Journal of Healthcare Engineering

Federated Learning Techniques in Public Healthcare and Medical Internet of Things Environments

Lead Guest Editor: Alireza Souri
Guest Editors: Mu-Yen Chen and Nima Jafari Navimipour

Federated Learning Techniques in Public Healthcare and Medical Internet of Things Environments

Journal of Healthcare Engineering

Federated Learning Techniques in Public Healthcare and Medical Internet of Things Environments

Lead Guest Editor: Alireza Souri
Guest Editors: Mu-Yen Chen and Nima Jafari Navimipour

Contents

Retracted: Exercise Rehabilitation Improves Heart Function and Quality of Life in Elderly Patients with Chronic Heart Failure
Journal of Healthcare Engineering
Retraction (1 page), Article ID 9809423, Volume 2023 (2023)

Retracted: Analysis of the Model for Sports Enhancing Human Health Using Data Mining
Journal of Healthcare Engineering
Retraction (1 page), Article ID 9807545, Volume 2023 (2023)

Retracted: Named Entity Recognition of Medical Text Based on the Deep Neural Network
Journal of Healthcare Engineering
Retraction (1 page), Article ID 9805297, Volume 2023 (2023)

Retracted: Recognition of Volleyball Player's Arm Motion Trajectory and Muscle Injury Mechanism Analysis Based upon Neural Network Model
Journal of Healthcare Engineering
Retraction (1 page), Article ID 9790589, Volume 2023 (2023)

Retracted: Biomechanical Analysis of the Human Knee Joint
Journal of Healthcare Engineering
Retraction (1 page), Article ID 9790572, Volume 2023 (2023)

Retracted: Effective CBMIR System Using Hybrid Features-Based Independent Condensed Nearest Neighbor Model
Journal of Healthcare Engineering
Retraction (1 page), Article ID 9789461, Volume 2023 (2023)

Retracted: Protective Effect of Amino Acids on the Muscle Injury of Aerobics Athletes after Endurance Exercise Based on CT Images
Journal of Healthcare Engineering
Retraction (1 page), Article ID 9785839, Volume 2023 (2023)

Retracted: Evaluation of Cardiac Space-Occupying Lesions by Myocardial Contrast Echocardiography and Transesophageal Echocardiography
Journal of Healthcare Engineering
Retraction (1 page), Article ID 9894289, Volume 2023 (2023)

Retracted: Atherosclerosis Vascular Endothelial Secretion Dysfunction and Smooth Muscle Cell Proliferation
Journal of Healthcare Engineering
Retraction (1 page), Article ID 9874048, Volume 2023 (2023)

Retracted: Efficacy of Super-Mini-PCNL and Ureteroscopy in Kidney Stone Sufferers and Risk Factors of Postoperative Infection
Journal of Healthcare Engineering
Retraction (1 page), Article ID 9872062, Volume 2023 (2023)

Contents

[Retracted] Intelligent Somatosensory Interactive Activities Restore Motor Function to Children with Autism
Qiang Wang, Xing Wang, and Lei Xu
Research Article (12 pages), Article ID 4516005, Volume 2022 (2022)

[Retracted] Effective CBMIR System Using Hybrid Features-Based Independent Condensed Nearest Neighbor Model
Hirald Dwaraka Praveena, Nirmala S. Guptha, Afsaneh Kazemzadeh, B. D. Parameshachari, and K. L. Hemalatha
Research Article (9 pages), Article ID 3297316, Volume 2022 (2022)

[Retracted] Meta-Analysis of Children's Acute Psychological Stress and Action Stress on Immune Function under Microscope Images
Hanjiang He, Yulin Tan, and Lihua Li
Research Article (12 pages), Article ID 6549805, Volume 2022 (2022)

[Retracted] Role of CT Images in the Diagnosis of Common Acute Abdominal Diseases in General Surgery
Yunguang Nan, Zuyan Zhang, Jianbo Zhang, Bo Jiang, Yuxi Zhu, and Li Zhang
Research Article (13 pages), Article ID 5732357, Volume 2022 (2022)

[Retracted] Protective Effect of Amino Acids on the Muscle Injury of Aerobics Athletes after Endurance Exercise Based on CT Images
Xianghai He and Yingjun Zhang
Research Article (13 pages), Article ID 5961267, Volume 2022 (2022)

[Retracted] Neuronal Apoptosis in Patients with Liver Cirrhosis and Neuronal Epileptiform Discharge Model Based upon Multi-Modal Fusion Deep Learning
Nannan Chi, Xiuping Wang, Yun Yu, Manman Wu, and Jianan Yu
Research Article (13 pages), Article ID 2203737, Volume 2022 (2022)

[Retracted] Bevacizumab Combined with Intensity-Modulated Radiation Therapy on Cognitive and Coagulation Function in Postoperative Glioma Patients
Guo-Shi Lin, Wei-Wei Wang, Hong Lin, and Rui-Sheng Lin
Research Article (8 pages), Article ID 9367919, Volume 2022 (2022)

[Retracted] Discussion on Protein Metabolism and Requirement of Aerobics Athletes during Training Based on Multisensor Data Fusion
Hua Gong, Shuang Chen, Shuo Yu, Dong Liu, Xin Li, Zeliang Shan, Fan Kong, Zhi Yan, and Feng Han
Research Article (12 pages), Article ID 6169150, Volume 2022 (2022)

Contents

[Retracted] Finite Element Analysis of Femoral-Acetabular Impingement (FAI) Based on Three-Dimensional Reconstruction
Xi Luo, Jun Zhang, Guofeng Cai, Yuqiong Wu, and Kun Ma
Research Article (13 pages), Article ID 2937056, Volume 2022 (2022)

[Retracted] Recognition of Volleyball Player's Arm Motion Trajectory and Muscle Injury Mechanism Analysis Based upon Neural Network Model
Jinxiang Zhao and Zengli Li
Research Article (15 pages), Article ID 8114740, Volume 2022 (2022)

[Retracted] Analysis of the Model for Sports Enhancing Human Health Using Data Mining
Ruiqing Wang and Lei Han
Research Article (9 pages), Article ID 3416255, Volume 2022 (2022)

[Retracted] Evaluation of Cardiac Space-Occupying Lesions by Myocardial Contrast Echocardiography and Transesophageal Echocardiography
Mingming Ren, Lei Huang, Xiaoqiang Ye, Zhifeng Xv, Chun Ouyang, and Zhen Han
Research Article (10 pages), Article ID 2066033, Volume 2022 (2022)

[Retracted] Exercise Rehabilitation Improves Heart Function and Quality of Life in Elderly Patients with Chronic Heart Failure
Xingyun Peng and Liuquan Tang
Research Article (12 pages), Article ID 8547906, Volume 2022 (2022)

Hindawi
Journal of Healthcare Engineering
Volume 2023, Article ID 9868954, 1 page
https://doi.org/10.1155/2023/9868954

Retraction

Retracted: Neuronal Apoptosis in Patients with Liver Cirrhosis and Neuronal Epileptiform Discharge Model Based upon Multi-Modal Fusion Deep Learning

Journal of Healthcare Engineering

Received 10 October 2023; Accepted 10 October 2023; Published 11 October 2023

This article has been retracted by Hindawi following an investigation undertaken by the publisher [1]. This investigation has uncovered evidence of one or more of the following indicators of systematic manipulation of the publication process:

(1) Discrepancies in scope
(2) Discrepancies in the description of the research reported
(3) Discrepancies between the availability of data and the research described
(4) Inappropriate citations
(5) Incoherent, meaningless and/or irrelevant content included in the article
(6) Peer-review manipulation

The presence of these indicators undermines our confidence in the integrity of the article's content and we cannot, therefore, vouch for its reliability. Please note that this notice is intended solely to alert readers that the content of this article is unreliable. We have not investigated whether authors were aware of or involved in the systematic manipulation of the publication process.

Wiley and Hindawi regrets that the usual quality checks did not identify these issues before publication and have since put additional measures in place to safeguard research integrity.

We wish to credit our own Research Integrity and Research Publishing teams and anonymous and named external researchers and research integrity experts for contributing to this investigation.

The corresponding author, as the representative of all authors, has been given the opportunity to register their agreement or disagreement to this retraction. We have kept a record of any response received.

References

[1] N. Chi, X. Wang, Y. Yu, M. Wu, and J. Yu, "Neuronal Apoptosis in Patients with Liver Cirrhosis and Neuronal Epileptiform Discharge Model Based upon Multi-Modal Fusion Deep Learning," *Journal of Healthcare Engineering*, vol. 2022, Article ID 2203737, 13 pages, 2022.

Hindawi
Journal of Healthcare Engineering
Volume 2023, Article ID 9865036, 1 page
https://doi.org/10.1155/2023/9865036

Retraction

Retracted: Based on the Auxiliary Effect of X-Ray in the Treatment of Severe Pneumonia in Children with Arterial and Venous Blood Gas

Journal of Healthcare Engineering

Received 10 October 2023; Accepted 10 October 2023; Published 11 October 2023

This article has been retracted by Hindawi following an investigation undertaken by the publisher [1]. This investigation has uncovered evidence of one or more of the following indicators of systematic manipulation of the publication process:

(1) Discrepancies in scope
(2) Discrepancies in the description of the research reported
(3) Discrepancies between the availability of data and the research described
(4) Inappropriate citations
(5) Incoherent, meaningless and/or irrelevant content included in the article
(6) Peer-review manipulation

The presence of these indicators undermines our confidence in the integrity of the article's content and we cannot, therefore, vouch for its reliability. Please note that this notice is intended solely to alert readers that the content of this article is unreliable. We have not investigated whether authors were aware of or involved in the systematic manipulation of the publication process.

In addition, our investigation has also shown that one or more of the following human-subject reporting requirements has not been met in this article: ethical approval by an Institutional Review Board (IRB) committee or equivalent, patient/participant consent to participate, and/or agreement to publish patient/participant details (where relevant).

Wiley and Hindawi regrets that the usual quality checks did not identify these issues before publication and have since put additional measures in place to safeguard research integrity.

We wish to credit our own Research Integrity and Research Publishing teams and anonymous and named external researchers and research integrity experts for contributing to this investigation.

The corresponding author, as the representative of all authors, has been given the opportunity to register their agreement or disagreement to this retraction. We have kept a record of any response received.

References

[1] H. Guo, H. Zhang, and F. Li, "Based on the Auxiliary Effect of X-Ray in the Treatment of Severe Pneumonia in Children with Arterial and Venous Blood Gas," *Journal of Healthcare Engineering*, vol. 2022, Article ID 5786630, 13 pages, 2022.

Hindawi
Journal of Healthcare Engineering
Volume 2023, Article ID 9857271, 1 page
https://doi.org/10.1155/2023/9857271

Retraction

Retracted: Data Mining-Based Analysis of Modern Chinese Medicine for the Treatment of Stable Angina Pectoris in Coronary Heart Disease

Journal of Healthcare Engineering

Received 10 October 2023; Accepted 10 October 2023; Published 11 October 2023

This article has been retracted by Hindawi following an investigation undertaken by the publisher [1]. This investigation has uncovered evidence of one or more of the following indicators of systematic manipulation of the publication process:

(1) Discrepancies in scope
(2) Discrepancies in the description of the research reported
(3) Discrepancies between the availability of data and the research described
(4) Inappropriate citations
(5) Incoherent, meaningless and/or irrelevant content included in the article
(6) Peer-review manipulation

The presence of these indicators undermines our confidence in the integrity of the article's content and we cannot, therefore, vouch for its reliability. Please note that this notice is intended solely to alert readers that the content of this article is unreliable. We have not investigated whether authors were aware of or involved in the systematic manipulation of the publication process.

Wiley and Hindawi regrets that the usual quality checks did not identify these issues before publication and have since put additional measures in place to safeguard research integrity.

We wish to credit our own Research Integrity and Research Publishing teams and anonymous and named external researchers and research integrity experts for contributing to this investigation.

The corresponding author, as the representative of all authors, has been given the opportunity to register their agreement or disagreement to this retraction. We have kept a record of any response received.

References

[1] M. Luo, Y. Hu, R. Bai, and Z. Xu, "Data Mining-Based Analysis of Modern Chinese Medicine for the Treatment of Stable Angina Pectoris in Coronary Heart Disease," *Journal of Healthcare Engineering*, vol. 2022, Article ID 3511974, 6 pages, 2022.

Hindawi
Journal of Healthcare Engineering
Volume 2023, Article ID 9854246, 1 page
https://doi.org/10.1155/2023/9854246

Retraction

Retracted: Research on Fitness Movement Monitoring System Based on Internet of Things

Journal of Healthcare Engineering

Received 10 October 2023; Accepted 10 October 2023; Published 11 October 2023

This article has been retracted by Hindawi following an investigation undertaken by the publisher [1]. This investigation has uncovered evidence of one or more of the following indicators of systematic manipulation of the publication process:

(1) Discrepancies in scope
(2) Discrepancies in the description of the research reported
(3) Discrepancies between the availability of data and the research described
(4) Inappropriate citations
(5) Incoherent, meaningless and/or irrelevant content included in the article
(6) Peer-review manipulation

The presence of these indicators undermines our confidence in the integrity of the article's content and we cannot, therefore, vouch for its reliability. Please note that this notice is intended solely to alert readers that the content of this article is unreliable. We have not investigated whether authors were aware of or involved in the systematic manipulation of the publication process.

In addition, our investigation has also shown that one or more of the following human-subject reporting requirements has not been met in this article: ethical approval by an Institutional Review Board (IRB) committee or equivalent, patient/participant consent to participate, and/or agreement to publish patient/participant details (where relevant).

Wiley and Hindawi regrets that the usual quality checks did not identify these issues before publication and have since put additional measures in place to safeguard research integrity.

We wish to credit our own Research Integrity and Research Publishing teams and anonymous and named external researchers and research integrity experts for contributing to this investigation.

The corresponding author, as the representative of all authors, has been given the opportunity to register their agreement or disagreement to this retraction. We have kept a record of any response received.

References

[1] Z. Yu, "Research on Fitness Movement Monitoring System Based on Internet of Things," *Journal of Healthcare Engineering*, vol. 2022, Article ID 5120556, 7 pages, 2022.

Hindawi
Journal of Healthcare Engineering
Volume 2023, Article ID 9836713, 1 page
https://doi.org/10.1155/2023/9836713

Retraction

Retracted: Finite Element Analysis of Femoral-Acetabular Impingement (FAI) Based on Three-Dimensional Reconstruction

Journal of Healthcare Engineering

Received 10 October 2023; Accepted 10 October 2023; Published 11 October 2023

This article has been retracted by Hindawi following an investigation undertaken by the publisher [1]. This investigation has uncovered evidence of one or more of the following indicators of systematic manipulation of the publication process:

(1) Discrepancies in scope
(2) Discrepancies in the description of the research reported
(3) Discrepancies between the availability of data and the research described
(4) Inappropriate citations
(5) Incoherent, meaningless and/or irrelevant content included in the article
(6) Peer-review manipulation

The presence of these indicators undermines our confidence in the integrity of the article's content and we cannot, therefore, vouch for its reliability. Please note that this notice is intended solely to alert readers that the content of this article is unreliable. We have not investigated whether authors were aware of or involved in the systematic manipulation of the publication process.

In addition, our investigation has also shown that one or more of the following human-subject reporting requirements has not been met in this article: ethical approval by an Institutional Review Board (IRB) committee or equivalent, patient/participant consent to participate, and/or agreement to publish patient/participant details (where relevant).

Wiley and Hindawi regrets that the usual quality checks did not identify these issues before publication and have since put additional measures in place to safeguard research integrity.

We wish to credit our own Research Integrity and Research Publishing teams and anonymous and named external researchers and research integrity experts for contributing to this investigation.

The corresponding author, as the representative of all authors, has been given the opportunity to register their agreement or disagreement to this retraction. We have kept a record of any response received.

References

[1] X. Luo, J. Zhang, G. Cai, Y. Wu, and K. Ma, "Finite Element Analysis of Femoral-Acetabular Impingement (FAI) Based on Three-Dimensional Reconstruction," *Journal of Healthcare Engineering*, vol. 2022, Article ID 2937056, 13 pages, 2022.

Hindawi
Journal of Healthcare Engineering
Volume 2023, Article ID 9834896, 1 page
https://doi.org/10.1155/2023/9834896

Retraction

Retracted: Contrast Agent and Molecular Imaging Meta-Analysis of the Clinical Effect of Intelligent Image Sensor Combined with Visual Training in the Treatment of Children with Intermittent Exotropia in China

Journal of Healthcare Engineering

Received 10 October 2023; Accepted 10 October 2023; Published 11 October 2023

This article has been retracted by Hindawi following an investigation undertaken by the publisher [1]. This investigation has uncovered evidence of one or more of the following indicators of systematic manipulation of the publication process:

(1) Discrepancies in scope
(2) Discrepancies in the description of the research reported
(3) Discrepancies between the availability of data and the research described
(4) Inappropriate citations
(5) Incoherent, meaningless and/or irrelevant content included in the article
(6) Peer-review manipulation

The presence of these indicators undermines our confidence in the integrity of the article's content and we cannot, therefore, vouch for its reliability. Please note that this notice is intended solely to alert readers that the content of this article is unreliable. We have not investigated whether authors were aware of or involved in the systematic manipulation of the publication process.

Wiley and Hindawi regrets that the usual quality checks did not identify these issues before publication and have since put additional measures in place to safeguard research integrity.

We wish to credit our own Research Integrity and Research Publishing teams and anonymous and named external researchers and research integrity experts for contributing to this investigation.

The corresponding author, as the representative of all authors, has been given the opportunity to register their agreement or disagreement to this retraction. We have kept a record of any response received.

References

[1] H. Sun, S. Bai, R. Liao, and A. Han, "Contrast Agent and Molecular Imaging Meta-Analysis of the Clinical Effect of Intelligent Image Sensor Combined with Visual Training in the Treatment of Children with Intermittent Exotropia in China," *Journal of Healthcare Engineering*, vol. 2022, Article ID 5387928, 12 pages, 2022.

Hindawi
Journal of Healthcare Engineering
Volume 2023, Article ID 9825050, 1 page
https://doi.org/10.1155/2023/9825050

Retraction

Retracted: Role of CT Images in the Diagnosis of Common Acute Abdominal Diseases in General Surgery

Journal of Healthcare Engineering

Received 10 October 2023; Accepted 10 October 2023; Published 11 October 2023

This article has been retracted by Hindawi following an investigation undertaken by the publisher [1]. This investigation has uncovered evidence of one or more of the following indicators of systematic manipulation of the publication process:

(1) Discrepancies in scope
(2) Discrepancies in the description of the research reported
(3) Discrepancies between the availability of data and the research described
(4) Inappropriate citations
(5) Incoherent, meaningless and/or irrelevant content included in the article
(6) Peer-review manipulation

The presence of these indicators undermines our confidence in the integrity of the article's content and we cannot, therefore, vouch for its reliability. Please note that this notice is intended solely to alert readers that the content of this article is unreliable. We have not investigated whether authors were aware of or involved in the systematic manipulation of the publication process.

In addition, our investigation has also shown that one or more of the following human-subject reporting requirements has not been met in this article: ethical approval by an Institutional Review Board (IRB) committee or equivalent, patient/participant consent to participate, and/or agreement to publish patient/participant details (where relevant).

Wiley and Hindawi regrets that the usual quality checks did not identify these issues before publication and have since put additional measures in place to safeguard research integrity.

We wish to credit our own Research Integrity and Research Publishing teams and anonymous and named external researchers and research integrity experts for contributing to this investigation.

The corresponding author, as the representative of all authors, has been given the opportunity to register their agreement or disagreement to this retraction. We have kept a record of any response received.

References

[1] Y. Nan, Z. Zhang, J. Zhang, B. Jiang, Y. Zhu, and L. Zhang, "Role of CT Images in the Diagnosis of Common Acute Abdominal Diseases in General Surgery," *Journal of Healthcare Engineering*, vol. 2022, Article ID 5732357, 13 pages, 2022.

Hindawi
Journal of Healthcare Engineering
Volume 2023, Article ID 9814324, 1 page
https://doi.org/10.1155/2023/9814324

Retraction

Retracted: Image Aided Recognition of Wireless Capsule Endoscope Based on the Neural Network

Journal of Healthcare Engineering

Received 10 October 2023; Accepted 10 October 2023; Published 11 October 2023

This article has been retracted by Hindawi following an investigation undertaken by the publisher [1]. This investigation has uncovered evidence of one or more of the following indicators of systematic manipulation of the publication process:

(1) Discrepancies in scope
(2) Discrepancies in the description of the research reported
(3) Discrepancies between the availability of data and the research described
(4) Inappropriate citations
(5) Incoherent, meaningless and/or irrelevant content included in the article
(6) Peer-review manipulation

The presence of these indicators undermines our confidence in the integrity of the article's content and we cannot, therefore, vouch for its reliability. Please note that this notice is intended solely to alert readers that the content of this article is unreliable. We have not investigated whether authors were aware of or involved in the systematic manipulation of the publication process.

In addition, our investigation has also shown that one or more of the following human-subject reporting requirements has not been met in this article: ethical approval by an Institutional Review Board (IRB) committee or equivalent, patient/participant consent to participate, and/or agreement to publish patient/participant details (where relevant).

Wiley and Hindawi regrets that the usual quality checks did not identify these issues before publication and have since put additional measures in place to safeguard research integrity.

We wish to credit our own Research Integrity and Research Publishing teams and anonymous and named external researchers and research integrity experts for contributing to this investigation.

The corresponding author, as the representative of all authors, has been given the opportunity to register their agreement or disagreement to this retraction. We have kept a record of any response received.

References

[1] B. Lu, "Image Aided Recognition of Wireless Capsule Endoscope Based on the Neural Network," *Journal of Healthcare Engineering*, vol. 2022, Article ID 3880356, 7 pages, 2022.

Hindawi
Journal of Healthcare Engineering
Volume 2023, Article ID 9812058, 1 page
https://doi.org/10.1155/2023/9812058

Retraction

Retracted: Automated System for Identifying COVID-19 Infections in Computed Tomography Images Using Deep Learning Models

Journal of Healthcare Engineering

Received 10 October 2023; Accepted 10 October 2023; Published 11 October 2023

This article has been retracted by Hindawi following an investigation undertaken by the publisher [1]. This investigation has uncovered evidence of one or more of the following indicators of systematic manipulation of the publication process:

(1) Discrepancies in scope
(2) Discrepancies in the description of the research reported
(3) Discrepancies between the availability of data and the research described
(4) Inappropriate citations
(5) Incoherent, meaningless and/or irrelevant content included in the article
(6) Peer-review manipulation

The presence of these indicators undermines our confidence in the integrity of the article's content and we cannot, therefore, vouch for its reliability. Please note that this notice is intended solely to alert readers that the content of this article is unreliable. We have not investigated whether authors were aware of or involved in the systematic manipulation of the publication process.

Wiley and Hindawi regrets that the usual quality checks did not identify these issues before publication and have since put additional measures in place to safeguard research integrity.

We wish to credit our own Research Integrity and Research Publishing teams and anonymous and named external researchers and research integrity experts for contributing to this investigation.

The corresponding author, as the representative of all authors, has been given the opportunity to register their agreement or disagreement to this retraction. We have kept a record of any response received.

References

[1] K. H. Abdulkareem, S. A. Mostafa, Z. N. Al-Qudsy et al., "Automated System for Identifying COVID-19 Infections in Computed Tomography Images Using Deep Learning Models," *Journal of Healthcare Engineering*, vol. 2022, Article ID 5329014, 13 pages, 2022.

Hindawi
Journal of Healthcare Engineering
Volume 2023, Article ID 9809423, 1 page
https://doi.org/10.1155/2023/9809423

Retraction

Retracted: Exercise Rehabilitation Improves Heart Function and Quality of Life in Elderly Patients with Chronic Heart Failure

Journal of Healthcare Engineering

Received 10 October 2023; Accepted 10 October 2023; Published 11 October 2023

This article has been retracted by Hindawi following an investigation undertaken by the publisher [1]. This investigation has uncovered evidence of one or more of the following indicators of systematic manipulation of the publication process:

(1) Discrepancies in scope
(2) Discrepancies in the description of the research reported
(3) Discrepancies between the availability of data and the research described
(4) Inappropriate citations
(5) Incoherent, meaningless and/or irrelevant content included in the article
(6) Peer-review manipulation

The presence of these indicators undermines our confidence in the integrity of the article's content and we cannot, therefore, vouch for its reliability. Please note that this notice is intended solely to alert readers that the content of this article is unreliable. We have not investigated whether authors were aware of or involved in the systematic manipulation of the publication process.

In addition, our investigation has also shown that one or more of the following human-subject reporting requirements has not been met in this article: ethical approval by an Institutional Review Board (IRB) committee or equivalent, patient/participant consent to participate, and/or agreement to publish patient/participant details (where relevant).

Wiley and Hindawi regrets that the usual quality checks did not identify these issues before publication and have since put additional measures in place to safeguard research integrity.

We wish to credit our own Research Integrity and Research Publishing teams and anonymous and named external researchers and research integrity experts for contributing to this investigation.

The corresponding author, as the representative of all authors, has been given the opportunity to register their agreement or disagreement to this retraction. We have kept a record of any response received.

References

[1] X. Peng and L. Tang, "Exercise Rehabilitation Improves Heart Function and Quality of Life in Elderly Patients with Chronic Heart Failure," *Journal of Healthcare Engineering*, vol. 2022, Article ID 8547906, 12 pages, 2022.

Hindawi
Journal of Healthcare Engineering
Volume 2023, Article ID 9807545, 1 page
https://doi.org/10.1155/2023/9807545

Retraction

Retracted: Analysis of the Model for Sports Enhancing Human Health Using Data Mining

Journal of Healthcare Engineering

Received 10 October 2023; Accepted 10 October 2023; Published 11 October 2023

This article has been retracted by Hindawi following an investigation undertaken by the publisher [1]. This investigation has uncovered evidence of one or more of the following indicators of systematic manipulation of the publication process:

(1) Discrepancies in scope
(2) Discrepancies in the description of the research reported
(3) Discrepancies between the availability of data and the research described
(4) Inappropriate citations
(5) Incoherent, meaningless and/or irrelevant content included in the article
(6) Peer-review manipulation

The presence of these indicators undermines our confidence in the integrity of the article's content and we cannot, therefore, vouch for its reliability. Please note that this notice is intended solely to alert readers that the content of this article is unreliable. We have not investigated whether authors were aware of or involved in the systematic manipulation of the publication process.

In addition, our investigation has also shown that one or more of the following human-subject reporting requirements has not been met in this article: ethical approval by an Institutional Review Board (IRB) committee or equivalent, patient/participant consent to participate, and/or agreement to publish patient/participant details (where relevant).

Wiley and Hindawi regrets that the usual quality checks did not identify these issues before publication and have since put additional measures in place to safeguard research integrity.

We wish to credit our own Research Integrity and Research Publishing teams and anonymous and named external researchers and research integrity experts for contributing to this investigation.

The corresponding author, as the representative of all authors, has been given the opportunity to register their agreement or disagreement to this retraction. We have kept a record of any response received.

References

[1] R. Wang and L. Han, "Analysis of the Model for Sports Enhancing Human Health Using Data Mining," *Journal of Healthcare Engineering*, vol. 2022, Article ID 3416255, 9 pages, 2022.

Hindawi
Journal of Healthcare Engineering
Volume 2023, Article ID 9805297, 1 page
https://doi.org/10.1155/2023/9805297

Retraction

Retracted: Named Entity Recognition of Medical Text Based on the Deep Neural Network

Journal of Healthcare Engineering

Received 10 October 2023; Accepted 10 October 2023; Published 11 October 2023

This article has been retracted by Hindawi following an investigation undertaken by the publisher [1]. This investigation has uncovered evidence of one or more of the following indicators of systematic manipulation of the publication process:

(1) Discrepancies in scope
(2) Discrepancies in the description of the research reported
(3) Discrepancies between the availability of data and the research described
(4) Inappropriate citations
(5) Incoherent, meaningless and/or irrelevant content included in the article
(6) Peer-review manipulation

The presence of these indicators undermines our confidence in the integrity of the article's content and we cannot, therefore, vouch for its reliability. Please note that this notice is intended solely to alert readers that the content of this article is unreliable. We have not investigated whether authors were aware of or involved in the systematic manipulation of the publication process.

Wiley and Hindawi regrets that the usual quality checks did not identify these issues before publication and have since put additional measures in place to safeguard research integrity.

We wish to credit our own Research Integrity and Research Publishing teams and anonymous and named external researchers and research integrity experts for contributing to this investigation.

The corresponding author, as the representative of all authors, has been given the opportunity to register their agreement or disagreement to this retraction. We have kept a record of any response received.

References

[1] T. Yang, Y. He, and N. Yang, "Named Entity Recognition of Medical Text Based on the Deep Neural Network," *Journal of Healthcare Engineering*, vol. 2022, Article ID 3990563, 10 pages, 2022.

Hindawi
Journal of Healthcare Engineering
Volume 2023, Article ID 9790589, 1 page
https://doi.org/10.1155/2023/9790589

Retraction

Retracted: Recognition of Volleyball Player's Arm Motion Trajectory and Muscle Injury Mechanism Analysis Based upon Neural Network Model

Journal of Healthcare Engineering

Received 10 October 2023; Accepted 10 October 2023; Published 11 October 2023

This article has been retracted by Hindawi following an investigation undertaken by the publisher [1]. This investigation has uncovered evidence of one or more of the following indicators of systematic manipulation of the publication process:

(1) Discrepancies in scope
(2) Discrepancies in the description of the research reported
(3) Discrepancies between the availability of data and the research described
(4) Inappropriate citations
(5) Incoherent, meaningless and/or irrelevant content included in the article
(6) Peer-review manipulation

The presence of these indicators undermines our confidence in the integrity of the article's content and we cannot, therefore, vouch for its reliability. Please note that this notice is intended solely to alert readers that the content of this article is unreliable. We have not investigated whether authors were aware of or involved in the systematic manipulation of the publication process.

Wiley and Hindawi regrets that the usual quality checks did not identify these issues before publication and have since put additional measures in place to safeguard research integrity.

We wish to credit our own Research Integrity and Research Publishing teams and anonymous and named external researchers and research integrity experts for contributing to this investigation.

The corresponding author, as the representative of all authors, has been given the opportunity to register their agreement or disagreement to this retraction. We have kept a record of any response received.

References

[1] J. Zhao and Z. Li, "Recognition of Volleyball Player's Arm Motion Trajectory and Muscle Injury Mechanism Analysis Based upon Neural Network Model," *Journal of Healthcare Engineering*, vol. 2022, Article ID 8114740, 15 pages, 2022.

Hindawi
Journal of Healthcare Engineering
Volume 2023, Article ID 9790572, 1 page
https://doi.org/10.1155/2023/9790572

Retraction

Retracted: Biomechanical Analysis of the Human Knee Joint

Journal of Healthcare Engineering

Received 10 October 2023; Accepted 10 October 2023; Published 11 October 2023

This article has been retracted by Hindawi following an investigation undertaken by the publisher [1]. This investigation has uncovered evidence of one or more of the following indicators of systematic manipulation of the publication process:

(1) Discrepancies in scope
(2) Discrepancies in the description of the research reported
(3) Discrepancies between the availability of data and the research described
(4) Inappropriate citations
(5) Incoherent, meaningless and/or irrelevant content included in the article
(6) Peer-review manipulation

The presence of these indicators undermines our confidence in the integrity of the article's content and we cannot, therefore, vouch for its reliability. Please note that this notice is intended solely to alert readers that the content of this article is unreliable. We have not investigated whether authors were aware of or involved in the systematic manipulation of the publication process.

In addition, our investigation has also shown that one or more of the following human-subject reporting requirements has not been met in this article: ethical approval by an Institutional Review Board (IRB) committee or equivalent, patient/participant consent to participate, and/or agreement to publish patient/participant details (where relevant).

Wiley and Hindawi regrets that the usual quality checks did not identify these issues before publication and have since put additional measures in place to safeguard research integrity.

We wish to credit our own Research Integrity and Research Publishing teams and anonymous and named external researchers and research integrity experts for contributing to this investigation.

The corresponding author, as the representative of all authors, has been given the opportunity to register their agreement or disagreement to this retraction. We have kept a record of any response received.

References

[1] S. Wang, "Biomechanical Analysis of the Human Knee Joint," *Journal of Healthcare Engineering*, vol. 2022, Article ID 9365362, 8 pages, 2022.

Hindawi
Journal of Healthcare Engineering
Volume 2023, Article ID 9789461, 1 page
https://doi.org/10.1155/2023/9789461

Retraction

Retracted: Effective CBMIR System Using Hybrid Features-Based Independent Condensed Nearest Neighbor Model

Journal of Healthcare Engineering

Received 10 October 2023; Accepted 10 October 2023; Published 11 October 2023

This article has been retracted by Hindawi following an investigation undertaken by the publisher [1]. This investigation has uncovered evidence of one or more of the following indicators of systematic manipulation of the publication process:

(1) Discrepancies in scope
(2) Discrepancies in the description of the research reported
(3) Discrepancies between the availability of data and the research described
(4) Inappropriate citations
(5) Incoherent, meaningless and/or irrelevant content included in the article
(6) Peer-review manipulation

The presence of these indicators undermines our confidence in the integrity of the article's content and we cannot, therefore, vouch for its reliability. Please note that this notice is intended solely to alert readers that the content of this article is unreliable. We have not investigated whether authors were aware of or involved in the systematic manipulation of the publication process.

Wiley and Hindawi regrets that the usual quality checks did not identify these issues before publication and have since put additional measures in place to safeguard research integrity.

We wish to credit our own Research Integrity and Research Publishing teams and anonymous and named external researchers and research integrity experts for contributing to this investigation.

The corresponding author, as the representative of all authors, has been given the opportunity to register their agreement or disagreement to this retraction. We have kept a record of any response received.

References

[1] H. D. Praveena, N. S. Guptha, A. Kazemzadeh, B. D. Parameshachari, and K. L. Hemalatha, "Effective CBMIR System Using Hybrid Features-Based Independent Condensed Nearest Neighbor Model," *Journal of Healthcare Engineering*, vol. 2022, Article ID 3297316, 9 pages, 2022.

Hindawi
Journal of Healthcare Engineering
Volume 2023, Article ID 9785839, 1 page
https://doi.org/10.1155/2023/9785839

Retraction

Retracted: Protective Effect of Amino Acids on the Muscle Injury of Aerobics Athletes after Endurance Exercise Based on CT Images

Journal of Healthcare Engineering

Received 10 October 2023; Accepted 10 October 2023; Published 11 October 2023

This article has been retracted by Hindawi following an investigation undertaken by the publisher [1]. This investigation has uncovered evidence of one or more of the following indicators of systematic manipulation of the publication process:

(1) Discrepancies in scope
(2) Discrepancies in the description of the research reported
(3) Discrepancies between the availability of data and the research described
(4) Inappropriate citations
(5) Incoherent, meaningless and/or irrelevant content included in the article
(6) Peer-review manipulation

The presence of these indicators undermines our confidence in the integrity of the article's content and we cannot, therefore, vouch for its reliability. Please note that this notice is intended solely to alert readers that the content of this article is unreliable. We have not investigated whether authors were aware of or involved in the systematic manipulation of the publication process.

In addition, our investigation has also shown that one or more of the following human-subject reporting requirements has not been met in this article: ethical approval by an Institutional Review Board (IRB) committee or equivalent, patient/participant consent to participate, and/or agreement to publish patient/participant details (where relevant).

Wiley and Hindawi regrets that the usual quality checks did not identify these issues before publication and have since put additional measures in place to safeguard research integrity.

We wish to credit our own Research Integrity and Research Publishing teams and anonymous and named external researchers and research integrity experts for contributing to this investigation.

The corresponding author, as the representative of all authors, has been given the opportunity to register their agreement or disagreement to this retraction. We have kept a record of any response received.

References

[1] X. He and Y. Zhang, "Protective Effect of Amino Acids on the Muscle Injury of Aerobics Athletes after Endurance Exercise Based on CT Images," *Journal of Healthcare Engineering*, vol. 2022, Article ID 5961267, 13 pages, 2022.

Hindawi
Journal of Healthcare Engineering
Volume 2023, Article ID 9894289, 1 page
https://doi.org/10.1155/2023/9894289

Retraction

Retracted: Evaluation of Cardiac Space-Occupying Lesions by Myocardial Contrast Echocardiography and Transesophageal Echocardiography

Journal of Healthcare Engineering

Received 1 August 2023; Accepted 1 August 2023; Published 2 August 2023

This article has been retracted by Hindawi following an investigation undertaken by the publisher [1]. This investigation has uncovered evidence of one or more of the following indicators of systematic manipulation of the publication process:

(1) Discrepancies in scope
(2) Discrepancies in the description of the research reported
(3) Discrepancies between the availability of data and the research described
(4) Inappropriate citations
(5) Incoherent, meaningless and/or irrelevant content included in the article
(6) Peer-review manipulation

The presence of these indicators undermines our confidence in the integrity of the article's content and we cannot, therefore, vouch for its reliability. Please note that this notice is intended solely to alert readers that the content of this article is unreliable. We have not investigated whether authors were aware of or involved in the systematic manipulation of the publication process.

In addition, our investigation has also shown that one or more of the following human-subject reporting requirements has not been met in this article: ethical approval by an Institutional Review Board (IRB) committee or equivalent, patient/participant consent to participate, and/or agreement to publish patient/participant details (where relevant).

Wiley and Hindawi regrets that the usual quality checks did not identify these issues before publication and have since put additional measures in place to safeguard research integrity.

We wish to credit our own Research Integrity and Research Publishing teams and anonymous and named external researchers and research integrity experts for contributing to this investigation.

The corresponding author, as the representative of all authors, has been given the opportunity to register their agreement or disagreement to this retraction. We have kept a record of any response received.

References

[1] M. Ren, L. Huang, X. Ye, Z. Xv, C. Ouyang, and Z. Han, "Evaluation of Cardiac Space-Occupying Lesions by Myocardial Contrast Echocardiography and Transesophageal Echocardiography," *Journal of Healthcare Engineering*, vol. 2022, Article ID 2066033, 10 pages, 2022.

Hindawi
Journal of Healthcare Engineering
Volume 2023, Article ID 9874048, 1 page
https://doi.org/10.1155/2023/9874048

Retraction

Retracted: Atherosclerosis Vascular Endothelial Secretion Dysfunction and Smooth Muscle Cell Proliferation

Journal of Healthcare Engineering

Received 1 August 2023; Accepted 1 August 2023; Published 2 August 2023

This article has been retracted by Hindawi following an investigation undertaken by the publisher [1]. This investigation has uncovered evidence of one or more of the following indicators of systematic manipulation of the publication process:

(1) Discrepancies in scope
(2) Discrepancies in the description of the research reported
(3) Discrepancies between the availability of data and the research described
(4) Inappropriate citations
(5) Incoherent, meaningless and/or irrelevant content included in the article
(6) Peer-review manipulation

The presence of these indicators undermines our confidence in the integrity of the article's content and we cannot, therefore, vouch for its reliability. Please note that this notice is intended solely to alert readers that the content of this article is unreliable. We have not investigated whether authors were aware of or involved in the systematic manipulation of the publication process.

In addition, our investigation has also shown that one or more of the following human-subject reporting requirements has not been met in this article: ethical approval by an Institutional Review Board (IRB) committee or equivalent, patient/participant consent to participate, and/or agreement to publish patient/participant details (where relevant).

Wiley and Hindawi regrets that the usual quality checks did not identify these issues before publication and have since put additional measures in place to safeguard research integrity.

We wish to credit our own Research Integrity and Research Publishing teams and anonymous and named external researchers and research integrity experts for contributing to this investigation.

The corresponding author, as the representative of all authors, has been given the opportunity to register their agreement or disagreement to this retraction. We have kept a record of any response received.

References

[1] J. Li, X. Fu, R. Yang, and W. Zhang, "Atherosclerosis Vascular Endothelial Secretion Dysfunction and Smooth Muscle Cell Proliferation," *Journal of Healthcare Engineering*, vol. 2022, Article ID 9271879, 13 pages, 2022.

Hindawi
Journal of Healthcare Engineering
Volume 2023, Article ID 9872062, 1 page
https://doi.org/10.1155/2023/9872062

Retraction

Retracted: Efficacy of Super-Mini-PCNL and Ureteroscopy in Kidney Stone Sufferers and Risk Factors of Postoperative Infection

Journal of Healthcare Engineering

Received 1 August 2023; Accepted 1 August 2023; Published 2 August 2023

This article has been retracted by Hindawi following an investigation undertaken by the publisher [1]. This investigation has uncovered evidence of one or more of the following indicators of systematic manipulation of the publication process:

(1) Discrepancies in scope
(2) Discrepancies in the description of the research reported
(3) Discrepancies between the availability of data and the research described
(4) Inappropriate citations
(5) Incoherent, meaningless and/or irrelevant content included in the article
(6) Peer-review manipulation

The presence of these indicators undermines our confidence in the integrity of the article's content and we cannot, therefore, vouch for its reliability. Please note that this notice is intended solely to alert readers that the content of this article is unreliable. We have not investigated whether authors were aware of or involved in the systematic manipulation of the publication process.

Wiley and Hindawi regrets that the usual quality checks did not identify these issues before publication and have since put additional measures in place to safeguard research integrity.

We wish to credit our own Research Integrity and Research Publishing teams and anonymous and named external researchers and research integrity experts for contributing to this investigation.

The corresponding author, as the representative of all authors, has been given the opportunity to register their agreement or disagreement to this retraction. We have kept a record of any response received.

References

[1] W. Yuan, Y. Li, Y. Dai, C. Luo, H. Zhang, and H. Xiong, "Efficacy of Super-Mini-PCNL and Ureteroscopy in Kidney Stone Sufferers and Risk Factors of Postoperative Infection," *Journal of Healthcare Engineering*, vol. 2022, Article ID 4733329, 7 pages, 2022.

Hindawi
Journal of Healthcare Engineering
Volume 2023, Article ID 9857376, 1 page
https://doi.org/10.1155/2023/9857376

Retraction

Retracted: Intelligent Somatosensory Interactive Activities Restore Motor Function to Children with Autism

Journal of Healthcare Engineering

Received 1 August 2023; Accepted 1 August 2023; Published 2 August 2023

This article has been retracted by Hindawi following an investigation undertaken by the publisher [1]. This investigation has uncovered evidence of one or more of the following indicators of systematic manipulation of the publication process:

(1) Discrepancies in scope
(2) Discrepancies in the description of the research reported
(3) Discrepancies between the availability of data and the research described
(4) Inappropriate citations
(5) Incoherent, meaningless and/or irrelevant content included in the article
(6) Peer-review manipulation

The presence of these indicators undermines our confidence in the integrity of the article's content and we cannot, therefore, vouch for its reliability. Please note that this notice is intended solely to alert readers that the content of this article is unreliable. We have not investigated whether authors were aware of or involved in the systematic manipulation of the publication process.

In addition, our investigation has also shown that one or more of the following human-subject reporting requirements has not been met in this article: ethical approval by an Institutional Review Board (IRB) committee or equivalent, patient/participant consent to participate, and/or agreement to publish patient/participant details (where relevant).

Wiley and Hindawi regrets that the usual quality checks did not identify these issues before publication and have since put additional measures in place to safeguard research integrity.

We wish to credit our own Research Integrity and Research Publishing teams and anonymous and named external researchers and research integrity experts for contributing to this investigation.

The corresponding author, as the representative of all authors, has been given the opportunity to register their agreement or disagreement to this retraction. We have kept a record of any response received.

References

[1] Q. Wang, X. Wang, and L. Xu, "Intelligent Somatosensory Interactive Activities Restore Motor Function to Children with Autism," *Journal of Healthcare Engineering*, vol. 2022, Article ID 4516005, 12 pages, 2022.

Hindawi
Journal of Healthcare Engineering
Volume 2023, Article ID 9806931, 1 page
https://doi.org/10.1155/2023/9806931

Retraction

Retracted: Bevacizumab Combined with Intensity-Modulated Radiation Therapy on Cognitive and Coagulation Function in Postoperative Glioma Patients

Journal of Healthcare Engineering

Received 1 August 2023; Accepted 1 August 2023; Published 2 August 2023

This article has been retracted by Hindawi following an investigation undertaken by the publisher [1]. This investigation has uncovered evidence of one or more of the following indicators of systematic manipulation of the publication process:

(1) Discrepancies in scope
(2) Discrepancies in the description of the research reported
(3) Discrepancies between the availability of data and the research described
(4) Inappropriate citations
(5) Incoherent, meaningless and/or irrelevant content included in the article
(6) Peer-review manipulation

The presence of these indicators undermines our confidence in the integrity of the article's content and we cannot, therefore, vouch for its reliability. Please note that this notice is intended solely to alert readers that the content of this article is unreliable. We have not investigated whether authors were aware of or involved in the systematic manipulation of the publication process.

Wiley and Hindawi regrets that the usual quality checks did not identify these issues before publication and have since put additional measures in place to safeguard research integrity.

We wish to credit our own Research Integrity and Research Publishing teams and anonymous and named external researchers and research integrity experts for contributing to this investigation.

The corresponding author, as the representative of all authors, has been given the opportunity to register their agreement or disagreement to this retraction. We have kept a record of any response received.

References

[1] G. Lin, W. Wang, H. Lin, and R. Lin, "Bevacizumab Combined with Intensity-Modulated Radiation Therapy on Cognitive and Coagulation Function in Postoperative Glioma Patients," *Journal of Healthcare Engineering*, vol. 2022, Article ID 9367919, 8 pages, 2022.

Hindawi
Journal of Healthcare Engineering
Volume 2023, Article ID 9806342, 1 page
https://doi.org/10.1155/2023/9806342

Retraction

Retracted: Effect Evaluation of Artificial Intelligence-Based Electronic Health PDCA Nursing Model in the Treatment of Mycoplasma Pneumonia in Children

Journal of Healthcare Engineering

Received 1 August 2023; Accepted 1 August 2023; Published 2 August 2023

This article has been retracted by Hindawi following an investigation undertaken by the publisher [1]. This investigation has uncovered evidence of one or more of the following indicators of systematic manipulation of the publication process:

(1) Discrepancies in scope
(2) Discrepancies in the description of the research reported
(3) Discrepancies between the availability of data and the research described
(4) Inappropriate citations
(5) Incoherent, meaningless and/or irrelevant content included in the article
(6) Peer-review manipulation

The presence of these indicators undermines our confidence in the integrity of the article's content and we cannot, therefore, vouch for its reliability. Please note that this notice is intended solely to alert readers that the content of this article is unreliable. We have not investigated whether authors were aware of or involved in the systematic manipulation of the publication process.

In addition, our investigation has also shown that one or more of the following human-subject reporting requirements has not been met in this article: ethical approval by an Institutional Review Board (IRB) committee or equivalent, patient/participant consent to participate, and/or agreement to publish patient/participant details (where relevant).

Wiley and Hindawi regrets that the usual quality checks did not identify these issues before publication and have since put additional measures in place to safeguard research integrity.

We wish to credit our own Research Integrity and Research Publishing teams and anonymous and named external researchers and research integrity experts for contributing to this investigation.

The corresponding author, as the representative of all authors, has been given the opportunity to register their agreement or disagreement to this retraction. We have kept a record of any response received.

References

[1] Y. Zhao, "Effect Evaluation of Artificial Intelligence-Based Electronic Health PDCA Nursing Model in the Treatment of Mycoplasma Pneumonia in Children," *Journal of Healthcare Engineering*, vol. 2022, Article ID 1956944, 10 pages, 2022.

Hindawi
Journal of Healthcare Engineering
Volume 2023, Article ID 9785028, 1 page
https://doi.org/10.1155/2023/9785028

Retraction

Retracted: Discussion on Protein Metabolism and Requirement of Aerobics Athletes during Training Based on Multisensor Data Fusion

Journal of Healthcare Engineering

Received 1 August 2023; Accepted 1 August 2023; Published 2 August 2023

This article has been retracted by Hindawi following an investigation undertaken by the publisher [1]. This investigation has uncovered evidence of one or more of the following indicators of systematic manipulation of the publication process:

(1) Discrepancies in scope
(2) Discrepancies in the description of the research reported
(3) Discrepancies between the availability of data and the research described
(4) Inappropriate citations
(5) Incoherent, meaningless and/or irrelevant content included in the article
(6) Peer-review manipulation

The presence of these indicators undermines our confidence in the integrity of the article's content and we cannot, therefore, vouch for its reliability. Please note that this notice is intended solely to alert readers that the content of this article is unreliable. We have not investigated whether authors were aware of or involved in the systematic manipulation of the publication process.

In addition, our investigation has also shown that one or more of the following human-subject reporting requirements has not been met in this article: ethical approval by an Institutional Review Board (IRB) committee or equivalent, patient/participant consent to participate, and/or agreement to publish patient/participant details (where relevant).

Wiley and Hindawi regrets that the usual quality checks did not identify these issues before publication and have since put additional measures in place to safeguard research integrity.

We wish to credit our own Research Integrity and Research Publishing teams and anonymous and named external researchers and research integrity experts for contributing to this investigation.

The corresponding author, as the representative of all authors, has been given the opportunity to register their agreement or disagreement to this retraction. We have kept a record of any response received.

References

[1] H. Gong, S. Chen, S. Yu et al., "Discussion on Protein Metabolism and Requirement of Aerobics Athletes during Training Based on Multisensor Data Fusion," *Journal of Healthcare Engineering*, vol. 2022, Article ID 6169150, 12 pages, 2022.

Hindawi
Journal of Healthcare Engineering
Volume 2023, Article ID 9763264, 1 page
https://doi.org/10.1155/2023/9763264

Retraction

Retracted: Meta-Analysis of Children's Acute Psychological Stress and Action Stress on Immune Function under Microscope Images

Journal of Healthcare Engineering

Received 1 August 2023; Accepted 1 August 2023; Published 2 August 2023

This article has been retracted by Hindawi following an investigation undertaken by the publisher [1]. This investigation has uncovered evidence of one or more of the following indicators of systematic manipulation of the publication process:

(1) Discrepancies in scope
(2) Discrepancies in the description of the research reported
(3) Discrepancies between the availability of data and the research described
(4) Inappropriate citations
(5) Incoherent, meaningless and/or irrelevant content included in the article
(6) Peer-review manipulation

The presence of these indicators undermines our confidence in the integrity of the article's content and we cannot, therefore, vouch for its reliability. Please note that this notice is intended solely to alert readers that the content of this article is unreliable. We have not investigated whether authors were aware of or involved in the systematic manipulation of the publication process.

Wiley and Hindawi regrets that the usual quality checks did not identify these issues before publication and have since put additional measures in place to safeguard research integrity.

We wish to credit our own Research Integrity and Research Publishing teams and anonymous and named external researchers and research integrity experts for contributing to this investigation.

The corresponding author, as the representative of all authors, has been given the opportunity to register their agreement or disagreement to this retraction. We have kept a record of any response received.

References

[1] H. He, Y. Tan, and L. Li, "Meta-Analysis of Children's Acute Psychological Stress and Action Stress on Immune Function under Microscope Images," *Journal of Healthcare Engineering*, vol. 2022, Article ID 6549805, 12 pages, 2022.

Hindawi
Journal of Healthcare Engineering
Volume 2023, Article ID 9753986, 1 page
https://doi.org/10.1155/2023/9753986

Retraction

Retracted: Study on Correlation between Body Cell Mass Index and Cognitive Impairment in Hemodialysis Maintaining Patients: A Cross-Sectional Study

Journal of Healthcare Engineering

Received 1 August 2023; Accepted 1 August 2023; Published 2 August 2023

This article has been retracted by Hindawi following an investigation undertaken by the publisher [1]. This investigation has uncovered evidence of one or more of the following indicators of systematic manipulation of the publication process:

(1) Discrepancies in scope
(2) Discrepancies in the description of the research reported
(3) Discrepancies between the availability of data and the research described
(4) Inappropriate citations
(5) Incoherent, meaningless and/or irrelevant content included in the article
(6) Peer-review manipulation

The presence of these indicators undermines our confidence in the integrity of the article's content and we cannot, therefore, vouch for its reliability. Please note that this notice is intended solely to alert readers that the content of this article is unreliable. We have not investigated whether authors were aware of or involved in the systematic manipulation of the publication process.

Wiley and Hindawi regrets that the usual quality checks did not identify these issues before publication and have since put additional measures in place to safeguard research integrity.

We wish to credit our own Research Integrity and Research Publishing teams and anonymous and named external researchers and research integrity experts for contributing to this investigation.

The corresponding author, as the representative of all authors, has been given the opportunity to register their agreement or disagreement to this retraction. We have kept a record of any response received.

References

[1] Q. Ou, C. Zhou, M. Tian, X. Yang, and Y. Zha, "Study on Correlation between Body Cell Mass Index and Cognitive Impairment in Hemodialysis Maintaining Patients: A Cross-Sectional Study," *Journal of Healthcare Engineering*, vol. 2022, Article ID 9023562, 9 pages, 2022.

Hindawi
Journal of Healthcare Engineering
Volume 2023, Article ID 9814324, 1 page
https://doi.org/10.1155/2023/9814324

Retraction

Retracted: Image Aided Recognition of Wireless Capsule Endoscope Based on the Neural Network

Journal of Healthcare Engineering

Received 10 October 2023; Accepted 10 October 2023; Published 11 October 2023

This article has been retracted by Hindawi following an investigation undertaken by the publisher [1]. This investigation has uncovered evidence of one or more of the following indicators of systematic manipulation of the publication process:

(1) Discrepancies in scope
(2) Discrepancies in the description of the research reported
(3) Discrepancies between the availability of data and the research described
(4) Inappropriate citations
(5) Incoherent, meaningless and/or irrelevant content included in the article
(6) Peer-review manipulation

The presence of these indicators undermines our confidence in the integrity of the article's content and we cannot, therefore, vouch for its reliability. Please note that this notice is intended solely to alert readers that the content of this article is unreliable. We have not investigated whether authors were aware of or involved in the systematic manipulation of the publication process.

In addition, our investigation has also shown that one or more of the following human-subject reporting requirements has not been met in this article: ethical approval by an Institutional Review Board (IRB) committee or equivalent, patient/participant consent to participate, and/or agreement to publish patient/participant details (where relevant).

Wiley and Hindawi regrets that the usual quality checks did not identify these issues before publication and have since put additional measures in place to safeguard research integrity.

We wish to credit our own Research Integrity and Research Publishing teams and anonymous and named external researchers and research integrity experts for contributing to this investigation.

The corresponding author, as the representative of all authors, has been given the opportunity to register their agreement or disagreement to this retraction. We have kept a record of any response received.

References

[1] B. Lu, "Image Aided Recognition of Wireless Capsule Endoscope Based on the Neural Network," *Journal of Healthcare Engineering*, vol. 2022, Article ID 3880356, 7 pages, 2022.

Hindawi
Journal of Healthcare Engineering
Volume 2022, Article ID 3880356, 7 pages
https://doi.org/10.1155/2022/3880356

Research Article

Image Aided Recognition of Wireless Capsule Endoscope Based on the Neural Network

Bin Lu

Department of Gastrointestinal Surgery, Affiliated Hospital of Shaoxing University (The Shaoxing Municipal Hospital), Shaoxing 312000, China

Correspondence should be addressed to Bin Lu; luchen131415@126.com

Received 19 January 2022; Accepted 22 March 2022; Published 7 April 2022

Academic Editor: Nima Jafari Navimipour

Wireless capsule endoscopy is an important method for diagnosing small bowel diseases, but it will collect thousands of endoscopy images that need to be diagnosed. The analysis of these images requires a huge workload and may cause manual reading errors. This article attempts to use neural networks instead of artificial endoscopic image analysis to assist doctors in diagnosing and treating endoscopic images. First, in image preprocessing, the image is converted from RGB color mode to lab color mode, texture features are extracted for network training, and finally, the accuracy of the algorithm is verified. After inputting the retained endoscopic image verification set into the neural network algorithm, the conclusion is that the accuracy of the neural network model constructed in this study is 97.69%, which can effectively distinguish normal, benign lesions, and malignant tumors. Experimental studies have proved that the neural network algorithm can effectively assist the endoscopist's diagnosis and improve the diagnosis efficiency. This research hopes to provide a reference for the application of neural network algorithms in the field of endoscopic images.

1. Introduction

Capsule endoscopy is a convenient, simple, and fast method of gastrointestinal examination, especially in the diagnosis of small bowel diseases. Small intestine capsule endoscopy technology is the starting point of capsule endoscopy. After more than ten years of development, capsule endoscopy has basically become an important inspection item for small bowel diseases. Compared with the traditional endoscope technology, the capsule endoscope can obtain the image of the entire digestive tract in real time during the whole process without feeling uncomfortable. The patient's entire digestive tract image can be displayed on the monitor; there are significant differences in the texture between the lesion area and the nonlesion area in the capsule endoscopic image, so the diagnosis of disease conditions by comparing textures in images has been widely used in clinical practice. Thousands of images will be generated during capsule endoscopic surgery. If the doctor reads and judges them one by one, it is easy to miss valuable information. Therefore, it is particularly important to find a computer-aided analysis method that has a good feature extraction effect on the capsule endoscopic image. Existing studies have shown that it is feasible to identify various abnormalities in capsule endoscopic images through convolutional neural networks. Gomes developed an unsupervised homography evaluation method in the capsule endoscope framework and then applied it to the capsule positioning system. The network can evaluate the homography between two images [1]. Leenhardt has developed a computer-aided diagnostic tool to detect vasodilation. The improved algorithm based on the convolutional neural network has high diagnostic performance and can detect vasodilation in the static frame of small bowel capsule endoscopy [2]. Sainju proposed a supervised method to automatically detect the bleeding area in the capsule endoscope frame or image. During surgery, segmentation methods can be used to obtain regions from the image, and a well-trained neural network can identify data patterns generated by bleeding and nonbleeding regions [3]. Aoki researched whether a system based on convolutional neural networks can reduce the reading time of endoscopists and increase disease detection rates. The results show that the

convolutional neural network system designed by the team can reduce reading time, but it has no significant effect on the detection rate of lesions [4]. Li proposed a new computer-aided system for detecting bleeding areas in capsule endoscopic images. This scheme is very effective for detecting bleeding areas and can be used to distinguish between normal and bleeding areas in capsule endoscopic images [5]. Shahril studied the recognition performance of the bleeding area of the capsule endoscope image based on the deep convolutional neural network algorithm and proposed a preprocessing technology classification, which can distinguish between the normal area and the bleeding area by improving the accuracy of the capsule endoscope image. Experiments show that compared with capsule endoscopy images that do not use this enhancement technology, capsule endoscopy images that use this enhancement technology have a better classification effect [6]. Chen proposed a general depth framework of spatio-temporal cascade to understand the most common content in the entire gastrointestinal video. Compared with other methods, their proposed network framework can perform noise content detection and terrain segmentation at the same time, thereby reducing the number of images that need to be inspected and segmenting images of different lesion areas more accurately [7]. Yiftach has developed a deep learning algorithm that can automatically grade Crohn's disease during capsule endoscopy. The conclusion shows that the convolutional neural network has achieved high accuracy in detecting severe Crohn's disease. Convolutional neural network-assisted capsule endoscopy readings in Crohn's disease patients can potentially facilitate and improve the diagnosis and monitoring of these patients [8]. The image recognition and machine learning technology in artificial intelligence can effectively reduce the endoscopic image reading work of gastroenterologists, reduce the workload of reading physicians, quickly identify various suspected lesions, and improve the diagnostic efficiency of the capsule endoscope. There are two main purposes. The first is to reduce the video of capsule endoscopy to increase the speed of capsule endoscopy, and the second is to perform image detection for specific diseases. However, image features mainly include shape, color, and texture, and feature extraction and selection directly affect the performance of subsequent image classifiers. The scene of the capsule endoscope image is complex and changeable, and there are uncertain factors such as bubbles, peristalsis, and lighting changes. Therefore, effective and automatic filtering of redundant images is still a problem. Based on deep learning, this research hopes to establish an effective capsule endoscopic diagnosis system, and the neural network is trained for prediction after preprocessing by extracting texture features that can significantly show the lesion to improve the speed and accuracy of doctors' diagnosis and help doctors make better diagnoses.

2. Methodology

2.1. Capsule Endoscopy. Capsule endoscopy is one of the advanced methods to detect and diagnose human digestive tract diseases. Compared with traditional inserting gastrointestinal endoscopes, capsule endoscopes have superior performance such as noninvasive, safe, and full-process detection [9–12]. The length of the capsule endoscope is about 20 mm and the diameter is about 10 mm. Its internal structure is shown in Figure 1. It is mainly composed of CMOS image sensor, lens, LED, ASIC transmitter, and power module.

The working principle of the capsule endoscope is shown in Figure 2. After the patient swallows the capsule endoscope, with the help of gravity and natural peristalsis of the gastrointestinal tract, the endoscope moves forward, passing through the mouth, esophagus, stomach, duodenum, jejunum, ileum, colon, and other parts, and finally discharged through the anus. During this process, the capsule endoscope will perform full range imaging (2–3 frames/sec) of the digestive tract it passes through, and the image will be stored in the data recorder carried by the patient through wireless transmission. According to statistics, the average residence time of the capsule endoscope in the digestive tract is about 8 hours, and thousands of color images can be collected during the entire process. Due to the characteristics of gastrointestinal peristalsis, there are often a large number of redundant images in the collected images, which have extremely high similarities. Doctors manually screen out images with lesions from these large numbers of images. Screening is labor intensive and inefficient, and it usually takes 2-3 hours to focus on carefully examining each frame. Since the endoscope has passed through different parts of the digestive tract, such as the stomach, duodenum, and colon, the color information, intestinal diameter, and movement state of each part are different, so the focus is not good during endoscopic shooting. The captured image scenes are also complex and changeable, with great differences in structure, color, and texture. There may be many uncertain factors, such as food residues, air bubbles, digestive juices, and blood. Therefore, how to quickly and automatically filter out redundant images in capsule endoscopy to improve the diagnosis efficiency of doctors is a hot issue in the field of neural network diagnosis technology and medical image processing.

2.2. Image Preprocessing. The RGB color model is a color superposition model based on human perception of colors, that is, three primary colors are added together in different ways to represent various colors. The RGB color model is device-oriented and is mainly used for the representation and display of images in the electronics industry. The laboratory color model is a color model based on physiological characteristics and has nothing to do with equipment. The color gamut of the lab color model is much larger than that of the RGB color model, CMYK color model, and human vision, and it makes up for the shortcomings of uneven color distribution in the RGB color model. Although lab color space is not often used, it has excellent results consistent with human visual analysis when analyzing certain images with specific color characteristics [13]. Usually, the original digital image we obtain is an RGB image, and the RGB image needs

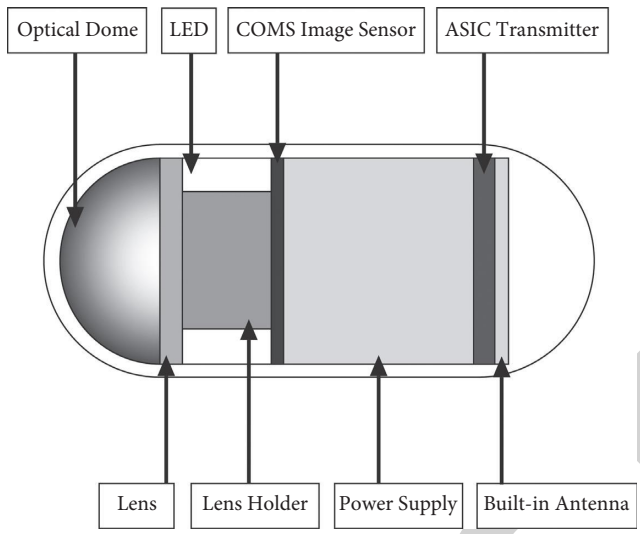

Figure 1: The structure of the capsule endoscope.

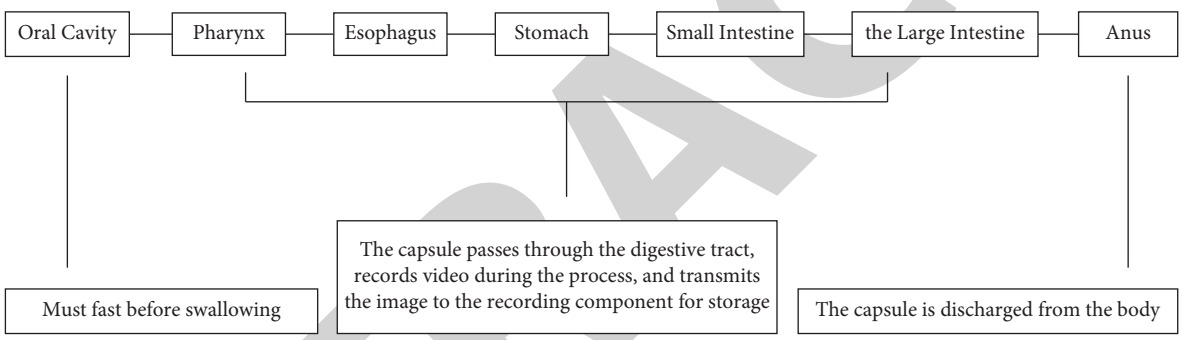

Figure 2: Schematic diagram of the capsule endoscope.

to be converted to XYZ color space first. Assuming the representation of the pixel in the RGB color space, first convert the RGB mode to the XYZ color space in the following way (XYZ is the coordinate system, X, Y, and Z are the 3 components of the target color space):

$$\begin{cases} R = \text{gamma}\left(\dfrac{r}{255.0}\right), \\ G = \text{gamma}\left(\dfrac{g}{255.0}\right), \\ B = \text{gamma}\left(\dfrac{b}{255.0}\right). \end{cases} \tag{1}$$

Among them, the gamma function is the gamma correction in the sRGB standard, which is usually defined as

$$\text{gamma}(x) = \begin{cases} \left(\dfrac{x + 0.055}{1.055}\right)^{2.4}, \text{if } (x) > 0.04045, \\ \dfrac{x}{12.92}, \text{others}, \end{cases}$$

$$\begin{cases} X = 0.4124 * R + 0.3576 * G + 0.1805 * B, \\ Y = 0.2126 * R + 0.7152 * G + 0.0722 * B, \\ Z = 0.0193 * R + 0.1192 * G + 0.9505 * B. \end{cases} \tag{2}$$

It can be seen from the above formula that when the X, Y, and Z components are very close to 1, the coefficients of R, G, and B are 0.950456, 1.0, and 1.088754, respectively. To map to the RGB mode in the same range, the formula for converting XYZ mode to lab mode is as follows:

$$\begin{cases} L = 116 f\left(\dfrac{Y}{Y_n}\right) - 16, \\ a = 500\left[f\left(\dfrac{X}{X_n}\right) - f\left(\dfrac{Y}{Y_n}\right)\right], \\ b = 200\left[f\left(\dfrac{Y}{Y_n}\right) - f\left(\dfrac{Z}{Z_n}\right)\right]. \end{cases} \tag{3}$$

Among them, X_n, Y_n, and Z_n are usually set to 95.047, 100.0, and 108.883, and

$$f(x) = \begin{cases} t^{1/3}, \text{if}\,(t) > \left(\dfrac{6}{29}\right)^3, \\ \dfrac{1}{3} * \left(\dfrac{29}{6}\right)^2 t, \text{others}. \end{cases} \tag{4}$$

2.3. Extract Texture Features. There are significant differences in the texture between the lesion area and the non-lesion area in the capsule endoscopic image [14–16], so it is very important to extract texture features. In this research, Daubechies function is chosen as the wavelet basis function [17]. The formula can be expressed as

$$\begin{aligned} Q^i &= \left\{L_a^i, H_\beta^i\right\}, \\ i &= 1, 2, 3; \\ \alpha &= 1, 2, 3; \\ \beta &= 1, 2, \ldots, 9. \end{aligned} \tag{5}$$

Among them, L represents the low frequency part of the image when it is decomposed in the horizontal and vertical directions; H represents the middle and high frequency part of the image; α represents the decomposition level; β represents the wavelet frequency band; and i represents the R, G, and B components of the image. Commonly used computer-aided analysis methods are mainly carried out in the low frequency band of the image. In this article, we choose the middle and high frequency bands to reconstruct the image and extract texture information. The selected subbands are represented as follows:

$$\begin{aligned} O^i &= \left\{H_\beta^i\right\}, \\ i &= 1, 2, 3; \\ \beta &= 1, 2, \ldots, 9. \end{aligned} \tag{6}$$

Calculate the matrix Wθ T, Tε{R, G, B} of the RGB components of the converted image. The pixel pair (m, n) in the matrix means the distance in the image is d, the color scale is m and n, and the number of occurrences of two pixels in the direction θ. In applications, θ is usually selected as 0°, 45°, 90°, and 135°. It can reflect the distribution characteristics of brightness, it can also reflect the location distribution characteristics between pixels of the same or close to brightness, and it is also a second-order statistical feature of image brightness changes. Then, normalize the obtained co-occurrence matrix, and write Wθ T (m, n) as the value of the pixel (m, n) into the normalized co-occurrence matrix, where $T \in \{R, G, B\}$, $\theta \in \{0°, 45°, 90°, 135°\}$. The expression is as follows:

$$\begin{aligned} E_T^\theta &= \sum_{m=1}^{D}\sum_{n=1}^{D}\left[w_T^\theta(m,n)\right]^2, \\ I_T^\theta &= \sum_{m=1}^{D}\sum_{n=1}^{D}(m-n)^2 w_T^\theta(m,n), \\ II_T^\theta &= -\sum_{m=1}^{D}\sum_{n=1}^{D} w_T^\theta(m,n)\log w_T^\theta(m,n), \\ A_T^\theta &= \frac{\sum_{m=1}^{D}\sum_{n=1}^{D}(m,n)w_T^\theta(m,n) - \mu_1^\theta\mu_2^\theta}{\sigma_1^\theta\sigma_2^\theta}, \\ \mu_1^\theta &= \sum_{m=1}^{D} m \sum_{n=1}^{D} w_T^\theta(m,n), \\ \mu_2^\theta &= \sum_{n=1}^{D} n \sum_{m=1}^{D} w_T^\theta(m,n), \\ \sigma_1^\theta &= \sum_{m=1}^{D}\left(m-\mu_1^\theta\right)^2 \sum_{n=1}^{D} w_T^\theta(m,n), \\ \sigma_2^\theta &= \sum_{n=1}^{D}\left(n-\mu_2^\theta\right)^2 \sum_{m=1}^{D} w_T^\theta(m,n). \end{aligned} \tag{7}$$

Among them, Eθ T, Iθ T, IIθ T, and Aθ T, respectively, represent the energy, contrast, entropy, and correlation of the co-occurrence matrix θ of each color component; D is the maximum color level of the image. In this study, $d = 1$ is used to construct the texture feature vector of the image based on the feature value calculated above, which can be given by the following formula.

$$Z_T = \left[\overline{E}_T^\theta, \widehat{E}_T^\theta, \overline{I}_T^\theta, \widehat{I}_T^\theta, \overline{II}_T^\theta, \widehat{II}_T^\theta, \overline{A}_T^\theta, \widehat{A}_T^\theta\right]. \tag{8}$$

Among them, $\overline{X}_T^\theta = \sum_{\theta\in\{0°,45°,90°,135°\}} X_T^\theta/4$, $\widehat{X}_T^\theta = \sqrt{\sum_{\theta\in\{0°,45°,90°,135°\}}(X_T^\theta - \overline{X}_T^\theta)^2/4}$; X$\in${E, I, II, A}, T$\in${R, G, B}, $\theta\in\{0°, 45°, 90°, 135°\}$. The 8-dimensional texture features of the RGB components obtained above are correspondingly added as the final extracted texture features:

$$F_{\text{texture}} = Z_R + Z_G + Z_B. \tag{9}$$

2.4. Network Training. This research is based on neural network algorithms to realize the recognition and segmentation of endoscopic images of digestive tract capsules. The support vector machine (SVM) is a statistical learning theory proposed and established by Vapnik et al. It is usually used for data classification and regression prediction. It has

many unique advantages in solving nonlinear, high-dimensional pattern, and small sample recognition problems [18–21]. The principle is as follows: find an optimal hyperplane that meets the classification requirements and maximize the distance between the edges on both sides of the hyperplane on the basis of ensuring the classification accuracy. Assuming that the number of samples in the training set is a and the training set is {{x1, y1), (x2, y2), ..., (xa, ya)}, the SVM maps the input to the high-dimensional feature space Λ to φ (X), and the corresponding classification function is

$$f(x) = \operatorname{sgn}(w \cdot \phi(x) + b). \tag{10}$$

In the formula, w and b represent the weight vector and the offset, respectively. According to the principle of structural risk minimization, formula (10) is transformed into

$$\min J = \frac{1}{2}\|w\|^2 + C\sum_{c=1}^{a}(\xi_c^* + \xi_c),$$
$$s.t.\begin{cases} y_c - w \cdot \phi(x) - b \le \varepsilon + \xi_c, \\ w \cdot \phi(x) + b - y_c \le \varepsilon + \xi_c^*, \\ \xi_c, \xi_c^* \ge 0, c = 1, 2, \ldots, a. \end{cases} \tag{11}$$

In the formula, ξ_c and ξ_c^* are the upper and lower limits of the relaxation factor, respectively; C represents the penalty factor. By adjusting C, a balance can be achieved between training error and generalization ability. Introducing the Lagrangian multiplier becomes a convex quadratic optimization problem:

$$L(w, b, \xi, \xi^*, \lambda, \lambda^*, \gamma, \gamma^*) = \frac{1}{2}\|w\| + C\sum_{c=1}^{a}(\xi_c + \xi_c^*) - \sum_{c=1}^{a}\lambda_c[\xi_c + \varepsilon - y_c + f(x_c)] - \sum_{c-1}^{a}\lambda_c^*[\xi_c^* + \varepsilon - y_c + f(x_c)] - \sum_{c=1}^{a}(\xi_c y_c - \xi_c^* y_c^*), \tag{12}$$

where λc and λ ∗ c represent Lagrangian multipliers. In order to speed up the solution, formula (10) is transformed into a dual form:

$$\psi(\lambda, \lambda^*) = -\frac{1}{2}\sum_{c,e=1}^{a}(\lambda_c - \lambda_c^*)(\lambda_e - \lambda_e^*)[\phi(x_c), \phi(y_e)] + \sum_{c=1}^{a}(\lambda_c - \lambda_c^*)y_c - \sum_{c=1}^{a}(\lambda_c - \lambda_c^*),$$
$$s.t.\begin{cases} w = \sum_{c,e=1}^{a}(\lambda_c - \lambda_c^*)x_c, \\ \sum_{c=1}^{a}(\lambda_c - \lambda_c^*) = 0, \\ 0 \le \lambda_c, \lambda_c^* \le C. \end{cases} \tag{13}$$

Introduce the function K (x_c, x) to replace the vector inner product (φ (x_c), φ (x)); then, the classification decision function of SVM is

$$f(x) = \operatorname{sgn}\left(\sum_{c=1}^{a}(\lambda_c - \lambda_c^*)K(x_c, x) + b\right). \tag{14}$$

3. Results

The data used are 1317 patients who underwent capsule endoscopy in our hospital from September 2016 to September 2020, including 1438 males and 879 females, aged 13–86 years old, with an average age of 45.23 years. Finally, a total of 22785313 capsule endoscopic images were obtained. Excluding redundant images collected in various parts of the digestive tract due to complex scenes, these images include food residues, bubbles, digestive juices, blood, and other uncertain factors that cause interference, and finally, 22565431 effective images are obtained. The images are divided into normal, inflammation, ulcers, polyps, lymphatic dilatation, hemorrhage, vascular disease, and bulge. A total of 1722499 images of the capsule endoscopy images of 300 patients were retained as a verification set to verify the performance of the model. A total of 5782 lesions were confirmed in 1317 patients. Then, according to the proportion and random selection method, each disease is divided into the training set and test set. Finally, there are 18881193 images in the training set and 3776238 images in the test set. The lesion samples in the image are all marked by an endoscopist with many years of hospital clinical experience. The data labeling work is divided into three steps: the

doctor first determines the patient's disease based on the previously recorded cases (such as polyps and ulcers) and then filters out the disease images from the capsule endoscopy video. Diseased images are provided by professionals. The doctor will label them one by one. Labels are divided into malignant tumors, benign lesions, and normal. Input the 3776238 test set images into the constructed convolutional neural network to verify the accuracy of the neural network. The convolutional neural network model constructed in this study can output malignant tumors, benign lesions, and normal results. Calculate the output results of the convolutional neural network model, and calculate the accuracy (Pr) of the model classification, the recall rate (Re) [22, 23], and the average accuracy (MA). The calculation is as follows:

$$\mathrm{Pr} = \frac{\mathrm{TP}}{\mathrm{TP} + \mathrm{FP}},$$
$$\mathrm{Re} = \frac{\mathrm{TP}}{\mathrm{TP} + \mathrm{FN}}, \tag{15}$$
$$\mathrm{MA} = \frac{\mathrm{TP} + \mathrm{TN}}{\mathrm{TP} + \mathrm{FN} + \mathrm{TN} + \mathrm{FP}}.$$

According to this formula, it can be seen that increasing the number of true positive samples can increase the accuracy rate, while reducing the number of false negative samples can increase the recall rate. The new sample greatly increases the number of true positive samples and reduces the number of false negative samples. Therefore, the use of new samples can improve accuracy and recall.

4. Discussion

According to Table 1, after inputting 3776238 sample images of the test set into the convolutional neural network algorithm model, the accuracy, recall, and average accuracy of the algorithm model are 96.47%, 96.13%, and 97.69%, respectively. The total accuracy of this study reached 97.69%, which shows that the convolutional neural network constructed in this study can effectively help doctors perform endoscopic image recognition. Among them, the highest average accuracy is the normal type and the lowest is the benign lesion. The reason may be that normal endoscopic images have no pathological features, so this algorithm can more accurately identify normal endoscopic images. Among the types of benign lesions, it may be because there are more types of benign lesions, and there are more items to be compared with the algorithm, which leads to inaccurate output results of the algorithm. There is a significant difference in the average reading time of capsule endoscopic images for each patient between manual reading and assisted reading models based on convolutional neural networks. In this study, the RGB color model was converted to the lab color model, and the endoscopic images of these two color models were input into the validation set sample data for analysis and comparison. The result analysis is given in Table 2.

Table 1: Neural network output result index table.

Norm	Pr (%)	Re (%)	MA (%)
Malignant tumor	96.76	95.34	97.92
Benign lesions	95.18	94.69	96.34
Normal	97.46	98.37	98.81
Total	96.47	96.13	97.69

Table 2: Comparison table of the output results of the two color modes.

Color mode	Pr (%)	Re (%)	MA (%)
RGB	75.24	76.34	73.12
Lab	96.47	96.13	97.69

According to Table 2, it can be concluded that the results obtained by inputting the validation set samples of the RGB color model into the convolutional neural network are significantly lower than using the lab color model, so it can be judged that the laboratory color model can improve the accuracy of computer recognition. Although the convolutional neural network proposed in this study can effectively identify the endoscopic image of the digestive tract, in actual use, due to the particularity of the digestive tract environment, there will be many uncertainties in the working image of the capsule endoscope. For example, food residues, bubbles, digestive juices, and blood increase the difficulty of processing and analyzing redundant images. Therefore, it is necessary to filter out these useless images when processing images. The result of this research is the result of screening out these redundant images, so some errors may occur in practical applications.

5. Conclusion

This research proposes a convolutional neural network model algorithm that can automatically recognize and classify endoscopic images of digestive tract capsules. First, the redundant image is filtered to obtain a valid endoscopic image and the RGB color model of the image is converted to a lab color model, the image features are extracted and the training set image is used to train the convolutional neural network, and finally, input the validation set image into the network model to verify the performance of the model. Based on the above experiments, it can be concluded that the convolutional neural network constructed in this study can effectively distinguish and recognize the images of the digestive tract capsule endoscopy. The time it takes is much shorter than the doctor's diagnosis time and can quickly make an accurate diagnosis, so it can effectively assist the doctor in the diagnosis and treatment process. The convolutional neural network we built can screen and identify thousands of endoscopic images in a short time and then divide the identified endoscopic images into three types: malignant tumors, benign lesions, and normal. The convolutional neural network algorithm proposed in this research requires a large number of annotated image databases for training. Therefore, in the future research process, the

Hindawi
Journal of Healthcare Engineering
Volume 2023, Article ID 9812058, 1 page
https://doi.org/10.1155/2023/9812058

Retraction

Retracted: Automated System for Identifying COVID-19 Infections in Computed Tomography Images Using Deep Learning Models

Journal of Healthcare Engineering

Received 10 October 2023; Accepted 10 October 2023; Published 11 October 2023

This article has been retracted by Hindawi following an investigation undertaken by the publisher [1]. This investigation has uncovered evidence of one or more of the following indicators of systematic manipulation of the publication process:

(1) Discrepancies in scope
(2) Discrepancies in the description of the research reported
(3) Discrepancies between the availability of data and the research described
(4) Inappropriate citations
(5) Incoherent, meaningless and/or irrelevant content included in the article
(6) Peer-review manipulation

The presence of these indicators undermines our confidence in the integrity of the article's content and we cannot, therefore, vouch for its reliability. Please note that this notice is intended solely to alert readers that the content of this article is unreliable. We have not investigated whether authors were aware of or involved in the systematic manipulation of the publication process.

Wiley and Hindawi regrets that the usual quality checks did not identify these issues before publication and have since put additional measures in place to safeguard research integrity.

We wish to credit our own Research Integrity and Research Publishing teams and anonymous and named external researchers and research integrity experts for contributing to this investigation.

The corresponding author, as the representative of all authors, has been given the opportunity to register their agreement or disagreement to this retraction. We have kept a record of any response received.

References

[1] K. H. Abdulkareem, S. A. Mostafa, Z. N. Al-Qudsy et al., "Automated System for Identifying COVID-19 Infections in Computed Tomography Images Using Deep Learning Models," *Journal of Healthcare Engineering*, vol. 2022, Article ID 5329014, 13 pages, 2022.

Hindawi
Journal of Healthcare Engineering
Volume 2022, Article ID 5329014, 13 pages
https://doi.org/10.1155/2022/5329014

Research Article

Automated System for Identifying COVID-19 Infections in Computed Tomography Images Using Deep Learning Models

Karrar Hameed Abdulkareem,[1] **Salama A. Mostafa**,[2] **Zainab N. Al-Qudsy**,[3] **Mazin Abed Mohammed**,[4] **Alaa S. Al-Waisy**,[5] **Seifedine Kadry**,[6] **Jinseok Lee**,[7] **and Yunyoung Nam**[8]

[1]*College of Agriculture, Al-Muthanna University, Samawah 66001, Iraq*
[2]*Faculty of Computer Science and Information Technology, Universiti Tun Hussein Onn Malaysia, 86400 Batu Pahat, Johor, Malaysia*
[3]*Computer Sciences Department, Baghdad College of Economic Sciences University, Baghdad, Iraq*
[4]*College of Computer Science and Information Technology, University of Anbar, 11 Ramadi, Anbar, Iraq*
[5]*Communications Engineering Techniques Department Information Technology Collage, Imam Ja'afar Al-Sadiq University, Baghdad, Iraq*
[6]*Faculty of Applied Computing and Technology, Noroff University College, Kristiansand, Norway*
[7]*Department of Biomedical Engineering, College of Electronics and Information, Kyung Hee University, Yongin-si, Gyeonggi-do 17104, Republic of Korea*
[8]*Department of Computer Science and Engineering, Soonchunhyang University, Asan 31538, Republic of Korea*

Correspondence should be addressed to Jinseok Lee; gonasago@khu.ac.kr and Yunyoung Nam; ynam@sch.ac.kr

Received 31 December 2021; Revised 29 January 2022; Accepted 18 February 2022; Published 30 March 2022

Academic Editor: Mu-Yen Chen

Coronavirus disease 2019 (COVID-19) is a novel disease that affects healthcare on a global scale and cannot be ignored because of its high fatality rate. Computed tomography (CT) images are presently being employed to assist doctors in detecting COVID-19 in its early stages. In several scenarios, a combination of epidemiological criteria (contact during the incubation period), the existence of clinical symptoms, laboratory tests (nucleic acid amplification tests), and clinical imaging-based tests are used to diagnose COVID-19. This method can miss patients and cause more complications. Deep learning is one of the techniques that has been proven to be prominent and reliable in several diagnostic domains involving medical imaging. This study utilizes a convolutional neural network (CNN), stacked autoencoder, and deep neural network to develop a COVID-19 diagnostic system. In this system, classification undergoes some modification before applying the three CT image techniques to determine normal and COVID-19 cases. A large-scale and challenging CT image dataset was used in the training process of the employed deep learning model and reporting their final performance. Experimental outcomes show that the highest accuracy rate was achieved using the CNN model with an accuracy of 88.30%, a sensitivity of 87.65%, and a specificity of 87.97%. Furthermore, the proposed system has outperformed the current existing state-of-the-art models in detecting the COVID-19 virus using CT images.

1. Introduction

Coronavirus disease 2019 (COVID-19) is a novel disease that rapidly spreads and affects the daily patterns of millions of people in the world. [1]. The infection causes pulmonary complications, such as severe pneumonia, which leads to death in several cases [1, 2]. The possible containment of this virus requires quick detection to ensure that the exposed person can be isolated as quickly as possible to mitigate the spread of the disease because it is highly contagious. Reverse transcription-polymerase chain reaction (RT-PCR) [1] is the standard method used to detect COVID-19; in this method,

sputum or nasopharyngeal swab is tested for the presence of the viral RNA. RT-PCR has the following limitations: the long time required to produce results, limited or lack of test materials in medical centers and hospitals [2], and relatively low sensitivity; this condition is not conducive to the main objective of detection of rapid positive samples for immediate isolation [3]. The utilization of medical images, such as chest X-ray images or computed tomography (CT) scans, can be an alternative solution for fast screening [4]. An early-stage identification of COVID-19 via imaging would allow rapid patient isolation and thus would reduce the spread of the disease [1]. However, physicians are trying hard to contain this disease. Thus, artificial intelligence- (AI-) based decision support tools should be developed to identify and use the image at the lung level in segmenting the infection [2]. AI, such as machine and deep neural network (DNN) techniques [5], has been increasingly used in recent years as the main tool to find solutions to diverse difficulties, such as object detection [6–8], image classification [9], and speech recognition [10]. In image processing [11], a convolutional neural network (CNN) has specifically produced outstanding results [12]. Many studies have presented the influence and strength of these techniques in image segmentation [13]. Image classification [14] and image segmentation [13] for medical imaging has also produced very good results using CNN architectures [15].

The most effective technique for detecting lung COVID-19 is CT because of its 3D image-forming capability of the chest, which enables it to produce lung pathology in greater resolution. Computer processing of a CT image is a popularly used technique in aiding clinical lung COVID-19 diagnostics. The use of a computer-supported identification process for lung COVID-19 can be divided into two: a detection system and an identification approach (usually abbreviated as CAD). The CAD approach categorizes the previously identified candidate lung COVID-19 as normal or nonnormal COVID-19 cases (i.e., normal anatomic structures). The detected lung inflammation is classified as normal or nonnormal as COVID-19 by the CAD approach [16]. The CAD can differentiate the lung inflammation as normal or nonnormal COVID-19 case by utilizing efficient features, such as shape, texture, and growth rates because a probability has a close relationship to shape, geometric size, and appearance in COVID-19. Thus, the precise diagnostic, speed, and automation levels are measurable terms that can present the achievement of a specific CAD approach [17].

Deep learning enhances the accuracy of the computerized process and assessment of CT image segmentation and identification and accelerates the critical task. The problem associated with lung inflammation classification into normal or nonnormal COVID-19 cases is considered in this study. However, several existing CT scan datasets for COVID-19 comprise hundreds of CT images and fall short of the demand [18]. Several available COVID-19 datasets also lack fine-grained pixel-level annotations; they also provide only the patient-level labels (i.e., class labels), which indicate whether the person is infected or otherwise [19, 20]. DNN, CNN, and stacked autoencoder (SAE) are proposed to implement COVID-19 identification. The research can be utilized directly as input to limit the difficult data reconstruction process during feature extraction and classification. This study constructs a large-scale CT scan dataset for COVID-19 that comprises pixel-level annotations to alleviate the limitations presented earlier. Then, we propose a CT diagnosis system for COVID-19 classification to provide explainable diagnostic results to medical staff battling COVID-19. We specifically use the gathered COVID-19 CT dataset from hundreds of COVID-19 cases containing thousands of CT images to train the employed deep learning models for better diagnosis performance. The proposed diagnosis method first identifies the suspected patients of COVID-19 using a classification model based on lung CT images. Then, the system provides the diagnosis explanations by applying activation mapping techniques. The proposed system can find the locations and areas of the lung radiography using fine-grained image techniques. Our method extensively accelerates and simplifies the diagnosis procedure for radiologists related medical personnel by providing them with explainable classification results. Accordingly, our contribution is summed up in three main points as follows:

(i) We showed that the proposed classification techniques and their implemented models can effectively improve the performance of COVID-19 diagnosis by using limited computational resources, few parameters, and only 746 chest CT scan samples

(ii) We proposed a new COVID-19 diagnostic model to perform explainable detection and precise COVID-19 case classification and show significant improvement over previous systems

(iii) The proposed CNN, DNN, and SAE use CT scans as a direct input to limit the complexity involved with data reconstruction during the deep learning and classification processes

This paper is structured in five sections, and the following section evaluates the previous studies, while Section 3 contains the presentation of the materials and methods for classifying lung CT images. Section 4 shows the produced experimental outcomes, and Section 5 elaborates the conclusion of our study.

2. Related Work

The complexity in the diagnostic of inflammatory and infectious lung disease using visual examination is still a challenge in developing an automated system for lung CT scan classification. The large number of patients requiring diagnosis is a source of errors for an acceptable standard as visual examination. Wang et al. [16] proposed a system to offer a clinical identification of the pathogenic examination using CNN-based automated technique in identifying distinct COVID-19 features. The dataset contained 217 cases and produced an accuracy of 82.9%. A fully automated framework was proposed by Li et al. [21], and it utilized a CNN for extracting the best features in detecting COVID-19 and distinguishing it from the healthy case and pneumonia

infection. The used dataset contained 400 CT scans and produced an overall accuracy of 96% in detecting COVID-19 cases. Xu et al. [22] proposed an automatic screening approach utilizing deep learning methods to distinguish CT samples detected with influenza-A viral pneumonia or COVID-19 from the sample of patients who had healthy lungs. The dataset contained 618 lung CT scans and produced an overall classification accuracy of 86.7%, as revealed by the experimental result. Song et al. [23] improved an automatic deep learning identification approach to aid medical personnel in detecting and recognizing patients infected by COVID-19. The gathered dataset contained CT scans of 86 healthy, 88 COVID-19, and 100 bacterial pneumonia samples. The proposed deep learning model could detect and classify bacterial pneumonia and COVID-19-infected samples with an accuracy of 95%. Hasan et al. [24] presented identification COVID-19 among COVID-19, healthy, and pneumonia CT lung scans using the integration of Q-deformed entropy handcrafted features and deep learning of extracted features. Preprocessing was utilized to limit the intensity difference influence amid CT cases in this study. In isolating the background of the lung CT scan, histogram thresholding was applied. Feature extraction was conducted on every lung CT scan using a Q-deformed entropy and deep learning methods. The long short-term memory (LSTM) type of neural network was employed to classify the extracted features. The combination of all features extracted meaningfully resulted in better execution of the LSTM network in accurately discriminating among COVID-19, healthy, and pneumonia samples.

Feature extraction complexity is one of some limitations in present classification models. Feature extraction algorithms play a vital role in gathering the significant variations in the spatial scattering of image pixels. The powerful discriminative capability of AI technologies, especially deep CNNs, is improving medical imaging solutions. However, deep learning algorithms, including CNNs need to be trained on large-scale datasets to show their capability. The majority of presently available CT scan datasets for COVID-19 [25, 26] comprise hundreds of CT images from tens of cases, which fall short of the requirement. Lack of fine-grained pixel-level annotations and provision of patient-level labels (i.e., class labels) that indicate whether the person is infected in the majority of the currently available COVID-19 datasets makes CNN models trained. Despite the establishment of several diagnosis systems for testing suspected COVID-19 cases by CT scan [27], most of them exhibit two constraints: (1) they are not suitably robust for versatile COVID-19 infections because they are trained on small-scale datasets; (2) they lack explainable transparency in assisting doctors during medical diagnosis because classification is performed on the basis of black-box CNNs.

The lung CT scan classification models in existing systems depend on deep learning methods to extract the best features. The classification performance between healthy and COVID-19 cases will improve further as a result of deep learning features. Proposing an efficient COVID-19, healthy, and COVID-19 lung classification in CT images applying the deep learning models is the motivation for this study. CNN, DNN, and SAE provide the means of developing a COVID-19 diagnosis method that can perform supervised learning and produce accurate detection.

3. Materials and Methods

There is a significant require for speedy testing and diagnostic of patients amid the COVID-19 widespread. Lung CT is an images methodology that is widely accessible and cost-effective and can analyze and diagnose intense respiratory trouble disorder in patients with COVID-19. It can be utilized to discover imperative features within the medical samples that present all the clinician information that can be used to diagnose and monitor the COVID patents. With the usage of versatile ultrasound transducers, lung CT samples can be effortlessly obtained. In any case, the CT image is frequently of destitute quality. It frequently needs a specialist clinician elucidation, which may be highly subjective and time-consuming. The main goal of this work is to develop a new COVID-19 identification framework proposed to automatically distinguish between COVID-19 infected subjects and healthy one via CT images using different deep learning methods.

3.1. CT Image Dataset. The dataset consists of 746 COVID-19 patient cases with their CT scan images and full clinical description (e.g., 349 images with confirmed COVID-19 infection, while 397 CT scans belong to individuals with a good health condition and no diagnosed pneumonia diseases) [25]. Free public radiology resources, including datasets, reference studies, case studies, and CT images, are provided on many international radiology websites, such as medRxiv and bioRxiv. The first COVID-19 dataset used in our study is obtained from medRxiv and bioRxiv for the period from January 19, 2020, to March 25, 2020. An example of chest CT scans for patients having COVID-19 is shown in Figure 1.

3.2. Automated COVID-19 Classification Methodology. This research aims to enhance the process of COVID-19 identification and diagnosis by minimizing the diagnostic error rate associated with human error in reading chest CT scans. In addition, it aims to help medical practitioners conduct fast identification to distinguish among the patients with confirmed COVID-19 infection, other pneumonia infections, and healthy people. The proposed system can be divided into three major phases: preprocessing of CT images, extraction of dominant features, and classification of selected features by DNN, CNN, and SAE classifiers to make the final decision. Figure 2 illustrates the components of the proposed COVID-19 identification.

3.2.1. CT Lung Preprocessing Stage. The quality of the image scan depends on the accuracy of the metrics, intensity, and variations of the reconstructed and consecutive slices of CT scan [28]. Normalization of the intensity through extracting deep features can help minimize the CT slice variations, enhance the classifier's performance, and accelerate the

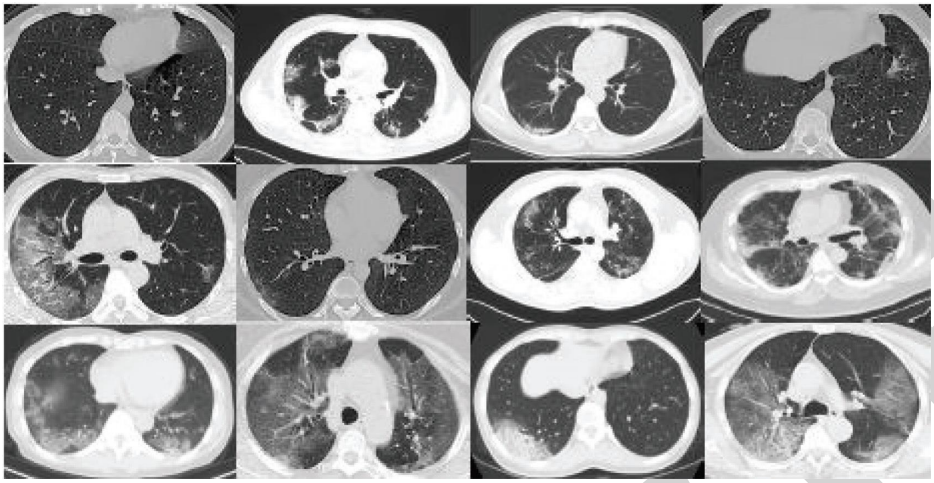

Figure 1: Positive cases for COVID-19 in CT scan images.

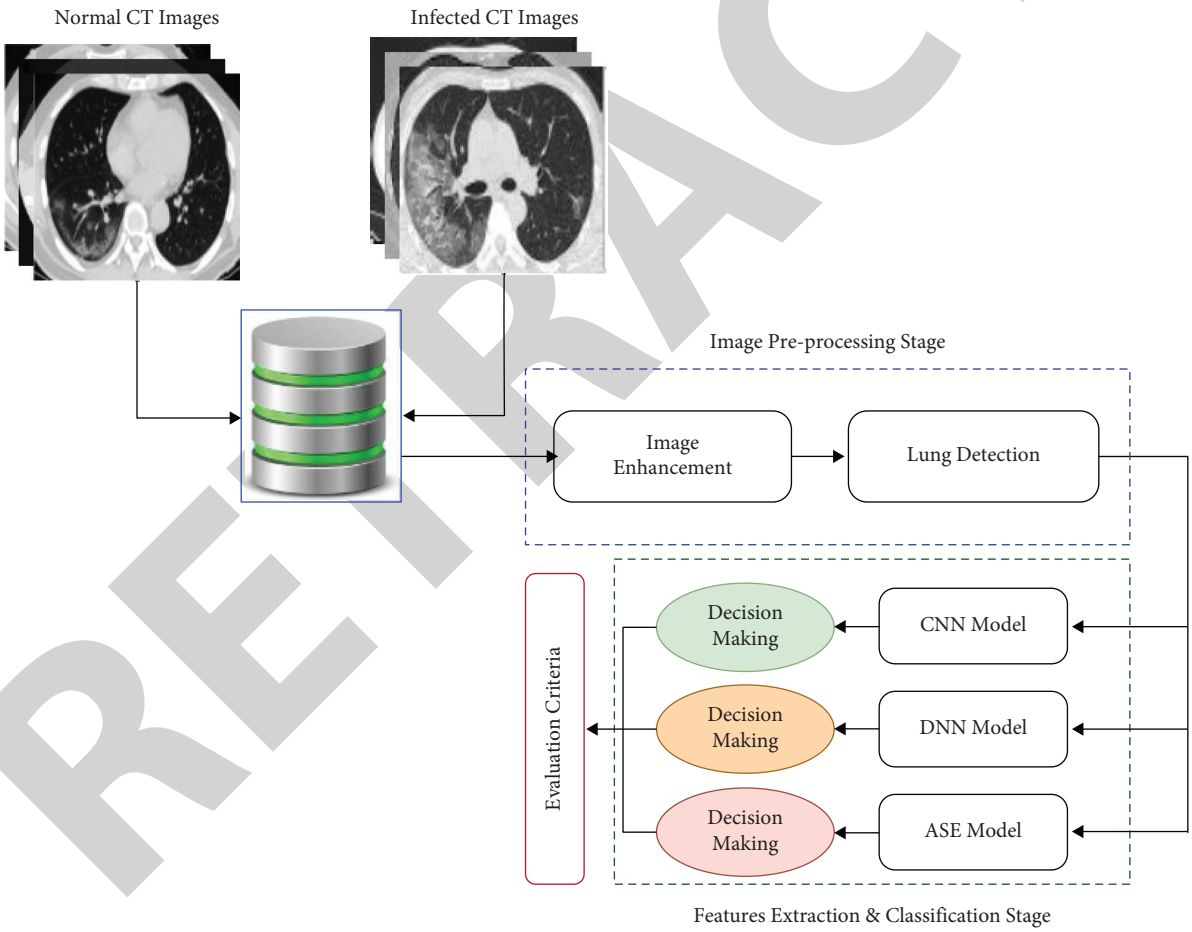

Figure 2: Proposed automated detection and classification of COVID-19 cases on CT images using deep learning models.

training process. This process also identifies lung boundaries to recognize the area of thoracic tissue surrounding the lung, which is represented as many unimportant pixels [29]. We use the histogram thresholding method that isolates each individual CT with intensity values larger than a set cut-off value from the CT lung background pixels. Then, the morphological dilation operation was applied to fill the gaps that appear in the sliced image. Any deficiencies found can be removed by connecting small objects. As a result, the shades of zeros and ones are applied to extract the more interesting area of the lung. Ones represent the lung area, and the background is represented by zeros [22]. Algorithm 1 describes the pseudocode of the steps of the chest CT scan. A sample of the segmented CT lung is illustrated in Figure 3.

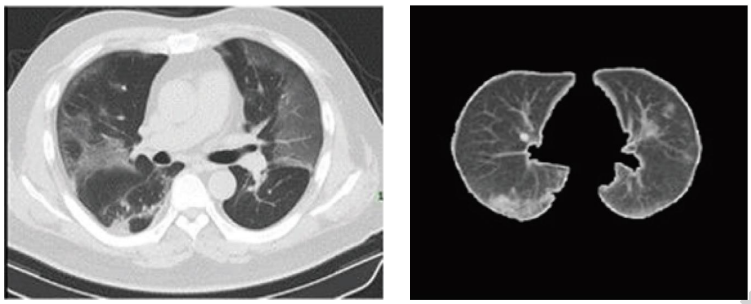

(a) (b)

Figure 3: CT lung classification: (a) original CT lung case and (b) segmented CT lung.

(i) - Preprocessing
(1) Begin
(2) $x_1 \longleftarrow$ read CT lung image (x_0);
(3) $x_2 \longleftarrow$ set image intensity (x_1);
(4) $x_3 \longleftarrow$ transform x_2 to a binary image (x_2);
(5) $x_4 \longleftarrow$ eliminate small substances from the image (x_3);
(6) $x_5 \longleftarrow$ fill holes and small gaps (x_4);
(7) $x_6 \longleftarrow$ multiply image x_5 pixels (x_5);
(ii) - Feature extraction
(8) For each feature extraction operator F_i do
(9) $f_i \longleftarrow$ extract features (x_6);
(10) $w_i \longleftarrow$ evaluate features (f_i);
(11) $bf_i \longleftarrow$ select best features (f_i, w_i);
(12) End for
(iii) - Classification
(13) For each classification operator C_j do
(14) [healthy, unhealthy] $\Longleftarrow c_{i,j} \longleftarrow$ classify (bf_i);
(iv) - Evaluation
(15) For each evaluation operator E_k do
(16) $e_{j,k} \longleftarrow$ evaluate classification ($c_{i,j}$);
(17) write results (bf_i, F_i, $c_{i,j}$, C_j, E_k, $e_{j,k}$);
(18) End for
(19) End for
(20) End

Algorithm 1: Deep learning-based COVID-19 diagnosis algorithm.

3.2.2. Deep Learning for Feature Extraction. The use of handcrafted features as input to the classifier with expert guidance may affect its performance. However, many deep learning techniques perform more successfully in extracting features, particularly in the computer vision domain. They also show efficiency in improving the accuracies of classification. In this study, the CNN technique is used to extract features efficiently. CNN is one of the successful classification methods in the computer vision domain. CNN is an improved version of the classical neural network by introducing new layers (convolutional, pooling, and fully connected) [30]. The convolutional layers consist of a number of trainable convolutional filters.

The filters change the entire input size to be specific amount known as stride(s) to yield integer dimensions of output size [31]. As a result of this process, the spatial dimensions of input size are considerably reduced after the convolutional layer. The original input size with a low number of features needs to be minimized by zero-filling each input to be assigned with zero value. In the feature maps, all negative values are turned to zeros via the rectified linear unit (ReLU) layer to maximize the feature maps nonlinearly. Thereafter, the pooling layers divide the feature maps into small nonoverlapped partitions to minimize the data dimensionality. For this purpose, the pooling layer has been supported by the max-pooling function in this research. A batch normalization layer performs normalization of the features to accelerate the training process. The fully connected layer is considered the most significant layer in CNN. The normalized feature map is inserted into this layer, and this layer acts as a classifier to yield the final results and label probabilities. Although CNN is a powerful method as a classifier, it has a disadvantage in terms of requiring

intensive parameter tuning. As a result, fewer convolution layers are used to reduce the complexity of CNN architecture and thus the parameter tuning process. CNN aims to extract highly significant features for a particular task. The network architecture, the number of convolutional layers, the filters size, and the CT partitions inserted into the network are major factors that affect the classification process. Therefore, they should be given more attention when applying CNN. In our study, the CT slice dimensions are set to (256×256) pixels to reduce computation complexity. For a given CT partition, the size of the convolutional layer and the number of zero-filling are determined via the following equations:

$$\begin{aligned}
\mathrm{Conv}_{\mathrm{width}} &= \frac{CT\mathrm{Slice}_{\mathrm{width}} - Cf_{\mathrm{width}} + \left(2 \times ZP_{\mathrm{width}}\right)}{S_{\mathrm{width}}} + 1, \\
\mathrm{Conv}_{\mathrm{height}} &= \frac{CT\mathrm{Slice}_{\mathrm{height}} - Cf_{\mathrm{height}} + \left(2 \times ZP_{\mathrm{height}}\right)}{S_{\mathrm{height}}} + 1, \\
ZP_E &= \frac{Cf_{\mathrm{width}} - 1}{2}, \\
ZP_{\mathrm{height}} &= \frac{Cf_{\mathrm{height}} - 1}{2}.
\end{aligned} \tag{1}$$

3.2.3. The Convolutional Neural Network (CNN). CNN is a neural network based on a multilayer approach. It consists of a set of convolution and fully connected layers; the latter acts as the standard layer of the neural network. The idea of CNN can be traced back to the 1960s [32]. It is based on three concepts: local perception, sharing of weights, and time or space sampling. Local perception is an efficient detection method that is currently attracting attention. This method mainly detects the local aspect of data to extract the basic features for the visual object in a picture, such as an angle or arc of an animal [15]. The advantage of CNN is the requirement of a few parameters compared with the number of hidden units for fully connected networks. CNN consists of two layers: the convolution and pool layers that collaborate [33]. It may affect a specific position of the features and make a confusion of uninterested feature location to focus on other relative positions of features. The pooling layer function relies on mean pooling and max-pooling operations. Mean pooling operation computes the neighborhood average of feature points, while max-pooling operation computes the maximum of feature points for the neighborhood. The size limitation of the neighborhood may cause a feature extraction error. The reason is that the mean deviation is due to errors of the estimated parameter and variance in the convolution layer. Estimated variance error can be decreased by mean pooling operation by preserving image background information. Estimated parameter error can be decreased by max-pooling operation by preserving image texture information.

The CNN architecture is illustrated in Figure 4. The CNN architecture comprises multiple layers. Every layer comprises multiple maps. Every map comprises numerous neural units. For the same map, neural elements share the weight of the convolution kernel. Every convolution kernel is shown as a feature. The edge of image features can be accessed. Additional CNN details are represented in Table 1. Image data, which are represented as input data, have high control of the deformation. The convolution kernel and parameter size generate the multiscale image feature convolution. The distinct angles of information are created in the space of feature.

3.2.4. The Deep Neural Network (DNN). A DNN is a basic neural network with more hidden nodes. An intensive computation of the input is conducted in the neural network because of the nonlinear transformation from each hidden layer to the output layer [34]. However, DNN is more efficient than the superficial network. As for the linearity of the activation function, each hidden layer should be represented as the nonlinear function $f(x)$. This condition is opposite to the individual hidden layer in the neural network, given that the hidden layer depth has no ability to improve the expression. The aspect of various sizes of the lung nodes is extracted from different network layers in the DNN processing phase. DNN has some issues with respect to problems associated with the local boundary and gradient spread. The original image is fed as the input in the training process to preserve more image information.

The DNN architecture comprises the input, hidden, and output layers. All these layers are interconnected to one another. DNN has no convolution layer. Training and label images are fed to the DNN. In the initial training, the random weight is assigned to every layer using Gauss distribution with bias equals to zero. Forward propagation is used for output calculation, while backpropagation is used for parameter updating. The depth structure of the neural network is illustrated in Figure 5. Additional neural network details are shown in Table 2. The DNN requires sorting out some issues related to its parameters, including the tuning of parameters, the growth of data size, and normalization [35, 36].

3.2.5. The Stacked Autoencoder (SAE). An SAE is an unsupervised learning algorithm having a multilayer neural network with SAE [37]. It consists of input, hidden, and output layers. The SAE architecture is shown in Figure 6. The input and output layers have the same number of neurons, while the hidden layer has less number of neurons. The SAE is composed of two phases: the coding and decoding phases. Mapping from the hidden and input layers occurs in the coding phase. Meanwhile, mapping the hidden layer to the output layer occurs in the decoding phase.

This research uses a combination of multiple autoencoders and softmax as a classification method to build an SAE network. The SAE network has several hidden layers and softmax as a final layer [38]. Sparse autoencoder, which is a variant of autoencoder, was introduced in [39]. SAE has very few active neurons. Masci et al. [40] proposed a convolutional autoencoder that trains high-dimensional image

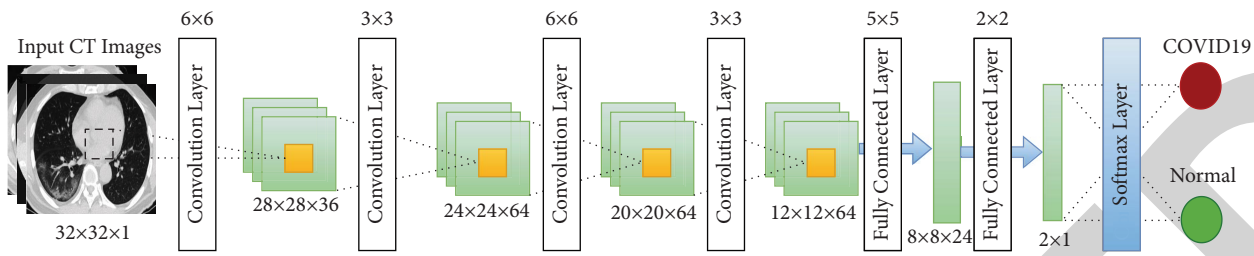

Figure 4: CNN architecture.

Table 1: CNN parameters.

Layer	Type	Input	Kernel	Output
1	Convolution layer	$32 \times 32 \times 1$	6×6	$28 \times 28 \times 36$
2	Max pooling	$28 \times 28 \times 36$	3×3	$24 \times 24 \times 64$
3	Convolution layer	$24 \times 24 \times 64$	6×6	$20 \times 20 \times 64$
4	Max pooling	$20 \times 20 \times 64$	3×3	$12 \times 12 \times 64$
5	Fully connected layer	$12 \times 12 \times 64$	5×5	$8 \times 8 \times 64$
6	Fully connected layer	$8 \times 8 \times 64$	2×2	2×1
7	Softmax layer	2×1 result	-	Identification output

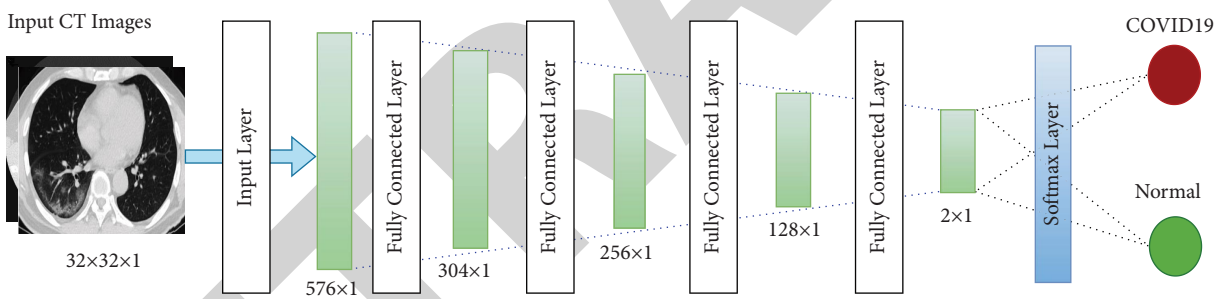

Figure 5: DNN architecture.

Table 2: DNN parameters.

Layer	Type	Input	Output
1	Input layer	$24 \times 24 \times 1$	576×1
2	Fully connected layer	576×1	304×1
3	Fully connected layer	304×1	256×1
4	Fully connected layer	256×1	128×1
5	Fully connected layer	128×1	64×1
6	Softmax layer	2×1	Identification output

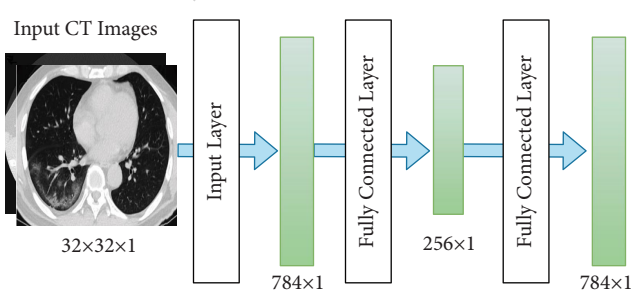

Figure 6: Sparse autoencoder.

data. However, this convolution structure has difficulty in training the autoencoder in a convolutional way because of the high computational load and complex architecture [41].

The architecture of the SAE neural network is shown in Figure 7. The hidden layer includes an individual hidden layer of the scattered autoencoder. Identification of pulmonary nodes is considered an image classification problem. Each scattered autoencoder removes the decoded layer by the end of the training process. Then, the encoding process is started to train the next output of SAE.

3.2.6. Loss Functions for Neural Network. In the loss function, the last element is used to restrain overfitting for the training procedure, and the aggregate of weights is distributed by n multiplied by 2. Dropout is also used to restrain overfitting. Random neurons are protected prior to backpropagation. Thus, updating parameters of shaded neurons is not allowed. DNN requires a large number of data as input for the neural network, and this condition requires large memory storage. Min_batch is used in the

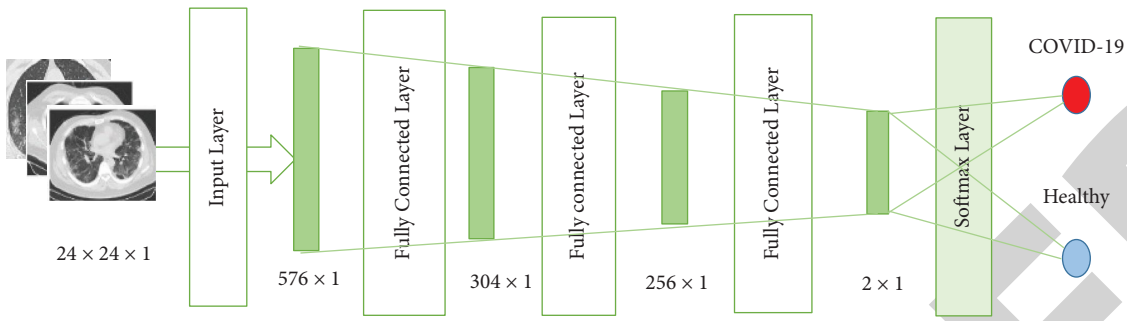

Figure 7: SAE architecture.

backpropagation to accelerate the updating process of parameters for solving the aforementioned issue. The loss function is formulated and explained as follows:

$$C(w,b) \equiv \frac{1}{2n}\sum_{x}\|y(x)-a\|^2 + \frac{1}{2n}\lambda\sum_{w} w^2. \quad (2)$$

Here, C represents the total function, w represents the weight, b represents the bias, n represents the training dataset instance numbers, and x is an input parameter that represents the values of the image pixel and output. The backpropagation method is adopted in DNN to update the b weight wand for enhancing accuracy by reducing the difference between the expected and actual values.

The leaky ReLU represents a neural network's activation function that helps improve the nonlinear modeling ability. The ReLU activation function is formulated as follows:

$$y = \begin{cases} x, & \text{if } x \geq 0, \\ 0, & \text{if } x < 0, \end{cases} \quad (3)$$

where x represents the weighted priority multiplication result and weight wand added to the y element to obtain the activation function output. The ReLU derivative can be 0 if $x < 0$; otherwise, it can be 1. ReLU can remove the gradient sigmoid activation function problem. However, the phenomenon of neuronal death can occur as the updating weight is stopped because of the continuous updating in the training process. In this situation, the ReLU output can be more than zero, which means the neural network output is offset.

This problem can be solved by applying the leaky ReLU method. This method is an activation function that can be represented as follows:

$$y = \begin{cases} x & \text{if } x \geq 0, \\ ax & \text{if } x < 0, \end{cases} \quad (4)$$

where a is set to 0.1. Notably, a is a fixed value in leaky ReLU, while a is not fixed in the ReLU.

3.2.7. Data Augmentation. Data augmentation refers to the differences in sizes of lung patterns. The size of lung patterns is regularly set to 28×28 to extract the aspects of the lung patterns, including the size and texture. Binary processing is used to obtain lung pattern images [42]. They can be approximately outlined. Subsequently, the lung pattern value is preserved as pixels in the advanced image. Finally, any noise perturbation that surrounds the lung patterns is removed [43]. The neural network training entails a large number of positive and negative samples. In this study, we first process the images' translation, flip, and rotation. Then, we insert them as the input of the neural network to maximize the size of the sample data. The large size of the sample data can positively affect the performance of the neural network in terms of enhancing the training process, improving the accuracy of testing, decreasing the loss function, and increasing the efficacy of the neural network.

4. Experimental Results and Discussion

This section presents the experiment configuration settings and the outcomes of the proposed systems based on the classification of the CT scan images. Two main subsections are presented as follows:

4.1. Experiment Settings. Caffe, a deep learning model based on expressiveness, modularity, and speed, is used in this research. A total of 746 CT scans are used, which comprise 349 CT scans for COVID-19 hospitalized individuals' CT scans for infected pneumonia patients, and 397 CT scans for healthy persons with no apparent chest infection. The first website publicly offers reference documents, radiology images, and patients' cases. The latter contains open access datasets with a wide archive of medical images with public viewing. The second website is a partnership on radiology. A total of 20% of the training data, which comprise approximately 448 images, are utilized for cross-validation. The same set of data applies to the three distinct architectures of the network.

The learning rate of the CNN is set to 0.02, and the batch size is set to 24 during network training to obtain the best results. The process of convolution and sampling is performed twice in the network. The kernel size is 6, and two layers of convolution are considered and consist of 36 filters. The pooling layer has a kernel size of two. The purpose of a dropout layer is being used to avoid overfitting. At least a softmax function with two fully connected layers is considered. The DNN contains a completely connected layer.

The 2D data input of 24×24 mapped into 576×1 is presented as an input image in the first layer. An entirely

connected layer of 304×1 is used in the second layer. The third layer is fully connected to 256×1. A dropout layer will be considered after the third layer, which includes a parameter of 0.5. Units will also be hidden in 30%. The fully connected layer is the fourth layer of 128×1 with ReLU as an activation function. The SAE structure also consists of a completely connected layer. The input and output neurons of the automotive encoder are the same. Thus, the autoencoder is the same as

$$H_{w,b}(x) = x. \tag{5}$$

Here, w and b are the crankiness and weight, respectively; x is the input factor. The neural networks correspond to the input image coding. The self-encoder creates the hidden layer, and it is primarily utilized in the identification process. This way cancels the self-encoder decoding portion. The coding factor of the SAE is utilized during training. The encoder creates a stack encoding component to add a confident number of training courses to the identification of the initializing neural network. The artifact characteristics are not evident after the encoder the image edge is formed. However, this condition triggers some reduction in classification accuracy. Table 3 offers information on the SAE.

Table 3: SAE parameters.

Layer	Type	Input	Output
1	Input layer	$24 \times 24 \times 1$	576×1
2	Fully connected layer	576×1	304×1
3	Fully connected layer	304×1	256×1
4	Fully connected layer	256×1	128×1
5	Softmax layer	2×1	Identification output

Table 4: Deep learning model results.

Deep learning models	Accuracy (%)	Sensitivity (%)	Specificity (%)
CNN	88.30	87.65	87.97
DNN	86.23	84.41	86.77
SAE	86.75	85.62	87.84

4.2. COVID-19 Classification Results. This section presents the classification of CT COVID-19 and normal cases. The classification results are based on the experiment outcomes of three deep learning models: CNN, DNN, and SAE. Accuracy, sensitivity, and specificity are used as evaluation indicators for the performance of the three mentioned models. The classification results of the three models are presented in Table 4.

The results show that the CNN has a sensitivity of 87.65%, a specificity ratio of 87.97%, and an accuracy of 88.30%. The accuracy, sensitivity, and specificity of DNN are 86.23%, 84.41%, and 86.77%, respectively. The good result is due to the fact that the operation of the convolution layer can be defined by the texture and shape of two distinct dimensions. A convolution kernel shares constraints throughout the procedure of convolution in diverse weights for diverse image features with a convolution kernel. Thus, the convolution operation is less than the fully connected operating conditions in terms of parameter number. The DNN has poor precision and sensitivity than the SAE. However, the former is better than the latter, given that it has a specificity ratio of 87.84%.

Better specificity provides a greater degree of detection of COVID-19 within a single set of data, and this feature can be more useful in slightly earlier diagnosis of pulmonary pathways. However, DNN increases the number of false-positive COVID-19 cases to a certain degree. The DNN and SAE are completely connected networks, but different generating methods are possible. In encoder training, SAE is generated by parsing; the DNN is generated directly from formation through the completely connected layer.

Unlike the previously published works that mainly depend on employing pretrained models in identifying the COIVD-19, we proposed to build a customized CNN model composed of two convulsion layers to reduce the number of hyperparameters and the model's complexity. On the contrary, the pretrained models such as ResNet and DenseNet have more complex architecture, which can present high computational load and execution time during training and validation processes. Furthermore, it is very difficult to change the main structure of the pretrained model by adding or removing some layers to find an optimal model's structure.

Certainly, the computing time of the model is an important problem in identifying the COVID-19 virus, where having a customized CNN model that required fewer CT images can significantly help the doctors in the early diagnosis of the COVID-19, especially when there is a very limited number of CT images with confirmed COVID-19 infection.

Finally, to compare the testing time required to produce the final decision per image of the proposed models and the current state-of-the-art works. Table 5 lists the seconds' testing time per image to produce the final prediction results. From this table, one can see that the proposed models have outperformed all the current state-of-the-art works in terms of generating the final decision. Although Kassani et al. [44] achieved a faster testing time than the proposed DNN model, it has inferior results than the other two models (CNN and SAE model).

The evaluation scenario with other benchmarked studies is presented in Table 6. For a fair comparison, the experiments in this study are done on the basis of the same dataset and hyper tuning parameters. However, the experimental results and data of the CNN parameters can still be improved. CT lung COVID-19 image cases that include normal and COVID-19 samples are shown in Figure 8.

Table 6 shows that the benchmarking process that determines the efficiency and reliability is the most essential step in common medical image processing and diagnosis research. Benchmarking is achieved by utilizing the best recent prediction COVID-19 methods based on CT lung COVID-19 images based on deep learning approaches in the literature. As aforementioned, further evaluation of the present COVID-19 prediction system in CT lung COVID-19

Table 5: The comparison of the proposed models with the current state-of-the-art works in terms of testing time.

Approaches	Testing time (s)
Wang et al. (2020) [16]	10
Xu et al. (2020) [22]	30
Kassani et al. (2020) [44]	0.03
CNN	0.002
DNN	0.04
SAE	0.02

Table 6: Comparison with benchmarked studies on CT lung COVID-19 images.

Study/year	Dataset (samples no.)	Accuracy (%)	Sensitivity (%)	Specificity (%)
Zhao et al. [42](2020)	275 CT scans	84.7	N/A	N/A
Amyar et al. [45] (2020)	1044 CT collected from 3 datasets	86	94	79
He et al. [46] (2020)	349 CT scans	86	N/A	N/A
Our proposed (CNN)	746 chest CT scans	88.30	87.65	87.97
Our proposed (DNN)	746 chest CT scans	86.23	84.41	86.77
Our proposed (SAE)	746 chest CT scans	86.75	85.62	87.84

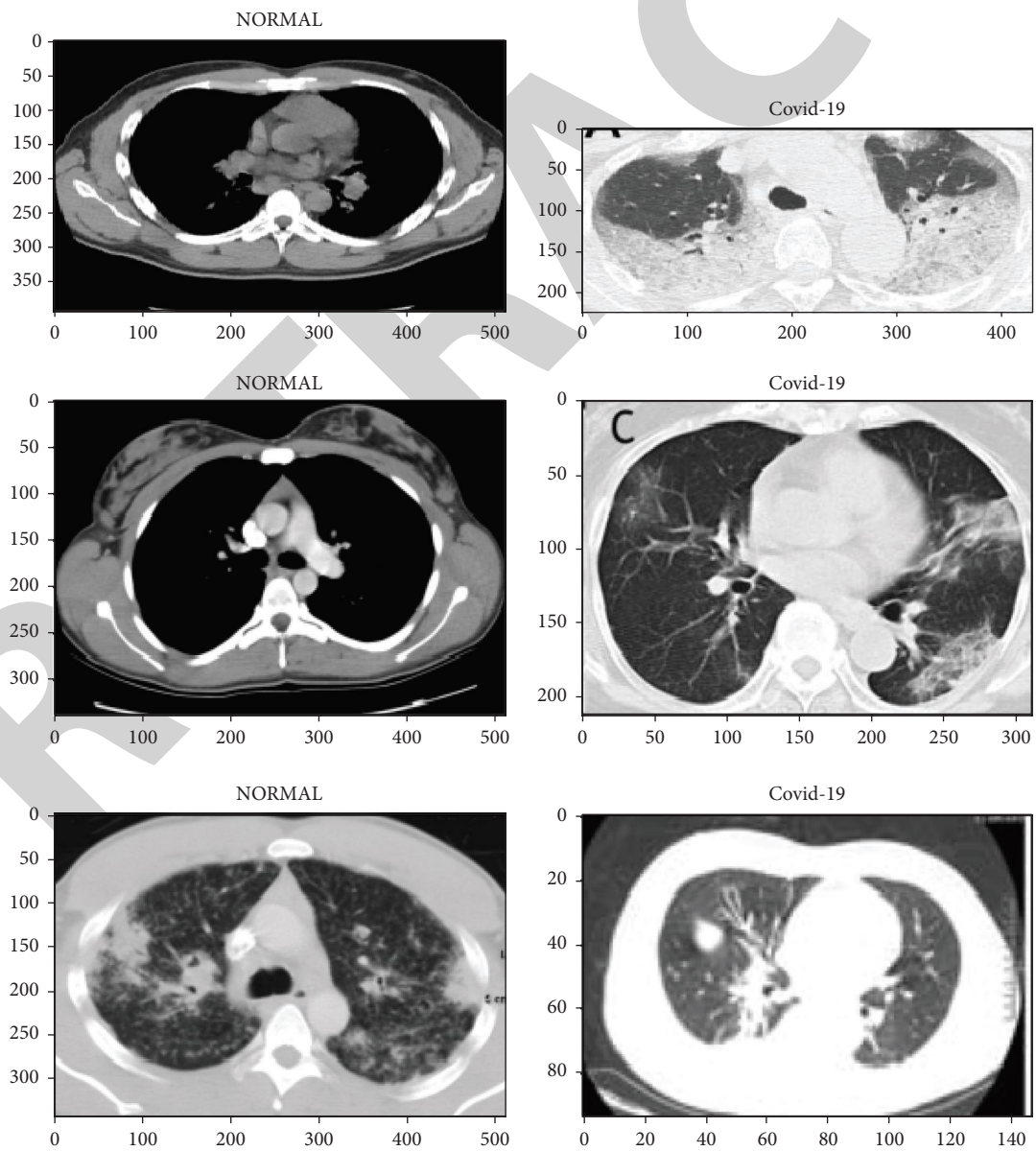

Figure 8: CT lung COVID-19 image cases that include normal and COVID-19 samples.

images is made by benchmarking it with the best three studies from the CT lung COVID-19 image classification [42, 45, 46]. Table 6 summarizes the results after benchmarking. Common trends of performance and major measurements are classification accuracy rate (CAR), sensitivity (Sen.), and specificity (Spe.). The CNN scores an accuracy of 88.30%, a specificity ratio of 87.97%, and a sensitivity of 87.65%. The best performance in all benchmarked studies is observed with an accuracy of 86%, a sensitivity of 94%, and a specificity ratio of 79%. The proposed system presents an acceptable and significant sensitivity performance compared with the benchmarked studies with high sensitivity ratio. Nevertheless, the proposed system outperforms all the benchmarked studies in terms of accuracy and specificity performance.

5. Conclusion

This study aims to explore and extensively test three deep learning models. The prediction is compared for normal and COVID-19 cases by using chest CT images. Several preprocessing stages are applied to CT images. First, data segmentation is applied to isolate the region of interest from the CT image background. Second, a data augmentation technique is used to increase the volume of CT images. Accordingly, adequate input can be provided for the deep learning models for directly affecting the performance of classification. The test outcomes indicate that CNN achieves the ideal execution compared with the DNN and SAE. Moreover, the CNN is superior to other models in terms of performance with an accuracy of 88.30%, a sensitivity of 87.65%, and a specificity ratio of 87.97%. Neural network layers in this study are comparatively small due to the constraints of the datasets. The proposed approach is anticipated to increase the accuracy of the other database. Furthermore, deep learning approaches can be used to assist physicians in mitigating this newly spreading disease with CT images to identify and distinguish early COVID-19 patients, recognize and segment images in the medical field, and predict the results of treating them. We also show that too excellent sensitivity can be obtained from CT images, which can address the need for early-stage detection of infected persons to limit the progression of the virus. We will further validate the performance of our technique on a large dataset. The process can be generalized for the good implementation of CAD frameworks for future medical image processes. This study is limited to three models as diagnosis systems. However, additional deep learning models will be explored in the future.

Data Availability

The datasets generated during and/or analysed during the current study are available in the Barrett, J.F. and Keat, N., 2004. Artifacts in CT: recognition and avoidance. Radiographics, 24(6), pp.1679-1691.

Ethical Approval

This article does not contain any studies with human participants or animals performed by any of the authors.

Conflicts of Interest

The authors declare that there are no conflicts of interest.

Acknowledgments

This work was partially supported by the Korea Medical Device Development Fund grant funded by the Korean Government (the Ministry of Science and ICT, the Ministry of Trade, Industry and Energy, the Ministry of Health and Welfare, and the Ministry of Food and Drug Safety) (KMDF_PR_20200901_0095 and NRF-2020R1A2C1014829) and the Soonchunhyang University Research Fund.

References

[1] M. Toğaçar, N. Muzoğlu, B. Ergen, B. S. B. Yarman, and A. M. Halefoğlu, "Detection of COVID-19 findings by the local interpretable model-agnostic explanations method of types-based activations extracted from CNNs," *Biomedical Signal Processing and Control*, vol. 71, Article ID 103128, 2022.

[2] A. Bhattacharyya, D. Bhaik, S. Kumar, P. Thakur, R. Sharma, and R. B. Pachori, "A deep learning based approach for automatic detection of COVID-19 cases using chest X-ray images," *Biomedical Signal Processing and Control*, vol. 71, Article ID 103182, 2022.

[3] K. Roosa, Y. Lee, R. Luo et al., "Real-time forecasts of the COVID-19 epidemic in China from february 5th to february 24th, 2020," *Infectious Disease Modelling*, vol. 5, pp. 256–263, 2020.

[4] T. Wang, A. Paschalidis, Q. Liu, Y. Liu, Y. Yuan, and I. C. Paschalidis, "Predictive models of mortality for hospitalized patients with COVID-19: retrospective cohort study," *JMIR Medical Informatics*, vol. 8, no. 10, Article ID e21788, 2020.

[5] A. S. Kardos, J. Simon, C. Nardocci et al., "The diagnostic performance of deep-learning-based CT severity score to identify COVID-19 pneumonia," *British Journal of Radiology*, vol. 95, no. 1129, Article ID 20210759, 2022.

[6] A. S. Al-Waisy, M. A. Mohammed, S. Al-Fahdawi et al., "COVID-DeepNet: hybrid multimodal deep learning system for improving COVID-19 pneumonia detection in chest X-ray images," *Computers, Materials & Continua*, vol. 67, no. 2, 2021.

[7] B. Majhi, R. Thangeda, and R. Majhi, "A review on detection of COVID-19 patients using deep learning techniques," in *Assessing COVID-19 and Other Pandemics and Epidemics Using Computational Modelling and Data Analysis*, pp. 59–74, Springer, New York City, 2022.

[8] O. I. Obaid, M. A. Mohammed, and S. A. Mostafa, "Long short-term memory approach for Coronavirus disease predicti," *Journal of Information Technology Management*, vol. 12, pp. 11–21, 2020.

[9] Z. A. A. Alyasseri, M. A. Al-Betar, I. A. Doush et al., "Review on COVID-19 Diagnosis Models Based on Machine Learning and Deep Learning Approaches," *Expert Systems*, vol. 39, Article ID e12759, 2021.

[10] J. Ruano, J. Arcila, D. R. Bucheli et al., "Deep learning representations to support COVID-19 diagnosis on CT-slices," *Biomedica*, vol. 42, no. 2, 2022.

[11] M. Ragab, K. Eljaaly, N. A. Alhakamy et al., "Deep ensemble model for COVID-19 diagnosis and classification using chest CT images," *Biology*, vol. 11, no. 1, p. 43, 2022.

[12] J. N. Hasoon, A. H. Fadel, R. S. Hameed et al., "COVID-19 anomaly detection and classification method based on supervised machine learning of chest X-ray images," *Results in Physics*, vol. 31, Article ID 105045, 2021.

[13] V. G. Biradar, H. C. Nagaraj, and H. A. Sanjay, "Leveraging X-ray and CT scans for COVID-19 infection investigation using deep learning models: challenges and research directions," in *Emerging Research in Computing, Information, Communication and Applications*, pp. 289–306, Springer, New York City, 2022.

[14] Q. Mastoi, M. S. Memon, A. Lakhan et al., "Machine Learning-Data Mining Integrated Approach for Premature Ventricular Contraction Prediction," *Neural Comput & Applic*, vol. 33, 2021.

[15] A. H. Barshooi and A. Amirkhani, "A novel data augmentation based on Gabor filter and convolutional deep learning for improving the classification of COVID-19 chest X-Ray images," *Biomedical Signal Processing and Control*, vol. 72, Article ID 103326, 2022.

[16] S. Wang, B. Kang, J. Ma et al., "A deep learning algorithm using CT images to screen for Corona virus disease (COVID-19)," *European Radiology*, vol. 31, no. 8, pp. 6096–6104, 2021.

[17] H. S. Maghdid, A. T. Asaad, K. Z. Ghafoor, A. S. Sadiq, S. Mirjalili, and M. K. Khan, "Diagnosing COVID-19 pneumonia from x-ray and CT images using deep learning and transfer learning algorithms," *Multimodal Image Exploitation and Learning*, vol. 11734, Article ID 117340E, 2021.

[18] U. Ozkaya, S. Ozturk, and M. Barstugan, "Coronavirus (COVID-19) Classification Using Deep Features Fusion and Ranking Technique," in *Big Data Analytics and Artificial Intelligence against COVID-19: Innovation Vision and Approach*Springer, New York City, 2020.

[19] P. K. Sethy and S. K. Behera, *Detection of Coronavirus Disease (Covid-19) Based on Deep Features*, Preprints, Basel, Switzerland, 2020.

[20] F. Shan, Y. Gao, J. Wang et al., "Abnormal lung quantification in chest CT images of COVID-19 patients with deep learning and its application to severity prediction," *Medical Physics*, vol. 48, no. 4, pp. 1633–1645, 2021.

[21] L. Li, L. Qin, Z. Xu et al., "Artificial Intelligence Distinguishes COVID-19 from Community Acquired Pneumonia on Chest CT," *Radiology*, vol. 296, no. 2, Article ID 200905, 2020.

[22] X. Xu, X. Jiang, C. Ma et al., "A Deep Learning System to Screen Novel Coronavirus Disease 2019 Pneumonia," *Engineering*, vol. 6, no. 10, 2020.

[23] Y. Song, S. Zheng, L. Li et al., "Deep learning enables accurate diagnosis of novel Coronavirus (COVID-19) with CT images," *IEEE/ACM Transactions on Computational Biology and Bioinformatics*, vol. 18, no. 6, pp. 2775–2780, 2021.

[24] A. M. Hasan, M. M. Al-Jawad, H. A. Jalab, H. Shaiba, R. W. Ibrahim, and A. a. R. Al-Shamasneh, "Classification of covid-19 Coronavirus, pneumonia and healthy lungs in CT scans using Q-deformed entropy and deep learning features," *Entropy*, vol. 22, no. 5, p. 517, 2020.

[25] J.-j. Zhang, X. Dong, Y. Cao, Y. Yuan, and Y. Yang, Y. Ya bin, Y. Q. Yan, C. A. Akdis, Y. D. Gao, A. Cezmi, and Y. A. dong Gao, "Clinical characteristics of 140 patients infected with SARS-CoV-2 in Wuhan, China," *Allergy*, vol. 75, no. 7, pp. 1730–1741, 2020.

[26] Y. Fang, H. Zhang, J. Xie et al., "Sensitivity of Chest CT for COVID-19: Comparison to RT-PCR," *Radiology*, vol. 296, no. 2, Article ID 200432, 2020.

[27] J. O. B. Diniz, D. B. P. Quintanilha, and A. C. Santos Neto, "Segmentation and quantification of COVID-19 infections in CT using pulmonary vessels extraction and deep learning," *Multimedia Tools and Applications*, vol. 80, no. 19, pp. 29367–29399, 2021.

[28] J. F. Barrett and N. Keat, "Artifacts in CT: recognition and avoidance," *RadioGraphics*, vol. 24, no. 6, pp. 1679–1691, 2004.

[29] A. Mansoor, U. Bagci, B. Foster et al., "Segmentation and image analysis of abnormal lungs at CT: current approaches, challenges, and future trends," *RadioGraphics*, vol. 35, no. 4, pp. 1056–1076, 2015.

[30] K. L. Hua, C. H. Hsu, S. C. Hidayati, W. H. Cheng, and Y. J. Chen, "Computer-aided classification of lung nodules on computed tomography images via deep learning technique," *OncoTargets and Therapy*, vol. 822 pages, 2015.

[31] F. Ciompi, K. Chung, S. J. Van Riel et al., "Towards automatic pulmonary nodule management in lung cancer screening with deep learning," *Scientific Reports*, vol. 7, no. 1, p. 46479, 2017.

[32] I. D. Apostolopoulos and T. A. Mpesiana, "Covid-19: automatic detection from x-ray images utilizing transfer learning with convolutional neural networks," *Physical and Engineering Sciences in Medicine*, vol. 43, no. 2, 2020.

[33] A. Abbas, M. M. Abdelsamea, and M. M. Gaber, "Classification of COVID-19 in chest X-ray images using DeTraC deep convolutional neural network," *Applied Intelligence*, vol. 51, no. 2, pp. 854–864, 2021.

[34] R. L. Kumar, F. Khan, S. Din, S. S. Band, A. Mosavi, and E. Ibeke, "Recurrent neural network and reinforcement learning model for COVID-19 prediction," *Frontiers in Public Health*, vol. 9, Article ID 744100, 2021.

[35] A. Badawi and K. Elgazzar, "Detecting Coronavirus from chest X-rays using transfer learning," *COVID*, vol. 1, no. 1, pp. 403–415, 2021.

[36] M. E. H. Chowdhury, T. Rahman, A. Khandakar et al., "Can AI help in screening viral and COVID-19 pneumonia?" *IEEE Access*, vol. 8, pp. 132665–132676, 2020.

[37] A. H. Elsheikh, A. I. Saba, H. Panchal, S. Shanmugan, N. A. Alsaleh, and M. Ahmadein, "Artificial intelligence for forecasting the prevalence of COVID-19 pandemic: an overview," *Healthcare*, vol. 9, no. 12, p. 1614, 2021.

[38] T. T. Nguyen, *Artificial Intelligence in the Battle against Coronavirus (COVID-19): A Survey and Future Research Directions*, Preprint, Basel, Switzerland, 2020.

[39] A. Ng, "Sparse auto-encoder," *CS294A Lecture notes*, vol. 72, pp. 1–19, 2011.

[40] J. Masci, U. Meier, D. Ciresan, and J. Schmidhuber, "Stacked convolutional auto-encoders for hierarchical feature extraction," in *Proceedings of the International Conference on Artificial Neural Networks*, pp. 52–59, Springer, Espoo, Finland, June 2011.

[41] S. Chen, H. Liu, X. Zeng, S. Qian, J. Yu, and W. Guo, "Image Classification Based on Convolutional Denoising Sparse Auto-Encoder," *Mathematical Problems in Engineering*, vol. 2017, Article ID 5218247, 2017.

[42] P. Afshar, S. Heidarian, N. Enshaei et al., "COVID-CT-MD, COVID-19 computed tomography scan dataset applicable in machine learning and deep learning," *Scientific Data*, vol. 8, no. 1, p. 121, 2021.

[43] E. Bhattacharya and D. Bhattacharya, "A review of recent deep learning models in COVID-19 diagnosis," *European Journal of Engineering and Technology Research*, vol. 6, no. 5, pp. 10–15, 2021.

[44] S. Hosseinzadeh Kassania, P. Hosseinzadeh Kassanib, M. J. Wesolowskic, K. A. Schneidera, and R. Detersa, "Automatic detection of Coronavirus disease (COVID-19) in

Hindawi
Journal of Healthcare Engineering
Volume 2023, Article ID 9865036, 1 page
https://doi.org/10.1155/2023/9865036

Retraction

Retracted: Based on the Auxiliary Effect of X-Ray in the Treatment of Severe Pneumonia in Children with Arterial and Venous Blood Gas

Journal of Healthcare Engineering

Received 10 October 2023; Accepted 10 October 2023; Published 11 October 2023

This article has been retracted by Hindawi following an investigation undertaken by the publisher [1]. This investigation has uncovered evidence of one or more of the following indicators of systematic manipulation of the publication process:

(1) Discrepancies in scope
(2) Discrepancies in the description of the research reported
(3) Discrepancies between the availability of data and the research described
(4) Inappropriate citations
(5) Incoherent, meaningless and/or irrelevant content included in the article
(6) Peer-review manipulation

The presence of these indicators undermines our confidence in the integrity of the article's content and we cannot, therefore, vouch for its reliability. Please note that this notice is intended solely to alert readers that the content of this article is unreliable. We have not investigated whether authors were aware of or involved in the systematic manipulation of the publication process.

In addition, our investigation has also shown that one or more of the following human-subject reporting requirements has not been met in this article: ethical approval by an Institutional Review Board (IRB) committee or equivalent, patient/participant consent to participate, and/or agreement to publish patient/participant details (where relevant).

Wiley and Hindawi regrets that the usual quality checks did not identify these issues before publication and have since put additional measures in place to safeguard research integrity.

We wish to credit our own Research Integrity and Research Publishing teams and anonymous and named external researchers and research integrity experts for contributing to this investigation.

The corresponding author, as the representative of all authors, has been given the opportunity to register their agreement or disagreement to this retraction. We have kept a record of any response received.

References

[1] H. Guo, H. Zhang, and F. Li, "Based on the Auxiliary Effect of X-Ray in the Treatment of Severe Pneumonia in Children with Arterial and Venous Blood Gas," *Journal of Healthcare Engineering*, vol. 2022, Article ID 5786630, 13 pages, 2022.

Hindawi
Journal of Healthcare Engineering
Volume 2022, Article ID 5786630, 13 pages
https://doi.org/10.1155/2022/5786630

Research Article

Based on the Auxiliary Effect of X-Ray in the Treatment of Severe Pneumonia in Children with Arterial and Venous Blood Gas

Hui Guo,[1] **Hua Zhang**,[1] **and Fuping Li**[2]

[1]*Department of Pediatric, Ji'an Matemal and Child Health Hospital, Jian 343000, Jiangxi, China*
[2]*Department of Radiology, Ji'an Matemal and Child Health Hospital, Jian 343000, Jiangxi, China*

Correspondence should be addressed to Hui Guo; 2111816103@e.gzhu.edu.cn

Received 11 January 2022; Revised 3 March 2022; Accepted 4 March 2022; Published 30 March 2022

Academic Editor: Nima Jafari Navimipour

Pediatric severe pneumonia clinical is a conceptual term for the diagnosis and treatment of pediatric clinical diseases. At present, domestic and foreign standards for clinical diagnosis of severe pneumonia, which is a childhood disease, are still inconsistent. At present, the first book of the main pediatric medical textbook in the society interprets the clinical definition of severe pneumonia in children as follows: severe pneumonia refers to pulmonary function in heart failure or other comorbidities in other important organs except the lung. This article is based on X-ray medical film and television examinations, through the analysis of arterial and venous blood gas in children with severe pneumonia to play a certain role in adjuvant therapy for children with pneumonia. Prospective clinical studies have found significant changes in the function of auxiliary coagulation and blood fibrinolysis indicators in patients with severe pneumonia in late childhood. The obvious difference between the pretreatment and the late-stage treatment for 1 week and the direct influence on the blood gas quantitative analysis and liver function of advanced patients provide a scientific basis for the diagnosis of typical advanced childhood severe pneumonia patients with adjuvant anticoagulant therapy. The data analysis of the clinical laboratory found that the blood coagulation and fibrinolysis functions of the typical patients with severe pneumonia in the typical late stage of childhood were significantly activated, and the anticoagulant antibody substances were significantly reduced, fibrinolytic coagulation inhibitors and anticoagulants are significantly increased, fibrinolytic activators are significantly reduced, and the body is in a procoagulant state for a long time. Adjuvant anticoagulation therapy through quantitative analysis of blood gas in patients can not only effectively increase the success rate of early treatment of typical late-stage severe pneumonia in children by 64.28% but also significantly reduce the inflammatory coagulation indexes of patients with late-stage severe pneumonia in children. The functions of coagulation, anticoagulation, and coagulation fibrinolysis have been significantly restored. The advantages of X-ray-based adjuvant treatment of severe pneumonia in children with arteriovenous blood gas are good contrast, clear imaging, and clear development of fine lesions or thick parts, and objective records are kept for comparison during review and consultation and discussion. The disadvantage is that the operation is more complicated, and it is not convenient to observe the activity function of the organ.

1. Introduction

Pneumonia bacterial infection disease is one of the most common pulmonary respiratory and nervous system diseases infection classification diseases, and many kinds of disease classification and diagnostic criteria have been developed clinically. It can be classified according to the type of pneumonia infection of various pneumonia-infected pathogens and can be divided into chronic pneumonia infection with bacterial viral tuberculosis pneumonia, viral pneumonia with bacterial tuberculosis pneumonia, and mycoplasmal viral tuberculosis pneumonia. It can also be classified according to the ways in which various types of pneumonia bacterial infections can be transmitted and can be divided into three types, pneumonia infectious tuberculosis pneumonia (community-acquired pneumonia, CAP) is obtained through adult community treatment, the hospital uses the treatment method to obtain pneumonia infectious tuberculosis pneumonia (hospital-acquired pneumonia, hap), and according to the inherent correlation of the human

lung respiratory system different types of acquired pneumonia (ventilator-associated pneumonia, VAP) and so on. Regardless of the clinical classification, the diagnosis of pneumonia mainly depends on medical history, clinical manifestations, and imaging examinations, especially imaging examinations, which can distinguish pneumonia from other acute respiratory inflammations with similar symptoms. At present, the first choice for the diagnosis of pneumonia is a chest X-ray (CXR). In larger hospitals, digital radiography (DR) with better image quality is generally used; in smaller hospitals, ordinary chest radiographs may still be used due to conditions.

The lungs are vital respiratory organs that continue to keep in touch with the external environment, always face the threat of various environmental pathogenic factors, and are plagued by infectious diseases such as pneumonia. As one of the most common respiratory diseases, pneumonia is a high incidence and common disease at all ages. Its pathogen can come from the external environment or from the upper respiratory tract, which is the passage between the lung and the external environment. At present, the clinical imaging method for diagnosing pneumonia is mainly radiography, in which chest X-ray is often used as the first choice, and chest CT is considered the gold standard. Therefore, this article is based on X-rays to diagnose severe pneumonia in children and study the effect of blood gas analysis on the adjuvant treatment of severe pneumonia in children.

In recent years, blood gas analysis and determination have been carried out on the treated infants with pneumonia in a timely manner, and its role in the treatment is now discussed. Judging whether it is complicated by respiratory failure, infants with pneumonia complicated by respiratory failure often have a poor prognosis, so early diagnosis and timely rescue should be made. Observation confirmed that the changes of blood gas in infants and young children with pneumonia were related to the size of the lesions, the presence or absence of mutations, and whether viral pneumonia was secondary to bacterial infection.

This is because the incidence of severe pneumonia in children has increased and the mortality rate is high. The use of X-rays to diagnose and analyze blood to treat pneumonia has become an important method. Wen-bo has proposed the diagnosis of microcomputed tomography (MCT). Computer tomography uses a microfocused X-ray tube and a cone X-ray beam, which can display sample images from more than 360 angles. The same image sample can directly obtain the real isotropic and similarity of the smaller volume three-dimensional image, improve the three-dimensional spatial image resolution, and reduce the comprehensive use of radiation, but the application field is limited [1]. Hsinlj found the symptoms of children diagnosed with severe pneumonia in the early stage; CT clinical symptoms and examination pathological signs and analysis summary of CT examination are important clinical diagnostic and imaging methods for diagnosing severe pneumonia in children. Its clinical features are mainly that the area of the small intestine is thicker and more uniform, and the intestinal wall is gradually calcified. And on this basis, its cells appear unevenly into the tube wall and then into the soft tissue to form a larger thickness or round shadow of the mass. But this test can only be used for patients with chronic irritable bowel syndrome [2]. The cut-off value in the Van D statistical model is obtained from the ROC chart and subjected to discriminant analysis. The diameter and CT changes of the entropy and uniformity values are evaluated by a stepwise selection method. The critical values of the parameters are determined and the statistical model of the sample to evaluate the efficiency is analyzed and used for RECIST verification and discriminant analysis to create the Kaplan–Meier survival curve, but the diagnostic method is more complicated and difficult to apply to the actual situation [3]. Fu W reported a dilated X-ray framing camera based on a gated microchannel plate (MCP) and time dilation technique. The camera expands the electronic signal with a pulsed photocathode (PC) for high temporal resolution. The temporal resolution of the camera is characterized by short X-ray pulses produced by a laser beam focused on a flat iron target. The fringe raw images are obtained, and the experimental results show that the temporal resolution of the camera is better than 10 ps [4]. The Rohr J dual-source scanner is interested in the pathological type and clinical distance of severe pneumonia in children. The quantitative parameters of dual-source CT can indirectly reflect the pathological type of pneumonia and play an important role in the diagnosis of pneumonia. However, due to its expensive assembly cost, it is difficult to spread and use in a large area [5]. Stasevych M uses the grid-shaped sacroiliac combined with a radiofrequency neuron (PSRN) recommended by the study to treat severe pneumonia in children. CT-guided PSRN is safer and more effective in reducing the overall pain intensity in the treatment of arthralgia and pelvic pain in AS patients. The principle of improving the physical function and movement of the spine has been replaced by today's advanced equipment [6]. Wolff K D explored the clinical importance of chest computed tomography (CT) in the surgical treatment of pneumonia, but the extent of treatment is still limited [7].

The clinical pathology research report divides the two groups of children with typical severe pneumonia and acute patients into two groups, the first group is severe pneumonia benign, and the second group is severe pneumonia malignant group. Collect the serum ultrasound images of the two groups, respectively, and then compare the image characteristics (including the size, boundary, morphology of the nodule, the level of the mucosal echo halo within the nodule, the peripheral echo halo, the vertical and horizontal contrast, the calcification of the mucosal inside the nodule, the density change of the vascular flow pattern, and the chest X-ray examination), and the average data of children's blood gas density analysis step by step. The analysis data obtained by the patient are gradually collected by downloading the ACCESS software program data; after that, the accuracy of the statistical analysis results is analyzed through the SPSS19.0 software program, and the analysis results obtained by the patients are analyzed and displayed in the form of calculation of the average value of accuracy and ±standard deviation, respectively. For children's serum TSH and the statistical values of the image characteristics of the serum

ultrasound image examination group, the χ^2 test was carried out to determine the difference between the two groups of data. And to analyze and compare the accuracy difference data between the two groups of data, establish the regression analysis model of the logistic group of the nonspecific condition group, and use the ultrasonic forward step-by-step tracking analysis method to analyze the regression model step by step. Main functions of the advanced arterial blood gas analysis training model: this model is composed of a simulated hand model and an electronic blood circulation device. It has real blood flow, can palpate the radial artery, and feels real. Pulse speed and strength can be adjusted.

2. Principle and Overview

2.1. Pathology of Pneumonia. According to the different causes of pneumonia, tracheal pneumonia caused by various biochemical factors is referred to as similar bacterial tracheal pneumonia, viral tracheal pneumonia, mycoplasma tracheal pneumonia, fungal tracheal pneumonia, and various types of parasitic tracheal pneumonia. The types of tracheal pneumonia caused by different physical and chemical environmental factors are referred to as radioactive tracheal pneumonia, oil-like tracheal pneumonia, inhalation tracheal pneumonia, or allergic tracheal pneumonia, respectively. According to the different regions and scopes of the inflammatory lesions of thoracic pneumonia that may be involved, it can be subdivided into large-scale pneumonia similar to lobular nonbronchitis, lobular nonbronchitis pneumonia, and various types of pneumonia similar to segmental nonbronchitis [8, 9]. According to the main source of infection and nature of its pneumonia lesions, it can generally be roughly divided into serous, fibrinous, purulent, hemorrhagic, caseous, and various types of punctate granulomatous and edematous tracheal pneumonia. In clinical disease, it usually refers to the selection of the latest clinical names of pneumonia diseases that can accurately reflect the early characteristics of acute tracheal pneumonia lesions and the nature of lung inflammation lesions and give them accurate names in the hospital. The most common clinical symptoms of acute tracheal pneumonia in the period of vigorous onset of juvenile pneumonia are acute pneumonia accompanied by chronic pneumonia with small bronchitis, which can also be called pneumonia similar to lobular nonbronchitis. It mainly includes general bronchial pneumonia and interstitial pneumonia, both of which are common and frequently occurring clinical diseases. Generally speaking, chronic bronchial pneumonia is mainly a kind of purulent airway inflammation with acute pneumonia and lobular pneumonia as the main pathological unit. It is mostly caused by certain pathogenic bacteria such as *Staphylococcus pneumoniae* and *Haemophilus influenzae* bacteria, which have relatively strong or weak pathogenic immunity, and they are more likely to occur in the lower lobe and dorsal side. Interstitial pneumonia is mostly exudative inflammation, which is often caused by infections such as viruses and mycoplasma [10, 11]. Lobular pneumonia not only occurs in children but also occurs in the elderly, chronic patients, and other people with weakened immunity. In addition to lobular mucosal pneumonia in young adults, large lobular mucosal pneumonia is also common, which is mostly caused by f 1, 3, 7, and 2 types of lobular pneumonia and streptococcal infections that are highly infectious. It is an acute alveolar intima and diffuse mucosal exudative interstitial inflammation involving all large lobes of the lung; Figure 1 shows the real pathological diagram of human body weight pneumonia:

It is generally believed that the diagnosis of pneumonia mainly relies on medical history and physical examination. In fact, imaging examinations are widely used. A common belief is that patients with suspected pneumonia should undergo chest X-ray examination once they are admitted to the hospital [12, 13]. Sometimes sputum microscopy and sputum culture are also performed to understand the types of pathogenic bacteria to assist in the diagnosis and treatment of some complex and refractory cases. Because the lung tissue with air is considered to be the blind spot of ultrasound imaging, the imaging diagnosis of lung diseases, including pneumonia, mostly relies on radiological examinations, mainly chest X-ray and CT. Ultrasound has never been used clinically as a routine imaging examination item for pneumonia, and this situation still persists in China. In recent years, some scholars have also carried out lung MR examinations. The specific pathological classification of pneumonia and common diagnosis methods are shown in Table 1.

It is generally believed that chest X-ray is the preferred imaging method for patients with pneumonia, and chest CT is the imaging standard for the diagnosis of pneumonia. It is clinically recognized that the diagnostic value of chest CT is better than X-ray, but the former cannot completely replace the latter [14, 15]. The vast majority of literature believes that the diagnostic accuracy of CT is significantly higher than that of chest X-ray, but CT has the disadvantages of expensive, relatively long examination time, and relatively large radiation dose. And critically ill patients who cannot be moved cannot receive CT examinations but can only receive bedside chest radiographs. The medical examination process for pneumonia is shown in Figure 2:

Chest X-ray and CT have been used to diagnose pneumonia for a long time and are very mature diagnostic methods. At present, the focus of these two radiological examinations is for radiologists to reduce radiation dose by improving scanning methods and scanning parameters and to strike a balance between radiation dose and image quality. For clinicians and patients, it is the ionization damage to human tissues and related protection issues, as well as the feasibility of other nonradioactive imaging for the diagnosis of pneumonia [16, 17].

2.2. X-Ray Imaging Principle and Data Acquisition. X-ray is a commonly used medical imaging method. The basic procedure of X-ray imaging is to irradiate the inspected area with X-rays, then collect the radiation passing through the inspected area, and analyze the collected radiation dose. The collected and observed air radiation and energy have a certain positive correlation with the air density coefficient of

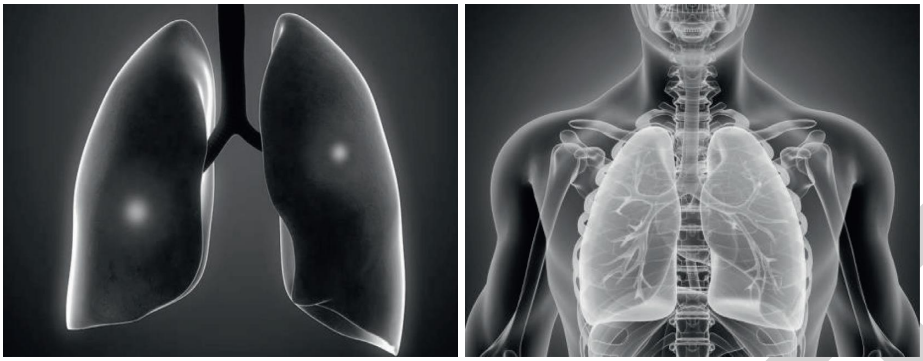

Figure 1: Pathological diagram of severe pneumonia.

Table 1: Classification of pneumonia and common diagnostic methods.

Types of pneumonia	Diagnosis method
Mycoplasma pneumonia	X-ray
Chlamydia pneumonia	CT
Staphylococcus aureus pneumonia	MR
Adenovirus pneumonia	X-ray

the entire room. Imagine that the two parts illuminated by the sun are composed of small circles or rectangles (small circles or voxels) of the same ball size. The basic radiation amount irradiated on each different voxel is generally the same, but the remaining basic radiation amount is different after each different voxel of different voxel density is irradiated. The basic radiation attenuation coefficient is generally calculated from the increased radiation dose of the exposure residual [18, 19]. According to the basic attenuation coefficient of each voxel, the radiation attenuation value greater than X can be calculated and obtained. The calculation formula is as follows:

$$X = 1000 * \frac{(\mu_m - \mu_w)}{\mu_w}. \quad (1)$$

Among them, m is the attenuation coefficient of a certain voxel, w is the attenuation coefficient of water, and the unit of the X-ray value is Hounsfield Unit (HU).

The delay time is analyzed, which made the algorithm in X-ray easier, so set the waiting time as Tback and rewind upper limit as TmaxBack:

$$C < 16. \quad (2)$$

Maximum avoidance index:

$$\text{Max}\,E = 10. \quad (3)$$

Maximum number of conflicts:

$$MC = 16. \quad (4)$$

Time slot:

$$\text{Slot} = \text{TbackN}. \quad (5)$$

N is a positive integer between 0 and the upper limit of backoff:

$$\text{TMaxBack} = 2^i - 1, i \in (10, 16). \quad (6)$$

Similarly, the probability P of all nodes is not transmitting a data frame, the probability P of a single node transmitting P, the probability P of multiple nodes transmitting, etc. For the waiting time for any conflict to reach the desired value EB(i), when the number of conflicts is greater than 10, the expected value remains EB(10) unchanged; otherwise, it is EB(i). The estimated delay time is as follows:

$$E[T_i] = P_m^i * P_r W_{i-1}. \quad (7)$$

W_{i-1} represents the number of data arrival times before the i-th collision, so the total contention period delay time expectation can be expressed as

$$E[T_i] = \sum_{i=0}^{MC} E[T_i]. \quad (8)$$

And the selection of the value of *i* in the backoff function is modified, for example, by selecting

$$i = \max\{1, \text{MaxE} - kC + 1\}. \quad (9)$$

Or the following is taken:

$$i = \min\{\text{TMback}, 2 * K\}. \quad (10)$$

The self-designed dynamic logarithmic BEB algorithm is adopted, and the K value adopts the dynamic logarithmic numerical method. And there are specific improvements to larger avoidance clues, specific settings:

$$\text{MaxE} = \text{fix}(\log_2(N))K = \text{fix}\left(\log_2\left(\frac{N}{2}\right)\right). \quad (11)$$

The backoff ceiling index is taken as:

$$b = \max(1, \text{fix}(\log_2(N) - k * i + 1)). \quad (12)$$

The minimum is 2 and the maximum is 10; backoff upper limit time is as follows:

$$\text{TMback} = (\log_2(b + 1) - 1) * T \pm \text{slot}. \quad (13)$$

Time slot:

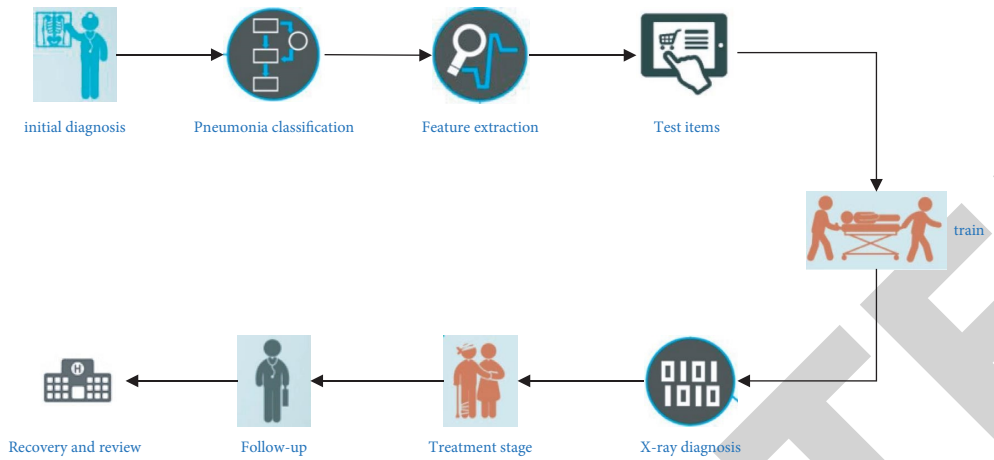

Figure 2: Medical examination process for pneumonia.

$$T \pm \text{slot} = 51.2 * 10\wedge(-3). \tag{14}$$

The expected value of backoff index, when less than or equal to 10, is as follows:

$$EB(i) = \text{fix}\left((\log_2(b+1) - 1) * \frac{T \pm \text{slot}}{\log_2(b+1)}\right). \tag{15}$$

Otherwise,

$$EB(i) = \text{fix}\left((\log_2(10) - 1) * \frac{T \pm \text{slot}}{\log_2(10)}\right). \tag{16}$$

When the Vikj function monotonously increases $w = 0$, it will be a parameter when the Vikj function monotonously decreases:

$$w = 1, F(F \in [0, 1]). \tag{17}$$

The equation guarantees

$$x[isikj]\text{new} \geq RVikj. \tag{18}$$

$$x[isikj]\text{new} \leq x[isikj]\text{old}. \tag{19}$$

While complex images have high entropy, entropy can be defined as follows:

$$\text{entropy} = -\sum_{i=1}^{N_i} P(i)\log_2 P(i). \tag{20}$$

The basic idea of edge detection is to detect the edge points in the image first and then connect the edge points into contours according to a certain strategy to form a segmentation area. Since the edge is the dividing line between the target and the background to be extracted, the target and the background can be distinguished only by extracting the edge, so edge detection is very important for digital image processing. X-ray values penetrating all voxels in the radiation section can generate an X-value matrix and then obtain an X-ray image. Chest computed tomography is a method of using X-ray computed tomography to examine the chest. The characteristics of the X-value matrix are shown in Figure 3:

The thickness of the scan is usually 1 to 10 mm. The breast usually contains soft tissues and other organs belonging to the human body, such as the gastrointestinal tract and soft tissues, bones, fat, and various other soft tissues. The width and position of the window must be set differently. Different lung display parts need to pay attention to the width of the window. The width of the door in the window position is 400–500 HU, and the height of the window is 0–50 HU. It is suitable for displaying breast augmentation display of breast soft tissues such as the vertical and horizontal muscular atrial septal muscles of the upper and lower chest and abdomen on both sides of the human body. The window width is 1000–2000HU, and the window height is 600–800HU, which is suitable for display and intestinal scanning. The enhanced application of computerized chest tomography and various high-resolution new types of computerized chest tomography is the common surgical methods for the chest using computerized tomography. Simple X-ray scanning is the most common scanning method and does not inject contrast agent into the blood vessel. An enhanced X-ray scan is an X-ray scan that uses a contrast agent. In blood vessels, X-ray resolution has very high spatial resolution and density resolution and can clearly show the detailed structure of the tissue. The comparison of X-ray spatial resolution and density resolution factor is shown in Figure 4:

2.3. Principles of Blood Gas. The measurement of arterial catheter blood gas-related indicators is one of the commonly used clinical vital signs management and monitoring technical indicators, which involves many types of monitoring items, among which the more typical cases are $PaCO_2$ and pH. $PaCO_2$ can directly reflect the effect of detecting the patient's alveolar blood ventilation, and it is one of the important monitoring indicators for the clinical judgment of the patient's respiratory blood pH imbalance. Through the numerical monitoring of this monitoring index, it can be directly found whether there may be residual imbalances of respiratory carbon dioxide retention in the body of patients with lung disease. In this article, combined with the

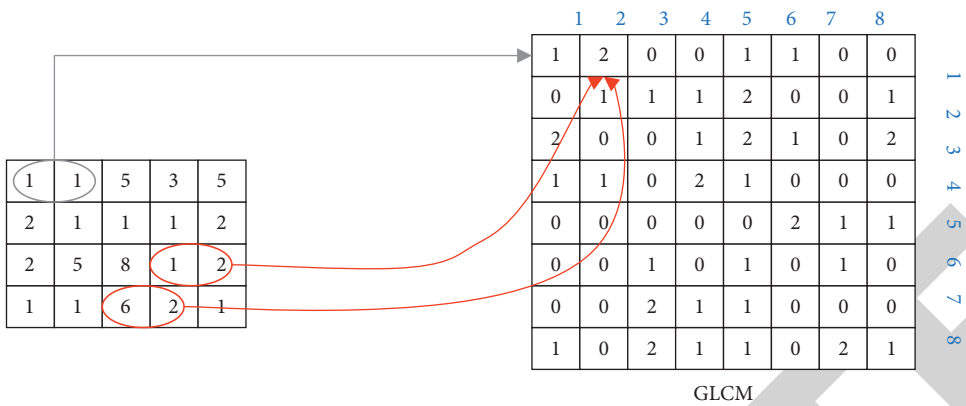

Figure 3: Schematic diagram of the characteristics of the X-value matrix.

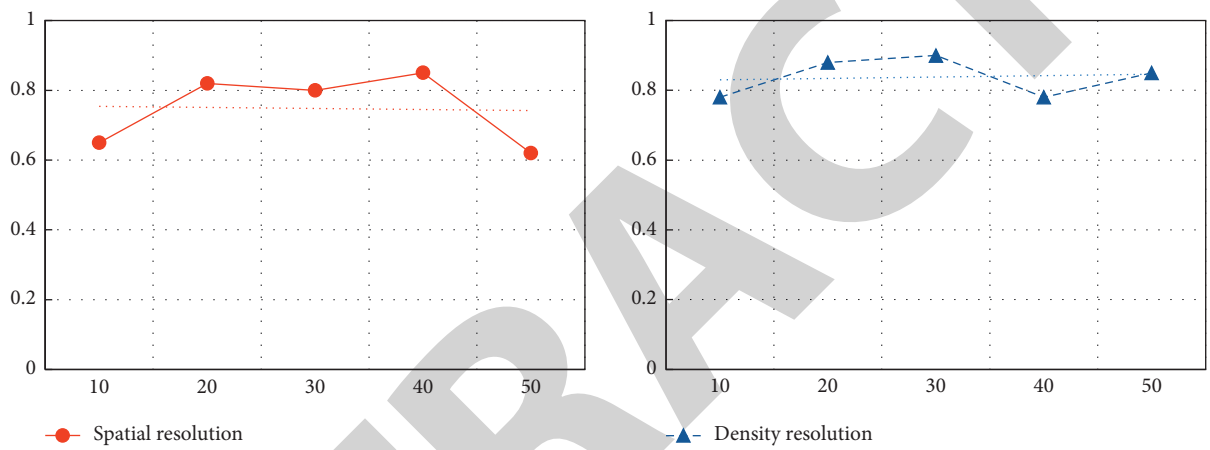

Figure 4: Comparison of X-ray spatial resolution and density resolution factor.

numerical analysis and monitoring of PH, the measurement results can directly assess whether there may be an imbalance of respiratory pH in patients with lung disease. At the same time, the analysis and determination of arterial catheter blood gas-related indicators is also one of the two key factors that clinically guide the clinical treatment and diagnosis of lung disease patients to predict the prognosis of the disease. The accuracy of analysis and measurement results of related technical indicators of arterial catheter blood gas indicators will directly affect its clinical value in practical medical applications. By analyzing the prognostic factors of patients' arterial catheter blood gas-related indicators analysis and measurement results, it is convenient to better formulate measures to take medical care and health management measures. Furthermore, it will gradually improve its related analysis indexes of arterial duct blood gas and the accuracy of the measurement results and give full play to its actual clinical application value for the measurement and analysis of arterial duct blood gas-related indexes.

It is well known that the X-ray beam generated by the medical X-ray generator is a mixed wave (white radiation) with rich frequency components. During X-ray inspection, the low-frequency components (i.e., low-energy X-ray photons) in such mixed waves may be absorbed in the interaction with the human body after passing through the human body for a certain distance. The lower the energy, the more likely the absorption. Some soft rays are absorbed even on the surface of the human body. These low-energy rays do not contribute to the X-ray image and only damage the human body. The more soft ray components are contained in the X-ray photon beam, and the medium (high) frequency high voltage power supply improves the X-ray image quality.

Early severe pneumonia in infants and young children is mainly an inflammation directly caused by bacterial infection of the respiratory tract in children. The disease mainly has the main characteristics of rapid onset, severe disease, and high fatality rate in children. Its main clinical symptoms are fever and dyspnea. Traditional oxygen therapy is currently an effective method for clinical treatment of the disease, but it is very easy to cause complications such as nasal mucosal ulcer, lung injury, and nasal septum injury in children, which limits its clinical application. The use of effective oxygen therapy measures is the key to improving the ventilatory function and ventilation status of infants and young children and controlling the progress of the disease. Warming and humidifying high-flow nasal catheter ventilation is a new type of oxygen therapy model based on the improvement of traditional oxygen therapy, which can effectively improve the tolerance of infants and young children. It can also assist in improving lung function and

significantly improve the ventilation status of infants with severe pneumonia. The mechanism and effect of blood gas analysis on the treatment of severe pneumonia in children are shown in Figure 5.

Arterial catheter blood gas blood analysis is an important clinical diagnostic method that can quickly and accurately reflect the internal and external environmental health of critically ill children. The test results also directly affect the treatment decisions of the children's clinical nursing doctors, especially for children with critical symptoms. I personally recommend that nurses choose to use professional arterial blood gas detection tools for children and have reached a consensus on improving the accuracy of clinical test results. Clinical nurses in the pediatric department of acute and critical illnesses are more recommended to choose or use various professional arterial blood gas collection devices (choose professional arterial blood gas blood collection devices or use professional arterial vaccinations or puncture-type special arterial blood gas blood collection devices); 490 clinical nurses chose to use ordinary disposable arterial injectors for arterial blood gas sampling, accounting for 32.3%. Ordinary liquid blood inflatable syringes usually use hard plastic liquid inflatable injection tubes. Diffusion analysis will directly affect the blood inert gas that has entered this blood inert gas index and various other external chemical substances, resulting in the blood inert gas index dispersion analysis index being inaccurate. The main reason is that it affects the results of pH, PO_2, and PCO_2 in this blood gas index dispersion analysis, the standard bicarbonate (SB), actual bicarbonate (AB), residual alkali (BE), and extracellular residual alkali (BEecf) related to PO_2 and PCO_2. Therefore, in order to effectively ensure the accuracy of the results of the blood gas analysis of the commonly used arterial catheters, various large-scale specialized medical institutions specifically stipulate that nurses should strictly follow the norms to use a new type of more professional and commonly used arterial stent catheter blood gas venous blood analysis and blood sampling device detection and identification device [20, 21].

In addition, when using a disposable blood metering syringe or a new type of arterial catheter blood gas blood sampling instrument that is commonly used as a common arterial small plate blood gas catheter blood quantitative analysis test result to identify specimens, one of the 60.5% of nurses would recommend the use of a freeze-dried saline solution containing calcium and heparin sodium for blood rinses. The experimental results show that the salt of heparin sodium has strong physical and chemical substance selectivity and chemisorption to the negative ion heparin calcium sodium of yang and yin. It will directly result in that other nurses exchange the commonly used anticoagulant with the sodium heparin calcium in the blood for ion exchange, affect the exchange of calcium and heparin sodium, magnesium, calcium, and heparin sodium magnesium, and use quantitative detectors and other methods to test the certainty and accuracy of the results. Therefore, a nurse is specifically recommended to use a lyophilized salt and a lyophilized salt-containing heparin sodium, or a self-filling, disposable type containing other commonly used anticoagulants, or nonuse of the new safety-type common arterial catheter blood gas blood sampling instrument testing equipment. The preset and nonused arterial catheter blood gas blood sampling devices are also authoritative international arterial blood sampling technical guides, specifically stipulating that the equipment is recommended for use by a nurse [22, 23].

3. Experiment and Design

3.1. Design of Experimental Control Group. Children with severe pneumonia present with obvious pathological changes such as pulmonary respiratory tract inflammation, sputum secretions, and high-concentration reactions in the respiratory airways. In addition, the children also have increased glucocorticoid-1 in plasma cells and decreased nitric oxide cell synthesis protein; platelets synthesize granule membrane protein-140; the platelet-activating factor is significantly increased; the ratio of thromboxane A2 to thromboprostaglandin 2 is imbalanced. These abnormalities may indicate that pneumonia is beneficial to the damage of the vascular mucosal endothelial layer and the exposure of thrombus collagen under the endothelium, which directly activates the platelets and prothrombin oxidase in the lungs of the children and leads to a hypercoagulable state. The results of clinical studies such as Lin Chunwang [24] showed that there is a hypercoagulable state in the lungs of children with severe pneumonia and causes the formation of acute microthrombosis in the lungs, D-deoxydimer (D-Dimor, dd) increased significantly, and the activity of AT-III decreased significantly. The activation time of thrombin kinase (TT) and the activation time of thrombin prokinase (APTT) in some children were significantly shorter than those in the normal infection control group, and the intra-arterial thrombin oxidase saturation (SaO_2) was significantly reduced. The prothrombin activation time (PT), activation time (APTT), TT, and DD of some children with normal infection were significantly higher than those of the normal infection control group. Although it is in the normal infection range, it is lower than the normal infection control group. The large differences in the results of the two clinical studies may be closely related to the severity of the lung infections and the duration of the disease in the two study subjects [25].

Adrenal secretory function, side effects of c-cell metabolism, and venous blood protein were analyzed by antibodies and venous blood flow from the blood flow monitoring of the arteries in the peripheral ventricle. The two methods of testing one ELISA at a time were used to test one PAl-1 twice. Both the normal control group and the long-term control group were physical examiners from the physical examination group of the health clinic of our hospital in Beijing in 2015. He asked for a health examination of peripheral upper peritoneal venous blood after fasting at 6 : 30 in the morning [26]. This prospective clinical study has obtained changes in the concentration of liver coagulation and other fibrinolytic liver functions in patients treated with chronic pneumonia in this community. The difference between the concentration before treatment and the patient's 1 week after treatment has an important impact

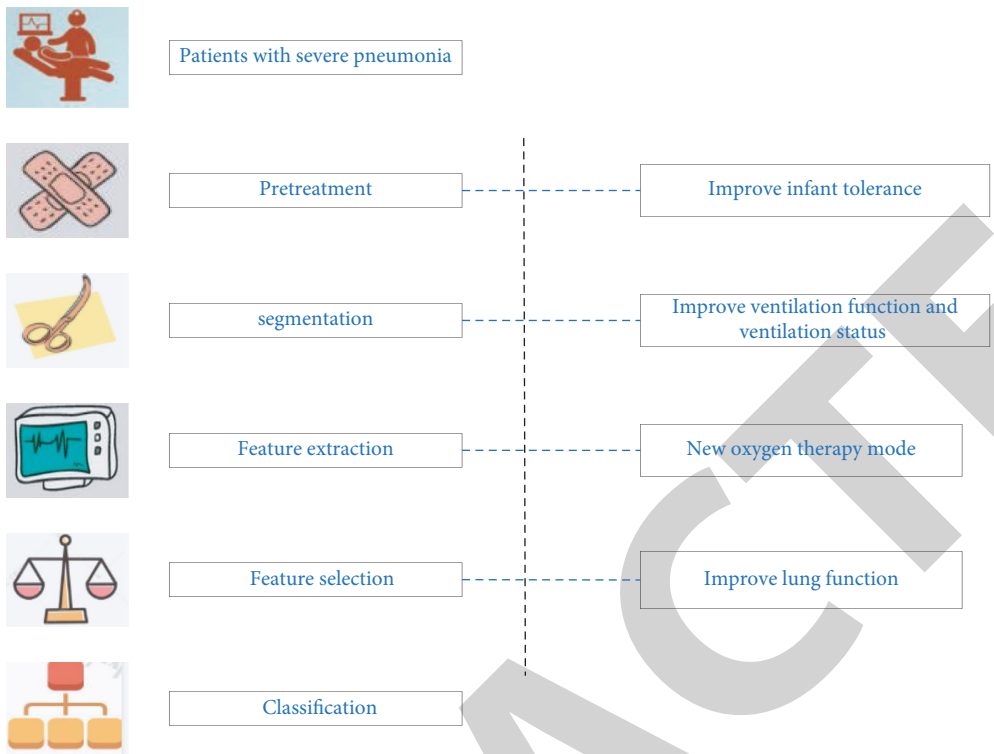

Figure 5: The mechanism and effect of blood gas analysis in the treatment of severe pneumonia in children.

on the analysis of the liver function of the treated patient's liver blood gas map. Moreover, the treatment of patients who may have other severe liver damage and whether it may affect other coagulation and fibrillary functions provides a scientific basis for diagnosing early pneumonia diagnosis and whether it is suitable for the application of other conditions anticoagulant treatment methods. Figure 6 shows the comparison of blood gas factor index data between children with severe pneumonia and the normal control group.

The research subject is a late-stage community resident who is hospitalized in the late-stage community and the patients with chronic pneumonia are the main investigation and research objects. The prospective big data analysis research is based on the analysis of the obvious damage to the overall liver function of the patient with chronic pneumonia obtained by a resident in the community at the time of the disease; the obvious difference between the prognosis before treatment and the late prognosis at 1 week of treatment, the objective analysis of the late systemic local blood gas structure of a severe late-type patient, and the direct damage to liver function; and whether a severely late-type patient undergoes significant changes in the degree of systemic liver function damage when receiving a viral infection in the late stage and whether it can directly affect the overall liver function of a severely late-stage patient, such as systemic local coagulation, anticoagulation, and local coagulation and fibrinolysis. A scientific basis is provided for whether the late treatment of severely ill late-type patients with chronic pneumonia in the advanced community who need long-term use of short-acting anticoagulants can become a direct treatment and diagnosis target so as to effectively help control or shorten the clinical recurrence period and course of severely ill advanced patients with chronic pneumonia in the advanced community, improve the prognosis, and reduce the late mortality of severely ill patients.

3.2. Experimental Equipment and Objects

3.2.1. Research Object. A total of 252 cases of children with severe pneumonia in children and children in the outpatient of the department of vascular medicine of a children's hospital were counted at the same time. There were 152 cases from 36 months to 6 years old at the same time and 200 cases over 6 years old. The relationship between the number of patients with severe pneumonia and their age is shown in Figure 7:

The basic criteria for the clinical diagnosis of acute severe pneumonia in children, the full text refers to the diagnosis concept of severe pneumonia in children in the WHO Children's Acute Pneumonia Respiratory Bacterial Infection Prevention and Control Program, and the diagnostic criteria for other chronic diseases in children refer to the 7th edition of Zhufutang Pediatrics. Chemical clinical diagnosis of pathogenic bacteria in sputum culture: based on the clinical chemistry diagnosis method, the sputum of children who meet the chemical screening was separated twice to isolate the same other pathogenic bacteria. Specimen identification of pathogenic strains of typical mixed acute infection: during the same period, two consecutive samples were analyzed and detected to isolate other different pathogenic bacteria, and

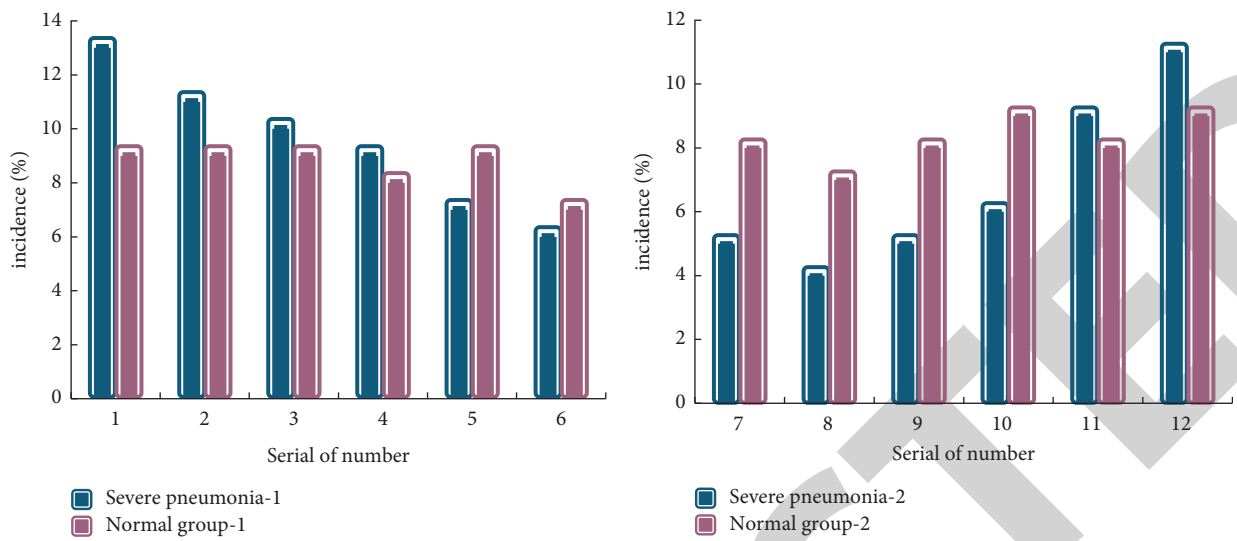

Figure 6: Blood gas factor index of children with severe pneumonia and normal control group.

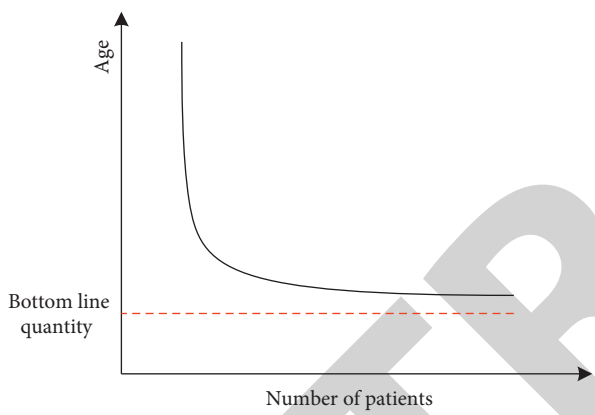

Figure 7: The relationship between the number of severely ill children and their age.

the child was determined to be a typical mixed acute infection pathogenic strain.

The experimental equipment is shown in Table 2:

Short analysis time: 17 critical parameter results are obtained in 35 seconds, and timely treatment plans are given to patients. Short cycle time: sample testing can be performed at any time, and the timeliness of sample testing will not be affected by maintenance. Automatic quality management (AQM) system monitors the entire inspection system and random errors in real time through calibration, quality control, and internal inspection of the system and corrects them in time.

3.3. Experimental Operation. The patient was admitted to the hospital for diagnosis, the chest patient was checked immediately after admission this week, and two X-ray lasers and radiographs were taken in the chest and abdomen to determine the location where the peripheral malignant lesion may occur and the extent of the lesion. Blood samples of sputum coagulative leukemia from peripheral lesions were collected and blood smears, blood analysis, and culture were performed. By combining the clinical symptoms of peripheral lesions and performing laboratory tests based on clinical examination signs, the peripheral lesions were diagnosed as children with severe pneumonia, and the main fluids were taken immediately for blood tests. After blood analysis and testing, the main blood tests for urine and liver routine, four items of coagulation, DD, AT-III, and four analyses of blood gas concentration were performed. The two main detection materials and ELISA methods were used to detect renal tubular coagulation function and CRP, respectively. The specific operation flow diagram for detecting the content of the above body characteristics is shown in Figure 8.

Taking the concentration of the standard substance as the abscissa, draw a standard curve on logarithmic graph paper, and find the corresponding concentration range on the standard curve. The specific operation steps for detecting t-PA in human blood and the comparison of inflammatory indexes between each group are shown in Table 3.

Using clinical retrospective medical history analysis method, the inspection indicators are as follows:

(1) Examination of the occurrence of complications in children

(2) Auxiliary medical examination of children, mainly including blood routine, blood meteorological analysis and blood electrolytes, blood coagulation and lung function at discharge, imaging, pathogen culture detection (mainly including searching for negative sputum cells, virus receptor antigens in the respiratory tract, blood and mycoplasma virus antibody culture tests, and negative sputum cell culture), and the results of drug susceptibility detection mainly used for pathogenic bacteria

(3) Combination therapy, including antibacterial hormone drug combination therapy, hormone drug therapy, supportive drug therapy, and the use of medical mechanical ozone ventilators

Table 2: Details of the experimental equipment.

Equipment name	Model	Origin
Blood gas analyzer	Raydu ABL-520 blood gas analyzer	Denmark
Lactic acid determination	Raydu ABL-520 blood gas analyzer	Denmark
Blood routine	Sysmex SF-3000 automatic blood cell analyzer	America
Coagulation	Diagnostica Stago coagulation analyzer	America
Low-temperature centrifuge	Beckman Coulter	America

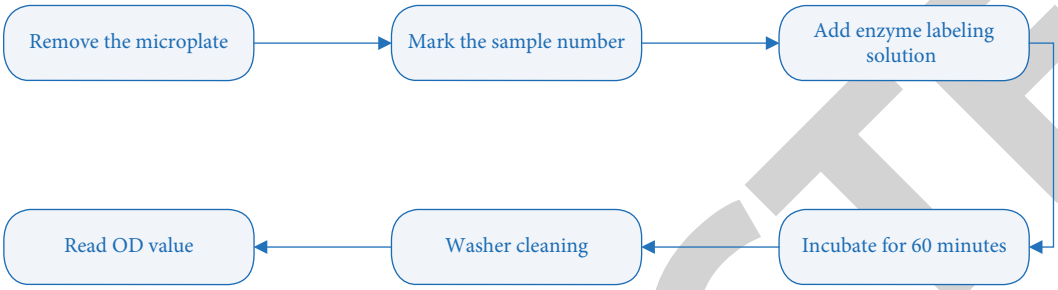

Figure 8: Operation flowchart for detecting PAl-1 in human blood.

Table 3: Comparison of inflammatory indexes between groups.

Group	WBC	GR (%)	PLT	CRP (mg/L)
A	10.12 ± 6.25	65.26 ± 12.26	312.58 ± 128.69	110.25 ± 76.58
B	8.26 ± 2.51	62.52 ± 10.36	325.26 ± 118.25	9.25 ± 8.14

(4) The prognosis of cure, mainly including the prognosis of cure, improvement, giving up, and finally death

4. Experimental Data Processing and Results

4.1. Data Collection and Processing. SPSS 17.0 statistical data analysis application software was used for statistical data analysis of the importance of statistical data samples of independent measurement laboratories. Before conducting important statistics on the data samples of independent measurement experiments, it is first necessary to carry out a comparison test of normality and variance. Those conforming to the positive and the same negative count standard deviation distribution are represented by the function formula that the variances are all mean ± standard deviation ($x \pm s$). The comparison of statistical means of variance between two groups generally mainly adopts the comparison test of variance t and negative t variance, and the comparison of statistical means of variance between multiple groups generally mainly adopts analysis of variance. Different from those who just fit the normal count standard deviation distribution, the variance is the median (including the three-quarter digits and the gap in the middle). The [m(Q)] function formula is an example to show that the statistical standard value positive rank and variance comparison test of two different independent statistical experimental data samples is performed. The standard value X2 test is generally used for the variance of the negative count measurement data. The high accuracy of $p < 0.05$ is an important statistical data analysis and practical significance. The detailed data are shown in Figure 9:

Severe pneumonia in children often occurs in heart and lung organs and local lung function and nervous system heart failure (multiple organ failure, MOF), and the early high incidence is common in June to December. Moderate viral A leukemia encephalopathy is more common in the early stage of the disease from 28 days to June. The comparison of coagulation and fibrinolysis indexes among patients is shown in Table 4.

5. Results

Of the 252 cases of acute high-risk severe pneumonia in all children, only (121/252) two cases have high-risk severe disease risk factors. These high-risk severe diseases have a total of 161 cases. Among them, acute pediatric cardiovascular and nervous system diseases, malnutrition, brain dysplasia (155/252) cases have high-risk clinical complications in the occurrence of the disease, and there are 231 cases of high-risk clinical complications of these diseases. Among them, acute pediatric respiratory failure and acute pediatric heart failure patients with severe diseases are the main clinical high-risk complications, accounting for 62.3% (144/231). The data of each part of the inspection method is shown in Figure 10.

Compared with the normal combined control group, patients with early symptoms of B pneumonia also reflect the abnormal blood index of the function of human blood clotting cells. The coagulation combined enzyme activation time (TT) has been shortened a lot ($p < 0.02$). The clinical symptoms of patients with type B pneumonia at the initial stage of blood coagulation treatment were that the partial pressure of oxygen ($Pa0_2$) and the saturation of intra-arterial coagulation of oxygen (S02) were significantly lower than

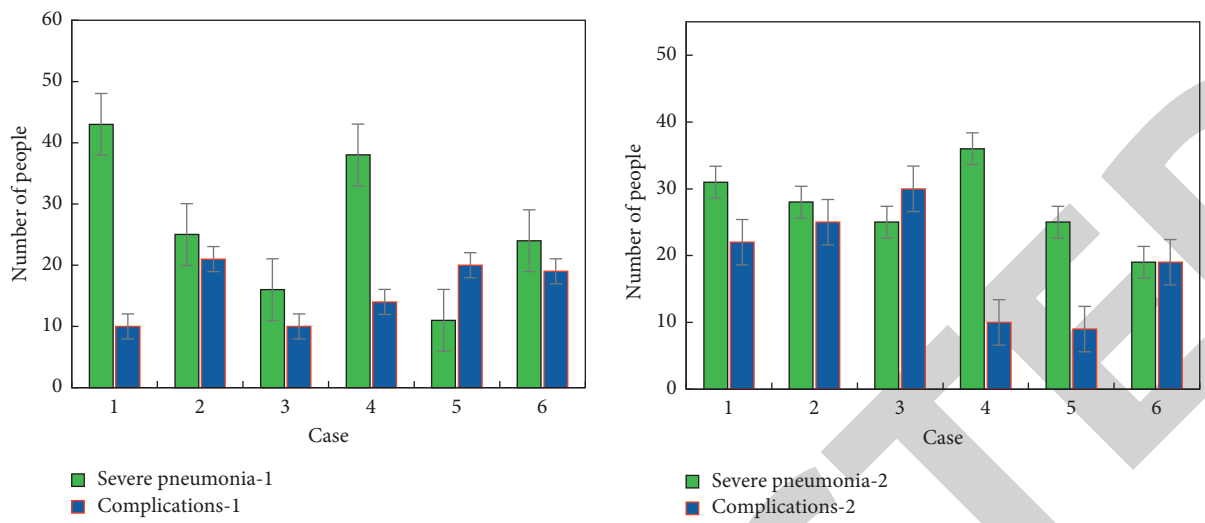

Figure 9: The data graph of the patient's and children's prevalence.

Table 4: Comparison of coagulation and fibrinolysis indexes between groups ($x \pm s$).

Test items	Group A	Group B	Group C
PT (s)	13.52 ± 1.06	13.58 ± 0.58	14.58 ± 1.69
APTT (s)	35.29 ± 1.25	39.52 ± 6.54	35.66 ± 4.89
TT (s)	17.25 ± 1.82	15.78 ± 4.89	15.89 ± 2.58
FIB (g/L)	3.12 ± 0.48	6.41 ± 2.18	5.10 ± 1.57

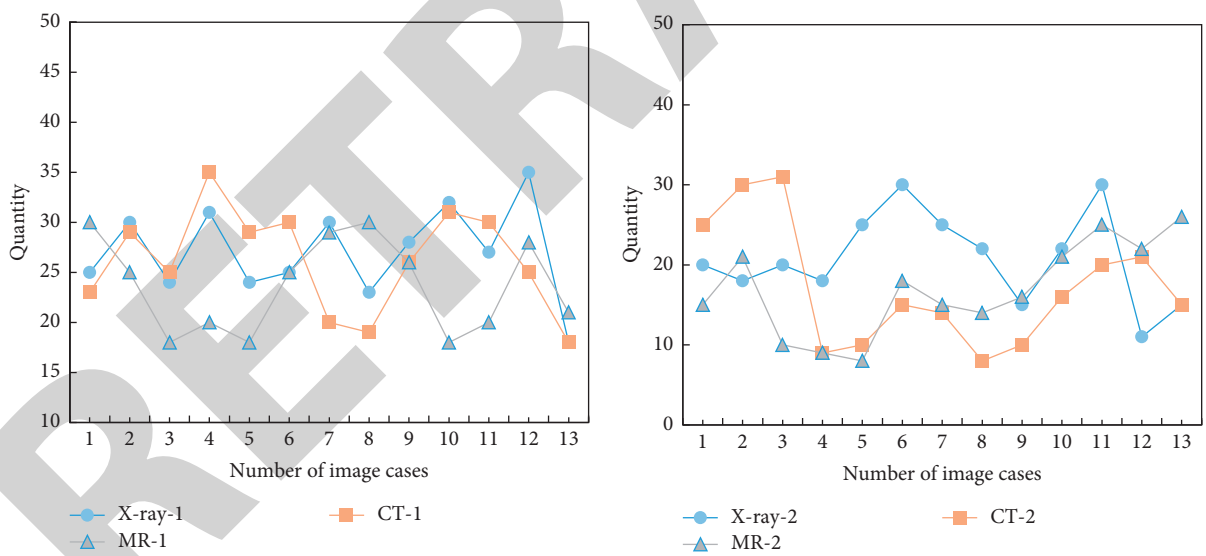

Figure 10: Examination method data for each part of the patient.

those of the normal combined control group ($p < 0.02$) and lactic acid (lac) was significantly increased ($p < 0.02$). Before the rehabilitation of patients with advanced pneumonia, the levels of blood pressure ($PaCO_2$) and bicarbonate ($HC0_3$-) were significantly different between the group using of carbon dioxide lysing enzyme to break down blood pressure ($PaCO_2$); in the normal treatment control group, there was no significant statistical fact ($p > 0.05$). After rehabilitation treatment, both were significantly lower than those in the normal treatment control group ($p > 0.05$). However, after diagnosing pneumonia in children with severe pneumonia based on X-rays, the targeted arterial and venous blood gas analysis and treatment of the children have increased the treatment rate by 64.28%.

6. Conclusion

This article mainly adopts a prospective fasting controlled clinical study test method, examining the patients before and after fasting and the hospital health doctor group before and

after comparison. In 252 children with severe pneumonia, based on chest X-ray radiation, the entire body of the patient was examined by optical video imaging of the chest and checked immediately afterward (groups *b* and c). And on the 7th day (group c) at 6 am in the morning, coagulation and urine routine test, four items of coagulation, and D-dimer were taken from the peripheral blood vessel and venous blood flow test piece on an empty stomach (antithrombin-Ill (AT-III), liver function, adrenal function, CRP, blood protein). Taking the peripheral arterial blood flow examination film and blood gas data analysis, compared with the normal oxygen inhalation control group, the main body kidney and liver functions of children with severe pneumonia and poor children have not suffered severe damage. It is not important to affect the hemostatic, anticoagulant, and inhibitory functions of coagulation protein fibrinolytic complex enzyme. One of the shortcomings of the current research of this research topic is that the duration of the research work of this topic is relatively short and the sample size is relatively small. In the future continuous research, the sample size in this study should be larger, and further study is warranted to understand the characteristics of clinical medical pathology, etiology, and drug resistance of children with acute severe pneumonia in the society. Moreover, in the future, its clinical medical background to analyze the factors that affect it and its pathological changes should be analyzed, the direct causal relationship between children with acute severe pneumonia and poor prognosis in children examined, high-risk factors identified, clinical evidence for the early diagnosis and prevention of severe pneumonia provided, and the rational clinical selection of antibiotics guided.

Data Availability

The data that support the findings of this study are available from the corresponding author upon reasonable request.

Conflicts of Interest

The authors declare that they have no conflicts of interest.

References

[1] W. B. Luo, Z. Y. Xue, and W. M. Mao, "Effect of heat treatment on the microstructure and micromechanical properties of the rapidly solidified Mg_(61.7)Zn_(34)Gd_(4.3) alloy containing icosahedral phase," *International Journal of Minerals Metallurgy and Materials*, vol. 26, no. 7, pp. 69–77, 2019.

[2] L. J. Hsin, L. A. Lee, T. J. Fang, C. T. Liao, and H. Y. Li, "The treatment effect of sialendoscopy on obstructive sialadenitis without sialoliothiasis," *International Journal of Head and Neck Science*, vol. 3, no. 2, pp. 108–114, 2019.

[3] B. van der Kolk, "Commentary: the devastating effects of ignoring child maltreatment in psychiatry - a commentary on Teicher and Samson 2016," *Journal of Child Psychology and Psychiatry*, vol. 57, no. 3, pp. 267–270, 2016.

[4] W. Fu, H. Cai, D. Wang, Y. Lei, and J. Liu, "Time resolved x-ray image of laser plasma interactions using a dilation framing camera," *Optik*, vol. 186, pp. 374–378, 2019.

[5] J. F. C. Rohr, A. Rozenblats, A. Rozenblats, G. Selga, and I. Čēma, "The influence of the oral microbiome on general health," *Stomatology Edu Journal*, vol. 8, no. 1, pp. 66–76, 2021.

[6] M. Stasevych, V. Zvarych, and V. Novikov, "Study of the antifungal action of the lacquer based on the GABA derivative of 2-chloro-N-(9,10-Dioxo-9,10-Dihydroanthracen-1-yl)Acetamide," *Biointerface Research in Applied Chemistry*, vol. 11, no. 2, pp. 8818–8824, 2021.

[7] K.-D. Wolff, A. Rau, J. Ferencz et al., "Effect of an evidence-based guideline on the treatment of maxillofacial cancer: a prospective analysis," *Journal of Cranio-Maxillofacial Surgery*, vol. 45, no. 3, pp. 427–431, 2017.

[8] W. A. Brooks, K. Zaman, D. Goswami et al., "The etiology of childhood pneumonia in Bangladesh," *The Pediatric Infectious Disease Journal*, vol. 40, no. 9S, pp. S79–S90, 2021.

[9] "Recommendations for the diagnosis, prevention and control of the 2019 novel coronavirus infection in children (first interim edition)," *Chinese Journal of Pediatrics*, vol. 58, no. 3, pp. 169–174, 2020.

[10] K. Maitland, S. Kiguli, P. Olupot-Olupot et al., "Randomised controlled trial of oxygen therapy and high-flow nasal therapy in African children with pneumonia," *Intensive Care Medicine*, vol. 47, no. 5, pp. 566–576, 2021.

[11] S. Zheng, S. Zhang, S. Hong, and Q. Lou, "Severe dyspnea and uncontrolled seizures following meperfluthrin poisoning: a case report," *BMC Pediatrics*, vol. 21, no. 1, pp. 51–56, 2021.

[12] N. Xu, P. Chen, and Y. Wang, "Evaluation of risk factors for exacerbations in children with adenoviral pneumonia," *BioMed Research International*, vol. 2020, no. 3, pp. 1–5, 2020.

[13] A. Andrés-Martín, A. E. Montaner, J. F. Mulet et al., "Consensus document on community-acquired pneumonia in children," *SENP-SEPAR-SEIP. Archivos de Bronconeumología*, vol. 56, no. 11, pp. 725–741, 2020.

[14] P. Wu and J. Wang, "Changes and significance of serum sB7-H3 and cytokines in children with mycoplasma pneumonae pneumonia," *Journal of the College of Physicians and Surgeons--Pakistan : JCPSP*, vol. 30, no. 3, pp. 268–271, 2020.

[15] S. O. Akech, D. W. Kinuthia, and W. Macharia, "Serum procalcitonin levels in children with clinical syndromes for targeting antibiotic use at an emergency department of a Kenyan hospital," *Journal of Tropical Pediatrics*, vol. 66, no. 1, pp. 29–37, 2020.

[16] J. T. Huang, X. L. Lu, Z. H. Xiao et al., "[Clinical effect of feeding with calorie-enriched formula in children with ventricular septal defect and severe pneumonia]," *Zhong Guo Dang Dai Er Ke Za Zhi*, vol. 21, no. 10, pp. 998–1004, 2019.

[17] F. Q. Kareem and A. M. Abdulazeez, "Ultrasound medical images classification based on deep learning algorithms: a review," *Fusion: Practice and Applications*, vol. 3, no. 1, pp. 29–42, 2021.

[18] J. Liu, F. Zhao, J. Lu, and H. Xu, "High mycoplasma pneumoniae loads and persistent long-term mycoplasma pneumoniae infection in lower airway associated with severity of pediatric mycoplasma pneumoniae pneumonia," *BMC Infectious Diseases*, vol. 19, no. 1, pp. 1–8, 2019.

[19] K. Çıkı, D. Doğru, B. Kuşkonmaz et al., "Pulmonary complications following hematopoietic stem cell transplantation in children," *Turkish Journal of Pediatrics*, vol. 61, no. 1, pp. 59-60, 2019.

[20] M. Singh Heer, H. Chavhan, V. Chumber, and V. Sharma, "A study of internet of medical things (IoMT) used in pandemic covid-19 for healthcare monitoring services," *Journal of*

Hindawi
Journal of Healthcare Engineering
Volume 2023, Article ID 9857376, 1 page
https://doi.org/10.1155/2023/9857376

Retraction

Retracted: Intelligent Somatosensory Interactive Activities Restore Motor Function to Children with Autism

Journal of Healthcare Engineering

Received 1 August 2023; Accepted 1 August 2023; Published 2 August 2023

This article has been retracted by Hindawi following an investigation undertaken by the publisher [1]. This investigation has uncovered evidence of one or more of the following indicators of systematic manipulation of the publication process:

(1) Discrepancies in scope
(2) Discrepancies in the description of the research reported
(3) Discrepancies between the availability of data and the research described
(4) Inappropriate citations
(5) Incoherent, meaningless and/or irrelevant content included in the article
(6) Peer-review manipulation

The presence of these indicators undermines our confidence in the integrity of the article's content and we cannot, therefore, vouch for its reliability. Please note that this notice is intended solely to alert readers that the content of this article is unreliable. We have not investigated whether authors were aware of or involved in the systematic manipulation of the publication process.

In addition, our investigation has also shown that one or more of the following human-subject reporting requirements has not been met in this article: ethical approval by an Institutional Review Board (IRB) committee or equivalent, patient/participant consent to participate, and/or agreement to publish patient/participant details (where relevant).

Wiley and Hindawi regrets that the usual quality checks did not identify these issues before publication and have since put additional measures in place to safeguard research integrity.

We wish to credit our own Research Integrity and Research Publishing teams and anonymous and named external researchers and research integrity experts for contributing to this investigation.

The corresponding author, as the representative of all authors, has been given the opportunity to register their agreement or disagreement to this retraction. We have kept a record of any response received.

References

[1] Q. Wang, X. Wang, and L. Xu, "Intelligent Somatosensory Interactive Activities Restore Motor Function to Children with Autism," *Journal of Healthcare Engineering*, vol. 2022, Article ID 4516005, 12 pages, 2022.

Hindawi
Journal of Healthcare Engineering
Volume 2022, Article ID 4516005, 12 pages
https://doi.org/10.1155/2022/4516005

Research Article

Intelligent Somatosensory Interactive Activities Restore Motor Function to Children with Autism

Qiang Wang,[1,2] Xing Wang ,[1] and Lei Xu[3]

[1]*School of Physical Education and Training, Shanghai University of Sport, Shanghai 200438, China*
[2]*School of Sports and Health, Guangdong Polytechnic of Science and Technology, Zhuhai 519090, Guangdong, China*
[3]*School of Physical Education, South China University of Technology, Guangzhou 510640, Guangdong, China*

Correspondence should be addressed to Xing Wang; 18930132117@163.com

Received 8 January 2022; Accepted 4 March 2022; Published 27 March 2022

Academic Editor: Nima Jafari Navimipour

So far, the biomedical community has not provided clear etiological conclusions and targeted drug treatments. Educational intervention and rehabilitation are the main ways to promote the development of autistic children's ability and change the quality of life. This research mainly explores how intelligent somatosensory interactive activities can restore motor function to children with autism. Case studies are used to investigate the current problems of hand movement training for children with autism and the effect of somatosensory games on rehabilitation training for autism. The experience of autistic children using somatosensory games for hand movement training was analyzed. Through the collection, sorting, and analysis of data, the influence of different factors on users' immersive experience is explored. It designs and implements the system's somatosensory game module, including a detailed introduction to the development platform and key technologies used in the development of the somatosensory game module, and shows the functions, program flow, main features, and implementation effects of the somatosensory game. The development process of the somatosensory interaction system is introduced in detail, including model making, character control, task flow control, collision detection, interactive interface, and natural interaction methods of gesture interaction and voice interaction. This study outlines the concepts related to autism and the characteristics of children with autism. It discusses the feasibility of applying somatosensory games to the hand movement training of children with autism and analyzes the development status and application of somatosensory games in detail to lay the foundation for follow-up research. Moreover, it defines the research content of somatosensory interactive training products and clarifies the design content and direction of the product. The comfort evaluation of the somatosensory game products designed in the study reached 92.9%. This research further proves that somatosensory games have a positive effect.

1. Introduction

The specific injuries and external environmental factors of preschool children with autism reduce their chances of participating in physical activities, resulting in poor physical fitness. Social skills deficiency is one of the core defects of autism, which poses a lifelong challenge to autistic patients. However, the cause of autism is unknown, and it is a disease that accompanies life. So far, many medical experts have made unremitting efforts to relieve the symptoms of autistic patients, help them integrate into society, and improve their quality of life.

Mapping process for the study is as follows: In the first phase, therapists or teachers selected children with autism who met the inclusion criteria. In the second stage, the PEDI scale was used to evaluate the two groups of subjects, and the pretest data were obtained. The third stage is to accept the intervention of somatosensory games. In the fourth stage, after the children in the experimental group received the somatosensory game intervention, the posttest data were obtained. Active intervention training has an important role and value for autistic individuals, families, and society. First of all, active intervention can effectively reduce the degree of symptoms of autistic individuals; promote the development of various abilities such as language, social interaction, cognition, sports ability, and social adaptation; and lay a good foundation for survival and social life. Many autistic individuals can be greatly improved after

active intervention training. During their adulthood, they can get jobs smoothly and become workers and creators of social wealth. This can bring good benefits to the society while reducing the cost of social welfare. This paper studies somatosensory interaction technology, applies natural human-computer interaction technology to training, and realizes the form of using computer technology to present training content. This paper realizes the interaction of multiple human senses and accurately distinguishes the participants in the training under the condition of interference. This achieves static gesture interaction and has achieved good practical results in application. At the same time, interactive gestures are used to replace most of the mouse operations. A desktop client for the cooperative ability training of children with autism spectrum disorder is realized. The use of sports games as an intervention can improve the motor ability of autistic children and can play a certain role in improving the daily behavior of autistic children. The purpose of this article is to design a more rigorous and scientific experimental plan based on previous research, to explore the effectiveness of somatosensory games in the intervention for children with autism, and to provide theoretical and data support for the application and promotion of somatosensory games.

2. Related Work

This paper uses the self-developed somatosensory game to intervene in children with autism and analyzes the effect of its intervention on the social skills, motor skills, and daily life skills of children with autism. After receiving intervention training, autistic individuals can return to society to participate in work. This not only can effectively reduce the cost of social welfare, but also provides the possibility of creating huge social benefits. Magnusson et al. believe that autism spectrum disorder (ASD) is a neurodevelopmental disorder. Its core characteristics are social communication barriers and atypical repetitive behaviors or restrictions on the scope of interest. These characteristics appear in the preschool stage and have a major and destructive effect in the subsequent developmental stage. It was able to reliably identify most cases well before the average age at diagnosis. This provides new opportunities for early intervention, but the availability of this intervention varies significantly among American communities, and its impact is not fully understood. Regarding the effectiveness of early enhancing behavioral interventions, there is a need for individualized therapy based on the genomic characteristics of individual patients. In addition, a new wave of research on the development of new therapies for newly elucidated causal effects will eventually change the clinical approach. These conditions occur in early childhood [1]. Salter and Stevens believe that a large number of new discoveries have recently given insight into the relationship between microglia and central nervous system (CNS) diseases. Understanding the physiological functions of these cells is essential to determine their role in disease [2]. Gandal et al. believe that the susceptibility of neuropsychiatric diseases involves a complex, polygenic, and pleiotropic genetic structure. However, little is known about how genetic variation can cause brain dysfunction or pathology. They use transcriptome analysis as a quantitative readout of molecular brain-based phenotypes for five major mental illnesses (autism, schizophrenia, bipolar disorder, depression, and alcoholism) and compare them with matched controls. This comprehensive system-level view of the neurobiological structure of major neuropsychiatric diseases shows ways of molecular convergence and specificity [3]. Lyall et al. believe that polychlorinated biphenyls (PCBs) and organochlorine pesticides (OCPs) are neurodevelopmental toxins, but few studies have examined the association with autism spectrum disorder (ASD). They aim to determine whether prenatal exposure to PCBs and OCPs affects the risk of ASD and nonautistic intellectual disability (ID) in offspring. They conduct a population-based case-control study in children born in Southern California. It includes children with ASD ($n = 545$) meeting the criteria of the Diagnostic and Statistical Manual of Mental Disorders 4th Edition (DSM-IV-TR) and ID ($n = 181$), as well as a general population (GP) control ($n = 418$). They compare the concentrations of 11 PCB homologues and 2 OCPs measured in stored serum samples of the second trimester between the diagnostic groups. Logistic regression is used to calculate the ratio (AOR) associated with ASD, and to calculate the ID, compared with the GP control, and the concentration of the primary research analyte [4]. Gilbert et al. believe that the understanding of the link between the human microbiome and diseases, including obesity, inflammatory bowel disease, arthritis, and autism, is rapidly expanding. The increase in throughput and accuracy of genomic DNA sequencing of microbial communities associated with human samples is supplemented by analysis of the transcriptome, proteome, metabolome, and immunome, as well as mechanical experiments in the model system. This greatly improves the ability to understand structure and function. However, there are still many challenges. In their comments, they focused on human research to describe these challenges and proposed using existing knowledge to quickly transform from correlation to causality and finally to a strategy that can be tried to solve the problem [5]. It can be found that the delay in the development of motor skills of children with autism is closely related to autism symptoms such as social communication disorders and repetitive stereotyped behaviors, emotional disorders, behavior disorders, and social adaptation skills. As the basis of the various fields, motor skills will play an important role in the overall development. Therefore, in the intervention in the fields of cognitive ability, language level, social communication skills, behavior, and emotion, it is also necessary to pay attention to the training of motor skills of children with autism. Somatosensory games intervention also has good effects on autistic children's daily living skills. In fact, educators already use somatosensory games in practice to improve skills related to daily living in children with autism.

3. Exploring Methods of Somatosensory Interactive Activities for the Recovery of Motor Function of Children with Autism

3.1. General Framework Design of Somatosensory Rehabilitation System. Kinect was used as a somatosensory interaction tool in this study. The system is divided into two modules in a targeted manner: somatosensory game module and data

management module. The overall framework of the system is shown in Figure 1. The data management module of the system can view and manage game data on the server in real time.

3.2. Voice Interaction Module. Because Baidu Voice has the advantages of low user cost, support for multiplatform development, and diverse functions, it is used in this research to realize the voice interaction based on WorldViz. When using Baidu Voice's speech synthesis and speech recognition modules, you need to download and install the corresponding SDK package before development. Since Python is the development language in this research, only online speech synthesis Python SDK and online speech recognition Python SDK can be selected.

In games, dynamic sounds are more random, can reflect the interaction of various elements in the game, give players timely information feedback, and can better convey emotions. Although the dynamic sound will not change with the player's operation, it plays an important role in setting off and creating the atmosphere. Therefore, in game design, both dynamic sound and static sound play a very important role. In the design of somatosensory games, appropriate dynamic and static sounds should be selected according to the psychology of children with autism.

The spatial recognition degree is one-dimensional, and the direction of the sound source can be judged. However, accurate sound source localization cannot be carried out, and it needs to be combined with other auxiliary information to be able to proceed further [6].

$$d < \frac{\lambda}{1 + \cos\phi}. \tag{1}$$

ϕ is the incident direction of the sound source.

The far-field model needs to satisfy the distance R between the array and the loudspeaker [7].

$$R > \frac{\lambda L^2}{\phi}. \tag{2}$$

Suppose the signal bandwidth is B and the array aperture is L; then, [8] one has the following:

$$\frac{L}{B} \leq 1. \tag{3}$$

The signal model with reverberation can be modeled as follows:

$$y(t) = H(t) * S(t) + N(t). \tag{4}$$

$S(t)$ is the source signal.

The formula of array manifold vector is as follows [9]:

$$\begin{aligned} \alpha(z) = a(\beta, \delta) &= \begin{bmatrix} e_1 & e_3 \\ e_2 & e_4 \end{bmatrix}, \\ z &= -\frac{2\tau}{\lambda} \begin{bmatrix} \sin\beta & \cos\varphi \\ \cos\varphi & \cos\beta \end{bmatrix}. \end{aligned} \tag{5}$$

Among them, z is the wave number information of the sound source.

The parameters that need to be estimated in the sound source localization problem are M incident angle information [10].

$$\begin{aligned} y(t)_{L\times 1} &= A(\delta, \varphi)_{L\times M} S(t) + n(t)_{L\times 1}, \\ A(\delta, \varphi)_{L\times M} &= \left[e^{-jz_1} \quad e^{-jz_2} \quad e^{-jz_3} \quad \ldots \quad e^{-jz_n} \right]. \end{aligned} \tag{6}$$

The signal received by the microphone array can be modeled as follows:

$$\begin{aligned} y(t) &= [y_1, y_2, y_3, \ldots, y_n], \\ y_i(t) &= \sum_{m=1}^{M} y(t - \eta) + n(t), \\ \lambda &= \mathrm{p}^T \frac{v}{c}. \end{aligned} \tag{7}$$

Among them, λ is the time delay of i sound source relative to the origin and m microphone [11].

3.3. Database Logical Architecture. In the first layer, all network-based C/S network applications should include connection processing, authentication, and security management. The second layer is the core part of MySQL, usually called SQL Layer. The functions provided by each storage engine are concentrated in this layer, such as stored procedures, triggers, and views. The database items are shown in Table 1.

In the storage engine layer, the storage engine is really responsible for the storage and extraction of data in MySQL, and the server communicates with the storage engine through API. Different storage engines have different functions, so that we can choose the appropriate storage engine according to our own needs. Compared with other databases, MySQL is a bit different, and its architecture can be applied and played well in many different scenarios. Mainly reflected in the storage engine, the plug-in storage engine architecture separates query processing from other system tasks and from data storage and extraction. The third layer, storage engine, is usually called StorageEngineLayer. That is, the implementation part of the underlying data access operation. Storage engines cannot parse SQL, nor can they communicate with each other. They simply respond to server requests. The logical structure of the database is shown in Figure 2.

The objective function is defined as the weighted sum of four error squares [12]:

$$\begin{aligned} E &= \gamma E + \gamma_1 E_S + \gamma_2 E_N B, \\ E_D &= \sum_{P \in T} \left\| S(P) - D_0(P) \right\|^2, \end{aligned} \tag{8}$$

where E_D is the distance between the estimated depth value $D_0(P)$ and the original depth value $S(P)$ at the pixel point p.

Rectangular window [13] is as follows:

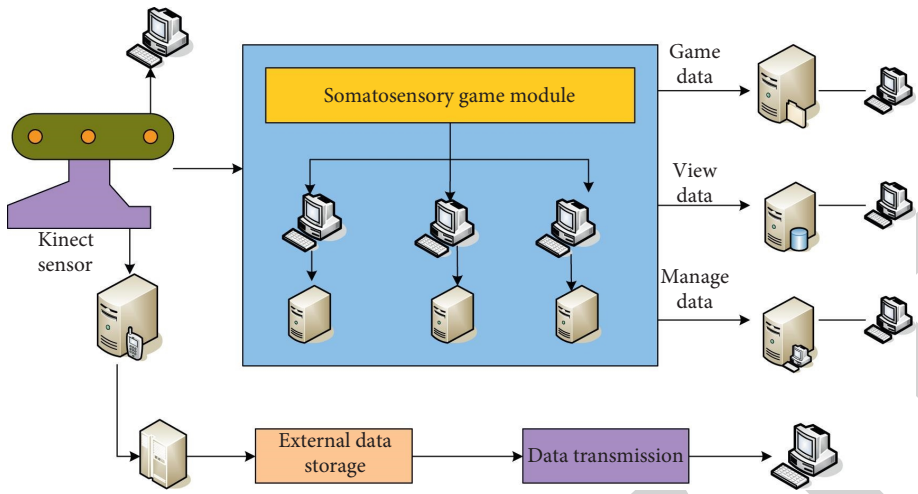

Figure 1: The overall framework of the system.

Table 1: Database items.

Field name	Type	Field description
Pro name	Varchar (32)	Project name
Pro code	Varchar (20)	Project code
Type	Varchar (20)	Project type
Researcher	Varchar (20)	Project contributor

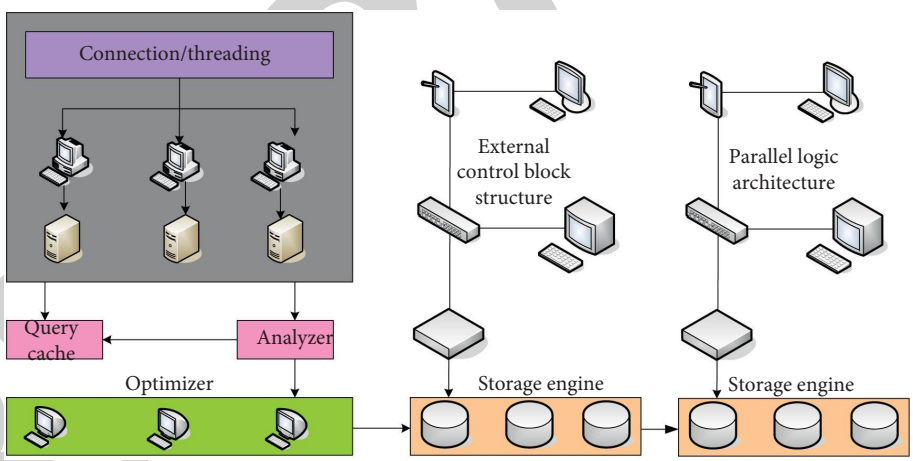

Figure 2: Database logical architecture.

$$w(n) = \begin{cases} 1, & 0 \le n \le m \\ 0, & else \end{cases}. \tag{9}$$

Hanning window is as follows:

$$w(n)_{\mathrm{h}} = \frac{(1 - \cos \delta/T)}{\gamma}. \tag{10}$$

Gaussian window is as follows:

$$w(n)_{\mathrm{g}} = e^{-\frac{1}{2}\left(\alpha - \frac{n}{n-1}\right)^2} = e^{-n^2/2\kappa}. \tag{11}$$

α is the mean value [14].

3.4. Game Menu Design. The game menu interface of this system adopts Metro style design. Metro is the main interface display style of Microsoft Windows 8 operating system. It has the advantages of intuitiveness, simplicity, and strong maneuverability and is widely recognized by users. It makes the system interface more concise and intuitive and clear at a glance, with an excellent touch experience. In the control of the system interface, besides using traditional input devices such as mouse, keyboard, and touchpad, it also supports the function of human control. The system interface adopts the "hover selection" method to realize the human body's control of the system interface. When operating the system, the player only needs to move the palm to

realize the menu selection function. There is a hand tool at the top of the system interface. When the player waves his/her hand to make a selection in the game menu, this hand tool will automatically track the position of the hand. Park your hand on the game you want to choose, and wait for the progress circle to fill up; then, the target game will be opened. This process will be completed within 2 seconds, and both left and right hands can realize the selection operation. It can get rid of traditional input devices, can easily control the system interface through the human body, and has a good control experience.

It represents its physical size in the physical coordinate system [15, 16].

$$\begin{bmatrix} u \\ v \\ 1 \end{bmatrix} = \begin{bmatrix} \frac{1}{dx} & 0 & u \\ 0 & \frac{1}{dy} & v \\ 0 & 0 & 1 \end{bmatrix} \begin{bmatrix} x \\ y \\ 1 \end{bmatrix},$$
$$\begin{bmatrix} x \\ y \\ 1 \end{bmatrix} = \frac{1}{z} \begin{bmatrix} f & -f\cot\varphi & 0 \\ 0 & \frac{f}{\sin\theta} & 1 \\ 0 & 0 & 0 \end{bmatrix} \begin{bmatrix} x_c \\ y_c \\ z_c \end{bmatrix}. \tag{12}$$

Assumptions are as follows:

$$B = A^{-T}A^{-1},$$
$$H^T A^{-T} A^{-1} H_2 = 0. \tag{13}$$

Therefore,

$$H_1^T A^{-T} A^{-1} H_1 = H_2^T A^{-T} A^{-1} H_2. \tag{14}$$

3.5. Children's Motor Function Coordination Test

3.5.1. Leg-Eye Coordination Test Items. Leg-eye coordination is one of the branches of visual-limb movement coordination. The leg-eye coordination test project simulates catching a ball. The test requires sensitive and rapid lower limb movement ability, not only to quickly accelerate or decelerate the movement, but also to pay attention to the direction and position of the ball. At the same time, it is necessary to maintain the balance of the limbs during the movement. In the scene of the tested virtual playground, facing the Kinect camera, the computer automatically attaches the "bucket" to the tested body, and the movement of the "bucket" can be controlled by moving the body. Both yellow and green baseballs will drop on the top of the screen, and the test is conducted by moving the lower body to pick up the baseballs that fall from the air. This requires the tester to quickly move his/her lower limbs to catch the ball while observing the drop of the baseball above. At the same time, it must be adjusted according to the score and falling speed represented by the baseball to ensure that enough baseballs are received so that the final score will be higher. The final test result is based on the number of balls received in 1 minute.

$$P_M = P_0 + P_V. \tag{15}$$

P_0 represents the position coordinates of the empty object, and its value is a fixed value, which can be set freely according to the specific situation; P_V is a random number.

$$V_i = V_{i-1} * 0.9. \tag{16}$$

V_i is the speed of the i-th ball [17].

3.5.2. Hand-Eye Coordination Test. The project is based on conventional evaluation methods such as the 2-hand coordination test, double maze test method, sandbag throwing, and precision throwing, and it combines the characteristics of Kinect somatosensory interaction technology and the development characteristics of children's motor ability. The design idea of this test task is orbital push ball. This task aims to test the hand-eye coordination ability of children when they push the ball. In the 3D virtual high-altitude scene, children use four gestures to drive the ball forward, while preventing the ball from falling off the air orbit. There will be some "red gems" in the middle of the track. Children need to control the small balls to collect the "red gems" to increase the score. During this test, the computer automatically records the number of "red gems" collected. When children collect "red gems," they need to convey the "red gems" they see to the brain and then control gestures to drive the ball to move to an accurate position. This is to control the speed of the ball and the displacement position of the ball. The more precise the children's gestures, the stronger the coordination and control ability of the muscles involved in sports, the higher the task completion, and correspondingly the higher their hand-eye coordination ability. If the child uses the wrong gesture during the operation, which causes the ball to fall off, the test is ended. The final test result is based on the number of "red gems" obtained without the ball falling. The lower right corner is the real-time three-dimensional animation of the human body, which can change according to the different movements of the human body. The testees can observe whether their movements are standard according to this picture.

3.5.3. Auditory-Physical Movement Coordination Test Items. Auditory-limb movement coordination ability refers to the coordination of the response actions from the auditory organs to the corresponding body parts. According to the common test methods such as "follow the rhythm" and "change rhythm continuously," the design idea of this task is to test the coordination ability of auditory-limb movement by "capturing the beat." In the virtual scene, there are 5 color buttons, among which red, yellow, and blue are valid metronome, and the rest are invalid metronome. If you increase the difficulty of the test in the future, you can use the metronome of all 5 colors. The three-color metronome

represents three different body movements, namely, raising the left hand, raising the right hand, and squatting. According to the prompts of the screen interface, the testee must maintain a high degree of attention and make corresponding physical movements in time to trigger the metronome. The distance of the different color beats on the screen is set according to the rhythm of the background music. Its perception of rhythm depends on the movement and hearing ability of the tested muscle system, as well as whether it can control the muscle movement in time when switching actions. If there is a rhythm error in the test process, it is often caused by the human muscles responding too fast or too slowly to the instructions of the brain. During the test, the computer automatically records the number of "metronomes" of different colors that are correctly triggered by the test. The test result is based on the correct number within a fixed time.

3.5.4. Balance Test Items. Static balance ability test consists of the following: normal standing with eyes open, normal standing with eyes closed, standing on one foot, and standing on one foot with eyes closed. The dynamic balance ability test mainly records the score, the maximum angular velocity, the average angular velocity, the percentage of the time spent in the front, middle, rear, and left and right areas in the total test time of the testers, the time the ball stays in the center zone and zones 1, 2, 3, and 4, as well as the test score level. According to the existing test methods, such as "single-leg balance," "jumping rope," and "toe walking," the "single-legged" task is designed. This project draws on the relevant indicators of the balance tester and the movement data of important bone points when the human body is standing on one foot. Hip Center is the key bone point of the human body when maintaining balance. The test indicators are as follows: the standing time on one foot, the total trajectory length of the skeletal point in the hip (Hip Center) within a fixed time, and the degree of shaking of the skeletal point [18].

$$LG = \sum_{i=1}^{n=1} \sqrt{(x_i - x_{i-1})^3 + (y_i - y_{i-2})^3}. \tag{17}$$

The formula is the converted two-dimensional position coordinates of the Hip Center collected by Kinect, and n is the number of collections. When the testee stands on one foot in the virtual test scene, Kinect will automatically recognize the one-foot standing action, start the test, and detect and identify the movement data of key bone points and the test time. If the tested feet touch the ground, the test automatically ends.

3.5.5. Coordination Test between Limbs. During the test, the shorter the time it takes to complete the four movements, the better the coordination ability between the limbs. The test result is based on the correct number within a fixed time.

Assuming that $p_i(f), p_i(f+1), p_i(f+2)$ is the coordinate position data of the part for 3 consecutive frames, then the displacement vector is [19] as follows:

$$\begin{aligned} d_i(f) &= p_i(f+1) - p_i(f), \\ d_i(f+1) &= p_i(f+2) - p_i(f+1). \end{aligned} \tag{18}$$

Connect the Kinect power supply, make sure that the various lines are connected correctly, and start the Kinect hardware device. Obtain the status information of the device, and then let the children under test enter the visual range of Kinect (0.5–4.5 m). Kinect will detect the child's position and return the child's position parameters. At the same time, related applications began to calculate and draw the user's human skeleton image. In addition, it listens and constantly updates the skeleton image information. In order to prevent people from entering the test area by mistake and causing interference, Kinect will automatically detect the user closest to the device and ignore the undetected bone points [20].

4. The Result of Recovery of Motor Function in Children with Autism

The evaluation results of the two groups of ABC scales before the experiment are shown in Table 2. There is no significant difference ($p > 0.05$) in S (sensation ability), R (communication ability), B (motor ability), L (language ability), $S2$ (self-care), and total scores of the two groups before the experiment, and they are comparable.

There was no significant difference ($p > 0.05$) in the scores of the experimental group after treatment. The results of the significance evaluation of the experimental group after treatment are shown in Figure 3.

There was no significant difference in S, R, B, L, $S2$, and total score of the experimental group after the experiment ($p > 0.05$). Table 3 shows the evaluation results of the ABC scale before and after the experiment in the control group.

The comparison results of the two groups of ABC scale evaluation scores before and after the experiment are shown in Figure 4. There is no significant difference ($p > 0.05$) in S, R, B, L, $S2$, and the total score between the two groups after the experiment.

The differences in perceived behaviors, gross movements, fine movements, language communication, cognitive behaviors, social behaviors, and self-care ability before and after training were statistically significant ($p < 0.0001$). The score comparison of various behaviors before and after training is shown in Table 4.

In cognition ($t = 4.449$, $p < 0.0001$), social ($t = 3.914$, $p < 0.0001$), and other aspects of the score difference before and after training, males are higher than females. This shows that the training effect on boys in these aspects is better than that on girls. The comparison of gender training effects is shown in Figure 5.

According to the classification criteria, the scores and total scores of 5 items are analyzed as shown in Table 5.

In order to give the subjects a more reasonable and targeted explanation, this article will analyze the test item scores of balance, hearing and limb coordination, limb coordination, hand-eye coordination, and leg-eye coordination, as shown in Table 6. The five test items are designed

Table 2: Evaluation results of the two groups of ABC scales before the experiment.

Subscale parameters	Experimental group ($n = 18$)	Control group ($n = 14$)	P
S (sensory ability)	9.83 ± 7.326	10.428 ± 5.543	0.802
R (communication ability)	10.889 ± 8.858	11.57 ± 7.165	0.816
B (exercise ability)	6.556 ± 6.401	8.36 ± 7.239	0.461
L (language ability)	12.833 ± 7.422	8.79 ± 7.106	0.130
$S2$ (self-care)	9.556 ± 6.061	8.57 ± 3.715	0.598

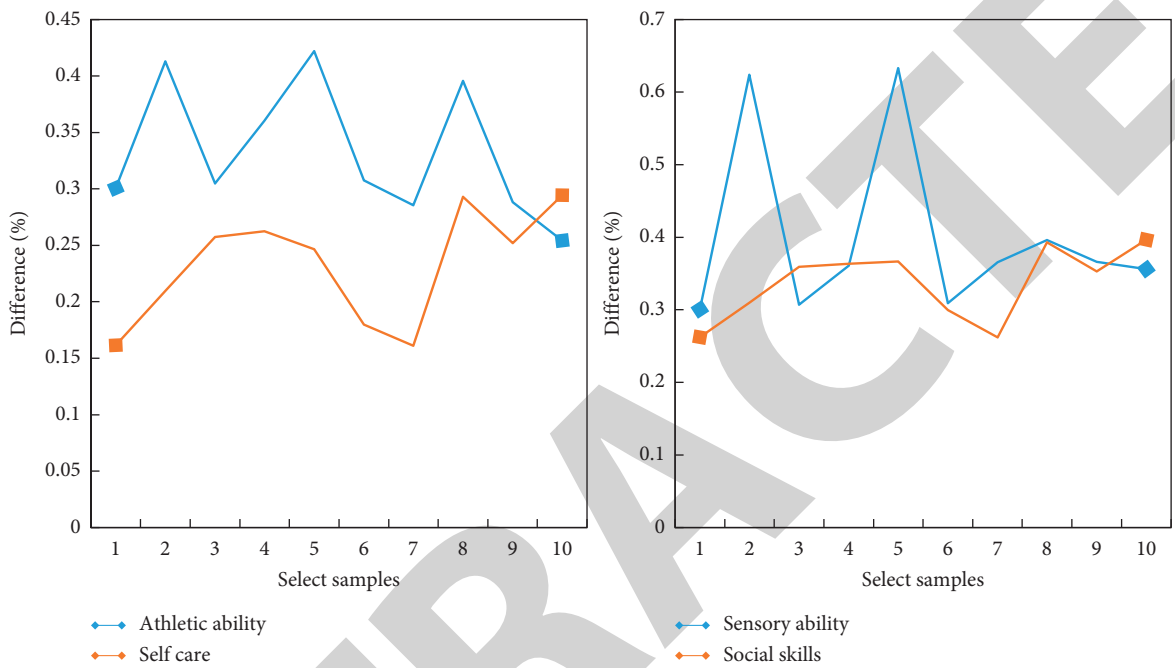

Figure 3: Significance evaluation results after treatment in the experimental group.

Table 3: Evaluation results of the ABC scale before and after the control group experiment.

Subscale parameters	Before the experiment	After the experiment	P
S (sensory ability)	$10.\ 428 \pm 5.543$	$11.\ 571 \pm 5.867$	0.680
R (communication ability)	11.57 ± 7.165	12.357 ± 6.368	0.396
B (exercise ability)	8.36 ± 7.239	11.214 ± 7.392	0.929
L (language ability)	8.79 ± 7.106	$11.\ 142 \pm 8.11$	0.114
$S2$ (self-care)	8.57 ± 3.715	10.928 ± 4.322	0.625

according to a certain element of the motor coordination ability, in order to explain the specific ability level of the subjects in a certain item. The scores of the 5 test items of the subjects were divided into 4 ability levels according to the standard deviation. We will analyze the 5 test items at different levels of progress at different ability levels.

It can be seen from Table 6 that in each project, there are 3 projects at ability level 1, and 2 projects at ability level 2. It can be seen from the results that most of the people with the first level of progress are at the level to be developed and the general middle level.

People at level 2 of progress are concentrated at level 2 of ability in each project. That is to say, most of the people at the second level of progress are at the general middle level. The ability level analysis is shown in Figure 6.

Pediatric Evaluation of Disability Inventory (PEDI) is a professional scale for functional assessment of children with low abilities. It can effectively detect the impairment of each field or energy area of children with disabilities, judge the efficacy of rehabilitation, formulate rehabilitation plans, and guide rehabilitation training. Statistical analysis of the data was performed, and the analysis results are shown in Figure 7. The scores of PEDI scale of daily living ability improved more obviously.

According to the weight ranking of evaluation indicators, in the interaction design of somatosensory games, the evaluation indicators have the largest weight. This shows that the evaluation index is more important and should be given priority in the design. The ranking of evaluation indicators is shown in Figure 8.

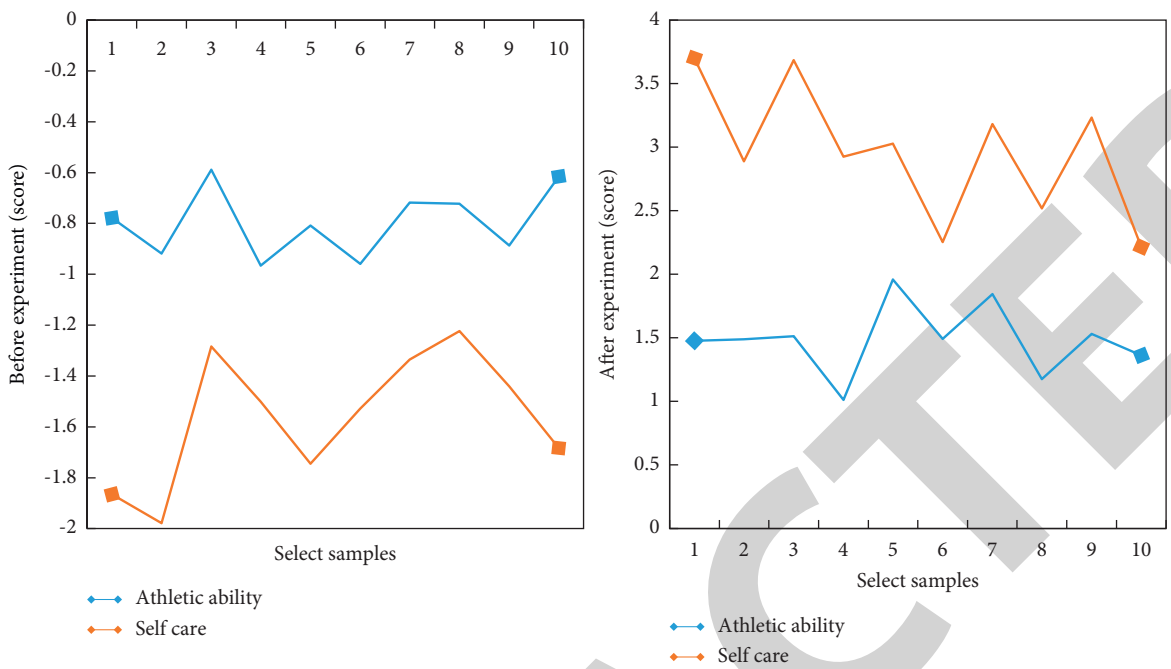

Figure 4: Comparison between the two groups of ABC scale evaluation scores before and after the experiment.

Table 4: Comparison of scores of various behaviors before and after training.

Subscale parameters	Before training	After training	Score difference before and after training
Perceptual behavior	23.76 ± 0.94	39.07 ± 0.99	15.31 ± 0.80
Gross movement	36.63 ± 1.21	55.71 ± 1.10	19.08 ± 0.79
Fine motor	31.64 ± 1.30	46.21 ± 1.18	14.57 ± 0.62
Language communication	25.03 ± 1.63	48.01 ± 1.64	22.98 ± 1.11
Cognitive behavior	17.64 ± 1.03	34.82 ± 1.18	17.18 ± 0.87
Social behavior	17.38 ± 0.74	30.85 ± 0.84	13.48 ± 0.65

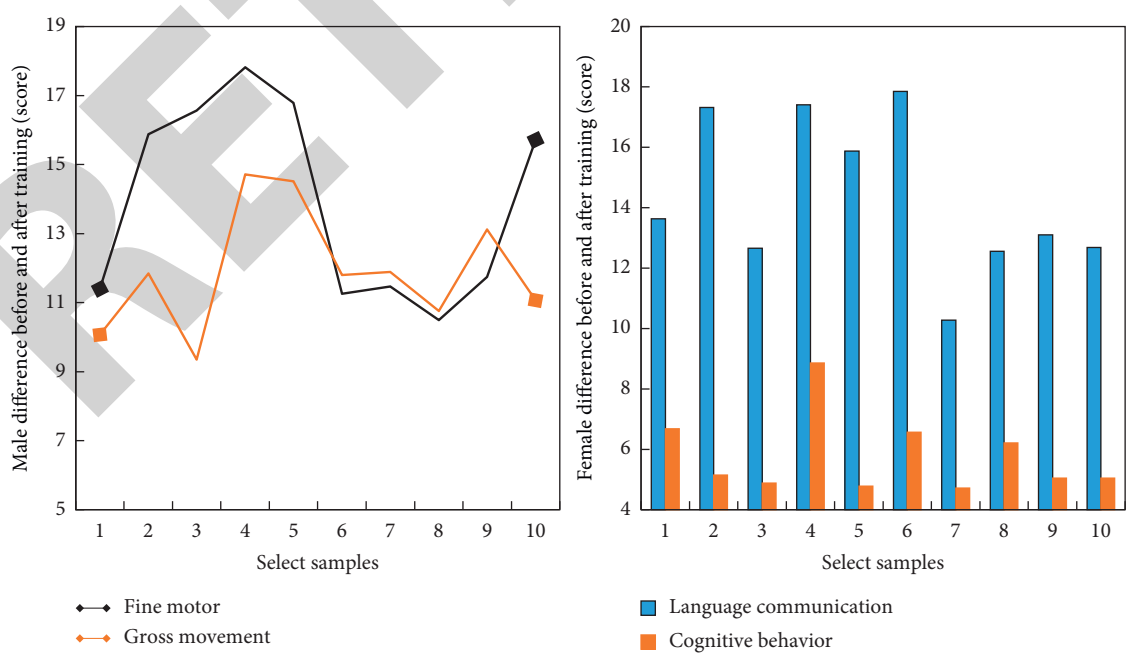

Figure 5: Comparison of gender training effects.

Table 5: Analysis of the scores and total scores of 5 items according to the classification criteria.

Project	Progress level one	Progress level two	Progress level three	Progress level four
Balance test	4	13	18	4
Auditory-physical coordination test	4	15	15	5
Limb coordination test	4	10	20	3
Hand-eye coordination test	5	14	17	4
Leg-eye coordination test	5	12	18	4
Total score	1	18	18	2

Table 6: Detailed analysis of the test item scores of balance, auditory-limb coordination, limb-limb coordination, hand-eye coordination, and leg-eye coordination.

Project	Progress level 1	Progress level 2	Progress level 3	Progress level 4
Balance test	1	0	0	0
Auditory-physical coordination test	1	0	0	0
Limb coordination test	1	0	1	0
Hand-eye coordination test	0	0	0	0
Leg-eye coordination test	0	1	0	1

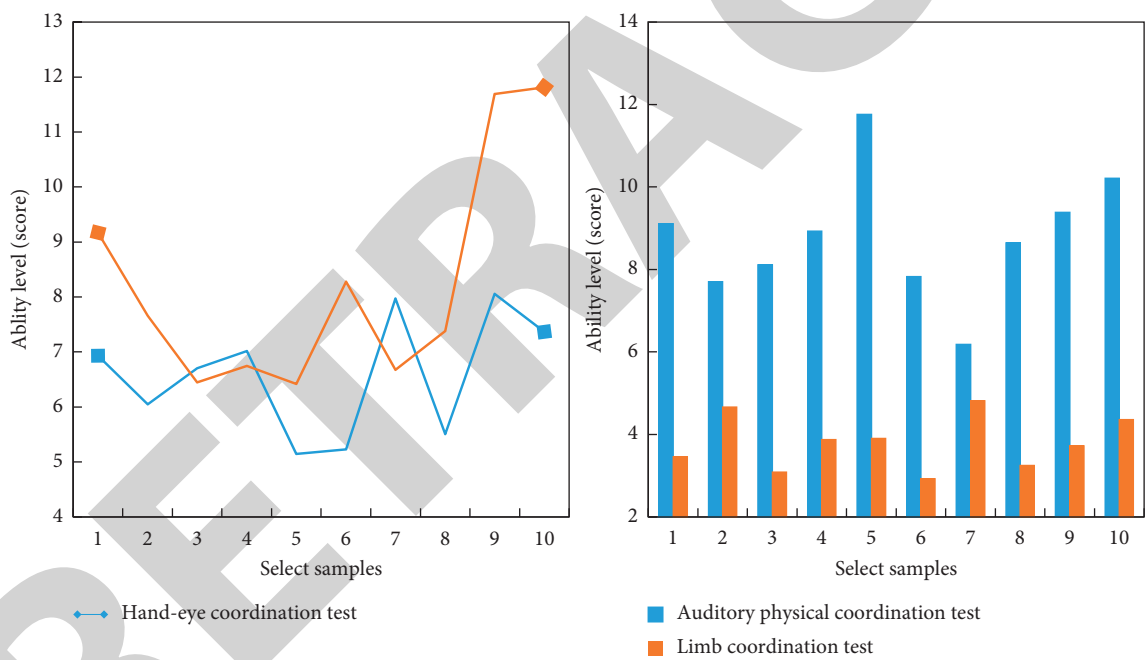

Figure 6: Ability level analysis.

It can be seen from Figure 8 that the simple screen, simple operation, and straightforward interface level in the evaluation index account for a larger weight. In order to save the cost of design, these indicators should be given priority in the design.

A total of 28 people participated in the design evaluation, including 10 teachers and 18 parents. 28 questionnaires were returned, of which 28 were valid questionnaires. 92.9% of people think that the training process can meet the requirements of comfort, 89.3% of people think that training aids can bring a positive experience to the training of autistic children, 100% of people think that the design plan meets the requirements of function, and 96.4% of people think that the design can achieve the desired effect and improve the user experience of the training process. The evaluation result of the system is shown in Figure 9.

5. Discussion

The structural characteristics of children with autism determine their functional status, and dysfunction affects their normal growth and development mode, which ultimately leads to structural changes. Social communication barriers restrict the reception and feedback of external information in children with autism, and repetitive stereotyped behaviors

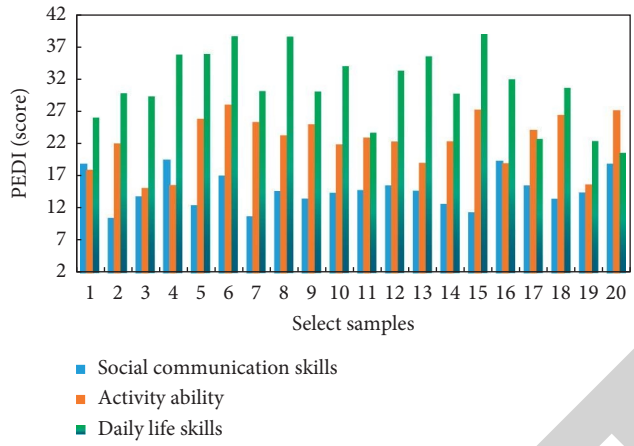

Figure 7: PEDI scale score.

restrict the development of complex continuous movements in children with autism [21].

Appropriate sports participation will have a positive impact on children's basic sports ability, quality of life, healthy lifestyle, emotions, and psychology. However, because children with autism are closed in their own world, they are unwilling to receive information from the outside world or even resistant to this. As an effective internal stimulating factor, sports are not easy to reject by children with autism, and sports can provide opportunities to increase the interaction and communication behavior of children with autism [22].

Exercise can enhance and is beneficial to physical and mental health, and cognitive and intellectual development. For example, activities such as hand-slapped basketball and foot-passing football improve children's hand-eye coordination and visual concentration; running and frog jumping on the road improve the coordination and flexibility of children's limbs and torso; and lifting small dumbbells, squatting, jumping, and frog jumping can increase the muscle strength of children's limbs, which is of great help to the improvement of physical coordination. Jogging can exercise children's endurance, and cardiopulmonary function can also be improved. The practice of abdominal breathing and blowing games can adjust the breathing pattern of children with autism and improve cardiopulmonary function. Repeated practice of all aspects of movement in sports can not only promote the improvement of athletic ability and lay a good foundation for the later development of motor skills, but also exercise self-control.

In order to better serve children with autism and let the rehabilitation of children with autism embark on a path of sustainable development, it is necessary to increase the rehabilitation staff and management team with rich experience and strong professional ability. Corresponding measures should be taken to stabilize the professional team of rehabilitation personnel and prevent the loss of employees. Rehabilitation personnel responsible for children with autism improve their rehabilitation skills and actively adjust their mentality through continuous learning. They accept short-term rehabilitation training for children with autism implemented by the Disabled Persons' Federation and other departments, learn the most cutting-edge rehabilitation skills in the field of children's autism rehabilitation, and skillfully apply them in rehabilitation work. Rehabilitation institutions check when personnel are admitted, recruit high-quality personnel based on the core competence requirements of child autism rehabilitation personnel, guide and promote the self-development of rehabilitation personnel through the assessment and review system, and improve the capabilities of rehabilitation personnel through the provision of systematic on-the-job training and academic exchanges.

To a certain extent, autism is a specific behavioral disorder and excessive syndrome, with the inability to carry out normal social activities like ordinary children. Therefore, it is particularly important to take effective and scientific interventions for stereotyped behaviors. There are many similarities between sensory integration disorder and stereotyped behavior in behavior performance, which is easy to cause confusion. Therefore, scholars who pay attention to this field explore the relationship between the two and come to the conclusion in the process of exploring the reasons for the occurrence of stereotyped behavior: the main internal reason for the occurrence of stereotyped behavior is to seek sensory stimulation [23].

In recent years, although the society as a whole has continuously deepened the understanding of autism, there is still a certain gap between the research on social support, social welfare, and security system of autistic children and foreign countries. Personnel engaged in education in special schools also urgently need a set of methods that have proven effective through theoretical and practical research to educate children with autism.

Often, many children with autism will show a clear sense of anxiety, and they will unconsciously relieve their anxiety through various stereotyped behaviors. This situation will cause children to be in an idle state, which will show stereotyped behaviors to seek various stimuli. Therefore, it is particularly important to seek professional treatment organizations to arrange reasonable treatment plans for children with autism and to provide children with a relaxing

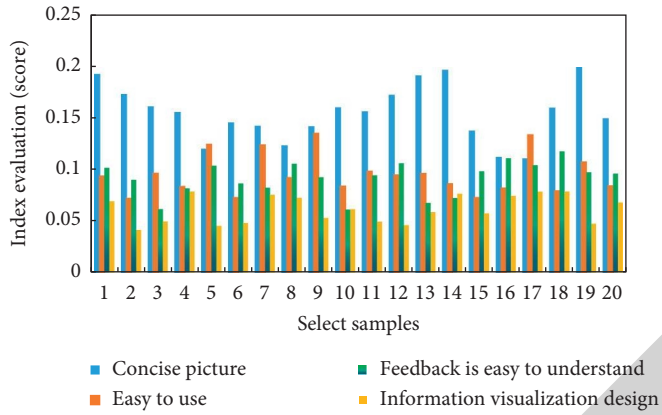

Figure 8: Ranking of evaluation indicators.

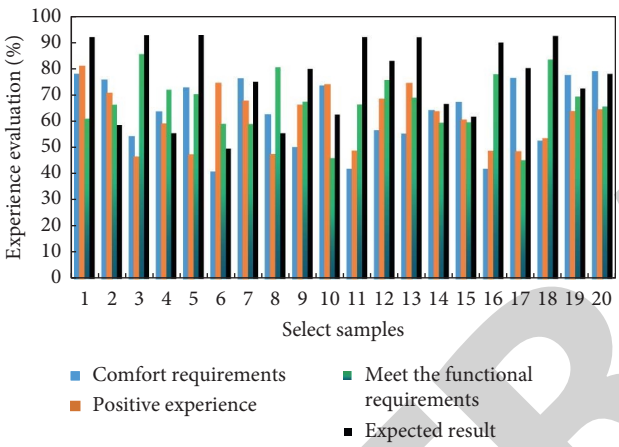

Figure 9: Evaluation results of the system.

and pleasant treatment environment. In addition, parents can scientifically and rationally arrange their children's treatment plan with the teacher, improve the efficiency of rehabilitation, and develop scientific and reasonable living habits [24].

The description and evaluation of the functional status of children with autism should be carried out by professionals. The functional status of children is a process of dynamic balance between the individual and the environment. In the evaluation, the child's family situation and the situation of the school or rehabilitation institution should also be fully considered. Rehabilitation training for children with autism is a long process and requires more care and support from the family and society. Therefore, a family-school or rehabilitation institution-society long-term close cooperation relationship should be established to jointly create a good rehabilitation training and living and learning environment for children with autism [25].

6. Conclusion

Studies have shown that somatosensory games are effective in rehabilitation training for children with autism. However, it is rare to design a somatosensory game based on the characteristics of autistic children from the perspective of interaction design and user experience design to enhance the initiative and enthusiasm of the training of children with autism, thereby improving the effect of training. Through the design and implementation of the experimental program, the subjects are trained in a planned way, and the effectiveness of the system is finally verified by analyzing the training data and evaluation data of the subjects. The use of advanced computer technology to partially replace the traditional training model also provides a certain reference. However, this study found that there are many problems in the use of somatosensory games for hand training in children with autism after field investigation, and training aids must be used to achieve the best results. This requires research on the form and function of training aids to improve the user experience of autistic children during training. Therefore, this research has great research prospects. Healthcare intervention based on intelligent interactive gesture technology can scientifically and effectively exercise the muscle strength and balance, throwing, jumping, and climbing abilities of children with autism; visual responses, anxiety responses, verbal communication, and interpersonal relationships were improved. Somatosensory games can effectively stimulate the learning motivation of children with autism and show good intervention effects. Therefore, in the intervention practice of children with autism, it is possible to appropriately combine somatosensory games on the basis of existing intervention methods to intervene in children with autism, to improve the intervention effect for children with autism.

Data Availability

No data were used to support this study.

Conflicts of Interest

The authors declare that there are no conflicts of interest with any financial organizations regarding the material reported in this manuscript.

Acknowledgments

This work was supported by Youth Innovative Talents Project of Guangdong Provincial Department of Education

Hindawi
Journal of Healthcare Engineering
Volume 2023, Article ID 9789461, 1 page
https://doi.org/10.1155/2023/9789461

Retraction

Retracted: Effective CBMIR System Using Hybrid Features-Based Independent Condensed Nearest Neighbor Model

Journal of Healthcare Engineering

Received 10 October 2023; Accepted 10 October 2023; Published 11 October 2023

This article has been retracted by Hindawi following an investigation undertaken by the publisher [1]. This investigation has uncovered evidence of one or more of the following indicators of systematic manipulation of the publication process:

(1) Discrepancies in scope
(2) Discrepancies in the description of the research reported
(3) Discrepancies between the availability of data and the research described
(4) Inappropriate citations
(5) Incoherent, meaningless and/or irrelevant content included in the article
(6) Peer-review manipulation

The presence of these indicators undermines our confidence in the integrity of the article's content and we cannot, therefore, vouch for its reliability. Please note that this notice is intended solely to alert readers that the content of this article is unreliable. We have not investigated whether authors were aware of or involved in the systematic manipulation of the publication process.

Wiley and Hindawi regrets that the usual quality checks did not identify these issues before publication and have since put additional measures in place to safeguard research integrity.

We wish to credit our own Research Integrity and Research Publishing teams and anonymous and named external researchers and research integrity experts for contributing to this investigation.

The corresponding author, as the representative of all authors, has been given the opportunity to register their agreement or disagreement to this retraction. We have kept a record of any response received.

References

[1] H. D. Praveena, N. S. Guptha, A. Kazemzadeh, B. D. Parameshachari, and K. L. Hemalatha, "Effective CBMIR System Using Hybrid Features-Based Independent Condensed Nearest Neighbor Model," *Journal of Healthcare Engineering*, vol. 2022, Article ID 3297316, 9 pages, 2022.

Hindawi
Journal of Healthcare Engineering
Volume 2022, Article ID 3297316, 9 pages
https://doi.org/10.1155/2022/3297316

Research Article

Effective CBMIR System Using Hybrid Features-Based Independent Condensed Nearest Neighbor Model

Hirald Dwaraka Praveena,[1] Nirmala S. Guptha,[2] Afsaneh Kazemzadeh,[3] B. D. Parameshachari,[4] and K. L. Hemalatha[5]

[1]*Department of Electronics and Communication Engineering, Sree Vidyanikethan Engineering College, Tirupati 517102, Andhra Pradesh, India*
[2]*Department of CSE-Artificial Intelligence, Sri Venkateshwara College of Engineering, Bengaluru 562157, India*
[3]*Shabakeh Pardaz Azarbaijan, Tabriz, Iran*
[4]*Department of Telecommunication Engineering, GSSS Institute of Engineering and Technology for Women, Mysuru 570016, India*
[5]*Department of ISE, Sri Krishna Institute of Technology, Bengaluru 560090, India*

Correspondence should be addressed to B. D. Parameshachari; paramesh@gsss.edu.in

Received 29 January 2022; Revised 28 February 2022; Accepted 8 March 2022; Published 26 March 2022

Academic Editor: Alireza Souri

In recent times, a large number of medical images are generated, due to the evolution of digital imaging modalities and computer vision application. Due to variation in the shape and size of the images, the retrieval task becomes more tedious in the large medical databases. So, it is essential in designing an effective automated system for medical image retrieval. In this research study, the input medical images are acquired from new Pap smear dataset, and then, the visible quality of acquired medical images is improved by applying image normalization technique. Furthermore, the hybrid feature extraction is accomplished using histogram of oriented gradients and modified local binary pattern to extract the color and texture feature vectors that significantly reduces the semantic gap between the feature vectors. The obtained feature vectors are fed to the independent condensed nearest neighbor classifier to classify the seven classes of cell images. Finally, relevant medical images are retrieved using chi square distance measure. Simulation results confirmed that the proposed model obtained effective performance in image retrieval in light of specificity, recall, precision, accuracy, and f-score. The proposed model almost achieved 98.88% of retrieval accuracy, which is better compared to other deep learning models such as long short-term memory network, deep neural network, and convolutional neural network.

1. Introduction

In recent times, medical imaging plays a crucial role in early treatment, diagnosis, and detection of several diseases [1]. Recently, medical imaging comprises of dissimilar imaging modalities such as ultrasound, fluoroscopy, computed tomography, and histopathology that helps in interpreting and understanding the dissimilar organs of the human body [2, 3]. In recent scenario, the medical facilities and hospitals create an enormous number of medical images, where it is a complex task to interpret medical images that needs extensive knowledge [4, 5]. So, researchers developed many support systems such as computer aided diagnosis system and content-based medical image retrieval (CBMIR), to assist radiologists or clinicians for interpreting the medical images [6, 7]. Among the available support systems, CBMIR system gained more attention among the researchers, which aids clinicians in finding the identical medical images during diagnosis [8]. Most of the developed CBMIR systems work based on image information such as edges, texture, color, and shape features are generally extracted from handcrafted feature extraction techniques [9–20]. Incompatibility

between high- and low-level image features leads to "semantic gap" that affects the overall system performance by creating an ambiguity between the extracted feature vectors and the query image [21–23].

In this research study, a new model is proposed for enhancing the performance of CBMIR in the large medical datasets. In this research, the input images are acquired from a new Pap smear dataset, which comprises of 917 cell images. Furthermore, image data augmentation is used to generate more training samples by performing random rotations, flips, and shear, where the total augmented samples are 1502 cell images. Next, preprocessing is accomplished using normalization technique for improving the contrast of acquired and augmented cell images, which help in achieving better retrieval performance. After data preprocessing, feature extraction is performed using two global descriptors such as modified local binary pattern (MLBP) and histogram of oriented gradients (HOG) for extracting the feature vectors. In this research, hybrid feature extraction has advantages such as reduces overfitting risk, speeds up the training process, increases the explainability of classifier, and improves the data visualization. Furthermore, an independent condensed nearest neighbor (ICNN) classifier is used for classifying the images of seven classes in a new Pap smear dataset, and then, the relevant medical images are retrieved by applying chi square distance. Lastly, the performance of the hybrid feature-based ICNN model is analysed by means of recall, precision, accuracy, f-score, and specificity.

This study is prearranged as follows; a few recent year papers on the topic "CBMIR" are surveyed in Section 2. The proposed hybrid feature-based ICNN model is briefly explained in Section 3. The experimental investigation of the proposed hybrid feature-based ICNN model is represented in Section 4. The conclusion of the present research work is stated in Section 5.

2. Related Works

Haripriya and Porkodi [24] implemented a new parallel deep convolutional neural network (PDCNN) algorithm for an effective CBMIR. The developed algorithm consists of higher level semantic, compact, and lower level content features that significantly handles the imbalanced dataset issues and decreases the DCNN training time in DICOM images. The compact and higher level feature descriptors, LBP, radon, and HOG, resolve the imbalanced dataset issue. In addition, data parallelism was accomplished in the DCNN algorithm for reducing the network training time by executing multiple central processing unit cores on a single computer. The developed algorithm obtained effective performance in CBMIR by means of f-measure, recall, and precision. However, the developed DCNN algorithm was computationally expensive, while using higher end graphics processing unit systems. Ahmed [25] introduced a new relevance feedback retrieval method (RFRM) to obtain better performance in CBMIR. In this study, feedback implementation was done based on voting, and then, feature extraction was accomplished by gray level co-occurrence matrix, and color moments for extracting feature coefficients. Additionally, the top images retrieved from every class were considered as voters that help to choose the effective similarity coefficients, and it were used for final searching mechanism. The statistical investigation showed that the presented model obtained better performance in CBMIR in terms of recall and precision on Kvasir dataset. However, the presented model consumes more time for searching mechanism because it treats each similarity coefficients with the same weight.

Öztürk [26] implemented a novel hash code generation approach for reducing the semantic space between the higher and lower feature vectors for imbalanced medical datasets. Initially, the discriminative feature vectors were extracted from the medical images by employing the CNN model, and then, the imbalance between the classes was reduced by using synthetic minority oversampling approach. In the third phase, deep stacked autoencoder was applied to convert the extracted feature vectors into 13 symbols or 13 character label for image retrieval. The simulation results confirmed that the developed approach obtained successful retrieval performance compared to state-of-the-art approaches. The direct use of feature vectors extracted from CNN was inadequate, due to its higher dimensionality nature that increases system complexity.

Veerashetty and Patil [27] used Gaussian filter for medical image enhancement, and then feature extraction was performed using Manhattan distance-based HOG (MHOG) for extracting the feature vectors from the denoised image. Lastly, Euclidean distance measure was used for similarity matching between the extracted feature vectors for relevant medical image retrieval. The experimental outcome showed that the developed MHOG approach improved retrieval accuracy upto 5% to 15% in CBMIR compared to state-of-the-art approaches. However, the developed MHOG approach extracts only color features, which were insufficient to obtain adequate results in the large medical datasets. Shakeel et al. [28] presented a new image retrieval system based on probabilistic neural network and improved watershed histogram thresholding technique. The developed system obtained high retrieval performance compared to the existing systems in terms of precision, recall, and accuracy on large medical dataset. The developed image retrieval system has some limitations such as flat valleys, noise sensitive, and computationally expensive.

Sampathila and Martis [29] used texture, shape, and color features to retrieve relevant medical images from large dataset. In this study, histogram-based cumulative distribution function and gray level co-occurrence-based Haralik's feature descriptor were applied for feature extraction. Additionally, the distance between the extracted feature vectors was determined using k-nearest neighbor technique for final medical image retrieval. The performance of the presented model was analysed in terms of recall, precision, and average accuracy. As a future extension, an image denoising technique need to be developed to decrease electronic noise, motion artifacts, processing error, and acquisition concern. In order to highlight the aforementioned problems, a novel hybrid features-based ICNN model is proposed for improving the performance of CBMIR. Lin

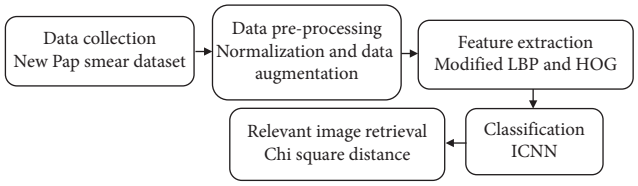

Figure 1: Workflow of the proposed model.

et al. [30] applied the CNN-based method for cell morphology for cervical cell classification in Pap smear. The cervical cell dataset is used to test the performance of the developed method and adaptively re-sampled image patches centred on nuclei. Several CNN models such as DenseNet, ResNet, GoogLeNet, and AlexNet were used to pretrained on ImageNet dataset and fine-tuned for dataset. The CNN learning performance is improved adding nucleus mask and cytoplasm as new information.

Allehaibi et al. [31] applied mask regional CNN (Mask RCNN) for cervical cell segmentation and VGG-like net is used to classify the image. The mask RCNN and transfer learning is applied for the segmentation in the image. The Herlev Pap Smear dataset was used to test the performance of the developed mask-RCNN model. The VGG-like Net is applied on whole segmented cell and improves the performance of the classification. Ghoneim et al. [32] applied the CNN-based model for the cervical cancer cell detection and classification system. The CNN model is applied to extract deep learned features and extreme learning machine (ELM) is applied for classification. The transfer learning and fine tuning are applied for CNN classification and the model is tested with autoencoder and multilayer perceptron (MLP) classifiers. The results show that the developed method has higher performance in classification than existing methods in cervical cancer cell detection.

2.1. Methodology. The proposed retrieval model includes five phases such as data collection: new Pap smear dataset, data preprocessing: normalization and data augmentation, feature extraction: modified LBP and HOG, classification: ICNN, and image retrieval: Chi square distance measure. However, the workflow of proposed model is indicated in Figure 1.

2.1.1. Data Collection. In this research study, the proposed hybrid feature-based ICNN model performance is tested by using new Pap smear dataset which totally comprises of 917 cell images [33, 34]. The subtypes in new Pap smear dataset is determined in

(i) Ninety eight cell images are normal columnar epithelial.

(ii) Seventy cell images are normal intermediate squamous epithelial.

(iii) Seventy four cell images are normal superficial squamous epithelial.

(iv) One hundred and six cell images are abnormal moderate squamous nonkeratinizing dysplasia.

Figure 2: Sample images of new Pap smear dataset.

Figure 3: Sample normalized images of new Pap smear dataset.

(v) One hundred and fifty cell images are abnormal squamous cell carcinoma in situ intermediate.

(vi) One hundred and ninety seven cell images are abnormal severe squamous nonkeratinizing dysplasia.

(vii) One hundred and eighty two cell images are abnormal squamous nonkeratinizing dysplasia. The sample images of new Pap smear dataset is graphically depicted in Figure 2.

2.1.2. Data Preprocessing. After collecting the data from new Pap smear dataset, image data augmentation technique is applied to expand the size of new Pap smear dataset by generating modified version of cell images in the dataset [35]. The image data augmentation technique is used for expanding the training sets that enhance the ability of the proposed hybrid feature-based ICNN model, where the total augmented samples are 1502 cell images.

Secondly, preprocessing is accomplished using normalization technique that modifies the range of pixel values to a normal distribution for enhancing the contrast of collected images [36]. Normalization technique transforms the cell image $I \longrightarrow \{\text{Min}, \ldots, \text{Max}\}$ into a new image with pixel values in the range (newMin, newMax) $I_N \longrightarrow \{\text{new Min}, \ldots, \text{new Max}\}$. The mathematical equation of linear normalization technique is defined as

$$I_N = (I - \text{Min})\frac{\text{new Max} - \text{new Min}}{\text{Max} - \text{Min}} + \text{new Min}, \quad (1)$$

where I states input cell image, I_N denotes normalized cell image, Max – Min denotes maximum and minimum pixel values, and new Max – new Min indicates new maximum and minimum pixel values, which ranges from 0 to 255. The sample normalized images of new Pap smear dataset is graphically indicated in Figure 3.

2.1.3. Hybrid Feature Extraction. After normalizing the images, feature extraction is accomplished using two global

descriptors, HOG [37] and modified LBP [38], to extract the feature vectors for better classification. The LBP is a simple and efficient feature descriptor, which works on the basis of gray-scale invariances that majorly depends on texture and local image patterns. In this descriptor, pixel values are weighted by power of two for storing the location of central pixel x_c which is mathematically represented in as

$$LBP\,(x, y) = \sum_{i=0}^{m-1} f\left(x_i - x_c\right)^{2i}, \quad f(x) = \left\{\begin{matrix} 1, x \geq 0 \\ 0, x \leq 0 \end{matrix}\right\}, \tag{2}$$

where x and y represent pixel position, which is utilized for determining the central pixel x_c, m indicates neighborhood image pixel, and x_i indicates gray value of central pixel x_c. In addition, the uniform model U is calculated in LBP feature descriptor, while the jumping time increases and the validation area is small. The uniform model U is calculated by

$$U\left(LBP(x, y)\right) = \left|f\left(x_{c-1} - x_i\right) - f\left(x_0 - x_i\right)\right| + \sum_{i=1}^{m-1}\left|f\left(x_c - x_i\right) - f\left(x_{c-1} - x_i\right)\right|. \tag{3}$$

In modified LBP descriptor, local difference vector D_p is calculated for central pixel x_c that delivers effective performance against the illumination condition, where the local difference vector D_p is mathematically depicted in

$$D_p = s_p \times m_p \left\{\begin{matrix} s_p = sign\left(D_p\right) \\ m_p = \left|D_p\right| \end{matrix}\right\}, \tag{4}$$

where s_p indicates sign of D_p and m_p denotes magnitude of D_p. HOG feature descriptor includes two important aspects: (i) captures the local appearance of cell image and (ii) completely invariance to illumination condition. At first, horizontal gradients G_H and vertical gradients G_V are calculated for normalized image I_N using

$$G_H = I_N \times [-1\,0\,1], \tag{5}$$

$$G_V = I_N \times [-1\,0\,1]^T. \tag{6}$$

Furthermore, the gradient magnitude $Gm(I_N)$ and angular orientation $\varnothing(I_N)$ are determined by using equations (7) and (8). The total extracted features HOG_{features} are determined by equation (9):

$$Gm\left(I_N\right) = \sqrt{G_V^2\left(I_N\right) + G_H^2\left(I_N\right)}, \tag{7}$$

$$\varnothing\left(I_N\right) = tan^{-1}\left(\frac{G_V\left(I_N\right)}{G_H\left(I_N\right)}\right), \tag{8}$$

$$HOG_{\text{features}} = B_{\text{img}} \times B_s \times N_b, \tag{9}$$

where N_b indicates bin number, B_s represents block size, and B_{img} denotes blocks per cell image. By using feature level fusion, the extracted 348 HOG features and 629 LBP feature vectors are combined and fed to the classifier for data classification.

2.1.4. Classification and Retrieval. The extracted feature vectors are fed to ICNN classification technique for classifying the samples of seven classes, which are mentioned in the data collection phase, and then, the relevant cell images are retrieved by finding the distance between extracted feature vectors using chi square distance measure. CNN is one of the extensively utilized image retrieval models in CBMIR, which is also called as Harts model. Initially, include the samples in reduced set, and then, every sample is validated by its nearest neighbor in the compressed set. The relevant cell images are classified if the label matches with the reduced set; orElse new image samples are added in the condensation. Though the iteration is repeated by the CNN model, until all the training image samples are correctly classified, one of the major advantages of the CNN model is it retains the sample captioning, which diminishes computational overhead and system storage. The CNN model usually works by including prototype in the existed prototype set, until the training image samples are classified properly. In this scenario, each class is divided into Voronoi likely areas that is mathematically determined in equations (10)–(12):

$$R_j = \cup_{i=1}^{n} V_{ji}, \quad j = 1, \ldots..c, \tag{10}$$

where V_{ji} indicates normalized value of ith and j^{th} variable, n represents total regions in class j, and R_j denotes Voronoi area. In this circumstance, the total number of classes is equal to parameter $c = 7$:

$$V_{ji} \cap V_{jk} = \varnothing, \quad i \neq k, \tag{11}$$

$$V_{ji} \cap V_{kl} = \varnothing, \quad j \neq k \text{ or } i \neq l, \tag{12}$$

where V_{kl} indicates the normalized value of kth and l^{th} variable and V_{jk} represents the normalized value of jth and k^{th} variable. In the CNN model, the regular or basic prototypes are arranged in an ascending order, and then, the training set is classified by using the arranged prototypes which are labeled one. Then, a representative image sample of every class is resolute on the basis of incorrectly classified samples for reclassification. In the CNN model, the reclassification is accomplished with expanded prototype sets.

The identification of incorrectly classified samples is a repetitive process that severely increases the system cost. To highlight this problem, the ICNN model is developed for calculating the subsets of training samples with nearest neighbor rules. The developed ICNN model utilizes triangular inequality that effectively identifies the worst case count and reduces the system computational cost. The developed ICNN model performs the following steps for image classification:

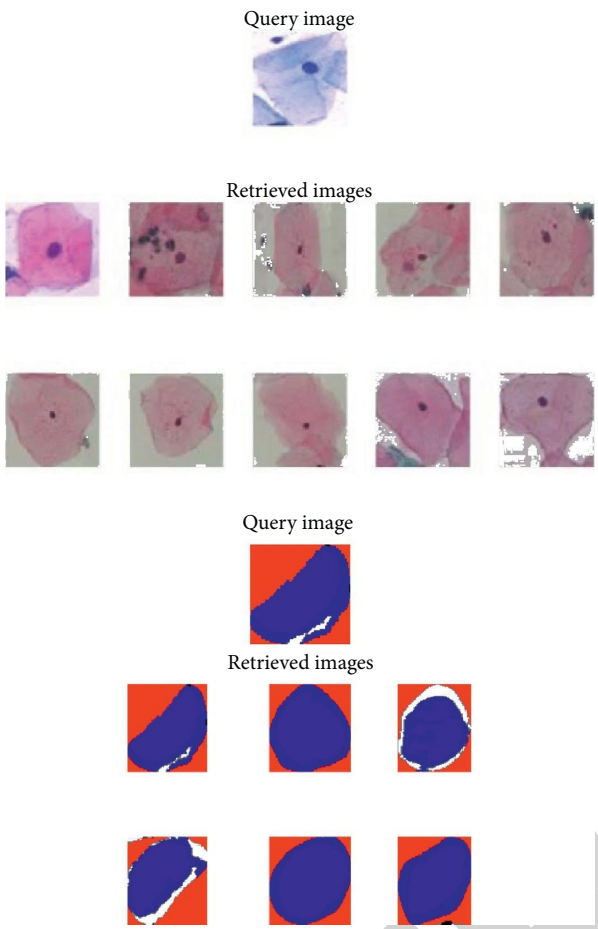

Figure 4: Sample retrieval images.

Step 1: in the training classes, each subset S starts with centroids in each class.

Step 2: in each iteration, the points q of T correspond to Voronoi cell points P, where the set of all points S closer to P are equivalent to the Voronoi cell points P. Once again, the different class labels are selected and included to S.

Step 3: the iteration stops, while no points are included to S (T is exactly classified using S). The ICNN model has subquadratic time complexity and order independent, where it needs maximum iterations to select and converge the points which are closer to the boundary. After classifying 7 classes, the relevant image retrieval is accomplished by using chi square distance measure. Sample retrieval images are graphically denoted in Figure 4.

3. Simulation Results

In this study, the proposed hybrid feature-based ICNN model performance is compared with a few existing classification techniques such as long short-term memory (LSTM) network, deep neural network (DNN), and CNN on a new Pap smear dataset. The proposed hybrid feature-based ICNN model is simulated using Python 3.7.3 software tool on a system with windows 10 operating system, Intel core i7 processor, and 8 GB RAM. The performance evaluation of the proposed hybrid feature-based ICNN model is carried out by using 70% training (1050 cell image) and 30% testing (450 cell image) of the data. The performance of the hybrid feature-based ICNN model is validated using various performance measures such as recall, precision, accuracy, f-score, and specificity. In this work, the performance measures are used for justifying the practical and theoretical benefit of the system. The mathematical expression of undertaken performance measures is represented in Table 1.

Table 1: Mathematical expression undertaken performance measures.

Performance measures	Mathematical expressions
Accuracy	$TP + TN/TN + TP + FN + FP$
Precision	$TP/FP + TP$
Specificity	$TN/TN + FP$
Recall	$TP/FN + TP$
F-score	$2TP/FP + 2TP + FN$

4. Quantitative Analysis

By inspecting Table 2, the performance analysis of dissimilar classifiers, LSTM, DNN, CNN, and ICNN, is carried out with individual HOG features, and their performance is validated in terms of precision, f-score, recall, specificity, and retrieval accuracy on a new Pap smear dataset. In this scenario, the combination is as follows: ICNN with HOG feature obtained maximum precision value of 98.45%, recall value of 98.13%, specificity of 97.92%, f-score of 97.64%, and retrieval accuracy of 97.78% in CBMIR. Related to the comparative classifiers, LSTM, DNN and CNN, the combination is as follows: ICNN with HOG features showed maximum of 1.57% and minimum of 0.53% improvement in retrieval accuracy. The graphical depiction of dissimilar classifiers with HOG features is indicated in Figures 5 and 6.

Correspondingly, in Table 3, the performance analysis of dissimilar classifiers is carried out with individual MLBP features, and their performance is evaluated in terms of precision, f-score, recall, specificity, and retrieval accuracy. As seen in Table 2, the combination is as follows: ICNN with MLBP features achieved a maximum precision value of 98.87%, specificity of 98.24%, recall of 98.81%, f-score value of 98.32%, and retrieval accuracy of 97.89% in CBMIR on a new Pap smear dataset. Hence, the combination is as follows: ICNN with MLBP features showed maximum of 1.45% and minimum of 0.35% improvement in retrieval accuracy related to comparative classifiers such as LSTM, DNN, and CNN. The graphical depiction of dissimilar classifiers with MLBP features is represented in Figures 7 and 8.

In Table 4, the performance analysis of dissimilar classifiers is carried out with hybrid features (HOG and MLBP) and validated by means of retrieval accuracy, precision, specificity, recall, and f-score. Related to individual feature extraction techniques and comparative classification methods, the combination is as follows: ICNN with hybrid features obtained maximum precision value of 99.90%, recall

Table 2: Performance analysis of dissimilar classifiers with HOG features.

	HOG features				
Classifiers	Precision (%)	Recall (%)	Specificity (%)	F-score (%)	Accuracy (%)
LSTM	96.44	95.92	96.41	96.84	96.21
DNN	97.14	96.71	97.25	97.12	96.49
CNN	97.6	97.54	97.62	97.52	97.25
ICNN	98.45	98.13	97.92	97.64	97.78

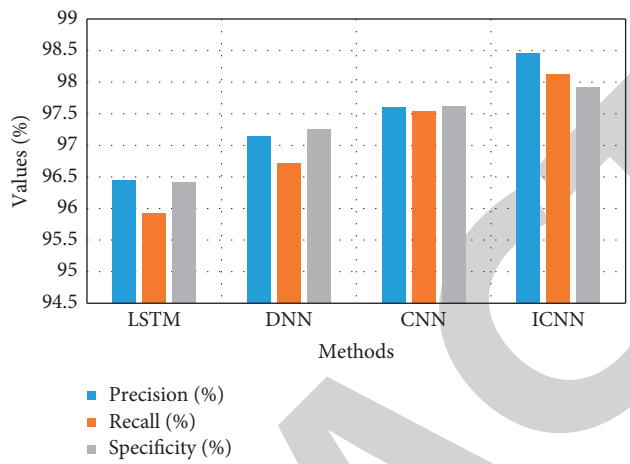

Figure 5: Graphical analysis of dissimilar classifiers with HOG features.

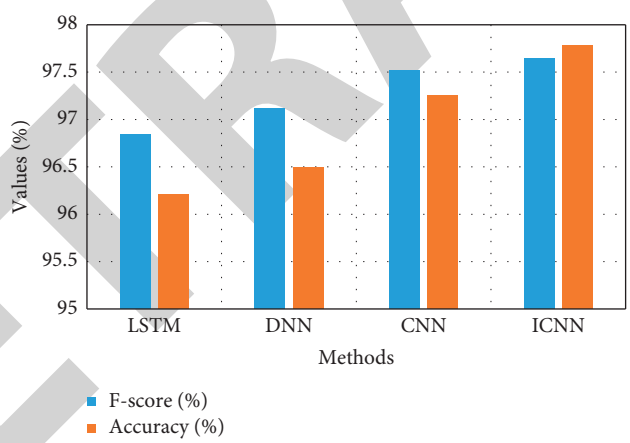

Figure 6: Graphical analysis of dissimilar classifiers with HOG features.

Table 3: Performance analysis of dissimilar classifiers with MLBP features.

	MLBP features				
Classifiers	Precision (%)	Recall (%)	Specificity (%)	F-score (%)	Accuracy (%)
LSTM	97.6	96.91	97.03	96.64	96.44
DNN	98.43	97.64	97.54	97.49	97.32
CNN	98.44	98.58	97.89	97.67	97.54
ICNN	98.87	98.81	98.24	98.32	97.89

value of 98.85%, specificity of 99.41%, f-score value of 99.48%, and retrieval accuracy of 98.88% in CBMIR on a new Pap smear dataset. In this research, the hybrid features (combination of color and texture feature vectors) effectively reduces the semantic space between the feature subsets that causes better image classification. Compared to CNN model, the ICNN model requires a minimum iteration to classify the seven classes of cell images. Graphical illustration of dissimilar classifiers with hybrid features (HOG and MLBP) is stated in Figures 9 and 10.

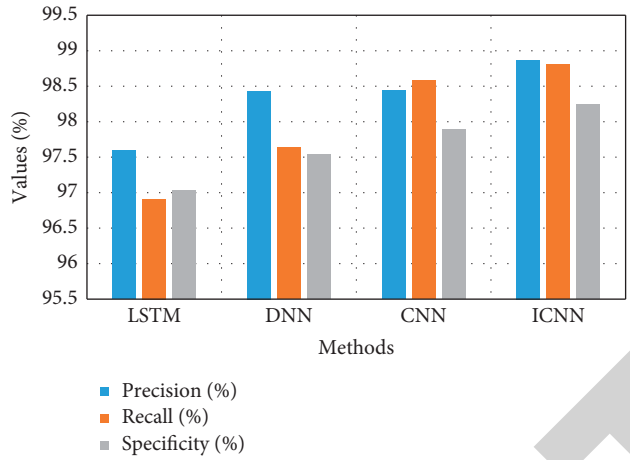

Figure 7: Graphical analysis of dissimilar classifiers with MLBP features.

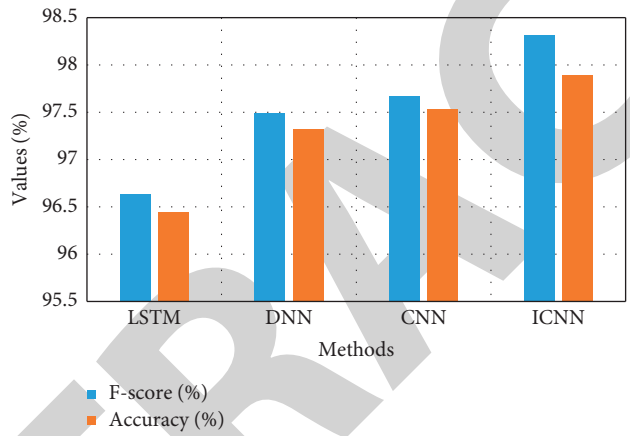

Figure 8: Graphical analysis of dissimilar classifiers with MLBP features.

Table 4: Performance analysis of dissimilar classifiers with hybrid features.

	Hybrid features (HOG and MLBP)				
Classifiers	Precision (%)	Recall (%)	Specificity (%)	F-score (%)	Accuracy (%)
LSTM	98.18	97.75	97.31	97.94	98.09
DNN	98.94	97.92	97.89	98.77	98.44
CNN	98.95	98.24	98.7	98.94	98.59
ICNN	99.9	98.85	99.41	99.48	98.88

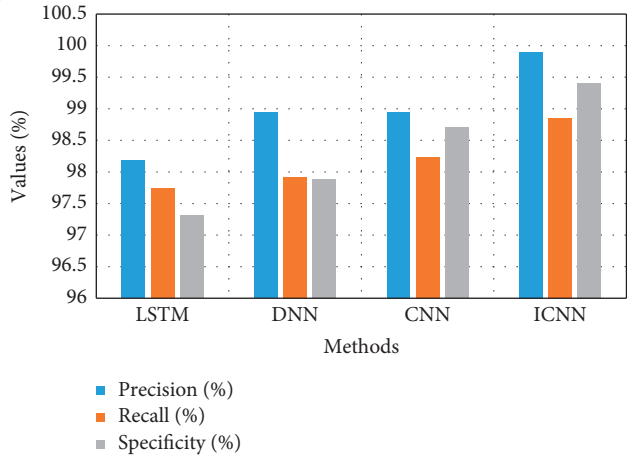

Figure 9: Graphical analysis of dissimilar classifiers with hybrid features.

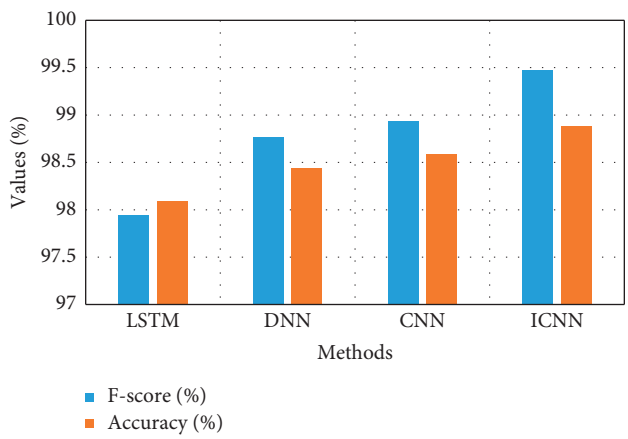

Figure 10: Graphical analysis of dissimilar classifiers with hybrid features.

Table 5: Performance analysis of dissimilar classifiers with hybrid features.

Methods	Accuracy (%)
GoogleNet [30]	71.3
Mask RCNN-Deep CNN [31]	95.9
CaffeNet + ELM [32]	98.2
ICNN	98.88

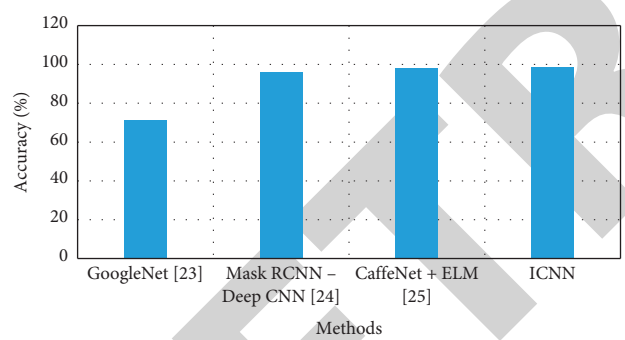

Figure 11: Graphical analysis of dissimilar classifiers with hybrid features.

The proposed method is compared with existing methods of GoogleNet [30], Mask RCNN + Deep CNN [31], and CaffeNet + ELM [32], as shown in Table 5. The proposed ICNN model has higher performance than existing methods in classification. The hybrid feature extraction and ICNN classifier improve the performance of the classification.

The proposed ICNN model accuracy is compared with existing methods such as GoogleNet [30], Mask RCNN [31], and CaffeNet + ELM [32], as shown in Figure 11. Existing CNN-based models have the limitations of overfitting problem. The hybrid feature extraction and ICNN model improves the performance of the classification.

5. Conclusion

In this research study, a new hybrid feature-based ICNN model is proposed to improve the performance of CBMIR in the large medical datasets. The proposed model comprises of two major steps in CBMIR such as feature extraction and classification. In this research, feature extraction is accomplished by using HOG, and MLBP descriptors for extracting the most discriminative texture feature vectors which effectively reduces the semantic space between the feature subsets and leads to better retrieval performance. The obtained discriminative feature vectors are given as the input to the ICNN model for classifying the classes of cell images, and then, the chi square distance measure is applied on the classified images for relevant image retrieval. The experimental results confirmed that the proposed hybrid feature-based ICNN model obtained significant performance in CBMIR by means of recall, precision, accuracy, f-score, and specificity. Related to comparative classifiers, LSTM, DNN, and CNN, we proposed hybrid feature-based ICNN model obtained maximum f-score of 99.48%, precision of 99.90%, recall of 98.85%, retrieval accuracy of 98.88%, and specificity of 99.41% in CBMIR on new Pap smear dataset. In the future work, a new feature selection algorithm can be included in the proposed model to further improve CBMIR by selecting the optimal feature vectors.

Data Availability

No data were used to support this study.

Conflicts of Interest

The authors declare that they have no conflicts of interest.

References

[1] M. Srinivas, R. R. Naidu, C. S. Sastry, and C. K. Mohan, "Content based medical image retrieval using dictionary learning," *Neurocomputing*, vol. 168, pp. 880–895, 2015.

[2] C. Zhang, L. Zhu, S. Zhang, and W. Yu, "TDHPPIR: an efficient deep hashing based privacy-preserving image retrieval method," *Neurocomputing*, vol. 406, 2020.

[3] D. B. Renita and C. S. Christopher, "Novel real time content based medical image retrieval scheme with GWO-SVM," *Multimedia Tools and Applications*, vol. 79, pp. 1–17, 2020.

[4] M. Kashif, G. Raja, and F. Shaukat, "An efficient content-based image retrieval system for the diagnosis of lung diseases," *Journal of Digital Imaging*, vol. 33, no. 4, pp. 971–987, 2020.

[5] L. Ma, X. Liu, Y. Gao, Y. Zhao, X. Zhao, and C. Zhou, "A new method of content based medical image retrieval and its applications to CT imaging sign retrieval," *Journal of Biomedical Informatics*, vol. 66, pp. 148–158, 2017.

[6] M. Garg and G. Dhiman, "A novel content-based image retrieval approach for classification using GLCM features and texture fused LBP variants," *Neural Computing & Applications*, vol. 33, pp. 1–18, 2020.

[7] M. K. Alsmadi, "Content-based image retrieval using color, shape and texture descriptors and features," *Arabian Journal for Science and Engineering*, vol. 45, no. No. 4, pp. 3317–3330, 2020.

[8] M. Owais, M. Arsalan, J. Choi, and K. R. Park, "Effective diagnosis and treatment through content-based medical image retrieval (CBMIR) by using artificial intelligence," *Journal of Clinical Medicine*, vol. 8, no. 4, p. 462, 2019.

Hindawi
Journal of Healthcare Engineering
Volume 2023, Article ID 9763264, 1 page
https://doi.org/10.1155/2023/9763264

Retraction

Retracted: Meta-Analysis of Children's Acute Psychological Stress and Action Stress on Immune Function under Microscope Images

Journal of Healthcare Engineering

Received 1 August 2023; Accepted 1 August 2023; Published 2 August 2023

This article has been retracted by Hindawi following an investigation undertaken by the publisher [1]. This investigation has uncovered evidence of one or more of the following indicators of systematic manipulation of the publication process:

(1) Discrepancies in scope
(2) Discrepancies in the description of the research reported
(3) Discrepancies between the availability of data and the research described
(4) Inappropriate citations
(5) Incoherent, meaningless and/or irrelevant content included in the article
(6) Peer-review manipulation

The presence of these indicators undermines our confidence in the integrity of the article's content and we cannot, therefore, vouch for its reliability. Please note that this notice is intended solely to alert readers that the content of this article is unreliable. We have not investigated whether authors were aware of or involved in the systematic manipulation of the publication process.

Wiley and Hindawi regrets that the usual quality checks did not identify these issues before publication and have since put additional measures in place to safeguard research integrity.

We wish to credit our own Research Integrity and Research Publishing teams and anonymous and named external researchers and research integrity experts for contributing to this investigation.

The corresponding author, as the representative of all authors, has been given the opportunity to register their agreement or disagreement to this retraction. We have kept a record of any response received.

References

[1] H. He, Y. Tan, and L. Li, "Meta-Analysis of Children's Acute Psychological Stress and Action Stress on Immune Function under Microscope Images," *Journal of Healthcare Engineering*, vol. 2022, Article ID 6549805, 12 pages, 2022.

Hindawi
Journal of Healthcare Engineering
Volume 2022, Article ID 6549805, 12 pages
https://doi.org/10.1155/2022/6549805

Research Article

Meta-Analysis of Children's Acute Psychological Stress and Action Stress on Immune Function under Microscope Images

Hanjiang He,[1] Yulin Tan,[2] and Lihua Li[1]

[1]*School of Medicine, Lishui University, Lishui 323000, Zhejiang, China*
[2]*School of Basic Medicine, Xiangnan University, Chenzhou 423000, Hunan, China*

Correspondence should be addressed to Lihua Li; lilihua@lsu.edu.cn

Received 30 December 2021; Accepted 23 February 2022; Published 23 March 2022

Academic Editor: Alireza Souri

The immune system is a complex system, mainly including immune cells and immune organs. When the human body is invaded by foreign substances, the immune system will play a role in resisting the attack of harmful substances and pure necrotic cells, which is the defense structure of the body. The purpose of this study was to analyze children's acute psychological stress and action stress, and judge the adverse effects on immune function. Through the stress experiment of rats, three experimental groups were set up, which were placebo control group, placebo stress group, and drug stress group. The experiments include material-level test, sugar preference test, body weight test, and lymphocyte test. The experimental data show that stress reaction not only causes negative emotions, but also reduces weight gain by about 5%, and sugar preference decreases by about 40% compared with the normal group. There was no significant difference in the number of granulocytes and intermediate cells in the blood, but the number of lymphocytes increased from 2.49×10^9/L to 5.03×10^9/L. It shows that acute psychological stress has an inhibitory effect on the immune function of the body; not only suitable load exercise can improve the immune function of the body but also the mechanism may be that moderate load exercise makes the rat axis has better adaptability, and improves hormones, cytokines, and cytokines. The secretion of neurotransmitters can maintain the stability of the body's immune function.

1. Introduction

1.1. Background and Significance. Today, the public health problems widely studied are anxiety and depression, which are closely related to the prevention and treatment of post-traumatic anxiety disorder. Long-term or short-term strong fear may exceed the individual's ability to adapt and tolerate, causing changes in the body's nervous system, cardiovascular system, immune system, endocrine system, and other microenvironments, eventually leading to body damage, forming a fear of stress injury. Fear and anxiety, as a common psychological pressure in social groups, affects the normal life and work of patients by affecting the cognitive function of the brain and the mechanism of microenvironment. Therefore, in recent years, scientists at home and abroad have been devoted to exploring the mechanism of fear, in order to find out the impact of children on the immune system in the case of acute psychological stress and behavioral stress, and conduct a meta-analysis based on a large amount of data to find out the cause of the disease and targeted treatment to eliminate the impact of the disease. The research mainly focuses on the following aspects: the influence of fear on knowledge, the memory regression mechanism of fear, and the influence of fear on the immune system. A meta-analysis based on the study of children's acute psychological stress and behavioral stress on immune function under the microscope can be very effective in treating children's acute stress response and reducing psychological damage to children.

1.2. Innovation. The experiment uses a meta-analysis method to study the basic experiments of this method as a statistical method that combines the results of several independent studies with the same research objective for quantitative system evaluation. The second method is the

inverse method of variation, also known as the weighted least squares method. This is the most common method after analysis. This method is based on the variability of research results. The relationship between the survey results was used as the total weight. The deviation is used to measure the degree of variance in a sample. The greater the variability, the greater the variability of the sample, and the less certainty the clustering parameter has, and the less the effect on the combined effect size. This method considers a fixed-effects model and a random-effects model. The simulation results show that this index has good statistical performance under various configurations.

The multiple data method was also used in the experiment. And the big data analysis framework created by this method is quite simple and efficient. At the same time, the parallel operation of multiple components is an attempt at a new approach to consolidating results. The majority of analytics surveys after many variables apply to the big data sector. The application of multivariate meta-analysis extends to the field of medical analysis, and the theory of multivariate meta-analysis has been developed. This is a method after multivariate analysis. To demonstrate the effect of this method, a sample of analysis and simulation experiments will be used together and selected multiple indicators to compare results. This makes the evaluation results more comprehensive and reliable.

1.3. Paper Organization. In this thesis, a meta-analysis is conducted on the impact of children's acute psychological stress and behavioral stress on immune function, and the whole process is related to observation under the microscope. The beginning of the thesis is to introduce the specific analysis of children's psychological conditions, the resulting psychological stress, and behavioral stress behavior, and finally lead to the impact on the immune function. After citing the research of several experts, it is found that a meta-analysis of the disease is carried out. Find out the reasons that affect immune function. In the method part, it analyzes the meta-analysis method, the risk assessment of deviation, the variance component model, and the multiple linear regression model, and has been applied in this article. In the experimental part, experiments were conducted on mice, and it was found that there were corresponding symptoms in the clinic to reflect the reasons for the impact of the patient's immune function. In the final discussion and summary part, using the results of clinical experiments in mice, it is concluded that acute psychological stress has an inhibitory effect on the immune function of the body and that proper load exercise cannot improve the immune function of the body.

2. Related Work

Exposure to stress results in physiological changes known as "stress response," which are the result of changes in the activity of the adrenal medullary hormone system, hypothalamus pituitary adrenal (HPA), and sympathetic nervous system (SNS). Rakhshan studied the effects of chronic physiological and psychological stress on ischemia/reperfusion (I/R) injury in isolated rat hearts and the role of the sympathetic nervous system in stress. The rat hearts were isolated and subjected to ischemia for 30 min and reperfusion for 120 min. Daily stress was induced one week before I/*R* induction. Sympathectomy is accomplished by injecting hydroxydopamine before stress induction. There were no significant changes in heart rate and coronary flow between the two groups. The left ventricular diastolic blood pressure (LVDP) and rate overstock (RPP) in the physiological stress group and the psychological stress group were significantly lower than those in the control group ($P < 0.05$), but there was no significant difference between the physiological stress group and the psychological stress group [1, 2].

Psychogenic fever is a psychosomatic disease related to stress, especially in young women. Some patients have extremely high core body temperature (TC) (up to 41°C) when affected by emotional events, while others show persistent low-grade hyperthermia (37–38°C) under chronic stress. The mechanism of psychogenic fever is not fully understood. However, clinical case reports show that psychogenic fever is alleviated not only by antipyretic drugs, but also by psychotropic drugs showing anti-anxiety and sedative effects, or by natural means or psychotherapy to solve patients' difficulties. Oka studies have shown that psychological stress increases TC through a mechanism different from infectious fever (requiring proinflammatory mediators), and the sympathetic nervous system, especially the nonshivering heat production in brown adipose tissue mediated by β3-adrenoceptor, plays an important role in the occurrence and development of psychological stress-induced high fever [3, 4].

The mechanism of stress inflammation leading to severe depressive disorder remains unclear. AMI studied the role of adenosine triphosphate (ATP)/purinergic 2×7 receptor (P2X7R) pathway and NLRP3 (nucleotide binding, leucine-rich repeats, containing three pyrimidine domains) inflammatory bodies in interleukin-1β (IL-1β) and stress-induced depressive behavior. The effects of acute restraint stress on extracellular ATP, glutamate, IL-1β, and tumor necrosis factor-α in hippocampus were measured by microdialysis, and the effects of acute restraint stress on NLRP3 inflammatory bodies were analyzed by Western blot. In the chronic unpredictable stress model, the effects of P2X7R antagonist on IL-1β, tumor necrosis factor α, anxiety, and depression behavior were observed [5].

3. Mathematical Basis

3.1. Multivariate Meta-Analysis. In many scientific research directions, in the discussion of similar problems, different researchers will adopt the same or different mathematical theoretical methods for research and experiment, but the conclusions drawn from the experimental results are indeed similar. In the current situation, we discuss and summarize different research results, and finally come to a conclusion [6]. This problem can be solved by using a meta-analysis, which provides quantitative average results for the answers. In order to improve the accuracy of the conclusion, we need to increase the number of samples, collect more samples to

explore the experiment, and effectively solve the problem of different experimental results. This is a quantitative review of the literature. It accepts the same results of several independent studies as the subjects [7]. In the implementation of strict research experiments, it is necessary to use good statistical methods to analyze and study the collected data, and to conduct an objective and quantitative comprehensive analysis of multiple research results. Figure 1 shows the specific workflow of Mate's analysis.

A meta-analysis is a statistical method used to compare and synthesize the results of studies on the same scientific question. Whether the conclusion is meaningful depends on the quality of the included studies and is often used for quantitative pooled analysis in systematic reviews. In the use of a meta-analysis, we must first determine the impact value of the results, which can be used to measure the quality of research results, such as correlation coefficient, relative ratio, and standard relative deviation, which can be used as the effect value. The fixed result value is the basis of postanalysis. Only in the reliable comprehensive analysis of the results can we make a reliable comprehensive analysis of the results. In practical research, more than one effect value is often needed to evaluate the experimental or research results. For example, in terms of work, the evaluation of an employee's daily work performance is not only based on the employee's completion of the work, but also on the employee's performance in other aspects, such as attendance, coworkers' relationship, and work completion quality [8]. In the medical field, heart disease drug testing is to measure blood pressure when the heart is contracting, and it is also necessary to measure blood pressure in the process of expansion; in the financial field, there are many indicators reflecting the liquidity risk of enterprises, such as liquidity indicators, quick ratio, and short-term multiple cash liabilities. When summarizing the above research results, many researchers will choose to conduct a meta-analysis on each result value and then summarize the results as the overall evaluation [9, 10]. However, for the same population, there is often a correlation between different impact values. If each result value is regarded as an independent individual and analyzed separately, the correlation between each result value will be ignored, which may lead to overestimation of the change of effect value, and the estimation value of effect value is biased. The multivariate meta-analysis solves the problem that the unit meta-analysis ignores the correlation of evaluation indicators when analyzing multiple effect values, making the evaluation results more accurate. In addition, compared with individual unit meta-analysis, multivariate meta-analysis takes into account the correlation between impact values and can get more effective conclusions. Therefore, this analysis method can provide more accurate conclusions or reduce errors when some studies lack effect values or there are some unavoidable reference deviations.

3.2. Risk Assessment of Bias. The research and implementation of systematic evaluation and meta-analysis have been widely used in the medical field, especially the increase

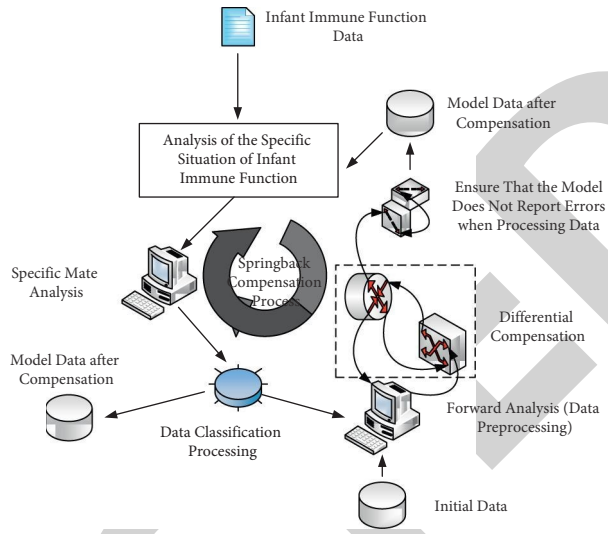

Figure 1: The specific workflow chart of a meta-analysis.

of randomized controlled trials and evidence-based medicine in recent years [11]. Researchers also regularly evaluate the quality of systematic reviews and meta-analysis studies. The schematic diagram of the researchers studying the immune function of young children is shown in Figure 2.

Multivariate analysis is a set of statistical theories and methods to study the relationship between multiple independent variables and dependent variables. Meta-analysis is a method of collecting data for quantitative and systematic evaluation. The quality of its conclusions depends not only on the preciseness of the postanalysis process, but also on the quality of the research literature itself and the reasonable control of deviation. Jada scale is also commonly used to analyze the quality of randomized controlled trials in a meta-analysis. Cochrane's participation in risk assessment tool has seven elements in six aspects of participation in risk assessment:

(1) Selection: including random sequence generation and allocation hiding.
(2) Implementation: including blinding of researchers and subjects.
(3) Measurement: blind evaluation of study outcome.
(4) Follow-up: research results of outcome data.
(5) Report: selective report of research results.
(6) Others: the origin of other biases.

According to the risk assessment criteria of bias, we made "low-risk bias," "high-risk bias," and "unclear." Cochrane embedded software contains risk assessment tools and provides risk-sharing assessment results' chart, and colors such as green, red, and yellow can be selected and also symbols such as "+,""-," and "?" were "low-risk bias," "high-risk bias," and "unclear."

Selection bias mainly involves three items: allocation sequence, baseline characteristics, and hidden grouping. However, with the release of the cyclone tool, the "low-risk" coincidence rate of the published animal experiments in

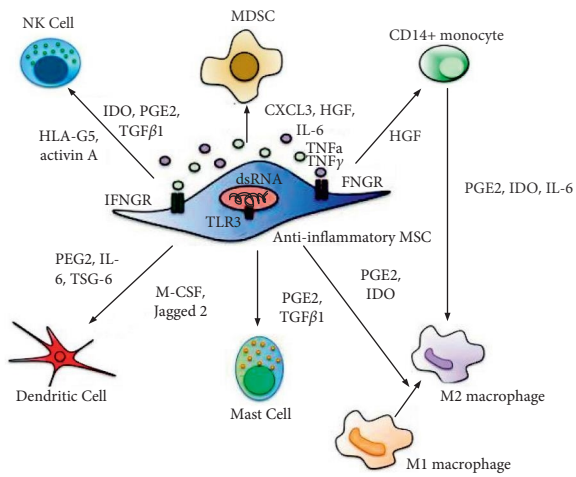

Figure 2: Schematic diagram of immune function.

these three items has been improved to some extent, but the actual proportion is less than 39%, of which the distribution sequence is only 12.74%, and the hidden grouping is less than 3%. Compared with clinical trials, the sample size of most animal experiments is small, and "random allocation" is not the standard practice mode in animal experimental research. Therefore, differences in some important baseline characteristics of animals between groups are more likely to affect the inference of experimental results. Moreover, randomization without hidden grouping still exaggerates the therapeutic effect. Therefore, we should pay more attention to the influence of baseline characteristics on the experimental results in future experiments, especially for the studies that have not been randomized or the sample size is relatively small. In addition, more attention should be paid to the implementation and development of random method and hidden grouping method in animal experimental research to reduce the selective bias.

3.3. Variance Component Model. The variance component model is a general term for both "random-effects model" and "mixed-effects model." Meta-analysis is a combination of multiple studies (hypothesis K) on the same problem. In the idea of selection equation, a variable model is used to conduct statistical treatment on a meta-analysis. The basic idea is to treat the problems studied by a meta-analysis as a distributed population [12]. The results of the first study are samples taken from the population. Since a meta-analysis is vulnerable to the risk of heterogeneity and bias, the following two are used to describe the idea of modeling meta-analysis in the selection equation [13].

3.3.1. Steady-State Model. The steady-state model shows that each study is homogeneous, and there is only one true effect value in each study time; that is, there is no difference between these studies. The difference of effect value directly observed from the study comes from the sampling error. The mathematical model is as follows:

$$y_i = \mu + \sigma_i \varepsilon_i, \varepsilon_i \sim N(0,1),$$
$$L(\beta \mid X, y) = \prod_{i=1}^{n} [\pi(X_i)]^{y_i} [1 - \pi(X_i)]^{1-y_i}, \quad (1)$$

where y_i is the estimated value of the effect value of the ith study, μ is the comprehensive effect value, and σ_i^2 is the variance of sampling in the population.

3.3.2. Random-Effects Model. The random-effects model means that the actual impact value of each study is different, and the value of each study is subject to normal distribution. Therefore, the difference should include the random error and sampling error in the actual result value in the final audit. The mathematical model is as follows:

$$y_i = \mu_i + \sigma_i \varepsilon_i, \mu_i \sim N(\mu, \tau^2), \varepsilon_i \sim N(0,1),$$
$$l(\beta) = \sum_{i=1}^{n} \{y_i \ln[\pi(X_i)] + (1 - y_i)[1 - \pi(X_i)]\}. \quad (2)$$

where y_i is the estimated value of the effect value of the ith study, μ is the comprehensive effect value, t^2 is the variance between groups, t 2s used to measure the heterogeneity among groups of studies, and σ_i^2 is the variance of intragroup sampling.

3.4. Multiple Linear Regression Model. One of the most common statistical models is multiple linear regression model, which is widely used in various fields. Through multiple linear regression model, the correlation between independent variable and dependent variable can be obtained, or dependent variable can be predicted through independent variable [14]. Under normal circumstances, a multiple linear regression model with multiple independent variables can be written as follows:

$$y_i = \beta_0 + \beta_1 x_{1i} + \beta_2 x_{2i} + \beta_3 x_{3i} + \cdots + \beta_k x k_{1i} + u_i, \quad i = 1, 2, 3, \ldots, n, \quad (3)$$

where x is the explanatory variable or independent variable and β is the correlation coefficient of each explanatory variable. Therefore, a multiple linear regression model is selected for the simulation experiment. The multiple regression model selected for the experiment is the quaternion regression model, and the model format is as follows:

$$y = \beta_0 + \beta_1 x_1 + \beta_2 x_2 + \beta_3 x_3 + \beta_4 x_4 + \varepsilon, \quad (4)$$

where y is the dependent variable, x_1-x_4 is the independent variable, β_0-β_4 is the five parameters of the model, and e is the random error term of the model. The variables of each model are sampled many times, and finally, multiple datasets are obtained. After receiving the data required by the simulation experiment, the data set is randomly divided into N parts for comparative analysis. After that, the simple average method and multivariate meta-analysis method were selected, and combined with the parameter estimation

of N data items, the multivariate analysis model was established [15, 16].

Define how many positive packets at a certain point are close to the point and how far the point is from the negative packet example as the diversity density of the point. The probability of diversity density is expressed as follows:

$$y(x) = \mathrm{ROOT}\left(x = t \mid C_1^+, \ldots, C_n^+, C_1^-, \ldots, C_m^-\right), \tag{5}$$

where x represents an independent point in the feature space, and t represents a factual concept. As such, the goal of the problem is to determine by maximizing the diversity density, namely,

$$\begin{aligned} &\arg\min_x \mathrm{ROOT}\left(x = t \mid C_1^+, \ldots, C_n^+, C_1^-, \ldots, C_m^-\right), \\ &\arg\min_x \prod_i \mathrm{ROOT}\left(x = t \mid C_i^+\right) \prod_i \mathrm{ROOT}\left(x = t \mid C_i^-\right). \end{aligned} \tag{6}$$

For positive or negative packets, the meaning of independent point x as a fact concept is also different. Assuming that the event only occurs if there is at least one cause for the event, the mathematical description of the model is as follows:

$$\begin{aligned} &\mathrm{ROOT}\left(x = t \mid C_i^+\right) = 1 - \prod_j \left(1 - \mathrm{ROOT}\left(x = t \mid C_{ij}^+\right)\right), \\ &\mathrm{ROOT}\left(x = t \mid C_i^-\right) = \prod_j \left(1 - \mathrm{ROOT}\left(x = t \mid C_{ij}^-\right)\right). \end{aligned} \tag{7}$$

The probability of an example appearing on a potential target is defined as the distance between the example and the potential target.

$$\begin{aligned} ROOT\left(x = t \mid C_{ij}\right) &= \left(-\left\|C_{ij} - x\right\|^2\right), \\ \left\|C_{ij} - x\right\|^2 &= \sum_n S_n\left(C_{ijn} - x_n\right)^2, \end{aligned} \tag{8}$$

where B_{ijn} represents the n attribute of B_{ij}, and s_n represents the correlation degree of the n attribute. In the logistic regression model, if the value of y_i is [0, 1], then

$$\begin{aligned} &P\left(y_i = 1 \mid M_i = m_i\right) = \gamma\left(m_i'\varepsilon\right), \\ &\gamma(x) = \frac{\exp(x)}{1 + \exp(x)} = (1 + \exp(-x))^{-1}. \end{aligned} \tag{9}$$

The parameter likelihood function of ε is

$$\begin{aligned} \mathrm{ROOT} &= \prod_{i=1}^{n} \left[\gamma\left(m_i'\varepsilon\right)\right]^{y_i} \left[1 - \gamma\left(m_i'\varepsilon\right)\right]^{1-y_i}, \\ \mathrm{ROOT} &= \sum_{i=1}^{n} y_i \log \gamma\left(m_i^T\varepsilon\right) + \left(1 - y_i\right)\log\left[1 - \gamma\left(m_i^T\varepsilon\right)\right]. \end{aligned} \tag{10}$$

The estimated variance can be obtained after derivation of the above formula with respect to parameter ε

$$\sum_{i=1}^{n} \left(\frac{y_i}{\gamma\left(m_i^T\varepsilon\right)} - \frac{1 - y_i}{1 - \gamma\left(m_i^T\varepsilon\right)}\right)\gamma''\left(m_i^T\varepsilon\right)m_i = 0. \tag{11}$$

By this, $\gamma''(x)$ means

$$\frac{\mathrm{d}}{\mathrm{d}x}\gamma''(x) = \frac{\exp(-x)}{(1 + \exp(-x))^2} = \gamma''(x)\left(1 - \gamma''(x)\right). \tag{12}$$

After calculation, the estimation equation can be simplified to

$$\sum_{i=1}^{n} m_i\left(y_i - \gamma\left(m_i^T\varepsilon\right)\right) = 0. \tag{13}$$

4. Experimental Design and Analysis

Machine learning is a multifield interdisciplinary subject involving probability theory, statistics, approximation theory, convex analysis, algorithm complexity theory, and other disciplines. It specializes in how computers simulate or realize human learning behaviors to acquire new knowledge or skills, and to reorganize existing knowledge structures to continuously improve their performance. Deep learning is to learn the inherent laws and representation levels of sample data, and the information obtained during these learning processes is of great help to the interpretation of data such as text, images, and sounds. Its ultimate goal is to enable machines to have the ability to analyze and learn like humans, and to recognize data such as words, images, and sounds. Deep learning is a complex machine learning algorithm that has achieved results in speech and image recognition far exceeding previous related technologies.

4.1. Experimental Animals. The rats used in the experiment are provided by Beijing Siberian Experimental Animal Co., Ltd., which are closed group, clean grade, and have license number identification. The animal rearing environment is in line with the relevant ethical requirements of animal experimental research.

4.2. Experimental Methods. Fifteen male rats, aged about 5 years old and weighing about 250g, were reared adaptively for 10 days in the environment of relative humidity 70%, illumination time 8 : 00–18 : 00, and temperature about 25°C. The experiment began one week later. Male rats were randomly divided into three groups: placebo control group, placebo stress group, and drug stress group, with 5 rats in each group. The placebo control group ate and drank normally without stress. The stress patterns of placebo stress group were fasting for one day, water deprivation for 8 hours, empty bottle stimulation for 3 hours, tail stimulation for 10 minutes, strange object stimulation for 8 hours, and immobilization for 3 hours. In addition to the above three different stress modes daily for 5 consecutive weeks in the fasting stress group, the same stress mode should not persist. 3 ml/D (5 mg/kg) of 0.7% normal saline and 4 ml/D (5 mg/kg) of hydrogen bromide solution were injected subcutaneously. The preference rate of sugar water = sugar water intake/total intake × 100% was calculated according to the preference degree of sugar water. Sugar preference was calculated before the beginning of stress stimulation, at the

end of the second and third weeks. The rats were randomly divided into a control group, a chronic stress group, and a chronic pain group. The technical route is shown in Figure 3.

4.3. Quality Control. It is necessary to strictly control the quality of each step. All personnel involved in the research should be trained uniformly to ensure homogeneity. In the process of the experiment, it needs to be completed on time according to the planned research method. The problems encountered in the experiment need to be dealt with in time and the research scheme should be improved. When recording the data, the trained team members should be unified to input the data, and the two people should check the data to ensure the authenticity and accuracy of the data to the maximum extent.

4.4. Statistical Methods. The software was used to conduct a meta-analysis on the data, and the related risk and its 93% confidence interval were selected as the results of binary variables. If the variable is continuous variable, the standard mean deviation and weighted average deviation shall be adopted when the measurement method and unit are consistent. As a result of the inconsistency between measurement method and measurement unit, continuous variable index is combined with weighted average difference, and binary classification index is combined with RR. When $p < 0.05$, the changes of the results were considered to be statistically significant. Subgroup analysis of heterogeneity indicators was performed to obtain the sources of heterogeneity, and sensitivity analysis (exclusion) was used to evaluate the overall results of the study.

5. The Effect of Stress on Immune Function

5.1. Changes of Substances after Stress. The changes of substance levels in the body before and after the stress reaction can be seen from the figure that the level of leptin has a considerable change before and after the stress reaction. From the figure, the change of leptin plasma concentration in rats is described in the figure: after the implementation of stress response stimulation, the leptin level of rats decreased to 54% of the normal in the process, and then gradually increased. After one day of stress reaction, the level of leptin basically returned to the basic level; in the rats in the placebo stress group, the leptin level showed a similar change with the previous group, gradually recovered to 58% of the normal during the operation, and then showed a gradual recovery trend, as shown in Figure 4.

Cortisol level in the first group of rats increased significantly during the stress reaction, gradually decreased, and then decreased to the basic level in the day after the stress response. As part of cardiopulmonary bypass (CPB), the level of leptin and cortisol in rats was negatively correlated after in vitro stimulation. In the placebo stress group, the cortisol level gradually increased from the stress reaction to the middle of the day, peaked at two hours after the reaction, and then decreased, but the change of cortisol level was not statistically significant.

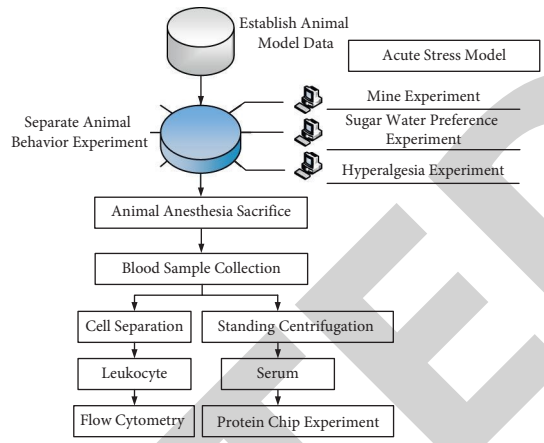

Figure 3: Technology roadmap.

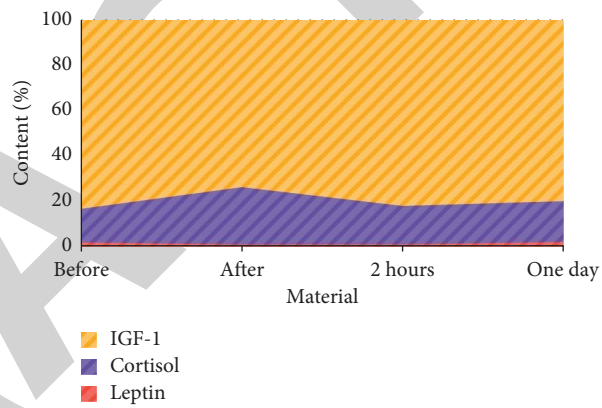

Figure 4: Changes of stress substance levels.

In the placebo control group, the level of IGF-1 increased significantly two hours after the stress reaction and then gradually decreased. It dropped to the basic level in one day after the reaction and decreased to a lower level after two days. There was a significant correlation between cortisol and IGF-1 levels. IGF-1 levels tended to be negatively correlated with leptin levels, but there was no significant difference between them. The changes of IGF-1 levels in the placebo stress group were similar to those in placebo control group.

5.2. Effect of Stress on Weight Gain. The weight gain of the control group and the experimental group during the 18-day restraint treatment was shown. Two-dimensional analysis of variance showed that there were significant differences in restraint, time, and the interaction between constraint and time. At the beginning of chronic restraint, there was no significant difference in body weight between the two groups, but the weight gain of rats in the experimental group was significantly slowed down from the fifth day. This result shows that our chronic restraint treatment can effectively induce chronic stress response in rats, as shown in Figure 5.

It can be seen from the figure that the weight gain of the control group is higher than that of the stress response group, and the weight jump-like growth appears on the ninth day. Although the difference of weight growth rate

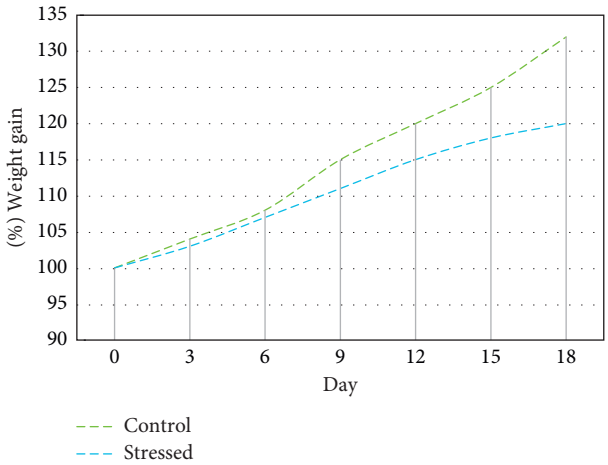

Figure 5: Weight gain rate.

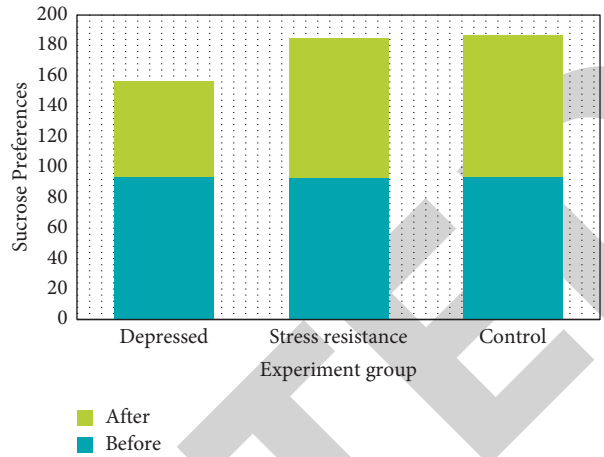

Figure 6: Sugar preference.

between the two experimental groups was not significant in the first six days, the difference of weight change rate was bigger with the increase of time. The weight of stress response group began to increase steadily on the 15th day.

5.3. Sugar Preference. Sugar water preference test was used to test the level of pleasure loss. The behavioral results of rats in this study showed that compared with the drug stress group and the placebo control group, the placebo stress group had less basic fine action, longer resting time, and lower preference for sugar solution, which indicated that chronic stress led to depression-like behavior, increased tension, decreased interest, and cognitive function of exploration. It is similar to fatigue, energy decline, psychomotor depression, and interest decline in patients with depression.

After three weeks of chronic unpredictable mild stimulation and control group mice, their emotional state was evaluated by sugar water preference test. Depressive behaviors were as follows: after chronic unpredictable mild stimulation, the consumption of sugar water was significantly lower than that before chronic unpredictable mild stimulation; the exploration time of new things after chronic unpredictable mild stimulation was significantly lower than that before chronic unpredictable mild stimulation. If the mice showed significant changes in this experiment, they were defined as chronic unpredictable mild stimulation-induced depression-like mice, and if the mice did not show significant changes in the three experiments, they were defined as chronic stress resistance mice, as shown in Figure 6.

The preference of sugar water is expressed by SPT value, SPT value = sugar water amount/(sugar water amount + pure water amount) × 100%. The first group of histograms shows the changes of SPT values before and after chronic unpredictable mild stimulation in depression-like mice induced by chronic unpredictable mild stimulation; the second group shows the changes of SPT values in chronic unpredictable mild stimulation of the chronic stress resistance group; the third group shows the changes of SPT values of control group mice in the same period. Chronic unpredictable mild stimulation resulted in a significant decrease in sugar preference in depression-like mice, but no significant change was observed in the chronic stress resistance group.

It can be seen from the figure that the SPT value of depression-like mice induced by chronic unpredictable mild stimulation was 94% before chronic unpredictable mild stimulation and 63% after chronic unpredictable mild stimulation, while the SPT value of mice in the chronic stress resistance group was 93% before chronic unpredictable mild stimulation and 92% after chronic unpredictable mild stimulation. Meanwhile, the SPT values of the control group were 94% and 93%, respectively, before and after the experiment. The results showed that the depression-like mice induced by chronic unpredictable mild stimulation showed a significant decrease in sugar water preference, while the mice in the chronic stress resistance group after chronic unpredictable mild stimulation did not change significantly.

5.4. Proportion of T Lymphocyte Subsets. After the experimental operation, 1 ml venous blood was drawn from rats on an empty stomach. The peripheral blood mononuclear cells were extracted by density gradient centrifugation. The proportion of T lymphocyte subsets (CD4 +, CD8 + and CD4 + / CD8 +) was detected by Beckman flow cytometry. The results showed that the proportion of CD4 + T lymphocytes increased in thymopentin group and Bozhi glycopeptide group compared with the placebo group, the difference was statistically significant, and there was no significant difference in CD8 + T lymphocyte among the three groups. CD4 + / CD8 + represents the ratio of *T* helper cells/*T* suppressor cells, referred to as CD4 + /CD8 +. The results showed that after 3 weeks of experiment, the ratio of CD4 + /CD8 + in thymopentin group and Bozhi glycopeptide group was higher than that in the placebo group, and the difference was statistically significant. Flow cytometry was used to detect the proportion of T lymphocyte subsets in human peripheral blood. The specific situation is shown in Figure 7.

After drug injection, the proportion of peripheral blood T lymphocytes was detected by flow cytometry. The

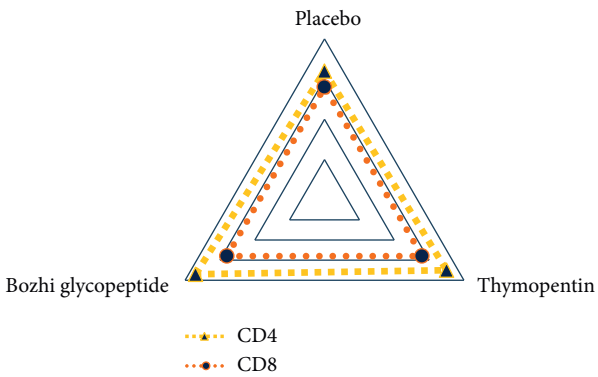

Figure 7: Proportion of lymphocyte subsets.

statistical results showed that compared with the placebo group, the difference of CD4 + in thymopentin group and Bozhi glycopeptide group was statistically significant, but the difference of CD8 + was not statistically significant.

5.5. The Effect of High-Intensity Exercise and Acute Psychological Stress on Behavior and Weight

5.5.1. Subjects and Feeding. The animals adapt to the laboratory environment for a week, during which they are stroked irregularly and for a short period of time every day to reduce the impact of the operation. At the same time, the high-intensity exercise group was placed on the animal treadmill for training every day, and the entire experimental period lasted for seven weeks. The weight comparison between rats in each group is shown in Table 1.

5.5.2. Dynamic Observation of Rat Behavior. The rats in the quiet control group were in good condition, with normal daily food intake, bright coat color, standing on the two legs of the box wall, many searching movements, and gentle temperament. The hair color of rats in the high-intensity exercise plus chronic psychological stress group is yellowish. With the continuation of exercise and psychological stress, the food intake gradually decreases, especially in the last week of the experiment, and the food intake per day is only equivalent to one meal in the quiet control group. The food intake and weight changes of rats in each group are shown in Figure 8.

It can be seen from Figure 8 that the rats in the quiet control group have been gaining weight steadily, followed by the rats in the chronic psychological stress group; the rats in the high-intensity exercise plus chronic psychological stress group have the smallest increase in weight; and the rats in the high-intensity exercise group have the smallest increase in weight between the latter two.

5.5.3. Results of Determination of Blood Urea Nitrogen Content. It can be seen from Table 2 that the high-intensity exercise plus chronic psychological stress group had higher blood urea nitrogen levels after exercise and psychological stress than in the psychological stress group ($P < 0.05$) and the quiet control group ($P < 0.01$); the blood urea nitrogen level at 24h after stress decreased significantly ($P < 0.05$); and the blood urea nitrogen level at 24h after psychological stress was much lower than that of the quiet control group ($P < 0.01$).

5.5.4. White Blood Cell Count Result. The variance analysis of high-intensity exercise and acute psychological stress on white blood cells (WBC) of rats is shown in Table 3.

It can be seen from Table 3 that there is no significant difference between each group and the quiet control group. But at the moment of psychological stress, the number of WBCs in group P was significantly higher than that in EP and *E* groups ($P < 0.05$), and there was no significant difference between the latter two groups. The effects of high-intensity exercise and acute psychological stress on the thymus index and spleen index of rats are shown in Tables 4 and 5.

It can be seen from Table 4 that there is no significant difference in the thymus index between the groups after long-term high-intensity exercise and chronic psychological stress immediately and after 24 hours.

5.6. Effects of Drugs on Immune Function. The traditional Chinese medicine compound is composed of *Astragalus* membranaceus, radix rehmanniae, Codonopsis pilosula, and Angelica sinensis, which are fermented by *Saccharomyces cerevisiae* and *Bacillus* subtilis. All the herbs were purchased from Wuhan Hanrongda Chinese Herbal Medicine Co., Ltd. The main production process is as follows: first, the raw materials are processed, the processed traditional Chinese medicine is dried and crushed, and then, the auxiliary materials and microbial agents are added according to a certain formula, mixed evenly, and then bagged for use.

The changes of blood lymphocytes and white blood cells in rats are shown in Table 6. It can be seen that the number of all kinds of cells in the blood of the rats in the third group of the experiment was not significant. After the beginning of the experiment, the number of lymphocytes and white blood cells increased significantly with the increase of the amount of traditional Chinese medicine, especially on the 10th and 15th days of the experiment; the 50 and 75g/*D* groups were significantly higher than the control group; and the highest number of lymphocytes and white blood cells appeared in the 100g/*D* groups on the 15th day, $03 \times 109/L$ and $1.97 \times 109/L$, respectively. At the same time, it was found that there was no significant difference in the number of blood granulocytes and white blood cells in all groups during the whole experimental period.

5.7. Effect of Different Load Exercise on IL-6 Content in Rats with Acute Psychological Stress. It can be seen from Table 7 and Figure 9 that the two-factor analysis of variance was used to test the effects of acute psychological stress and exercise on the IL-6 content of rats. The results showed that the analysis of the 10-minute exercise acute psychological stress (S1P1) group and minute exercise in the difference of

Table 1: Weight comparison between rats in each group.

Group	Deal with	N	Weight(g)
EP1	High-intensity exercise plus psychological stress immediate group	8	200.32 ± 13.62
EP2	24-h group after high-intensity exercise plus psychological stress	8	208.17 ± 12.73
E3	High-intensity exercise immediate group	8	208.14 ± 17.33
E4	24-h group after intensive exercise	8	210.39 ± 11.47
P5	Chronic psychological stress immediate group	8	199.93 ± 20.56
P6	24-h group after chronic psychological stress	8	197.43 ± 14.56
C	Quiet control group	8	199.72 ± 13.26
Total	—	56	204.27 ± 15.67

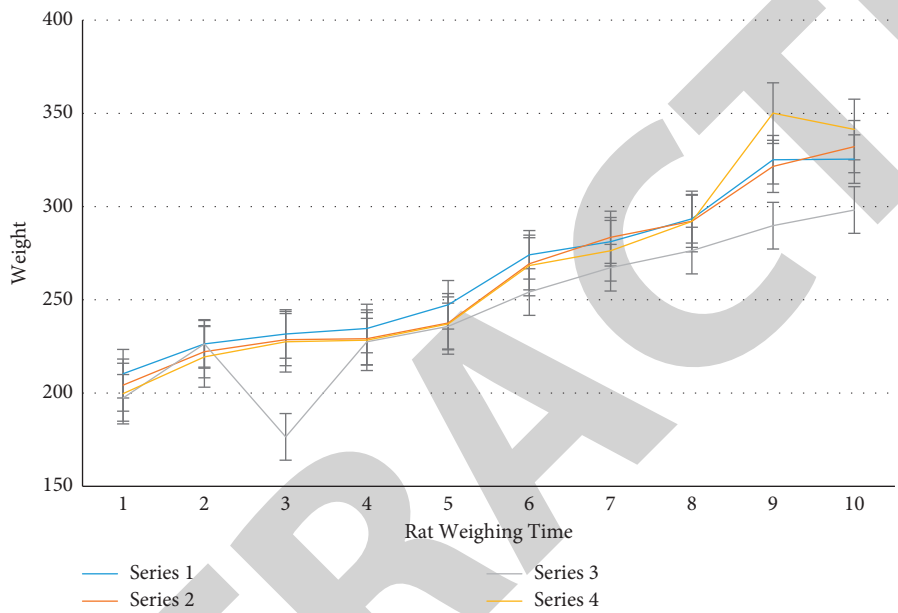

Figure 8: Rat body weight change.

Table 2: Comparison of blood urea nitrogen content.

Group	N	Blood urea nitrogen
EP1	7	188.32 ± 23.94
EP2	7	172.94 ± 19.33
E3	6	210.22 ± 30.62
E4	8	173.41 ± 41.27
P5	7	183.79 ± 24.09
P6	6	146.32 ± 24.71
C	7	207.32 ± 10.51

Table 3: Comparison of rat white blood cells (WBC).

Group	N	Blood urea nitrogen
EP1	7	7.36 ± 1.98
EP2	5	9.06 ± 2.13
E3	6	7.02 ± 1.24
E4	8	7.39 ± 2.18
P5	7	9.62 ± 1.26
P6	8	9.00 ± 3.40
C	7	8.90 ± 1.69

IL-6 in P1 group, F = 5.613, $P < 0.05$, suggesting that the difference in IL-6 content between S1P1 group and S0P1 group is significant, and the IL-6 content of S1P1 group is higher than that of P1 group. Analyze the difference in IL-6 between the 60-minute exercise acute psychological stress (S1P2) group and the minute exercise (P2) group, $F = 24.742$, $P < 0.01$, suggesting that the IL-6 content difference between the S1P2 group and the P2 group is very significant sex, and the IL-6 content of S1P2 group was lower than that of P2 group. The results of experiments conducted through the above multiple methods show that these methods can be

Table 4: Thymus index comparison.

Group	N	Blood urea nitrogen
EP	13	0.0013 ± 0.0005
E	14	0.0014 ± 0.0003
P	16	0.0012 ± 0.0003
C	7	0.0013 ± 0.0002

Table 5: Thymus index comparison.

Group	N	Blood urea nitrogen
EP	13	0.0028 ± 0.0008
E	14	0.0025 ± 0.0003
P	16	0.0029 ± 0.0004
C	7	0.0023 ± 0.0002

It can be seen from Table 5 that the spleen index of group P is much higher than that of group C and E ($P < 0.01$).

Table 6: Effects of drugs on immune function.

	0g/d	25 g/d	50 g/d	75 g/d	100 g/d
Granulocyte	3.41×10^9/L	3.58×10^9/L	3.82×10^9/L	3.92×10^9/L	4.01×10^9/L
White blood cell	1.72×10^9/L	1.83×10^9/L	1.92×10^9/L	1.84×10^9/L	1.97×10^9/L
Lymphocyte	2.45×10^9/L	3.41×10^9/L	3.89×10^9/L	4.35×10^9/L	5.03×10^9/L

Table 7: Effects of different load exercises on the content of IL-6 in rats with acute mental stress.

	No exercise (P0)	30 minutes of exercise (P1)	60 minutes of exercise (P2)
Psychological stress (S1)	220.28 ± 72.21	452.17 ± 34.04	294.25 ± 82.11
No psychological stress (S0)	348.45 ± 63.54	429.12 ± 54.02	464.36 ± 97.19

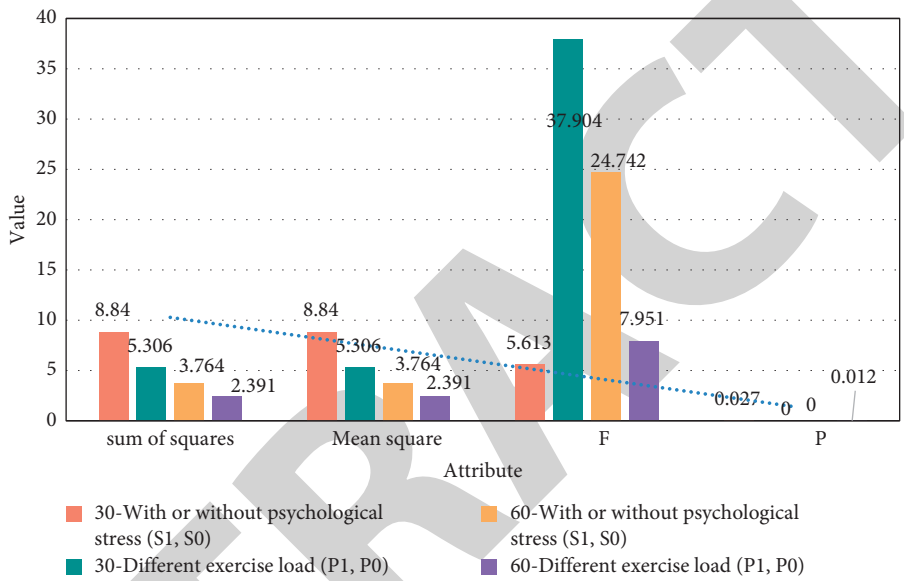

Figure 9: The effect of exercise on the content of IL-6 in rats with acute psychological stress.

used clinically to conduct a meta-analysis of children's acute psychological stress and behavioral stress, and use a microscope to study and analyze the specific conditions of patients.

6. Conclusions

Stress response is a kind of physical defense. If the response to stress is very strong and takes a long time, it is harmful to the body, and often there will be pathological changes, known as the pathological response of stress, and this phenomenon is called general adaptation syndrome. Initially, stress refers to the biological response of human or animal organisms to environmental stimuli, which may be caused by many different requirements on the body, not specific. Stress refers to the environment or internal needs beyond the adaptability of individual, society or body organization system, or people have special physiological or psychological needs, and thus produce unusual or unexpected reactions. Stress response is a nonspecific defense response to harmful stimuli. This mechanism includes stimulation of sympathetic nerve and inhibition of sympathetic nerve. Effective control and interruption of stress response have a positive impact on the mechanism. The increase of catecholamine excretion caused by stress reaction can cause many cardiovascular reactions. Insulin secretion decreases, and glucose secretion increases. Catecholamine produced by stress reaction is an important factor in the development of tumor. Professor Rakhshan's research is aimed at the effects of chronic physiological and psychological stress on ischemia/reperfusion (I/R) injury of isolated rat hearts and the role of the sympathetic nervous system in stress, and there is no relevant change in the human body. Professor Oka's research shows that psychological stress increases TC through a mechanism different from infectious fever (which requires pro-inflammatory mediators) and the sympathetic nervous system. His research lacks the support of experimental data, so I do not want this experiment to do a lot of experiments.

This meta-analysis provides a reference for the characteristics of children's psychological acute stress. It is hoped that the research results can provide a possible research direction for clinicians in treating children's immune function impairment caused by stress reaction. This study only analyzes the cognitive effect of stress-induced simple graphics in rats, and the following research should analyze spatial knowledge and knowledge-related attention factors. Due to the limited number of relevant high-quality studies

and the small sample size, the validity of the evidence in the conclusion is limited to a certain extent. Therefore, it is expected to have a higher quality, large sample multicenter study to further explore the efficacy of stress-induced immune damage. The medical image fusion research based on deep belief network introduces medical images in detail. In this article, the microscope observation experiment provides a large number of research methods, which makes the experiment very smooth, and deep neural network multimodal medical image based on multi-objective differential evolution. Fusion technology describes the application of deep neural networks in image fusion and provides a research direction for this article; the study of drug synergistic effect prediction based on dynamic mutation and differential evolution provides a good explanation of the synergistic effect of drugs. Different drugs are used to work together in one body, which can effectively illustrate the results of the experiment.

In order to carry out normal immune regulation, human body must have a complete and coordinated immune system composed of immune cells, immune cells and immune organs. The thymus and bone marrow of malignant gland and central immune organ are the mature sites of T lymphocyte and B lymphocyte, respectively. Spleen has the function of filtering blood and bleeding, but as the largest immune organ of human body, it is more for the maturation of various immune cells and when pathogenic bacteria invade the human body's fungi and cells. This study is to conduct a meta-analysis of the effects of children's acute psychological stress and behavioral stress on the immune function, and use a microscope to conduct specific observations on white mice. The experimental research results show that the evaluation of animal models and the study of the physiological mechanism of psychological disorders are of great significance. This research provides a reliable pressure model for the neural mechanisms and methods that express different degrees of fear in the subsequent visual pathways to transmit and receive sensory information.

Data Availability

The data that support the findings of this study are available from the corresponding author upon reasonable request.

Conflicts of Interest

The authors declare that they have no conflicts of interest.

Acknowledgments

This work was supported by the Natural Science Foundation of Zhejiang Province, China (LY17H100001).

References

[1] K. Rakhshan, A. Imani, M. Faghihi, F. Nabavizadeh, M. Golnazari, and S Karimian, "Evaluation of chronic physical and psychological stress induction on cardiac ischemia/reperfusion injuries in isolated male rat heart: the role of sympathetic nervous system," *Acta Medica Iranica*, vol. 53, no. 8, pp. 482–490, 2015.

[2] L. Chang, "Research on prediction algorithm of employees' psychological stress based on multifeature fusion," *Security and Communication Networks*, vol. 2021, Article ID 6917191, 9 pages, 2021.

[3] O. Takakazu, "Psychogenic fever: how psychological stress affects body temperature in the clinical population," *Temperature*, vol. 2, no. 3, pp. 368–378, 2015.

[4] N. Mao, "The role of music therapy in the emotional regulation and psychological stress relief of employees in the workplace," *Journal of Healthcare Engineering*, vol. 2022, Article ID 4260904, 7 pages, 2022.

[5] M. Iwata, K T. Ota, X Y. Li et al., "Psychological stress activates the inflammasome via release of adenosine triphosphate and stimulation of the purinergic type 2x7 receptor," *Biological Psychiatry*, vol. 80, no. 1, pp. 12–22, 2016.

[6] K. Gourounti, "Psychological stress and adjustment in pregnancy following assisted reproductive technology and spontaneous conception: a systematic review," *Women & Health*, vol. 56, no. 1, pp. 98–118, 2015.

[7] L. Wang, L.-L. Guo, L.-H. Wang et al., "Oxidative stress and substance P mediate psychological stress-induced autophagy and delay of hair growth in mice," *Archives of Dermatological Research*, vol. 307, no. 2, pp. 171–181, 2015.

[8] R. A. Caparros-Gonzalez, B. Romero-Gonzalez, H. Strivens-Vilchez, R. Gonzalez-Perez, O. Martinez-Augustin, M. I. Peralta-Ramirez et al., "Hair cortisol levels, psychological stress and psychopathological symptoms as predictors of postpartum depression," *PLoS One*, vol. 12, no. 8, Article ID e0182817, 2017.

[9] K. Miura, Y. Egawa, T. Moriki et al., "Microscopic observation of chemical modification in sections using scanning acoustic microscopy," *Pathology International*, vol. 65, no. 7, pp. 355–366, 2015.

[10] X. Cheng, B. Yang, A. Hedman, T. Olofsson, H. Li, and L. Van Gool, "NIDL: a pilot study of contactless measurement of skin temperature for intelligent building," *Energy and Buildings*, vol. 198, no. SEP, pp. 340–352, 2019.

[11] Z. Y. Yuan, X. Q. Guo, Z. Haibin, C. Cheng, W. Guang, H. Fei et al., "Intermittent microscopic observation of structure change and mineral reactions of high phosphorus oolitic hematite in carbothermic reduction," *ISIJ International*, vol. 57, no. 7, pp. 1149–1155, 2017.

[12] R. M. Gorgoll, E. Yücelen, A. Kumamoto, N. Shibata, K. Harano, and E. Nakamura, "Electron microscopic observation of selective excitation of conformational change of A single organic molecule," *Journal of the American Chemical Society*, vol. 137, no. 10, pp. 3474–3477, 2015.

[13] L. Anderson, N. Oldridge, D. R. Thompson et al., "Exercise-based cardiac rehabilitation for coronary heart disease,"

Hindawi
Journal of Healthcare Engineering
Volume 2023, Article ID 9825050, 1 page
https://doi.org/10.1155/2023/9825050

Retraction

Retracted: Role of CT Images in the Diagnosis of Common Acute Abdominal Diseases in General Surgery

Journal of Healthcare Engineering

Received 10 October 2023; Accepted 10 October 2023; Published 11 October 2023

This article has been retracted by Hindawi following an investigation undertaken by the publisher [1]. This investigation has uncovered evidence of one or more of the following indicators of systematic manipulation of the publication process:

(1) Discrepancies in scope
(2) Discrepancies in the description of the research reported
(3) Discrepancies between the availability of data and the research described
(4) Inappropriate citations
(5) Incoherent, meaningless and/or irrelevant content included in the article
(6) Peer-review manipulation

The presence of these indicators undermines our confidence in the integrity of the article's content and we cannot, therefore, vouch for its reliability. Please note that this notice is intended solely to alert readers that the content of this article is unreliable. We have not investigated whether authors were aware of or involved in the systematic manipulation of the publication process.

In addition, our investigation has also shown that one or more of the following human-subject reporting requirements has not been met in this article: ethical approval by an Institutional Review Board (IRB) committee or equivalent, patient/participant consent to participate, and/or agreement to publish patient/participant details (where relevant).

Wiley and Hindawi regrets that the usual quality checks did not identify these issues before publication and have since put additional measures in place to safeguard research integrity.

We wish to credit our own Research Integrity and Research Publishing teams and anonymous and named external researchers and research integrity experts for contributing to this investigation.

The corresponding author, as the representative of all authors, has been given the opportunity to register their agreement or disagreement to this retraction. We have kept a record of any response received.

References

[1] Y. Nan, Z. Zhang, J. Zhang, B. Jiang, Y. Zhu, and L. Zhang, "Role of CT Images in the Diagnosis of Common Acute Abdominal Diseases in General Surgery," *Journal of Healthcare Engineering*, vol. 2022, Article ID 5732357, 13 pages, 2022.

Hindawi
Journal of Healthcare Engineering
Volume 2022, Article ID 5732357, 13 pages
https://doi.org/10.1155/2022/5732357

Research Article

Role of CT Images in the Diagnosis of Common Acute Abdominal Diseases in General Surgery

Yunguang Nan,[1] Zuyan Zhang,[2] Jianbo Zhang,[1] Bo Jiang,[1] Yuxi Zhu,[1] and Li Zhang[2]

[1]*General Surgery, Shuyang Benevolent Hospital, Suqian 223600, Jiangsu, China*
[2]*Imaging Department, Shuyang Benevolent Hospital, Suqian 223600, Jiangsu, China*

Correspondence should be addressed to Yuxi Zhu; 345419092@qq.com and Li Zhang; 161841356@masu.edu.cn

Received 8 December 2021; Accepted 16 January 2022; Published 23 March 2022

Academic Editor: Alireza Souri

Acute abdomen is a clinical emergency disease with acute abdominal pain as the main prominent feature. Through severe disease changes in intra-abdominal, extrapelvic, and retroperitoneal tissues and organs, symptoms and clinical signs led by abdominal pain are formed. This article mainly explores the role of CT imaging diagnosis in common acute abdominal diseases in general surgery. In this paper, the use of computer-aided CT scan imaging technology in pulmonary nodules was firstly investigated, and the image segmentation algorithms based on CT images were given, including the spatial domain fuzzy C-mean clustering separation algorithm and the spatial domain fuzzy clustering level set semiautomatic separation algorithm, then the treatment of acute abdomen under the concept of ERAS was explored, and the treatment of ERAS under CT images of the acute abdomen was analyzed and studied. The empirical research results show that the ERAS's concept is guided by the undergoing national nutritional support with the traditional perioperative management. Compared to 12.9% of complications in traditional CPM groups, the recall rate of complications after ERAS group was only 6.01%, the improvement was obvious and the results were statistically significant ($P < 0.05$). Postoperative hospitalization time was also 4.62 days from 7.93 days, thus controlling the clinical risks of perioperative periods, providing a benefit to patient life.

1. Introduction

Surgical emergencies often require emergency surgery, and clinicians tend to focus on saving patients' lives, while often neglecting to anticipate the disturbance of patients' internal environment, intraoperative damage control, postoperative recovery, and their own feelings during the perioperative period. The introduction of the FTS concept has fundamentally changed the clinicians' way of thinking. It requires the clinician to pay attention to the patient's preoperative psychological and physiological status, avoid unnecessary invasive operations to reduce various stress reactions, pay attention to intraoperative warming and control the amount of rehydration to facilitate the recovery of various physiological functions after surgery, and require the patient to eat and get out of bed as early as possible after surgery to prevent various complications. All these are aimed at making the patients' perioperative physiological functions close to or return to the normal level as soon as possible, reducing pain and restoring health as soon as possible.

With the continuous development of computer application technology, computer-aided CT imaging technology has been widely used in the medical industry, and CT imaging technology uses digital image processing technology to analyze medical image processing data in order to obtain auxiliary signals that are of practical use to physicians in clinical treatment. As with traditional medical examinations, the use of CT imaging technology in clinical applications will reduce the pressure on physicians to read films, improve the accuracy and effectiveness of treatment, and reduce inconsistencies in treatment conclusions due to physician experience and knowledge levels during treatment; in the long run, the use of computer-aided creation of CT imaging products is of great significance in improving current medical technology.

According to the research progress at home and abroad, different scholars also have some collaborative research in

CT imaging diagnosis: Zhang S used the classical LeNet-5 model to classify pulmonary nodules in chest CT images, including benign and malignant pulmonary nodules, and different degrees of malignancy of malignant nodules. A 10-folder cross-validation (CV) was also implemented to demonstrate the robustness of the training classification model. The results showed that LeNet-5 migration learning was effective in classifying lung nodules from chest CT images, with mean Top-1 accuracy rates of 97.041% and 96.685%, respectively [1]. The objectives of the Li Y study were to determine the rate of radiologist misdiagnosis of coronavirus disease (COVID-19) in 2019 and assess the performance of chest CT in the diagnosis and management of COVID-19. CT features of COVID-19 are reported and compared with those of other viruses to familiarize radiologists with possible CT patterns. The results of the study found that chest CT had a low rate of missed diagnosis of COVID-19 (3.9%, 2/51) and could be used as a standard method for rapid diagnosis of COVID-19 to optimize patient management. However, CT is still limited in identifying specific viruses and differentiating them [2]. Metintas et al. aim to compare the diagnostic yield and safety of CT scan-guided pleural biopsy using an Abrams needle (CT-ANPB) with ultrasound-assisted pleural biopsy using a cutting needle (US–CNPB). For patients with CT scans showing pleural effusion and associated pleural thickening, the preferred diagnostic intervention is CT-ANPB, and US-CNPB should be used primarily in cases where only pleural thickening but not pleural effusion is found [3]. Ropelle et al. summarize that the hypothalamus is a brain region that collects information about the nutritional status of the body and controls the release of multiple metabolic signaling molecules (e.g., insulin and leptin) to maintain homeostasis in the body. Studies have shown that physical activity reorganizes the set point of nutritional homeostasis through anti-inflammatory signaling mediated by interleukin (IL)-6 and IL-10 in the rodent hypothalamus. Thus, IL-6 and IL-10 are important physiological factors in exercise-mediated central insulin and leptin actions, linking them to hypothalamic endoplasmic reticulum stress and inflammation [4, 5]. Dijk et al. investigated improved prediction of XER12m and STIC12m with patient-specific features based on CT image biomarkers (IBM). The prediction of XER12m could be significantly improved by adding the IBM "ShortRunEmphasis" (SRE), which quantifies parotid tissue heterogeneity, to a model with mean contralateral parotid dose and XERbase [6]. Dong et al. propose an averaging image-induced nonlocal mean (aviNLM) filter for each energy-specific image recovery. The proposed aviNLM algorithm produces recovery results by performing a nonlocal weighted averaging operation for noise-energy specific images, where there is a nonlocal weight matrix between the target and prior images. Experimental results show that the current aviNLM algorithm has the potential to reduce radiation dose by reducing mAs in SCT imaging, and it may be useful for some other clinical applications, such as in myocardial perfusion imaging and radiotherapy [7]. The Hao et al. study aimed to transform the edge-preserving region noise smoothing paradigm into a texture-preserving framework for LdCT image reconstruction, while preserving the advantages of the MRF neighborhood system in edge preservation. To demonstrate the feasibility of the proposed reconstruction framework, experiments using clinical patient scans were performed. The experimental results showed that significant gains were obtained from the a priori knowledge of LdCT image reconstruction using the commonly used Haralick texture measurements. Therefore, it is hypothesized that texture-preserving LdCT reconstruction is superior to the edge-preserving region smoothing paradigm in texture-specific clinical applications [8, 9]. Helma et al. explored the efficiencies of data mining and machine learning algorithms induced by mutant moiety (SAR) from nonmutated data concentration. From the application's machine learning technology, the rule learner Part and support vector machines give the best results, although the difference between the learning algorithms is small [10]. However, these scholars did not explore the role of common acute abdominal conditions in general surgery in conjunction with diagnostic CT imaging.

The innovation of this paper is reflected in discussing the application of computer-aided CT scan images in pulmonary nodules and proposing an image segmentation algorithm based on CT images and then exploring the treatment of acute abdomen under the concept of ERAS and analyzing the study of ERAS for acute abdomen under CT images.

2. Experimental Methods for the Diagnosis of Common Acute Abdominal Diseases in General Surgery Based on CT Images

2.1. Application of Computer-Aided CT Scan Images in Lung Nodules. For a long time, the interpretation of medical pictures has been performed by radiologists, and experienced physicians can determine whether a suspicious shadow is benign or malignant by examining the grayscale value, size, margin, location, and other signal characteristics of the suspicious shadow in medical pictures, but usually an in-depth puncture is required to extract a small number of biopsies for pathological analysis before a final diagnosis can be made. However, physicians' understanding of medical images is influenced by many factors, including the complexity of the imaging mechanism of medical images and the differences in the performance of various medical imaging devices, which inevitably lead to conditions such as large individual differences, blurred boundaries, and prominent noise and artifacts in the resulting images [11]. Moreover, the pathology of pulmonary nodule formation is unclear, the lesion characteristics are diverse, and the clinical examination lacks specific norms, which makes the examination, identification, and classification of pulmonary nodules more difficult [12]. Therefore, making an accurate judgment based on a patient's image is sometimes not a simple task. The opinions of different doctors sometimes differ when examining the same image and are highly subjective [13]. At the same time, reading a large number of images is unbearable for physicians, who need to reduce the number of images read and the time spent on each image to make a

quick judgment, which can easily lead to misdiagnosis and missed cases [14]. Therefore, it is crucial to develop computer programs to help physicians read and analyze medical images through computer support.

However, for computer-assisted therapy, useful signals must be found in the images to make judgments. For example, Figure 1 shows the computer-aided CT image analysis [15]. Because of the partial volume effect and artifacts, there are often cases of different images of the same disease or even different diseases in the images, which causes great problems for computer-aided therapy [16]. While high-performance CAD systems often give medically accurate opinions, which in turn greatly improve the effectiveness and thus the accuracy of treatment, reduced-performance CAD systems not only often yield unsatisfactory results, but also increase the psychological burden on medical staff and even mislead them, thus achieving the opposite effect [17]. Although many research results have been obtained on CAD techniques for pulmonary nodules, and some CAD systems have been commercialized, these research results and application conditions are not perfect, or they are only effective for a certain type of suspected shadow, and their use is limited. Therefore, the current therapeutic efficacy of CAD systems does not yet meet the requirements of conventional medical imaging treatment for the characterization of benign and malignant pulmonary nodules [18].

Under the circumstances that the current CAD system cannot handle the diagnosis of pulmonary nodules, it is always advantageous to explore new solutions. The main purpose of this paper is to summarize the previous research results in various stages of lung nodule detection, and at the same time to try to design and develop a CAD system specifically for lung nodules with a new idea of lung nodule diagnosis, in order to expect to reduce the burden of medical personnel and to detect lung nodules more effectively [19]. Figure 2 shows the computer-assisted virtual drug screening process.

Lung cancer is extremely harmful to people's health. At present, the most effective way to deal with lung cancer is through regular lung CT scans, early detection of lung nodules, and timely diagnosis to improve survival rate [20]. A CAD system with high accuracy plays a pivotal role in reducing omissions or misdiagnosis by doctors and has important use value and practical significance.

2.2. Theories of Image Segmentation Algorithms Based on CT Images

2.2.1. Fuzzy C-Means Clustering Segmentation Algorithm in Spatial Domain. The fuzzy C-mean (FCM) clustering algorithm regards the pixels of the picture as a sample set and distinguishes the pixels of the picture according to the principles of similarity within the class and separation between classes [21]. FCM algorithm is the largest separation calculation used in fuzzy clustering calculation, and it is also commonly used in the field of medical vision image separation.

The typical FCM algorithm originated from K-means clustering calculation. After repeated iterations of the algorithm, all cost functions are simplified and clustered:

$$G = \sum_{a=1}^{K} \sum_{b==1}^{D} l_a - c_b^2. \tag{1}$$

The objective function of the FCM algorithm is

$$G = \sum_{a=1}^{K} \sum_{b==1}^{D} t_{ab}^h l_a - c_b^2, \tag{2}$$

where t_{ab} is a member function of the algorithm and must meet the following requirements:

$$\begin{gathered} \forall a, b, \sum_{b=1}^{D} t_{ab} = 1; \quad t_{ab} \in [0, 1], \\ \sum_{a=1}^{A} t_{ab} > 0. \end{gathered} \tag{3}$$

Member function t_{ab} and cluster center c_b can be solved iteratively according to the following formula until the objective function value is the smallest:

$$\begin{gathered} t_{ab} = \frac{l_a - c_b^{-2/(h-1)}}{\sum_{k==1}^{D} l_a - c_k^{-2/(h-1)}}, \\ c_b = \frac{\sum_{a=1}^{A} t_{ab}^h l_a}{\sum_{a=1}^{A} t_{ab}^h}. \end{gathered} \tag{4}$$

If the pixel characteristic value of an image is similar to the characteristic value of a cluster center level variable, then the image is given a higher fuzzy affiliation value; assuming that the difference between the image characteristic value and the characteristic value of a cluster center is large, then the image is given a lower fuzzy affiliation value [22]. The classic fuzzy C-means clustering algorithm can accurately separate the images initially, but the separation effect is not ideal for images with inconsistent gray levels and weak edge features.

The composition function operation method is described by the following formula:

$$t_{ab} = \frac{t_{ab}^m r_{ab}^n}{\sum_{k=1}^{D} t_{kb}^m r_{kb}^n}. \tag{5}$$

r_{ab}^n is the constructed spatial domain function including the membership degree of the neighboring pixels:

$$r_{ab}^n = \sum_{k \in A_a} t_{kb}. \tag{6}$$

In the clustering calculation, the expression of the spatial function method can be introduced into formula (4) and modified as a fuzzy membership degree.

2.2.2. Semiautomatic Segmentation Algorithm of Fuzzy Clustering Level Set in Spatial Domain. The FCM algorithm, after subdividing the graphical pixel point aggregation, uses

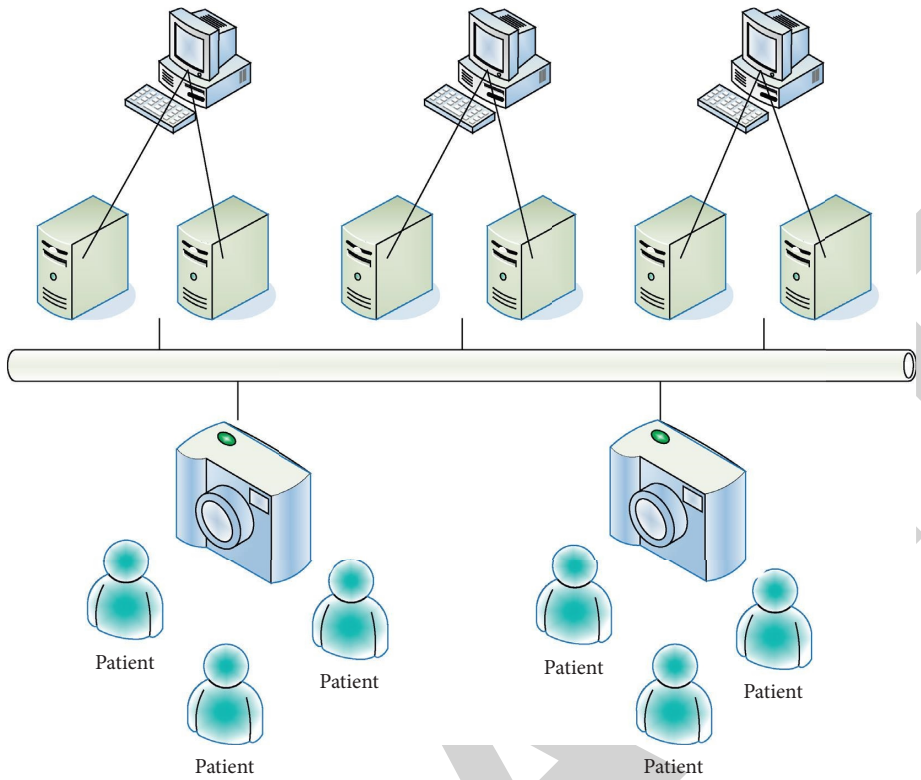

Figure 1: Computer-aided CT image analysis.

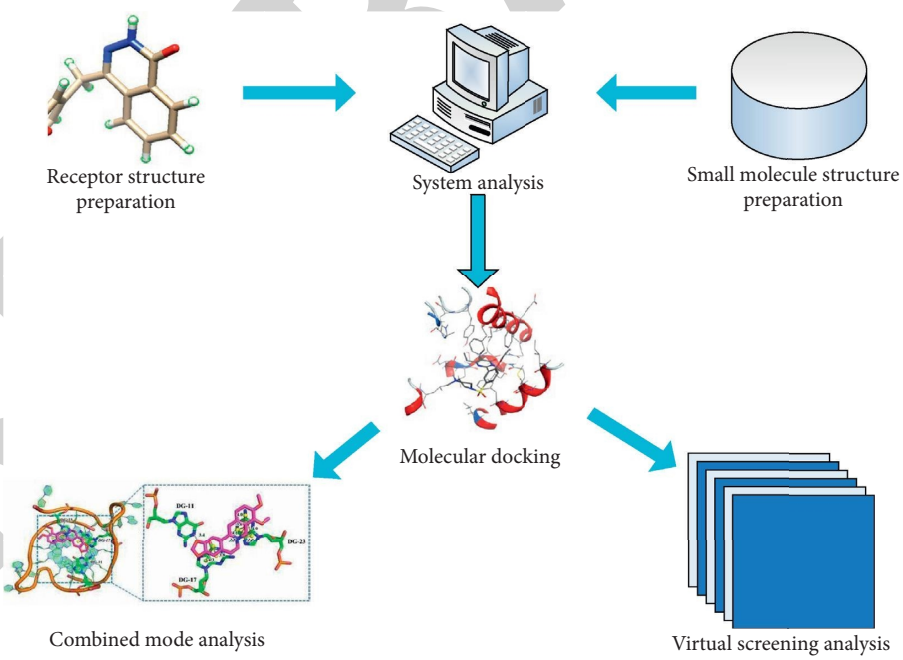

Figure 2: Computer-aided virtual drug screening.

the level set cutting operator to express a function in the highest one-dimensional space (called level set function) as a zero level set to cut the target contour shape and uses the curve evolution of the active contour model to cut the graph, as shown in Figure 3.

The traditional level set cut approach in the curve evolution step, for determining the sign of the level set function with the time distance function approach, must be periodically initialized, which leads to an excessive amount of statistics for the algorithm and unstable cut results

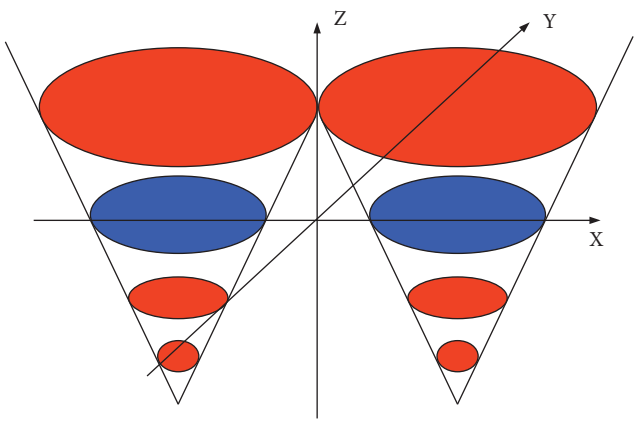

Figure 3: Schematic diagram of the evolution of the level set function.

[23, 24]. Moreover, the statistical time and quantization steps must also comply with the Courant–Friedrichs–Lewy (CFL) requirements, so the average value is usually taken to be smaller.

According to the above problems, you can choose a high-speed level set subdivision calculation that does not need to be initialized. The evolution formula of the level set algorithm is defined as

$$\frac{\partial \varphi}{\partial o} = t\gamma(\varphi) + \gamma(j, \varphi). \tag{7}$$

Here, φ is the signed distance function; $\gamma(\varphi)$ is the degree to which the level set function φ deviates from φ, and the expression is

$$\gamma(\varphi) = \triangle\varphi - \operatorname{div}\left(\frac{\nabla\varphi}{|\nabla\varphi|}\right), \tag{8}$$

where $\gamma(j, \varphi)$ is to guide the level set function to converge towards the boundary of the target of interest, and the expression is

$$\gamma(j, \varphi) = \rho\omega(\varphi)\operatorname{div}\left(\frac{\nabla\varphi}{|\nabla\varphi|}\right) + sj\omega(\varphi). \tag{9}$$

Here, ρ and s are constants. The expressions of $\omega(\varphi)$ and j are

$$\omega(a) = \begin{cases} \frac{1}{2\tau}\left[1 + \cos\frac{\pi a}{\tau}\right], & |a| \le \tau, \\ 0, & |a| \ge \tau, \end{cases} \tag{10}$$
$$j = \frac{1}{1 + \left|\nabla\left(J_\alpha \otimes L\right)\right|^2}.$$

The level set algorithm initializes the level set function by establishing a region, instead of using the signed distance function to initialize it. Express the initialization function as

$$\varphi_0(a, b) = \begin{cases} -D, & \varphi_0(a, b) < 0, \\ D, & \text{otherwise}, \end{cases} \tag{11}$$

where D is a fixed constant.

The level set evolution formula adopts the finite difference method to discretize the calculation, and the obtained level set function iterative equation is

$$\varphi^{k+1}(a, b) = \varphi^k(a, b) + \beta\left[t\gamma\left(\varphi^k\right) + \gamma\left(j, \varphi^k\right)\right], \tag{12}$$

where β refers to the time step.

Both fuzzy C-mean clustering and level set separation calculations are very good image separation models and have been widely used in industrial image separation, but when the algorithms are applied to the field of medical image separation, each has limitations and is not widely adaptable [25]. The fuzzy clustering algorithm clusters the splitting objects for image pixel point similarity without affecting the spatial extent signal and boundary information of the image; while the horizontal set segmentation algorithm requires manual initialization, so the calculation of the splitting conclusion is not fixed, and for different types of horizontal separation objects, different types of parameters need to be set preferably, and if the parameters are chosen properly, the image separation effect is good, and on the contrary, the effect is not good [26].

Based on these problems, a level set calculation based on spatial domain fuzzy clustering is given to perform the segmentation of CT images of malignant cancers of the liver and kidney. The calculation first uses the spatial domain fuzzy C-mean clustering algorithm for the initial aggregation of image segmentation and then reinitializes the level set function based on the aggregation results.

The initial level set function is defined as

$$\varphi_0(a, b) = -4\tau(0.5 - E_k) \tag{13}$$

where τ is a parameter in the Dirac function and E_k is a binary image:

$$E_k = U_k \ge e_0, \quad e_0 \in (0, 1). \tag{14}$$

In the fuzzy level centralized split calculation, the parameter settings during the level set evolution will also affect the final split conclusion of the medical image. Therefore, for different types of medical images, the control parameter selection values need to be adjusted appropriately [27].

The parameters are automatically initialized according to the following formula:

$$\begin{cases} i = \int \omega(\varphi_0)\mathrm{d}a\mathrm{d}b, \\ \mu = \int H(\varphi_0)\mathrm{d}a\mathrm{d}b, \\ \aleph = \frac{\mu}{i}. \end{cases} \tag{15}$$

$H(\varphi_0)$ represents the Heaviside function, and the expression is

$$H(\varphi_0) = \begin{cases} 1, & \varphi \ge 0, \\ 0, & \varphi < 0, \end{cases}$$
$$\begin{cases} t = \frac{0.2}{\aleph}, \\ \rho = \frac{0.1}{\aleph}. \end{cases} \tag{16}$$

The balloon force parameter is rewritten as follows:

$$J(E_k) = 1 - 2E_k. \tag{17}$$

The function term $\gamma(j, \varphi^k)$ in the level set evolution equation and iterative expression can be rewritten as

$$\gamma(j, \varphi^k) = \rho\,\omega(\varphi)\mathrm{div}\left(\frac{\nabla\varphi}{|\nabla\varphi|}\right) + J(E_k)j\omega(\varphi). \tag{18}$$

The level set segmentation calculation combined with the spatial domain fuzzy cluster analysis method fully considers the image space domain information, and the balloon force parameter covers the signal after the spatial domain fuzzy cluster analysis method, and the level set function can be initialized manually after the fuzzy cluster analysis method results, thus reducing the problem of unstable operation results caused by automatic initialization [28].

The basic idea of regional growth is to collect pixels with similar properties to constitute a region. Specifically, one seed pixel is found to be a growing point of the growing region and then combined with the same or similar properties of the seed pixels in the neighborhood of the seed pixels into the region where the seed pixels are located. These new pixels as new seed pixels continue the above process until the pixels that are not satisfied can be included. Such a zone is growing. The core of the threshold segmentation method is how to find an appropriate threshold. The most commonly used threshold method is based on the method of gray histogram, such as the maximum interclass equation method (OTSU), minimum error method, maximum entropy method, and the like. Such methods typically use a fixed global threshold for the entire image. If there is a shadow or brightness distribution in the image, the segmentation effect will be affected. Different thresholds are employed in different regions of the image based on local thresholds, which have a better segmentation effect relative to the global threshold method, which is also referred to as an adaptive threshold method. The selection of the threshold is generally based on the local statistical information, such as local variance, partial contrast, and surface fitting threshold. Whether it is a global threshold or a partial threshold, the threshold method is usually affected by noise. In order to obtain better segmentation results, it is often also necessary to combine with other image processing techniques such as image denoising. The advantage of threshold segmentation is that the calculation is simple, the operation is high, and the speed is fast. The selection of the threshold needs to be determined according to the specific problem, generally determined by experiments. For a given image, the optimal threshold can be determined by analyzing the method of the histogram, such that when the histogram is clearly present, two peak midpoints can be selected as the optimal threshold, as shown in Figure 4.

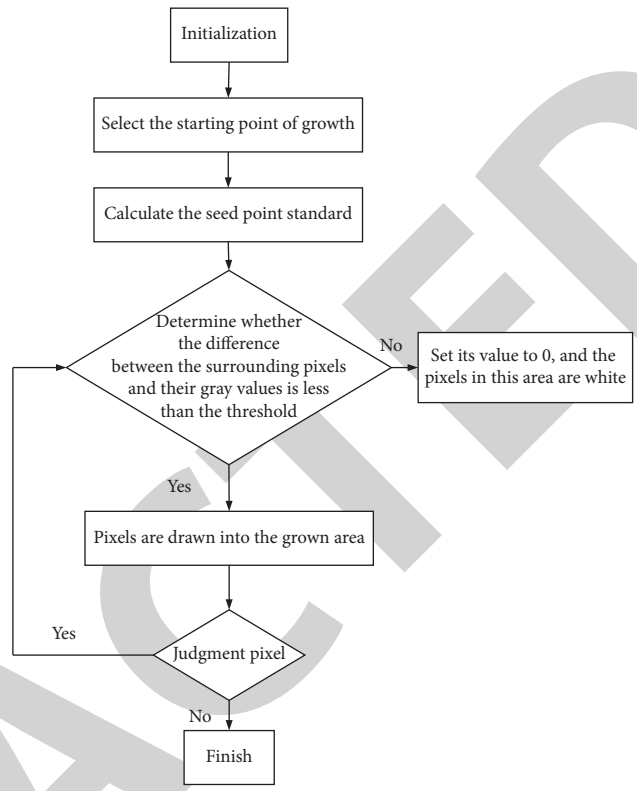

Figure 4: Segmentation flowchart based on the threshold region growing algorithm.

3. Experimental Results of Common Acute Abdominal Diseases in General Surgery Based on CT Images

3.1. Treatment of the Acute Abdomen under the ERAS Concept. Enhanced recovery after surgery (ERAS) refers to the implementation of various proven methods in the perioperative period to reduce the stress and complications of surgical patients. Reduce physical and psychological trauma and stress, reduce fatality rate and shorten hospital stay, and speed up the recovery of patients. Since its introduction, the ERAS concept has been used in various elective surgeries, such as upper gastrointestinal perforation, acute cholecystitis, and acute appendicitis [29]. Many studies have been reported on the use of the ERAS concept in the perioperative period of clinical surgical emergencies requiring emergency surgery, and the research results have shown that the application of the ERAS concept in the perioperative period of emergency abdominal diseases can achieve good clinical results corresponding to those in elective surgery, and the results of these studies have shown that the application of the ERAS concept to the perioperative period of acute abdomen can achieve good clinical outcomes in elective surgery and create a new model of perioperative management in clinical surgery. Acute abdomen is characterized by rapid onset, rapid changes, complex causes, and heavy morbidity, and the stressful stimuli caused by the onset and perioperative period are more severe than those caused by elective laparoscopic lesions, so the ERAS concept is urgently needed. In this study, we attempted to explore the importance of perioperative nutritional support therapy in the diagnosis of acute abdomen under the ERAS concept.

The case selected in this study was collected in hospitalization in a rehabilitation area of a hospital, and thirty patients with patients in income national standards. According to the order before and after admission, follow

the proportion of 1 : 1 and follow the simple digital table to randomly divide the treatment group and control group, 15 cases. All kinds of diseases are divided into two groups according to simple randomization, namely, ERAS group and CPM group. Among them, the acute abdomen cases in parallel emergency treatment have been selected as an object, mainly involving acute appendicitis, acute gallbladder inflammation, acute intestinal obstruction, upper digestive pipe perforation, and acute pancreatitis. And they are classified here.

There was no statistically significant difference in the composition of patients between the ERAS group and the CPM group, and the differences in age, gender, nutritional status before surgery, and surgical methods between the two groups were not statistically significant. Figure 5 shows the composition of the two groups of patients, and Figure 6 shows the comparison of the general conditions of the two groups of patients admitted to the hospital. Among them, A means acute appendicitis, B means acute cholecystitis, C means acute intestinal obstruction, D means gastrointestinal perforation, and E means acute pancreatitis.

Intraoperative nutrient metabolism is mainly based on restrictive infusion and regulation of blood glucose, while the patient is under intraoperative anesthesia with intraperitoneal injection, but because the organism remains in a state of stress, the surgery also causes an inductive stimulation of the organism, resulting in increased catabolism. Under stressful conditions, the human organism produces sympathetic excitation and launches various management systems including renin-angiotensin-aldosterone system and hypothalamic-pituitary hormone, etc., while many active hormones in the above management systems, such as aldosterone and antidiuretic hormone, also have a great impact on the balance of fluids in the body. Table 1 shows the comparison of NRS2002 scores between the two groups of patients. Through statistical treatment, acute appendicitis, acute gallbladders, acute intestinal obstruction, digestive tract perforation, and acute pancreatitis P values are greater than 0.05, and there is no significant difference.

In the general preoperative period, the proposed patient may not take in enough fluid or lose too much due to loss of appetite, fasting, diarrhea, nausea, etc. This results in a large loss of body fluids and insufficient effective circulating blood volume, while the traditional rehydration is the sum of the preoperative loss, the required amount, and the intraoperative and postoperative loss. The large amount of rehydration increases the effective circulatory load of patients, which can lead to gastrointestinal vascular edema, heart failure, pulmonary edema, etc., and the increase of overload effective circulation causes the oversaturation of bacterial and extrabacterial fluids, and the physiological function is constrained to a certain extent, which directly affects the postoperative wound healing, and when aggravated, it can also cause intestinal mucosal edema and prevent the normal repair of intestinal functions and even cause postoperative complications. Therefore, the rehydration method should be controlled to prevent unnecessary postoperative complications caused by excessive burden of systemic fluid and promote the recovery of the body after surgery. The theory of ERAS suggests the use of epidural anesthesia, which inhibits parasympathetic stimulation signaling and thus reduces the release of stress-related hormones, which has a favorable negative impact on glucose metabolism disorders and multiple fluid homeostasis. The dose of glucose injected during surgery should also be appropriately controlled, and the phenomenon of insulin resistance in the postoperative period should be reduced. Table 2 compares the surgical methods of the two groups of patients.

3.2. Treatment of the Acute Abdomen by ERAS Based on CT Images. Compared with the CPM group, the duration of postoperative recovery of colorectal function was significantly reduced in the ERAS group, and this difference was more statistically significant ($P < 0.05$). Compared with the CPM group, the ERAS group had earlier time to first bed activity and first meal and also had lower postoperative pain level, and this difference was more statistically significant ($P < 0.05$). Figure 7 shows the comparison of the relevant indexes of the two groups of acute appendicitis patients after the operation of acute cholecystitis patients. The nutritional method for acute abdomen surgery under the ERAS concept is water intake for six hours after the operation; liquid food is gradually started on the first day after the operation and then slowly added every day according to the patient's tolerance until the full dose.

How to provide proper nutritional protection after surgery depends on the nutritional status before surgery and the gastrointestinal function status after surgery. ERAS advocates early postoperative diet, and early feeding stimulation can shorten the duration of gastrointestinal ischemia, thereby reducing the reperfusion injury to the gastrointestinal mucosa and improving the peristalsis of the large intestine, thereby promoting the repair of intestinal function. Under normal circumstances, supine patients need to be given about 20–25 kcal of heat energy per kilogram weight per day, but if the patient is still able to move independently, it needs to increase the energy consumption of about 5 kcal/(kg d). The transition of nutrient sources from intestinal nutrition to conventional diet cannot be accomplished overnight and must be gradually improved with the patient's tolerance status. Usually, one-fourth of the full dose can be given on the first day, but the nutrients must fully meet the patient's needs for healing and recovery; one-half of the full dose can be given after the second day, and the full dose of enteral nutrition can be given after the third day if circumstances permit. For patients who cannot receive enteral nutrition in a short period of time, they can choose to combine enteral nutrition with parenteral nutrition. As shown in Figure 8, it is a comparison of the indicators of the two groups of patients with acute intestinal obstruction after surgery and those with gastrointestinal perforation, where a represents the date of intestinal function returning to normal, b represents the date of first getting out of bed, and c represents the time of first eating. Figure 9 is a picture of a patient with complete intestinal obstruction observed on the basis of CT images. The left picture in Figure 10 shows a perforation of the digestive tract observed on the basis of CT

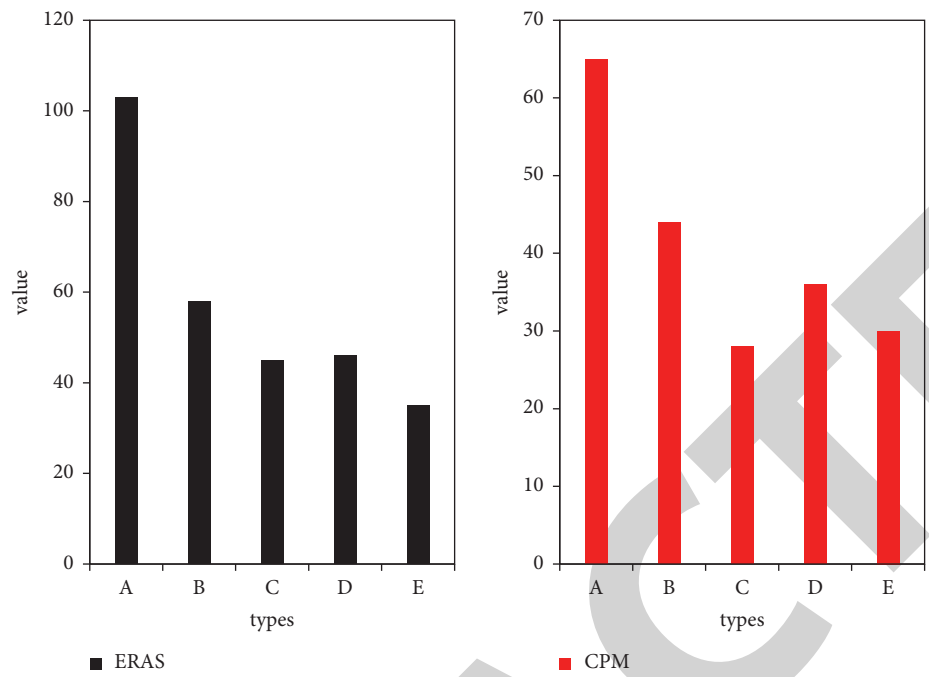

Figure 5: Disease composition of the two groups of patients/case.

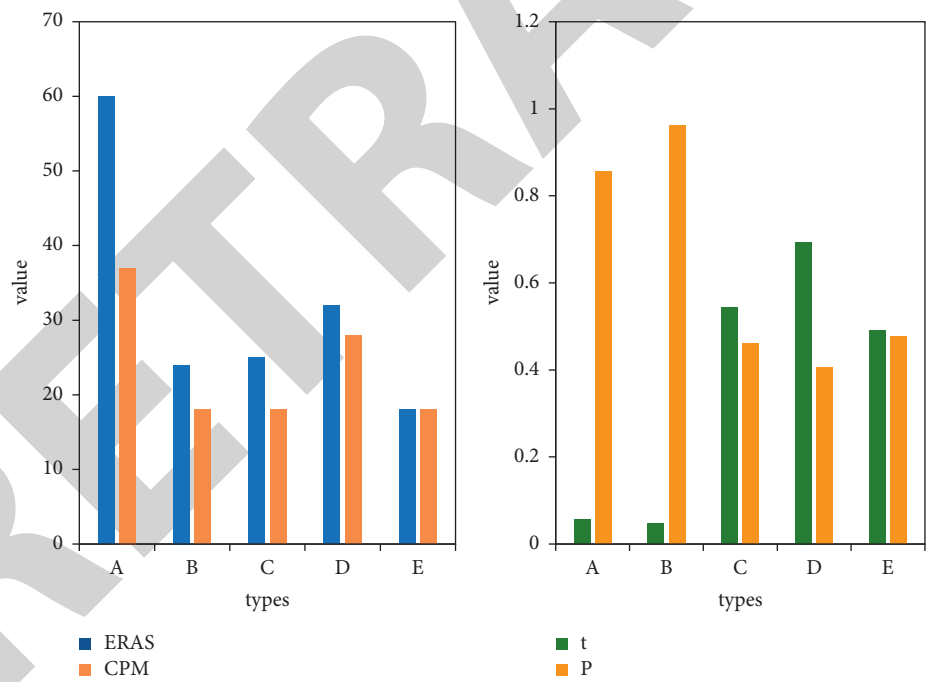

Figure 6: Comparison of the general conditions of the two groups of patients admitted to the hospital/case.

Table 1: Comparison of NRS2002 score between two groups of patients/case.

Group	Acute appendicitis		Acute cholecystitis		Acute intestinal obstruction		Digestive tract perforation		Acute pancreatitis	
	>3	<3	>3	<3	>3	<3	>3	<3	>3	<3
ERAS	19	79	9	36	19	24	26	20	14	19
CPM	13	49	8	47	9	15	14	19	15	17
T	0.319		0.169		0.249		1.298		0.597	
P	0.571		0.678		0.609		0.249		0.441	

Table 2: Comparison of surgical methods between the two groups of patients/case.

Group	Acute appendicitis		Acute cholecystitis		Acute intestinal obstruction		Digestive tract perforation		Acute pancreatitis
	Simple appendectomy	Appendectomy + abscess removal	Cholecystectomy	Cholecystectomy + bile duct exploration	Bowel arrangement	Bowel resection and anastomosis	Perforation repair	Bowel resection and anastomosis	Abdominal abscess removal
ERAS	90	13	23	33	21	24	29	20	36
CPM	49	11	19	22	12	10	23	9	29
T	0.691		0.411		0.149		0.988		-
P	0.401		0.519		0.701		0.309		-

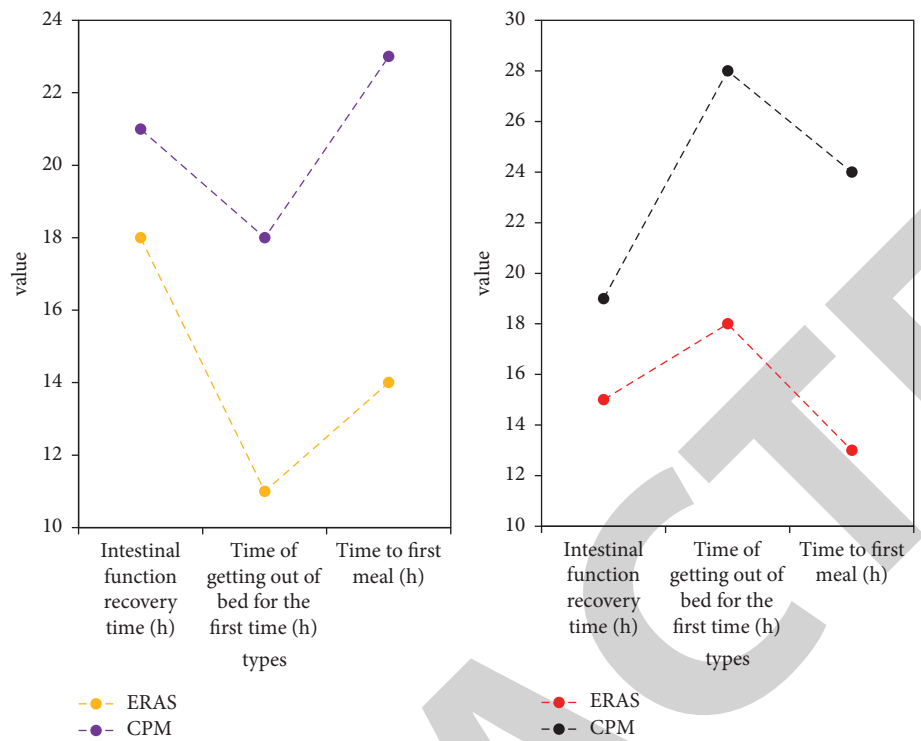

Figure 7: Comparison of related indexes of (a) two groups of patients with acute appendicitis after surgery and (b) two groups of patients with acute cholecystitis.

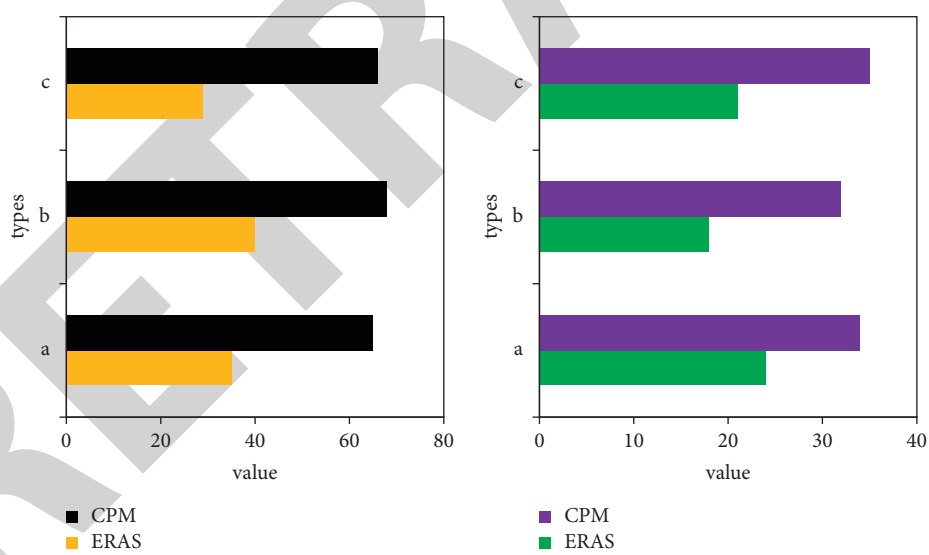

Figure 8: Comparison of related indexes between (a) the two groups of patients with acute intestinal obstruction after surgery and (b) the two groups of patients with gastrointestinal perforation.

images, and the right picture shows a normal abdominal radiograph observed on CT images.

Postoperative pain can prolong the patient's bed rest or delay the return of bowel function to normal, but not every pain medication is suitable for perioperative application; for example, opioid analgesics can reduce intestinal peristalsis and increase the risk of postoperative intestinal obstruction, which can prolong the time to the first meal; ERAS emphasizes epidural pain pump + administration of NSAIDs, while reducing opioid analgesics for multimodel pain treatment can somewhat reduce this adverse effect. Table 3 shows the comparison of the relevant indexes of the two groups of patients with acute pancreatitis after operation.

Table 4 compares the clinical outcomes of the two groups of patients. ERAS combined with some optimization initiatives in the perioperative period can increase the possibility of early postoperative transdigestive nutrition, such as nonroutine preoperative cleaning of the gastrointestinal

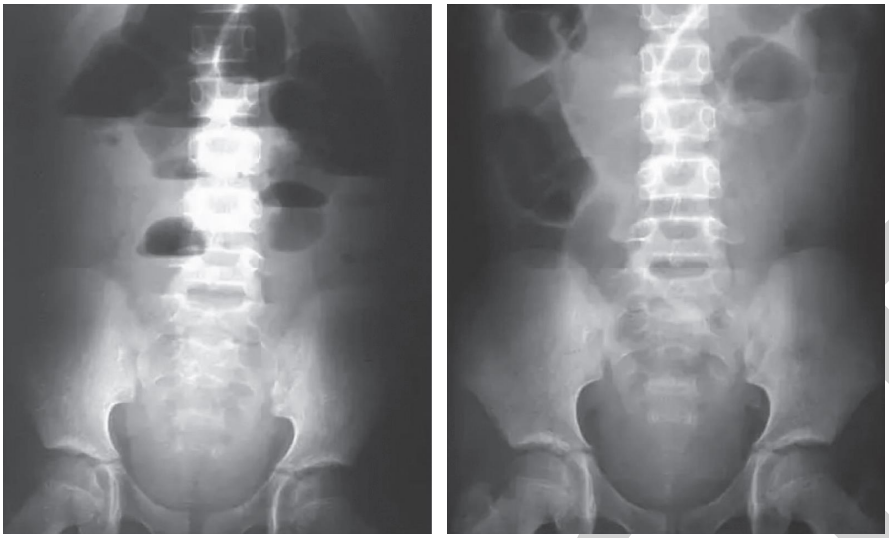

Figure 9: Complete intestinal obstruction.

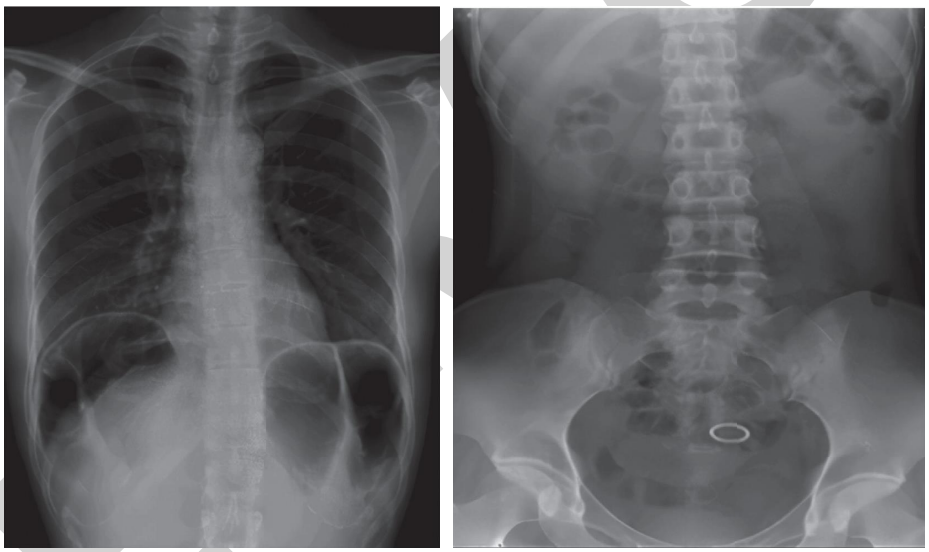

Figure 10: (a) Perforation of the digestive tract; (b) a normal abdominal slice.

Table 3: Comparison of related indexes of two groups of patients with acute pancreatitis after operation.

Group	Intestinal function recovery time (h)	Time of getting out of bed for the first time (h)	Time to first meal (h)
ERAS	35	31	33
CPM	47	37	49
T	5.98	3.387	7.821
P	<0.001	0.001	<0.001

Table 4: Comparison of clinical results between the two groups of patients.

Group	Postoperative complications/case (%)	Postoperative hospital stay (d)
ERAS	18	5.34
CPM	26	9.07
T	8.012	19.987
P	0.05	<0.001

tract, early postoperative removal of nasogastric and urinary catheters, restrictive rehydration, epidural anesthesia and less damaging surgical methods, early postoperative activity, and multimodal postoperative analgesia, reducing stressful stimuli caused by disease and the postoperative environment, thus minimizing the impact on the nutritional and metabolic systems. This reduces the incidence of postoperative comorbidities, shortens the duration of postoperative hospitalization, reduces medical expenses, and promotes the ultimate goal of recovery. The ERAS concept has outstanding advantages for lower perioperative nutritional support and comparison with conventional perioperative management, as ERAS offers benefits to patients by shortening the postoperative hospitalization time frame.

4. Discussion

The main objective of nutritional support in combination with other perioperative optimization measures is to reduce the stressful stimulation of the patient, thus reducing the postoperative disruption of nutrition and metabolism, reducing the incidence of postoperative comorbidities, reducing the length of hospital stay, and reducing medical expenses, in order to achieve the goal of accelerated recovery of the patient. The results of this investigation showed that perioperative nutritional support under the concept of ERAS had outstanding advantages compared with traditional perioperative management methods, and the postoperative complication rate in the ERAS group was only 6.01% compared with 12.9% in the traditional CPM group, which was a statistically significant improvement ($P < 0.05$). The postoperative hospital stay was also reduced from 7.93 days to 4.62 days, thus controlling the clinical risk during the perioperative period and bringing benefits to patients. Compared with the CPM group, the rapid recovery of gastrointestinal function and the first meal in the ERAS group after surgery were significantly earlier than those in the CPM group. This was achieved through a combination of enhanced communication with patients and families before surgery to obtain full cooperation, nonroutine placement of nasogastric tubes, epidural intraperitoneal infusion anesthesia treatment and analgesia, small postoperative incisions, control of the amount of vomiting and diarrhea, reduction of opioid analgesics within perioperative resourcefulness, and the results of a series of measures such as early postoperative bedtime activities.

5. Conclusions

In the postoperative treatment of acute abdominal disease, we advocate individualized treatment, specific solutions for various conditions of patients, and carefully grasp the nutrient requirements of patients, metabolic function, and nutrient giving pathways and effects, so that we can achieve the desired goal of postoperative nutritional support care for acute abdominal disease. In the case of patients with acute abdomen, nutritional support under the ERAS concept has made it possible to provide patients with shorter hospital stays, significantly improved organ function, significantly improved nutrient status, and increased comfort, and there is no increase in the number of patients, with good publicity and promotion, thus providing the greatest possible benefit to patients. The standardized and reasonable management of nutritional support in the peripheral period can enhance the immune function, adjust metabolism, maintain tissue and organ function and control inflammatory response, and thus improve the outcome of surgical care, which is the development direction that must be pursued by surgical nutrient caregivers in the future. In patients with acute abdomen undergoing emergency surgery, the use of perioperative nutrient support measures under the theory of accelerated repair surgery can effectively improve the nutritional status of patients, accelerate postoperative recovery, and reduce surgical complications, thereby reducing the length of hospitalization and optimizing clinical outcomes. The core of accelerating the surgery of rehabilitation is to reduce surrounding wound stress and promote rapid recovery of each organ function. Perioperative wound stress response is the earliest effect on gastrointestinal function, but the last one continues. Perioperative treatment measures have different degrees of gastrointestinal function recovery after surgery, and improper treatment will result in postoperative gastrointestinal function recovery delays. In this regard, we will further study.

Data Availability

The data that support the findings of this study are available from the corresponding author upon reasonable request.

Disclosure

Yunguang Nan and Zuyan Zhang are the co-first authors.

Conflicts of Interest

The authors declare that they have no conflicts of interest.

Authors' Contributions

Yunguang Nan and Zuyan Zhang authors contributed equally to this work.

References

[1] S. Zhang, F. Sun, N. Wang et al., "Computer-aided diagnosis (CAD) of pulmonary nodule of thoracic CT image using transfer learning," *Journal of Digital Imaging*, vol. 32, no. 6, pp. 995–1007, 2019.

[2] Y. Li and L. Xia, "Coronavirus disease 2019 (COVID-19): role of chest CT in diagnosis and management," *AJR. American journal of roentgenology*, vol. 214, no. 6, pp. 1280–1286, 2020.

[3] M. Metintas, H. Yildirim, T. Kaya et al., "CT scan-guided Abrams' needle pleural biopsy versus ultrasound-assisted cutting needle pleural biopsy for diagnosis in patients with pleural effusion: a randomized, controlled trial," *Respiration*, vol. 91, no. 2, pp. 156–163, 2016.

[4] E. R. Ropelle, M. B. Flores, D. E. Cintra et al., "IL-6 and IL-10 anti-inflammatory activity links exercise to hypothalamic

Hindawi
Journal of Healthcare Engineering
Volume 2023, Article ID 9785839, 1 page
https://doi.org/10.1155/2023/9785839

Retraction

Retracted: Protective Effect of Amino Acids on the Muscle Injury of Aerobics Athletes after Endurance Exercise Based on CT Images

Journal of Healthcare Engineering

Received 10 October 2023; Accepted 10 October 2023; Published 11 October 2023

This article has been retracted by Hindawi following an investigation undertaken by the publisher [1]. This investigation has uncovered evidence of one or more of the following indicators of systematic manipulation of the publication process:

(1) Discrepancies in scope
(2) Discrepancies in the description of the research reported
(3) Discrepancies between the availability of data and the research described
(4) Inappropriate citations
(5) Incoherent, meaningless and/or irrelevant content included in the article
(6) Peer-review manipulation

The presence of these indicators undermines our confidence in the integrity of the article's content and we cannot, therefore, vouch for its reliability. Please note that this notice is intended solely to alert readers that the content of this article is unreliable. We have not investigated whether authors were aware of or involved in the systematic manipulation of the publication process.

In addition, our investigation has also shown that one or more of the following human-subject reporting requirements has not been met in this article: ethical approval by an Institutional Review Board (IRB) committee or equivalent, patient/participant consent to participate, and/or agreement to publish patient/participant details (where relevant).

Wiley and Hindawi regrets that the usual quality checks did not identify these issues before publication and have since put additional measures in place to safeguard research integrity.

We wish to credit our own Research Integrity and Research Publishing teams and anonymous and named external researchers and research integrity experts for contributing to this investigation.

The corresponding author, as the representative of all authors, has been given the opportunity to register their agreement or disagreement to this retraction. We have kept a record of any response received.

References

[1] X. He and Y. Zhang, "Protective Effect of Amino Acids on the Muscle Injury of Aerobics Athletes after Endurance Exercise Based on CT Images," *Journal of Healthcare Engineering*, vol. 2022, Article ID 5961267, 13 pages, 2022.

Hindawi
Journal of Healthcare Engineering
Volume 2022, Article ID 5961267, 13 pages
https://doi.org/10.1155/2022/5961267

Research Article

Protective Effect of Amino Acids on the Muscle Injury of Aerobics Athletes after Endurance Exercise Based on CT Images

Xianghai He[1] and Yingjun Zhang[2]

[1]*School of Physical Education and Health, Yulin Normal University, Yulin 537000, Guangxi, China*
[2]*Medical School, Hunan University of Medicine, Huaihua 418000, Hunan, China*

Correspondence should be addressed to Yingjun Zhang; zhangyingjun82@163.com

Received 12 January 2022; Revised 23 February 2022; Accepted 26 February 2022; Published 19 March 2022

Academic Editor: Alireza Souri

During the training process, the aerobics athletes gradually increase their technical movements, the appreciation of the movements has been gradually improved, and the injuries of the athletes themselves have also gradually become serious. Based on CT image analysis, we study the protective effect of amino acids on aerobics athletes' muscle injury after endurance exercise. There are three major substance metabolism disorders in patients with muscle sclerosis, which are mainly manifested as decreased glucose tolerance and insulin resistance. Some patients develop muscle-derived diabetes. At the same time, the synthesis of lipids such as cholesterol and apolipoproteins decreases, the production of ketone bodies increases and the body uses more ketones for energy. The BCAA/AAA factor refers to the branched-chain amino acid/aromatic amino acid (BCAA/AAA) value. In amino acid metabolism, plasma albumin decreased significantly, the ratio of amino acids was unbalanced, and BCAA/AAA decreased, which was more likely to induce muscular encephalopathy. Using computer tomography (CT) to study the protective effect of amino acids on muscle injury, 32 aerobics athletes were randomly divided into an intervention group (Ig) and a control group (CG), each with 16 people. After 64-slice spiral CT scanning of muscles and three-dimensional reconstruction, the intervention group and the control group participated in aerobic endurance training 3 weeks in advance to establish a muscle microinjury model. The intervention group took the preprepared BCAA, while the control group did not take it. After three weeks of training, there will be one hour and three hours of aerobics competition. We need to detect changes in blood glucose (BS), creatine kinase (SCK), lactate dehydrogenase (LD), alanine (ALA), and alanine aminotransferase (AA) before and after exercise and 1 hour after exercise and record AVS athletes' pain analysis table. We successfully established the muscle injury model, letting all athletes' VAS score in 6–8 points; after 1 hour of exercise, the measurement results were the same as those of 2 hours. Therefore, after endurance training, the blood glucose content of the intervention group gradually decreased and returned to the original level after 2 hours of exercise, while the control group was lower than the level of exercise after 2 hours of exercise; the content of alanine in the two groups decreased more after 2 hours of exercise; the results of serum creatine kinase in the intervention group were higher than those in the control group after exercise. In the intervention group, lactate dehydrogenase increased rapidly at 2 hours after exercise; the alanine aminotransferase in the intervention group increased after exercise, but there was no significant change in the control group. It is also concluded that the longer the exercise time and the more energy consumption, the more effective the branched-chain amino acids supplement will be. The obtained imaging data can provide a more intuitive and accurate basis for the scientific selection of athletes, and amino acids can promote the synthesis of hormones, accelerate the synthesis of proteins and other products, reduce the content of creatine kinase in the blood, and protect the rapid recovery of muscle damage.

1. Introduction

Competitive aerobics [1] is evolved from fitness aerobics, with many similar characteristics. For example, music is an indispensable element of both. Athletes arrange their own movements according to the music rhythm and theme background and use their flexibility and strength to complete a set of difficult and natural movements. Aerobic exercise [2] has seven basic steps. Designers can arrange and combine them at will to get better display effect and improve

performance difficulty. Therefore, competitive aerobics is not only a simple sport but also a combination of wisdom. At the same time, in order to make the athletes perform the choreographer's designed movements perfectly, we must improve their own physical quality. Perfect body shape, soft toughness, and strong body strength are essential. Although competitive aerobics is not included in the current Olympic Games, with its separation from fitness aerobics, more and more countries begin to attach importance to it. This is possible in the future Olympic Games. Although our country has made some progress in the field of aerobics, after all, China has not been exposed to this project for a long time. Therefore, it is necessary and urgent to study the protective effect of BCAA on muscle injury after endurance exercise.

In the study of muscle injury, classifying CT images of muscle injury based on historical data can provide early prevention and treatment of some lesions, improve the cure rate, and assist doctors in the diagnosis of muscle injury. In machine learning, image labels are used to label the attributes of the entire image, which are used to train a classifier based on the entire CT image. One might think that hospitals would store labels on CT images.

Although the treatment of muscle strain has made substantial progress, muscle strain is still a very destructive disease, the incidence of muscle injury is still very high, and different from other diseases, skeletal muscle is the most abundant human tissue, and bone and iliac muscle injury is one of the most common sports injuries, so muscle strain urgently needs new and effective treatment methods. Mesenchymal stem cells (MSCs) have become important target cells for tissue engineering research and other diseases treatment because of their unique characteristics such as abundant sources, simple preparation, multidirectional differentiation ability, and low tumorigenicity. It is exciting that MSC [3] has achieved initial success in the treatment of muscle injury. The study of muscle injury found that when muscle injury occurs, an inflammatory response occurs in the first stage, and inflammatory cells can freely invade, due to vascular tear or vascular permeability increased significantly, leading to the accumulation of inflammatory factors in the injured site. After several hours of damage, white blood cells and monocytes eventually become macrophages. Macrophages have two functions. First, they remove necrotic muscle fibers by phagocytosis. Secondly, together with fibroblasts, they produce chemotactic signals, such as growth factors, cytokines, and chemokines. The extracellular matrix also contains growth factors, which become active when tissue is damaged. The next stage is the repair phase. The first is muscle fiber regeneration, also known as mycoplasma or basal layer muscle fiber regeneration under satellite cells. Muscle satellite cells proliferate and eventually differentiate into myoblasts. Muscle injuries have always plagued athletes, and along with athletes' training and competition, muscle injuries will have a greater negative impact on training effects and competition results to a certain extent. In severe cases, they may even cause muscle damage, causing athletes to stop training and withdraw from competitions. Therefore, it is very necessary to grasp the changes of muscle injury. Because these new myoblasts fuse with the injured muscle fiber, both ends of the injured muscle fiber are refilled. The second repair stage is the process of connective tissue forming cancer scar tissue. Scar tissue provides a location for fibroblasts to invade granulation tissue. However, if these fibroblasts proliferate excessively, the injured muscle will form scar tissue, which not only interferes with the repair process but also blocks the process of muscle regeneration. In addition, due to the injury, the nerve tissue in the muscle is damaged, which makes the muscle fiber lose the nerve innervation and the nutritional function of nerve cells, which is not conducive to the healing process of the injured muscle. HGF, IL-1, and IL-6 are secretory factors that stimulate satellite activity. In a word, it is an indisputable fact that there is a protective function of muscle after injury.

Abnormal amino acid metabolism is mainly manifested in the decrease of serum albumin, the increase of blood ammonia, and the imbalance of amino acid ratio. The liver is the main place for protein synthesis. It can synthesize almost all plasma proteins except immune proteins. In liver cirrhosis, liver function declines due to the damage and number of liver cells, as well as unreasonable diet restrictions, resulting in a significant decrease in plasma albumin and hypoproteinemia. However, hypoalbuminemia easily induces brain edema, makes brain cell dysfunction, and promotes the occurrence of hepatic encephalopathy. Branched-chain amino acids [4] are essential amino acids for the human body, including leucine, isoleucine, and valine. They are called "branched-chain amino acids" because they have typical side chains. BCAAs [5] have a variety of physiological functions. BCAAs are not only the basic unit of the peptide chain but also involved in the synthesis of sterols, ketones, and glucose. The final products of BCAAs metabolism are acetyl coenzyme A and succinyl coenzyme A, which enter the mitochondria and generate energy through the tricarboxylic acid cycle. In addition, BCAAs, especially leucine, can activate the mTOR signaling pathway and promote protein synthesis, cell metabolism, and cell growth. However, excessive BCAA is harmful. High BCAAs were positively correlated with dyslipidemia, insulin resistance, obesity, and type 2 diabetes. Although most amino acids are synthesized and decomposed in the liver, the metabolism of BCAAs is mainly concentrated in nonliver tissues, such as the myocardium, neurons, and kidney. Therefore, the changes of BCAAs metabolism may be involved in the occurrence and development of CHF metabolic remodeling. However, so far, there is no data to prove whether there is a correlation between plasma BCAAs level and CHF. In addition, in the normal body, the metabolic waste ammonia enters the ornithine cycle to synthesize urea through the liver, while liver cell metabolism is impaired in liver cirrhosis, the ornithine cycle is blocked, and a large amount of ammonia accumulates in the body, so blood ammonia rises. In patients with liver cirrhosis, the body environment is disordered, especially the metabolism of amino acids. Due to insufficient intake of plasma amino acids and increased consumption of peripheral muscle tissue in patients with liver cirrhosis, BCAA is lower than normal.

If the protective effect of muscle injury is not in place, it will do great harm to the muscle, and the athletes can neither play the real state nor participate in high-intensity sports in time, which will have a great impact on the collective and individual. In the process of generating muscle CT images, due to machine performance or scanning technology and other reasons, there will be large differences in the quality of the generated images. Therefore, the preprocessing of images has become an indispensable stage before data analysis. Moreover, as the amount of data continues to increase, the preprocessing operations involving manual participation have been unable to meet the needs. In this paper, the research on the protective effect of branched-chain amino acids on muscle injury of aerobics athletes after endurance training has solved this problem. The main structure of this paper is as follows: firstly, the development status of branched-chain amino acids is elaborated, and the muscle injury is briefly introduced; secondly, the model of muscle injury after endurance exercise of aerobics athletes is established, in which the mechanism of endurance exercise, the repair method of muscle injury, the training scheme of aerobic endurance exercise, and the successful target of muscle injury in endurance exercise are established. Then, it introduces the protective effect of BCAA on muscle injury after endurance training, including the composition and function of BCAA, the mechanism of BCAA catabolism, the physiological function of BCAA, the biosynthesis pathway of BCAA, and the protection mechanism of BCAA on muscle injury. Surface electromyography is one of the methods to assess muscle fatigue. It is a noninvasive technology that records, measures, and evaluates skeletal muscle function through the skin surface above the muscle. The real-time monitoring of fatigue and the fatigue status of specific muscles can be measured, and the mutual changes of biomechanics and physiology in the process of muscle fatigue can be obtained. Finally, through the formulation of an endurance exercise program, the experimental results of sports injury show that proper supplement of branched-chain amino acids can reduce the contents of creatine kinase and lactate dehydrogenase in blood, protect muscle tissue structure, and alleviate muscle injury caused by endurance training.

2. Establishment of the Muscle Injury Model of Aerobics Athletes after Endurance Exercise

2.1. Overview of Endurance Sports. Combining the popular deep learning or machine learning with tomography helps not only in image analysis but also in image reconstruction. The most widespread application of machine learning in CT image reconstruction is depth imaging [6]. Endurance exercise [7] usually refers to the ability to perform certain high-intensity behaviors for a long time. Functional ability refers to the ability to use functional potential effectively and the psychological strength of athletes which are important factors to determine the endurance level of aerobics athletes. The invention provides a CT image prediction method based on deep learning. Because the aerobics competition time is generally 1 minute 20 seconds ± 5 seconds, aerobics athletes have been carrying out high-intensity, high difficulty movement, which will make the heartbeat faster than the general action. Therefore, the vast majority of aerobics coaches do not think they are engaged in aerobic exercise. For homogeneous materials, the incident intensity and output intensity of single-energy X-rays conform to Lambert–Beer's law.

$$I = I_0 e^{-uax}. \tag{1}$$

For nonuniform objects, that is, different attenuation coefficients everywhere, the object can be divided into small units to calculate the attenuation characteristics. That is, when the outgoing beam of the previous unit is the incident beam of the next unit, it can be expressed as follows in the form of cascade in mathematics:

$$I = I_0 e^{-u_2 ax} e^{-u_1 ax} e^{-u_3 ax} \cdots e^{-u_t ax} = I_0 e^{\sum_{n=1}^{N} u_n ax}. \tag{2}$$

The incident X-ray intensity I_0 does not change, so

$$\frac{I}{I_0} = e^{-u_2 ax} e^{-u_1 ax} e^{-u_3 ax} \cdots e^{-u_t ax} = e^{\sum_{n=1}^{N} u_n \nabla x}. \tag{3}$$

Most of the sports injuries of outstanding competitive aerobics athletes in China are concentrated.

Born during the training period, the high difficulty of training, high intensity, and long time are the main reasons for the high probability of injury to athletes during this period, mostly in the wrists, ankles, and knees. Through some physiological knowledge, we can know that when a person is engaged in anaerobic exercise for more than 8 seconds, the energy of the body mainly comes from the conversion of glycogen and glucose, which will produce lactic acid. In the process of conversion, lactic acid accumulation will definitely cause muscle soreness, and some will become powerless from heart exercise; this is also an important reason why many aerobics athletes often make mistakes after the competition. Take the logarithm of both sides of the equal sign of the above equation to get the following:

$$P = -\ln\left(\frac{I}{I_0}\right) = \ln\left(\frac{I_0}{I}\right) = \sum_{n=1}^{N} \mu_n \nabla x. \tag{4}$$

When the unit size is infinitely small, we can get

$$p = p(y) = \sum_{n=1}^{N} \mu(x, y) \cdot \nabla X. \tag{5}$$

Aerobic capacity refers to the work done by the body to provide energy from the oxidative decomposition of energy substances under the condition of sufficient oxygen supply. It is based on the characteristics of skeletal muscle, neuromodulation ability, energy supply characteristics, etc. It is one of the important indicators of human health.

Therefore, in order to achieve good results, aerobics athletes must carry out endurance training in daily training. When your body adapts to a certain intensity of exercise, even if you will still feel tired in the future, your resistance will be greatly improved, and your endurance will also be improved, as shown in Figure 1:

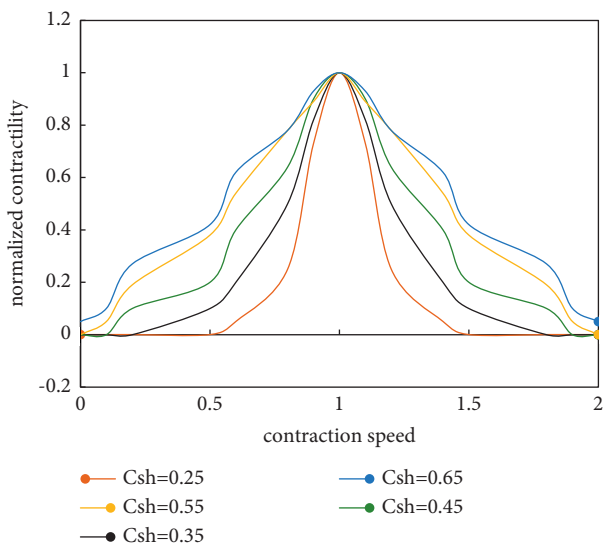

Figure 1: Contraction force-speed curve and contraction force-length curve.

At the same time, competitive aerobics is a kind of anaerobic exercise, which is obviously different from other anaerobic sports such as 100 meters dash. Because it does not have a single exercise composition, it contains a variety of sports, so in anaerobic training, we should also pay attention to aerobic training. Aerobic exercise and anaerobic exercise are not antagonistic, but interrelated.

$$W_{ij} = \frac{N^{11}N^{00} - N^{01}N^{10}}{N^{11}N^{00} + N^{01}N^{10}}, \tag{6}$$

$$W_{sv} = \frac{2}{L(L-1)} \sum_{i=1}^{L-1} \sum_{k=i+1}^{L} W_{i,j}. \tag{7}$$

In order to get rid of the long-term physical training, the athletes must combine the two kinds of sports to improve their endurance. No sport has only one mode of energy supply, just the proportion of which mode. Therefore, although aerobic exercise is a kind of anaerobic exercise, we should pay attention to the training of aerobic exercise, so that the oxygen uptake of muscles can be improved [8].

$$L_{ij} = \frac{N^{11}N^{10} - N^{01}N^{10}}{\sqrt{\left(N^{11} + N^{10}\right)\left(N^{01} + N^{00}\right)\left(N^{11+}N^{01}\right)\left(N^{10} + N^{00}\right)}}. \tag{8}$$

2.2. Establishment Mechanism of Muscle Injury. The common symptom of exercise-induced muscle injury is muscle soreness, which is transmitted by myelinated type III afferent nerve fibers and unmyelinated type IV afferent nerve fibers. The measure of inconsistency is

$$W_{isij} = \frac{N^{01} + N^{10}}{N^{11} + N^{01} + N^{10} + N^{00}}. \tag{9}$$

There are 6 types of unpaired difference measures:

(1) Entropy measurement method:

$$Q = \frac{1}{N} \sum_{j=1}^{N} \frac{1}{(L - (L/2))} \min\left\{l\left(Z_j\right)\left(L - l\left(Z_j\right)\right)\right\}. \tag{10}$$

(2) Kohavi–Wolpert measurement method:

In 1996, Kohavi and Wolpert proposed the KW measurement method as follows:

$$KW = \frac{1}{NL^2} \sum_{j=1}^{N} l\left(z_j\right)\left(L - l\left(z_j\right)\right). \tag{11}$$

From this, the relationship between KW and it can be drawn:

$$KW = \frac{L-1}{2L} Dis_{sv}. \tag{12}$$

(3) Interrater agreement $\mathfrak{R}$ measurement:

$$\overline{p} = \frac{1}{NJ} \sum_{j=1}^{N} \sum_{i=1}^{L} y_{i.j}. \tag{13}$$

Then, the calculation formula of κ is

$$\kappa = 1 - \frac{(1/L)\sum_{j=1}^{N} l\left(z_j\right)\left(L - l\left(z_j\right)\right)}{N(L-1)\overline{P}(1-\overline{P})}. \tag{14}$$

(4) Difficulty θ metric:

$$\theta = \mathrm{Var}(X). \tag{15}$$

(5) Generalized diversity measurement:

$$P(1) = \sum_{i=1}^{L} \frac{i}{L} p_i, \qquad p^2 = \sum_{i=1}^{L} \frac{i(i-1)}{L(L-1)} p_i. \tag{16}$$

(6) CFD measurement:

$$\mathrm{CFD} = \begin{cases} 0, \\ \dfrac{1}{1 - P_0}, \displaystyle\sum_{i=1}^{L} \frac{L-i}{L-1} P_i. \end{cases} \tag{17}$$

It is generally believed that myelinated type III fibers transmit tingling sensation, while unmyelinated type IV fibers transmit dull pain. The latter is more common in delayed onset muscle soreness. In addition, pain is caused by chemicals released during muscle injury and repair, including prostaglandins, vasodilators, serotonin, histamine, and potassium ions.

The development process of the muscle injury model is divided into four stages. The characteristics of muscle injury caused by endurance exercise are delay, different exercise

intensity, time, and muscle contraction mode, and the duration is from several minutes to two weeks or more. The four stages are as follows:

(1) Initial stage: it is generally believed that the primary injury is caused by mechanical stretch or metabolic factors. Mechanical stretching can damage the membrane of muscle cells (causing calcium ions to enter muscle cells), sarcoplasmic reticulum (resulting in decreased calcium regulation), and muscle contractile components. Metabolic factors include high body temperature, low pH, insufficient mitochondrial oxidation, and increased free radicals. At this stage, the main cause of muscle injury that more research shows is calcium overload and free radical accumulation. However, many of the features of this phase are not clear. This process is mainly related to the causes of the change, and further research is needed. This paper uses Euclidean distance as the similarity measure of the K-means algorithm. Euclidean distance is the distance between points in n-dimensional space.

$$d = \sqrt{\sum_{k=1}^{n} \left(x_{1k} - x_{2k}\right)^2}, \tag{18}$$

$$d = \sqrt{(a-b)(a-b)^T}. \tag{19}$$

(2) Spontaneous phase: this stage refers to the destruction of the cellular structure by the intrinsic proteolytic system and lipid peroxidation system of muscle fibers, usually occurring hours before phagocytes invade the injured site. In this stage, the damage of proteolytic enzyme, lysosomal enzyme, lysophosphatidylcholine, and prostaglandin on local tissues is the main reason.

$$d_j(X) = \max_{i=1}^{l} c_{i,j}(X), \quad j = 1, 2, \ldots, m. \tag{20}$$

(3) Phagocytosis: it usually occurs 4–6 hours after exercise, lasting for 2–4 days. At this stage, phagocytes invade the injured site, and the protein degradation part of the injured muscle fiber is engulfed. At this stage, it is generally believed that white blood cells (mainly neutrophils, monocytes, and macrophages) play a broad role in the inflammatory response to muscle injury. They have three main functions in the process of muscle injury and repair: attack and decompose debris (neutrophils and macrophages), scavenge cell debris (macrophages), and cell regeneration (macrophages). It is difficult to separate the spontaneous phase from the phagocytic phase.

(4) Regeneration: after degradation, some macrophages participate in muscle repair. In the phagocytosis stage of muscle injury, the surviving satellite cells differentiate into myoblasts and fuse to form new muscle tubules. In this process, macrophages will still invade, and the invasion of macrophages is a necessary prerequisite for regeneration, which may stimulate satellite cell division in some way. However, up to now, there is not enough evidence to prove that the ultrastructural changes of EIMI have cumulative damage.

Studies have shown that strenuous exercise and stretching can activate satellite cells to produce mitosis and proliferation, so as to make muscle fibers proliferate or repair damaged muscle fibers. The activation of satellite cells is related to the nature and intensity of stimulation and the response ability of muscle fibers. This stage usually occurs 4–6 days after exercise. Contractile proteins in damaged muscle fibers begin to regenerate. After 10 days, the muscle structure gradually returned to normal.

2.3. Repair Methods of Muscle Injury. There are different treatments for muscle injury [9]. According to the severity of the injury, surgical or nonsurgical methods can be adopted. There are many alternatives to nonsurgical treatment (conservative treatment). Drug therapy is one of them. Drugs are divided into traditional Chinese medicine and Western medicine. According to the different ways of use, it can be divided into oral and external use. China is the birthplace of traditional Chinese medicine, which has rich drug resources, long history experience, and systematic theoretical guidance. "See, smell, ask, cut," "pill, powder, ointment, Dan" is the essence of Chinese medicine. Maximum oxygen uptake and ventilatory threshold are important indicators for assessing aerobic capacity, as well as key indicators for formulating exercise intensity. Therefore, assessing the aerobic capacity of athletes is of great significance for mastering the training effects of athletes and understanding the gap between athletes of different levels. The human body uses a large number of muscles for long-term intense exercise, and when the cardiopulmonary function and the ability of the muscles to use oxygen reach their limit level, the amount of oxygen that can be taken in a unit of time is called the maximum oxygen uptake. The CT value reflects the degree of absorption of X-rays by the human body, thereby showing the density of different tissues. Generally speaking, the CT value of the bone cortex with the highest density of the human body is +1000 Hu, while the air is −1000 Hu. The larger the attenuation coefficient of human tissue to X-ray, the higher the CT value. A medical diagnosis can be made by comparing the calculated CT value with the standard CT value of the corresponding part. Common CT values of human tissues are shown in Table 1.

The CT value of bone tissue is greater than 500, the CT value of coagulation is between 74 and 94, and the CT value of fat is between -10 and 100.

For thousands of years, traditional Chinese medicine (TCM) has played an irreplaceable role in treating diseases and saving people. The invention and application of traditional Chinese medicine in China has a long history, and more than 10000 kinds of traditional Chinese medicine have been used so far. Traditional Chinese medicine

Table 1: CT values of human tissues.

Organize	CT value	Organize	CT value	Organize	CT value
Bone tissue	>500	Blood clotting	74~94	Fat	−10~100
Calcium	90~400	Blood	23~45	Water	0

compound is the characteristic and advantage of traditional Chinese medicine. The so-called medicine is limited, the prescription is infinite, the medicine has the individuality specialty, the prescription has the group clever use, the disease manifests by the card, and the medicine uses the card to form the prescription. "Monarch, minister, assistant, and envoy" is the principle of prescription, while "mutual order, mutual food, and mutual diarrhea" is the law of action. It is based on the holistic view of traditional Chinese medicine and the concentrated embodiment of syndrome differentiation and treatment. In recent years, the research of traditional Chinese medicine compounds used to eliminate sports fatigue and injury has gradually become a hot spot in sports medicine research. The traditional Chinese medicine compound system is the basic characteristic of traditional Chinese medicine. It has incomparable advantages in eliminating, preventing, and repairing sports diseases. We need to understand its medicinal value and clinical application and provide a reliable basis and data for the development of new drugs.

2.4. Endurance Exercise Program of Aerobics Athletes. During exercise, oxygen is transported to skeletal muscles, and aerobic metabolism produces energy to contract skeletal muscles. These muscle contractions allow the body to keep moving and meet the intensity of exercise. As the exercise load increases, the energy required to meet this exercise intensity also increases. Therefore, the increase in oxygen uptake will meet the energy demand. Through in-depth interviews with experts, combined with the essence of this study, an elite competitive aerobics athlete endurance training program was constructed. A routine training program was constructed for testing, as shown in Table 2.

2.5. Marks of Successful Model Establishment. Muscle injury caused by high-intensity and unaccustomed exercise can change the function, metabolism, and morphological structure of muscle. Its function is mainly manifested in the decrease of muscle contraction strength and speed. Like muscle fatigue, it is the external manifestation of muscle injury and should not be used as evidence and mark to judge muscle injury. In terms of morphology, both optical microscope and electron microscope can be used as the most direct evidence of muscle injury. At the same time, the increase of muscle enzyme activity, myoglobin, and muscle protein degradation products detected by biochemical method [10] can also be used as indirect evidence and markers of muscle injury. In sports practice, the content of muscle cells leaking into serum is a common index to reflect the degree of muscle cell injury. Of course, with the development of magnetic resonance imaging (EMG), some noninvasive markers of muscle injury, such as MRI, have been used to evaluate muscle condition.

Brain CT manifestations of congenital amino acid metabolism disease are as follows. Congenital amino acid metabolism disease mainly affects the nervous system and is one of the important causes of mental retardation in children. In addition, the ultrastructural changes of skeletal muscle only account for a small part of muscle fiber. In addition, for human experiments, due to the limitations of experimental methods, many deep injured muscles are not easy to biopsy. Therefore, some ultrastructural changes of muscle are often ignored in this field, which leads to different experimental results. In order to find the exact evidence and mark of Amy's morphology, it is necessary to conduct in-depth research in this field.

In recent ten years, more and more attention has been paid to the biochemical changes during exercise muscle load and recovery period, which is sensitive and accurate indirect evidence. The biochemical indicators of muscle injury mainly include the increase of serum enzyme activity, especially the activity of creatine kinase; the increase of serum myoglobin (MB), and the increase of muscle protein conversion and urinary 3-methylhistidine excretion.

3. Protective Effect of Branched-Chain Amino Acids on Muscle Injury after Endurance Training

3.1. Composition and Function of Branched-Chain Amino Acids. Branched-chain amino acid is an organic compound containing basic amino acids and the acid Clostridium. It is the basic material of protein molecules. Protein is the basis of all tissues of the body and plays a decisive role in life phenomena and life processes. Protein is composed of a variety of amino acids through skin bonds, which is a phthalic acid amide bond connecting amino acid units. Incomplete protein metabolism and dysfunction are often caused by the lack of essential amino acids [11]. The protein in food enters the human body through the intestines and stomach.

The most commonly used method of measuring maximum oxygen uptake is to perform a limit test in a laboratory. In order to allow the subjects to reach the maximum oxygen uptake, the test program adopts an incremental load method in the laboratory. The test method of respiratory function during exercise is a breath-by-breath analysis method to reach its maximum effort and to reach the maximum oxygen uptake in a specific time. There are differences between male and female athletes in their physiological structures, as well as differences in mechanistic response, effect results, and injury frequency. According to gender, we further subdivided the distribution of injury positions of high-level competitive fitness athletes, identified the areas with higher self-injury rates of male and female athletes, analyzed their characteristics, and improved the athletes' resistance to injury, as shown in Figure 2.

Table 2: Routine training program of aerobic athletes' sports endurance.

Exercise content	Practice times/group	Practice form	Practice requirements
Push-up	35 × 5 groups	Do push-ups continuously with no time limit	Shoulder and elbow level
From both ends	35 × 5 groups	Keep practicing	When folding, the fingers touch the toes and the open shoulders must touch the ground
400 m turn back	Time recording × 3 groups 2′ × 5 groups	In the standard 400 m runway, the time is recorded. 10 m distance, calculate the round-trip mark	Reach your limit speed. Touch the mark with your fingers
Split (left, right, horizontal)	1′ × 5 group	Place 30 cm pads on the front legs and back to keep the split position	Keep the upper body upright with both hands on the front knee
Supporting swivel (right angle, split leg)	20 laps × 5 groups	On the ground, a complete 360° is used to calculate the number of turns	During practice, except for supporting hands, other parts should not touch the ground
Raise your hips	45 × 3 groups	Continuous contact information, jump back from the push-up state to push-up state, calculate the number of times	Push-up, shoulder parallel to elbow, body folding angle less than 80 degrees, hand touching ankle joint
Straddle jump	40 × 5 groups	Continuous without time limit	Both feet across the horizontal line at the same time, count the number
Vertical split leg (left and right)	40 × 3 groups	With both hands on the ground, one leg to do a continuous vertical split	The opening is 360 degrees
Obstacle endurance training (long jump, high platform, climbing handstand, high leg lift, standing, and lying support)	(5 times + 3times + 8 meters + 50 times + 30 times) × 5 groups	Form: 20 people in the range of five exercises on average, practice clockwise, in turn, a circle into a group	The practice process is compact and needs to realize direct and seamless connection between groups

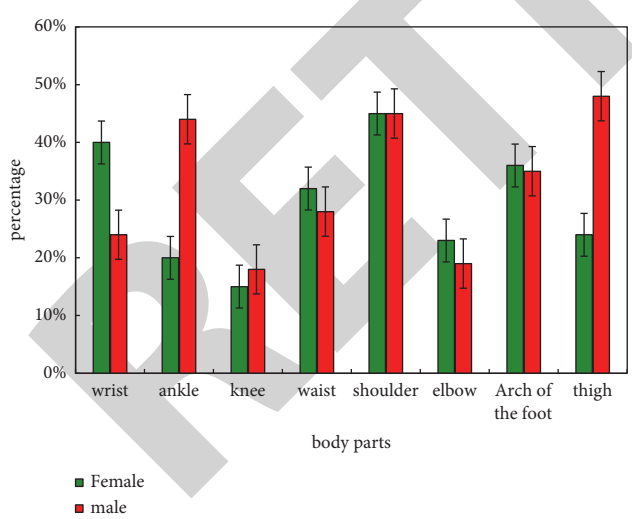

Figure 2: Our country's high-level competitions, health, and beauty, male and female athletes, and the distribution of the main sports injury positions.

Its absorption process is first decomposed into different amino acids by various enzymes and then transported to various organs of the body for protein synthesis. Therefore, amino acids are essential substances for the human body. Food containing more amino acids not only has high nutritional value but also is easy to digest and absorb and participates in human energy metabolism, as shown in Figure 3.

With the emergence of lactic acid threshold, the reason for the corresponding changes in ventilation is as follows: with the increase of exercise intensity, when the energy produced by aerobic metabolism cannot meet the oxygen demand of human exercise, the proportion of glycolysis energy supply gradually increases, and its by-products lead to increased blood lactic acid concentration. At this time, the body uses the bicarbonate buffer system in order to buffer lactic acid and produces sodium lactate and carbonic acid, resulting in an increase in carbon dioxide production. Observation and statistical results of muscle histochemical staining and fluorescent labeling can indicate that a certain degree of damage and loss of muscles occurs after fast downhill running, which is more serious on the day after exercise, there is an obvious recovery on the 4th day after exercise, and some muscle fibers are overrecovered on the day after exercise. There is hyperplasia performance after slow downhill running and uphill running, the muscles have no obvious damage or loss, or the damage and loss are very slight, as shown in Figures 3 and 4.

Amino acid is one of the most important elements in life, and it is widely used in medicine, food, and health care. In recent years, great progress has been made in physiology, pharmacology, and medicine. It is of great significance to study the synthesis of amino acids and their derivatives. The

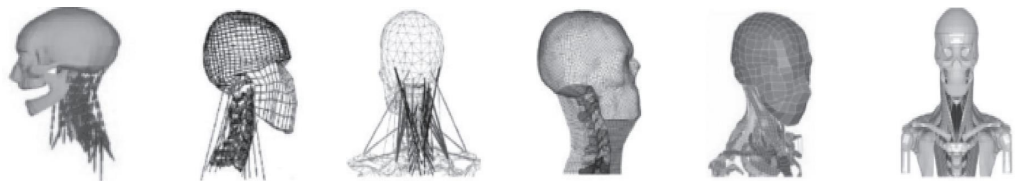

De Jager etc. 1994 Yang etc. 1998 Wittek etc. 2001 Meyer etc. 2004 Ejima etc. 2005 Hedensitma etc. 2008

Figure 3: Examples of related head and neck models.

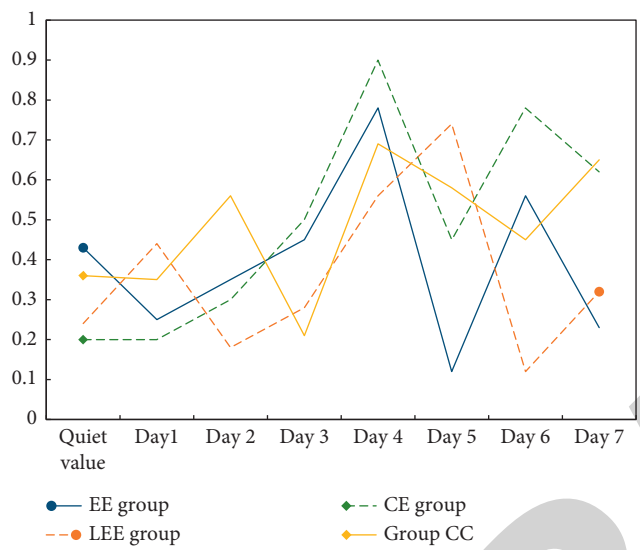

Figure 4: Comparison of changes in muscle cytoskeleton proteins after the initial and repeated exercises in each group.

protection of amino acids is very important. This step has laid a solid foundation for the synthesis of necessary intermediates and has a decisive significance for the study of skin synthesis.

3.2. Catabolism Mechanism of Branched-Chain Amino Acids. In kinesiology, the ventilation threshold refers to the inflection point at which the increase in ventilation volume during exercise is faster than the increase in oxygen uptake. A person's ventilatory threshold reflects the level of endurance and lactic acid accumulation. As exercise intensity increases, breathing becomes faster, more stable, and faster. When the breathing volume exceeds the normal ventilation volume, then the ventilation threshold is reached.

BCAAs, including leucine, isoleucine, and valine, are essential amino acids for the human body. Food is the only source of BCAAs. The body maintains the level of BCAAs mainly by regulating the catabolism of BCAAs. BCAAs are the main energy supply amino acid and the only amino acid metabolized outside the liver. Leucine is the only ketogenic amino acid, isoleucine is a glycogen and ketogenic amino acid, vand aline is a glycogen amino acid. Although the molecular basis and regulatory mechanism of BCAAs uptake are still unclear, its downstream activation pathway is mainly through L-amino acid transporter and bidirectional transport of L-glutamine and L-leucine. Leucine, isoleucine, and valine are decomposed to produce corresponding ortho keto-iso-acetic acid, ortho keto-1-methylvaleric acid, and ortho keto-isovaleric acid, referred to as branched keto acids. Under the catalysis of mitochondrial branched-chain keto dehydrogenase complex, branched-chain keto acid can irreversibly oxidize decarboxylate to acetyl coenzyme A and succinyl coenzyme A and enter the tricarboxylic acid cycle. Reduced nicotinamide adenine dinucleotides enter the respiratory chain from the tricarboxylic acid cycle to participate in electron transport and finally generate ATP, as shown in Figure 5:

(1) Regulation of enzyme activity [12]: feedback inhibition and feedback inhibition play an important role in the regulation of amino acid synthesis. Corynebacterium glutamicum can precisely and precisely regulate the synthesis of branched-chain amino acids through the combined action of complex feedback inhibition and feedback inhibition, thus maintaining the balance of branched-chain amino acids. Threonine deaminase was only inhibited by L-Ile, but not by valine and leucine. When L-Ile was insufficient, threonine deaminase activity was higher. On the premise of high affinity for α - ketobutyric acid, the synthesis rate of L-Ile in cells is much higher than that of other branched-chain amino acids; when the content of L-Ile in cells increases, the activity of threonine deaminase decreases, and the intracellular ketones decrease. Due to feedback inhibition, when the content of branched-chain amino acids reaches the demand, the inhibited branched-chain amino acids will be fed back, and then the synthesis of branched-chain amino acids will be reduced. The advantages of using cross-linking technology to detect protein interactions are as follows: it can detect weak interactions; it can detect transient interactions with different proteins at different stages of a dynamic process, such as glycosylation; linking reagents and cross-linking can occur in vivo.

(2) Gene regulation [13]: there are many regulatory mechanisms of gene expression, including transcriptional regulation, attenuation, carbon metabolism inhibition, and global regulatory factor expression regulation.

3.3. Physiological Function of Branched-Chain Amino Acids. BCAAs play an important role in physiology. Firstly, BCAAs are not only important raw materials for protein synthesis in

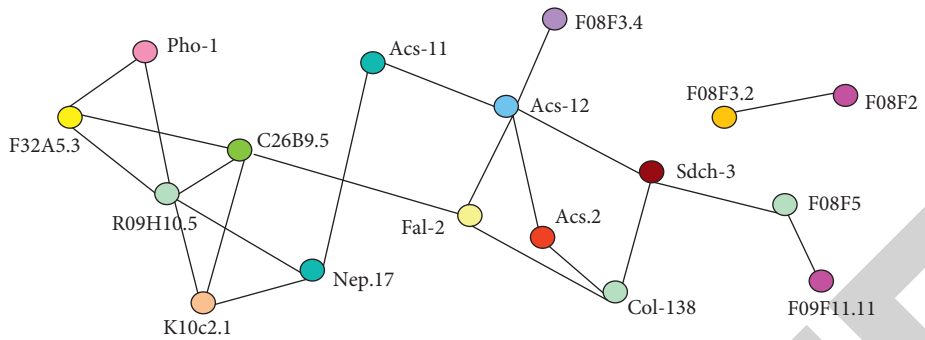

Figure 5: Network diagram of the interaction of sudden variants of different proteins.

vivo but also involved in the synthesis of sterols, ketones, and grapes. Secondly, BCAAs are the most important energy supply amino acid in aircraft, and they are an important energy substance. They can provide energy to the body through a series of biochemical reactions. Thirdly, BCAAs, especially leucine, are important signal molecules. They can activate the mTOR signaling pathway and promote protein synthesis, cell metabolism, cell growth, autophagy, neurotransmitter synthesis, carbohydrate utilization, and lipid metabolism. Therefore, BCAAs are essential to maintain the normal growth and function of cells and organs. Finally, BCAAs play an important role in mRNA translation. BCAAs, especially leucine, can enhance signal transduction at the beginning of mRNA translation. BCAAs can activate mTOR by phosphorylating its downstream effectors S6K1 and 4E BP1 and then act on eukaryotic initiation factor eif4f to enhance the stability of mRNA; BCAAs can also act on eIF2 · GTP · met-tRNAiMet in an unknown way, promoting the formation of a complex with ribosomal protein S6, thus promoting the initiation of mRNA translation.

3.4. Biosynthesis Pathway of Branched-Chain Amino Acids. Branched-chain amino acids include Ile, Leu, and Val, and their biosynthesis pathway only exists in plants and microorganisms [14]. The synthesis of L-Ile begins with aspartic acid and is catalyzed by a series of enzymes. Using pyruvic acid as a precursor, l-leu and L-Val were synthesized by a series of enzymes. In the biosynthesis of branched-chain amino acids, aspartic acid and threonine are two intermediate amino acid products, while lysine and methionine are two by-products of the bypass pathway. Among the enzymes involved in the biosynthesis of branched-chain amino acids, acetyl hydroxyl synthase, acetyl lactate isomerase, dihydroxy acid dehydratase, and branched-chain amino acid transaminase are the common enzymes in the biosynthesis of branched-chain amino acids. At present, there are few reports about BCAA in *Bacillus*. The research on the regulation of BCAA synthesis and metabolism mainly focuses on *Escherichia coli* and *Corynebacterium glutamicum*.

3.5. Protective Mechanism of Branched-Chain Amino Acids on Muscle Injury. Aerobic capacity is the most basic ability for athletes and the general population. It reflects an individual's health level and is an important indicator for evaluating athletic ability. Therefore, it is also a hot spot for scholars at home and abroad. Among the indicators for assessing aerobic capacity, the maximum oxygen uptake is an important indicator for evaluating cardiorespiratory endurance, and the maximum oxygen uptake and ventilation threshold are the basis for formulating exercise intensity and are the physiological indicators for athlete selection.

It is proved that branched-chain amino acids play an important role in the regulation of myocardial ischemia, blood pressure, and myocardial ischemia. In order to protect the athletes from myocardial injury, it can reduce myocardial injury by taking calcium [15]. Supplement of branched-chain amino acids in endurance training can reduce serum creatine poisoning. The simulation result is compared with the experimental result curve of Kerrigan et al. The simulation curve is basically located in the experimental channel, and the limit load is in good agreement with the experimental result. The displacement of the femur when it reaches the ultimate load is different from the experimental results, which is caused by the different ages of the experimental samples, as shown in Figures 6 and 7.

Supplementation of branched-chain amino acids [16] can reduce muscle injury associated with endurance exercise. It is found that exercise can promote the oxidation of branched-chain amino acids and increase the demand for branched-chain amino acids. Supplement of the branched-chain [17] nitrogen acid before and after exercise can reduce muscle injury caused by exercise and improve protein synthesis.

4. Results and Discussion

4.1. VAS Score of Muscle Injury. According to the VAS pain [18] score table, the degree of muscle injury of each athlete is counted, as shown, as shown in Figure 8.

The higher the score is, the more serious the muscle injury is. According to the score, we can see that they mainly focus on 6–8 points, accounting for 44% of the total number of people. The second was 4–6, accounting for 34% of the total. It can be seen that the establishment of the muscle injury model is very successful, most people have a relatively large degree of muscle soreness, only a few people have reached the maximum [19] pain, very few people have an insufficient muscle injury, but the overall impact can be ignored. Muscle fatigue (muscle fatigue) is a decrease in

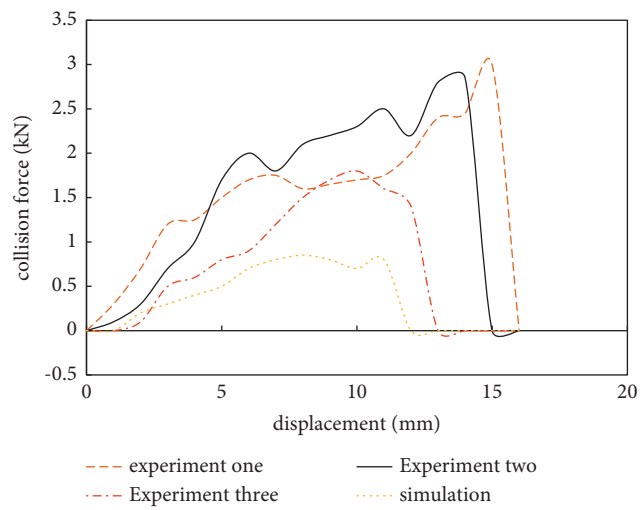

Figure 6: Femur dynamic three-point bending (collision force-displacement).

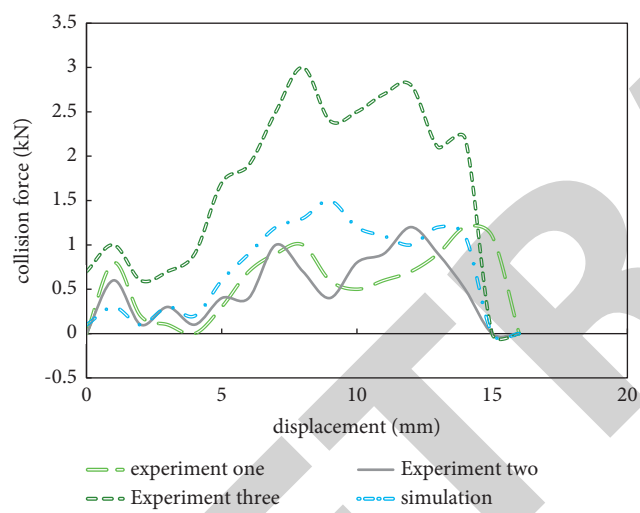

Figure 7: Fibula dynamic three-point bending (collision force-displacement).

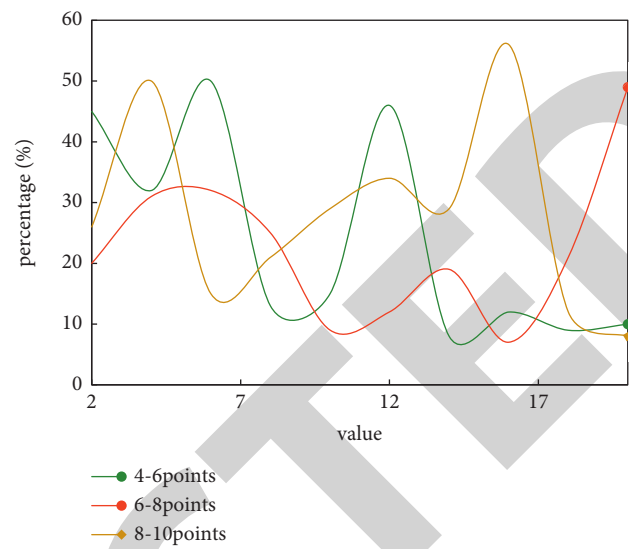

Figure 8: Pain analysis after global muscle injury.

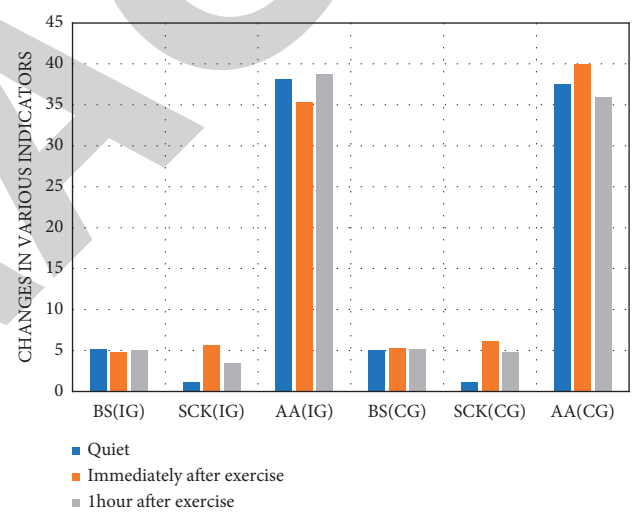

Figure 9: Changes of serum creatine kinase, alanine, and alanine aminotransferase in two groups.

muscle ability to work with repeated work (referring to "local muscle fatigue"). Motor muscle fatigue (exercise-induced muscle fatigue) refers to the movement caused by muscle maximum contraction force or maximum output power temporary decline in the physiological phenomenon and is the muscles in the process of contraction due to local muscle metabolism changes, morphological structure change, and nervous system function changes caused by a continuous, dynamic complex process.

4.2. Changes of Blood Indexes in the Intervention Group and Control Group after Endurance Exercise. After endurance training, the changes of blood glucose [20] and alanine aminotransferase in the intervention group were not very obvious, as shown in Figure 9.

The activity of serum creatine kinase changed after endurance training, increased by 4.72 but began to decline after 1 hour, but it was still higher than that before the competition. In the control group, there was no significant change in blood glucose. Serum creatine kinase and alanine aminotransferase increased significantly after the exercise. Serum creatine kinase began to decrease after 1 hour, which was higher than that before exercise, but glutamic pyruvic transaminase decreased at 1 hour until lower than that before exercise, as shown in Table 3.

The changes of alanine in the intervention group first increased and then decreased, reaching the peak at the end of the exercise. However, the content of LDH has been in the rising stage, even if the content of LDH [21] after exercise is higher than that before and after exercise. The content of alanine in the control group decreased significantly immediately after exercise and recovered to a part after 1 hour, but it was still lower than that before exercise. Compared with the intervention group, LDH showed a downward

Table 3: Changes of blood glucose and lactate dehydrogenase in two groups.

	Quiet	Immediately after exercise	1 hour after exercise
Intervention group			
ALA	257.6	325.4	296.6
LD	237.15	240.0	285.9
Control group			
ALA	294.7	199.4	220.5
LD	341.6	285.17	290.8

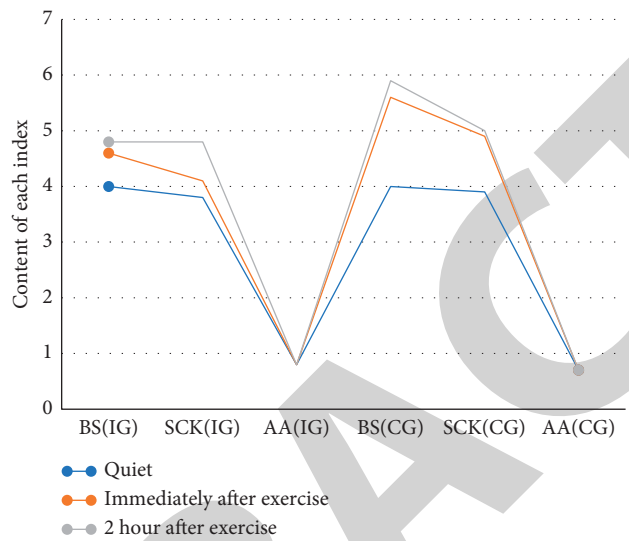

Figure 10: Changes of serum creatine kinase, lactate dehydrogenase, and alanine aminotransferase before and after endurance test in two groups.

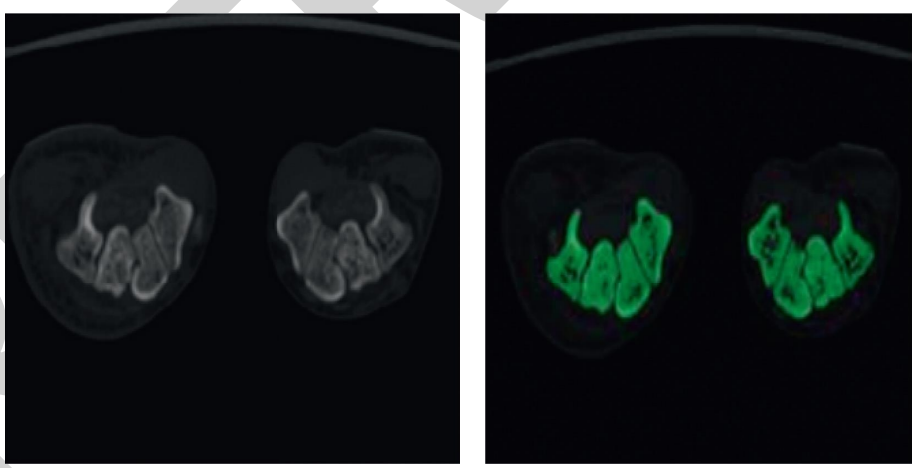

(a) (b)

Figure 11: Before and after tomographic images. (a) Raw tomographic image of the carpal bone. (b) Tomographic image after carpal threshold segmentation.

trend; that is, the LDH of athletes taking branched-chain amino acids had a significant upward trend.

4.3. Changes of Three Substances before and after Exercise and 2 Hours after Exercise. After receiving the designed endurance training, there was no significant change in alanine aminotransferase in the control group 2 hours after exercise, as shown in Figure 10.

The contents of creatine kinase and lactate dehydrogenase in the control group were measured immediately after exercise and 2 hours after exercise. The results showed that the contents of creatine kinase [22] and lactate dehydrogenase increased significantly, as shown in Figure 11.

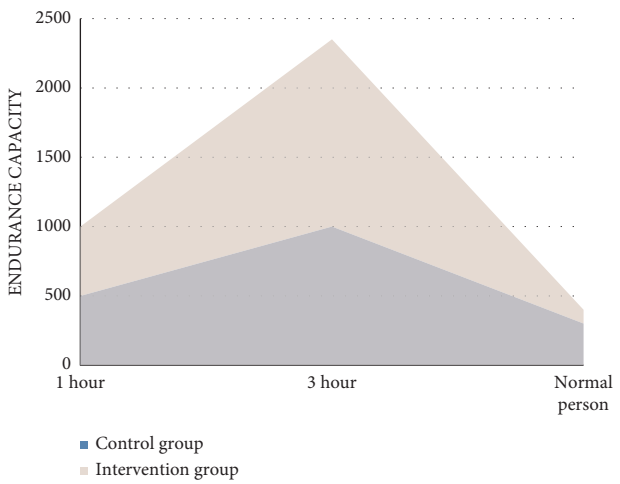

Figure 12: Effect of chain amino acids on the endurance of aerobics athletes.

According to the nature of the CT image and the different CT values of the bones and soft tissues of the wrist, the segmentation is performed by setting the threshold range. First, select an appropriate threshold [23]. For example, if the CT value is too high, parts with thin bones or slightly lower density cannot be included, forming false holes or irregular fissures; too low will also include other structures at the edge of the bone in the imaging range and make the edges blurred, and some structural levels cannot be distinguished. But it should be adjusted appropriately according to the bone density, as shown in Figure 11.

In the intervention group, the serum creatine kinase and lactate dehydrogenase were only measured immediately after exercise, which were significantly increased compared with those without exercise, but still lower than those in the control group. The level of creatine kinase in serum was also much lower than that in the control group at 2 hours after exercise.

4.4. Effect of Branched-Chain Amino Acids on Endurance of Aerobics Athletes. The endurance of the experimental group in the endurance test after taking BCAA is much higher than that of the control group and the people who receive any training. The longer the exercise time, the more energy consumption, the more effective the branched-chain amino acids supplement will be, as shown in Figure 12.

5. Conclusion

For people with abundant fast-twitch fibers, such as sprinters, the ratio of fast-twitch fibers is higher than that of slow-twitch fibers, because sprinters need strong explosive power, and the fast-twitch fibers have a relatively large diameter and can provide great power output. Therefore, sprinters tend to have thicker lower limbs and a high proportion of fast-twitch fibers. Competitive aerobics athletes must have the quality of coordination, flexibility, and sports tolerance. Complex gymnastics is a challenge for athletes. A little inattention will cause muscles to pull up, which will lead to an instant collapse of the overall body coordination. In order to avoid the occurrence of this kind of event, this paper puts forward the protective effect of branched-chain amino acids on muscle injury of aerobics athletes after endurance exercise. According to the experimental results, the measurement results after 1 hour of exercise are the same as those of 2 hours. Therefore, after endurance training, the blood glucose content of the intervention group gradually decreased and returned to the original level after 2 hours of exercise, while the control group was lower than the level of exercise after exercise and 2 hours later; the content of alanine in both groups showed a downward trend after exercise, and the decrease was more after 2 hours; the blood creatine kinase in the intervention group was measured immediately after exercise In the intervention group, lactate dehydrogenase increased rapidly at 2 hours after exercise, while that in the control group increased immediately after exercise; the content of alanine aminotransferase in the intervention group increased after exercise, but there was no significant change in the control group. Finally, it is found that the longer the exercise time is, the more effective the BCAA plays in protecting muscle injury. From the above experimental results, we found that branched-chain amino acids can be used as a drug to promote protein synthesis to repair muscle injury, which can reduce the pain caused by muscle injury, which is worthy of application for athletes in all walks of life who are troubled by muscle injury. The advantage of this paper is to discuss that amino acids based on CT images can play a protective role in aerobics athletes' muscle damage after endurance exercise, and CT can be well used to protect muscle damage, but the experiment in this paper is not so perfect, in the data collection. There are still many shortcomings.

Data Availability

No data were used to support this study.

Conflicts of Interest

The authors declare no conflicts of interest.

Authors' Contributions

All authors have read the manuscript and approved for submission.

Acknowledgments

This work was supported by the Hunan Provincial Natural Science Foundation of China (Grant no. 2019JJ40202) and the Scientific Research Fund of Hunan Provincial Education Department, China (Grant no. 18C1135).

References

[1] None, "Racket sports stave off death better than swimming or aerobics," *Nursing Standard*, vol. 31, no. 19, p. 16, 2017.

Hindawi
Journal of Healthcare Engineering
Volume 2023, Article ID 9868954, 1 page
https://doi.org/10.1155/2023/9868954

Retraction

Retracted: Neuronal Apoptosis in Patients with Liver Cirrhosis and Neuronal Epileptiform Discharge Model Based upon Multi-Modal Fusion Deep Learning

Journal of Healthcare Engineering

Received 10 October 2023; Accepted 10 October 2023; Published 11 October 2023

This article has been retracted by Hindawi following an investigation undertaken by the publisher [1]. This investigation has uncovered evidence of one or more of the following indicators of systematic manipulation of the publication process:

(1) Discrepancies in scope
(2) Discrepancies in the description of the research reported
(3) Discrepancies between the availability of data and the research described
(4) Inappropriate citations
(5) Incoherent, meaningless and/or irrelevant content included in the article
(6) Peer-review manipulation

The presence of these indicators undermines our confidence in the integrity of the article's content and we cannot, therefore, vouch for its reliability. Please note that this notice is intended solely to alert readers that the content of this article is unreliable. We have not investigated whether authors were aware of or involved in the systematic manipulation of the publication process.

Wiley and Hindawi regrets that the usual quality checks did not identify these issues before publication and have since put additional measures in place to safeguard research integrity.

We wish to credit our own Research Integrity and Research Publishing teams and anonymous and named external researchers and research integrity experts for contributing to this investigation.

The corresponding author, as the representative of all authors, has been given the opportunity to register their agreement or disagreement to this retraction. We have kept a record of any response received.

References

[1] N. Chi, X. Wang, Y. Yu, M. Wu, and J. Yu, "Neuronal Apoptosis in Patients with Liver Cirrhosis and Neuronal Epileptiform Discharge Model Based upon Multi-Modal Fusion Deep Learning," *Journal of Healthcare Engineering*, vol. 2022, Article ID 2203737, 13 pages, 2022.

Hindawi
Journal of Healthcare Engineering
Volume 2022, Article ID 2203737, 13 pages
https://doi.org/10.1155/2022/2203737

Research Article

Neuronal Apoptosis in Patients with Liver Cirrhosis and Neuronal Epileptiform Discharge Model Based upon Multi-Modal Fusion Deep Learning

Nannan Chi,[1] Xiuping Wang,[2] Yun Yu,[3] Manman Wu,[4] and Jianan Yu[2]

[1]*Digestive Department, the First Affiliated Hospital of Jiamusi University, Jiamusi 154000, Heilongjiang, China*
[2]*Department of Neurology, the First Affiliated Hospital of Jiamusi University, Jiamusi 154000, Heilongjiang, China*
3Medical Education Department, the First Affiliated Hospital of Jiamusi University, Jiamusi 154000, Heilongjiang, China
[4]*Graduate Department, Jiamusi University, Jiamusi 154000, Heilongjiang, China*

Correspondence should be addressed to Jianan Yu; yujianan@jmsu.edu.cn

Received 16 December 2021; Revised 8 February 2022; Accepted 10 February 2022; Published 17 March 2022

Academic Editor: Alireza Souri

Neurons refer to nerve cells. Each neuron is connected with thousands of other neurons to form a corresponding functional area and carry out complex communication with other functional areas. Its importance to the human body is self-evident. There are also many scholars studying the mechanism of apoptosis. This paper proposes a study of neuronal apoptosis in patients with liver cirrhosis and neuronal epileptiform discharge models based on multi-modal fusion deep learning, aiming to study the influencing factors of abnormal neuronal discharge in the brain. The method in this paper is to study multi-modal information fusion methods, perform Bayesian inference, and analyze multi-modal medical data. The function of these research methods is to obtain the relationship between the independence of information and the intersection of information among modalities. In the neuronal epileptiform discharge model, the mRNA expression level of the necroptotic signaling pathway related protein was detected, and the mechanism of neuronal necrosis in patients with liver cirrhosis was explored. Experiments show that the neuron recognition rate has been increased from 67.2% to 84.5%, and the time has been reduced, proving the effectiveness of deep learning.

1. Introduction

1.1. Background. In medical imaging, the use of deep learning for automatic diagnosis has become an unstoppable power [1, 2]. However, it is limited by factors such as data acquisition channels, and most of the existing researches focus on single-modality images. However, single-modal images are often very limited in the expression of pathological information. Therefore, it is very necessary to obtain more comprehensive pathological information by studying the image data of multiple modalities. Addressing the issue of the single-modal interaction being very much affected by user operations and the interaction efficiency being low, this paper constructs the fusion of gestures, voice, sensor information, and intelligent interaction methods at the decision-making level. Furthermore, this paper proposes an intelligent navigation interaction model oriented to multi-modal fusion. First of all, this paper establishes three modal information data sets and intention analysis to construct multi-modal information intersection and information independent functions. Next, based on the directed graph, this paper proposes an interaction strategy to realize the understanding of the user's intention of multi-modal information fusion. Finally, this paper proposes a navigation interaction mode based on multi-modal intention understanding. It can correctly guide the user's operation behavior and solve the problem of difficult operation.

1.2. Significance. The purpose of this research and application was to provide better medical resources for small and medium medical institutions. It is of great significance for telemedicine and medical care where education and experimental conditions are obviously lacking [3, 4]. In the

first homogenous multimodal image for the liver cirrhosis grading task, this paper employs histogram equalization technique to enhance image detail and contrast. It optimizes the enhancement of liver cirrhosis, and has better classification indicators than previous methods. In the second heterogeneous ultrasound and electronic medical record for the early diagnosis of cardiovascular disease, in view of various factors such as data acquisition channels, the research of multi-modal ultrasound imaging is rarely involved, and ultrasound imaging has an irreplaceable role for special populations. This article uses the fusion method of homogenous multi-modal imaging and heterogeneous electronic medical records for hospital data for practical project applications. And, this article has carried on the visual explanation analysis to the training process of the homology multi-modal ultrasound image fusion. It has a strong practical guiding significance.

1.3. Related Work. For the neuron epileptiform discharge model, many scholars have carried out research on it. With the recent resurgence of neural networks and the proliferation of large amounts of unlabeled multi-modal data, Vukoti V believes that recommendation systems and multimodal retrieval systems based on continuous representation spaces and deep learning methods are becoming more and more concerned. He introduced an alternative to advanced multi-modal fusion. The cross-modal conversion is realized by projecting the symmetrical encoder onto the bidirectional deep neural network [5]. Luo proposed a new multi-modal medical image fusion method based on environmental information. The experimental result is that compared with some typical fusion methods, the fusion method he proposed can effectively suppress color distortion and provide better fusion quality [6]. LiS proposes a point-to-point convolutional network called attention-based multi-modal fusion network, which is used to infer the task completion status of a 3D scene from a single-view RGB. Compared with the previous method that only used the extraction of semantic features from RGB-D images, the method he proposed uses the experience of inferring semantic segmentation from RGB-D images. The results show that his method achieves gains of 2.5% and 2.6% on the synthetic SUNCG-RGBD data set NYUv2 data set, respectively [7]. Kumthekar A proposed a technology based on deep learning technology for automatic cloud detection in multispectral images. These different initial layers are designed to increase the width of the network by replacing the standard convolutional layer. They extract multi-scale features without loss of resolution and maintain the same output size as the input image size. Reducing the computational complexity by reducing the number of parameters, using fewer spectral bands and deconvolution [8]. The classification accuracy of the model developed by Zhang differs significantly when applied to an independent test data set. He explored two potential training strategies to solve the over-fitting problem in AF detection [9]. Liu proposed a multi-task deep learning method, which may exist in the open world of unknown classes for simultaneous classification and reconstruction. He compared the reconstructed data with the original data. Due to the lack of labels, the data is not well represented in the underlying features. He proposed two strategies based on extreme value theory, which are used in few-shot and multi-shot scenes respectively [10]. Demianenko believes that the synchronous burst firing of neuron action is a typical manifestation of brain epileptiform activity, and this firing is reflected in the EEG as a burst seizure [11]. The purpose of Zhang is to study the regulatory effect of LIUS on epileptiform discharges in mouse hippocampal slices and its underlying mechanism. The results showed that LIUS suppressed the amplitude, rate and duration of the discharge. For interictal discharge, LIUS inhibits the spontaneous spike activity of mouse pyramidal neurons and eliminates epileptiform resistance [12].

1.4. Innovation. In this thesis, the Li-Pilo continuous high-frequency induced epileptiform discharge model and the primary culture hippocampal neuron spontaneous repetitive epileptiform discharge model induced by magnesium-free external fluid were used in this thesis. This article uses behavioral analysis and a number of molecular biology research methods to study the effect of MK2206 on the AKT/NF-KB signaling pathway and hippocampal neuron necrosis. This article proposes some practical applications of trained models, which have excellent reference value in medical diagnosis. (1) Images of different modalities adopt a unified feature extraction method. It can be seen from the visualization data of the early diagnosis task of cardiovascular disease that the experiment did not make full use of the motion wave group modal image and the Doppler spectrum image. (2) At the feature fusion level, this instrument performed a simple splicing operation. This paper does not carry out correlation analysis on the extracted features of different modalities, and explore the potential connections between them.

2. Research Methods of Neuronal Apoptosis

2.1. Multimodal Information Fusion Method. Modality is a subdivision concept of media. Each source of information and different manifestations can be called a modality. Multimodality in this article refers to the existence of multiple media forms for the description of the same object. According to the data media form and source of the description object, this article can divide the modalities into homogenous modalities and heterogeneous modalities. For example, images, texts, and electrical signals belong to heterogeneous multi-modality. The different sequence images produced by the same magnetic resonance equipment or the different description images produced by the same color ultrasound equipment are all homologous multimodality [13].

By analyzing the user's possible intentions during operation, this article will obtain the relationship between information independence and the intersection of information and modalities. Therefore, this paper establishes the multi-modal information intersection function and

information independent function. First, recognition is performed based on various modal inputs such as sensor information, gesture information, and voice information recognition. Then, based on the recognition result, it is determined whether it is an information cross function or an information independent function [14]. When the user's behavior status is set to Taks_$T \in \{T1, T2, \ldots Tn\}$, the information cross function $F1(\text{Taks\_}T, M)$ is:

$$F_1(\text{Taks}_T, M) = \begin{cases} T1(t_1 \cap a_4 \cap v_1) \neq \varnothing \\ \text{or} \\ t_1 \cap a_4 \neq a_4 \cap v_1 \neq \varnothing, \\ T2(t_9 \cap a_8), \\ T3(t_{10} \cap a_9), \\ T4(t_5 \cup a_1 \neq \varnothing) \\ \text{or} \\ (t_7 \cup a_1) \neq \varnothing, \\ T5(t_{11} \cap a_6 \neq \varnothing), \\ \vdots \\ Tn(t_{n+1} \cap a_{n+2} \neq \varnothing). \end{cases} \tag{1}$$

In (1), Taks_$T \in \{T1, T2, \ldots Tn\}$, the current behavior state Taks_T of the user is determined by judging the information merge function of different modalities. The information independent function $F\ d(\text{Taks\_}T, M)$ is

$$Fd(\text{Taks}_T, M) = \begin{cases} T13 & t_3 \neq \varnothing, \\ T14 & v_3 \neq \varnothing, \\ T15 & v_4 \neq \varnothing, \\ T16 & a_3 \neq \varnothing, \\ T17 & a_{10} \neq \varnothing. \end{cases} \tag{2}$$

In (2), Taks_$T \in \{T13, T2, \ldots T17\}$, the current behavior state Taks_T of the user is determined according to the information independent function. According to the multi-modal information fusion strategy, different behavior states Taks_T of users are judged. Determine the user's intention under the current trigger condition and establish the following rules:

$$\begin{cases} \text{Taks\_}T \neq \varnothing \longrightarrow e_{17}, \\ \text{Taks\_}T = \varnothing \longrightarrow \varnothing. \end{cases} \tag{3}$$

The main goal of canonical correlation analysis is to find linear projections of data from various data sources with the greatest correlation [15]. Canonical correlation analysis is a linear mathematical model. It is a multivariate statistical analysis method suitable for multi-source heterogeneous data, multi-view, and multi-scale analysis. Its purpose is to identify and quantify the relationship between two sets of variables, focusing on the correlation between the linear combination of one set of variables and the linear combination of another set of variables. The idea is to first solve the linear combination of the two variable sets to maximize the correlation coefficient [16]. Then, select the pair with the highest correlation coefficient from the linear combination pairs that are not related to the first selected linear combination pair, and so on. These selected linear combination pairs are called canonical variables, and their correlation coefficients are called canonical correlation coefficients. The canonical correlation coefficient measures the strength of the connection between these two sets of variables. This maximization technique aims to map the high-dimensional relationship between the two sets of variables to some typical variables [17].

Ultrasound image feature extraction model InceptionV3 is used in the experiment of this article to first divide the ultrasound image into four modal data sets with each modal as a unit. Then, train on each data set and save the best classification model. These four optimal models are the feature extraction models of four modes [18]. The feature extraction dimension of each mode is 128.

After the multi-modal feature fusion, this article chooses the XGBoost model as the classification model. XGBoost is mainly improved based on the gradient boosting decision tree, so the essence of XGBoost is still a combination of multiple regression trees, and each round of training is based on the previous generation. Assuming there are n samples, each independent sample is defined as xn, and the value range of n is (1,n). For each sample, the prediction result yn of XGBoost is equal to the superposition of the predicted values of K trees completed by the model training [19]. The formula is as follows:

$$\hat{y}_n = \sum_{k=1}^{K} f_k(x_n), \quad f_k \in F. \tag{4}$$

Among them, f_k represents the function of the k-th tree, and F represents the space of the tree. The objective function of the model is as follows:

$$L(\varnothing) = \sum_n l(\hat{y}_n, y_n) + \sum_k \Omega f_k. \tag{5}$$

The optimization direction of the function is to minimize $L(\varnothing)$. Among them, the loss function l, the regular term $\sum_k \Omega f_k$, and O represent the complexity of the tree, which can be further expressed as follows:

$$\Omega(f) = yT + \frac{1}{2\gamma}\|\omega_i\|^2. \tag{6}$$

Among them, the number of leaf nodes is represented by T, and the score of the i-th leaf node is represented by ω_i. Because the objective function is not convenient to optimize, the Taylor series is used to further optimize the function. The formula is as follows:

$$\begin{aligned} \omega_n^* &= \frac{\sum_{n\in \text{In}} \partial l\left(y_n, \hat{y}_n^{n-1}\right)}{\sum_{n\in \text{In}} \partial^2 l\left(y_n, \hat{y}_n^{n-1}\right)} + \gamma, \\ L^{-n}(q) &= \frac{-1}{2} \sum_{j=1}^{T} \left\{ \frac{\left[\sum_{n\in \text{In}} \partial l\left(y_n, \hat{y}_n^{n-1}\right)\right]^2}{\sum_{n\in \text{In}} \partial^2 l\left(y_n, \hat{y}_n^{n-1}\right)} \right\} + \gamma T. \end{aligned} \tag{7}$$

In practice, it is impossible to list the shapes of all trees for optimal calculation, so the tree is split and calculated to obtain the final objective function:

$$L_{\text{splot}} = \frac{1}{2\left\{\left[\sum_{n\in I_L}\partial l\left(y_n, \hat{y}_n^{n-1}\right)\right]^2 / \sum_{n\in I_L}\partial^2 l\left(y_n, \hat{y}_n^{n-1}\right) + \gamma\right\}} + \frac{\left[\sum_{n\in I_n}\partial l\left(y_n, \hat{y}_n^{n-1}\right)\right]^2}{\sum_{n\in I_n}\partial^2 l\left(y_n, \hat{y}_n^{n-1}\right) + \gamma} - \gamma. \tag{8}$$

Therefore, in order to merge the information between multiple modes in parallel with more reasonable weights, reduce the mutual cancellation of information between different modes, and improve accuracy, as it is necessary to set the initial value of the weight of each mode reasonably [20]. The experiments in this article are performed on each input data, and the accuracy of the segmentation results of each modal image is obtained by statistics. Using this as prior knowledge, this article expresses it as fusion weights to achieve better segmentation results.

Based on the characteristics of MRI images, it is determined that there are four modal images (Flair, T1, T1c, T2) that are closely related to the segmentation results. The weights of Flair modal images are set to $\alpha, \beta, \gamma, \theta$, respectively, as shown in Figure 1.

2.2. Deep Learning and Bayesian Inference. Deep learning is a type of machine learning algorithm that meets the following characteristics. Deep neural network is not a "black box model," and its theoretical basis relies on general approximation theory and Bayesian inference [21–23]. Among them, the general approximation theory is described as follows:

Define s as any continuous nonlinear sigmoid function, namely,

$$\sigma(x) = \begin{cases} 1\, x \longrightarrow +\infty, \\ 0\, x \longrightarrow -\infty. \end{cases} \tag{9}$$

Define $G(x)$ as a linear combination of σ, namely:

$$G(x) = \sum_{n=1}^{N} \alpha_n \sigma\left(y_n^t + b_n\right). \tag{10}$$

Among them, $x \in \partial^n$, $yn \in \partial^n$, α_n, $b_n \in \partial$. Let In denote the n-dimensional unit cube $[0,1]^n$, and the continuous function space on In is denoted as C(In), then given any $f \in C(\text{In})$, $\forall \grave{o} > 0$, $\exists G(x)$ satisfies:

$$|G(x) - f(x)| < \grave{o}, \quad x \in \text{In}. \tag{11}$$

The Bayesian inference theory is described as follows: The prior distribution $p(\theta|\alpha)$, which is usually not easy to observe. The sample distribution $p(X|\theta)$ is also called the likelihood function, which can be considered as the marginal likelihood function of the distribution parameters represented by $L(\theta|X) = p(X|\theta)$. The marginal likelihood function represents the marginal distribution of parameter observation data.

$$p(X|\alpha) = \int p(X|\theta) * p(\theta|\alpha) d\theta. \tag{12}$$

Bayesian inference expresses the posterior probability as the product of the likelihood function and the prior probability, namely:

$$p(\theta|x, \alpha) = \frac{p(x|\theta) * p(\theta|\alpha)}{p(x|\alpha)} \propto p(x|\theta) p(\theta|\alpha). \tag{13}$$

The mentioned general approximation theory and Bayesian inference theory are regarded as the theoretical basis of deep learning networks.

2.3. Multimodal Medical Data

2.3.1. HU Value Processing. For DICOM-type stored CT images, the commonly used Python processing library interface cannot automatically convert the read value to Hu value, so manual conversion is required [24]. For CT images, there is a specific measurement method in the medical field, namely, the Heng's Unit (HU), also known as the CT value. It is a linear mapping of the linear attenuation coefficient of the measured medium, which reflects the degree of absorption of X-rays by the tissue.

$$H = \text{pixel} * S + I. \tag{14}$$

The slope represented by S and the intercept represented by I can be read from DICOM format images. It represents the slope and intercept of the conversion. pixel represents the gray value of a pixel.

2.3.2. Histogram Equalization. This article can enhance the overall contrast effect of the image, especially when there is no significant difference in the contrast of the useful part of the image [25]. Histogram equalization is a method of adjusting the contrast using an image histogram. Histogram equalization provides better brightness distribution on the histogram. It improves local contrast without affecting the overall contrast. The specific conversion process is as follows: Calculate the number of times each pixel value in the gray image appears in the gray image.

$$\begin{aligned} p_x(n) &= p(x = n) \\ &= \frac{n_i}{n}, \quad 0 \le n < H. \end{aligned} \tag{15}$$

H is the maximum gray value in the image, n is the number of pixels in the image, and $P(n)$ is the ratio of the number of times the pixel value n is displayed in the image to all pixels in the image. Define cumulative distribution function, cumulative normalized histogram, corresponding to Px. The formula is as follows:

$$Cdf_x(n) = \sum_{j=0}^{n} p_x(j). \tag{16}$$

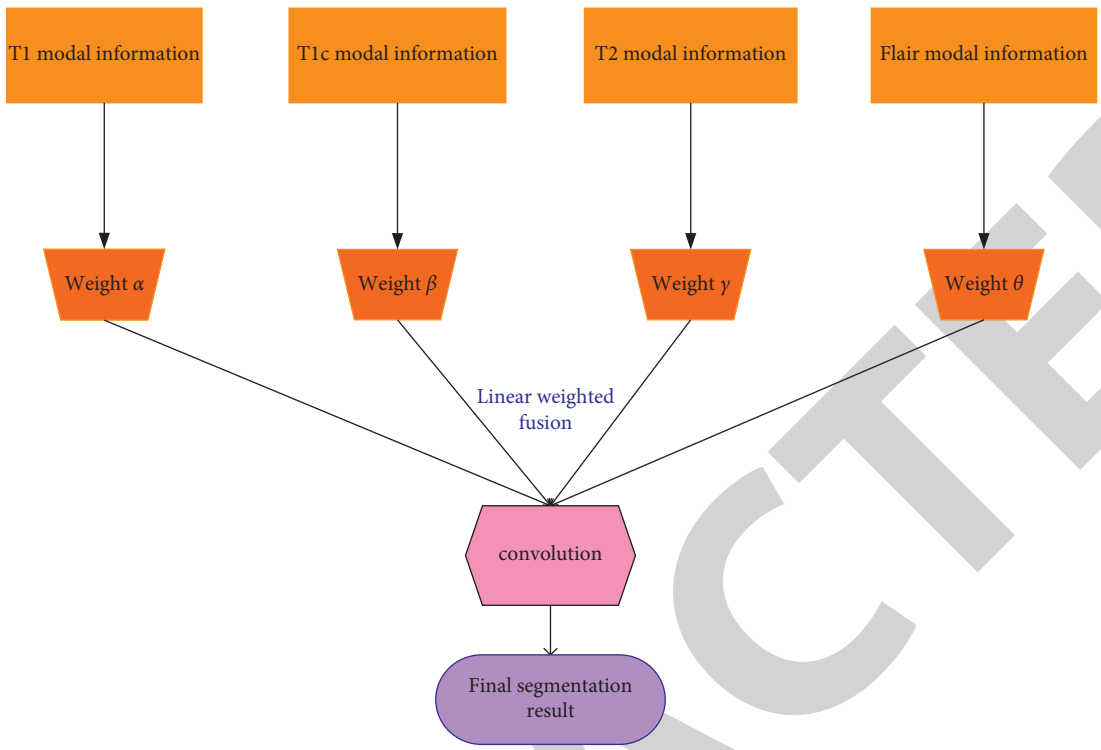

Figure 1: Linear weighted fusion structure diagram.

Create a mapping transformation formula like $y = T(x)$, and perform a formula transformation on each value in the original grayscale image. The generated y cumulative probability function can be linearized in all value ranges for a long time, and the formula is as follows:

$$Cdf_y(n) = iK, \tag{17}$$

where K is a constant. According to the nature of CDF:

$$\begin{aligned} Cdf_y(y') &= Cdf_y(T(k)), \\ &= Cdf_y(k), \end{aligned} \tag{18}$$

where k belongs to [0,1], and finally the histogram equalization result can be obtained by the following formula:

$$y' = y(\max\{x\} - \min\{x\}) + \min\{x\}. \tag{19}$$

3. Experiments on Factors Affecting Neuronal Apoptosis

3.1. Extraction of Neuron Signals. The basic unit of the human brain nervous system is the neuron cell, that is, the biological neuron. It is composed of about 10 billion neurons, and each neuron is connected to about 10,000 other neurons [26]. Figure 2 shows the main structure of a single neuron cell, which is composed of cell bodies, axons, and dendrites.

The main difference between nerve cells in the human brain and cells in other parts of the body is that nerve cells can generate, transmit, and process electrical signals. The neuron cell body is divided into inner and outer parts by cell membrane, resulting in different potentials inside and outside the membrane. Normally, the external potential is higher than the internal potential to form the internal and external potential difference, that is, the membrane potential. The membrane potential of neuron cells changes with synapses and the potential changes can be accumulated. That is to say, the membrane potential of the neuron is the sum of the potentials produced by all the synapses connected to it. If the membrane potential gradually rises above a certain threshold, the neuron will produce a neuron pulse, and the number of pulses emitted by the neuron cell when excited is affected by the neuron membrane potential [27]. There is a certain time delay when nerve information is transmitted through synapses, which is generally 0.3ms–1.0 ms for warm-blooded animals.

The neuron firing sequence ISI refers to the time interval between the peak and the peak of the neuron firing pulse. Assuming that a pulse is generated at time t, the elements in the sequence of ISIs that define the peak-to-peak interval of adjacent action potentials can be represented in Figure 3.

The map of neuron firing is drawn with the time interval of each spike in the neuron firing sequence as the abscissa, and the next spike time interval as the ordinate. The map can reflect some special recurring neuron firing patterns. In the biological nervous system, there are many different forms of charged ions in neuron cells, and it also has neurotransmitters that transmit electrical and chemical signals. At present, most researches are sodium ion, potassium ion, calcium ion, and so on. These ions are the basis for nerve cells to transmit and process information. Normally, the concentration of sodium and calcium ions in neuron cells is lower than that outside the neuron cell membrane, while the

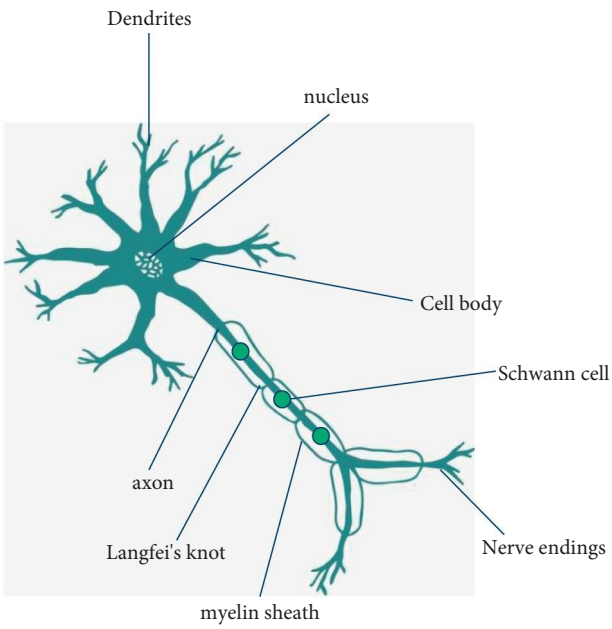

Figure 2: Neuron structure.

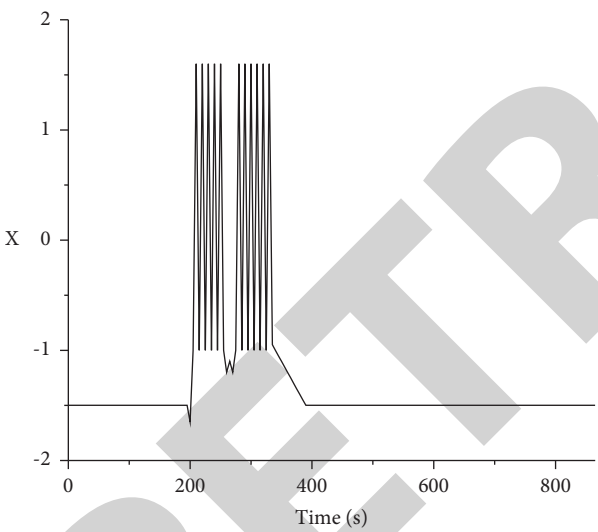

Figure 3: Diagram of ISIs sequence calculation.

concentration of potassium ions is higher than that outside the neuron cell membrane. At the same time, the neuron cells remain relatively static due to the barrier function of the cell membrane in the static state, and have different permeability to different ions in different states. When the neuron cell membrane is in a static state, the neuron cell membrane is more permeable to potassium ions than sodium ions and calcium ions. Therefore, more positive charges on the neuron cell membrane form an internal and external potential difference [28]. When the movement of internal and external ions reaches a relative balance, a constant potential difference between the inside and outside of the membrane will form, that is, the resting potential.

Figure 4 shows the simulation results of the H-R model of normal and rapid firing of a single neuron. The horizontal axis represents the simulation time, and the vertical axis represents the membrane potential value.

Figure 4 shows the firing model of a single HR neuron, with parameters $r = 0.0021$ and $I = 3.024$. It can be seen from the simulation results that the discharge model of the HR neuron model is determined by the control parameter r. But this parameter is not necessarily the only parameter that controls the model type [29]. From the figure, it can be inferred that when r fluctuates in a certain numerical interval, an irregular neuron firing model can be obtained, that is, a rapid firing model. As shown in the figure, after many simulation tests, the interval is [0.0014,0.0091]. According to relevant data, $r = 0.0021$ is selected here. The characteristic of this discharge model is that the discharge appears as a "cluster..

When r is greater than 0.0091 and less than a certain value, here we take $r = 0.022$ to obtain a regular neuron firing model. Its characteristic is that each discharge interval is approximately equal, and the sequence interval ISI changes little. From the simulation results, it can be inferred that there is a specific value from the irregular model to the regular model.

By fixing the input current I and changing r, the simulation results and ISIs sequence of different control parameters are obtained, as shown in Figure 5:

The upper picture shows the neuron firing pattern, and the lower picture shows the corresponding ISIs sequence scatter diagram. It can be seen from the neuron firing model image that when the value of I is very small, the neuron appears in a chaotic firing state [30]. When I increases, the chaotic state transitions to the discharge state. From the corresponding ISIs sequence scatter image, it can be seen that when I increases, the value of ISI gradually decreases and the frequency gradually increases.

Figure 6 is the time interval sequence ISIs of the regular issuance model, where $I = 3.024$ and $r = 0.022$. It can be seen from the simulation diagram that a neuron has one impulse every time it fires, and the abscissa indicates the time point when the pulse is obtained. The interval between the two pulses is the ISI, and the pulse distribution is relatively uniform.

Studies have confirmed that the AKT/NF-KB signaling pathway is closely related to epilepsy. AKT plays an important role in cell proliferation, migration, and cell survival, and NF-KB is an important downstream target protein of AKT. MK2206 is a specific allosteric inhibitor of AKT. It can inhibit the phosphorylation of AKT, thereby inhibiting AKT activation. MK2206 can effectively inhibit the proliferation of a variety of malignant tumor cells, promote tumor cell apoptosis, and exhibit good anti-tumor activity [31]. Necroptosis is a new type of cell death discovered in recent years, which is regulated by special death signaling pathways. Receptor interacting proteins 1 and 3 are very important regulatory proteins in the necroptotic signaling pathway.

3.2. Establish a Neuron Epileptiform Discharge Model. The experimental subjects were mice, and the experimental group and control group mice were euthanized. Then,

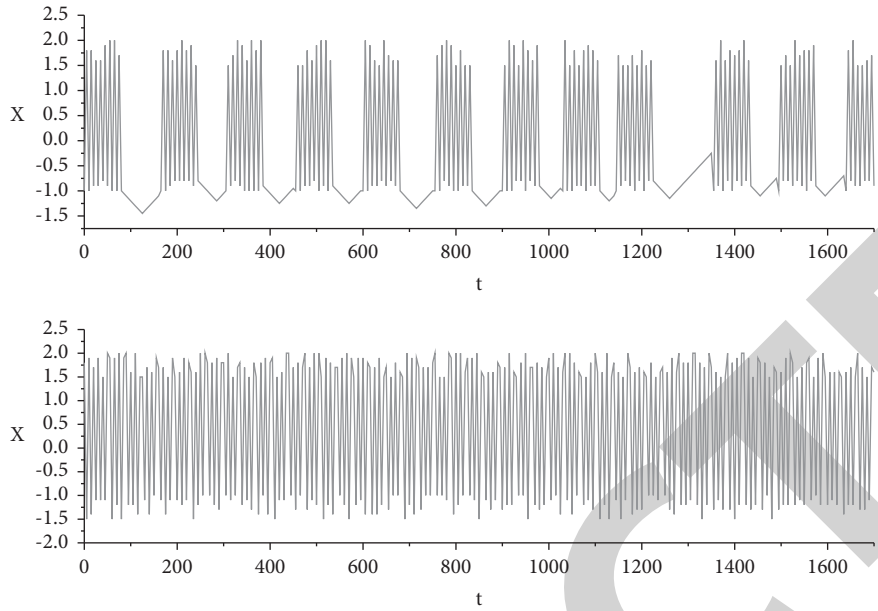

Figure 4: (a) Rapid firing model and (b) regular firing model.

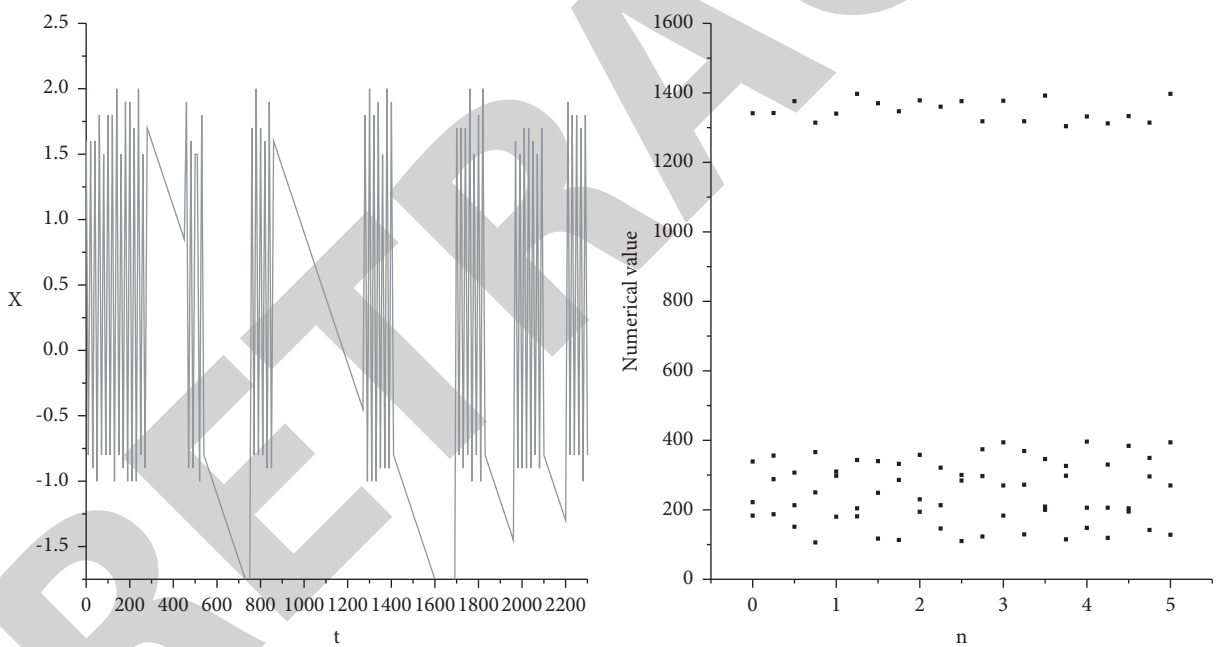

Figure 5: Neuron firing model and ISIs sequence diagram ($r = 0.0021$).

hippocampal tissues on both sides of the ice surface were separated after washing with physiological saline, the left and right hippocampus were put into the labeled imported coming cryotubes, and stored in liquid nitrogen tanks. Bilateral hippocampus was used for experiments, the left hippocampus was used to extract total protein, and the right hippocampus was used to extract nuclear and cytoplasmic proteins. Three rats in each group were directly decapitated to take their brains for paraffin sectioning. The brain tissues were placed in 4% paraformaldehyde and immersed for 24 hours for paraffin embedding. Paraffin tissue sections were used for HE staining and NISSLE staining of the hippocampal tissue. The sample size of the experimental pilo90 mg group was 8, the Racine score reached SE5, and the Racine score did not reach SE3. The epilepsy rate was 62%. The sample size of the control pilo90 group was 10, the Racine score reached SE10, and the Racine score did not reach SE0. The epileptic rate was 100%. The sample size of the control pilo30 group was 16 rats, the Racine score reached SE8, and the Racine score did not reach SE8, and the epileptic rate was 50%. Compared with the control pilo90 mg group, the epilepsy rate of the experimental pilo90 mg group was significantly reduced ($p < 0.05$), as shown in Table 1 and Figure 7.

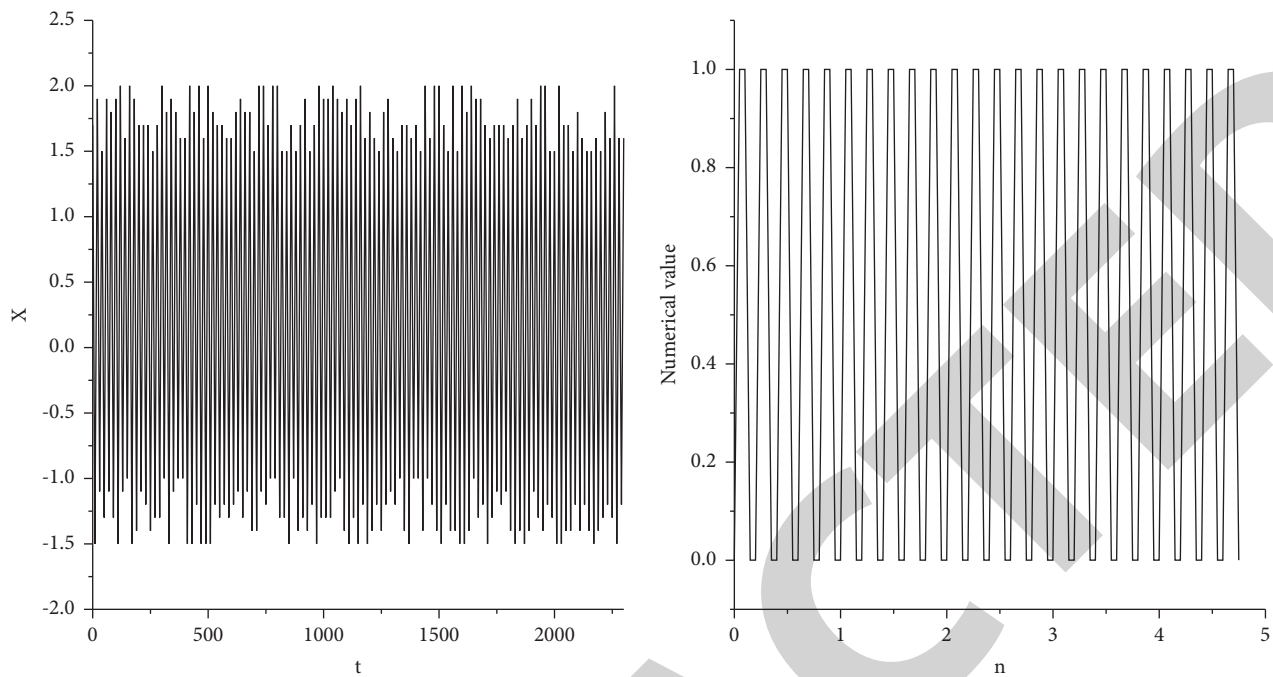

Figure 6: Regular discharge pattern and its time interval sequence ISIs.

Table 1: Comparison of epilepsy rate between the experimental group and control group.

	Racine score reached SE	Racine score does not reach SE	Sample size	Epilepsy rate (%)
Experimental group pilo 90 mg	5	3	8	62.50
Control group pilo 90 mg	10	0	10	100.00
Control group pilo 30 mg	8	8	16	50.00

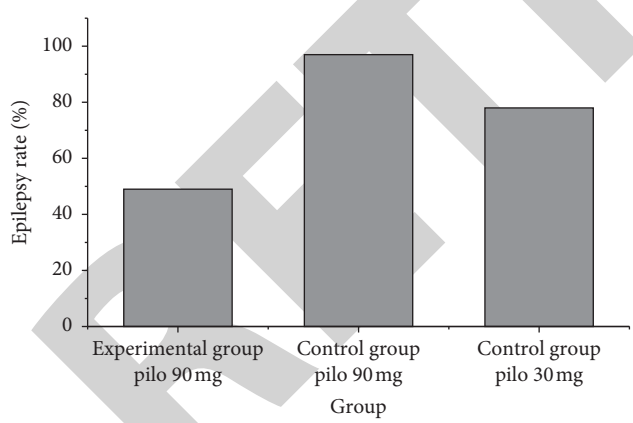

Figure 7: Comparison of epilepsy rate between pilo90 in the experimental group and pilo90 in the control group: $p = 0.017 < 0.05$.

The mice in the experimental group and the two control groups had no obvious abnormal changes after being injected with lithium chloride. Peripheral cholinergic reactions such as erect hair, salivation, eye congestion, etc., began to appear within a few minutes after intraperitoneal injection of pilocarpine, which lasted for about ten minutes. Different degrees of seizures occur simultaneously or sequentially, such as staring, less moving, blinking, chewing, sniffing, and groping. It can be seen that the head and neck are raised and there are tremors repeatedly [32]. The seizures develop further, with nodding tremor, unilateral or bilateral forelimb twitching, and they are in a semi-upright posture. It often leads to spasms of the hind limbs, followed by falling backwards or rotating, and seizures of tonic-clonic all over the body. During the course of the disease, the mice appeared sluggish. After SE lasted for 60 minutes, intraperitoneal injection of diazepam terminated the seizure, and the mice were in a state of inhibition and consumption, with reduced response and activity.

Comparing the experimental pilo90 mg group with the control pilo90 mg, the incubation period was significantly prolonged, $p = 0.046 < 0.05$. Compared with the control pilo90 mg group and the control pilo30 mg group, the incubation period was significantly shortened $p = 0.002 < 0.01$, as shown in Table 2 and Figure 8.

MK2206 has a specific inhibitory effect on AKT and has good safety. At present, its research on tumor diseases has entered the second clinical phase, and there is no research report on MK2206 in epilepsy. This article requires in-depth research, and Mk2206 is expected to become a new method of epilepsy treatment.

Studies have confirmed that the AKT/NF-KB signaling pathway is closely related to epilepsy. MK2206 is a specific allosteric inhibitor of AKT. Due to the excellent efficacy and safety in tumor treatment, it has now entered the second phase of clinical research. Necroptosis is a new method of

Table 2: SE latency results of each group (mean ± SEM).

Group	SE latency (min)
Experimental group pilo 90 mg	11.577 ± 1.295
Control group pilo 90 mg	8.239 ± 1.563
Control group pilo 30 mg	5.689 ± 2.756

The incubation period of the experimental pilo90 mg group was significantly longer than that of the control group pilo90 mg

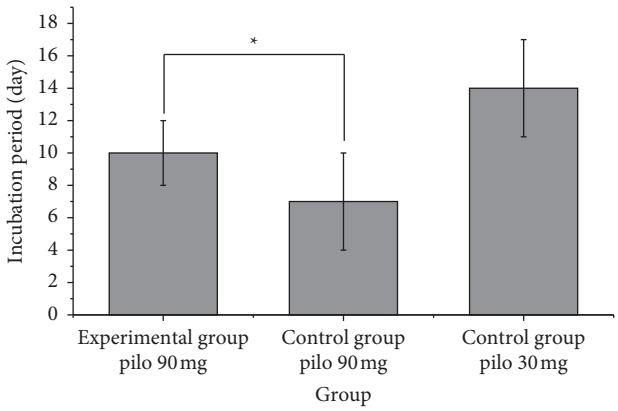

Figure 8: The incubation period of pilo90 in the experimental group compared with the pilo90 in the control group.

cell death discovered in recent years, and it has become a research hotspot at present. It has been shown that in most cells, the binding of death receptors and ligands can activate the apoptotic pathway. If caspase is over-activated, the apoptotic pathway is blocked and the cells enter the necrotic pathway, leading to necroptosis. In addition, cells can also cause cell necrosis by triggering pathogen recognition receptors. Such receptor families usually include toll-like receptors, cytoplasmic receptors, and RIG-like receptors. These receptors can recognize the molecular family of bacteria or viruses related to pathogens, such as lipopolysaccharide LPS, flagella, etc., thereby inducing innate immunity and leading to cell death. In addition to the mentioned pathways that mediate necroptosis, researchers have also found that calcium ion concentration, phospholipase, intracellular reactive oxygen species, and calpain can mediate necroptosis. In the process of cell proliferation, excessive DNA damage caused by aerobic stress can lead to excessive activation of RIP1, which leads to cell necrosis [33]. Studies have found that RIP3 can control the balance between apoptosis and necrosis pathways, which means that apoptosis and necrosis can be transformed. In the cell, if the expression level of RIP3 is high, the cell will die. Conversely, if the expression of RIP3 is low, the cells will undergo apoptosis.

3.3. Diagnosis of Liver Cirrhosis Based on Deep Learning. In the previous chapter, this article gave a general analysis and overview of the establishment of neuron epileptiform discharge model, and conducted research and verification on the ideas and algorithms involved in each module. In order to consider the accuracy and universality of neuron technology, this paper proposes to use a multi-modal high-precision fusion algorithm for optimization. Based on various performance indicators, this article will also verify the high-precision indoor and outdoor scene recognition technology based on multi-modal fusion in order to achieve better results. Medical imaging is an important tool for the study of clinical diseases. It plays an irreplaceable role in the early screening, treatment and subsequent rehabilitation, detection and management of the disease. However, the traditional artificial medical imaging diagnosis method still has many problems, such as the imbalance between the supply and demand of the doctor and the patient, and the heavy burden of the hospital staff. Medical imaging diagnosis is highly subjective and requires high experience. With the rapid development of deep learning in the image field, many deep learning methods have gradually been used in the processing and analysis of medical images in recent years to assist doctors in automatic diagnosis and improve work efficiency. However, considering the complexity of medical recognition tasks and the small sample size of medical images, the current mainstream research is monomodal imaging research, which still has some shortcomings. Because single-modal images are often unable to comprehensively and accurately express relevant pathological information, multiple images of different modalities can reflect the relevant information of the lesion from different aspects, making up for the lack of data and the disadvantages of a single information perspective. Therefore, based on multi-modal image data, the use of deep learning for early disease screening is of great significance for improving the accuracy of medical task recognition and assisting doctors in decision-making and diagnosis [34, 35]. This article focuses on the research of multi-modal medical imaging, and mainly conducts two groups of disease classification experiments based on multi-modal medical imaging.

The network model is pretrained through the large-scale data associated with the sample set to obtain the initialization parameters. Its effectiveness is that the network model is multi-level when learning sample features. And, the level is different; its characteristic expression is also different. With the deepening of the level, the greater is the difference of the learned sample information. In the lower level, the characteristics of the image described are less different, such as the color, contour, shape, size, and edge. The sample set image has a certain similarity and relevance to the pretrained sample set image. So, these low-level parameters can be shared. This article uses MNIST natural images. The dogs and cats in the data set are used as pretraining samples, as shown in Figure 9.

In deep learning, the deeper the model, the more neural nodes, and a larger sample set is needed to optimize many parameters of the model. If the sample set is small, each parameter cannot be trained to the best, and it is very easy to produce over-fitting. The research in this article is the image recognition of liver pathology in the medical field. The number of sample sets is far less than that of the natural image sets in life. In the transfer learning method, the natural image set by MNIST is used as the starting domain of Di, and one thousand classifications are used as the learning task Ti.

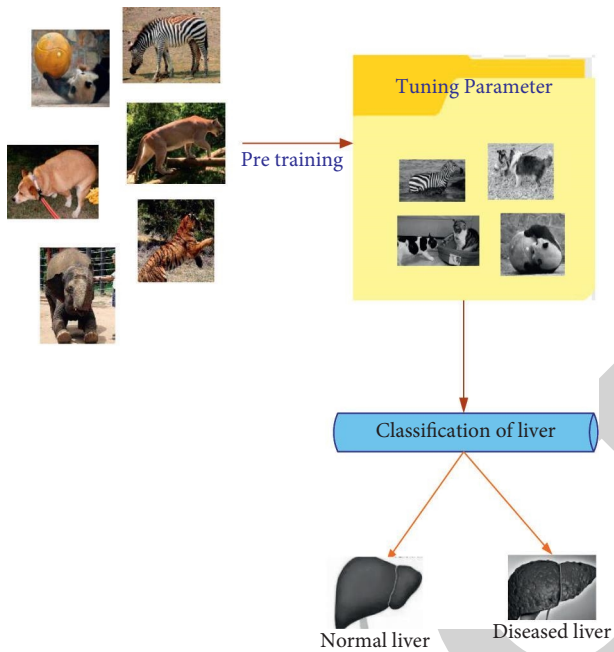

Figure 9: Schematic diagram of transfer learning.

Table 3: Squeeze model parameter table.

Parameter\Structure	fire2	fire3	fire4	fire5	fire6
S1∗1	48	16	16	64	16
E1∗1	16	16	64	16	16
E2∗2	48	16	64	16	16

After pretraining, the model parameters are retained, and then the model is applied to the medical liver pathology images in this paper for training. Finally, it improves the pan-China capability of the model and effectively prevents over-fitting. Many methods and applications have also confirmed its advantages [36]. The current transfer learning methods are mainly concentrated in two aspects: one is to keep the learned parameters unchanged and use them directly, and the other is to fine-tune the learned parameters.

Based on the explanation, this article established the SqueezeNet convolutional neural network model. The 1.2 million images in the ImageNet dataset have undergone thousands of classification trainings to obtain a pretrained classification model. The model parameters are shown in Table 3.

This article selects 1500 pathological images of the liver. Among them, 1,000 are used as the training sample set (600 are normal livers, 400 are affected by cirrhosis), and 500 are test samples (300 are normal livers and 200 are affected by cirrhosis). The experimental environment is the Linux system, Intel i5CPU, running memory 8G, running using caffe framework. This article adopts the second transfer learning method, fine-tuning training, using natural image sets for pretraining, and applying the obtained parameters to medical images to fine-tune the parameters. As shown in the comparison in Figure 10, this will further improve performance and increase the recognition rate of the original image. The recognition rate is increased from 67.2% to 84.5%, and the time will be reduced. This proves the effectiveness of transfer learning.

This article adds typical deep learning models such as AlexNet, GoogleNet, and LeNet for comparison. After reducing the model size to verify the performance of the lightweight convolutional neural network structure SqueezeNet with fewer parameters, the comparison results are shown in Table 4.

The model can distinguish each liver pathology image and give the probability of the class each pathology sample belongs to [37]. For example, the result of the first medical pathological image of liver cirrhosis is that 99.4% belong to cirrhosis, and 0.5% belongs to normal liver. And, the judgment given by the fourth normal liver sample model is that 99.5% are normal livers and 0.5% is diseased. It can be seen that it is very important and helpful for the practical application of clinical medical diagnosis, and it can help physicians to identify which disease the pathological image belongs to. The physician can also refer to the probability results given by the model. Because this article only trains patients with liver cirrhosis, the results will only show the probability of normal disease and liver cirrhosis. If a variety of liver diseases can also be trained and applied, after completing the training, it will give the probability of each disease.

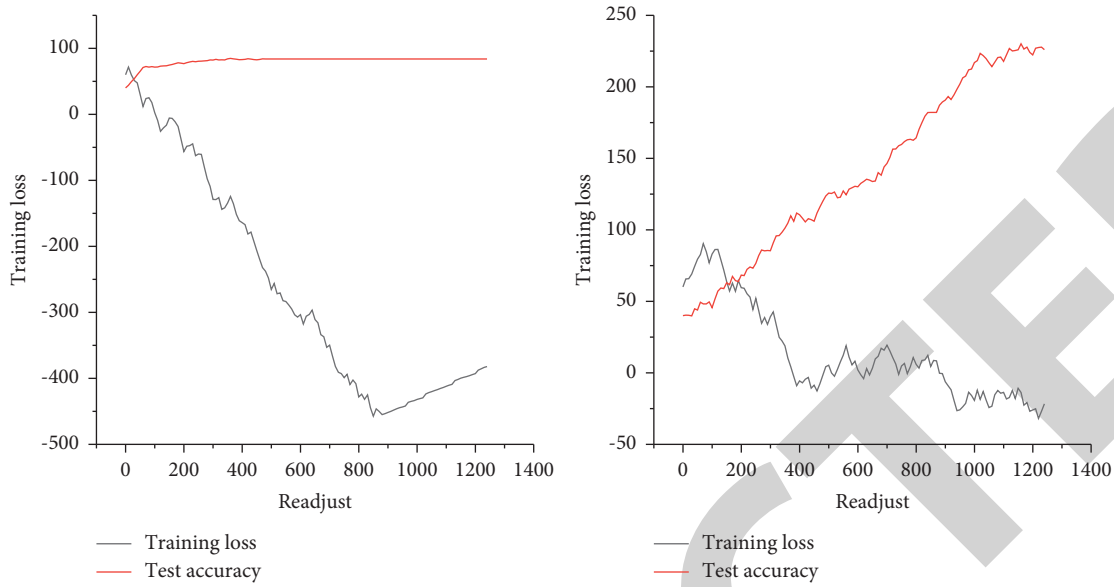

Figure 10: Comparison curve of transfer learning (the left picture shows the method after transfer learning).

Table 4: Comparison table of typical deep learning models.

Experiment	Method	Accuracy (%)	Test time (s)
1	AlexNex	75.57	53
2	SqueezeNet	71.69	41
3	GoogleNet(V2)	60.96	54
4	SqueezeNet + TL	80.64	46
5	SqueezeNet + TL + C-SVM	73.99	55

4. Discussion

Although this article has made some progress on the basis of other scholars' research, the content of this thesis is not perfect due to time constraints. The follow-up research can be carried out in the following contents: This article studies the firing pattern, coding, and parameters of HR neurons. Follow-up can be combined with another research topic on synapses to form a neural network circuit composed of HR neurons to simulate the algorithm and performance of the neural network. This paper only studies the synchronization of 3 and 4 neurons in the fully connected network and the synchronization of 4 neurons in the star network and the nearest neighbor connection network. Later, the number of neurons can be increased, and the synchronization problem of larger-scale neuron networks can be studied.

5. Conclusion

This article mainly studies the neuron model's firing pattern and the influence of parameters on the pattern and neuron information coding. As for the research of the neuron model, domestic and foreign research is in the exploratory stage, so the research has certain difficulty. Although there are some related neuron models, and most of these models are based on physiology. It is difficult to realize large-scale neural network networking. The content and results of this thesis are just basic work for further research on neural networks. This article adopts the method of multi-modal fusion deep learning, fine-tuning the training; the neuron recognition rate is increased from 67.2% to 84.5%%, and the time is also reduced, which proves the effectiveness of deep learning.

Data Availability

The data that support the findings of this study are available from the corresponding author upon reasonable request.

Conflicts of Interest

The author(s) declare no potential conflicts of interest with respect to the research, author-ship, and/or publication of this article.

Acknowledgments

This work was supported by Youth Innovative Talent Training Support Program of Jiamusi University (JMSUQP2021010)

References

[1] A A. Adegun, S. viriri, and R O. Ogundokun, "Deep learning approach for medical image analysis," *Computational Intelligence and Neuroscience*, vol. 2021, Article ID 6215281, 9 pages, 2021.

[2] B. Huang, F. Yang, M. Yin, X. Mo, and C. Zhong, "A review of multimodal medical image fusion techniques," *Computational and Mathematical Methods in Medicine*, vol. 2020, Article ID 8279342, 16 pages, 2020.

[3] Q. Zhang, Y. Du, Z. Wei, H. Liu, X. Yang, and D. Zhao, "Spine medical image segmentation based on deep learning," *Journal*

of Healthcare Engineering, vol. 2021, Article ID 1917946, 6 pages, 2021.

[4] B. J. Sowmya Bj, A. Shikhar, R. Utkarsha, and A. Singh, "Data analytics assisted internet of things towards building intelligent healthcare monitoring systems," *Journal of Organizational and End User Computing*, vol. 30, no. 4, pp. 83–103, 2018.

[5] V. Vukotic, C. Raymond, and G. Gravier, "A crossmodal approach to multimodal fusion in video hyperlinking," *IEEE Multimedia*, vol. 25, no. 2, pp. 11–23, 2018.

[6] X.-Q. Luo, Z.-C. Zhang, B.-C. Zhang, and X.-J. Wu, "Contextual information driven multi-modal medical image fusion," *IETE Technical Review*, vol. 34, no. 6, pp. 598–611, 2017.

[7] S. Li, C. Zou, Y. Li, X. Zhao, and Y. Gao, "Attention-based multi-modal fusion network for semantic scene completion," in *Proceedings of the AAAI Conference on Artificial Intelligence*, Article ID 11409, NY USA, February 2020.

[8] A. Kumthekar and G. R. Reddy, "An integrated deep learning framework of U-Net and inception module for cloud detection of remote sensing images," *Arabian Journal of Geosciences*, vol. 14, no. 18, pp. 1–13, 2021.

[9] X. Zhang, J. Li, Z. Cai, L. Zhang, Z. Chen, and C. Liu, "Overfitting suppression training strategies for deep learning-based atrial fibrillation detection," *Medical, & Biological Engineering & Computing*, vol. 59, no. 1, pp. 165–173, 2021.

[10] S. Liu, Q. Shi, and L. Zhang, "Few-shot hyperspectral image classification with unknown classes using multitask deep learning," *IEEE Transactions on Geoscience and Remote Sensing*, vol. 22, no. 99, pp. 1–18, 2020.

[11] L. E. Demianenko, E. P. Poddubnaya, I. A. Makedonsky, I B. Kulagina, and S M. Korogod, "Hypothermic suppression of epileptiform bursting activity of a hyppocampal granule neuron possessing thermosensitive TRP channels (a model study: biophysical and clinical aspects)," *Neurophysiology*, vol. 49, no. 1, pp. 1–11, 2017.

[12] Z. Zhang, W. Qiu, H. Gong et al., "Low-intensity ultrasound suppresses low-Mg2+-induced epileptiform discharges in juvenile mouse hippocampal slices," *Journal of Neural Engineering*, vol. 16, no. 3, Article ID 036006, 2019.

[13] L. Xiang, Y. Chen, W. Chang et al., "Deep-learning-based multi-modal fusion for fast MR reconstruction," *IEEE Transactions on Biomedical Engineering*, vol. 66, no. 7, pp. 2105–2114, 2019.

[14] L. Ma, F. Ju, J. Wan, and X. Shen, "Emotional computing based on cross-modal fusion and edge network data incentive," *Personal and Ubiquitous Computing*, vol. 23, no. 3-4, pp. 363–372, 2019.

[15] S. H. Amiri and M. Jamzad, "Leveraging multi-modal fusion for graph-based image annotation," *Journal of Visual Communication and Image Representation*, vol. 55, no. AUG., pp. 816–828, 2018.

[16] P. H. Dinh, "A novel approach based on Three-scale image decomposition and Marine predators algorithm for multi-modal medical image fusion," *Biomedical Signal Processing and Control*, vol. 67, no. 2, pp. 1–14, 2021.

[17] M. G. Huddar, S. S. Sannakki, and V. S. Rajpurohit, "Multi-level context extraction and attention-based contextual inter-modal fusion for multimodal sentiment analysis and emotion classification," *International Journal of Multimedia Information Retrieval*, vol. 9, no. 2, pp. 103–112, 2020.

[18] B. Palkar and D. Mishra, "Fusion of multi-modal lumbar spine images using Kekre's hybrid wavelet transform," *IET Image Processing*, vol. 13, no. 12, pp. 2271–2280, 2019.

[19] D. Mukherjee, R. Mondal, P. K. Singh, R. Sarkar, and D. Bhattacharjee, "EnsemConvNet: a deep learning approach for human activity recognition using smartphone sensors for healthcare applications," *Multimedia Tools and Applications*, vol. 79, no. Part 2, pp. 1–28, 2020.

[20] B. Karg and S. Lucia, "Efficient representation and approximation of model predictive control laws via deep learning," *IEEE Transactions on Cybernetics*, vol. 50, no. 9, pp. 3866–3878, 2020.

[21] S. Wandale and K. Ichige, "Design of sparse arrays via deep learning for enhanced DOA estimation," *EURASIP Journal on Applied Signal Processing*, vol. 2021, no. 1, pp. 1–13, 2021.

[22] K. Ding, M. Liu, X. Wei et al., "Comparison of MR-PWI quantitative and semi-quantitative parameters for the evaluation of liver fibrosis," *BMC Medical Imaging*, vol. 21, no. 1, p. 8, 2021.

[23] J. Ramalhinho, H. F. J. Tregidgo, K. Gurusamy, D. J. Hawkes, B. Davidson, and M. J. Clarkson, "Registration of untracked 2D laparoscopic ultrasound to CT images of the liver using multi-labelled content-based image retrieval," *IEEE Transactions on Medical Imaging*, vol. 40, no. 3, pp. 1042–1054, 2021.

[24] A. Brunetti, L. Carnimeo, G. F. Trotta, and V. Bevilacqua, "Computer-assisted frameworks for classification of liver, breast and blood neoplasias via neural networks: a survey based on medical images," *Neurocomputing*, vol. 335, pp. 274–298, 2019.

[25] V. Alhassan, C. Henry, S. Ramanna, and C. Storie, "A deep learning framework for land-use/land-cover mapping and analysis using multispectral satellite imagery," *Neural Computing & Applications*, vol. 32, no. 12, pp. 8529–8544, 2020.

[26] A. V. Chizhov, D. V. Amakhin, A. V. Zaizev, and L. G. Magazanik, "AMPAR-mediated interictal discharges in neurons of entorhinal cortex: experiment and model," *Doklady Biological Sciences*, vol. 479, no. 1, pp. 47–50, 2018.

[27] Z. Yu, D. Lei, G. Yang, and D. Lei, "Simulation and experimental study of DC electric field distribution characteristics of rat hippocampal slices in vitro," *Review of Scientific Instruments*, vol. 87, no. 6, pp. 22–35, 2016.

[28] G. Sun, H. Liu, K. Liu et al., "Effect of grouped ST36 or RN12 on gastric motility and sensation," *World Journal of Traditional Chinese Medicine*, vol. 3, no. 1, pp. 33–39, 2017.

[29] N. M. Egorov, V. I. Ponomarenko, I. V. Sysoev, and M. V. Sysoeva, "Simulation of epileptiform activity using network of neuron-like radio technical oscillators," *Technical Physics*, vol. 66, no. 3, pp. 505–514, 2021.

[30] B. Hu, D Wang, Z Xia et al., "Regulation and control roles of the basal ganglia in the development of absence epileptiform activities," *Cognitive Neurodynamics*, vol. 14, no. 1, pp. 137–154, 2020.

[31] P. Selvaraj, J. W. Sleigh, H. E. Kirsch, and A. J Szeri, "Closed-loop feedback control and bifurcation analysis of epileptiform activity via optogenetic stimulation in a mathematical model of human cortex," *Physical Review*, vol. 93, no. 1, Article ID 13309, 2016.

[32] W. Song, Y. Liu, C. Wu et al., "The expression of IGFBP6 after spinal cord injury: implications for neuronal apoptosis," *Neurochemical Research*, vol. 42, no. 2, pp. 1–13, 2016.

[33] C. Nucci, L. Morrone, and L. Rombolà, "Multifaceted roles of nitric oxide in the lateral geniculate nucleus: from visual signal transduction to neuronal apoptosis," *European Journal of Organic Chemistry*, vol. 139, no. 2-3, pp. 163–173, 2017.

[34] H.-T. Li, X.-Z. Zhao, X.-R. Zhang et al., "Exendin-4 enhances motor function recovery via promotion of autophagy and inhibition of neuronal apoptosis after spinal cord injury in rats," *Molecular Neurobiology*, vol. 53, no. 6, pp. 4073–4082, 2016.

Hindawi
Journal of Healthcare Engineering
Volume 2023, Article ID 9806931, 1 page
https://doi.org/10.1155/2023/9806931

Retraction

Retracted: Bevacizumab Combined with Intensity-Modulated Radiation Therapy on Cognitive and Coagulation Function in Postoperative Glioma Patients

Journal of Healthcare Engineering

Received 1 August 2023; Accepted 1 August 2023; Published 2 August 2023

This article has been retracted by Hindawi following an investigation undertaken by the publisher [1]. This investigation has uncovered evidence of one or more of the following indicators of systematic manipulation of the publication process:

(1) Discrepancies in scope
(2) Discrepancies in the description of the research reported
(3) Discrepancies between the availability of data and the research described
(4) Inappropriate citations
(5) Incoherent, meaningless and/or irrelevant content included in the article
(6) Peer-review manipulation

The presence of these indicators undermines our confidence in the integrity of the article's content and we cannot, therefore, vouch for its reliability. Please note that this notice is intended solely to alert readers that the content of this article is unreliable. We have not investigated whether authors were aware of or involved in the systematic manipulation of the publication process.

Wiley and Hindawi regrets that the usual quality checks did not identify these issues before publication and have since put additional measures in place to safeguard research integrity.

We wish to credit our own Research Integrity and Research Publishing teams and anonymous and named external researchers and research integrity experts for contributing to this investigation.

The corresponding author, as the representative of all authors, has been given the opportunity to register their agreement or disagreement to this retraction. We have kept a record of any response received.

References

[1] G. Lin, W. Wang, H. Lin, and R. Lin, "Bevacizumab Combined with Intensity-Modulated Radiation Therapy on Cognitive and Coagulation Function in Postoperative Glioma Patients," *Journal of Healthcare Engineering*, vol. 2022, Article ID 9367919, 8 pages, 2022.

Hindawi
Journal of Healthcare Engineering
Volume 2022, Article ID 9367919, 8 pages
https://doi.org/10.1155/2022/9367919

Research Article

Bevacizumab Combined with Intensity-Modulated Radiation Therapy on Cognitive and Coagulation Function in Postoperative Glioma Patients

Guo-Shi Lin, Wei-Wei Wang, Hong Lin, and Rui-Sheng Lin

Department of Neurosurgery, Zhangzhou Affiliated Hospital of Fujian Medical University, Zhangzhou, Fujian 363000, China

Correspondence should be addressed to Rui-Sheng Lin; yxy0516@fjmu.edu.cn

Received 4 January 2022; Revised 10 February 2022; Accepted 12 February 2022; Published 12 March 2022

Academic Editor: Nima Jafari Navimipour

To examine the influences of bevacizumab combined with intensity-modulated radiation therapy (IMRT) on postoperative brain glioma, particularly its impact on coagulation function and cognitive function, the complete clinical data of 156 patients undergoing glioma surgery in the neurosurgery department of our hospital between March 2015 and October 2018 were retrospectively analyzed. All patients underwent glioma surgery and were then assigned to the observation group (Obs group, $n = 79$, received bevacizumab combined with IMRT) or the control group (Con group, $n = 77$, received IMRT without bevacizumab) for analysis during postoperative treatment. The patients' short-term efficacy was evaluated, and their serum markers and coagulation function were compared, as well as the cognitive function, the occurrence of adverse reactions during treatment, the Karnofsky performance status (KPS) score, and quality of life after treatment. Patients' survival was followed up within 2 years after surgery. The Obs group showed a notably higher clinical remission rate and clinical control rate (DCR) than the Con group after treatment. The Obs group showed notably lower levels of interleukin-2 (IL-2), vascular endothelial growth factor (VEGF), IL-6, and epidermal growth factor (EGF), experienced notably shorter prothrombin time (PT) and activated partial thromboplastin time (APTT), and showed higher fibrinogen (FIB) and D-dimer (D-D) levels than Con group. The Obs group showed notably better cognitive function, KPS score, and quality of life than the Con group, but no notable difference was observed between them in the incidence of adverse reactions ($P > 0.0500$). The survival rates in the Obs group were higher than in the Con group. For patients with glioma, postoperative bevacizumab combined with IMRT delivers substantially higher clinical efficacy by lowering serum marker levels and improving cognitive function without significantly affecting coagulation function.

1. Introduction

Glioma is a frequently seen primary intracranial brain tumour, and its pathological types include astrocytoma, oligodendroglioma, ependymoma, and mixed glioma, of which astrocytoma is the most frequently seen one [1]. Glioma is characterized by high incidence, recurrence, and mortality [2]. Clinical symptoms mainly include increased intracranial pressure, neurological dysfunction, cognitive dysfunction, seizures, etc. [3]. Glioma is more frequently seen among individuals above 40 years old, with a higher incidence among the elderly over 60 years old. The World Health Organization classifies gliomas into grades I–IV at the pathological level, of which grades I-II and grades III-IV are considered as low-grade gliomas and high-grade gliomas, respectively [4]. Low-grade gliomas have relatively better prognosis than high-grade gliomas, with an overall survival period of about 5–10 years, but about 30% of low-grade gliomas recurrence can further malignant lesions to higher pathological grades glioma [5]. The treatment effect of high-grade glioma is very unsatisfactory, among which glioblastoma has a median survival time of only 18 months and 5-year survival time lower than 10% [6].

At the current stage, surgical resection is still the preferred therapy for glioma [7], whereas, due to the characteristics of invasive growth of gliomas, the boundary of tumour lesions in cases with low-grade or high-grade gliomas is not clear, and it is difficult to completely remove the

lesions by surgery, especially high-grade gliomas. The main mode after treatment failure is local recurrence [8]. In order to kill residual glioma, prevent postoperative recurrence, and reduce postoperative recurrence rate, patients with glioma often take adjuvant radiotherapy after surgery. Intensity modulated radiotherapy (IMRT) is a commonly used adjuvant method to kill residual cancer cells and prevent tumour recurrence in recent years [9]. IMRT has the characteristics of precise localization and can adjust the irradiation dose of the target region according to the shape and position of the tumour. While killing the cancer cells, it can minimize the radiation damage to the surrounding normal tissues and effectively control the growth, metastasis, and diffusion of the tumour [10, 11]. However, due to the poor sensitivity of glioma to radiotherapy, the postoperative IMRT alone has very limited preventive value for recurrence.

At the same time, recent research has indicated the high level of vascular endothelial growth factor (VEGF) as one crucial factor promoting tumour invasive growth [12]. Therefore, from this perspective, it is a new idea to use drugs that antagonize the biological function of VEGF for combination therapy. Bevacizumab has been approved by the US Food and Drug Administration as one antivascular agent for the therapy of recurrent high-grade gliomas [13]. However, there are some concerns with the use of bevacizumab, including the potential for tumour hemorrhage and venous thrombosis [14]. Now, studies on coagulation function and cognitive function of patients after glioma with bevacizumab combined with IMRT have not been reported. From the perspective of coagulation function and cognitive function, this study retrospectively analyzed the impacts of bevacizumab + IMRT on postoperative patients with glioma and its impacts on cognitive function and coagulation function, providing more evidence for clinical treatment of glioma.

2. Materials and Methods

2.1. Subjects. The complete clinical data of 156 patients undergoing glioma surgery in the neurosurgery department of our hospital between March 2015 and October 2018 were retrospectively analyzed. All patients continued to receive treatment postoperatively, with the choice of treatment initially based on patient willingness to undergo surgery and individual patient circumstances. In the light of different treatment means, patients were assigned to the control group (Con group, receiving postoperative intensity modulated radiation therapy, $n = 77$) and observation group (Obs group, receiving postoperative bevacizumab combined with intensity modulated radiation therapy, $n = 79$). This study was carried out under the ethical standards of clinical trials and approval of the hospital's Medical Ethics Committee (Approval number: 2021KYB203).

2.2. Inclusion and Exclusion Criteria. The inclusion criteria were as follows: (1) all with typical clinical manifestations such as headache and vomiting, loss of vision, and a clear diagnosis of glioma and treated with surgical resection, pathological grade III-IV; (2) all who started radiotherapy after the healing of the surgical incision (2–4 weeks); (3) age <80 years and expected survival >3 months; (4) Karnofsky (KPS) score ≥60; (5) those who had not been previously treated with any of the drugs used in this study; (6) complete clinical information.

Exclusion criteria were as follows: (1) patients with contraindications of surgery, radiotherapy, or allergy to drugs used in this study; (2) patients who have received chemotherapy or head and neck tumour sensitization radiotherapy; (3) presence of other cranial diseases or other serious pathological changes of tissues, organs, and systems; (4) poor treatment coordination, mental disorders; (5) incomplete clinical information.

2.3. Treatment Protocol. In both groups, intensity modulated conformal radiotherapy was performed with 6MV-X radiation at 2–4 weeks after surgery: Each patient was required to lie in a comfortable supine position to make a U-shaped thermoplastic mask for the head, and the head frame and thermoplastic mask were used to fix the position. According to CT and MRI examination results of patients before and after surgery, the lesion status was determined and target areas were marked, which were divided into tumour target area (GTV), clinical target area (CTV), and planned target area (PTV). Residual lesions in T1-weighted enhanced images, abnormal signals in water-inhibited T2, and intraoperative cavity were assigned as GTV1, residual lesions in T1-weighted enhanced images and intraoperative cavity were assigned as GTV2, and residual lesions in T1-weighted enhanced images were assigned as GTVp. CTV1 was obtained by GTV1 extending 1.5–2.0 cm outward. PTV1 was obtained by CTV1 expanding 0.3–0.5 cm outwards, CTV2 by GTV2 expanding 1.0–1.5 cm outwards, and PTV2 by CTV2 expanding 0.3–0.5 cm outwards. Radiotherapy dose: PTV1 was 54 Gy/30 times, PTV2 was 60 Gy/30 times, and CTV was 642–66.0 Gy/30 times. The segmentation dose was 1.8 Gy for PTV1, 2.0 Gy for PTV2, and 2.14–2.20 Gy for CTV, five times a week.

The Obs group was treated with bevacizumab in addition to IMRT, and bevacizumab was intravenously injected into 500 mL normal saline with 5–10 mg/kg bevacizumab every 2 weeks for 3 months (about 6 cycles).

2.4. Observation Indicators

(1) Short-term efficacy assessment: Three months after the end of radiotherapy, all patients underwent imaging examinations. Based on the Response Assessment in Neuro-Oncology (RANO) standard [15], the efficacy was classified into complete response (CR), partial response (PR), stable disease (SD), and progressive disease (PD). Clinical remission rate = (CR + PR)/total number of cases ×100%; clinical control rate = (CR + PR + SD)/total number of cases ×100%.

(2) All patients received relevant hematological examination before radiotherapy and during follow-up. Serum marker detection: Fasting weekly venous

blood was collected from each patient in the morning prior to treatment and 3 months after the end of radiotherapy, and the serum was separated for detection after standing at room temperature for natural coagulation and 20-min centrifugation (3000 r/min). Interleukin-2 (IL-2), IL-6, VEGF, and epidermal growth factor (EGF) were quantified using ELISA, with corresponding kits provided by Shanghai Enzyme-Linked Biotechnology Co., LTD. (article numbers: ml058063, ml058097, ml064281, and ml058660) under guidelines of the kits.

Coagulation function test: Venous blood was acquired from the elbow of every patient prior to radiotherapy and at 3 months after the end of radiation therapy and mixed with anticoagulant containing 0.109 mol/L sodium citrate (9 : 1), followed by 10-min centrifugation (3000 r/min) with shaking, and plasma was taken for measurement. The coagulation indexes, including prothrombin time (PT), prothrombin time (TT), fibrinogen (FIB), activated partial thromboplastin time (APTT), and fibrinolytic index (D-dimer, D-D), were measured through one automatic coagulation analyzer (STA-R Evolution, France).

(3) Cognitive function assessment: All patients were assessed for cognitive function before surgery, before postoperative radiation therapy, and at the end of 3 months of radiation therapy using the Mini-Mental State Examination (MMSE) [16]. With a total score of 30 points, the main components included memory (3 points), orientation (10 points), recall (3 points), attention and calculation (5 points), and verbal ability (9 points). A higher score implies better cognitive function, and a total score of <27 suggests cognitive impairment.

(4) Occurrence of adverse reactions and complications: During the treatment, intracranial pressure increase, gastrointestinal reaction, skin ulceration, bone marrow suppression, liver function injury, and other conditions were recorded in the 2 groups.

(5) Health status and quality of life (QOL) score: The two groups were compared in the Karnofsky performance status (KPS) score [17] and QOL score [18] before and 3 months after radiotherapy. With a higher score implying better health, KPS scores are within 0–100, using 0 points for death and 100 points normal condition, without any symptoms or signs. QOL score includes 12 dimensions including appetite, pain, spirit, sleep, fatigue, understanding and cooperation of colleagues, own knowledge of cancer, attitude towards therapy, understanding and cooperation of family, daily life, facial expression, and adverse reaction to therapy. With a full score of 60, each dimension is divided into five grades. A lower score implies worse QOL: 51–60: very good, 41–50: good, 31–40: fair, 21–30: poor, and < 20: very poor.

(6) Long-term survival rate: The 1-year and 2-year survival of patients were followed up from the date of surgery to December 2020, and the median survival inches were calculated.

2.5. Statistical Methods. The normal approximation method in PASS 15.0 (NCSS Statistical Software, Kaysville, Utah) was adopted for the calculation of sample size. A preliminary analysis was conducted to the data at the level of bilateral test $\alpha = 0.0500$. Assuming that the two-year survival rates of the Obs and Con groups were 74% and 50%, respectively, and 80% power was required, the sample size of each group was at least 61 cases, with 122 cases in total. Based on 20% loss rate, at least 77 cases should be included in each group, a total of 154 cases.

Statistical data were analyzed using SPSS 22.0 software package (IBM Corp., Armonk, NY, USA); GraphPad Prism 6.0 (GraphPad Software, La Jolla California USA) was used to visualize the data. Comparisons of count data [N (%)] were conducted via the $\chi 2$ test and fisher's exact test, and intergroup and introgroup comparisons of measurement data in normal distribution (Mean ± SD) were performed by independent sample T test and paired T test, respectively. We analyzed differences between groups at all time points (before surgery, before radiotherapy, and after radiotherapy) using repeated measures analysis of variance (ANOVA) and then the Bonferroni post hoc test. Kaplan–Meier analysis was applied to overall survival. With $\alpha = 0.0500$ as test standard, $P < 0.0500$ implies a notable difference.

3. Results

3.1. Summary of Patients' General Baseline Information. No significant differences were identified in the patients' general baseline information between the control group and observation group ($P > 0.0500$), indicating a comparability (Table 1).

3.2. Short-Term Efficacy in Two Groups. The Obs group showed notably higher RR and DCR than the Con group 3 months after radiotherapy (all $P < 0.0500$, Table 2).

3.3. Changes of Serum Marker Levels in Two Groups. No notable difference was observed in the contents of IL-2, IL-6, VEGF, and EGF between the 2 groups before postoperative radiotherapy ($P > 0.0500$), while 3 months after radiotherapy, the contents of them in both groups dropped notably, with greatly lower levels in the Obs group than those in the Con group (all $P < 0.0500$, Figure 1).

3.4. Changes in the Coagulation Indexes of Two Groups. The two groups were similar in TT before and after radiotherapy ($P > 0.0500$). Three months after radiotherapy, both groups experienced notably shortened PT and APTT and showed notably increased FIB and D-D contents, with

Table 1: General baseline information ($\bar{x} \pm s/n(\%)$).

	Control group ($n = 77$)	Observation group ($n = 79$)	χ^2/t	P
Gender [n(%)]			0.0219	0.8821
Male	41(53.2)	43(54.4)		
Female	36(46.8)	36(45.6)		
Average age (years, $\bar{x} \pm s$)	57.32 ± 6.43	58.02 ± 6.95	0.6526	0.5150
Pathological pattern			0.3095	0.8566
Neuroastrocytoma	47(61.0)	45(57.0)		
Oligodendroglioma	16(20.8)	19(24.1)		
Mixed glioma	14(18.2)	15(18.9)		
Lesion			1.2584	0.8685
Frontal lobe	32(41.6)	30(38.0)		
Occipital lobe	11(14.3)	14(17.7)		
Temporal lobe	19(24.7)	20(25.3)		
Parietal lobe	13(16.9)	11(13.9)		
Others	2(2.5)	4(5.1)		
Postoperative pathological grading			0.0855	0.7700
III	46(59.7)	49(62.0)		
IV	31(40.3)	30(38.0)		
Tumour diameter (cm, $\bar{x} \pm s$)	4.12 ± 0.87	4.02 ± 1.04	0.6506	0.5163
Degree of surgical resection			0.2059	0.6500
Complete excision	52(67.5)	56(70.9)		
Partial excision	25(32.5)	23(29.1)		
Combined underlying disease			0.2627	0.6083
Diabetes	15(19.5)	14(17.7)		
Hypertension	21(27.3)	25(31.6)		

Chi-square test, fisher's exact test, or independent sample t-test between groups.

Table 2: Intergroup comparison of short-term efficacy [n(%)].

Group	CR	PR	SD	PD	RR	DCR
Control group ($n = 77$)	9(11.7)	33(42.8)	22(28.6)	13(16.9)	42(54.5)	64(83.1)
Observation group ($n = 79$)	19(24.1)	42(53.1)	13(16.5)	5(6.3)	61(77.2)	74(93.7)
χ^2	10.5030				8.9341	4.2551
P	**0.0148**				**0.0028**	**0.0391**

Notes: CR: complete response; PR: partial response; SD: stable disease; PD: progressive disease; RR: response rate; DCR: disease control rate; chi-square test or fisher's exact test between groups. The bolded part represents statistical significance, $p < 0.05$.

notably shorter PT and APTT and notably higher FIB and D-D contents in the Obs group than those in the Con group (all $P < 0.0500$, Table 3).

3.5. Cognitive Functions. Attention, memory, orientation, and computation, language ability, recall ability, and MMSE total score of the two groups before postoperative radiotherapy were notably higher than those before surgery ($P < 0.0500$), without notable difference between the 2 groups ($P > 0.0500$). Three months after the end of radiotherapy, the scores of all indicators of cognitive function and the total MMSE scores of the two groups elevated notably, with notably higher scores of all indicators and the total MMSE scores in the Obs group than those in the Con group ($P < 0.0500$, Table 4).

3.6. Occurrence of Adverse Reactions. The Obs group had 35, 2, 9, and 3 cases of gastrointestinal reaction, skin ulceration, bone marrow suppression, and liver function injury, respectively, with a total incidence of 62%. The Con group had 32, 3, 8, and 2 cases of gastrointestinal reactions, skin ulceration, bone marrow suppression, and liver function injury, respectively, with a total incidence of 58.4%. The two groups were similar in the incidence and total incidence of adverse reactions ($P > 0.0500$, Table 5).

3.7. KPS Score and QOL. No notable difference was observed between the two groups in KPS and QOL scores before radiotherapy ($P > 0.0500$). KPS and QOL scores in both groups greatly increased 3 months after radiotherapy ($P < 0.0500$), with notably higher KPS score and QOL score in the Obs group than those in the Con group ($P < 0.0500$, Figure 2).

3.8. Long-Term Survival. The Obs group showed notably higher 2-year survival rates than the Con group ($P < 0.0500$, Figure 3).

4. Discussion

Infiltrating growth is the most prominent biological behavior of glioma, including infiltrating along white matter

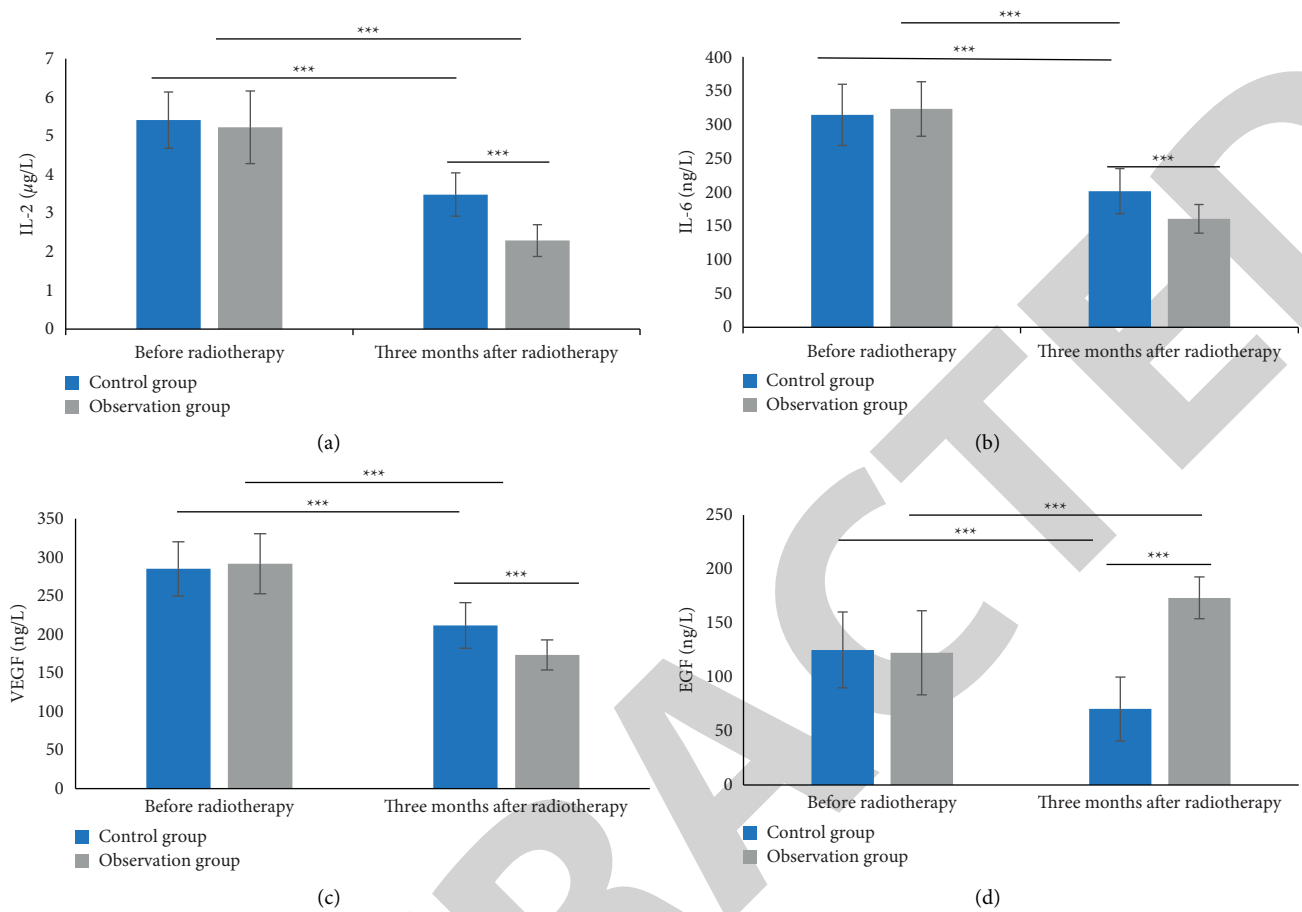

Figure 1: Serum marker levels of two groups in different time points. (a) Comparison of IL-2 level between two groups before and after radiotherapy. (b) Comparison of IL-6 level between two groups before and after radiotherapy. (c) Comparison of VEGF level between two groups before and after radiotherapy. (d) Comparison of EGF level between two groups before and after radiotherapy. $^{***}P < 0.001$ using paired t-test within group and independent sample T test between groups.

Table 3: Comparison of coagulation indexes ($\bar{x} \pm s$).

Time point	Group	TT (s)	PT (s)	APTT (s)	FIB (g/L)	D-d (mg/L)
Before radiotherapy	Control group ($n = 77$)	17.85 ± 1.34	11.07 ± 1.17	24.52 ± 2.41	2.93 ± 0.31	0.32 ± 0.14
	Observation group ($n = 79$)	17.69 ± 1.43	11.32 ± 1.25	24.02 ± 2.49	3.01 ± 0.37	0.35 ± 0.11
t		0.7207	1.2889	1.2739	1.4619	1.4903
P		0.4722	0.1994	0.2046	0.1458	0.1382
3 months after radiotherapy	Control group ($n = 77$)	17.63 ± 1.56	10.18 ± 1.21*	23.37 ± 2.51*	3.41 ± 0.27*	0.50 ± 0.13*
	Observation group ($n = 79$)	17.52 ± 1.50	9.98 ± 1.04*	21.05 ± 2.04*	3.69 ± 0.35*	0.59 ± 0.18*
t		0.4489	1.9842	6.3427	5.5846	3.5723
P		0.6541	**0.0490**	**<0.0001**	**<0.0001**	**0.0005**

Notes: TT: thrombin time; PT: prothrombin time; APTT: activated partial thromboplastin time; FIB: fibrinogen; D-D : D-Dimer; $*P < 0.0500$, compared to the same group before radiotherapy using paired t-test and independent sample T test between groups. The bolded part represents statistical significance, $p < 0.05$.

myelin fibers, nerve cells, and vascular tissue [19]. Since glioma cells migrate and grow invasive in the tumour area, surgical resection has limited efficacy for removing migrating tumour cells, and patients often relapse in a short period of time. However, surgical resection of partial lesions also enhances the efficacy of subsequent adjuvant therapy, prolonging the overall survival of patients to a certain extent. Postoperative radiotherapy is a conventional method to remove residual glioma lesions and prevent recurrence. Nevertheless, the long-term survival of postoperative radiotherapy alone is unsatisfactory. It is well known that solid tumour growth depends on continuous and extensive angiogenesis [20]. Glioma is a tumour rich in blood vessels. The new blood vessels caused by endothelial cell proliferation are closely related to the degree of biological invasion and malignancy of glioma [21]. Over the past few years, a large number of studies have pointed out the angiogenesis mediated by VEGF as a crucial link in the development of

Table 4: Comparison of cognitive functions ($\bar{x} \pm s$).

Time point	Group	Orientation	Registration	Calculation and attention	Recall	Language and visuospatial function	MMSE score
Before surgery	Control group ($n = 77$)	5.45 ± 0.51	1.50 ± 0.42	2.11 ± 0.39	1.11 ± 0.26	5.82 ± 0.85	21.23 ± 4.03
	Observation group ($n = 79$)	5.37 ± 0.42	1.53 ± 0.37	2.09 ± 0.32	1.17 ± 0.21	5.91 ± 0.77	21.59 ± 3.88
T		1.0707	0.4737	0.3505	1.5876	0.6934	0.5684
P		0.2860	0.6364	0.7264	0.1144	0.4891	0.5706
Before radiotherapy	Control group ($n = 77$)	$7.74 \pm 0.92^{*}$	$2.07 \pm 0.40^{*}$	$3.12 \pm 0.32^{*}$	$1.49 \pm 0.27^{*}$	$7.03 \pm 0.76^{*}$	$26.33 \pm 2.05^{*}$
	Observation group ($n = 79$)	$7.86 \pm 0.83^{*}$	$2.11 \pm 0.36^{*}$	$3.17 \pm 0.30^{*}$	$1.53 \pm 0.22^{*}$	$7.10 \pm 0.64^{*}$	$26.66 \pm 2.07^{*}$
T		0.8558	0.1099	1.0071	1.0156	0.6229	1.0002
P		0.3934	0.9127	0.3155	0.3114	0.5343	0.3188
3 months after radiotherapy	Control group ($n = 77$)	$8.12 \pm 0.77^{*\#}$	$2.37 \pm 0.40^{*\#}$	$3.49 \pm 0.29^{*}\#$	$1.79 \pm 0.31^{*\#}$	$7.60 \pm 0.74^{*\#}$	$26.99 \pm 1.89^{*\#}$
	Observation group ($n = 79$)	$8.35 \pm 0.64^{*\#}$	$2.49 \pm 0.32^{*\#}$	$3.63 \pm 0.33^{*\#}$	$1.91 \pm 0.23^{*\#}$	$7.83 \pm 0.68^{*\#}$	$27.54 \pm 1.16^{*\#}$
t		2.0310	2.0717	2.8119	2.7506	2.0222	2.1967
P		0.0440	0.0400	0.0056	0.0067	0.0449	0.0296

Note. $^{*}P < 0.0500$ *vs.* the same group before surgery; $^{\#}P < 0.0500$ *vs.* the same group before radiotherapy; paired t-test and independent sample T test between groups.

Table 5: Adverse reactions in the two groups [n(%)].

Group	Gastrointestinal reaction	Skin eruptions	Myelosuppression	Hepatic injury	Total incidence rate
Control group ($n = 77$)	32(41.6)	3(3.8)	8(10.4)	2(2.6)	45(58.4)
Observation group ($n = 79$)	35(44.3)	2(2.5)	9(11.4)	3(3.8)	49(62.0)
χ^2	0.1199	0.2340	0.0404	0.1810	0.2091
P	0.7291	0.6286	0.8407	0.6705	0.6475

Chi-square test between groups.

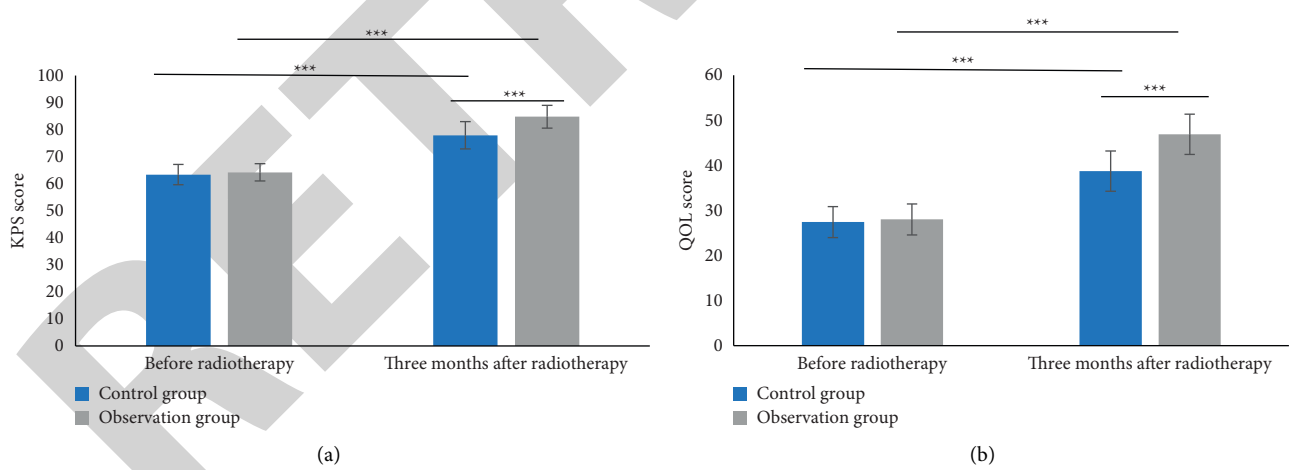

Figure 2: Intergroup comparison of KPS and QOL scores. (a) Comparison of KPS score between two groups before and after radiotherapy. (b) Comparison of QOL score between two groups before and after radiotherapy; $^{***}P < 0.001$ using paired t-test within group and independent sample T test between groups.

glioma [22]. Bevacizumab [23] is a targeted drug that specifically antagonizes VEGF and can produce biological effects that bind to VEGF and antagonize its promotion of angiogenesis. More and more data indicate that the combination of antiangiogenesis and chemoradiotherapy may improve the therapeutic effect [24]. This study was for clarifying the application value of bevacizumab + IMRT in cases with postoperative glioma. However, most previous studies focused on the overall survival of cancer treatment. With the progress of society, a growing number of people

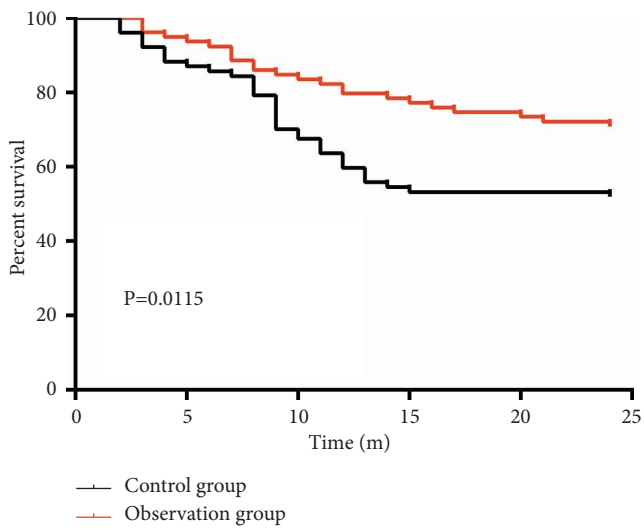

Figure 3: Kaplan–Meier analysis of 2-year overall survival.

began to focus on the impact of cancer therapy on the QOL and physical function.

In this study, we found notably higher overall efficacy, higher 1-year and 2-year survival rates, and longer median survival time in the Obs group than those in the Con group. These results suggested the ability of bevacizumab combined with IMRT in lifting the postoperative efficacy of glioma and prolonging the survival time of patients. We believed that bevacizumab may normalize tumour blood vessels and effectively reduce the hypoxic state in tumour while killing local tumour with IMRT, thus improving the efficacy of radiotherapy. Bevacizumab also selectively inhibits tumour-related angiogenesis and regeneration. After further analysis of the effect of bevacizumab, serum marker levels of patients were observed, and it was found that serum IL-2, IL-6, VEGF, and EGF in the 2 groups notably decreased after therapy, with notably lower levels in the Obs group than those in the Con group. Both IL-2 and IL-6 are cytokines that can promote the proliferation of tumour cells and the growth of vascular endothelial cells [25]. VEGF can directly act on endothelial cells and promote their proliferation to induce the formation of new blood vessels, while EGF can directly act on tumour cells to promote the growth of lesions [26]. These data implied that IL-6, IL-2, EGF, and VEGF produced in large quantities in the local lesions can be released into the blood circulation, and radiotherapy kills glioma cells and reduces the content of molecules related to proliferation activity in serum, but their effects were further enhanced with the addition of bevacizumab. All the above results indicate that bevacizumab combined with IMRT has stronger killing effect on tumour cells.

However, studies have found that the risk of deep vein thrombosis after brain tumour surgery is increased, which is mainly related to the secretion of hypercoagulable substances in the brain tissue during surgery [27]. Therefore, we detected the coagulation system function indicators of patients and found notably shorter PT and APTT and notably higher FIB and D-D contents in the Obs group than those in the Con group. Studies have pointed out that the shortening of APTT and PT indicates the hypercoagulable state of blood, which can be adopted for evaluating the risk of thrombosis and cardiovascular events in humans [28]. As a coagulation function protein molecule, FIB has the highest content in blood and is converted into fibrin catalyzed by thrombin, which affects the coagulation state in blood vessels. D-D, a specific degradation product of crosslinked fibrin, is also a specific indicator for secondary fibrinolysis evaluation and a major marker of thrombosis and hypercoagulability [29]. The increase of FIB and D-D indicates that the blood viscosity is elevated and thrombosis is likely to occur. Due to the injury of brain tissue in the process of surgery, a large number of tissue factors are secreted for activating the exogenous coagulation pathway of the body and eventually activating the endogenous coagulation pathway of the body, which is the disorder of the coagulation and anticoagulation system. However, with the addition of bevacizumab to the treatment, the incidence of abnormal coagulation function in patients increases, which has a certain risk. In addition, we found better improvement of cognitive function and higher KPS and QOL in the Obs group than those in the Con group. The results indicated that bevacizumab effectively improved the cognitive function and body function of patients. Patients with glioma are prone to postoperative complications of cerebral edema, which can affect cognitive function. Foreign literature has reported that bevacizumab can relieve radioactive brain edema and improve neurological function [30]. The results of this study also confirmed this point.

5. Conclusion

The application of bevacizumab combined with IMRT effectively improves the short-term efficacy and survival rate of patients after glioma surgery, with significant clinical treatment effect and good application value and development prospect. However, this study also has limitations; the use time of bevacizumab in our study is not long-term. According to the results of this study, medium- and short-term use of bevacizumab can improve the curative effect of patients, but does long-term use have the same effect or is there any impact on the incidence of venous thrombosis? Therefore, the results of this study need further verification in randomized prospective studies with a larger sample size. In addition to coagulation function, the influencing factors on thrombosis should be comprehensively considered in combination with other factors such as patient age, tumour itself, chronic disease, and operation, so as to ensure the safe application of bevacizumab.

Data Availability

The clinical data used to support the findings of this study are included within the article.

Conflicts of Interest

The authors declare that they have no conflicts of interest.

Hindawi
Journal of Healthcare Engineering
Volume 2023, Article ID 9785028, 1 page
https://doi.org/10.1155/2023/9785028

Retraction

Retracted: Discussion on Protein Metabolism and Requirement of Aerobics Athletes during Training Based on Multisensor Data Fusion

Journal of Healthcare Engineering

Received 1 August 2023; Accepted 1 August 2023; Published 2 August 2023

This article has been retracted by Hindawi following an investigation undertaken by the publisher [1]. This investigation has uncovered evidence of one or more of the following indicators of systematic manipulation of the publication process:

(1) Discrepancies in scope
(2) Discrepancies in the description of the research reported
(3) Discrepancies between the availability of data and the research described
(4) Inappropriate citations
(5) Incoherent, meaningless and/or irrelevant content included in the article
(6) Peer-review manipulation

The presence of these indicators undermines our confidence in the integrity of the article's content and we cannot, therefore, vouch for its reliability. Please note that this notice is intended solely to alert readers that the content of this article is unreliable. We have not investigated whether authors were aware of or involved in the systematic manipulation of the publication process.

In addition, our investigation has also shown that one or more of the following human-subject reporting requirements has not been met in this article: ethical approval by an Institutional Review Board (IRB) committee or equivalent, patient/participant consent to participate, and/or agreement to publish patient/participant details (where relevant).

Wiley and Hindawi regrets that the usual quality checks did not identify these issues before publication and have since put additional measures in place to safeguard research integrity.

We wish to credit our own Research Integrity and Research Publishing teams and anonymous and named external researchers and research integrity experts for contributing to this investigation.

The corresponding author, as the representative of all authors, has been given the opportunity to register their agreement or disagreement to this retraction. We have kept a record of any response received.

References

[1] H. Gong, S. Chen, S. Yu et al., "Discussion on Protein Metabolism and Requirement of Aerobics Athletes during Training Based on Multisensor Data Fusion," *Journal of Healthcare Engineering*, vol. 2022, Article ID 6169150, 12 pages, 2022.

Hindawi
Journal of Healthcare Engineering
Volume 2022, Article ID 6169150, 12 pages
https://doi.org/10.1155/2022/6169150

Research Article

Discussion on Protein Metabolism and Requirement of Aerobics Athletes during Training Based on Multisensor Data Fusion

Hua Gong,[1] Shuang Chen,[2] Shuo Yu,[3] Dong Liu,[4] Xin Li,[5] Zeliang Shan,[6] Fan Kong,[7] Zhi Yan,[1,8] and Feng Han[8]

[1]*Liaoning Normal University Sports Institute, Dalian 116029, Liaoning, China*
[2]*Department of Medical Health, Xing'an Vocational and Technical College, Ulanhot 137400, Inner Mongolia, China*
[3]*Sports Department of Liaoning Agricultural Technical College, Yingkou 115009, Liaoning, China*
[4]*Health College, Polus International College, Chengdu 610103, Sichuan, China*
[5]*Physical Education Department, Luxun Academy of Fine Arts, Dalian 116029, Liaoning, China*
[6]*Rehabilitation and Nursing Institute, Tianfu College of Swufe, Chengdu 610103, Sichuan, China*
[7]*School of Physical Education and Health, Dalian University of Technlogy, Dalian 116029, Liaoning, China*
[8]*Orthopaedics, Dalian Port Hospital, Dalian 116001, Liaoning, China*

Correspondence should be addressed to Feng Han; 2438383590@mail.dlut.edu.cn

Received 10 January 2022; Accepted 12 February 2022; Published 12 March 2022

Academic Editor: Nima Jafari Navimipour

Competitive aerobics has emerged as a highly competitive sport beyond its own physical limit. Modern competitive aerobics competition is very fierce; athletes cannot only rely on a specific competitive skill to achieve good results. Protein is the physical basis of life activity. The life activity of human body is closely related to protein, and protein is closely related to human exercise ability. This article aims to study protein metabolism and demand of aerobics athletes during training based on multisensor data fusion. A total of 26 female aerobics athletes were randomly divided into two groups: exercise group and exercise + nutrition group. According to the characteristics of human motion, a comprehensive measurement acquisition sensor system for collecting human motion information is designed and implemented, and the system is used to monitor the subject's protein condition in real time. The subjects took protein nutrient solution before breakfast every day. The dynamic recognition algorithm designed in this paper also has shortcomings, and the monitoring protein method based on gait and other signs is not completely correct. The experiment lasted for 7 weeks. The results showed that the level of serum transferrin receptor decreased significantly in the quiet + nutrition group for 4 weeks, which was significantly different from that at 0 and 3 weeks in the same group ($P < 0.01$) and was significantly different from that in the same group at 7 weeks ($P < 0.05$). In the exercise group, the level of serum transferrin receptor increased significantly at 5 weeks, compared with the same group at 0 and 3 weeks ($P < 0.05$).

1. Introduction

The technical level of competitive aerobics is affected by factors such as physical quality, psychological quality, technical ability, sense of music, and expressiveness of athletes. The development of computer technology can be used for the daily training of competitive gymnastics, so the aerobics technology of athletes can use advanced computer technology. When aerobics athletes fail to exercise for a long time, protein can provide energy up to 5%–18% of the total exercise energy consumption. Exercise can make the human body protein metabolism change, but different nature of the exercise produced different effects, so protein requirements for athletes at different events are not the same. Accurately identifying the athlete's protein condition can accurately understand the physical condition and improve the target point and realize the personalized and precise supplement of the athlete. Nanopore sensing technology can detect protein changes from a single-molecule level, effectively improving the accuracy of detecting athletes' protein conditions. This

topic uses nanopore single-molecule sensors to carry out experimental studies on single-protein molecules and protein interaction relationships.

The effect of exercise on lipoprotein metabolism has been studied for many years. Although there are some differences in the results due to different exercise modes, intensity, and research objects, a large number of epidemiological and clinical investigations have confirmed the following: No matter for men, women, old people, or children, China-Africa daily health life habits and lack of exercise or low fitness levels and many cardiovascular disease risk factors and incidence of coronary heart disease (CHD) were positively correlated, while regular exercise can effectively reduce blood lipids and lipoproteins and make the original plasma lipoprotein atherosclerosis develop in a good direction, and at the same time, it can control and reduce the risk factors of cardiovascular disease or coronary heart disease and slow down the adverse effects of aging [1, 2]. In order for the human body to exercise normally, the human body needs to consume more protein energy and supplementary food to promote the normal operation of the body.

Some scholars asked 166 athletes to maintain a scientific diet for three consecutive days, train more than 3 hectares of specific physical activities per week, and then be converted into macronutrients by a nutritionist. During Goodyear and other snow and ice athletes' training, the daily protein requirements were as follows: when the training amount was small, male speed skating athletes were 139 g/d and female athletes were 95 g/d. Skiing events male athletes were 110 g/d and female athletes were 64 g/d. When the training volume is large, the speed skaters are 165 g/d for men and 106 g/d for women [3]. At the same time, it is suggested that when the amount of exercise increases, the urine nitrogen excretion of athletes increases, and the nutrition level of protein can be understood by hemoglobin measurement. Crouse et al. found that the local levels of insulin and amino acids in muscles play an important role in controlling the synthesis of myostatin, and the reduction of insulin secretion caused by hunger reduces the synthesis rate of skeletal muscle protein by more than 50%, which is related to inhibiting the initiation of protein synthesis [4].

The innovation of this paper is the use of sensors to monitor protein changes in gymnasts, enabling visualization of athletes' protein requirements. At present, because calisthenics is very important to the development of students' physical quality, major universities widely carry out this sport. The aerobics center of each province will bring some aerobics trainers to participate in the intensive training, so that they will be fully prepared for the higher level of competition, as a professional aerobics athlete to achieve outstanding results. Aerobics athletes' training is not only the most basic technical movement training but also physical training. The results showed that the serum transferrin receptor level in the quiet + nutrition group decreased significantly after 4 weeks, which was significantly different from that of the same group at 0 weeks and 3 weeks ($P < 0.01$) and significantly different from that of the same group at 7 weeks ($P < 0.05$). In the exercise group, the serum transferrin receptor level was significantly increased at week 5, which was significantly different from that of the same group at weeks 0 and 3 ($P < 0.05$), showing that the serum transferrin receptor level at weeks 0 and 3 was significantly lower than that at week 5.

2. Protein Demand and Monitoring

2.1. Physiological Functions of Proteins. Human life is inseparable from proteins, which are an important part of human cells. Proteins have different structures and have many physiological functions. Their main functions are as follows.

2.1.1. Catalytic Function. In order to maintain the balance of human functions, the human body needs to produce some chemical reactions. Enzyme is a catalyst, and many chemical reactions are completed under the action of enzymes, so it can effectively control the metabolism of the human body and expel wastes from the body. According to scientific testing, the main components of the human body are more than 1,000 kinds of enzymes and proteins. Proteins have certain catalytic functions, so they are important substances to maintain human body functions [5].

2.1.2. Transportation Function. The human body is an organic whole, and blood circulation and oxygen transport need carriers. Protein is an effective carrier and an effective tool to ensure the normal transport of the human body. Effective transport of human body functions requires its normal operation to effectively complete its transport and guarantee its organic circulation [6].

2.1.3. Motor Function. The movement of the human body mainly relies on muscles to complete, and protein is the main component of muscles. There is a certain relationship between muscle contraction and relaxation and protein quality. The muscles of athletes are usually more developed than our ordinary people because athletes have a certain standard of diet, and there are requirements for daily intake of protein, fat, water, and so on [7, 8].

2.1.4. Hormone Function. In biology, the main component of many hormones is protein, which has a certain therapeutic effect on patients in medicine. Protein and polypeptide hormones are important hormones in animals, which regulate and control the physiological activities of animals. For example, insulin can reduce blood sugar. Glucagon has 3485 polypeptides of 29 amino acid residues. Its effect is exactly opposite to that of insulin, which can promote glycogen decomposition and gluconeogenesis and increase blood glucose concentration. Hormones are often available in people's lives, but the use of hormones should be reduced to a certain extent to cause damage to the human body. Proteins have certain hormonal functions and are the main components of hormones [9]. The flow chart of physiological function of protein is shown in Figure 1.

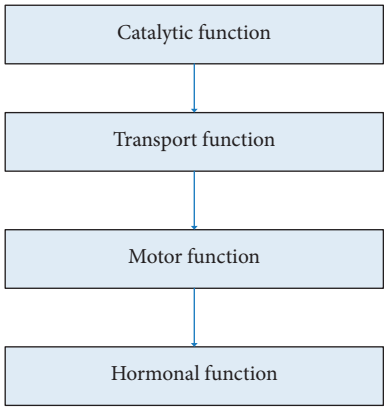

Figure 1: Flow chart of protein physiological function.

2.2. Function of Protein during Exercise.

(1) Protein is the basic structure of cells. Protein is the main component of cells, accounting for more than 80% of the dry weight of cells; proteins constitute the cell membrane and intracellular materials and regulate genetic information. The tissue cells of the body are in a balance of constant aging and renewal, and protein is the raw material for maintaining tissue repair and regeneration. Physical exercise can strengthen the metabolism of the human body. Therefore, it can strengthen the bones and muscles and increase the content of protein in the body [10].

(2) Proteins have physiological functions of regulating the body. All biochemical reactions in the body require the participation of enzymes with catalytic activity (with very few exceptions), and enzymes are essentially proteins. Proteins play an important role in regulating the acid-base balance of body fluids. When intense exercise leads to the enhancement of enzyme metabolism, blood proteins play an important role in buffering, thus keeping the internal environment of the body relatively stable. Many of the hormones regulating human physiological functions are composed of compounds of different amino acids and proteins, such as insulin and pituitary hormones regulating blood glucose levels [11].

(3) Proteins participate in energy supply during exercise. During long and intensive exercise, proteins, especially the free amino acids in the human body, can also participate in energy supply as energy materials, but the overall participation ratio is not high, generally accounting for 5%–18% of the total energy consumption. Amino acids derived from tissue protein regeneration also contribute a certain amount of energy. However, in exercise, protein takes a relatively small proportion in energy supply. Only when the body consumes insufficient sugar and fat in the body does the body break down protein to produce amino acids and obtain energy [12].

2.3. Effects of Exercise on Protein Metabolism

2.3.1. The Influence of Strength Training on Protein Metabolism. The athlete receives the strength movement training for a long time, can promote the protein anabolism obviously, and increases the muscle strength and the volume. Strength training makes the volume of training muscle increase, muscle fiber thicken, and strength enhanced. This adaptation occurs in fast-twitch muscle fibers. The main reason for muscle enlargement is the increase of muscle protein, including the increase of contractile protein. In addition, the amount and strength of connective tissue, tendons, and ligaments surrounding muscle fibers also increase.

Strength training can stimulate insulin secretion; for example, centripetal movement training can increase the sensitivity of muscle cells to insulin stimulation. Centrifugal exercise reduced the sensitivity of muscle cells to insulin stimulation, and this reduction lasted for more than two days after exercise. Metabolic studies have shown that this change is related to the reduction of the glucose transport rate by centrifugal motion, which leads to the slowdown of the glycogen synthesis rate. The sensor designed in this paper observes this feature and completes the monitoring task based on this principle. This temporary insulin resistance and inhibition of glycogen regeneration can lead to hyperinsulinemia, which may increase the rate of myoprotein synthesis.

2.3.2. The Influence of Endurance Training on Protein Metabolism. Endurance training increased the number and volume of mitochondria, as well as the activity of mitochondrial proteins and constituent enzymes. During endurance exercise, arginine stimulates insulin secretion. Aerobic exercise inhibits insulin secretion, increases insulin receptor sensitivity, and improves glucose tolerance. The effect of this movement also affects the metabolism of the body during the quiet state, so that the fluctuation frequency of insulin secretion remains unchanged, while the amount of insulin secretion decreases at each peak. Insulin and amino acids play an important role in controlling the synthesis of muscle protein in local muscles. Reduced insulin secretion caused by starvation reduced the rate of skeletal muscle protein synthesis in animals by more than 50%. The mechanism is related to inhibiting the initiation of protein synthesis and involves the phosphorylation of the translation regulator eukaryotic promoter 4E (EIF-4E) binding protein 1 (4E-BP1). In this process, insulin-like growth factor I (IGF-I) promotes phosphorylation of 4E-BP1 and dissociation of the 4E-Bp1-EIF-4E complex, promoting protein synthesis. Therefore, the decrease of insulin level caused by endurance exercise is one of the mechanisms controlling muscle protein synthesis. This is reflected in the difference of muscle mass between endurance athletes and strength athletes and also reflects the physiological adaptation mechanism of the body to meet the needs of different forms of exercise.

2.4. Endurance Exercise and Protein Metabolism. When the human body carries out physical exercise, the proportion of protein energy supply is generally small, accounting for about 5%–7% of the total thermal energy needs. However, with the gradual depletion of glycogen in exercise, the proportion of protein energy supply also increases correspondingly, and the maximum can rise to about 15% of the total thermal energy needs. It can be seen that the main exercise type that has great influence on protein metabolism is endurance exercise.

During prolonged endurance exercise, the limited sugar reserves in the body are consumed in large quantities and the gluconeogenic pathway of amino acids is activated. After the removal of amino acids, most of the carbon skeleton in the body can enter the tricarboxylic acid cycle or glycolytic metabolism pathway. After oxidation, energy is generated, which can also be converted into glucose to help maintain blood sugar concentration. Among them, alanine and glutamine accounted for about 30% of amino acid isoglucose. In the process of body movement, pyruvate produced by myoglycogen oxidation reacts with amino acids such as lysine to form alanine. In this step, the amino acids that provide amino acids are converted to ketoacids, which enter the aerobic metabolic pathway for oxidative energy supply. The generated alanine enters the blood and is transported to the liver, where it is regenerated into glucose through the glucogenic metabolic pathway of the liver, so as to increase the source of blood glucose in exercise, so it is called alanine glucose circulation. The glucose-generating process of glutamine also has a similar glutamine-glucose cycle.

2.5. The Protein Requirement of Athletes. The diet of athletes must have scientific standards. The protein intake of athletes has a certain relationship with sports, weight, and so on. The same sports, different genders, different weights, and different training intensities have certain standards for protein intake. A nutritionist needs to make a reasonable diet according to the actual situation of the athlete to promote the healthy growth of the athlete. Studies have shown that the daily protein requirement of long-term moderate intensity exercise is 2.5–3.0 /kg body weight. The daily protein requirement of athletes in bunker weight and speed and strength events is 2.4–2.59/kg body weight. The protein requirement of athletes is a general standard, and there are certain differences in the research data of experts and scholars in different industries. Strictly speaking, different athletes have certain differences in protein requirements. Nutritionists need to consume protein reasonably according to the physical condition of athletes, scientifically adjust the physical functions of athletes, and maximize their training effects.

2.6. The Relationship between Protein Metabolism and Exercise

2.6.1. Protein Synthesis. Protein cooperation is related to the intensity of exercise; the greater the intensity of exercise, the slower the protein synthesis. In animal experiments, a fast-running mouse made protein about 70 percent slower than a normal mouse. Therefore, there is a certain relationship between protein metabolism and sports. Athletes synthesize protein more slowly than ordinary people, which plays a certain role in protein maintenance of body functions. Therefore, scientific data must be used to illustrate the relationship between protein and sports.

2.6.2. Oxidation of Amino Acids. Experimental studies by experts show that the oxidation of leucine is enhanced during endurance exercise (its oxidation speed is directly proportional to the intensity of exercise, and the oxidation speed is 5–6 times faster than that at the maximum oxygen uptake). But whether it increases the oxidation of all amino acids remains to be proven. The intermediate metabolism of certain amino acids produces metabolites of the triolic acid cycle, which is good for muscle metabolism during exercise because it increases the oxidation capacity of the trialic acid cycle to the ethylene glycol produced by glucose and free fatty acids. In addition, metabolites of these amino acids are converted to pyruvates by phosphoenol spindle kinase and pyruvate kinase. Increased pyruvate production can lead to increased amino acid oxidation during exercise. The oxidation of amino acids is an important process of the human body. Human life is inseparable from oxygen. Oxygen is an important part of the blood.

2.6.3. Glucogenesis. Sugar is also an important part of the human body; exercise can consume an amount of sugar in the human body, but too much exercise can consume too much sugar, promote human hypoglycemia, and can seriously cause death. Glycosylation of amino acids is increased during exercise. It has been proved that the internal organs' absorption of gluconeoplasms is enhanced during exercise and is proportional to the intensity and duration of exercise. The gluconeogenesis process is a potentially important way to utilize amino acids because it facilitates glucose supplementation and thus prevents hypoglycemia during exercise.

In a word, a man's life is associated with many elements, but the protein is an important element; the human body needs a certain amount of protein a day to maintain body balance; athletes requirements according to the actual situation have effects on protein metabolism of human movement; athletes must have a reasonable intake of protein throughout the day to ensure normal training, which is a key factor in improving athletes' performance.

2.7. Current Situation of Physical Training of Aerobics Athletes in Chinese Colleges and Universities

2.7.1. Lack of Basic Training. Looking at the present, for the aerobics athletes in our country's universities, although they are aerobics athletes, they are not completely the professional first-line members of the aerobics; their aerobics basis and physical health status are not very ideal, and there is also relatively a lack in the physical basic training. As far as the aerobics competition is concerned, the movement is more

difficult. If the athletes feel weak in the second half of the competition, this must be caused by the lack of physical energy reserves of the athletes themselves. Then the coordination of movements may be reduced, and the endurance has a downward trend, which will have a great impact on the range, precision, and difficulty of some movements.

2.7.2. The Combination of Physical Training and Technical Training Is Not Close Enough. During the daily training of aerobics athletes, the coaches only pay attention to whether the athletes have difficult movements but ignore the endurance level of the athletes. In this way, the athletes will spend more time and energy on the training of difficult movements but ignore the training of their own physical strength. For an excellent aerobics athlete, physical training and professional technical training are linked together and are inseparable; for athletes to get good results, skills and tactics training and physical training are essential.

2.7.3. Single Training Content and Lack of Diversity. Chinese aerobics athletes only pay attention to the physical fitness training, such as sensitivity, flexibility, and coordination. If this single-training method is used for a long time, it will cause the separation of technical training and physical training and will eventually affect the performance. However, if, contrary to what has been mentioned above, too much attention is paid to the ability of calisthenics and too little attention is paid to physical training, the same athlete's physique will rapidly decline and ultimately fail to achieve satisfactory results.

2.8. Single-Molecule Detection Method of Protein. Laser-induced fluorescence method refers to irradiating a sample with a laser and then detecting the fluorescence reflection of the sample. It has the advantages of high sensitivity and good selectivity. The chemiluminescence method will detect the chemiluminescence intensity of the sample to show its concentration. It has the advantages of high sensitivity, simple instrumentation, and fast analysis speed. The disadvantages are serious interference and poor photoselectivity.

Biomechanics tools mainly include optical tweezers, magnetic tweezers, and atomic force microscopes.

(1) The optical tweezers method uses a focused laser beam to generate radiation pressure to form an optical trap and realizes molecular manipulation by applying force to the particles in the trap. The schematic diagram is shown in Figure 2.

(2) The magnetic tweezers method observes and analyzes the movement of sample molecules by applying force to magnetized beads in a gradient magnetic field. The schematic diagram is shown in Figure 3.

(3) The atomic force microscopy method investigates the surface structure and properties of sample molecules by detecting the interatomic interaction force between the sample surface and a miniature force-sensitive element. Using the optical detection method or the tunnel current detection method, the position change of the microcantilever corresponding to each scanning point can be measured, so that the information of the surface topography of the sample can be obtained. The schematic diagram is shown in Figure 4.

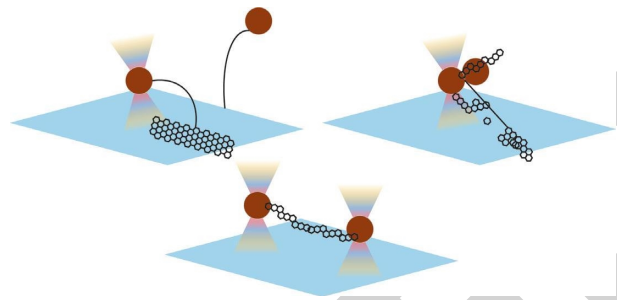

Figure 2: Working principle of mechanical tools for single-molecule detection: optical tweezers.

This section studies the influence of electrolyte solution pH on protein translocation events in pores. The experiment uses BSA molecules as the research object. Bovine serum albumin (BSA), also known as the fifth component, is a globulin in bovine serum. Fitting the curve by the function of molecular time distribution, it can be seen that as the pH of the solution increases, the molecular penetration speed increases accordingly, and the greater the pH of the solution is, the more obvious the molecular penetration speed rises.

Figures 5(a) and 5(b) show the distribution diagram transit time of BSA molecules in two salt solutions with different pH = 6/8/10. It can be found that the via time of BSA molecules increases with the pH of the solution. However, the passage times in the solutions with pH equal to 6 and 8 are similar. The passage time of the latter is slightly shorter than that of the former. The passage time in the solution of pH 10 is significantly better than that in the first two solutions.

3. Protein Metabolism and Requirement of Athletes during Training

3.1. Collection and Processing of Test Samples. In this study, venous blood was collected from the athletes on Monday morning after taking the nutrition for 0, 3, 5, and 7 weeks for a total of 4 times for 7 weeks. The application of physical or chemical methods to remove or inhibit certain coagulation factors in the blood and prevent blood coagulation is called anticoagulation. The subjects prepared EDTA anticoagulation and ordinary vacuum blood collection vessels. 1 ml whole blood was extracted with the EDTA tube, and then 4 ml whole blood was extracted with the ordinary vacuum tube. The EDTA tube was immediately used for blood count in three categories.

3.2. Indicator Testing and Methods. The test indicators used in this study included hemoglobin, red blood cell count, hematocrit, serum iron, serum ferritin, serum transferrin, and serum transferrin receptor.

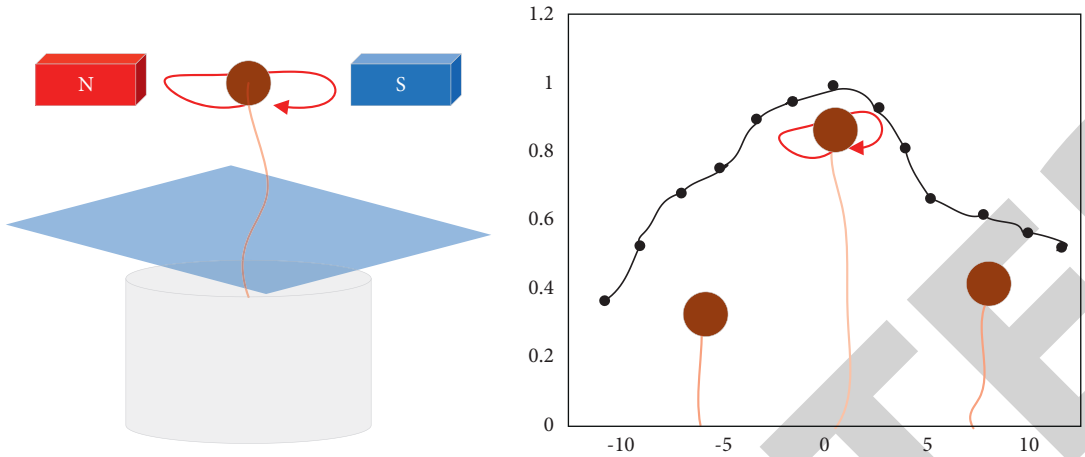

Figure 3: Working principle of mechanical tools for single-molecule detection: magnetic tweezers.

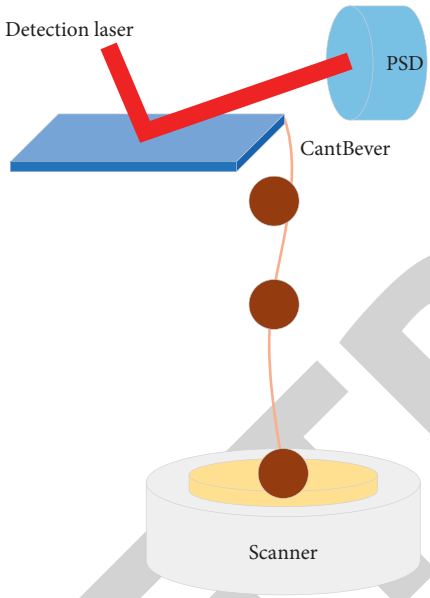

Figure 4: Working principle of mechanical tools for single-molecule detection: atomic force microscope.

3.3. Determination of Serum Ferritin. adding 125I-ferritin to the ferritin standard or sample, it will generate a competitive immune response under a certain amount of specific antibody. The binding amount of ferritin to antibody is related to the ferritin content in standard or sample. After separating the binding part and the free part with immune separating agent, the radioactivity of the binding part was measured and the binding rate was calculated. The serum was provided by the Biotechnology Research Institute. The detection range was 5–320 ng.ml^{-1}, and the detection limit of the cartridge was 2 ng.ml^{-1} for 2 h at 37°C. The intragroup coefficient of variation was less than 4.0%, and the intergroup coefficient of variation was less than 11.9%. The number of pulses within 1 min of the complex was counted on the sn-6958 intelligent counter.

3.4. The Structure Design of the Plantar Pressure Sensor. The plantar pressure sensor is a portable device used to measure the interaction force between the sole of the foot and the shoe during walking. By collecting pressure change data, the pressure measuring shoe can identify and judge the human gait and provide gait for the recognition of human behavior patterns information. In order to calculate the protein consumption and requirements of athletes, an actual picture of production foot pressure measurement shoes was made, as shown in Figure 6.

The purpose of choosing sandals for the shoe body of the measuring shoes is to facilitate the mounting of other hardware and facilitate the subjects to wear in the experiment, while the addition of insoles can protect the sensor and its wiring, enhance the reliability of the system, and increase the comfort of the wearer. The pressure data collection process is shown in Figure 7.

During exercise, people have different tolerances for different parts of the body, as well as different pressure trends. The resistance value of the pressure sensor changes with the change of the pressure received. The pressure measurement circuit board needs a certain method to convert the resistance change signal into an electrical signal, thereby indirectly measuring the pressure value. Pressure sensors are distributed in various parts of the sole of the foot, and the pressure measuring board converts the resistance signal into an analog voltage signal through signal conditioning and then obtains the pressure at each point. The main physical parameters and performance indicators of the membrane pressure sensor are shown in Table 1.

This study requires the subjects to wear measurement equipment for a long period of time to perform different exercises. During the long-term exercise, the soles of the feet are stressed and the periodic motions are frequent. If the membrane pressure sensor is not properly arranged, it is easy to produce measurement points. Problems such as offset and damage to the measurement wire make the measurement data incomplete, incorrect, and incomparable at different times.

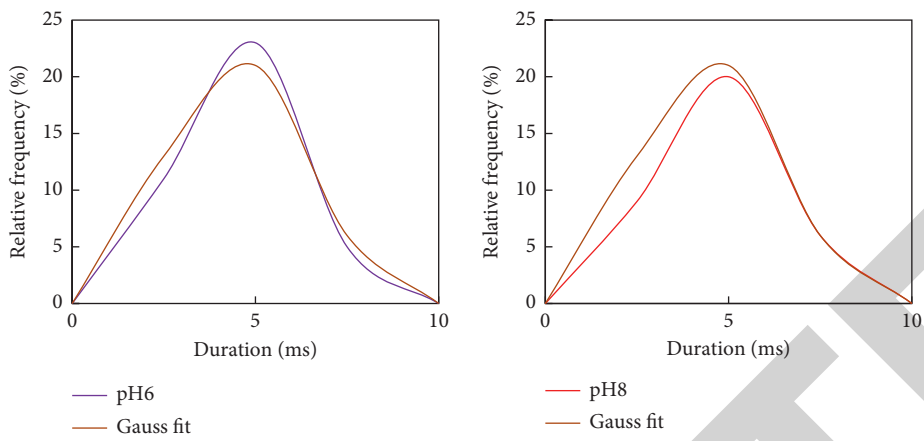

Figure 5: The effect of electrolyte solution pH on protein translocation time.

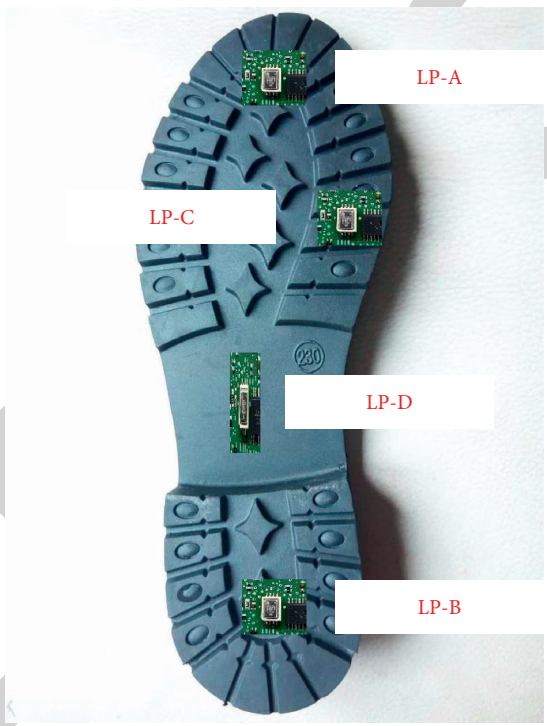

Figure 6: Foot pressure measurement shoe.

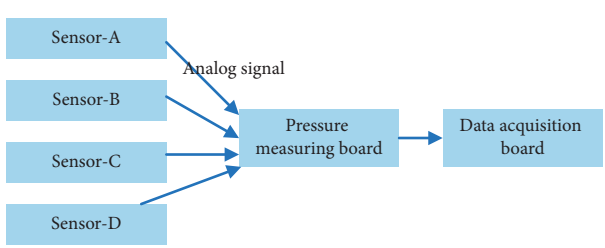

Figure 7: Pressure data collection process.

The foot pressure measurement system adopts a thin film pressure sensor and a piezoresistor as the sensor probe. The varistors are arranged in a matrix. As shown in Figure 8, each thin film pressure sensor can be arranged in the pressure measuring shoe as shown in the figure, and the measuring wire can be bent and arranged to solve this problem.

Table 1: Physical parameters and performance indicators.

Parameter		Unit
Thickness	0.25	mm
Length	26.2	mm
Width	15.1	mm
Induction zone diameter	10.7	mm
Measuring pressure range	0–500	N
Nonlinearity	< ±3%	-
Hysteresis	< ±4.5%	-
Response time	< 5	Us

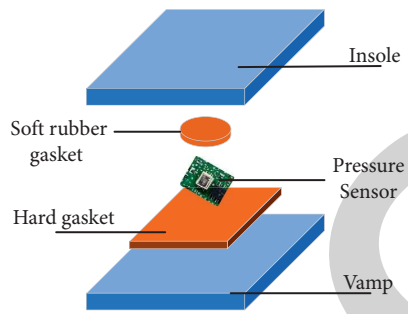

Figure 8: Pressure sensor layout.

4. Study on Protein Metabolism and Requirement of Athletes during Training

4.1. Effect of Protein Nutrition Taken by Aerobics Athletes

(1) A total of 26 female aerobics athletes were selected to participate in the experiment. Among them, 14 female athletes were randomly divided into two groups: sports group (7 with an average training period of 3.4 years) and sports + nutrition group (7 with an average training period of 4.2 years). In addition, 12 female college students (not trained) were also randomly divided into two groups: the quiet control group (6) and the quiet + nutrition group (6). The subjects took protein nutrient solution every day before breakfast. The experiment lasted for 7 weeks. The exercise group trained for 5 days a week (all days except Saturday and Sunday), 3–5 hours a day. During the experiment, no other nutritional health products were used except for normal diet and protein supplements. The changes of hemoglobin before and after the experiment are shown in Table 2 and Figure 9.

(2) According to the data of the aerobics athletes in each group above, compared with week 0, the hemoglobin in the quiet + nutrition group at 5 weeks and 7 weeks increased significantly, and the increase at week 7 was larger, with a very significant difference ($P < 0.01$), and the hemoglobin level increased by 12 g/L. There was no significant increase in 2 weeks ($P > 0.05$). The hemoglobin level in the exercise group decreased significantly at 5 weeks compared with that at 0 or 3 weeks, and there was a significant difference between 5 weeks and 3 weeks ($P < 0.05$). The hemoglobin level decreased by 6 g/L at 5 weeks compared with that at 0 weeks. In the exercise + nutrition group, there was a significant increase in hemoglobin level at weeks 7, 0, or 3, and there was a very significant difference ($P < 0.01$). The hemoglobin level at week 5 was 8.17 g/L higher than that at week 0. There was no significant difference between 5 weeks and 0 weeks or 3 weeks ($P > 0.05$). The hemoglobin levels in the groups are shown in Figure 10.

4.2. Changes in Protein Metabolism before and after the Experiment.

(1) The serum transferrin receptor level in the quiet + nutrition group decreased significantly at 4 weeks, which was significantly different from that at 0 weeks and 3 weeks ($P < 0.01$) and significantly different from that at 7 weeks ($P < 0.05$). In the exercise group, the serum transferrin receptor level increased significantly at week 5, which was significantly different from that of the same group at weeks 0 and 3 ($P < 0.05$), showing that the serum transferrin receptor level at weeks 0 and 3 was significantly lower than that at week 5. There was a significant difference ($P < 0.01$) between week 5 and week 7: the level of serum transferrin receptor at week 7 was far lower than that at week 5. The changes in serum transferrin receptor (Nmol/L) in each group were compared, and specific experimental data are shown in Table 3 and Figure 11.

(2) Serum transferrin receptor levels in the quiet + nutrition group at 5 weeks were significantly lower than those in the same group at 0 weeks and 3 weeks ($P < 0.01$) and those in the same group at 7 weeks ($P < 0.05$). In the

Table 2: hemoglobin level (G/L) among groups.

	Quiet control group (6)	Quiet + nutrition group (6)	Exercise group (7)	Exercise + nutrition group (7)
0 weeks	126.22 ± 6.45	126.23 ± 5.56	127.89 ± 4.34	122.12 ± 3.67
3 weeks	125.23 ± 11.67	133.23 ± 10.34	131.45 ± 12.89	122.89 ± 5.23
5 weeks	132.56 ± 3.18	134.33 ± 4.72	121.89 ± 3.43	126.12 ± 4.83
7 weeks	132.12 ± 4.54	135.66 ± 2.34	124.76 ± 3.36	130.22 ± 2.23

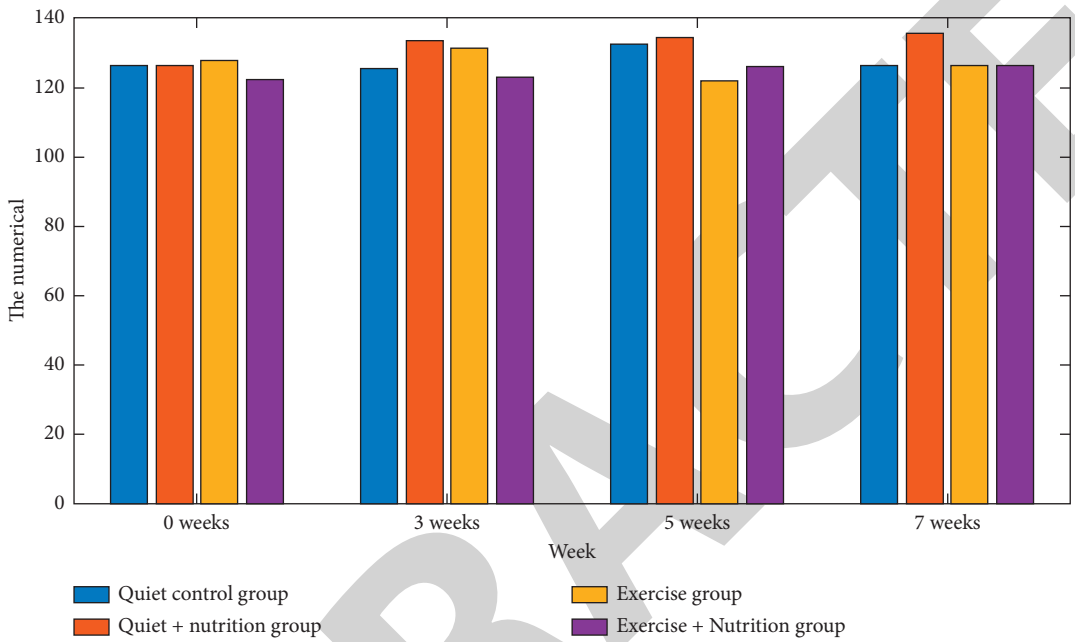

Figure 9: Comparison of hemoglobin level (G/L) among groups.

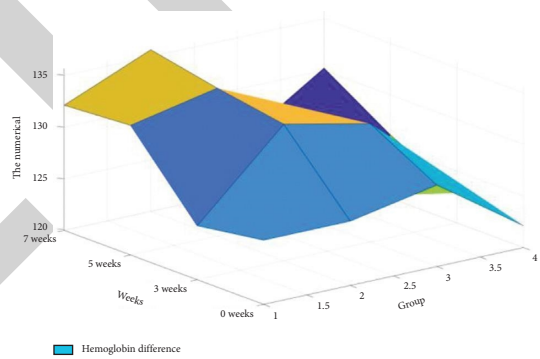

Figure 10: Hemoglobin levels in the groups.

exercise group, the serum transferrin receptor level increased significantly at week 5, which was significantly different from that of the same group at weeks 0 and 3 ($P < 0.05$), showing that the serum transferrin receptor level at week 0 and 3 was significantly lower than that at week 5. There was a significant difference between week 5 and week 7 ($P < 0.01$): the serum transferrin receptor level at week 7 was much lower than that at week 5. Specific data of serum transferrin receptor levels are shown in Figure 12.

Table 3: Comparison of the changes of serum transferrin receptor (Nmol/L) in each group.

	Quiet control group (6)	Quiet + nutrition group (6)	Exercise group (7)	Exercise + nutrition group (7)
0 weeks	14.65 ± 0.57	14.66 ± 0.53	14.38 ± 0.56	14.33 ± 0.56
3 weeks	14.86 ± 0.42	14.54 ± 0.57	14.45 ± 0.56	14.65 ± 0.57
5 weeks	14.54 ± 0.56	13.19 ± 0.42	15.33 ± 0.54	14.33 ± 1.20
7 weeks	14.68 ± 0.55	14.52 ± 0.89	14.23 ± 0.92	14.27 ± 1.39

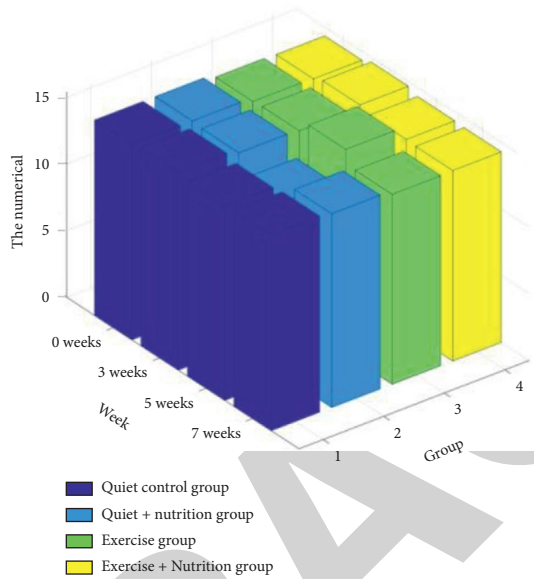

Figure 11: Comparison of the changes of serum transferrin receptor (Nmol/L) in each group.

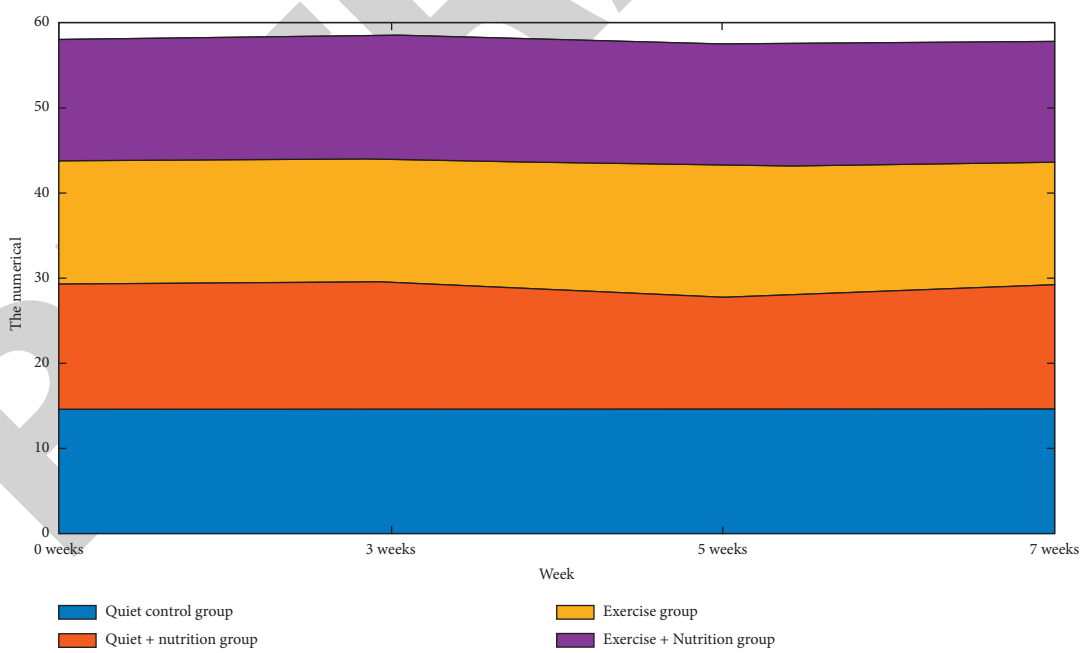

Figure 12: The specific data of serum transferrin receptor levels.

5. Conclusion

(1) To participate in aerobics exercise for a long time, after heavy load exercise training, the body protein is consumed in large quantities, may accompany the phenomenon of appetite decline, and should be in the normal diet on the basis of an appropriate amount of exogenous protein supplement. For example, in order to delay the central fatigue caused by endurance exercise, in addition to scientific control of exercise load, and gradually produce biological adaptation, exogenous supplement of branched-chain amino acids can have a good recovery effect on the body. However, the supplement of branched-chain amino acids is not the more the better. Since a large dose of branched-chain amino acids can lead to the increase of blood ammonia, which may lead to hepatic encephalopathy, the supplement of branched-chain amino acids is often combined with the supplement of sugars, which can simultaneously reduce the fatty acids produced by fat decomposition and the decomposition of branched-chain amino acids.

(2) According to the research in this paper, proteins are the main components that form cell structures and are biochemical catalysts and important regulators of gene expression. Any life activity of human body cannot leave the function of protein. Especially when the body is in a state of heavy exercise load and competition, the consumption of athletes increases, and the protein in the body will be catabolized. Providing high-quality protein and amino acid nutrition can supplement the function loss of athletes, enhance muscle strength, and promote hemoglobin synthesis, which is of great significance for accelerating the elimination of fatigue.

(3) Amino acids and proteins are important for aerobics athletes, but a large amount of high-protein diet harms the body. First, in the process of consuming a high-protein diet, once the protein exceeds the need, it is stored in the form of fat, which directly or indirectly increases blood cholesterol, triglyceride, and LDL levels, as well as HDL and long-term consumption of high-protein foods increases the incidence of hypertension, coronary heart disease (CHD), and atherosclerosis. The results showed that the serum transferrin receptor level in the quiet + nutrition group decreased significantly after 4 weeks, which was significantly different from that of the same group at 0 weeks and 3 weeks ($P < 0.01$) and significantly different from that of the same group at 7 weeks ($P < 0.05$). In the exercise group, the serum transferrin receptor level was significantly increased at week 5, which was significantly different from that of the same group at weeks 0 and 3 ($P < 0.05$), showing that the serum transferrin receptor level at weeks 0 and 3 was significantly lower than that at week 5.

(4) This article focuses on the transition from the detection of a single-protein molecule to protein interaction. First, it explores the basic physical properties of a single-protein molecule and the transport of a single-protein molecule in a confined nanopore and then develops antigen and antibody specificity. Based on the characteristics of human plantar pressure data collected by multisensor fusion technology, this paper designs a set of dynamic recognition algorithms for monitoring key gait events and monitors key protein information of athletes.

Data Availability

No data were used to support this study.

Conflicts of Interest

The authors declare that there are no conflicts of interest with any financial organizations regarding the material reported in this manuscript.

Acknowledgments

This work was supported by the National Key R&D Program of China (2019YFF0301805).

References

[1] N. Demirci and M. A. Ziyagil, "Effects of quercetin supplementation on lipid and protein metabolism after classic boxing training," *Journal of Education and Training Studies*, vol. 5, no. 4, p. 74, 2017.

[2] C. N. Matias, D. A. Santos, P. B. Júdice et al., "Estimation of total body water and extracellular water with bioimpedance in athletes: a need for athlete-specific prediction models," *Clinical Nutrition*, vol. 35, no. 2, pp. 468–474, 2016.

[3] N. Smit and D. Goodyear, "Tilikum crossing, bridge of the people," vol. 50, pp. 46–44, 2016.

[4] B. Crouse and R. N. Golden, "A strategic approach to addressing the rural Wisconsin physician shortage," *Wisconsin Medical Journal : Official Publication of the State Medical Society of Wisconsin*, vol. 115, no. 4, pp. 210-211, 2016.

[5] W. K. Mitchell, D. J. Wilkinson, B. E. Phillips, J. N. Lund, K. Smith, and P. J. Atherton, "Human skeletal muscle protein metabolism responses to amino acid nutrition," *Advances in Nutrition An International Review Journal*, vol. 7, no. 4, pp. 828S–838S, 2020.

[6] H. Astrid, O. D. Steven, S. Annemie, and V. L. Luc, "Is cancer cachexia attributed to impairments in basal or postprandial muscle protein metabolism?" *Nutrients*, vol. 8, no. 8, p. 499, 2016.

[7] T. Ren, Y. Zhu, X. Xia, Y. Ding, J. Guo, and J. Kan, "Zanthoxylum alkylamides ameliorate protein metabolism disorder in stz-induced diabetic rats," *Journal of Molecular Endocrinology*, vol. 58, no. 3, pp. 113–125, 2017.

[8] G. N. Marzuca-Nassr, K. F. Vitzel, L. G. D. Sousa et al., "Effects of high epa and high dha fish oils on changes in signaling associated with potein metabolism induced by hindlimb suspension in rats," *Physiological Reports*, vol. 4, no. 18, p. 1, 2016.

[9] A. A. Cassidy, R. J. Saulnier, S. G. Lamarre, and J. V. Planas, "Adjustments of protein metabolism in fasting arctic charr, *Salvelinus alpinus*," *Plos One*, vol. 11, no. 4, Article ID e0153364, 2016.

[10] D. C. M. Simoes and I. Vogiatzis, "Can muscle protein metabolism be specifically targeted by exercise training in

Hindawi
Journal of Healthcare Engineering
Volume 2023, Article ID 9834896, 1 page
https://doi.org/10.1155/2023/9834896

Retraction

Retracted: Contrast Agent and Molecular Imaging Meta-Analysis of the Clinical Effect of Intelligent Image Sensor Combined with Visual Training in the Treatment of Children with Intermittent Exotropia in China

Journal of Healthcare Engineering

Received 10 October 2023; Accepted 10 October 2023; Published 11 October 2023

This article has been retracted by Hindawi following an investigation undertaken by the publisher [1]. This investigation has uncovered evidence of one or more of the following indicators of systematic manipulation of the publication process:

(1) Discrepancies in scope
(2) Discrepancies in the description of the research reported
(3) Discrepancies between the availability of data and the research described
(4) Inappropriate citations
(5) Incoherent, meaningless and/or irrelevant content included in the article
(6) Peer-review manipulation

The presence of these indicators undermines our confidence in the integrity of the article's content and we cannot, therefore, vouch for its reliability. Please note that this notice is intended solely to alert readers that the content of this article is unreliable. We have not investigated whether authors were aware of or involved in the systematic manipulation of the publication process.

Wiley and Hindawi regrets that the usual quality checks did not identify these issues before publication and have since put additional measures in place to safeguard research integrity.

We wish to credit our own Research Integrity and Research Publishing teams and anonymous and named external researchers and research integrity experts for contributing to this investigation.

The corresponding author, as the representative of all authors, has been given the opportunity to register their agreement or disagreement to this retraction. We have kept a record of any response received.

References

[1] H. Sun, S. Bai, R. Liao, and A. Han, "Contrast Agent and Molecular Imaging Meta-Analysis of the Clinical Effect of Intelligent Image Sensor Combined with Visual Training in the Treatment of Children with Intermittent Exotropia in China," *Journal of Healthcare Engineering*, vol. 2022, Article ID 5387928, 12 pages, 2022.

Hindawi
Journal of Healthcare Engineering
Volume 2022, Article ID 5387928, 12 pages
https://doi.org/10.1155/2022/5387928

Research Article

Contrast Agent and Molecular Imaging Meta-Analysis of the Clinical Effect of Intelligent Image Sensor Combined with Visual Training in the Treatment of Children with Intermittent Exotropia in China

Haonan Sun,[1] Shimiao Bai,[2] Rujuan Liao,[3] and Aijun Han[3]

[1]*Chinese Medicine Ophthalmology, Hebei University of Chinese Medicine, Hebei Provincial Hospital of Traditional Chinese Medicine, Shijiazhuang 050000, Hebei, China*
[2]*Chinese Medicine Ophthalmology, Hebei Provincial Hospital of Traditional Chinese Medicine, Shijiazhuang 050000, Hebei, China*
[3]*Strabismus and Pediatric Ophthalmology, Hebei Eye Hospital, Hebei Provincial Key Laboratory of Ophthalmology, Hebei Provincial Clinical Research Center for Eye Diseases, Xingtai 054000, Hebei, China*

Correspondence should be addressed to Aijun Han; hajjunge@126.com

Received 23 December 2021; Accepted 15 February 2022; Published 12 March 2022

Academic Editor: Mu-Yen Chen

At present, the main treatment for strabismus is still surgical treatment, but there is no unified standard for the evaluation of the timing of surgery. This study mainly explores the clinical effects of using meta-analysis of intelligent image sensors combined with visual training to treat children with intermittent exotropia. Cochrane systematic reviews collect, evaluate, and synthesize an increasing number of original clinical research results to obtain the comprehensive effect of relevant interventions, so as to provide real and reliable evidence for health decision-making and clinical practice. It uses scientific, clear, and reproducible research methods to reduce the influence of biased factors, so it is different from traditional reviews. Cochrane systematic reviews are especially suitable for certain interventions when the pros and cons of interventions are difficult to determine based on the results of a single clinical study or when there are large differences in the clinical application process. Poor quality systematic reviews can mislead policymakers and clinicians. In the meta-analysis, the Cochrane systematic evaluation method of evidence-based medicine was used to comprehensively search the published literature research on the treatment of intermittent exotropia with vision training. Using the Cochrane system evaluation method, computer search of CENTRAL, MEDLINE, Embase, Chinese Biomedical Literature Database, Chinese Journal Full-text Database, manual retrieval of relevant conference documents, and inclusion of all clinical trial documents of visual training in children with intermittent exotropia was conducted. Patients with intermittent exotropia were selected, simultaneous vision, fusion function, and far stereo vision with the same vision machine were measured, and near stereo vision with a stereo vision chart was measured. The number of simultaneous vision, fusion function, and distance and near stereo vision "with" and "without" cases were recorded for all patients, and the relationship with age of onset, type of strabismus, degree of strabismus, and degree of control was counted. Among them, 91 patients who underwent strabismus correction surgery were followed up for at least 6 months with correct eye position. The presence or absence of simultaneous vision, fusion function, far stereo vision, and near stereo vision were recorded and compared with preoperative. The number of recovery and nonrecovery cases was recorded, and the relationship between the age of operation, the type of strabismus, the degree of strabismus, and the degree of control was counted. It was statistically analyzed by SPSS22.0. The results of the meta-analysis showed that in terms of the effective rate of fundus lesions, the visual training group was better than the nontraining group, and the difference between the two groups was statistically significant (RR = 1.32, 95% CI: (1.25, 1.40), $P < 0.0001$). This study provides guidance for the early rehabilitation of children with intermittent exotropia.

1. Introduction

Due to the rapid development of children's visual function, most scholars believe that early intervention in the treatment of eye position will achieve a more ideal correction effect, especially for the far stereo effect before surgery. This will help restore the visual function of the binocular and achieve a more ideal result, so the treatment of strabismus is imminent.

The image sensor plays a key role in visual restoration. This study shows that in addition to reasonable surgical treatment, the maintenance of the third-level visual function of the binocular also plays a key role. The detailed inspection of the three-level visual function before the operation and postoperative training can predict the long-term surgical effect.

High-resolution image sensors can be easily used. Due to the daily use of cameras, microphones, and smart devices, the improvement of wireless interactive media sensor networks has been greatly improved. Seo *D* believes that oil spills in the oceans. He developed an oil spill point test device (SOPD), and the performance of the device was proved [1]. Nweke HF believes that the human activity recognition system was developed as part of a framework that can continuously monitor human behavior in the fields of environmental assisted living. His focus is an in-depth summary of deep learning methods. He introduced the characteristics, advantages, and limitations of the method. He not only divided the research into generative methods and differentiated methods. In addition, the review proposed classification and evaluation procedures, and discussed public data sets for the recognition of human activity by mobile sensors. Finally, he outlined and explained some of the challenges of improvement [2]. Ramesh S believes that the secure multihop routing mechanism in the surveillance area can be incorporated into a multimedia sensor that can read detection data composed of recorded images and videos. In addition, the method enables him to predict and fight against malicious, untrustworthy, defective nodes. Compared with the current trust model used for wireless video sensor network security, the proposed trust decision model has improved reliability, flexibility, and low memory [3]. Ho A J believes that evaluating the relationship between the first overcorrection of patients with exotropia and the success of long-term surgery. The records to determine the preoperative stereoscopic acuity deviation and the postoperative stereoscopic acuity deviation are analysed. The follow-up interval is as follows: 1 year and 2 years. He used analysis of variance to compare the demographic data of each group and the angle of deviation before and after surgery. A statistically significant difference in the deflection angle after remote fixation in each group (all comparisons were $P < 0.003$). The outflow of group A 2 years ago was greater than that of group B. Among the patients who were initially overcorrected [4], Huh J retrospectively analyzed the medical records of 237 patients undergoing strabismus surgery. Age, gender, preoperative deflection, inhibition state, and near stereopsis were investigated. The inhibition state is divided into no inhibition, alternating inhibition, or continuous inhibition. At the last visit, the target motion alignment was external deviation or an internal deviation of 2 PD. The average age of surgery was 8.2 ± 3.2 years, and these patients respectively showed no inhibition, alternating inhibition, or sustained inhibition. The preoperative exotropia angle of all 12 patients was greater than 20 pd. Most patients undergoing intermittent exotropia surgery have achieved successful movement alignment and fusion after surgery. However, when the preoperative exotropia angle is greater than 20 pd, successful motion correction cannot guarantee the recovery of inhibition. The preoperative factors and functional effects he discovered are still unclear and are worthy of further study [5]. The stability of the child's eye position is not controlled. The presurgery examination requires a combination of strabismus and visual function. This is not only a guideline for surgery, but also a basis for predicting long-term changes in eye position after surgery and for training and recovery of postoperative functions. In order to achieve the ultimate goal of functional cure, first a detailed and comprehensive examination of the eyes must be carried out before the operation, especially the examination of the binocular function. Second, we must choose a reasonable and effective surgical method, and guide the functional rehabilitation training through a binocular function examination after the operation.

Clinically, there are many factors that affect the binocular vision development of patients with intermittent exotropia, including the age of the patient, the type of strabismus, the degree of strabismus, and the degree of control. Observing the relationship between various factors and binocular vision development and recovery is of great significance for judging the severity of the condition of patients with intermittent exotropia, choosing the appropriate timing of surgery, and guiding clinical work. In this study, the binocular vision training of patients after strabismus correction using a home-use synoptic machine was used to observe the binocular visual function rehabilitation of patients after strabismus correction and to explore effective treatment methods for improving or rebuilding binocular visual function after strabismus correction.

2. Intelligent Image Sensor Combined with Visual Training to Treat Children with Intermittent Exotropia

2.1. Types and Standards. All clinical controlled trials on visual sensors, visual training, and intermittent exotropia published and unpublished from 2017 to November 2020 at home and abroad. Helicoptia (including internal and external strabismus) and other types of strabismus were not included in this study. The cases in this group were all from the hospital from January 1, 2017 to December 31, 2020, when they were diagnosed with intermittent exotropia in children and admitted to the hospital for strabismus correction. The medical history of the children in this group is relatively complete. There is no history of strabismus treatment, no AV sign, no obvious vertical strabismus, nystagmus, normal eye movements, stable fixation in both

eyes, and no other ocular symptoms. There are no other systemic diseases and mental disorders. The operating age of the children was 3–16 years old, with an average age of 8.66 years.

2.1.1. Selection Criteria

(1) Children with intermittent exotropia who underwent strabismus correction surgery in the hospital from July 2017 to August 2019 were included, and all children who underwent strabismus correction surgery for the first time. All children who have no A-V signs, who are not accompanied by vertical dissociative strabismus and nystagmus, and have normal binocular movement. Those who are generally in good condition, without diabetes, high blood pressure, cardiovascular disease, blood system disease, and no mental disorders.

(2) The timing of surgery for intermittent exotropia: when the child or the child's family notices that the eye position is too frequent or the angle is too large, conservative treatment will not be effective; the eye position control score of the child has reached the surgical index, and the eye position control ability grading based on office examinations by Mohney and Holmes was used, and general control ability above level 3 requires surgical treatment; the binocular vision function is impaired, and the squint is at least > -15△.

2.1.2. Exclusion Criteria. The exclusion criteria were as follows: those who are accompanied by organic ocular diseases; obvious abnormal eye movements; accompanied by nystagmus or other types of strabismus; a past medical history of strabismus correction; a past medical history of premature delivery and fetal dysplasia; and those whose medical record data collection is incomplete.

2.2. Binocular Vision Training on the Synoptic Machine. Synoptic binocular fusion training: adjusting the position of the mandibular platform and the distance between the pupils according to different examiners, and adjusting the positions of the lens tubes on both sides to zero. Simultaneous visual function inspection: using the tiger cage picture (10°) to check the simultaneous visual function. The side of the mirror is simply fixed. The examiner can adjust the position of the side mirror hose of the squint eye and put the tiger into the cage. The degree at this time is the degree of conscious strabismus, and the record is regarded as "have" at the same time; then, the light source can be turned on alternately until there is no eye movement in the eyes, and the degree at this time is the objective strabismus degree. When the examiner has simultaneous vision, replace the flower butterfly picture (10°) to check the fusion function, and the person who can integrate the two pictures into a complete picture is recorded as "Yes." On the basis of the existence of the fusion function, replace the random spot picture to check the distance stereo vision, and record the result as "Yes" or "No." Simultaneous vision, fusion function, and distance stereo vision before and after the operation were recorded as "recovery", and those with no function after the operation were recorded as "no recovery". The binocular vision training of the synoptic machine is shown in Figure 1.

In the meta-analysis, the effect size presented by the initial research may not be exactly the same as that required by the meta-analysis, which requires proper conversion of those effect sizes that are inconsistent with the meta-analysis to meet the requirements of the meta-analysis [6, 7].

$$\mathrm{OR} = \left(\frac{a}{b}\right)\left(\frac{c}{d}\right) = \frac{ad}{bc}. \tag{1}$$

The quantitative variables were as follows: weighted mean difference (WMD), standardized mean difference (SMD), and Hedges' g. Take Hedges'g calculation as an example [8].

$$\begin{aligned} SMD &= \frac{(\overline{X}_1 - \overline{X}_2)}{S}, \\ \text{Hedges}'\, g &= \mathrm{SMD} * J, \\ J &= 1 - \left[\frac{3}{4} * (N_1 + N_2 - 3)\right]. \end{aligned} \tag{2}$$

$\overline{X}_1$ is the mean of the case group. $\overline{X}_2$ is the mean of the control group [9, 10].

Convert the log odds ratio into a standardized mean difference [11].

$$\begin{aligned} \mathrm{SMD} &= \lg \mathrm{OR} \times \frac{\sqrt{3}}{\pi}, \\ V_R &= \frac{3}{\pi^2} \times V_R. \end{aligned} \tag{3}$$

lgOR is the logarithmic ratio [12, 13].

Convert the standardized mean difference to the log odds ratio [14].

$$\begin{aligned} \lg \mathrm{OR} &= \mathrm{SMD} * \frac{\lambda}{3}, \\ V_{\mathrm{OR}} &= V_{\mathrm{SMD}} * \frac{\lambda^2}{3}. \end{aligned} \tag{4}$$

Convert the correlation coefficient into a standardized mean difference (SMD) [15, 16].

$$\begin{aligned} \mathrm{SMD} &= \frac{2}{\sqrt{1 - R^2}}, \\ V_{\mathrm{OR}} &= \frac{4V}{(1 - R)^3}. \end{aligned} \tag{5}$$

Extract research data according to standardized tables. When different researchers get different data, they can resolve disputes through discussion and negotiation and reach consensus and unanimous opinions. Research features and data extraction information are mainly the year of

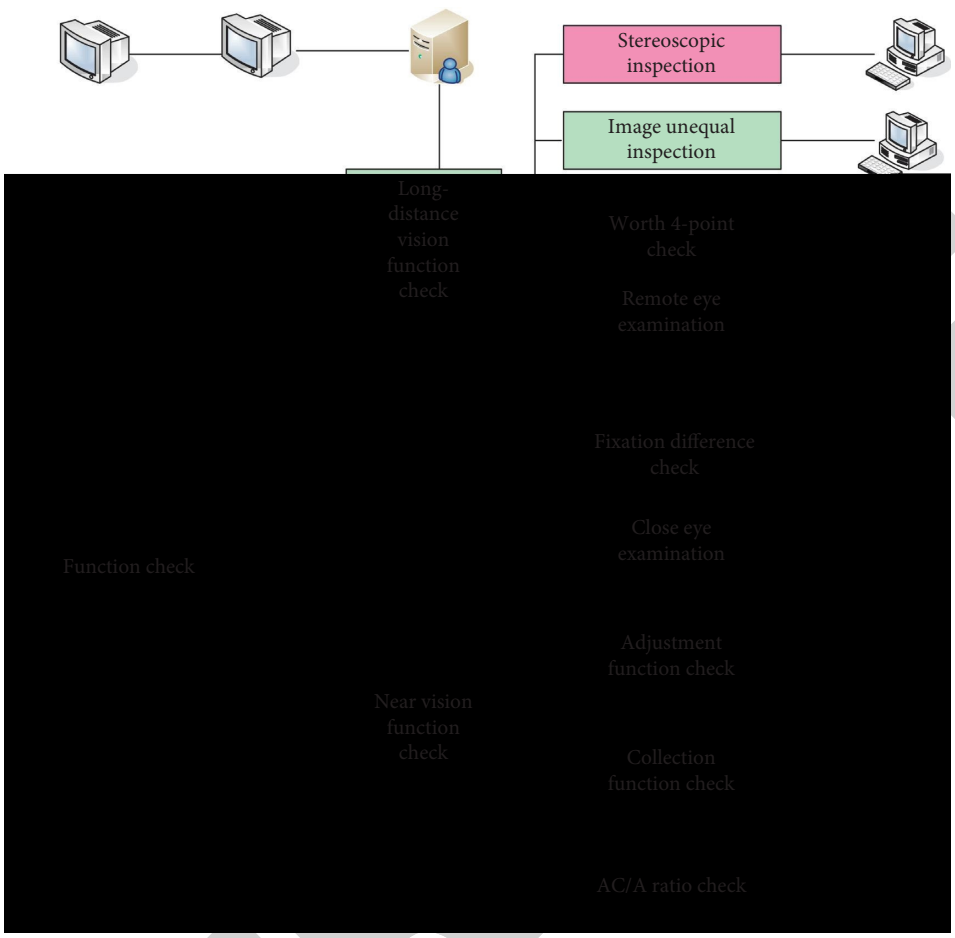

Figure 1: Binocular vision training on the same vision machine.

publication of the paper, the country or region, the size of the sample of patients included in the study, age composition, sex ratio, and prevalence. The correlation coefficient is as follows [17]:

$$R = \frac{\text{SMD}}{\sqrt{\text{SMD}^2 + A}}. \tag{6}$$

A is the parameter related to the sample size n_1, n_2 of the two sets of data in the correlation analysis [18, 19].

The simplest random effects meta-regression model is as follows [20]:

$$Y_{\text{i}} = \chi + \alpha + \beta. \tag{7}$$

Among them, random effect α satisfies $E(\alpha) = 021, 22$.

The general form of the random effect (or mixed effect) meta-regression model can be written as follows [23]:

$$Y_{\text{i}} = \text{x}\chi^T + \alpha_i + \beta_i. \tag{8}$$

2.3. Examination of Double Heel Fusion Function Reconstruction before and after Common Strabismus. Check items of binocular fusion function after operation: Bagolini linear inspection, Worth four-point light inspection, Titmus inspection, and Yan Shaoming digital stereo vision inspection chart.

2.3.1. Inspection Method

(1) Routine ophthalmological examination: uniformly uses the international standard visual acuity chart to check naked vision and corrected vision (5 m), slit lamp, and ophthalmoscope examination.

(2) Eye movement examination: place the point light source 0.5 m in front of the patient's eyes and observe the patient's eye movements in 9 directions. If an abnormality is found, cover one eye and observe the eye movement of one eye to rule out paralytic and restrictive exotropia.

(3) Strabismus degree measurement: cover the patient's single-eye IH before each measurement to destroy its fusion function to obtain an accurate strabismus degree. The inspection method is corneal reflection, triangular prism + alternate covering method: alternately covering and not moving, record the angle of the triangular prism at this time. When the degree of strabismus is large, try not to superimpose the prism on the single eye and place it in front of both

eyes. If the patient has refractive errors, it is performed with corrective glasses.

(4) Control score: according to the Mohnry score, control is divided into 0–5 levels. Class 3 and below are recorded as the good control group, and 3 and above are recorded as the poor control group. At least two assessments are performed for each patient, and the assessment will be performed again when the difference between the two is large.

(5) Simultaneous vision, fusion function, and distance stereo vision were checked by the same vision machine, and the near stereo vision was measured by Yan Shaoming's stereo vision chart.

Q test (Cochran's Q) is a common statistical method, its essence is χ^2 test [24, 25].

$$Q = \sum_{i=1}^{n} W_i (Y - M). \tag{9}$$

The calculation formula of I^2 is as follows:

$$I^2 = \frac{(Q - DF)}{Q}. \tag{10}$$

The value of I^2 is between 0 and 1.

On the statistic Q, estimation can be obtained

$$H = \sqrt{\frac{Q}{(K-1)}}, \tag{11}$$

where K is the corresponding number of individuals.

$$\phi_L^2 = \frac{\sum_i w (y - \overline{y})^2 - (n-1)^2}{\sum_i w - \sum_i w^2 / \sum_i w}. \tag{12}$$

Among

$$\overline{y} = \frac{\sum_i w y}{\sum_i w}. \tag{13}$$

For a given κ, the estimate of γ is as follows:

$$\gamma(\kappa^2) = \frac{\sum_i w_i (\phi^2) y}{\sum_i w_i (\gamma^2) y}. \tag{14}$$

2.4. Strabismus Screening

(1) Preliminary screening: 2 ophthalmologists who have been trained in eye position examinations are responsible for the preliminary screening. The first eye position, corneal reflection method (33 cm), covering-uncovering (gazing at 33 cm, 6 m), and alternate covering were adopted to determine the patients with intermittent exotropia.

(2) Confirmation: when the two judges agree that the eye position is abnormal or the two judges are inconsistent, the deputy chief physician of the same strabismus specialist will review and confirm. Using the corneal reflection method (33 cm), cover-uncover (watch at 33 cm, 6 m), alternate cover, eye movement inspection, prism, linear mirror, etc.

2.5. Anterior Segment and Fundus Examination. 2 attending ophthalmologists used slit lamps (Shangbang Medical Equipment Co., Ltd., LS-6) to check the conditions of the outer eyes, conjunctiva, cornea, anterior chamber, iris, pupil, and lens of both eyes. Using a direct ophthalmoscope (Vision Technology, YZ6E) to check the vitreous body and fundus (optic disc, macula, blood vessel, retina, etc.) of both eyes, and record abnormal results in detail.

Binocular vision function check:

(i) Four-hole lamp: usually checked in a dark room. After instructing the patient to wear red on the left and green on the right, they sit 5 meters away from the four-hole lamp (there is a distance of 1 meter) and light the four-hole light source.

(ii) Titmus stereo vision inspection chart: the principle is to use a polarizer to observe the polarized light stereogram to determine stereo vision, and its false negatives are high. The principle is to use two-color filters to display three-dimensional graphics.

2.6. Meta-Data Analysis. Meta-analysis data and publication bias analysis were completed using the software RevMan 5.3, Meta-Disc 1.4, and Stata14.0. Relative risk (RR) and its 95% CI were used. X^2 test was used to analyze the heterogeneity between the studies ($P < 0.1$ as the test level) [26, 27]. When I^2<50%, there is a low possibility of heterogeneity, and the fixed effects model is adopted; I^2 is between 50% and 100%, and there is a substantial possibility of heterogeneity. When there is a table value of 0 in the four grid tables, add 0.5 to correct the calculation. In the four-grid table, when a study contains two tables with a value of 0, the article and the study are excluded. The meta-data analysis method is shown in Figure 2 [28, 29].

Using weighted least squares estimation or maximum likelihood estimation, the regression coefficient β can be estimated as follows:

$$\beta(\chi^2) = \left(X^T V^{-1}\right)^{-1} \left(X^T V^{-1} (\gamma^2)\right)^{-1} Y. \tag{15}$$

Among

$$X = \left(x_1^T, \ldots, x_i^T\right). \tag{16}$$

The data deletion diagnostic statistics based on the likelihood function are as follows:

$$LD(\delta) = 2[L(\theta|Y) - G(\theta|Y)]. \tag{17}$$

Where $L(\theta|Y)$ represents the likelihood function based on the observation data Y and the parameter θ.

The standard linear model has the following form:

$$Y = X\chi + \phi. \tag{18}$$

The estimate that the least squares estimation method knows is as follows:

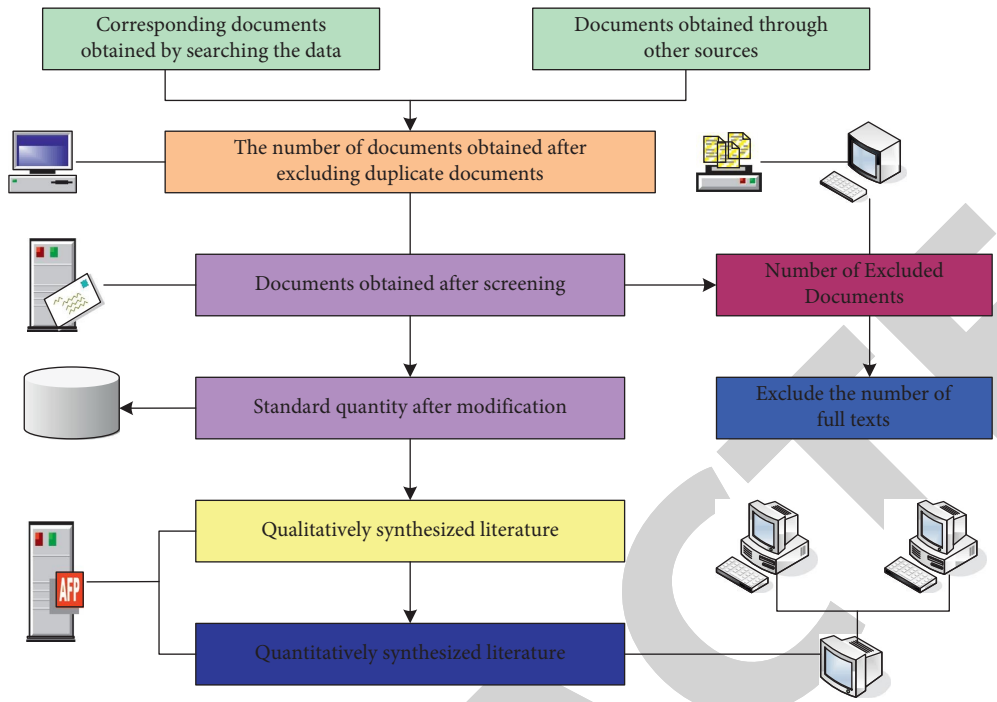

Figure 2: Meta-data analysis method.

$$\hat{\phi} = \left(X^T X\right)^{-1} X^T Y. \tag{19}$$

The number of people alive and at risk in the t-th interval $(t-1, t)$ is as follows:

$$\begin{aligned} R(t) &= R(t-1) - D(t-1) - C(t), \\ R_N(t) &= R_N(t-1) - D_N(t-1), \end{aligned} \tag{20}$$

where $R_N(t-1)$ is the number of surviving and at-risk populations in the time interval $(t-2, t-1)$.

2.7. Statistical Processing. The data are represented by the average value ± standard deviation. The comparison between the measurement data groups is by t-test, and the comparison between the count data is represented by X^2. When $P < 0.05$, the statistics between groups are meaningful.

3. Meta-Analysis Results of Clinical Effects in Children

The patients in this study had an operating age of 0–13 years old, and the development of binocular monocular function was basically mature at about 9 years old. A total of 69 cases were reported, of which 38 cases were orthotopic. The comparison of different ages is shown in Table 1.

There were 103 patients in this study. The course of disease was (39.22 ± 26.07) months. They were divided into 2 groups according to the course of disease ≤ 3 years and >3 years, $P = 0.043 < 0.05$, the difference was statistically significant. The comparison of disease course is shown in Table 2.

Table 1: Comparison of different ages.

Operating age	Eye position at last follow-up		Total
	≤±8PD	>±8PD	
0-5month	38 (55.1%)	31 (44.9%)	69
6–12month	18 (52.9%)	16 (47.1%)	34
Total	56 (54.4%)	47 (45.6%)	103

Table 2: Comparison of disease course.

Course of disease	Eye position at last follow-up		Total
	≤±8PD	>±8PD	
≤3 years	35 (63.6%)	20 (36.4%)	55
>3 years	21 (43.75%)	27 (56.25%)	48
Total	56 (54.4%)	47 (45.6%)	103

Preoperative Worth 4-point fusion function test results: there were 15 cases with mid-to-long-term ocular alignment, 40 cases with mid-to-long-term ocular alignment, and 42 cases with undercorrection or overcorrection. The results of the Worth 4-point fusion function inspection are shown in Table 3.

Figure 3 shows the distribution of the stereoscopic acuity of patients before and after surgery. In group A, 18.8% (3/16) had better stereo vision after operation than before operation, and 42.2% (19/45) in group D had better stereo vision after operation.

Comparison of binocular fusion function before and after operation the comparison of binocular fusion function in patients with intermittent exotropia before and after ocular position correction is shown in Table 4.

Table 3: Worth 4-point fusion function inspection results.

Worth 4 points before surgery	Eye position at last follow-up		Total
	≤±8PD	>±8PD	
Normal	15 (75.0%)	5 (25.0%)	20
Abnormal	40 (48.8%)	42(51.2%)	82
Total	55 (53.9%)	47(46.1%)	102

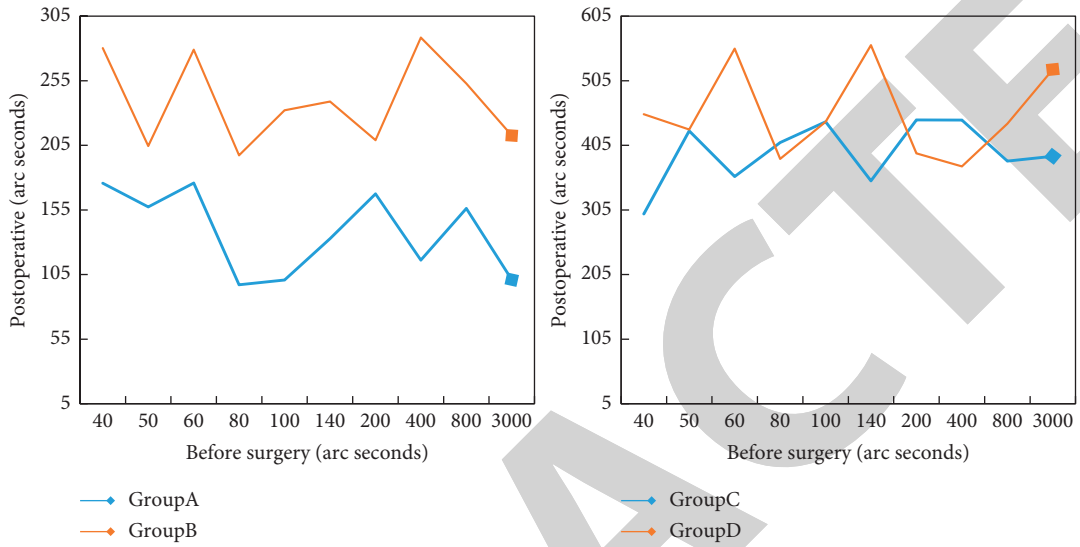

Figure 3: The distribution of stereoscopic acuity of patients before and after surgery.

Table 4: Comparison of binocular fusion function in patients with intermittent exotropia before operation and after eye position correction.

Preoperative	Postoperative		
	Central fusion	Peripheral fusion	No fusion
Central fusion	22	0	22
Peripheral fusion	28	11	40
No fusion	26	12	52
Total	76	23	114

The scores of each item of Child IXTQ (children's self-evaluation form) in the strabismus group were lower than those in the normal control group. The comparison of the strabismus group and the normal control group such as item 1 "Worry about eye problems" (51.84 ± 27.08 vs. 70.83 ± 31.19), item 2 "Close one eye under strong light, it will feel very annoying" (62.50 ± 32.46 vs. 85.61 ± 24.04), which has a significant difference ($P < 0.05$). Figure 4 shows the statistics of parents' doubts about their children.

In the Proxy IXTQ, Parent IXTQ score, and Parent IXTQ surgical dimension scores in the synoptic hypertropia group ($P < 0.05$). Further comparison Proxy and IXTQ: Group A vs. Group C ($P = 0.012$); parent IXTQ, among the surgical dimension, which the difference was significant and statistically significant. The quality of life of IXT with large strabismus at a distance is lower than that of small strabismus. Among them, parents' concerns about their children, especially the worry about surgery, are significant. Figure 5 shows the statistical scores of the different distance visual strabismus groups.

The range of strabismus for children in the strabismus group is 20–100 PD. Among them, 22 cases (32.35%) were $20 \leq PD < 40$, 32 cases (47.06%) were $40 < PD < 60$, and 14 cases (20.59%) were $PD > 60$. It can be seen that myopia is also mainly concentrated in 20–60PD. The strabismus groups were divided into group *D* (20SPD<40), group E ($40 < PD < 60$), and group F (PD260), and compared the differences in IXTQ scores among the three groups. The comparison of different squint ranges is shown in Figure 6.

Evaluating 8 published articles based on Cochrane risk assessment judgement items, the difference between the evaluation results based on the abovementioned IPD jointly published literature information and the evaluation results based only on the published literature report is shown in Table 5.

A total of 29 (72.5%) articles with low-risk bias based on published literature reports, unclear 5 (12.5%), and high-risk bias 6 (15%). A total of 20 (50%) low-risk biases were assessed based on published literature reports combined with intermittent exotropia reviews, unclear 1 (2.5%), and high-risk bias 19 (47.5%). The published literature report and Cochrane assessment are shown in Figure 7.

In the study, the effective rate of vision improvement in children with intermittent strabismus was observed. The results of the meta-analysis showed that in terms of the effective rate of vision improvement, the visual training treatment group was better than the nonvisual training

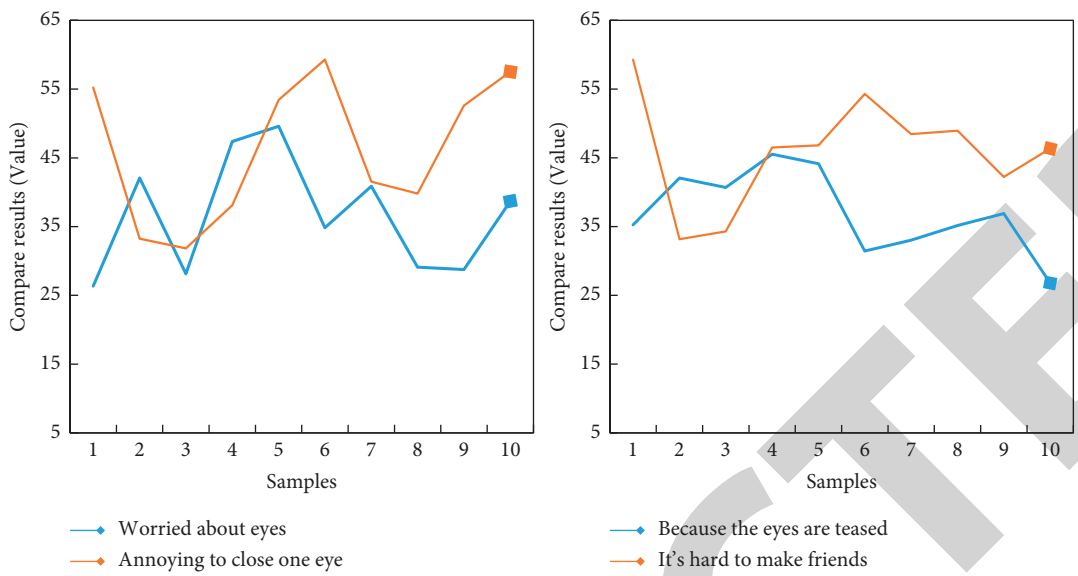

Figure 4: Statistics of parents' doubts about their children.

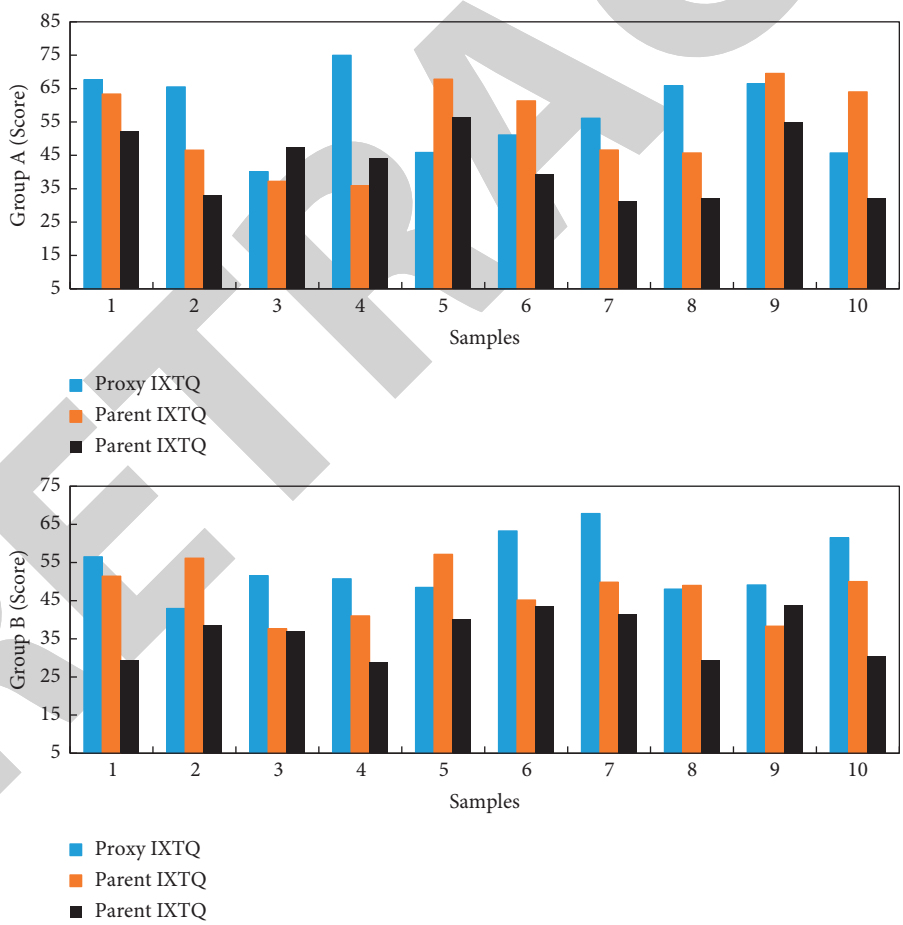

Figure 5: Statistical scores of different distance visual strabismus groups.

group. The meta-analysis of the efficiency of visual acuity improvement is shown in Figure 8.

In the study, the effective rate of fundus improvement of children with intermittent exotropia treated by visual training and nonvisual training was compared. A total of 2228 children were included, including 1124 in the treatment group. The meta-analysis results show that in terms of the effective rate of fundus lesions, the visual training group

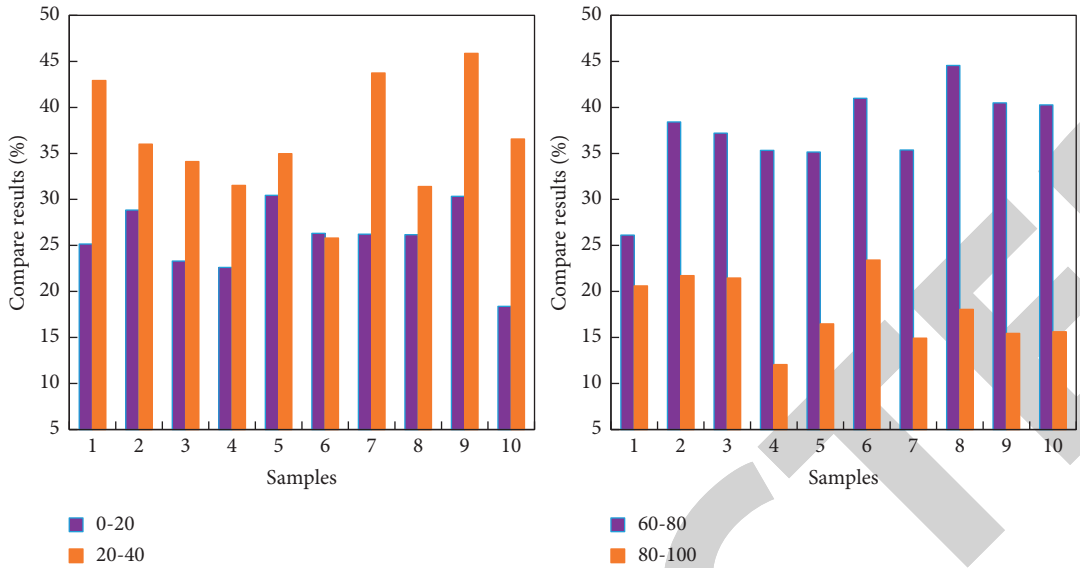

Figure 6: Comparison of different squint ranges.

Table 5: Differences between the evaluation results of the IPD joint publication of literature information and the evaluation results based on the published literature report only.

Method	Evaluation results based on published literature			Published literature and review joint evaluation results		
Random sequence generation	Low risk	Not clear	High risk	Low risk	Not clear	High risk
Random concealment	8	1	1	7	1	1
Blinding	6	2	1	6	1	1
Incomplete knot	2	1	6	2	1	6
Bureau report	6	2	1	2	1	6
Selective knot	7	1	1	3	1	5

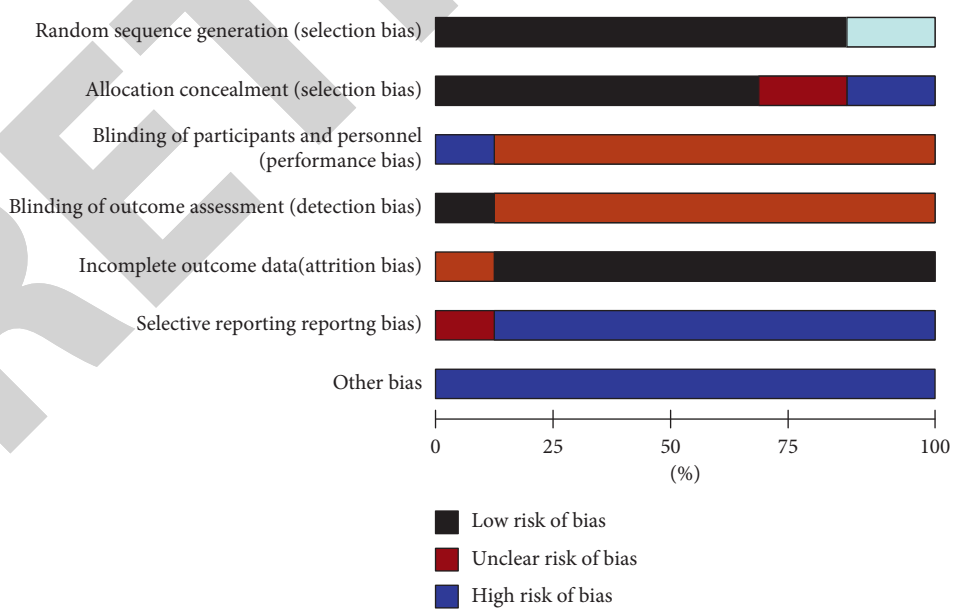

Figure 7: Cochrane assessment of published literature report.

is better than the nontraining group (RR = 1.32, 95% CI: (1.25,1.40), $P < 0.0001$). The meta-analysis of the efficiency of fundus improvement is shown in Figure 9.

An effective funnel chart for fundus improvement is shown in Figure 10. The funnel chart results show that the points distributed on both sides of the vertical line are not

Study	Experimental Events	Total	Control Events	Total	Weight	Risk Ratio M-H. Random.95% CI
1	18	50	33	50	19.7%	1.09 [0.84,1.42]
2	28	38	15	40	13.4%	2.18 [1.42,3.34]
3	6	40	26	40	19.2%	1.23 [0.93,1.62]
4	22	68	41	66	21.7%	1.33 [1.07,1.65]
5	2	30	12	31	12.1%	2.15 [1.34,3.45]

Heterogeneity.Chi^2 = 2.49, df = 9(P=0.98); I^2=0%
Test for overall effect: Z = 5.50 (P<0.00001)

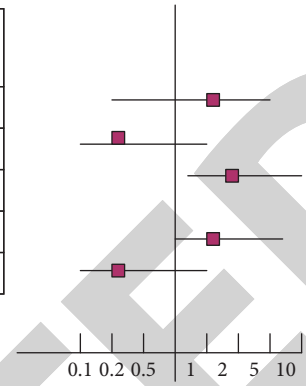

Figure 8: Meta-analysis of the effective rate of vision improvement.

Study	Experimental Events	Total	Control Events	Total	Weight	Risk Ratio M-H. Random.95% CI
1	43	50	40	50	6.2%	1.07 [0.90, 1.28]
2	32	38	22	40	3.3%	1.53 [1.12, 2.09]
3	35	40	17	40	4.2%	1.30 [1.01, 1.66]
4	50	62	32	60	6.7%	1.13 [0.92, 1.38]
5	25	36	32	30	2.2%	1.60 [1.01, 2.55]

Heterogeneity.Chi^2 = 1.49, df = 6(P=0.66); I^2=0%
Test for overall effect: Z = 8.50 (P<0.00001)

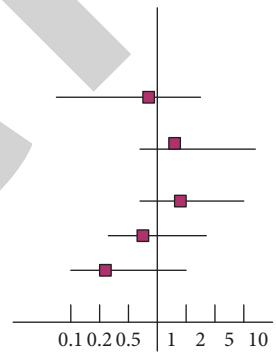

Figure 9: Meta-analysis of the effective rate of fundus improvement.

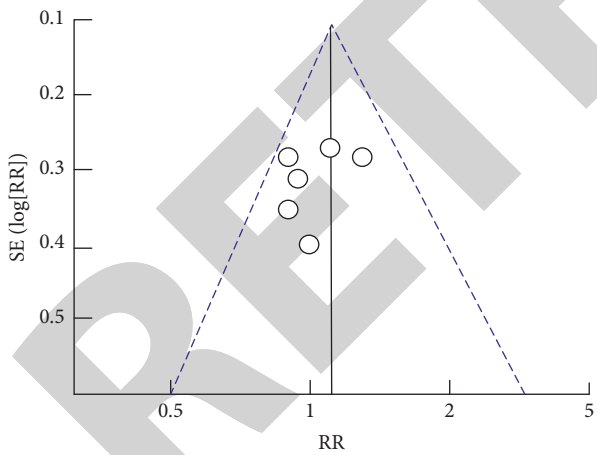

Figure 10: Funnel chart of effective fundus improvement.

completely symmetrical, indicating that there is a certain risk of bias between the studies.

4. Discussion

Intermittent exotropia is more common in clinical diagnosis and treatment, and its fundamental differences include hidden strabismus and intermittent positioning. Some patients often do not pay attention to outdoor exercises, and they will get diseases. Almost all cases of this disease occur at a young age. The incidence in early childhood is very low, and it is obvious after 3 years of age. According to the incidence of intermittent exotropia, it is divided into two types: progressive and nonprogressive. The convergence and adjustment of progressive patients gradually decline, and the orbital axis gradually separates, resulting in monocular depression. The possibility of squinting has also increased, and the angle of squint has also increased. If the exposure time of exotropia becomes longer, the brain will actively screen strabismus as the main source of vision, so that strabismus will continue.

On the one hand, low vision can cause eye fatigue and tingling of the retina, and even cause serious consequences such as cataracts and blindness, which cause great harm to the health of children. On the other hand, poor eyesight will children, affect future education and employment. In addition, in children with weak eyesight, due to changes in the growth of the eye axis, protruding eyeballs may be caused, leading to the formation of goldfish eyes, which may have adverse effects on the children. Therefore, poor eyesight will not only affect the daily study, life and work of children, but also cause serious harm to physical and mental health.

In the past few decades, in order to investigate the risk factors of intermittent exotropia, many countries in the world have conducted a series of large-scale studies. These studies show that intermittent exotropia is related to factors such as geography, race, heredity, habits, gender, growth development, youth, age, education level, nutrition, and

other factors. And it is also related to factors such as outdoor activities and close work. The impact of close work on vision has always been a concern.

Children's eye diseases, including refractive errors, strabismus, and amblyopia, as well as various congenital diseases, will cause a higher incidence of these three eye diseases. Patients with amblyopia are most likely to have loss of corrected vision and cause strabismus problems. The incidence of more common eye diseases is about 1% to 5%, and is mainly common in childhood in Asian demographics. Therefore, the development of binocular vision is one of the important issues that ophthalmologists pay attention to. When treating patients with strabismus, it is not only necessary to correct the position of the eyes, but also to pay attention to the visual function of the eyes. Most scholars believe that the state of binocular vision is one of the important factors in judging the severity of the disease, especially the severity of strabismus based on the state of binocular vision. The accommodative function of the eye and surgery are of guiding importance for strabismus. In addition, some scholars believe that the importance of the degree of intermittent strabismus disease needs to be evaluated as an indicator. In the past, there have been many studies on the recovery of binocular function in intermittent exotropia, but the effect of recovery of binocular function is uncertain.

Intermittent exotropia is one of the typical clinical symptoms for most children, and sometimes amblyopia of the eyes occurs. Patients with exotropia are usually in the process of the onset of imminent loss of visual function. If the ability to compensate is completely lost, it may affect the patient's physical and mental health. After the operation, if the eye position is maintained and the patient's vision is normal, the binocular vision may be restored. Based on the premise of tracking the position of the positive eyeball after surgery, observe the main reasons that actually affect the recovery of binocular vision. The recovery needs to be adjusted slowly. The binocular vision system is divided into two central forms: correct stereo vision and peripheral binocular single vision which forms a convergence force. If intermittent exotropia occurs, the discontinuous separation of the axis of the eye may cause abnormal retina correspondence, and the binocular vision cannot continue to stimulate the normal eyeball position, which will affect the development of binocular vision. However, in clinical research, if the patient is too young, the degree of cooperation and the reliability of the test results will be reduced. The possibility of excess correction will increase, which will have a certain impact on the treatment of children with amblyopia. However, when the binocular visual function is counted, there is no difference in the age of onset at all levels. For this study, by choosing the age span, for further research, more patients who are sensitive to eyes with developed vision can be selected in the future.

Development of binocular vision with types and strabismus. Although patients with intermittent exotropia have different degrees of strabismus, they are all associated with the formation of suppressive dark spots or abnormal retinal correspondence. Regarding various types of strabismus, the report shows that among the several subtypes of intermittent exotropia, patients who have undergone separation basically have the highest preservation rate of stereopsis. The main reasons after surgery that affect the reconstruction of the eyes include the age of the operation and the degree of control. On the premise of better combining ability, the younger the operation age, the better the restoration of binocular vision can be controlled.

Stereo vision examination occupies an important position in the clinical research of ophthalmology, and is used to evaluate patients with strabismus, amblyopia, and children with cataract corneal refraction correction surgery. For patients with stereo vision, as an ophthalmology research, the evaluation of treatment effects, the timing of surgery is very important, and it is an important clinical indicator. For the treatment of patients with intermittent strabismus, correcting the position of the eyes is only the first step in the treatment, the restoration of binocular vision is a true sensory treatment, and stereo vision is the most convenient, intuitive and most important reflection of binocular vision.

5. Conclusion

Strabismus is a common eye disease in children. In order to strengthen the screening of school-age children and preschool children and avoid irreversible visual disturbances, it is necessary to find and treat them as soon as possible. This study collected clinical data of children with intermittent exotropia in hospital and analyzed the age of onset, type, degree of strabismus, degree of control, and the relationship between the development of simultaneous vision, fusion function, and near and far stereo vision. Another option is to perform strabismus correction surgery in the hospital and follow-up for at least half a year for patients with orthopedic eyes. The age of surgery, the type of strabismus, the degree of strabismus, and the degree of control are counted to guide the timing of surgery. It is still necessary to increase the sample size and consider the relationship between the development of binocular visual function from more aspects. The inspection mechanisms of different binocular fusion inspection methods are different, and the detection sensitivity of binocular fusion is also different, but they can explain the existence of binocular fusion from different aspects.

Data Availability

No data were used to support this study.

Conflicts of Interest

The authors declare no conflicts of interest.

References

[1] D. Seo, S. Oh, S. Shin, M. Lee, Y. Hwang, and S. Seo, "Smartphone compatible on-site fluorescence analyzer for spilled crude oil based on CMOS image sensor," *Sensors and Actuators B: Chemical*, vol. 289, pp. 93–99, 2019.

Hindawi
Journal of Healthcare Engineering
Volume 2023, Article ID 9806342, 1 page
https://doi.org/10.1155/2023/9806342

Retraction

Retracted: Effect Evaluation of Artificial Intelligence-Based Electronic Health PDCA Nursing Model in the Treatment of Mycoplasma Pneumonia in Children

Journal of Healthcare Engineering

Received 1 August 2023; Accepted 1 August 2023; Published 2 August 2023

This article has been retracted by Hindawi following an investigation undertaken by the publisher [1]. This investigation has uncovered evidence of one or more of the following indicators of systematic manipulation of the publication process:

(1) Discrepancies in scope
(2) Discrepancies in the description of the research reported
(3) Discrepancies between the availability of data and the research described
(4) Inappropriate citations
(5) Incoherent, meaningless and/or irrelevant content included in the article
(6) Peer-review manipulation

The presence of these indicators undermines our confidence in the integrity of the article's content and we cannot, therefore, vouch for its reliability. Please note that this notice is intended solely to alert readers that the content of this article is unreliable. We have not investigated whether authors were aware of or involved in the systematic manipulation of the publication process.

In addition, our investigation has also shown that one or more of the following human-subject reporting requirements has not been met in this article: ethical approval by an Institutional Review Board (IRB) committee or equivalent, patient/participant consent to participate, and/or agreement to publish patient/participant details (where relevant).

Wiley and Hindawi regrets that the usual quality checks did not identify these issues before publication and have since put additional measures in place to safeguard research integrity.

We wish to credit our own Research Integrity and Research Publishing teams and anonymous and named external researchers and research integrity experts for contributing to this investigation.

The corresponding author, as the representative of all authors, has been given the opportunity to register their agreement or disagreement to this retraction. We have kept a record of any response received.

References

[1] Y. Zhao, "Effect Evaluation of Artificial Intelligence-Based Electronic Health PDCA Nursing Model in the Treatment of Mycoplasma Pneumonia in Children," *Journal of Healthcare Engineering*, vol. 2022, Article ID 1956944, 10 pages, 2022.

Hindawi
Journal of Healthcare Engineering
Volume 2022, Article ID 1956944, 10 pages
https://doi.org/10.1155/2022/1956944

Research Article

Effect Evaluation of Artificial Intelligence-Based Electronic Health PDCA Nursing Model in the Treatment of Mycoplasma Pneumonia in Children

Yan Zhao

Department of Pediatrics in Affiliated Hospital, North Sichuan Medical College, Nanchong 637000, Sichuan, China

Correspondence should be addressed to Yan Zhao; lijijun4468@nsmc.edu.cn

Received 21 December 2021; Accepted 28 January 2022; Published 11 March 2022

Academic Editor: Alireza Souri

The PDCA cycle, also known as Deming's cycle, mainly includes four stages: planning, implementation, inspection, and processing. As a kind of atypical pneumonia with fever and cough, mycoplasma pneumonia harms the health of many children. The purpose of this study is to investigate the anti-inflammatory and antimycoplasma effects and safety of artificial intelligence e-health PDCA nursing mode on pediatric MPP, to investigate its clinical efficacy, to observe the changes of serum cytokines (IL-10, IL-2, IL-4, IFN-γ), and to explore the mechanism of action and possible targets for the treatment of MPP, to provide a new basis for clinical treatment of MPP. The experimental results show that in the experimental group using PDCA nursing mode, the total satisfaction is 97.22%, higher than the control group of 94.44%; in the experimental group, the hospital stay and symptom disappearance time were significantly shortened by four hours. The satisfaction of nursing staff was significantly increased in statistical significance ($P < 0.05$). Therefore, in a statistical sense, the artificial intelligence e-health PDCA nursing mode can significantly improve the clinical symptoms of MPP children with wind-heat stagnation of lung syndrome and phlegm-heat closure of lung syndrome, improve the treatment effect of childhood mycoplasma pneumonia epidemic, shorten the time of hospitalization and symptom disappeared, and play a great auxiliary role in the treatment of childhood mycoplasma pneumonia.

1. Introduction

1.1. Research Background. Mycoplasma pneumonia (MPP) is a kind of atypical pneumonia with fever, severe irritant dry cough, and mild pulmonary signs. The main cause of the disease is the infection of pathogenic mycoplasma *pneumoniae* (MP). In recent years, studies have shown that the incidence of MPP has increased significantly, and it is even the primary pathogen in some age stages, accounting for about 30% of CAP, and the onset age tends to be younger. With the widespread use of antibiotics, the drug resistance rate of MP varies from 3.6% to 36.4%, showing an increasing trend. The drug resistance rate of MPP children varies greatly in specific regions due to the influence of regional, climate, and other factors. Some studies showed that in vitro drug resistance experiments were as high as 90–100%, suggesting that the situation of MP drug resistance was very serious. In addition, the long-term and widespread application of antibiotics is prone to various problems such as drug resistance of superbacteria, loss of regulation of bacterial community, and double opportunistic infection. Therefore, how to improve the clinical efficacy and safety of drug treatment of MPP and reduce the drug resistance rate has become the difficulty of clinical breakthrough.

The clinical manifestations of "pneumonia cough" are mainly "heat, cough, phlegm, wheeze, and panting." The external cause is that the external evil invades the lungs, and the lungs lose their function of sending out and descending. Internal causes are mainly responsible for the weakness of children's viscera, Yin and Yang and juvenile organs, the imbalance of strength and weakness of the five viscera, and the fragile and unstable correlation, and the evil spirit is easy to be committed by the guest; or the righteous qi in the body is weak, the function of the spleen and stomach is low, and it

is easy to be infected with evil qi. The fundamental treatment lies in syndrome differentiation and treatment. Different syndromes and treatment methods are different. With the development of this disease, modern TCM experts, based on their practical experience in diagnosis and treatment, have carried out syndrome differentiation and treatment on MPP from different perspectives, so as to fully explore the great advantages of TCM in China.

Artificial intelligence is a new technical science that studies and develops theories, methods, technologies, and application systems for simulating, extending, and expanding human intelligence. Artificial intelligence is a branch of computer science that attempts to understand the essence of intelligence and produce a new type of intelligent machine that responds in a similar way to human intelligence.

The name of PDCA comes from the initials of the English words Plan, Do, Check, Act, also known as the improvement cycle. The methodology describes the four steps of the system to achieve continuous improvement and defines our continuous approach to improving product and process quality. The introduction of PDCA management mode in medical treatment will be a more efficient cooperation mode for hospitals, patients, and medical staff.

1.2. Research Status at Home and Abroad. At home and abroad related to electronic health, the PDCA mode of nursing research, and child mycoplasma pneumonia, Lin WC sees that artificial intelligence (AI) technology provides a promising approach for the analysis of electronic health records more modal datasets, such as to provide an overview of different methods of artificial intelligence applied to the electronic medical record data in the field of ophthalmology. Although AI technology has been widely used in imaging data, studies using AI technology for clinical data from electronic medical records are limited [1]. SUBBA enables real-time monitoring and intervention in healthcare. Electronic health records (EHRs), mandatory in the most developed countries, can use evidence-based tools to help make safer decisions about patient care. However, there are few examples applied to the PDCA nursing model [2]. Wang K used transcriptome sequencing to identify gene expression and selective splicing profiles to gain insight into the pathogenesis of severe MPP. Bronchoalveolar lavage fluid (BALF) samples from 3 children with severe MPP and 3 children with mild MPP were deeply sequentially analyzed, calculated and annotated, and quantitatively analyzed. Gene expression analysis showed that compared with mild MPP, children with severe MPP had 14 upregulated genes and 34 downregulated genes, but there was a need to improve the nursing model to improve it [3]. In management, the PDCA cycle management model is a general management model, which has been widely used in hospital nursing quality management in recent years. Through the effective application of this management model, the work efficiency of nursing staff can be continuously improved.

1.3. Main Innovation. Routine nursing often appears normative and has a lack of planning and other problems, resulting in the reduction of the effect of medical adjuvant treatment and slow recovery of patients, and nursing adverse events also occur frequently. In this article, PDCA nursing mode was added in the treatment process of chlamydia pneumonia in children to increase effective nursing intervention. A comparative analysis was conducted from multiple perspectives, such as the length of stay between the experimental group and the control group. It can be seen that PDCA nursing can alleviate the symptoms of children, improve the satisfaction of patients and nursing staff, shorten the length of hospital stay and symptom disappearance time, and reduce nursing adverse events. PDCA nursing mode changes the retrospective case analysis method adopted by traditional management through continuous quality improvement. It carries out three-level ward rounds or nursing rounds for difficult cases or cases that need assistance from the superior in nursing. The form of PDCA can be 1–2 times a month and can be used to improve nursing operations and procedures. The basic principle of its operation is that everything needs to be planned in advance, so that the nursing process is orderly, reduce the occurrence of repeated nursing, excessive nursing, omission nursing, and so on. This article innovatively introduced PDCA nursing mode in the treatment of children with mycoplasma pneumonia and added the wavelet transform theory of artificial intelligence to make the whole nursing mode intelligent.

2. Proposed Method

Wavelet transform has a better effect on nursing mode management and is one of the key research directions of researchers now. The core idea of wavelet analysis is as follows: firstly, the wavelet is stretched and shifted, and then, the correlation between the image and the wavelet is studied. In fact, the wavelet is a function, which fluctuates in the local area.

2.1. Principle of Wavelet Transform. In a broad sense, intelligent robot refers to the humanoid or other forms of artificial machines with some human abilities. It is generally believed that intelligent robot should have perception ability, planning ability, movement ability, and coordination ability. Although the intelligence level of the robots developed at present is still not very high and there is still a big gap between them and the real-life intelligence, at present, rich achievements have been made in the research of intelligent robots at home and abroad, and they continue to penetrate into all fields of human activities [4, 5]. On the basis of existing technology, people customize various types of robots according to the actual needs of all walks of life for detection, disaster relief, transportation, delivery, cleaning, etc., and these robots can replace people to accomplish some high-risk, monotonous work, to a great extent, the human liberation, causes humans to do more creative work and improve the social productivity.

2.2. One-Dimensional Wavelet Transform Algorithm. In some commonly used signal analysis methods, Fourier transform is a kind of analysis method that researchers like

to use very much. However, Fourier transform is a pure frequency-domain method, so frequency information in local time period cannot be obtained [6, 7]. Although STFT can be used to analyze the characteristics of signals in the time domain and the frequency domain at the same time, it is not conducive to analyzing pulse signals because of the fixed time window. Wavelet transform is a new theory deduced based on Fourier transform. Compared with Fourier transform, wavelet transform is a time-frequency multiresolution analysis method starting from local angle [8, 9].

The function $\phi(t)$ satisfies the following admissibility conditions:

$$C_\phi = \int_{-\infty}^{+\infty} |\omega|_{|\psi(\omega)|} d\omega < \infty, \tag{1}$$

where $\psi(t)$ is the parent wavelet and $\psi(\omega)$ is the Fourier transform of $\psi(t)$. After multiple stretching and translation operations on the parent wavelet, the family of wavelet functions $\psi_{m,n}(t)$ can be obtained as follows [10, 11]:

$$\psi_{m,n}(t) = \frac{1}{\sqrt{m}} \psi(t-n), \tag{2}$$

where m is the scale factor and n is the displacement factor.

Discrete wavelet analysis is adopted in this article, and the discrete wavelet $\psi_{s,w}(t)$ is defined as follows [12]:

$$\psi_{s,w}(t) = \frac{1}{\sqrt{m_0^w}} \psi\left(t - qn_0 m_0^w\right), \tag{3}$$

where s and w are integers, m_0 is an integer greater than 1, and n_0 is a constant greater than zero. The discrete wavelet transform of the function $f(t)$ is [13]

$$WT_f(s,w) = < f(t), \psi_{s,w}(t) > = \int_{-\infty}^{+\infty} f(t)\overline{\psi_{s,w}(t)}dt, \tag{4}$$

where denotes the inner product and $\overline{\psi_{s,w}(t)}$ denotes the complex conjugate of $\psi_{s,w}(t)$. Direct use of a low-pass filter may lose the contour feature information of the signal, and direct use of a high-pass filter may retain a lot of interference components, so only two filtering methods cannot be directly selected in pulse signal processing. Although the signal waveform after Fourier transform denoising will become relatively smooth, it will lose a lot of details. The use of wavelet transform can overcome the above contradictions and has a significant advantage in the study of the detailed characteristics of signals [14, 15].

Generally speaking, the wavelet coefficient of noise is small. When the coefficient is less than a certain set threshold, this part can be treated as caused by noise and all of it can be set to zero. When the value is greater than the set threshold, it can be considered that it is mainly caused by useful signals, and it can be kept unchanged, or it can be contracted by a fixed amount as shown in following the formula [16, 17]:

$$\begin{aligned} \widehat{\omega}_{j,k} &= \begin{cases} \omega_{j,k}, \left|\omega_{j,k}\right| \geq \lambda \\ 0, \left|\omega_{j,k}\right| < \lambda \end{cases}, \\ \widehat{\omega}_{j,k} &= \begin{cases} sign\left(\omega_{j,k}\right)\left(\left|\omega_{j,k}\right| - \lambda\right), \left|\omega_{j,k}\right| \geq \lambda \\ 0, \left|\omega_{j,k}\right| < \lambda \end{cases}. \end{aligned} \tag{5}$$

In the new threshold function, the part less than λ is still treated in the same way as the method mentioned above; the part greater than λ is treated by combining two classical functions with variable μ, under the limit condition $\mu \longrightarrow 0$ and the part greater than λ is treated as a hard threshold function. When the limit condition $\mu \longrightarrow 1$ is satisfied, the improved soft threshold function is used for the part greater than λ. The new threshold function is shown in the following formula [18, 19]:

$$\widehat{\omega}_{j,k} = \begin{cases} (1-\mu)\omega_{j,k} + sign\left(\omega_{j,k}\right)\left(\left|\omega_{j,k}\right| - \exp(\lambda - 1), \left|\omega_{j,k}\right| \geq \lambda \right. \\ 0, \left|\omega_{j,k}\right| < \lambda \end{cases}. \tag{6}$$

According to the formula, the improvement of the new threshold function lies in that, and the part of $|w_{j,k}| \geq \lambda$ is replaced by the content shown in the above formula and retained as the new wavelet coefficient. The basic idea of the improved method is derived from the weighted average combination of soft and hard threshold functions. It not only has the advantages of the two methods but also overcomes their respective shortcomings. Compared with the traditional hard and soft threshold functions, the new threshold function has higher reconstruction accuracy and better denoising effect. In addition, the traditional soft threshold function has the problem of discontinuous derivative, while the new threshold function is continuous derivative, which is more convenient in dealing with other kinds of mathematical problems and has a wider range of practical application, so it has obvious advantages. Therefore, this article uses the method after the improved threshold function to realize the denoising of pulse signal [20].

When the wavelet energy is used as the eigenvector of the pulse category, the rate of the pulse recognition process may be affected due to the large number of wavelet scale division and the larger dimension of the eigenvector. Principal component analysis (PCA) technology can reduce the loss and can be used to simplify the pulse feature vector, obtain the principal component feature parameters with less dimension, and it can show almost all information, which can improve the system identification efficiency. The process of reducing the dimension of pulse signal feature vector E by using principal component analysis technique is as follows:

(1) The m n-dimensional eigenvectors E obtained are written into a dimensional data matrix $n \times m$. The matrix E is normalized according to the following formula, and the normalized matrix is obtained to eliminate the interference of data dimension:

$$E_{ij}^{*} = E_{ij} - \overline{E}_i, \tag{7}$$

where $\overline{E_i}$ is the sample mean and s_i is the sample standard deviation.

(2) Calculate the covariance matrix E^* of the normalized matrix according to the following formula:

$$c = {}_{m-1}^{1} \sum {}_{j-1}^{m} \left(E_{ij}^{*} - \overline{E_i^{*}}\right)\left(E_{ji}^{*} - \overline{E_j^{*}}\right) = {}_{m-1}^{1} E^{*} E^{*T}, \tag{8}$$

(3) Calculate the eigenvalues of C and their eigenvectors, adjust the corresponding eigenvectors according to the eigenvalues, and obtain the unit orthogonal matrix according to the Schmidt algorithm.

(4) Calculate the cumulative contribution rate of eigenvalues, set the extraction index as η, and get the number of main elements k and corresponding main vectors V^* that meet the requirements.

(5) Calculate the projection of the normalized matrix E^* on the main vector $X = (x_{ij})_{k\times m}$, and obtain the low-dimensional eigenvector $X = [X_1, X_2, \ldots, X_k]$ according to the following formula:

$$X = V^{*T} E^{*}. \tag{9}$$

In this article, the eigenvalue, contribution rate, and cumulative contribution rate of each component of the 8-dimensional eigenvector obtained from the wavelet energy are shown in Table 1.

2.3. Two-Dimensional Wavelet Transform Algorithm. Simply put, the one-dimensional wavelet is extended to the two-dimensional wavelet, and the one-dimensional wavelet transform is equivalent to the two-dimensional wavelet transform when the two-dimensional image data are carried out independently in the horizontal and vertical directions:

$$W_f\left(a, b_x, b_y\right) = \iint f(x, y)\psi_{a,b_x,b_y}(x, y)dxdy, \tag{10}$$

where b_x and b_y represent the translation on two dimensions, a represents the scale factor, $f(x, y) \in L_2(R)$ is a two-dimensional arbitrary function, and $W_f(a, b_x, b_y)$ is a two-dimensional wavelet transform coefficient.

The inverse transform of two-dimensional wavelet transform is

$$f(x, y) = \frac{1}{c_\psi} \iiint w_f\left(a, b_x, b_y\right)\overline{\psi_{a,bx,by}}dxdy. \tag{11}$$

Under the action of the same principle, the above theoretical methods can be pushed to higher dimensions. The two-dimensional wavelet transform is to carry out the discrete transform on the image, and carry out the multiscale decomposition and reconstruction of the wavelet based on the obtained discrete transform:

Let W_j be the closure on the set $\left\{\phi_{jk}(t); k \in Z\right\}$ linearly spanned, and then

$$L^2(R) = \cdots \oplus W_{j-1} \oplus W_j \oplus W_{j+1} \oplus \cdots. \tag{12}$$

Yeah, there is a unique solution to $f(t) \in L^2(R)$:

$$f(t) = \cdots + g_{-1}(t) + g_0(t) + g_1(t) + \cdots. \tag{13}$$

One of $g(t) \in W_k, k \in Z$. For each k, let us think about it：

$$V_k = \cdots + W_{k-2} + W_{k-1}, k \in Z. \tag{14}$$

Each V_k is the set of all the displacements $\phi_{jk}(t)$ containing the scale $\leq k - 1$.

Wavelet reconstruction is the inverse process of wavelet decomposition. Reconstruction is to synthesize the multiscale wavelet into the original signal source by using the wavelet coefficient under the multiresolution obtained by wavelet decomposition. Reconstruction is not completed immediately after decomposition, which can complete the process of image defogging and so on.

The application of wavelet transform to image processing mainly has the following advantages:

(1) Wavelet transform can cover the whole part of the image.

(2) The wavelet transform theory is to use the filter that selects the image suitable, so that the correlation between different features of the information extracted from the image can be reduced or removed to the maximum extent.

(3) The theory of wavelet transform has the characteristics of frequency conversion. High frequency resolution and low time resolution can be used in the low frequency part of the image, and low frequency resolution and high time resolution can be used in the high frequency part of the image.

(4) Fast algorithm can be used in the actual operation of wavelet transform; that is, Mallat wavelet decomposition method is often used.

Because of these advantages of the wavelet transform, this article uses the wavelet transform method and will further analyze the wavelet transform in the following description.

2.4. PDCA Nursing Model. PDCA cycle is a continuous spiraling cycle rising process, which can be divided into four stages and eight steps, and each stage is gradual in order to promote the improvement of project quality.

The first is the quality management planning stage: the task of this stage is mainly to determine the quality objectives of the project, formulate implementation plans, and plan management measures. It can be roughly divided into four specific steps: 1. study the status quo of the project and find out the quality defects of the project. 2. Analyze the causes of project quality defects and all influencing factors. 3. Find out the main reasons and factors that cause quality problems. 4. For the results of the previous step, make targeted quality

Table 1: Eigenvalues and contributions of each component.

Principal component	Characteristic value	Contribution rate (%)	Cumulative contribution rate (%)
1	3.029	41.27	41.27
2	2.4481	31.84	73.11
3	1.0321	14.51	87.62
4	0.6352	7.36	94.98
5	0.3526	2.83	97.81
6	0.1568	1.82	99.63
7	0.0785	0.35	99.98
8	0.0023	0.02	100

improvement measures, and determine the expected goals and detailed implementation plans.

PDCA can be divided into four stages. The first stage is, P stage, the planning stage. In this stage, in order to form a certain planning scheme, an enterprise needs to clarify its performance objectives and then further determine relevant performance appraisal indicators through top-level design, planning, and inspection. The second stage, stage *D*, is the execution stage. This stage is to carry out the plan formed in the planning stage, and all the work will be carried out in an orderly manner according to the plan. The third stage—stage C, is the feedback stage. This stage is to analyze and feedback the implementation effect of the implementation stage, to monitor the progress, to check the original plan, and to find out the situation beyond the plan and point out the deficiencies. The fourth stage—A stage, is the improvement stage. This stage is to reflect on the problems found in the third stage, acknowledge or deny, and advantages need to be further developed, and deficiencies need to summarize experience and to improve efficiency.

PDCA has the following characteristics: first, a large ring set small ring. The PDCA cycle is a large cycle with a smaller PDCA cycle. The smaller level PDCA cycle is formulated according to the larger level PDCA cycle. The larger level PDCA cycle plays its role thanks to the effective execution of the smaller level PDCA cycle, recurrent relationship.

Second, keep improving and rising. PDCA will solve some problems and accumulate new experience every time it completes a cycle. A large number of problems will be improved and improved in the cycle process. New goals and contents will also appear in each cycle, so as to improve the management level of enterprises and achieve the development of enterprises.

Third, pay attention to the A cycle. In the PDCA cycle, stage A, the improvement stage, is the key. Stage A is the process of improving the problems found in the previous three stages, and it is the key step from quantitative change to qualitative change. Only by improving the problems found can we constantly push things forward. If there is no improvement stage, then things cannot be completed and improved, only the same, so stage A is a key link to promote the development of things.

In view of the above advantages, this article innovatively applied the PDCA cycle mode in the treatment of mycoplasma pneumonia in children.

2.5. Support Vector Machine Method Based on Machine Learning. In recent years, with the development of science and technology, people gradually use intelligent computers to replace some tedious manual labor and mental labor, and have achieved remarkable results. For example, using computers to recognize human speech by learning, learn checkers, detect rare diseases, detect credit card fraud problems, driverless cars, etc. These are achieved through the intelligent learning of the computer. Machine learning is one of the important frontier disciplines that combine computer science and information science.

The simplest classification model in SVM is the maximum margin classifier W. In a linear classification problem, define a linear function for

$$g(a) = w^T a + b, \tag{15}$$

where a is the vector representation of the sample data, and the dimension can be very high. Assuming that the threshold is 0, the category to which the sample a belongs is determined according to the positive or negative of the $g(a)$ value.

In order to maximize the target geometric interval, it can be transformed to solve the following optimization problem as

$$F = \min \frac{1}{2}\|w\|^2. \tag{16}$$

The maximum geometric interval is achieved here, where $\|w\|^2$ is a parameter that controls the classification surface. Using the Lagrangian function to derive the dual form of the above optimization problem is

$$L = \sum_{i=1}^{n} \alpha_i - \frac{1}{2}\left|\sum_{i,j=1}^{n} \alpha_i \alpha_j b_i b_j\right|, \tag{17}$$

where the Lagrangian coefficient α_i is the solution of the optimization problem.

Since many data in the real world are noisy, the feature space generally cannot be separated. In order to balance model performance and generalization, slack variables are introduced, which can allow a small number of error points and outliers. The optimization problem is finally transformed into the following:

$$F = \min \frac{1}{2}\|w\|^2 + C\sum_{i=1}^{n} \xi_i. \tag{18}$$

The measurement of the expiratory flow rate is an index that mainly reflects the degree of obstruction of the large airway. It is more sensitive and objective than clinical symptoms to reflect the degree of airway obstruction and changes in the condition of asthma patients. Monitoring expiratory flow rate can help detect early signs of disease deterioration before symptoms appear, where C is the penalty coefficient. Similarly, using the Lagrange multiplier method, the above optimization problem is transformed into the following dual problem as

$$L = \sum_{i=1}^{n} \alpha_i - \frac{1}{2}\left(\sum_{i,j-1}^{n} \alpha_i \alpha_j b_i b_j a_i^T\right). \quad (19)$$

Solve the above problem, solve the coefficient α_i, and get the optimal classification plane. The above is the main idea of SVM to deal with the classification problem. At present, support vector machines have achieved good results in the application of many real problems.

3. Comparative Experiment of PDCA Nursing Mode

3.1. Experimental Data. A total of 72 hospitalized children diagnosed as MPP from December 2019 to March 2020 in the 5th District of Pediatrics of the First Affiliated Hospital of Jiangxi University of Chinese Medicine were recruited and randomly divided into two groups, with 36 children in each group. All the children in the experiment were informed and approved by their guardians, and signed the relevant medical confirmation letters, which were in line with the clinical diagnostic criteria of mycoplasma pneumonia in children. Infants with mental diseases or other major diseases were strictly controlled to participate in the experiment.

Among the 36 patients in the experimental group, 18 were male and 18 were female. The age distribution ranged from 1 to 13 years, with an average age of 7.7 ± 0.1 years. The course of disease was 1 to 6 days, and the mean course of disease was 4.7 ± 0.6 days. In the control group, there were 18 male children and 18 female children. The age distribution ranged from 1 to 13 years, with an average age of 6.9 ± 0.4 years. The course of disease was 1 to 6 days, and the mean course of disease was (5.5 ± 0.3) *d*. There was no significant difference in general data between the two groups ($P > 0.05$), which was comparable.

3.2. Nursing Methods. The 36 children in the control group were treated with routine nursing methods. During the experiment, the nursing staff needed to check the physical conditions of the children regularly, and timely informed the doctors of any abnormal conditions in terms of the severity of symptoms, the respiratory rate and the peak expiratory value of the children, and other indicators. The 36 children in the observation group were treated with the PDCA nursing method, and different nursing structures were used in the routine nursing process. The specific PDCA nursing mode is shown in Figure 1.

(1) Formulation of nursing plan: nursing staff should also take into full consideration the physical condition, family background, psychological factors, social factors, and other factors of children with mycoplasma pneumonia before making the plan. Because the nurses themselves will also have differences, which will affect the experimental effect, so before the start of the experiment, the nurses participating in the experiment should be trained uniformly, and their operation should be standardized to avoid the influence of the experimental results due to their own reasons.

(2) Application of nursing plan: for children with a generally younger age, their logical awareness is low and they are unable to self-resolve their emotions. At this time, the medical staff need to stabilize the mood of the child patient according to the actual situation of the child, cooperate with playing video and music, provide the child with toys, divert the child's attention during the treatment process, reduce their pain and discomfort, and in the process of treatment, actively guide parents to cooperate with the hospital to treat their children. These nursing programs will effectively guarantee and improve the therapeutic effect.

(3) The implementation of nursing evaluation: in the nursing process, a detailed nursing plan should be developed to standardize the behaviors of the nursing staff, evaluate the regular performance, and find, discuss, and solve problems in a timely manner. For children's health problems, nurses should report to the organized seminar in a timely manner, and the experts will discuss and solve them.

(4) The development of nursing summary work: For the problems existing in the nursing process, the nursing staff should record, summarize, and report in time, and formulate the corresponding report uniformly after the end of the experiment. Nursing staff should also find their own shortcomings and advantages in the process of this experiment, and further improve themselves, to help children overcome the disease.

3.3. Evaluation Index and Method. The evaluation indexes include the following: (1) the satisfaction of nursing staff in the training process; (2) time of symptom disappearance; (3) peak expiratory flow rate; (4) length of hospital stay; and (5) forced expiratory volume. Among them, in the whole nursing process, the degree of satisfaction to the nursing staff is divided into three indicators: satisfaction, basic satisfaction, and dissatisfaction. Because the children are young, they are filled in by the families of the children. The calculation formula of total satisfaction is as follows: (satisfaction + basic satisfaction)/36 × 100.00%.

Statistical Methods SPSS 24 statistical software was used for data processing. Measurement data were expressed as mean ± standard deviation, and the χ^2 test was used. Enumeration data were expressed as (m, %), and the difference was statistically significant when $P < 0.05$ was used.

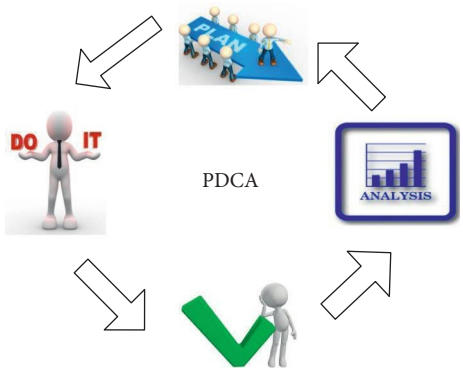

Figure 1: PDCA nursing model diagram.

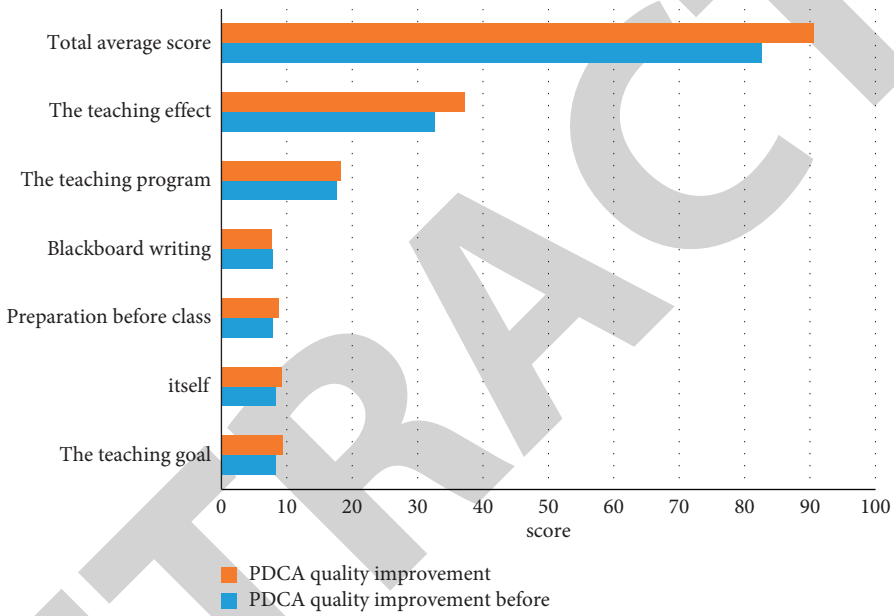

Figure 2: Comparison of average scores before and after PDCA quality improvement.

Table 2: Comparison of students' test scores before and after PDCA quality improvement.

Group	Number of cases	Theory	Operation
Before quality improvement	50	82.7 ± 6	93.7 ± 2.3
Quality improvement	50	89.6 ± 3.7	95.0 ± 1.0
t		-6.89	-3.6
p		<0.05	0.001

3.4. Training of Nurses. Before the start of the experiment, we conducted corresponding training for the nurses participating in the experiment, and the training period lasted for one month. As can be seen from the data collected from the training quality evaluation form, the average score for teaching objectives (full score: 10) is 9.4, and the average score for teaching attitude (full score: 10) is 9.6. The average score was 9.3, pre-class preparation (full score: 10) 8.8, blackboard writing (full score: 10) 7.7, teaching procedure (full score: 20) 18.2, and teaching effect (full score: 40) 37.2. The comparison of the average scores before PDCA quality improvement and after PDCA quality improvement is shown in Figure 2.

As can be seen from Table 2, the average score of the nursing staff after quality improvement was 95, 94, 96, 9.88, and 96% in the theoretical operation examination. It can be seen that the passing rate of students has been significantly improved after the quality improvement as shown in Table 2.

4. Comparison and Analysis of PDCA Nursing Mode before and after

4.1. Satisfaction Comparison. The total nursing satisfaction of the observation group was 97.22%, which was higher than 94.44% in the control group, and the difference was statistically significant ($P < 0.05$). In the table, 21 patients were satisfied with the evaluation, which was higher than 19 patients in the control group. The PDCA nursing mode has an auxiliary effect on the treatment of mycoplasma pneumonia in children, as shown in Table 3.

Table 3: Satisfaction comparison table.

Group	Number of cases	Satisfied	Basically satisfied	Dissatisfied	Total satisfaction (%)
Control group	36	21	14	1	97.22
Observed group	36	19	15	2	94.44

Table 4: Comparison of hospitalization time and symptom disappearance time.

Group	Number of cases	Length of stay	Time of symptom disappearance
Control group	36	12.8 ± 2.8	1.2 ± 0.4
Observed group	36	16.5 ± 3.3	2.8 ± 2.1
T value		5.239	4.289
P value		<0.05	<0.05

Table 5: Comparison of the peak expiratory flow rate.

Group	Number of cases	Peak expiratory flow rate
Control group	36	43.29 ± 12.03
Observed group	36	27.12 ± 16.27
T value		6.178
P value		<0.05

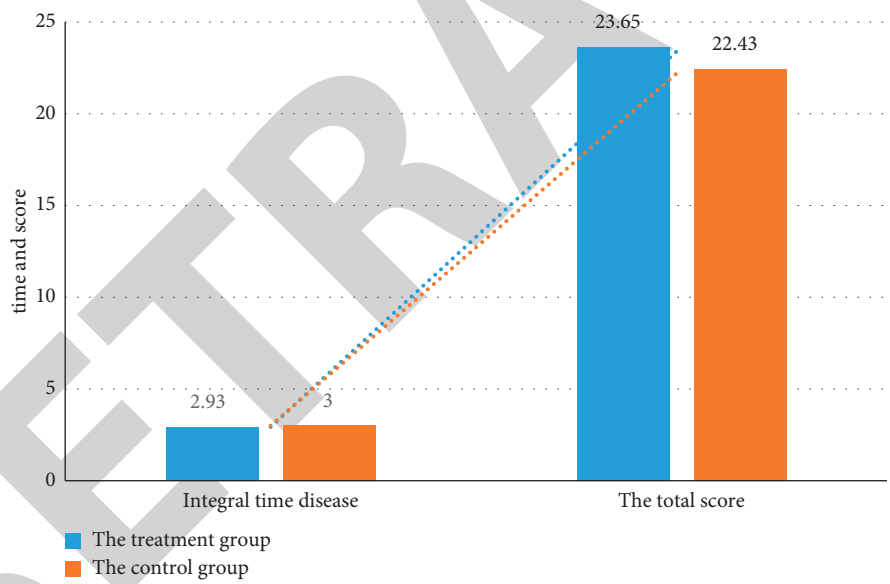

Figure 3: Comparison of treatment time.

4.2. Comparison of Hospital Stay and Symptom Disappearance Time between the Two Groups. The length of stay in the experimental group was about 12.8 days and the time of symptom disappearance was about 1.2 days, whereas the length of stay in the control group was about 12.8 days and the time of symptom disappearance was about 1.2 days. The length of stay in the experimental group was lower than that in the control group, and the differences were statistically significant ($P < 0.05$), as shown in Table 4.

4.3. Comparison of Peak Expiratory Velocity between the Two Groups. After active nursing, the peak expiratory velocity of the experimental group was about 43.27, which was better than that of the control group (27.12), and the difference was statistically significant ($P < 0.05$), as shown in Table 5.

4.4. Comparison of Treatment Time. As can be seen from Figure 3, the treatment market duration consumed by the experimental group was slightly lower than that of the control group, and the score of consumption duration was also higher than that of the control group.

As shown in Figure 3, the therapeutic market duration consumed by the experimental group was 2.93, and the duration of the control group was 3, which was slightly lower than that of the control group.

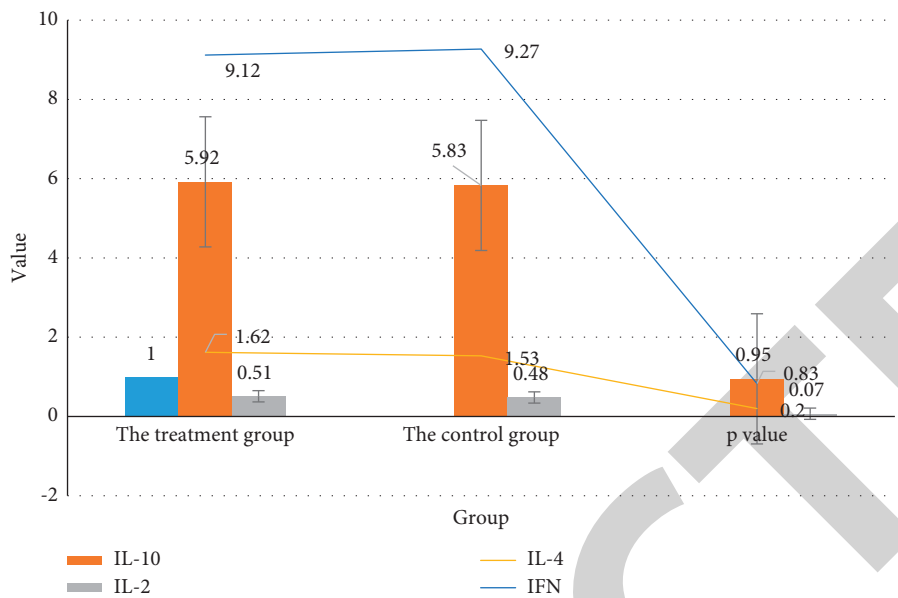

Figure 4: Comparison of cytokine levels.

Table 6: Comparison of curative effect between the two groups after treatment.

	The number of cases	Cure	Effective	Upturn	Invalid	Efficient (%)	*P* values
The treatment group	36	5	18	12	1	97.22	0.055
The control group	36	1	14	18	3	91.67	

Table 7: Comparison of forced expiratory volume.

Group	Number of cases	Forced expiratory volume
Control group	36	53.03 ± 12.53
Observed group	36	32.58 ± 12.69
T value		9.327
P value		<0.05

Table 8: Nursing staff satisfaction comparison.

Group	n	Very satisfied	Satisfied	Basically satisfied	Dissatisfied
Trained	12350	3730 (30.2)	3260 (26.4)	3433 (27.8)	1927 (15.6)
Untrained	16258	7868 (48.4)	5072 (31.2)	2243 (13.8)	1075 (6.6)
χ^2		963.618	78.344	865.114	651.728
P		<0.001	<0.001	<0.001	<0.001

4.5. Comparison of Cytokine Levels. As can be seen from Figure 4, the drug residues of patients in the experimental group were higher than those in the control group, but statistically speaking, only the level of IL-2 was significantly improved.

4.6. Comparison of Curative Effect. As shown in Table 6, the treatment effect of the experimental group was significantly better than that of the control group, and the improvement of the treatment effect was statistically significant.

4.7. Forced Expiratory Volume Comparison. The forced expiratory volume index of the experimental group was about 53.03, which was better than that of the control group (32.58), and the difference was statistically significant ($P < 0.05$), as shown in Table 7.

4.8. Nursing Staff Satisfaction Comparison. As can be seen from Table 8, not only the satisfaction of patients in the experimental group is higher than that of the control group, but also the satisfaction of nursing staff in the experimental group.

Hindawi
Journal of Healthcare Engineering
Volume 2023, Article ID 9874048, 1 page
https://doi.org/10.1155/2023/9874048

Retraction

Retracted: Atherosclerosis Vascular Endothelial Secretion Dysfunction and Smooth Muscle Cell Proliferation

Journal of Healthcare Engineering

Received 1 August 2023; Accepted 1 August 2023; Published 2 August 2023

This article has been retracted by Hindawi following an investigation undertaken by the publisher [1]. This investigation has uncovered evidence of one or more of the following indicators of systematic manipulation of the publication process:

(1) Discrepancies in scope
(2) Discrepancies in the description of the research reported
(3) Discrepancies between the availability of data and the research described
(4) Inappropriate citations
(5) Incoherent, meaningless and/or irrelevant content included in the article
(6) Peer-review manipulation

The presence of these indicators undermines our confidence in the integrity of the article's content and we cannot, therefore, vouch for its reliability. Please note that this notice is intended solely to alert readers that the content of this article is unreliable. We have not investigated whether authors were aware of or involved in the systematic manipulation of the publication process.

In addition, our investigation has also shown that one or more of the following human-subject reporting requirements has not been met in this article: ethical approval by an Institutional Review Board (IRB) committee or equivalent, patient/participant consent to participate, and/or agreement to publish patient/participant details (where relevant).

Wiley and Hindawi regrets that the usual quality checks did not identify these issues before publication and have since put additional measures in place to safeguard research integrity.

We wish to credit our own Research Integrity and Research Publishing teams and anonymous and named external researchers and research integrity experts for contributing to this investigation.

The corresponding author, as the representative of all authors, has been given the opportunity to register their agreement or disagreement to this retraction. We have kept a record of any response received.

References

[1] J. Li, X. Fu, R. Yang, and W. Zhang, "Atherosclerosis Vascular Endothelial Secretion Dysfunction and Smooth Muscle Cell Proliferation," *Journal of Healthcare Engineering*, vol. 2022, Article ID 9271879, 13 pages, 2022.

Hindawi
Journal of Healthcare Engineering
Volume 2022, Article ID 9271879, 13 pages
https://doi.org/10.1155/2022/9271879

Research Article

Atherosclerosis Vascular Endothelial Secretion Dysfunction and Smooth Muscle Cell Proliferation

Junxi Li, Xinying Fu, Renyi Yang, and Wei Zhang

Hunan University of Chinese Medicine, Changsha 410000, Hunan, China

Correspondence should be addressed to Wei Zhang; zhangwei1979@hnucm.edu.cn

Received 30 December 2021; Accepted 11 February 2022; Published 9 March 2022

Academic Editor: Nima Jafari Navimipour

Atherosclerosis is a chronic inflammatory disease of the arterial wall and the main cause of cardiovascular disease and cerebrovascular disease. In recent years, the mortality rate of atherosclerotic diseases has become higher and higher. This article aims to study the dysregulation of atherosclerotic vascular endothelial secretion and smooth muscle cell proliferation, and put forward and practice the pathological research of atherosclerotic disease. This article describes in detail atherosclerosis, endothelial dysfunction, and smooth muscle cell proliferation, and studies the causes of atherosclerosis. Research results indicate that atherosclerotic vascular endothelial dysfunction also has a great influence on the proliferation of smooth muscle cells. Many genes and environmental factors can regulate the functions of endothelial cells, vascular smooth muscle cells, and mononuclear macrophages and affect the formation of atherosclerosis. At the same time, diabetes, hypertension, hyperlipidemia, obesity, etc. are the main causes of atherosclerosis. The number of patients with cardiovascular and cerebrovascular diseases dying from atherosclerosis in the country is increasing, and the proportion is close to 30%.

1. Introduction

Atherosclerosis (AS) is a type of inflammatory disease that mostly occurs in the large and medium blood vessels in the body, and the annual mortality rate is also increasing. There are many reasons for the occurrence of atherosclerosis, such as dietary habits, environmental factors, and induction of other diseases, the etiology is not yet fully understood. The pathological changes in AS are caused by a large number of highly specific reactions of molecules. When the disease occurs, the initial changes in the blood vessel wall occur on endothelial cells (EC). Endothelial cells are located in the vascular intima and are the component of the vessel wall that has the fullest contact with blood. Because of its smooth surface, it is conducive to blood flow, so it serves as the first protective barrier for the vascular intima. The multiple influences induced by growth factors and cytokines lead to dysfunction of the inner membrane of the tube wall. The destruction of EC can lead to lipid permeability, increase the aggregation of macrophages, form foam cells, and recruit T lymphocytes and platelets. Endothelial cell injury will stimulate smooth muscle cells to change their functions, gradually begin to migrate, proliferate, and move to the intima, resulting in the formation of plaques on the blood vessel wall. Therefore, the pathogenesis of AS is to change the function of smooth muscle cells (SMCs).

Atherosclerosis is the main pathological basis of cardiovascular disease. Atherosclerosis narrows the diameter of blood vessels and induces the formation of thrombosis. At the same time, coronary artery embolism causes acute myocardial insufficiency and intracellular metabolic disorders. Atherosclerosis is the main pathological basis of cardiovascular disease and cerebrovascular disease. Its etiology is a complex process with multiple factors and multiple stages. The participation of multiple cells and the appearance of abnormal genes play an important role. Through the study of the pathology of atherosclerosis, the influencing factors of cardiovascular and cerebrovascular diseases can be discovered in time, so as to better improve the diagnosis efficiency of doctors, and at the same time, it can also provide better treatment for patients with cardiovascular and cerebrovascular diseases.

Cardiovascular and cerebrovascular diseases have extremely high morbidity and mortality, prompting a large number of researchers to increase their research efforts on cardiovascular and cerebrovascular diseases. In the study of endothelial cell dysfunction, Gimbrone stated that endothelial dysfunction in the susceptible areas of arterial vascular system disease is an important factor in the pathobiology of atherosclerotic cardiovascular disease. Gimbrone traced the evolution of the concept of endothelial cell dysfunction, focusing on the latest insights into the cellular and molecular mechanisms that play a key role in the occurrence and progression of atherosclerotic lesions [1]. Childs found in the study of atherosclerosis that advanced atherosclerotic lesions contain senescent cells, but the role of these cells in atherosclerosis is still unclear. At the same time, Childs's research shows that these cells are harmful in the entire disease pathogenesis [2]. Both Ketelhuth and Childs have studied atherosclerosis, Ketelhuth stated in his research that atherosclerosis is a chronic inflammatory disease caused by the retention and accumulation of cholesterol-containing lipoproteins in the arterial wall, especially low-density lipoproteins. At the same time, Ketelhuth's research shows that a large number of clinical and experimental data support the adjustment of the adaptive immune system that can be used to treat and prevent atherosclerosis [3]. Needham is different from other researchers in that he applies the content of atherosclerosis to other medical research fields. Needham stated that depression is a common but undiagnosed and untreated mental disorder. He also used data on atherosclerotic mediators from South Asians living in the United States to examine the association between different acculturation strategies and symptoms of depression [4]. During the more than two decades of follow-up based on the community atherosclerosis risk study, Warren compared the risk of future outcomes with different definitions of prediabetes based on fasting blood glucose concentration, HbA1c, and 2-hour blood glucose concentration. Warren's research aims to analyze the correlation between definitions and results to provide a comparison of different definitions [5]. In order to further explore the mechanism of atherosclerosis, researchers have also conducted many studies on vascular smooth muscle cells. In order to verify whether miR-22-3p can play a role in regulating the function of human arterial smooth muscle cells and the formation of new intima, Huang used real-time quantification and fluorescence in situ hybridization to detect the expression of miR-22-3p in human arteries. In addition, Huang also performed a luciferase reporter gene test to identify miR-22-3p target genes. Finally, the rat carotid artery balloon injury model was used to determine the role of miR-22-3p in neointima formation [6]. Sun used hematoxylin and eosin staining to check the thickness of the arterial wall in the distal pulmonary artery isolated from the lungs of healthy volunteers and PAH patients. The expression level of MEG3 was analyzed by qPCR to determine whether long-chain noncoding RNA maternally expressed gene 3 (MEG3) is involved in PAH-related vascular remodeling [7]. Although these researchers have conducted a large number of related studies on atherosclerosis, most of these researchers have not proposed specific and feasible related methods that can be used to prevent and treat atherosclerosis. And, in the course of their research, patients' age groups were not distinguished, and the relationship between diseases and age groups could not be explained very well.

The innovation of this article is to study the relationship between atherosclerotic vascular endothelial dysfunction and smooth muscle cell proliferation. The contents of vascular endothelial function, atherosclerosis, smooth muscle cell proliferation, etc. Were introduced in detail, and related experiments and analyses were carried out on the factors that induce atherosclerotic diseases. And the multiple linear regression method is used to predict and analyze the high incidence of cardiovascular diseases.

2. Atherosclerosis and Smooth Muscle Cell Proliferation

2.1. Vascular Endothelial Function and Atherosclerosis. Vascular endothelial dysfunction includes decreased endothelial cell-mediated vasodilation, fibrinolytic ability, and hemodynamic disturbances, among which the main manifestation is the decrease in the ability to relax blood vessels. The reason may be that the synthesis or release of NO by endothelial cells itself is reduced, or the above two conditions exist at the same time. And the reduction of NO bioavailability, which is caused by the abnormal function of NO synthase, leads to the reduction of NO synthesis, or (and) the increase of NO degradation caused by reactive oxygen species [8]. Finally, the vasodilation function is reduced to varying degrees, mainly due to the endothelium-dependent relaxation function, while reducing its ability to fight atherosclerosis, providing more favorable conditions for the formation and development of atherosclerotic plaque. At present, it is confirmed that vascular endothelial cells are damaged to initiate atherosclerosis and play an important role [9]. Atherosclerosis of arterial blood vessels is considered to be the basis of various groups of vascular diseases. It is believed that its occurrence and development is a chronic inflammatory process, mainly through the joint action of a variety of inflammatory cells and inflammatory mediators in the body [10]. Arteriosclerosis can be formed in the circulation of blood vessels in various systems and organs of the body, such as renal arteries and coronary arteries. Abnormal complex carbohydrates and lipids can accumulate in the diseased blood vessel. At the same time, a large amount of calcium deposits in the inner layer of the blood vessel and excessive fibrous tissue proliferation will eventually cause the wall of the involved artery to become thicker and harder, and even lose its elasticity; further, the vascular cavity is narrowed and even completely blocked, resulting in an increase in the occurrence of various types of cardiovascular and cerebrovascular diseases. Current research shows that atherosclerosis-related cardiovascular disease has become the most common cause of death in the world. The mortality rate of related diseases each year even exceeds that of cancer, which poses a great threat to human health, and at the same time causes a huge economic burden and

psychological pressure on our society and families. Early detection and timely correction of vascular endothelial function damage-related factors are of great significance for the prevention of cardiovascular and cerebrovascular diseases [11]. The detection of the patient's vascular endothelial function is of great significance for assessing the patient's atherosclerosis and severity, early prediction of the occurrence of cardiovascular disease, and evaluation of the effect before and after drug treatment.

Factors related to vascular endothelial dysfunction

The factors that cause vascular endothelial function damage and dysfunction are currently known to include metabolic syndrome including obesity, diabetes, insulin resistance, hypertension, lipid metabolism disorders, nonalcoholic fatty liver, and classic risk factors such as smoking, age, and men. These factors can cause abnormalities in human hemodynamics and metabolic changes, including increased blood viscosity and increased vascular pressure. Through some pathophysiological reactions such as increasing oxidative stress, inducing inflammation, reducing NO synthase activity, and promoting the adhesion between leukocytes and vascular endothelial cells, it eventually leads to vascular endothelial dysfunction [12]. Figure 1 shows the related factors that cause vascular endothelial dysfunction.

(2) Detection method of vascular endothelial function

According to the nature of each inspection method, it is divided into equipment inspection and biochemical method inspection.

2.1.1. Equipment Inspection

① Blood flow-mediated vasodilation

The specific method is to place the blood pressure device at the distal end of the upper brachial artery of the forearm. The inflation pressure of the cuff is higher than the systolic pressure or the pressure of 200 mmHg given to it. After 5 minutes, the contraction forms reactive hyperemia, increasing intravascular blood flow and shear stress, which increases the release of NO from the endothelium and promotes vasodilation. In addition, sublingual administration of nitroglycerin will increase the concentration of extrinsic NO, thereby promoting vasodilation. At the same time, two-dimensional plane high-resolution ultrasound is used to detect the diameter of the proximal brachial artery before and after the compression change, and calculate the rate of change of the artery diameter. If endothelial dysfunction occurs, FMD% will be lower than healthy people [13].

②Quantitative coronary angiography in which vasoactive substances are injected into the coronary arteries

The specific method is to inject acetylcholine and other vascular substances into the coronary arteries through a catheter to cause endothelium-dependent vasodilation, use Doppler conductive wire to measure coronary blood flow, and evaluate the endothelial function of the coronary circulation [14].

③Laser speckle imaging

The specific method is to detect changes in the blood flow of the skin microcirculation before and after the hyperemia, after acetylcholine penetrates the skin, or after the occlusion causes reactive hyperemia to evaluate the endothelial function.

2.1.2. Biochemical Examination. There are several molecules and particles related to endothelial function damage and blood circulation repair, and endothelial function can be evaluated by detecting these molecules and particles. At present, the biomarkers of endothelial function generally used in clinical research include asymmetric dimethylalanine, soluble E-selenium, iron hexaenoic acid, and factor circulating endothelial precursor cells [15].

2.1.3. Repair of Vascular Endothelial Injury. A certain degree of vascular endothelial dysfunction in the early stage can be reversed, so the evaluation of vascular endothelial function is of great significance and can detect early vascular endothelial dysfunction [16]. The early stage of vascular endothelial function damage has a certain degree of repairability, and maintaining the structural and functional integrity of vascular endothelial cells is important for the recovery of early vascular endothelial dysfunction. Repairing endothelial cells after an injury is a crucial issue in preventing atherosclerosis-related cardiovascular diseases. Researchers have found some methods for treating early vascular endothelial injury through a large number of experiments. Figure 2 shows some of the methods discovered by researchers that can be used to repair the vascular endothelial injury.

2.1.4. Atherosclerosis. Cardiovascular disease is the most common disease that puts human health in a dangerous state. Athenian Roma arteriosclerosis is the main pathological basis of cardiovascular disease. Atherosclerosis is characterized by a high incidence, a high recurrence rate, a high obstruction rate, and a high mortality rate. With the intensification of population aging, the number of patients with hypertension, hyperlipidemia, and diabetes is increasing year by year, not only the incidence of middle-aged and elderly people is increasing, but the incidence of young people is also increasing [17]. The fact that atherosclerotic disease has caused a huge burden on the family and society is becoming clear. Atherosclerosis is a vascular disease that accumulates in the large and medium arteries and is characterized by the deposition and inflammation of lipids. Atherosclerosis involves a variety of vascular cells such as endothelial cells, smooth muscle cells, Mclovac, and lymphocytes [18]. There are many causes of atherosclerotic disease; Figure 3 lists the general causes of atherosclerosis.

With the development of imaging technology and ultrasound technology, there are currently a variety of

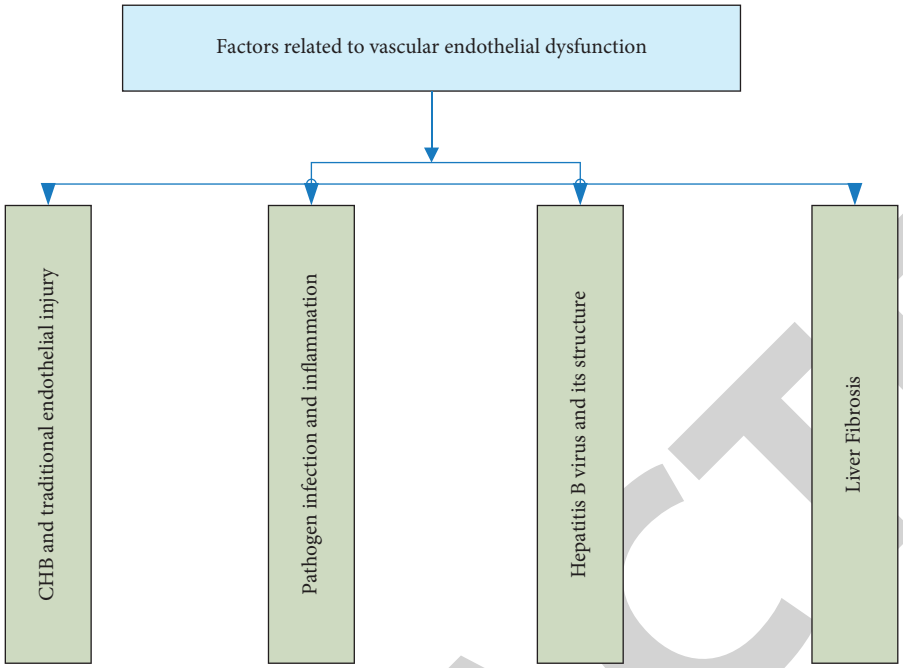

Figure 1: Related factors causing vascular endothelial dysfunction.

Figure 2: Treatment of early vascular endothelial injury.

common clinical imaging examination methods that can directly image the blood vessel condition. Generally speaking, they can be divided into a noninvasive examination and invasive examination. Noninvasive examinations include cervical angiography, cervical vascular ultrasound, high-resolution MRI, etc. Invasive examinations include digital side-effect angiography, intravascular ultrasound, endovascular endoscopy, etc. [19]. Figure 4 shows the common medical imaging examination methods for vascular diseases:

2.2. Hemodynamics. Blood circulation dynamics is the science of studying blood deformation and flow. It uses a high degree of computer technology and numerical calculation methods to investigate the effect of blood and plasma viscosity on the body. With the rapid development of computer technology and numerical calculation methods, more and more scholars use computers to perform numerical simulation calculations on blood circulation dynamics, which is currently the main research method [20].

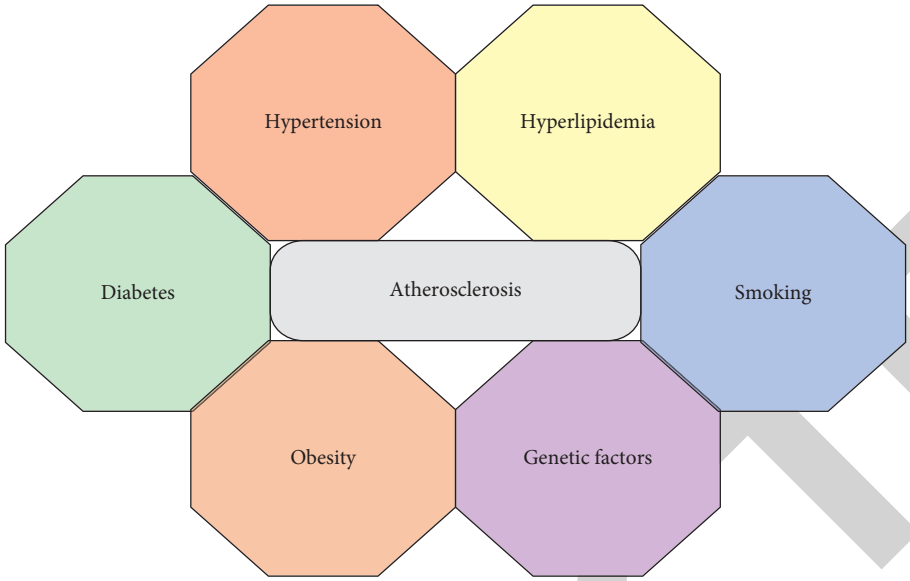

Figure 3: Causes of atherosclerosis.

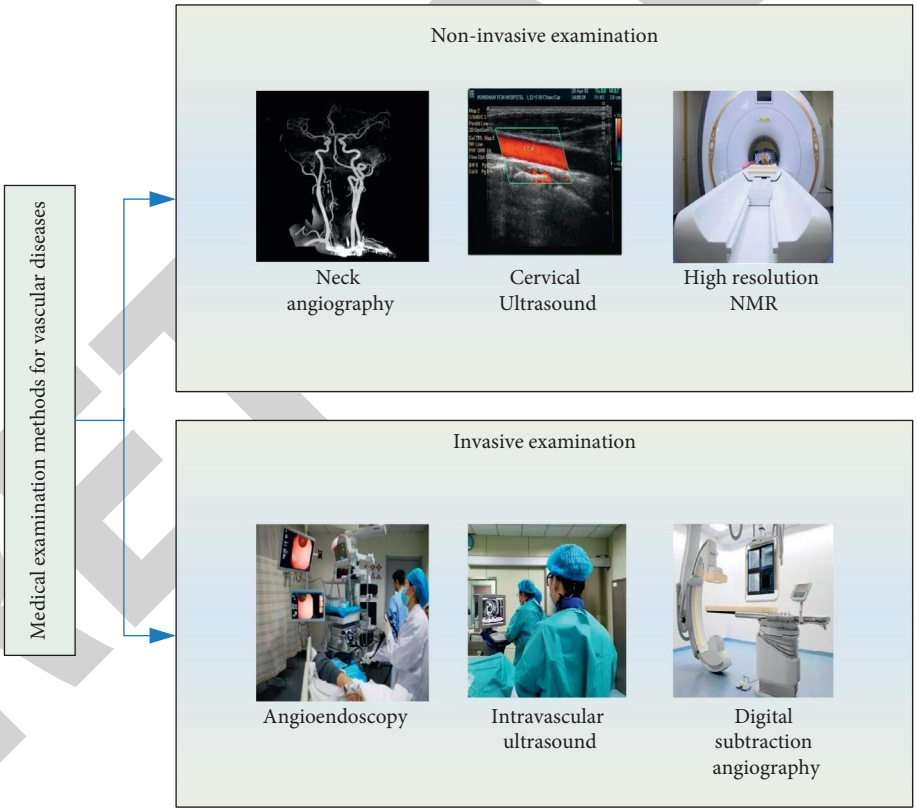

Figure 4: Common medical imaging examination methods for vascular diseases.

2.2.1. Hemodynamic Model

(1) Basic Equation of Fluid Motion. According to the law of conservation of mass, the continuity equation satisfied by the fluid is as follows:

$$\frac{\alpha p}{\alpha q} + \nabla \cdot (p * v) = 0, \tag{1}$$

where p stands for fluid density and v stands for flow velocity.

All fluids are compressible fluids under actual conditions, but in the case of low-speed moving liquids or gases with small temperature differences, they can usually be approximated as incompressible fluids. When the density p is constant, the continuity equation of the fluid can be simplified to the following equation:

$$\nabla \cdot v = 0. \tag{2}$$

The energy equation of fluid motion is as follows:

$$\frac{Na}{Nz} + I\frac{N}{Nz}\left(\frac{1}{p}\right) = TP + \frac{1}{p}\left[\frac{\alpha}{\alpha m}\left(l\frac{\alpha Z}{\alpha m}\right) + \frac{\alpha}{\alpha n}\left(l\frac{\alpha Z}{\alpha n}\right) + \frac{\alpha}{\alpha b}\left(l\frac{\alpha Z}{\alpha b}\right)\right] + \Phi. \tag{3}$$

In equation (3), l is the thermal conductivity, Z is the temperature, and Φ is the energy consumption function, which represents the mechanical work that is discharged by the fluid every unit time and unit mass due to viscosity.

If the fluid is an ideal fluid, $v = (a, b, c)$ is set in the Cartesian coordinate system, and the differential motion equation is shown as follows:

$$\begin{aligned}
p\left(\frac{\alpha_a}{\alpha_z} + a\frac{\alpha_a}{\alpha_x} + b\frac{\alpha_a}{\alpha_y} + c\frac{\alpha_a}{\alpha_o}\right) &= -\frac{\alpha_l}{\alpha_x} + T_a,\\
p\left(\frac{\alpha_b}{\alpha_z} + a\frac{\alpha_b}{\alpha_x} + b\frac{\alpha_b}{\alpha_y} + c\frac{\alpha_b}{\alpha_o}\right) &= -\frac{\alpha_l}{\alpha_y} + T_b,\\
p\left(\frac{\alpha_c}{\alpha_z} + a\frac{\alpha_c}{\alpha_x} + b\frac{\alpha_c}{\alpha_y} + c\frac{\alpha_c}{\alpha_o}\right) &= -\frac{\alpha_l}{\alpha_o} + T_c.
\end{aligned} \tag{4}$$

When the fluid is a Newtonian fluid, if $v = (m, n, t)$ is set in the Cartesian coordinate system, the following equation should be satisfied when it is solved:

$$\begin{aligned}
&\frac{\alpha_m}{\alpha_x} + \frac{\alpha_n}{\alpha_y} + \frac{\alpha_t}{\alpha_z} = 0,\\
&p\left(\frac{\alpha_m}{\alpha_o} + m\frac{\alpha_m}{\alpha_x} + n\frac{\alpha_m}{\alpha_y} + t\frac{\alpha_m}{\alpha_z}\right) = -\frac{\alpha_p}{\alpha_x} + \frac{\alpha}{\alpha_x}\left(\delta\frac{\alpha_m}{\alpha_x}\right) + \frac{\alpha}{\alpha_y}\left(\delta\frac{\alpha_m}{\alpha_y}\right) + \frac{\alpha}{\alpha_z}\left(\delta\frac{\alpha_m}{\alpha_z}\right) + T_m,\\
&p\left(\frac{\alpha_n}{\alpha_o} + m\frac{\alpha_n}{\alpha_x} + n\frac{\alpha_n}{\alpha_y} + t\frac{\alpha_n}{\alpha_z}\right) = -\frac{\alpha_p}{\alpha_y} + \frac{\alpha}{\alpha_x}\left(\delta\frac{\alpha_n}{\alpha_x}\right) + \frac{\alpha}{\alpha_y}\left(\delta\frac{\alpha_n}{\alpha_y}\right) + \frac{\alpha}{\alpha_z}\left(\delta\frac{\alpha_n}{\alpha_z}\right) + T_n,\\
&p\left(\frac{\alpha_t}{\alpha_o} + m\frac{\alpha_t}{\alpha_x} + n\frac{\alpha_t}{\alpha_y} + t\frac{\alpha_t}{\alpha_z}\right) = -\frac{\alpha_p}{\alpha_z} + \frac{\alpha}{\alpha_x}\left(\delta\frac{\alpha_t}{\alpha_x}\right) + \frac{\alpha}{\alpha_y}\left(\delta\frac{\alpha_t}{\alpha_y}\right) + \frac{\alpha}{\alpha_z}\left(\delta\frac{\alpha_t}{\alpha_z}\right) + T_t.
\end{aligned} \tag{5}$$

Here, m, n, and t represent the velocity components in the x, y, and z directions, respectively, and T_m, T_n, and T_t represent the generalized source terms of the momentum equation.

$$\begin{aligned}
T_m &= L_x + T_x,\\
T_n &= L_y + T_y,\\
T_t &= L_z + T_z.
\end{aligned} \tag{6}$$

For incompressible fluids, T_m, T_n, and T_t are all zero. When physical strength is not considered, $L_x = L_y = L_z = 0$; when inertial force is considered, $L_x = L_y = 0, L_z = -pj$.

When the fluid moves, the fluid called viscous stress has the resistance to the relative movement between two adjacent layers, but the ideal fluid without viscosity does not exist in objective reality [21]. According to the law of momentum preservation, the navigation tracking equation of fluid

motion is derived, which is used to illustrate the motion law of the motion law of viscous fluid:

$$p\left(\frac{\alpha_m}{\alpha_o} + m \cdot \nabla m\right) = -\nabla y + \nabla \cdot \partial,$$
$$\partial = 2\chi(\varepsilon)M, \tag{7}$$
$$M = 1/2\left(\nabla m + \nabla m^o\right),$$

where p is the fluid density and y is the pressure.

2.2.2. Newtonian Fluid. Unlike ideal fluids, actual fluids have a viscous effect, which can roughly distinguish between Newtonian fluids and non-Newtonian fluids. Newtonian fluids have low viscosity and are easily deformed due to external forces. The internal frictional force is proportional to the deformation speed of the fluid. After the stress is applied by the Newtonian fluid, the shear stress between the fluid layers is proportional to the deformation speed of the fluid [22]. The formula of Newton's law of viscosity is expressed as follows:

$$\theta = \alpha \frac{dx}{dy}. \tag{8}$$

The widely used equations of fluid motion are derived from Stokes' mathematical reasoning. The composition relationship of Newtonian fluid can be written as follows [23]:

(1) Tangential stress

$$\theta_{ab} = \theta_{bz} = \alpha\left(\frac{\delta_x}{\delta_b} + \frac{\delta_p}{\delta_a}\right),$$
$$\theta_{bc} = \theta_{cb} = \alpha\left(\frac{\delta_q}{\delta_b} + \frac{\delta_p}{\delta_c}\right), \tag{9}$$
$$\theta_{ca} = \theta_{ac} = \alpha\left(\frac{\delta_q}{\delta_a} + \frac{\delta_x}{\delta_c}\right).$$

(2) Normal stress

$$\nu_{aa} = -l + 2\alpha\frac{\delta_x}{\delta_a} - \frac{2}{3}\alpha\nabla \cdot m,$$
$$\nu_{bb} = -l + 2\alpha\frac{\delta_y}{\delta_b} - \frac{2}{3}\alpha\nabla \cdot m, \tag{10}$$
$$\nu_{cc} = -l + 2\alpha\frac{\delta_z}{\delta_c} - \frac{2}{3}\alpha\nabla \cdot m.$$

The above equations are called the generalized Newtonian viscosity law, and fluids that satisfy these equations are Newtonian fluids. For Newtonian fluids that cannot be compressed, the equation of motion can be simplified as follows:

$$k\left(\frac{\delta_m}{\delta_i} + m \cdot \nabla m\right) = -\nabla \cdot l + \alpha\nabla^2 m. \tag{11}$$

Based on this, the kinematic viscosity coefficient z is the ratio of the fluid's kinematic viscosity coefficient α to the fluid density k. The expression of the formula is as follows:

$$z = \frac{\alpha}{k}. \tag{12}$$

The blood flow in the blood vessel was investigated, and it was found that if the diameter of the blood vessel exceeds 1 mm, the intrinsic viscosity coefficient of the blood will be close to a constant, and the blood at this time can be approximated as a Newtonian fluid. Normally, the diameter of the blood flow of the artery is large, which satisfies this condition.

2.3. Smooth Muscle Cells. Studies have shown that vascular smooth muscle cells are important cells constituting the vascular wall, and the proliferation and migration of vascular smooth muscle cells play an important role in the formation of arteriosclerosis. After the vascular intima is injured, endothelial cells, inflammatory cells, and platelets will release growth factors, reticulin, and other related regulatory factors. These factors will promote the contraction of vascular smooth muscle cells, promote cell proliferation and migration, and cause intimal hyperplasia or intimal hyperplasia, leading to the formation of arteriosclerosis.

Smooth muscle is distributed in several internal organs, arranged in parallel in the internal organs, forming smooth muscle bundles or layers, forming the digestive tube, respirator, genitourinary organ, blood, and other tubes or cavity walls [24]. Smooth muscle cells have two basic characteristics, there is no horizontal stripe pattern of skeletal tendons and cardiomyocytes. Smooth muscle cells are distributed in most organs in the human body. Figure 5 shows the distribution of smooth muscle cells in the human body.

The proliferation of vascular smooth muscle cells (VSMCs) is one of the general cytopathological basis of atherosclerosis, hypertension, and vascular restenosis. The risk factors of cardiovascular disease can damage the vascular endothelial function, especially the appearance of growth factors, which act on VSMC membrane receptors, activate intracellular signal transmission pathways, and ultimately cause the emergence of nuclear genes and promote the excessive proliferation of VSMCs [25, 26].

Cell proliferation is one of the basic characteristics of life activities and the result of orderly regulation of a series of genes. Under physiological conditions, VSMC means regular reproduction and death, maintaining the balance between the two. In many pathological conditions, the external environment will cause specific cytokine pathology, especially the increase of growth factors, and then regulate the appearance of specific genes by stimulating the signal transmission network. As a result, the proliferation of VSMC cannot be controlled, leading to a series of symptoms. Figure 6 shows the signal transduction pathways related to VSMC proliferation:

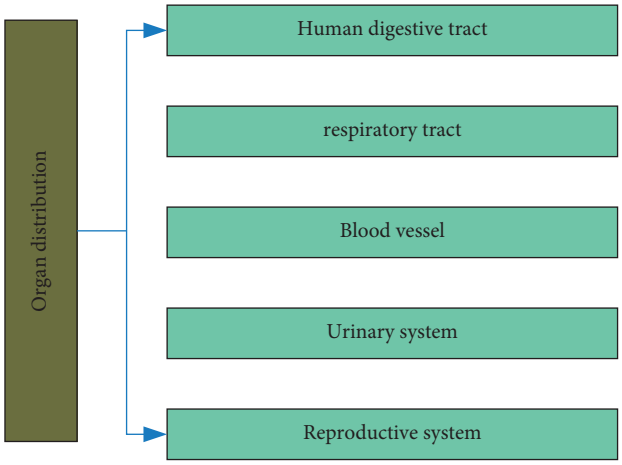

Figure 5: Organ distribution of smooth muscle cells.

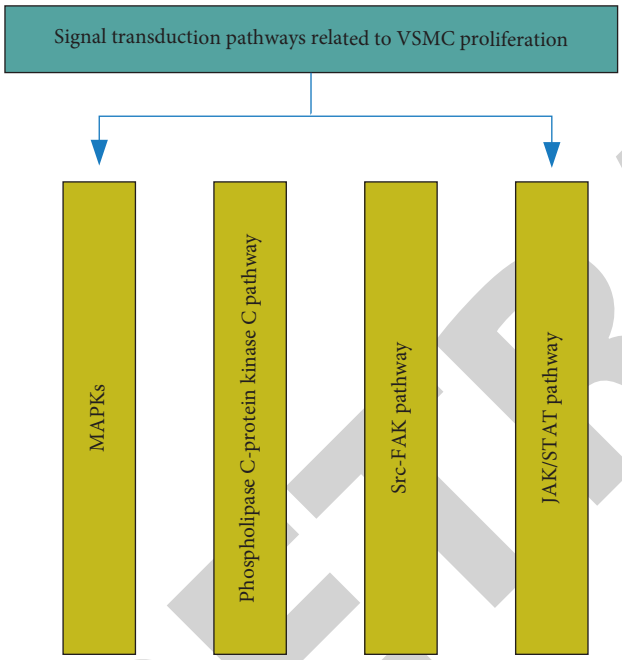

Figure 6: Signal transduction pathways related to VSMC proliferation.

3. Atherosclerosis Experiment Based on Machine Learning Method

3.1. Single Factor Investigation Experiment on the Distribution of Risk Factors and Intracranial and Extracranial Artery Stenosis. In this experiment, 600 patients with cardiovascular and cerebrovascular diseases were investigated, which were divided into three groups, namely the young group (<30), the middle-aged group (31–55), and the elderly group (>56). The number of male and female patients in each group is different, including 360 male patients and 240 female patients. Table 1 lists the distribution of intracranial and extracranial artery stenosis in different age groups obtained in this experiment.

Hypertension, diabetes, etc. are also causes of atherosclerosis. During the experiment, blood pressure and blood sugar were measured in 600 patients with cardiovascular and cerebrovascular diseases, which was used to investigate the correlation between hypertension, diabetes, and other intracranial and extracranial artery stenosis. Table 2 lists the statistical table of the survey results.

In addition to investigating the relationship between diabetes, hypertension, coronary heart disease, etc. and intracranial and extracranial artery stenosis, this experiment also focused on patients with a history of smoking and drinking. Table 3 lists the results of the experimental investigation on the correlation between the history of smoking and drinking and the distribution of intracranial and extracranial artery stenosis.

3.2. Distribution Characteristics of Risk Factors in Different Ages and Genders. There are many reasons for atherosclerosis, mainly smoking, drinking, obesity, high blood pressure, hyperlipidemia, diabetes, coronary heart disease, and so on. At the same time, the main reasons for patients of different age groups are also different. In this experiment, the distribution characteristics of risk factors for atherosclerosis in different age groups were studied. Table 4 and 5 are a comparison table of the distribution characteristics of atherosclerotic disease risk factors in different age groups and different gender groups, respectively.

3.3. Investigation and Experiment Related to Atherosclerotic Vascular Disease. This experiment investigated the domestic atherosclerotic vascular disease in recent decades, mainly investigating the mortality, urban and rural distribution, and age distribution of atherosclerotic vascular disease. In the investigation, statistical software is used to preprocess the data, and data classification and regression analysis are used to fit and analyze the data. Table 6 lists the survey results of this experiment.

4. Related Experiments of Atherosclerotic Diseases Based on Deep Learning

4.1. Experimental Results of Single Factor Investigation on the Distribution of Risk Factors and Intracranial and Extracranial Artery Stenosis. According to the experimental data in Tables 1 and 2, the distribution of intracranial and extracranial artery stenosis can be obtained, as shown in Figure 7:

According to Figure 7, it can be concluded that with the increase of age, the proportion of intracranial artery stenosis continues to decrease, but the proportion of intracranial combined intracranial artery stenosis continues to increase. In addition, it can be concluded from Figure 7 that hypertension (78.6%) and diabetes (53.2%) are more likely to cause intracranial stenosis with extracranial arteries, while patients with coronary heart disease are more likely to cause simple extracranial artery stenosis.

4.2. The Experimental Results of the Distribution Characteristics of Risk Factors in Different Ages and Genders. According to the experimental data in Tables 4 and 5, the distribution characteristics of atherosclerotic disease risk factors of different ages and genders can be drawn, as shown in Figure 8:

Table 1: Distribution of intracranial and extracranial artery stenosis in different age groups.

	No arterial stenosis	Intracranial stenosis	Extracranial stenosis	Intracranial combined extracranial
Youth group	12	16	3	8
Middle age group	123	178	16	58
Elderly group	56	70	10	50

Table 2: Correlation analysis of hypertension, diabetes, coronary heart disease, and the distribution of intracranial and extracranial artery stenosis.

	No arterial stenosis	Simple intracranial	Simple extracranial	Intracranial combined extracranial
Hypertension	106 (52.8%)	162 (63.4%)	26 (61.2%)	91 (78.6%)
Diabetes	58 (35.1%)	101 (42.6%)	16 (41.8%)	60 (53.2%)
Coronary heart disease	29 (15%)	52 (19.6%)	14 (32.8%)	26 (22%)

Table 3: Correlation analysis between the history of smoking and drinking and the distribution of intracranial and extracranial artery stenosis.

	No arterial stenosis	Simple intracranial	Simple extracranial	Intracranial combined extracranial
Smoking history	88 (49.2%)	150 (50.6%)	18 (56%)	60 (53%)
Drinking history	49 (27%)	79 (29.6%)	13 (34%)	42 (34.8%)

Table 4: Comparison of the distribution characteristics of atherosclerotic disease risk factors in different age groups (%).

	Youth group (%)	Middle age group (%)	Elderly group (%)
Smoking history	43.2	63.9	36.8
Drinking history	19.1	34.2	19.6
Obesity	78	63	53.2
Hypertension	54.2	65.8	66.2
Diabetes	32.1	40.2	42
High uric acid	7.5	15.1	11.2
Coronary heart disease	4.2	17.5	53.8

Table 5: Distribution characteristics of atherosclerotic disease risk factors in different gender groups (%).

	Male (%)	Female (%)
Smoking history	69.1	19.2
Drinking history	42.1	2.8
Obesity	63.5	57.4
Hypertension	62	65
Diabetes	36.6	50.2
High uric acid	15.3	6.8
Coronary heart disease	18.8	24.9

Table 6: Investigation results of atherosclerotic vascular disease.

	1995 (%)	1998 (%)	2000 (%)	2005 (%)	2010 (%)	2015 (%)
Mortality rate	19.8	18.7	20.1	19.2	23.8	28.1
Urban mortality	15.6	18.9	20.5	19.3	18.8	17.6
Rural mortality	12.1	13.0	14.4	16.8	17.1	17.9

According to Figure 8, obesity has a great influence on the vascular health of people of all ages, especially in the youth group, obesity has the greatest impact on cerebrovascular, reaching 78%. Among different genders, women's cerebrovascular disease is more closely related to hypertension. Figure 9 shows the incidence of hypertension in China in the past few years.

It can be seen from Figure 9 that the incidence of hypertension has been increasing year by year in recent years, showing an upward trend like atherosclerosis, and the probability of hypertension in people over 70 years old has reached more than 50%. From the statistics shown in Figure 9, it can be concluded that hypertension is an important factor in inducing atherosclerosis.

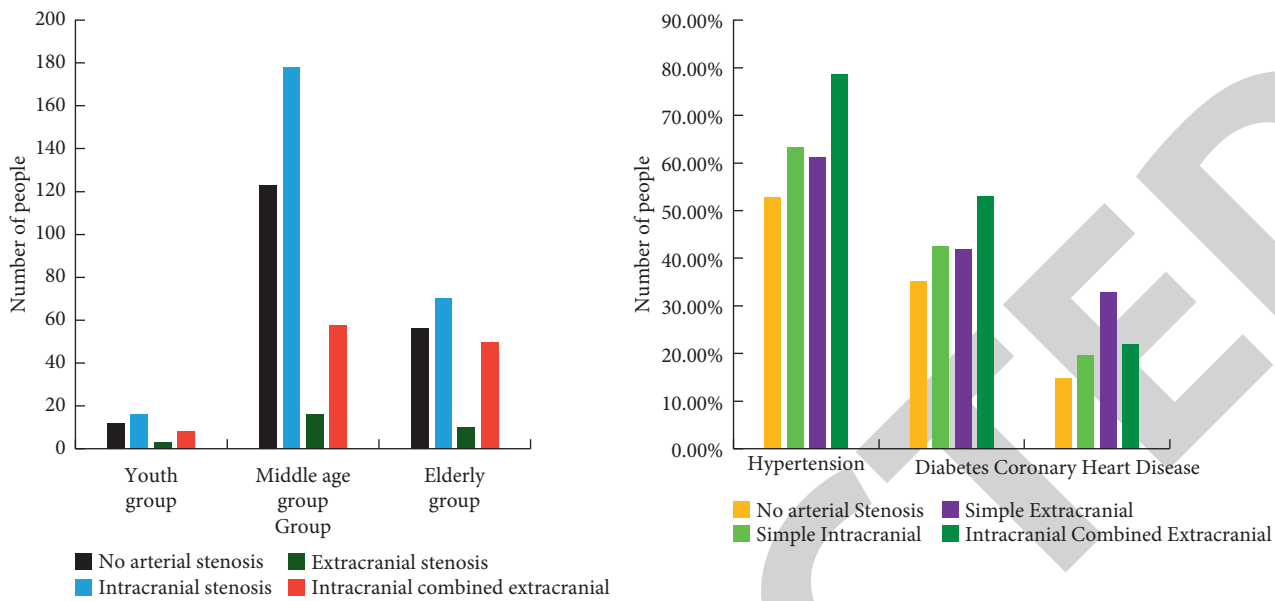

Figure 7: Distribution of intracranial and extracranial artery stenosis.

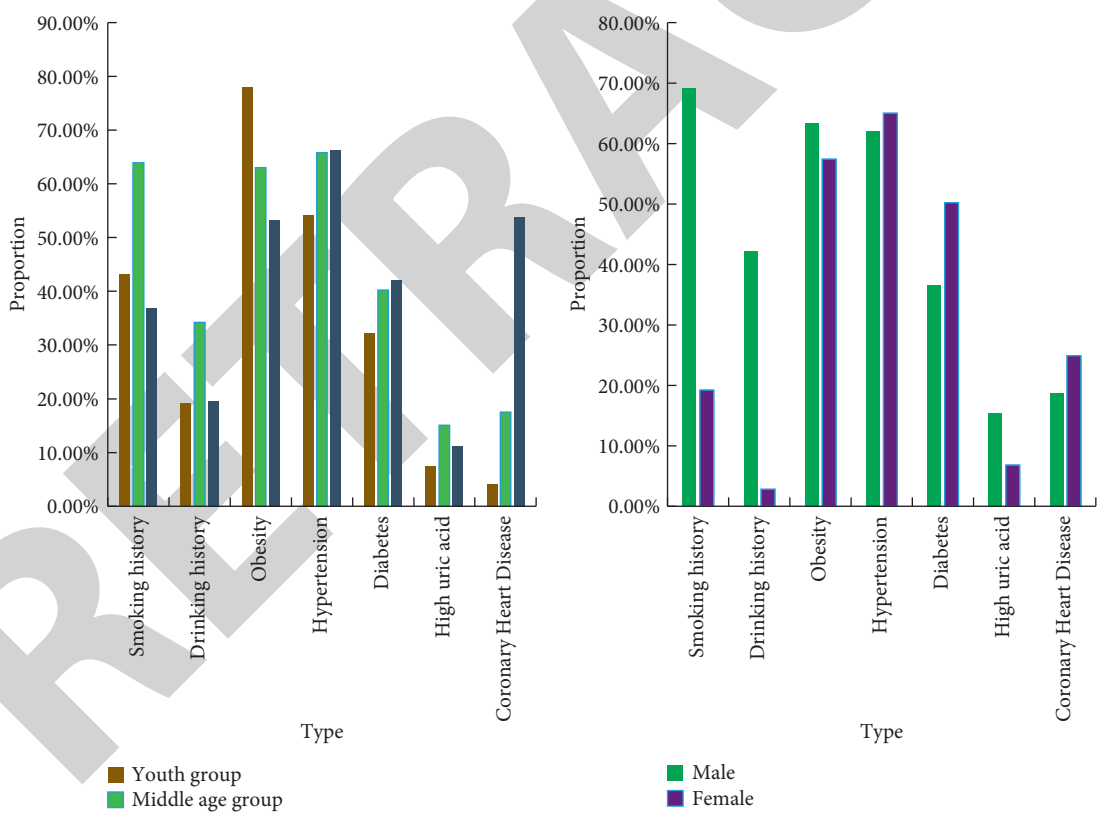

Figure 8: Distribution characteristics of atherosclerotic disease risk factors of different ages and genders.

4.3. The Results of Investigations Related to Atherosclerotic Vascular Diseases. According to the experimental data in Table 6 and other related data, a statistical chart of the mortality results of various diseases in China in recent years can be obtained, as shown in Figure 10:

It can be seen from Figure 10 that in recent years, the incidence of atherosclerotic vascular diseases in China has been on the rise, and the death rate has exceeded the mortality rate of tumor diseases. As of 2015, domestic deaths from cardiovascular and cerebrovascular diseases accounted for nearly 30% of all causes of death. Moreover, it can be concluded from Figure 10 that the mortality rate of atherosclerotic diseases among rural residents has increased.

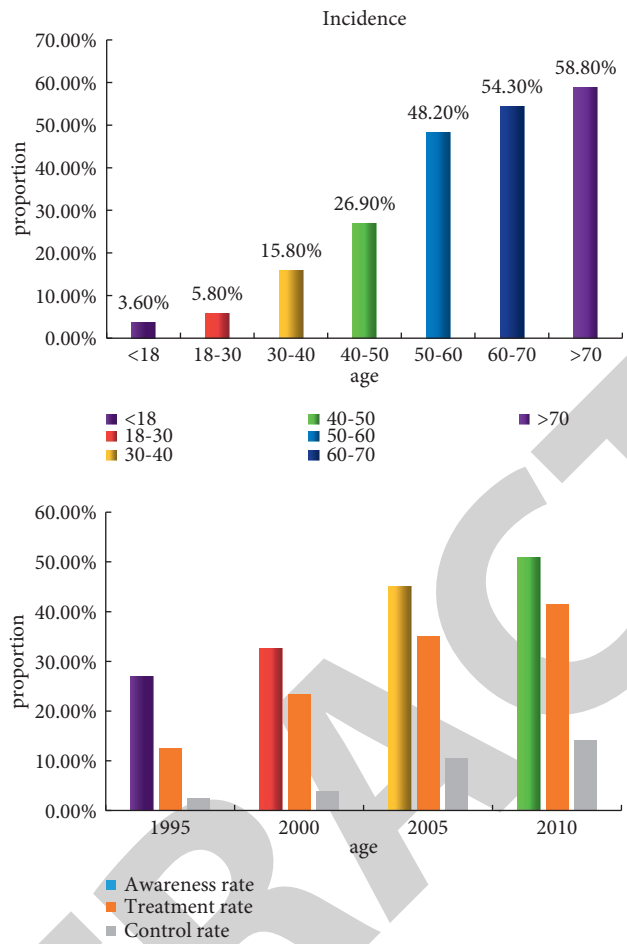

Figure 9: The incidence and control rate of hypertension in recent years.

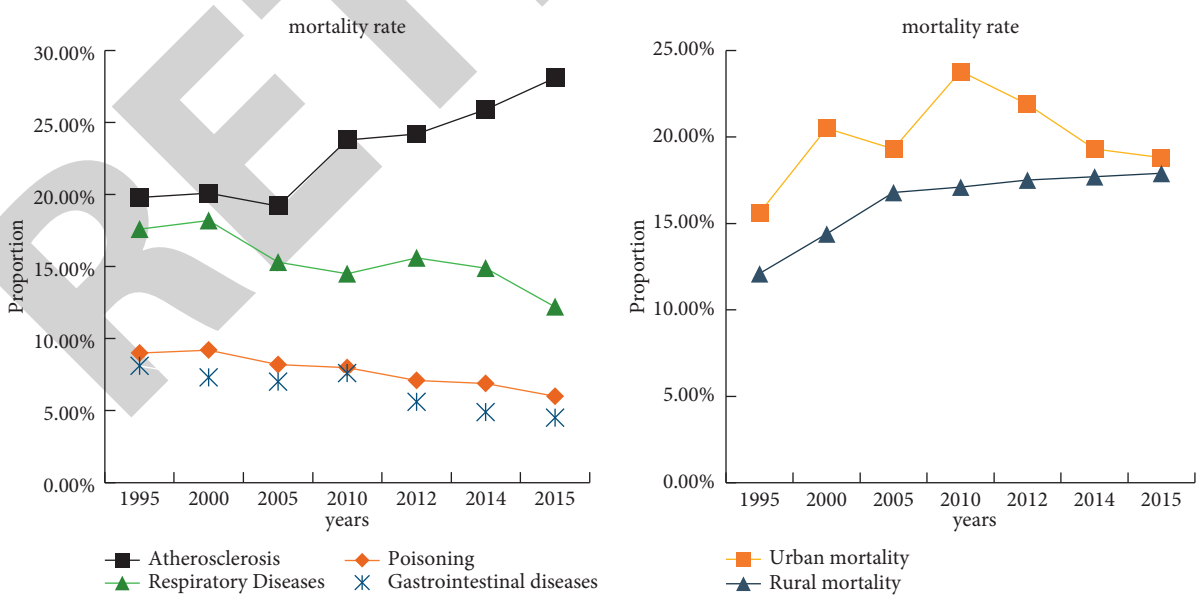

Figure 10: Comparison of mortality rates of various diseases in China in recent years.

5. Conclusions

AS is a chronic inflammatory disease involving the mediators of the aorta and middle arteries throughout the body, and is one of the main causes of cardiovascular disease and cerebrovascular disease. Through the experimental research in this article, it is found that atherosclerosis is greatly affected by factors such as hypertension, hyperlipidemia, diabetes. At the same time, atherosclerotic vascular endothelial dysfunction also has a great impact on the proliferation of smooth muscle cells. A variety of genes and environmental factors can regulate the functions of endothelial cells, vascular smooth muscle cells and mononuclear macrophages to affect the formation of atherosclerosis. And it was found in research that the incidence and mortality of atherosclerosis in China have been increasing in recent years. Atherosclerosis has also become the main cause of death due to cardiovascular and cerebrovascular diseases, accounting for nearly 30%.

Data Availability

No data were used to support this study.

Disclosure

The authors confirm that the content of the manuscript has not been published or submitted for publication elsewhere.

Conflicts of Interest

The authors declare no conflicts of interest.

Authors' Contributions

All authors have seen the manuscript and approved to submit to your journal.

Acknowledgments

This study was supported by the National Natural Science Foundation of China (nos. 81774032 and 82174218), Natural Science Foundation of Hunan Province of China (nos. 2020JJ2024 and 2018JJ3391), Education Department of Hunan Province of China (no. 19A374), National College Student Innovation and Entrepreneurship Training Program of China (nos. S202110541015 and S202010541006), and Provincial College Student Innovation and Entrepreneurship Training Program of China (no. J2020-010).

References

[1] M. A. Gimbrone and G. García-Cardeña, "Endothelial cell dysfunction and the pathobiology of atherosclerosis," *Circulation Research*, vol. 118, no. 4, pp. 620–636, 2016.

[2] B. G. Childs, D. J. Baker, T. Wijshake, C. A. Conover, J. Campisi, and J. M. van Deursen, "Senescent intimal foam cells are deleterious at all stages of atherosclerosis," *Science*, vol. 354, no. 6311, pp. 472–477, 2016.

[3] D. F. J. Ketelhuth and G. K. Hansson, "Adaptive response of T and B cells in atherosclerosis," *Circulation Research*, vol. 118, no. 4, pp. 668–678, 2016.

[4] B. L. Needham, B. Mukherjee, P. Bagchi et al., "Acculturation strategies and symptoms of depression: the mediators of atherosclerosis in South Asians living in America (MASALA) study," *Journal of Immigrant and Minority Health*, vol. 20, no. 4, pp. 792–798, 2018.

[5] B. Warren, P. Pankow, K. Matsushita, and N. R. Daya, "Comparative prognostic performance of definitions of prediabetes: a prospective cohort analysis of the Atherosclerosis Risk in Communities (ARIC) study," *Lancet Diabetes & Endocrinology*, vol. 5, no. 1, pp. 34–42, 2016.

[6] S.-c. Huang, M. Wang, W.-b. Wu et al., "Mir-22-3p inhibits arterial smooth muscle cell proliferation and migration and neointimal hyperplasia by targeting HMGB1 in arteriosclerosis obliterans," *Cellular Physiology and Biochemistry*, vol. 42, no. 6, pp. 2492–2506, 2017.

[7] Z. Sun, X. Nie, S. Sun et al., "Long non-coding RNA MEG3 downregulation triggers human pulmonary artery smooth muscle cell proliferation and migration via the p53 signaling pathway," *Cellular Physiology and Biochemistry*, vol. 42, no. 6, pp. 2569–2581, 2017.

[8] J. Y. Luo, D. Fu, Y. Q. Wu, and Y Gao, "Inhibition of the JAK2/STAT3/SOSC1 signaling pathway improves secretion function of vascular endothelial cells in a rat model of pregnancy-induced hypertension," *Cellular Physiology and Biochemistry: International Journal of Experimental Cellular Physiology, Biochemistry, and Pharmacology*, vol. 40, no. 3-4, pp. 527–537, 2016.

[9] S. A. S. Johnson, J. J. Lin, C. J. Walkey, M. P. Leathers, C. Coarfa, and D. L. Johnson, "Elevated TATA-binding protein expression drives vascular endothelial growth factor expression in colon cancer," *Oncotarget*, vol. 8, no. 30, pp. 48832–48845, 2017.

[10] A. Danoff, M. A. Kendall, J. S. Currier, T. Kelesidis, A. M. Schmidt, and J. A. Aberg, "Soluble levels of receptor for advanced glycation endproducts (RAGE) and progression of atherosclerosis in individuals infected with human immunodeficiency virus: actg NWCS 332," *Inflammation*, vol. 39, no. 4, pp. 1354–1362, 2016.

[11] B. Spring, A. C. Moller, L. A. Colangelo, and N. Siddique, "Healthy lifestyle change and subclinical atherosclerosis in young adults coronary artery risk development in young adults (CARDIA) study," *Circulation*, vol. 130, no. 1, pp. 10–17, 2016.

[12] J. Y. Yeon, K. K. Cheon, P. M. Hee, and K. Seo, "Atherosclerosis is exacerbated by chitinase-3-like-1 in amyloid precursor protein transgenic mice," *Theranostics*, vol. 8, no. 3, pp. 749–766, 2018.

[13] C. Napoli, V. Crudele, A. Soricelli, and F. P. Mancini, "Primary prevention of atherosclerosis: a clinical challenge for the reversal of epigenetic mechanisms?" *Circulation*, vol. 125, no. 19, pp. 2363–2373, 2016.

[14] X. Y. Tian, K. Ganeshan, C. Hong et al., "Thermoneutral housing accelerates metabolic inflammation to potentiate atherosclerosis but not insulin resistance," *Cell Metabolism*, vol. 23, no. 1, pp. 165–178, 2016.

[15] Y. Baumer, S. Mccurdy, M. Alcala et al., "CD98 regulates vascular smooth muscle cell proliferation in atherosclerosis," *Atherosclerosis*, vol. 256, pp. 105–114, 2017.

[16] W. Hong, G. Peng, B. Hao et al., "Nicotine-induced airway smooth muscle cell proliferation involves TRPC6-dependent

Hindawi
Journal of Healthcare Engineering
Volume 2023, Article ID 9872062, 1 page
https://doi.org/10.1155/2023/9872062

Retraction

Retracted: Efficacy of Super-Mini-PCNL and Ureteroscopy in Kidney Stone Sufferers and Risk Factors of Postoperative Infection

Journal of Healthcare Engineering

Received 1 August 2023; Accepted 1 August 2023; Published 2 August 2023

This article has been retracted by Hindawi following an investigation undertaken by the publisher [1]. This investigation has uncovered evidence of one or more of the following indicators of systematic manipulation of the publication process:

(1) Discrepancies in scope
(2) Discrepancies in the description of the research reported
(3) Discrepancies between the availability of data and the research described
(4) Inappropriate citations
(5) Incoherent, meaningless and/or irrelevant content included in the article
(6) Peer-review manipulation

The presence of these indicators undermines our confidence in the integrity of the article's content and we cannot, therefore, vouch for its reliability. Please note that this notice is intended solely to alert readers that the content of this article is unreliable. We have not investigated whether authors were aware of or involved in the systematic manipulation of the publication process.

Wiley and Hindawi regrets that the usual quality checks did not identify these issues before publication and have since put additional measures in place to safeguard research integrity.

We wish to credit our own Research Integrity and Research Publishing teams and anonymous and named external researchers and research integrity experts for contributing to this investigation.

The corresponding author, as the representative of all authors, has been given the opportunity to register their agreement or disagreement to this retraction. We have kept a record of any response received.

References

[1] W. Yuan, Y. Li, Y. Dai, C. Luo, H. Zhang, and H. Xiong, "Efficacy of Super-Mini-PCNL and Ureteroscopy in Kidney Stone Sufferers and Risk Factors of Postoperative Infection," *Journal of Healthcare Engineering*, vol. 2022, Article ID 4733329, 7 pages, 2022.

Hindawi
Journal of Healthcare Engineering
Volume 2022, Article ID 4733329, 7 pages
https://doi.org/10.1155/2022/4733329

Research Article

Efficacy of Super-Mini-PCNL and Ureteroscopy in Kidney Stone Sufferers and Risk Factors of Postoperative Infection

Wenbing Yuan, Yingyi Li, Yu Dai, Cheng Luo, Hui Zhang, and Haijun Xiong

Urology Surgery, Baoji City People's Hospital, Baoji 721000, Shannxi Province, China

Correspondence should be addressed to Haijun Xiong; 20200720192@nxmu.edu.cn

Received 30 December 2021; Revised 10 February 2022; Accepted 11 February 2022; Published 8 March 2022

Academic Editor: Nima Jafari Navimipour

To investigate the efficacy of super-mini-PCNL (SMP) and ureteroscopy in kidney stone (KS) sufferers and learn the risk factors of postoperative infection. A retrospective analysis was performed on 180 KS sufferers who were diagnosed and treated in our hospital from May 2019 to May 2021. They were enrolled into an observation group (OG, $n = 104$) and a control group (CG, $n = 76$) based on different treatment methods. Therein, the former was treated with SMP, while the latter was treated with ureteroscopy. The operation time, blood loss, hospital stay, recent stone-free rate (one week after operation), changes of serum creatinine (SCr), blood urea nitrogen (BUN), and cystatin C (CysC) levels before and after operation and complications were compared. Those sufferers were assigned to infected and uninfected groups based on their postoperative infection. The risk factors were assessed through logistic regression, and the model formula was established. The predictive value of this model for infection was tested through RO. Compared with CG, the operation time of the OG was longer, the blood loss and hospital stay were lower ($P < 0.05$), and the stone-free rate was higher ($P < 0.05$). Renal function indexes before and after treatment ($P > 0.05$) and postoperative complications revealed no significant difference ($P > 0.05$). Logistic regression analysis manifested that preoperative urinary tract infection (OR: 4.690, 95% CI: 1.170–18.802), preoperative blood glucose level (OR: 11.188, 95% CI: 2.106–59.442), positive urine culture (OR: 10.931, 95% CI: 2.453–48.705), and infectious stones (OR: 3.951, 95% CI: 1.020–15.300) were independently related to infection. The risk prediction equation is $\text{logit}(p) = -8.913 + 1.545 \times X1 + 2.415 \times X2 + 2.392 \times X3 + 1.374 \times X4$, with a goodness-of-fit value of 0.545. The AUC is 0.930, so SMP is superior to ureteroscopy in KS sufferers. Preoperative urinary tract infection, preoperative blood glucose level, positive urine culture, and infectious stones are independently related to infection.

1. Introduction

1.1. Incidence of Renal Calculi. Kidney stone (KS) is one of the familiar diseases of urinary system. Statistics show that 5–15% of the global population is plagued by KS [1]. A survey found that the number of KS sufferers increased by 70% from 1994 to 2010 [2]. In another study, from 1992 to 2009, the rate of visits to emergency departments for stones increased by 91% [3]. Not only that, due to the mounting sufferers from population, obesity and metabolic syndrome (independent risk factors for KS), the annual cost of treatment in the US exceeds $10 billion in the medicare system [4]. Although most stones will not have long-term consequences, it was once thought that KS is related to chronic kidney disease (CKD) [5]. In addition, the recurrence rate is very high: 50% within 5–10 years and 75% within 20 years [6]. Thus, choosing an effective treatment plan is the key to improve the current situation.

1.2. Progress in the Treatment of Renal Calculi. Chinese urology guidelines for diagnosis and treatment believe that conservative treatment can be considered for stone diameter < 0.4 cm, and 90% of them may pass spontaneously; however, for stones <0.6 cm, with a smooth surface, no obstruction of the lower urinary tract, and staying in the local area for less than 2 weeks, drug stone removal is the first choice [7], but it takes a long time so that most patients cannot bear the pain caused by the disease. Clinically, there are many surgical treatment schemes for KS. There are

mainly five schemes: traditional open lithotripsy, extracorporeal shock wave lithotripsy (ESWL), laparoscopic lithotripsy, percutaneous nephrolithotomy (PCNL), and flexible ureteroscopic lithotripsy (FURL), among which ESWL and PCNL are still in the front line [8]. PCNL still plays a vital role in urology surgery, which protects a large number of KS sufferers against open surgery [9]. Although PCNL has a high stone-free rate, patients need massive transfusions during operations, and the duration is long, which will inevitably increase the occurrence of complications such as vital organ injury and hemopneumothorax [10]. As efficacy develops, super-mini-PCNL (SMP) has been generalized in clinical practice [11]. The SMP channel is usually F10-14. Comparatively speaking, such a small channel is less traumatic and bleeding. Nowadays, new ureteroscopes and related auxiliary equipment are also developing continuously, which not only improves safety and shortens the operation time, but also reduces the incidence of complications, particularly bleeding. Ureteroscopy also achieved a higher stone-free rate than SMP [12], which has become an alternative surgical scheme for clinicians.

Purpose of the Study. But for surgical treatment of stones ≤2 cm, SMP or ureteroscopy is still disputed. In this research, we retrospectively analyzed the influence of SMP and ureteroscopy on the efficacy of KS sufferers and assessed the risk factors of postoperative infection by logistic regression, so as to provide a reference for clinical surgical treatment.

2. Methods and Data

2.1. Clinical Data of Patients. A retrospective analysis was performed on 180 KS sufferers diagnosed and treated in our hospital from May 2019 to May 2021. In the light of different treatment methods, they were assigned to an observation group (OG, $n = 104$) and a control group (CG, $n = 76$). Therein, the former was treated with SMP, while the latter was treated with ureteroscopy with the consent of the Medical Ethics Committee.

2.2. Inclusion and Exclusion Criteria

2.2.1. Inclusion Criteria. The inclusion criteria were as follows: KS sufferers with imaging analysis, intravenous pyelography, and abdominal plain film (diameter ≤2 cm); it was ineffective after ESWL; and patients or their families who signed an informed consent form.

2.2.2. Exclusion Criteria. The exclusion criteria were as follows: those who were intolerable about this operation or drugs; those complicated with tumor or congenital organ defects; the ureter has anatomical malformations such as stenosis and ectopia; pregnant women; and those aged <18 years old.

2.3. Surgical Treatment Plan. The treatment plan of SMP is as follows: anesthetized sufferers were in the lithotomy position; the affected side was inserted into a retrograde ureteroscope to guide them to a prone position under the cystoscope. Under B-ultrasound, the renal calyces were punctured with F13 SMP kits, the delaser optical fiber was placed, and an incision was made in the skin to expand it to F14 along the guide wire. The metal sheath was retained, a percutaneous nephrolithotomy channel was created, and then a ureteroscope or human standard nephrolithotomy was put in. An ultrasonic lithotripsy system was used for lithotripsy (frequency 25 Hz/energy 1.0 J/power 20 W) to obtain stones < 3 mm. With normal saline, the crushed stones were washed out through the sheath along the inner wall of the sheath, and the F6 double-J tube was maintained; 1–4 weeks later, the nephrostomy tube was removed.

The treatment plan of ureteroscope is as follows: sufferers were in the same position. The ureter superfine nephroscope was put in, the F5 tube was set up in the renal pelvis to dilate the ureter, 0.035 < 3 mm ultrasmooth guide wire was employed to retain and send it to the ureteroscope, and a 200 μm smooth guide wire was placed into the soft endoscope sheath to locate stones (frequency 15–20 Hz/energy 1.0–1.5 J/power 10–25 W). The stones were crushed until the diameter <3 mm. The F5 double-J tube was maintained after the stone fragments were collected by the stone extraction basket and pulled out 1–4 weeks later, and the F14 tube was removed after nephrostomy. Antibiotics were routinely utilized in both groups after operations to prevent infection.

2.4. Clinical Index Test. Peripheral blood (5 mL) was collected, then isolated at 3000 rpm/min, and centrifuged for 10 min to obtain the supernatant. Serum creatinine (SCr), blood urea nitrogen (BUN), and cystatin C (CysC) levels were tested. CysC was tested by enhanced immunoturbidimetry, BUN by ELISA, and SCr by the picric acid method, under the Beckman 5800 automatic biochemical analyzer. All the CysC, BUN, and SCr kits were offered by the manufacturers, and all the steps were based on the instructions and were completed by the same inspection team in line with the aseptic operation rules.

2.5. Outcome Measures. The primary outcome measures were as follows: the perioperative indicator changes (operation time, blood loss, and hospital stay) and stone-free rate one week after operation (clearance rate = stone-free rate/primary stone quantity × 100%) of both groups were compared. The renal function, such as SCr, BUN, and CysC, was compared before and after the operation.

The secondary outcome measures were as follows: the clinical data (gender, age, stone diameter, past medical history (hypertension and diabetes), smoking, and alcoholism), complications (infection, delayed bleeding, fever, and urinary fistula), and the overall incidence were tested (total incidence = cases/total number × 100%). Sufferers were assigned to the infected ($n = 15$) or uninfected groups ($n = 166$) based on their infection. The risk factors were assessed through logistic regression.

2.6. Statistical Analysis. Data were processed via SPSS 20.0 and then visualized by GraphPad Prism 8 software. Specifically, the independent sample t-test was conducted for

intergroup comparison and the paired t-test for intragroup comparison, both expressed in t. The rank-sum test was utilized for ranked data expressed by Z, and the chi-square test was performed on counting data. The risk factors were assessed via logistic regression (forward was utilized for univariate analysis and backward LR for multivariate analysis). The Hosmer–Lemeshow test was used to correct the discrimination and goodness-of-fit of the ROC curve model. $P < 0.05$ was statistically different.

3. Results

3.1. Clinical Data Comparison. It was found that there was no statistical difference in gender, age, stone diameter, previous medical history, smoking, and alcoholism history between both groups (Table 1; $P > 0.05$).

3.2. Comparison of Perioperative Indicators. It was found that both the operation time and hospitalization time of patients in the CG were higher than those in the OG, with statistical differences (Figures 1(a) and 1(b); $P < 0.001$). Besides, the blood loss in the CG was higher (Figure 1(c); $P < 0.001$).

3.3. Comparison of Recent Stone-Free Rates. The recent stone-free rate of the OG was higher than that of the CG, with statistical differences (Table 2; $P < 0.05$).

3.4. Renal Function Changes. It was found that the BUN, SCr, and CysC levels in both groups were lower after treatment than before treatment, with statistical differences ($P < 0.001$). But the three levels revealed no marked difference after the operation (Figures 2(a)–2(c); $P > 0.05$).

3.5. Comparison of Postoperative Complications. CG had 6 cases of postoperative infection, 3 of delayed bleeding, 2 of fever, and 2 of urinary fistula. While in the OG, there were 9 cases of postoperative infection, 3 of delayed bleeding, 1 of fever, and 1 of urinary fistula. There was no difference in the incidence of complications between the two groups ($P > 0.05$). And the total incidence rate of both groups also showed no statistical difference (Table 3; $P > 0.05$).

3.6. Analysis of Infection Risk Factors. Finally, sufferers were assigned to the infected ($n = 15$) and uninfected groups ($n = 166$) based on their infection, and clinical data were collected (Table 4). Signal and multivariant logistic regression demonstrated that urinary tract infection (OR: 4.690, 95% CI: 1.170–18.802), preoperative blood glucose level (OR: 11.188, 95% CI: 2.106–59.442), positive urine culture (OR: 10.931, 95% CI: 2.453–48.705), and infectious stones (OR: 3.951, 95% CI: 1.020–15.300) were independent risk factors for infection (Tables 5 and 6; $P < 0.05$). The risk prediction equation was established based on multivariate logistic regression: $\text{logit}(p) = -8.913 + 1.545 \times X1 + 2.415 \times X2 + 2.392 \times X3 + 1.374 \times X4$, and the regression equation goodness-of-fit was tested through the Hosmer–Lemeshow test ($P = 0.545$). The established model was used to test the AUC of postoperative infection in KS sufferers with a value of 0.930 (specificity: 93.33% and sensitivity: 81.81%) (Figure 3 and Table 7). According to the risk prediction score model established, the probability of postoperative infection in patients with infectious stones is 60.00%, and that of ineffectiveness after treatment in RA patients whose disease course is less than 2 years is 80.60%.

4. Discussion

As living standards changes and dietary structure develops, KS incidence has been growing. It is a human mineralized disease with a complicated etiology [13]. Data statistics reveal that KS is highly likely to relapse, and the 5–10-year recurrence rate has reached more than 50% [14]. Its formation cause is vague, which is affected not only by individual factors such as urinary tract, metabolism, and gene abnormalities, but also by the environment (such as geography, climate, and diet) [15]. Medication is a frequently used treatment at present [16]. But due to the slow onset and long treatment period, it is difficult to achieve the desired effect, which makes the surgical treatment of stones popular [17]. Clinically, the traditional treatment scheme for stones is mainly open surgery. However, open surgery has caused great trauma to patients, sometimes requiring multiple operations to remove stones, and the probability of postoperative complications is high, causing serious damage to renal function [18]. Therefore, these two treatment schemes are gradually being replaced by minimally invasive surgery.

ESWL is noninvasive and repeatable, with no anesthesia, low cost, and no wound on the body surface. It is also an outpatient treatment. It can crush stones in any part of the kidney [19]. Admittedly, it is not completely harmless. It can cause irreversible complete loss of renal function, and infection, bleeding, irreversible damage of renal function, and renal parenchyma may occur during treatment [20]. Moreover, the efficacy is relevant to many factors such as the shape and size of stones, with a high recurrence rate.

SMP and ureteroscopy have become the main surgical schemes for clinical treatment. Nevertheless, there is still controversy about the two schemes. To this end, we compared the effects of the two on the efficacy of patients. BUN is a proteinmetabolism product, which will obviously increase when the glomerular filtration rate is reduced to 50% of normal [21]. SCr is a crucial indicator of renal excretion function. When renal function is damaged, its content in human body will dramatically increase. The sensitivity of CysC is extremely high, and its content will rise rapidly in the early stage of kidney injury. The abovementioned changes of the three are essential criteria for clinical evaluation of renal function. Furthermore, we discovered the renal function indexes decreased after treatment with no difference. Moreover, there is no difference in the incidence of postoperative complications, which suggests that the two surgical schemes can substantially improve the prognosis of patients with renal injury without increasing the incidence of postoperative complications. The operation time and

Table 1: Basic figures (n (%)).

Factor		CG ($n = 76$)	OG ($n = 104$)	P value
Gender	Male ($n = 116$)	46 (60.53)	70 (67.31)	0.348
	Female ($n = 64$)	30 (39.47)	34 (32.69)	
Age	≥40 years old ($n = 82$)	36 (47.37)	46 (44.23)	0.676
	<40 years old ($n = 98$)	40 (52.63)	58 (55.77)	
Stone diameter	≥1 cm ($n = 141$)	58 (76.32)	83 (79.81)	0.574
	<1 cm ($n = 39$)	18 (23.68)	21 (20.19)	
Past medical history	Diabetes ($n = 44$)	16 (21.05)	28 (25.93)	0.365
	Hypertension ($n = 61$)	25 (32.89)	36 (34.62)	0.810
History of smoking	Yes ($n = 123$)	50 (65.79)	73 (70.19)	0.530
	No ($n = 57$)	26 (34.21)	31 (29.81)	
History of alcoholism	Yes ($n = 34$)	12 (15.79)	22 (21.15)	0.364
	No ($n = 146$)	64 (84.21)	82 (78.85)	

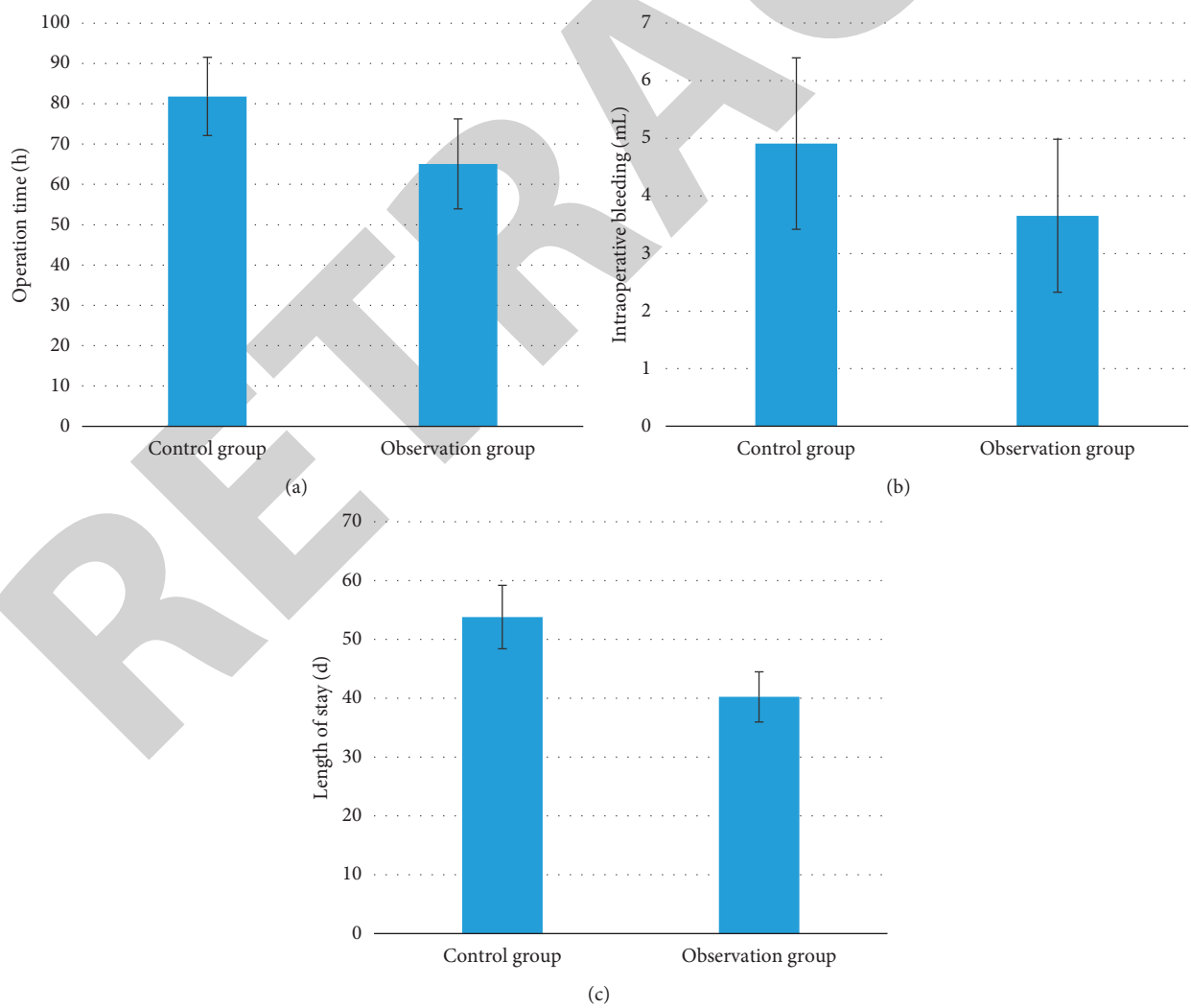

Figure 1: Perioperative indicator comparison. (a) Comparison of operation time between both groups. (b) Comparison of hospital stay between both groups. (c) Comparison of intraoperative blood loss between both groups. $^{***}P < 0.001$.

Table 2: Recent stone-free rate (n (%)).

Group	Cleared	Not cleared	$\chi 2$ value	P value
CG ($n = 76$)	57 (75.00)	19 (25.00)	7.690	0.006
OG ($n = 104$)	94 (90.38)	10 (9.62)		

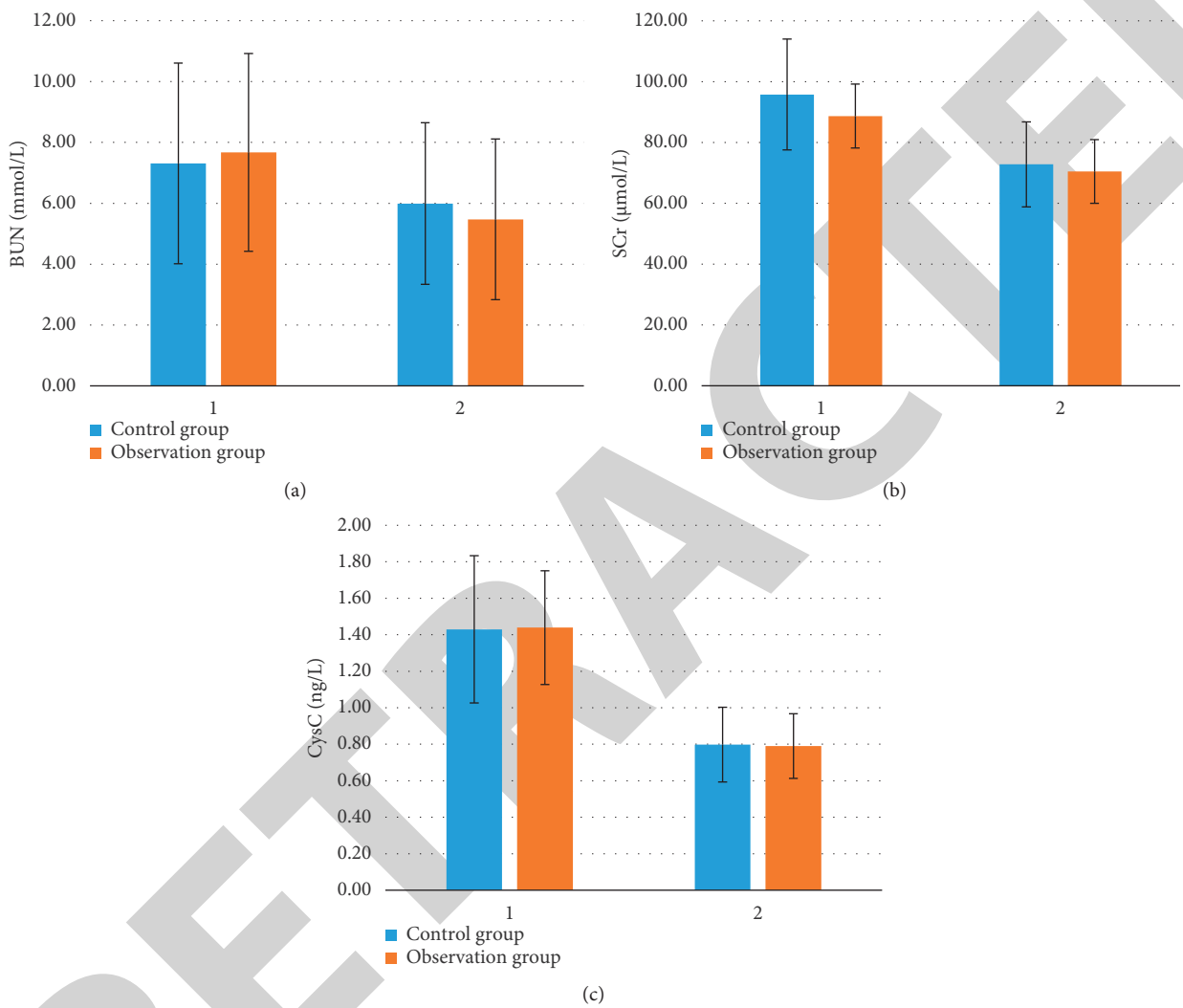

Figure 2: Renal function indexes of patients before and after operation. (a) Changes of BUN levels before and after treatment. (b) Changes of SCr levels before and after treatment. (c) Changes of CysC levels before and after treatment. $^{***}P < 0.001$.

hospital stay of SMP were shorter than those of ureteroscopy, and the blood loss during the operation was lower. Not only that, the recent stone-free rate of patients treated by SMP was higher. This is largely due to the negative pressure suction system of SMP, which ensures its stone removal efficiency well. With the help of the negative pressure suction device, the crushed stones can be quickly sucked out from the suction sheath to the collection bottle, which improves the removal rate, reduces the use of the net basket and the lithotripsy forceps, and accelerates the operation speed. In the process of ureteroscopy, only a 200 μm holmium laser is adopted for lithotripsy; the instrument is single, and the efficiency is low, which is greatly influenced by the stone hardness.

Postoperative infection is the challenge for all surgical patients after an operation. This research examined the postoperative infection of patients. Logistic regression analysis manifested that preoperative urinary tract infection, preoperative blood glucose level, positive urine culture, and infectious stones were related to infection. For that, the urinary tract infection process and urinary calculus formation are relevant and complementary, and the presence of urinary tract infection before operation will increase the risk of postoperative infection. Higher blood glucose increases plasma osmolality and reduces immunologic cellular activity, thus lowering the body's resistance to pathogenic bacteria and increasing the incidence of infection. Prior research found that positive urine culture and infectious

Table 3: Complications.

Group	Infection	Delayed bleeding	Fever	Urinary fistula	Total incidence rate
CG ($n = 76$)	6 (7.89)	3 (3.94)	2 (2.63)	2 (2.63)	13 (17.11)
OG ($n = 104$)	9 (8.65)	3 (2.88)	1 (0.96)	1 (0.96)	14 (13.46)
$\chi 2$ value	0.033	0.154	0.747	0.747	0.457
P value	0.856	0.695	0.387	0.387	0.499

Table 4: Assignment table.

Factor	Assignment
Gender (X)	Male = 1, female = 2
Age (X)	≥40 = 1, <40 = 2
Diameter of stones (X)	≥1 cm = 1, <1 cm = 2
Operation time (X)	Raw data are used as continuous variables
History of diabetes (X)	Yes = 1, no = 2
History of hypertension (X)	Yes = 1, no = 2
Preoperative urinary tract infection (X)	Yes = 1, no = 2
Preoperative blood glucose level (X)	≥6.1 mmol/L = 1, <6.1 mmol/L = 2
Positive urine culture (X)	Yes = 1, no = 2
Infectious stones (X)	Yes = 1, no = 2
Infection (Y)	Infected = 1, uninfected = 2

Table 5: Logistic univariate analysis.

	β	S.E	χ^2 value	P value	OR value	95% CI
Sex	0.107	0.571	0.035	0.851	1.113	0.363–3.411
Age	−0.560	0.570	0.966	0.326	0.571	0.187–1.745
Diameter of stones	−0.301	0.614	0.240	0.625	0.740	0.222–2.467
Operation time	0.004	0.020	0.034	0.855	1.004	0.965–1.044
History of diabetes	0.128	0.611	0.044	0.834	1.136	0.343–3.767
History of hypertension	0.486	0.685	0.502	0.478	1.625	0.424–6.221
Preoperative urinary tract infection	1.386	0.572	5.872	0.015	4.000	1.303–12.275
Preoperative blood glucose level	2.538	0.777	10.664	0.001	12.652	2.758–58.031
Positive urine culture	2.337	0.668	12.221	<0.001	10.348	2.792–38.355
Infectious stones	2.118	0.582	13.239	<0.001	8.312	2.656–26.011
Surgical plans	−0.05	0.55	0.008	0.927	0.951	0.323–2.796

Table 6: Logistic multivariate analysis.

	B	S.E	χ^2 value	P value	OR value	95% CI
Preoperative urinary tract infection	1.545	0.708	4.758	0.029	4.690	1.170–18.802
Preoperative blood glucose level	2.415	0.852	8.031	0.005	11.188	2.106–59.442
Positive urine culture	2.392	0.762	9.842	0.002	10.931	2.453–48.705
Infectious stones	1.374	0.691	3.956	0.047	3.951	1.020–15.300

stones were relevant to postoperative infection, which was associated with our results. Therefore, patients should be examined as early as possible before the operation and treated promptly to reduce the risk of infection. Finally, we constructed the risk model of infection prediction based on regression results. By fitting and drawing the ROC curve, we calculated that the area of the model under the curve of infection prediction was 0.930, which was ideal.

We also determined that the efficacy of SMP was better than that of ureteroscopy and analyzed the postoperative infection factors. Nevertheless, this research still has some limitations. Firstly, it is a retrospective study with a limited sample size, so it is impossible to increase the comparability of the research like the random control group experiment in sample selection. Secondly, patients cannot be followed up for long periods. It is well known that KS is likely to recur, but it is indistinct whether the two kinds of surgery affect postoperative recurrence. Thus, we hope to conduct randomized controlled trials and perfect our findings on inflammation through long-term follow-up.

To sum up, the efficacy of SMP in treating KS sufferers is better than that of ureteroscopy. Preoperative urinary tract

Hindawi
Journal of Healthcare Engineering
Volume 2023, Article ID 9854246, 1 page
https://doi.org/10.1155/2023/9854246

Retraction

Retracted: Research on Fitness Movement Monitoring System Based on Internet of Things

Journal of Healthcare Engineering

Received 10 October 2023; Accepted 10 October 2023; Published 11 October 2023

This article has been retracted by Hindawi following an investigation undertaken by the publisher [1]. This investigation has uncovered evidence of one or more of the following indicators of systematic manipulation of the publication process:

(1) Discrepancies in scope
(2) Discrepancies in the description of the research reported
(3) Discrepancies between the availability of data and the research described
(4) Inappropriate citations
(5) Incoherent, meaningless and/or irrelevant content included in the article
(6) Peer-review manipulation

The presence of these indicators undermines our confidence in the integrity of the article's content and we cannot, therefore, vouch for its reliability. Please note that this notice is intended solely to alert readers that the content of this article is unreliable. We have not investigated whether authors were aware of or involved in the systematic manipulation of the publication process.

In addition, our investigation has also shown that one or more of the following human-subject reporting requirements has not been met in this article: ethical approval by an Institutional Review Board (IRB) committee or equivalent, patient/participant consent to participate, and/or agreement to publish patient/participant details (where relevant).

Wiley and Hindawi regrets that the usual quality checks did not identify these issues before publication and have since put additional measures in place to safeguard research integrity.

We wish to credit our own Research Integrity and Research Publishing teams and anonymous and named external researchers and research integrity experts for contributing to this investigation.

The corresponding author, as the representative of all authors, has been given the opportunity to register their agreement or disagreement to this retraction. We have kept a record of any response received.

References

[1] Z. Yu, "Research on Fitness Movement Monitoring System Based on Internet of Things," *Journal of Healthcare Engineering*, vol. 2022, Article ID 5120556, 7 pages, 2022.

Hindawi
Journal of Healthcare Engineering
Volume 2022, Article ID 5120556, 7 pages
https://doi.org/10.1155/2022/5120556

Research Article

Research on Fitness Movement Monitoring System Based on Internet of Things

Zhenhao Yu

Shanxi University, Taiyuan 030006, China

Correspondence should be addressed to Zhenhao Yu; yzh_sxdx@sxu.edu.cn

Received 21 December 2021; Accepted 31 January 2022; Published 8 March 2022

Academic Editor: Mu-Yen Chen

A multiuser motion-monitoring system based on MEMS is proposed for fitness movement, it is used to monitor the three important parameters of movement type, movement times, and movement cycle in the body movement and supports the simultaneous use of multiple users. The specific content of the method: (1) In terms of system design, a motion-monitoring system framework based on the Internet of things is proposed considering the motion-monitoring scene oriented to intelligent fitness. (2) In the aspect of algorithm, the relevant research of motion pattern recognition and cycle calculation method is carried out. For action pattern recognition, SVM-based algorithm to adapt to different computing capabilities of the scene is applied. (3) Experiments on 7 kinds of actions show that the proposed deep neural network has a good learning effect on small datasets, the recognition accuracy of the proposed deep neural network reaches 97.61%, and the recognition accuracy of SVM also reaches over 96%. In the 50 times of operation cycle calculation experiments, the frequency statistics algorithm has reached 100% of the calculation accuracy, and the calculation results of the operation cycle are close to the real value, which proves the validity of the method of cycle calculation. The experiment proves that the zero-crossing detection and wavelet analysis methods have a good overall effect and can accurately count and calculate the period when the number of actions is more, improve fitness efficiency, and provide guarantee for human health.

1. Introduction

In today's society, the times are constantly developing, and people's requirements for material life will gradually improve, living standard has been satisfied at the same time, began to pursue a healthy lifestyle, and basically is based on physical exercise. Running is one of the most important activities for people to carry out physical exercise, it is one of the most popular fitness activities in the world at present, it is highly evaluated in the medical and sports circles, and it is also the most scientific and effective way to keep one's body and mind. It can effectively strengthen the muscle and bone function of the limbs, improve the cardiopulmonary function, and play a great role in weight loss [1]. At present, more popular sports exercise tools or fitness equipment have been developed. With the development of society, some jobs require people to have a good physical fitness to adapt, which strengthens the importance of physical exercise, but due to the restriction of some objective factors, such as climate, environment, and venue, people pay more and more attention to indoor exercise, and treadmill fitness has become the preferred way for people to exercise [2]. From a physical point of view, on the ground or on a treadmill, the motion is almost the same, but from a mechanical point of view, on a treadmill, since the belt can drive the lower limbs, the movement force and force become more flexible, which can save people's leg force [3]. It is conceivable that the treadmill enters the gym or home as a matter of course [4]. In the process of physical exercise, guidance from professionals is essential. Nowadays, in most places for physical exercise, such as gyms, rehabilitation training centers and physical education classes in schools, there are coaches or related professionals to demonstrate the correct movements and monitor the movement status of the athletes. No matter in the field of fitness, rehabilitation training or physical education, correct exercise under the guidance of professionals

is an important guarantee to improve the training effect and prevent sports injury. At present, the portable equipment or large medical equipment used for monitoring the basic parameters of the human body has little value except for recording and monitoring [5]. From the point of view of the bodybuilder, it is not to bring the best fitness effect. In view of the above situation, the combination of treadmill fitness and sports health monitoring, the collection and storage of fitness people in the running of the physiological parameters, and through certain analysis and processing, the body and sports conditions of the bodybuilders are presented in time, so that the bodybuilders can check their current health index in real time and understand their exercise situation [6]. Therefore, the domestic and foreign research continues, and Krespi et al. combined the actual needs of users, according to the software engineering development process to design the server system. While realizing the access to the server by ordinary PC browser, android application of mobile terminal is developed to realize the mobile terminal [7]. Shi studied and demonstrated the marine environment monitoring system based on Internet of Things technology [8]. Xu et al. designed an intelligent blood glucose monitoring system based on Internet of Things technology and sensor technology [2]. Liu et al. studied the load grade index corresponding to the action, grasped the dynamic change rule of the action according to the movement monitoring index, analyzed the corresponding index of subjective sensation and the method of determining the percentage of exercise intensity, and formulated the calculation formula of the optimal target action and the heart rate index corresponding to the exercise load grade [9]. In the current research, a MEMS-based multiuser motion-monitoring system is proposed. The recognition experiments of seven types of movements show that the proposed deep neural network has a good learning effect on small datasets, reaching 97.61% of the recognition accuracy, and the SVM has also reached over 96% of the recognition accuracy. In the 50 times of operation cycle calculation experiments, the frequency statistics algorithm has reached 100% of the calculation accuracy, and the calculation results of the operation cycle are close to the real value, which proves the validity of the method of cycle calculation.

2. Design of Motion-Monitoring System Based on Internet of Things

2.1. System Design. A multiuser body movement monitoring system based on MEMS is proposed, and the system consists of sensors, wireless access points, cloud servers, and data receiving terminals. As shown in Figure 1, each sensor node contains a MEMS-based attitude module for collecting action information. Sensors used by multiple users can be connected to a wireless access point through WIFI, and data can be uploaded to the cloud server through the wireless access point. In the cloud server, the machine learning algorithm and wavelet analysis method are used to centrally process the data, and action description information is generated for each user, including action type, action times, and action cycle. The results of motion analysis can be downloaded to any data terminal such as mobile phone or computer through the Internet.

Multiuser action monitoring based on MEMS is a process integrating data acquisition, data transmission, data preprocessing, action recognition, and cycle calculation. The overall algorithm flow is shown in Figure 2. In the research, the nine-axis attitude module based on MPU9250 is used to collect the body motion information, the attitude module can realize the data collection including three-dimensional acceleration, three-dimensional angular velocity and 3D euler angle (angle), at the same time, the initial attitude solution, digital filtering and Kalman filtering are carried out, and the final time-series signal is generated, and the signal is then transmitted through a serial port to the ESP8266 wireless transmission module. The ESP8266 wireless transmission module supports the wifi transmission standard and can upload the action data to the cloud server through the gateway. In order to facilitate debugging, a computer in the local area network is selected as the data processing server, and the action data received by ESP8266 is transmitted to the server through socket for subsequent processing [10, 11]. In the server, the raw data is verified and unpackaged and then stored temporarily as a CSV file, which is still essentially a time-series signal. Next, the motion recognition system reads these files, preprocesses them, and uses pretrained machine learning and deep learning models to identify and classify the movements. Finally, the number statistics and period calculation of the timing signal are carried out based on wavelet and zero-crossing check. After the above steps, a comprehensive description of the categories, times, and periods of an action can be obtained.

The MEMS sensor has its advantages in small volume, low power consumption, and low cost and is widely used in various fields. MEMS-based MEMS human motion information acquisition system uses MEMS accelerometer, MEMS gyroscope, and MEMS magnetometer as the core measurement devices to form its pose measurement unit. The measurement accuracy of the MEMS sensor directly affects the accuracy of the human motion information collection system, so it is necessary to analyze the error of each MEMS sensor used in the human movement information collection system and correct it, which is of great significance for the establishment of the mathematical model of the MEMS sensor.

2.2. SVM. In order to realize the motion-monitoring system, MEMS-based inertial sensor is used to collect motion in hardware. In terms of algorithm, SVM is used as one of the classification models with relatively popular and good generalization ability.

Support vector machine (SVM) is one of the most popular supervised learning methods. The proposed action recognition algorithm uses SVM, so the basic theory of SVM is introduced in the following. Before the advent of deep learning, SVM was long regarded as the best performing classification algorithm, especially suitable for application scenarios without any prior knowledge of the relevant field. The main reasons are the following three features of SVM:

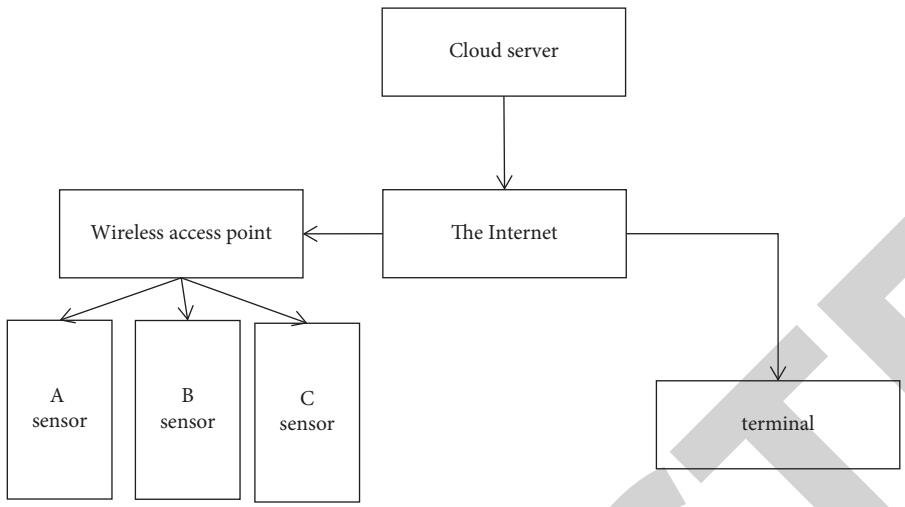

Figure 1: Hardware framework of multiuser action monitoring system.

(1) SVM has good data generalization ability. SVM is a classifier that maximizes the classification interval, the classification hyperplane constructed by SVM ensures the maximum distance to sample points, so it has excellent generalization performance and is not easy to overfit.

(2) SVM uses the so-called "kernel method" to map the linearly indivisible data in the low-dimensional plane to the high-dimensional space, making it linearly separable. Therefore, a linear hyperplane generated by SVM in a high-dimensional space is usually not linear in the original space.

(3) SVM retains almost all the training samples during the whole process of training and reasoning, which is a nonparametric method. However, only a few training samples play a role in the actual operation, which is called support vector. Therefore, SVM not only has the characteristics of parametric model against overfitting but also has the flexibility of nonparametric model when expressing complex functions.

The use process of SVM can be divided into the training process and reasoning process. The training process is the process of SVM learning rules from the preprepared action samples and delineating the optimal classification hyperplane, and the reasoning process is the process of giving the predicted category according to the data to be tested. Before training the model, the original data of the sensor should be extracted to get the training set. In the training process, the given training set X can be expressed as

$$X = [x_1, x_2, \ldots x_n]^T, \tag{1}$$

where n is the number of samples and x_i is the vector representation of the ith training sample.

For SVM, the optimization objective is to find a classification hyperplane with the maximum spacing, and the optimization process can be expressed as

$$\min \frac{1}{2}\|w\|^2 + C\sum_{i=1}^{n}\zeta_i$$
$$s.t. y\left[(wx_i) + b\right] \geq 1 - \varsigma_i \left(i = 1, 2, \ldots, n; \zeta_i \geq 0\right), \tag{2}$$

where w is the normal vector of the classified hyperplane, b is the offset, c is the penalty coefficient of the support vector machine, ζ is the loss term, and y is the classification label with A value of +1 or −1. This is a typical convex quadratic programming problem, and its Lagrange coefficient can be obtained by the Lagrange multiplier method, which can be expressed as

$$a = [a_1, a_2, \ldots a_n]. \tag{3}$$

In essence, the process of SVM optimization in the training phase is the process of finding Lagrange coefficient. In the reasoning stage, the vector representation of the action to be measured and the Lagrange coefficient are substituted into the following formula:

$$g(x) = \sum_{i=1}^{n} a_i y_i (x_i, x') + b. \tag{4}$$

The value of g(x) can be obtained. By comparing the value of g(x) with +1 and −1, the predicted category of the action to be tested can be obtained.

In the framework of support vector machine, Guyon proposed the SVM-RFE feature selection algorithm for sorting features. The core idea of SVM is to establish an optimal.

Hyperplane $(w \cdot x + b = 0)$ as decision surfaces and maximizes classification interval $(2/\|w\|^2)$. In dealing with nonlinear and high-dimensional pattern recognition, SVM is linearly separable by mapping kernel function to high-dimensional space. For l training sample $\{(x_i, y_i), i = 1, 2, \ldots, l\}$ and $x_i \in R^m$, $y_i \in \{-1, 1\}$, the objective function satisfying constraint conditions is

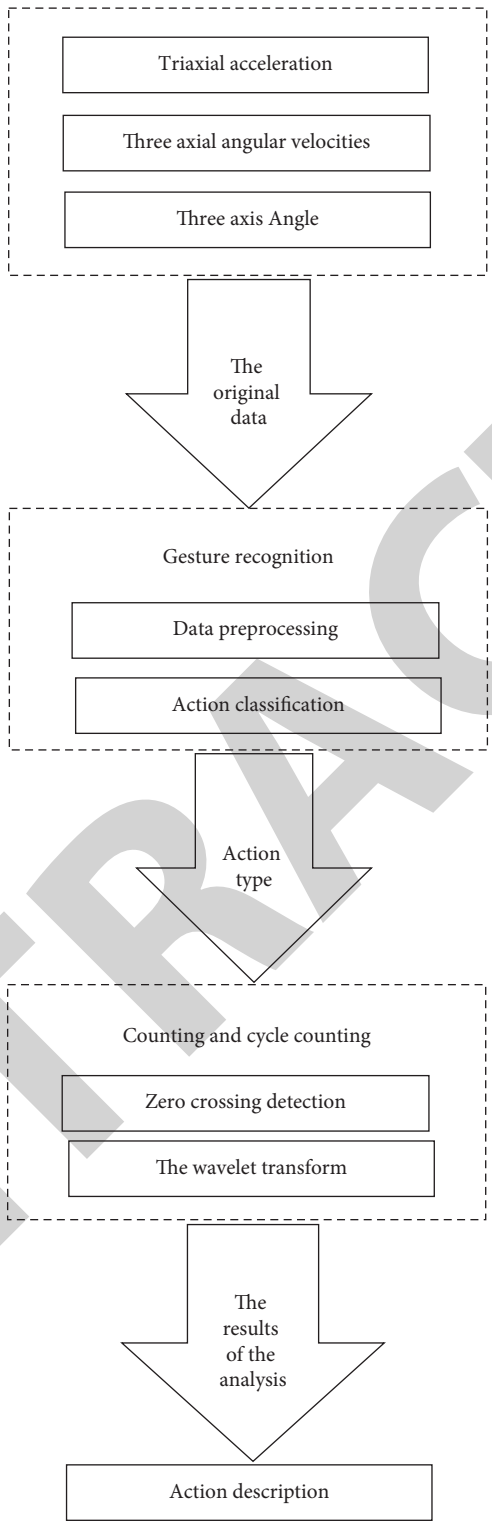

Figure 2: Algorithm framework of action monitoring system.

$$\left\{ \min J = \frac{1}{2}\|w\|^2 + C\sum_{i=1}^{l}\xi_i, s.t \begin{cases} y_i\left(w \cdot x_1 + b\right) \geq 1 - \xi_i \\ \xi_i > 0 \end{cases}, i = 1, 2, \ldots, l. \right. \tag{5}$$

The decision function of the SVM model is finally obtained by Lagrange duality theorem and quadratic programming:

$$\begin{cases} f(x) = \operatorname{sgn}(w \cdot x + b), \\ w = \sum_{i=1}^{l} a_i y_i x_i. \end{cases} \tag{6}$$

Therefore, in the decision function, the weight w is a linear combination of the support vectors whose A is not 0, and the larger the feature weight is, the more discriminant information it contains. In addition, if the ith feature is removed, the influence on the objective function can be calculated by Taylor formula expansion.

$$\Delta J(i) = \frac{\partial J}{\partial w_i} \Delta w_i + \frac{\partial^2 J}{\partial w_i^2} (\Delta w_i)^2. \tag{7}$$

On the optimal solution of J, only the second order is considered, so,

$$\Delta J(i) \approx (\Delta w_i)^2. \tag{8}$$

When the ith feature is deleted, $\Delta w_i = w_i$, so, SVM-RFE measures the importance of feature weight and uses w2 as the feature ranking criterion.

3. Simulation Experiment

Seven types of body movements were selected for recognition. These movements include four types of dumbbell movements and three types of leg exercises, respectively, dumbbell bending lift, dumbbell side flat lift, dumbbell shoulder push, dumbbell bird, sitting posture leg lift, and standing posture leg lift. These seven kinds of movements are common body exercise movements, with strong representativeness. Among them, there is a high similarity between some movements, such as leg raising by sitting posture and leg raising by standing posture, which poses a certain challenge for the classifier and can fully verify the classification ability of different models. In terms of data, the self-built dataset was used in this study, which was composed of 420 samples in total. A total of six people provided samples for the dataset, including three men and three women, each of whom provided 70 data samples, including 10 for each type of action. When recording data, each participant wore only one attitude acquisition module. For dumbbell action, the posture acquisition module is worn at the wrist. For lower limb movements, the posture acquisition module is worn at the ankle. The weight of the dumbbell used in the dumbbell action is 2.5 kg. In terms of data set allocation, 80% of all samples are used as training set and 20% as the test set. For the deep learning model, 20% of the training set is taken as the verification set.

Figure 3 shows the variation trend of SVM accuracy and loss in training. It can be seen from Figure 3(a) that the training loss and the validation loss continue to decline in the trend until they stop at the 200th training round, during this process, the validation loss is basically consistent with the training loss, in Figure 3(b), the training accuracy and verification accuracy always rise in the trend, and the final difference is not significant, which indicates that the model has learned the law in the data well to a certain extent.

As can be seen from the abovementioned experimental results, SVM achieves the recognition accuracy of more than 96%, higher than the comparison algorithm, while the accuracy of the multilayer perceptron is the lowest among the four models. It can be seen that in 84 test samples, only two dumbbell shoulder pushes were mistakenly classified into dumbbell side lift, which indicates that the SVM model proposed can be well used for action recognition in small datasets. As can be seen from the confusion matrix of SVM, this method is prone to misclassification for the two types of leg movements, which is because the two types of movements are similar, SVM does not perfectly separate the two types of actions based on features from a single sensor. Although SVM does not reach the highest accuracy, it does not have an obvious gap with the deep learning model, so it is more suitable for scenarios with low computing power and also has practical significance.

The purpose of the experiment is to verify the accuracy of counting and cycle calculation. For this experiment, whether the results are objective or not is largely affected by the number of trials. Especially for the action count, the effectiveness of the analysis method can be demonstrated only when the result is still accurate under the condition of sufficient number of times. In this experiment, 50 movements were repeated, which is much higher than the number of times required for a single exercise and can verify the accuracy of the algorithm. In the experimental process, in addition to the use of sensors to record the action, it also uses a stopwatch to time the cycle of each action, as the actual standard.

Table 1 shows the sensitive axes of the seven movements in the dataset obtained according to the abovementioned calculation method. It can be seen that for the movements of the limbs rotating around the joints, the sensitive axis is generally angular velocity, for vertical limb movements such as shoulder push and heel lift, the sensitive axis is acceleration.

Next, the experiment took dumbbell bending as an example, repeated 50 times, and calculated the number of times and period according to the sensitive axis data. Finally, the measured value was compared with the actual value and analyzed. In this experiment, the calculated and actual values of 50 precise cycles are shown in Figure 4. The dotted line marked with the box is the measured value obtained by the calculation method of using the period, the solid line marked with the triangle is the actual value recorded by using the stopwatch, the vertical axis is the period of action in seconds, and the horizontal axis is the number of actions.

Firstly, it can be seen from the length of the curve in the figure that the action count of the algorithm is very accurate, and the statistical result of 50 times is completely consistent with the actual value. Secondly, the overall fitting of the two curves in the figure is good, with an average error of only 0.08s and an average error rate of 4.03%. The maximum error of the calculated results is 0.25s, and the maximum

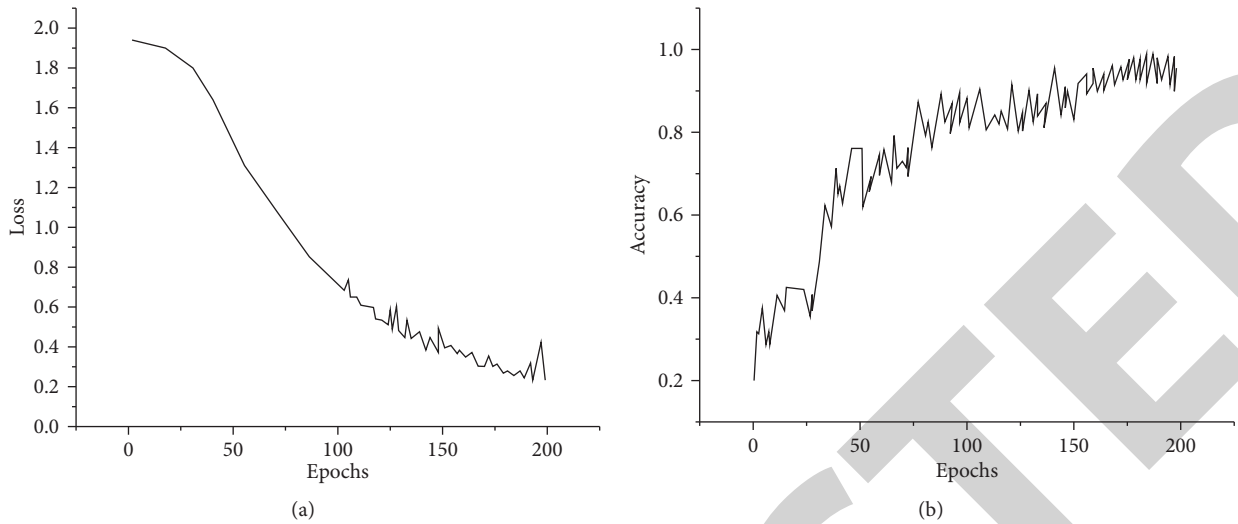

Figure 3: (a) Changes in training loss and validation loss. (b) Changes in training accuracy and verification accuracy.

Table 1: Sensitive axes for different actions.

Action type	Sensitive axis
Bending	Angular velocity on the *X*-axis
Levelly obeying	Angular velocity on the *X*-axis
Shoulder vertebra	Y-acceleration
The birds	X angular velocity
Seated leg lifts	Z angular velocity
Standing leg lifts	Z angular velocity
Lift heel	Y-acceleration

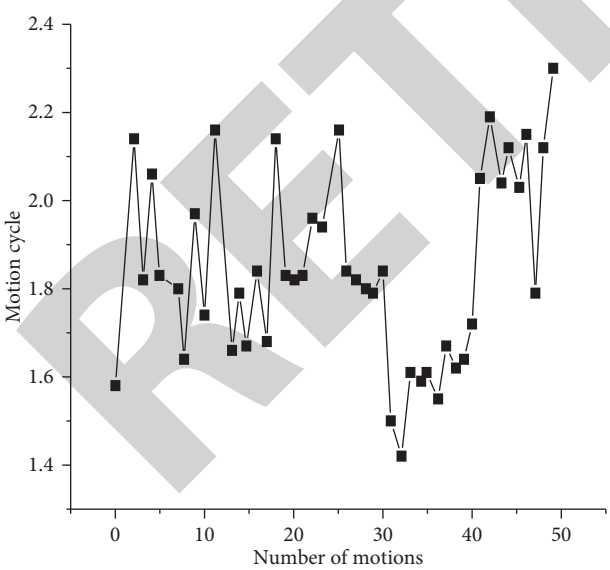

Figure 4: Action count and cycle calculation results.

error rate is 13.5%, which occurs only at the end points of the curve. Therefore, the experiment proves that the method of zero-crossing detection and wavelet analysis has a good overall effect and can realize the action count and period calculation more accurately even when the number of actions is more.

As people's attention to sports gradually improve, the concept of healthy life, based on MEMS sports information collection system has extremely important application value, and people can use the system to get more professional sports guidance, in the process of active participation in sports to prevent sports damage, at the same time, the system with big data technology can achieve a more comprehensive sports information analysis function. In this case, the MEMS-based on human movement information collection system adopts modular and miniaturization design, by a variety of measurement units that meet the standards of wearable devices and higher accuracy of attitude estimation algorithm and positioning algorithm, effectively improving the information collection accuracy of the system and applicability and expansion ability in different application scenarios.

4. Conclusions

A MEMS-based multiuser motion-monitoring system is proposed to monitor the three important parameters of movement type, movement times, and movement cycle in body movement and to support multiuser simultaneous use. The specific content of the method are as follows: (1) In terms of system design, a motion-monitoring system framework based on the Internet of Things is proposed considering the motion-monitoring scene oriented to intelligent fitness. (2) In the aspect of algorithm, the relevant research of motion pattern recognition and cycle calculation method is carried out. For action pattern recognition, the SVM-based algorithm to adapt to different computing capabilities of the scene is used. (3) In the aspect of system development, the hardware platform including data acquisition bracelet, wireless access point, and PC is developed as well as the software platform integrating data receiving, action recognition, and cycle computing module. The hardware platform and the software platform jointly constitute the experimental platform. Related experiments are carried out based on the developed software and hardware

Hindawi
Journal of Healthcare Engineering
Volume 2023, Article ID 9805297, 1 page
https://doi.org/10.1155/2023/9805297

Retraction

Retracted: Named Entity Recognition of Medical Text Based on the Deep Neural Network

Journal of Healthcare Engineering

Received 10 October 2023; Accepted 10 October 2023; Published 11 October 2023

This article has been retracted by Hindawi following an investigation undertaken by the publisher [1]. This investigation has uncovered evidence of one or more of the following indicators of systematic manipulation of the publication process:

(1) Discrepancies in scope
(2) Discrepancies in the description of the research reported
(3) Discrepancies between the availability of data and the research described
(4) Inappropriate citations
(5) Incoherent, meaningless and/or irrelevant content included in the article
(6) Peer-review manipulation

The presence of these indicators undermines our confidence in the integrity of the article's content and we cannot, therefore, vouch for its reliability. Please note that this notice is intended solely to alert readers that the content of this article is unreliable. We have not investigated whether authors were aware of or involved in the systematic manipulation of the publication process.

Wiley and Hindawi regrets that the usual quality checks did not identify these issues before publication and have since put additional measures in place to safeguard research integrity.

We wish to credit our own Research Integrity and Research Publishing teams and anonymous and named external researchers and research integrity experts for contributing to this investigation.

The corresponding author, as the representative of all authors, has been given the opportunity to register their agreement or disagreement to this retraction. We have kept a record of any response received.

References

[1] T. Yang, Y. He, and N. Yang, "Named Entity Recognition of Medical Text Based on the Deep Neural Network," *Journal of Healthcare Engineering*, vol. 2022, Article ID 3990563, 10 pages, 2022.

Hindawi
Journal of Healthcare Engineering
Volume 2022, Article ID 3990563, 10 pages
https://doi.org/10.1155/2022/3990563

Research Article

Named Entity Recognition of Medical Text Based on the Deep Neural Network

Tianjiao Yang,[1] Ying He ,[1] and Ning Yang[2]

[1]*College of Electronic Information, Qingdao University, Qingdao, Shandong 266071, China*
[2]*Qingdao Lanzhi Modern Service Industry Digital Engineering Technology Research Center, Qingdao, Shandong 266071, China*

Correspondence should be addressed to Ying He; yinghe@qdu.edu.cn

Received 31 December 2021; Accepted 26 January 2022; Published 7 March 2022

Academic Editor: Alireza Souri

Medical text data records detailed clinical data; named entity recognition is the basis of text information processing and an important part of mining valuable information in medical texts. The named entity recognition technology can accurately identify the information needed in medical texts and help medical staff make clinical decision-making, evidence-based medicine, and epidemic disease monitoring. This paper proposes a hybrid neural network medical text named entity recognition model. First, a coding method based on a fully self-attentive mechanism is proposed. The vector representation of each word is related to the entire sentence through the attention mechanism. It determines the weight distribution by scoring the characters or words in all positions and obtains the position information in the sentence that needs the most attention. The encoding vector at each position is integrated with the context information of full sentence, which solves the ambiguity problem. Second, a multivariate convolutional decoding method is proposed. This method can effectively pay attention to the characteristics of medical text named entity recognition in the decoding process. It uses two-dimensional convolutional decoding to associate the current position word with surrounding words to improve decoding efficiency while extracting features from the logic of the preceding and following words. Using the same number of convolution kernels as the entity category, it can effectively extract effective features from the label dimension. Besides, according to the characteristics of the named entity recognition task, a special mixed loss is designed. The experimental results verify that the proposed method is effective, and it is improved compared with some existing medical text named entity recognition methods.

1. Introduction

With the vigorous development of artificial intelligence, natural language processing (NLP) has always been a research hotspot. The ever-increasing performance of computing devices and the ever-developing algorithms have resulted in the emergence of a large number of excellent new algorithms for natural language processing on a large number of tasks. For the ever-changing Internet industry, how to combine the existing massive text data and natural language processing technology to mine the valuable data information in the massive text is a very challenging task. Artificial intelligence technology is entering all aspects of modern society and is gradually playing an irreplaceable role in all walks of life, and natural language processing technology is changing people's lives [1–5].

When it comes to proper names and phrases, named entity identification is the most important part of the process. There are a variety of downstream activities that rely on named entity identification as a building block, including information extraction, knowledge graphs, automated question answering, and machine translation. Named entities in nonspecific domain text data generally refer to specific referring entities. In specific field data such as medical data, named entities are mostly entities such as genes, diseases, and drugs. Named entity recognition system extracts entities from unstructured unlabeled text and performs sequence labeling tasks according to different standard rules [6–10].

At present, medicine is developing rapidly, and a large amount of medical information exists in various forms of text in an unstructured form. It can provide a large amount of professional data and knowledge for scientific research and teaching. With the popularization of informatization, a large amount of medical data has been accumulated in various business systems of hospitals, and these data have the characteristics of being heterogeneous, distributed, fragmented, and so on. The use of computers to process and analyze huge amounts of medical text data requires further research and development of natural language processing technologies corresponding to medical texts. The mining of medical text data is a cross-discipline of computer and medicine. It often involves machine learning, deep learning, artificial intelligence, and other fields in the field of computer science. In order to effectively analyze and mine these data through existing analysis methods, medical data needs to be structured. Through the use of natural language processing, named entity recognition of text data in the medical field will lay the foundation for the structured representation of data. Using effective computer algorithms and improving the accuracy of algorithm recognition is an indispensable link in medical text data mining. Medical text named entity recognition aims to identify specific text blocks in specific medical texts. It is extremely important in extraction of disease treatment relationship, gene function recognition, and semantic relationship extraction of molecular biology ontology concepts. Different from traditional named entity recognition, the medical field pays more attention to entities such as symptoms, organs, treatment methods, drugs, and diseases. However, due to the lack of standard naming methods in medical research, few models can achieve very satisfactory results. So medical text named entity recognition is still a very difficult issue [11–15].

In order to solve the problems existing in medical text entity recognition, this paper conducts corresponding research based on deep neural network. This work designs a medical text named entity recognition model with hybrid neural network. According to the characteristics of word ambiguity and structural complexity of medical text, a fully self-attentive coding mechanism is designed, which integrates contextual information into the coding of each word. It eliminates the problem of the disappearance of the long-distance transmission gradient caused by the use of time series model coding. At the decoding end, a multivariate convolutional decoding method is proposed to allow it to fully capture information in different feature dimensions. In addition, according to the characteristics of the named entity recognition task, a special mixed loss is designed, so that the convolution kernel can perform feature modeling for each label category.

2. Related Work

The method based on rules and dictionaries was mainly based on artificially defined rules and pattern matching to generate dictionaries and extract medical entities from existing medical dictionaries. Literature [16] used custom vocabulary and grammatical rules to identify medical knowledge in X-ray reports. Literature [17] used medical dictionaries to extract medical concepts from clinical texts and achieved good results. Although the method based on dictionaries and rules was simple to implement, the accuracy was closely related to the manually formulated rules and the quality of constructing medical dictionaries. It not only required researchers to fully analyze the corpus but also needed to have experience in the medical field. In addition, due to the rapid development of medical research, it was becoming more and more difficult to construct high-quality medical dictionaries. Normally, most dictionaries could not cope with large-scale and diversified medical data. In addition, the effect of this method was greatly reduced in practical applications due to the irregularities in the naming of entities in medical texts.

Methods based on machine learning consider it was a sequence labeling issue. The corresponding label for each character in the input sequence was predicted and the entity in the sentence was identified according to the label sequence. Literature [18] used a semi-Markov model to label conceptual entities in sequence. By adopting four tags and introducing concept mapping features and context features, it had obtained a better entity recognition effect. Literature [19] combined support vector machines with conditional random fields to identify entities in electronic medical records. Literature [20] used statistical models to extract concepts from clinical texts from multiple data sources and used BioTagger-GM to train the model to learn labels. Literature [21] used SVM and maximum entropy model, combined with rules to identify named entities in electronic medical records. These methods could achieve good and stable results in entity recognition tasks but to a large extent depend on artificially formulated features. This had limited the scope of application of this method.

Named entity recognition methods based on deep learning were used in entity extraction tasks. Literature [22] introduced the attention mechanism to recognize chemically named entities based on the deep learning model, which solved the problem of label inconsistency. Literature [23] trained two-way language model vectors on massive unlabeled corpus and added feature vectors to the original two-way recurrent neural network and CRF model for semisupervised sequence labeling. Literature [24] combined Bi-RNN and CRF and introduced n-gram features to identify five types of entities in Chinese clinical electronic medical records. Literature [25] proposed a transfer bidirectional recurrent neural network, which automatically extracted medical concepts such as diseases and treatments from Chinese electronic medical records. Literature [26] used the minimum feature engineering method and proposed two deep neural networks. Unsupervised learning was used to generate word vectors from a large number of unlabeled corpora to perform named entity recognition tasks. This method was superior to the existing CRF model, which shows the effectiveness of unsupervised learning. In order to establish high-precision drug entity recognition and clinical concept extraction, literature [27] combined the bidirectional LSTM with the CRF model to form BiLSTM-CRF model and used the dataset in the health field to train to get richer and professional word vectors, avoiding the manual construction

of features. Literature [28] used large-scale unlabeled corpus to learn multiple representations of entity categories and mined the semantic relationship between clinical medical entities and text words. Literature [29] proposed a model combining speech and self-matching attention mechanism. This improved the accuracy and performs well in clinical entity recognition. Literature [30] proposed a deep residual network with attention mechanism to extract medical information. It enhanced the recognition characteristics of different types of entities by combining the attention mechanism of character position. Literature [31] introduced word level information on the basis of the BiLSTM model. Different features based on dictionaries were combined to identify entities such as diseases and drugs in Chinese electronic medical records and obtain better recognition results. Compared with machine learning methods, methods based on deep learning could automatically learn features. They did not require manual definition, had strong generalization ability, and could better analyze entity performance.

3. Method

To effectively identify medical text entities, this paper proposes a hybrid neural network (HNN) as illustrated in Figure 1. FSAE refers to fully self-attentive encoder. MCD refers to multivariate convolutional decoder. The rest of this section will explain the composition of the network in detail.

3.1. Fully Self-Attentive Encoder. This section focuses on the characteristics for medical text named entity recognition tasks, such as the ambiguity of words and characters and the disappearance of the long-distance transmission gradient of the temporal neural network framework. A fully self-attentive coding model is proposed to extract features for medical text named entity recognition tasks. It can directly transmit information regardless of the distance between words or characters in a sentence, and there is no restriction on the characteristics of time series data.

3.1.1. Motivation. The existing named entity recognition algorithms basically treat sentences as time series data. The reason for this is based on the assumption that the reading habit is to read sequentially in a fixed direction, which is in line with the characteristics of time series data. Text-named entity recognition model with deep learning that has achieved good result uses time series model as the main framework, and the sentences are input into the model. Compared to RNN, the network structure of LSTM adds input gates, forget gates, and output gates. This makes it possible to decide which information needs to be forgotten and which information needs to be passed on to the next time step. This solves the problem of explosion or disappearance of the information gradient caused by the long-distance sequence of RNN to a certain extent. But, for the task of naming entities in medical texts, there are still shortcomings. The vocabulary of medical texts is more

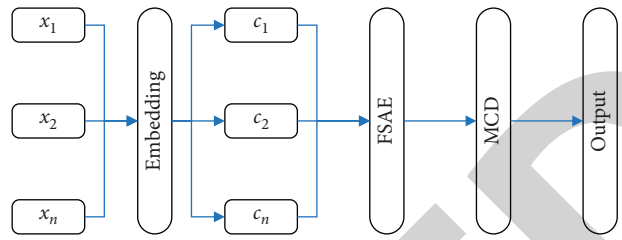

Figure 1: The structure of the HNN.

polysemous, and, generally, only by reading the whole sentence can we clearly judge the meaning of some words in the sentence.

How to make each word better integrate its context information when encoding a sentence has become the key to the effectiveness of the task of medical text named entity recognition. In addition, time series neural network models such as LSTM and GRU have very high requirements for hardware. Their structure determines that four fully connected layers are required in the core of each LSTM. If the time step of LSTM is very long and the number of layers is very deep, then the volume of the model will be quite huge; and because of the time sequence of LSTM, it cannot accelerate the calculation in parallel, which will cause medical text named entity recognition to use LSTM and other time series models as framework training on any dataset, which is a huge test for the hardware.

Therefore, this paper proposes a fully self-attentive encoder to replace the above-mentioned temporal model to model the corpus. The fully self-attentive mechanism pays attention to the words in all positions in the sentence when extracting the characteristics of the characters in each position and scores these words according to the degree of influence on the current word. In this way, the feature vector of each word will be fused with contextual information that is valid for it.

The fully self-attentive encoder does not have the timing characteristics of the time series model, so it cannot distinguish the sequence of words in the sentence. However, this article does not use additional coding information to increase the sequence characteristics of words, mainly based on the assumptions made by people's habits in fast reading in daily life. Combined with the characteristics of named entity recognition for medical text, the task does not require natural language processing tasks such as translation and question answering, and the semantics of the entire sentence can be extracted very accurately and completely. Instead, it only needs to extract the key entity words and judge their categories. Aiming at this characteristic, there is only a need to perform effective feature extraction on the part of the entity and pay attention to other key words in the sentence which affect its word meaning. In this way, it is possible to avoid the complexity of the model that the time series model needs to extract the semantics of the entire sentence, as well as the interference caused by the important local feature extraction part. In addition, the operation of the fully self-attentive mechanism is based on matrix operations, which determines that it can accelerate calculations in parallel through GPUs.

3.1.2. Structure. The fully self-attentive encoder does not use a timing model. Instead, in the encoding process of each position, all the words or word embedding vectors in the sentence are input into the self-attentive mechanism to calculate the weight assigned to each position. Finally, the code of the current position is obtained. The structure of the fully self-attentive coding model is shown in Figure 2.

$$E = [e_1, e_2, e_3, \ldots, e_n], \tag{1}$$

where n is the length for input and e_i is the word vector after embedding.

The word vector matrix E is input to the self-attentive mechanism n times, and the output of the i-th input is

$$a_i = \mathrm{Att}(e_i; E). \tag{2}$$

There is no priority when inputting, and input operations can be performed at the same time. Splice the full attention code a_i obtained each time into the final output of the fully self-attentive code:

$$A = [a_1, a_2, a_3, \ldots, a_n]. \tag{3}$$

3.1.3. Working Mechanism. The self-attentive mechanism encodes each word, which can effectively extract contextual information features into the current word hiding vector. This makes it pay attention to the position in the sentence related to the classification of its named entity.

From a macro perspective, the recurrent neural network encodes the words in an input sentence by combining all the previously processed information with the currently encoded words to generate a target vector. The self-attentive mechanism for word encoding will directly focus on all words in the sentence and assign weights according to the influence of these words on the current encoded word. Theoretically, if certain words are not related to the named entity classification of the current word, the assigned weight can be infinitely close to zero.

The realization of the self-attentive mechanism is viewed from a micro perspective. First, the self-attentive mechanism generates three vectors for each word or word embedding vector, the query vector, the key vector, and the value vector. These three vectors are the dot product of the embedding vector and three custom parameter matrices. The three parameter matrices are also optimized through top-down neural network training. After getting the three vectors, you need to use them to score all the words in the sentence. First, use the query vector of the currently encoded word and the key vector of all words including itself to do a dot product. The value obtained is the influence of all words in the sentence on the word. The larger the value is, the more important the word is to the currently encoded word. Then use the softmax function to normalize the scores so that scores obtained are all positive and the sum of all the scores is equal to 1. Here, the softmax score of each word is equivalent to its contribution to the word encoding at the current position. Finally, multiply the value vector of each word by its corresponding softmax score, and the final vector

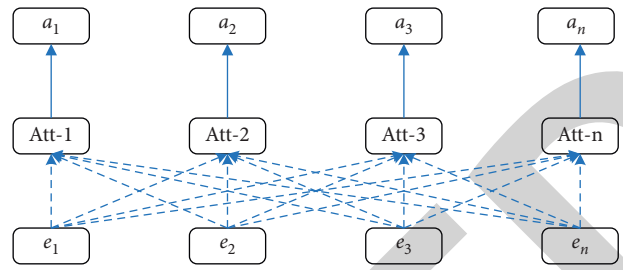

Figure 2: The structure of FSAE. The model input is the word vector after word embedding.

of the sum of the vector values is the self-attentive vector of the word at the current position. The goal of the model here is to weaken words that are not related to the current word as much as possible, and the value of softmax is as small as possible. It can be seen that the word hidden vector encoded in this way fully integrates the context information needed by oneself and can effectively pay attention to the position of the word related to the entity recognition classification. Moreover, it can prevent the weakening and disappearing of information transmission caused by too long sentences and too far apart words.

The output matrix formula of the fully self-attentive coding layer of the model can be expressed as

$$A = \mathrm{soft\,max}\left(W_q W_k^T W_v\right), \tag{4}$$

where W_q, W_k, and W_v are three parameter matrixes.

3.2. Multivariate Convolutional Decoder. This section proposes a multivariate convolutional decoding framework to solve the problem of entity nesting that often occurs in medical text named entities. At the same time, it enables each word to be associated with the grammar and word meaning information of adjacent words in the decoding process. In addition, multiple filters are used in the convolution process to decode each tag category separately to optimize the feature extraction in the tag dimension as much as possible.

3.2.1. Motivation. At present, named entity recognition tasks mainly use CRF (Conditional Random Fields) as the decoding layer of the model. The main reason why CRF are used for decoding is that they can incorporate dependencies in named entity tags. The parameter of CRF is $P \in \mathbb{R}^{(t+2)\times(t+2)}$, where t is the number of tags in the current named entity recognition, and P_{ij} represents the transfer score from the i-th tag to the j-th tag. Therefore, current label for the sentence is judged based on the position that has already been marked. The score of the input sentence $f = [f_1, f_2, \ldots, f_n]$ with the output label $g = [g_1, g_2, \ldots, g_n]$ is

$$\mathrm{score}(f, g) = \sum_{i=1}^{n} h_{i,g_i} + \sum_{i=1}^{n+1} P_{g_{i-1},g_i}, \tag{5}$$

where h_i is the hidden vector output from the previous layer such as Bi-LSTM. The scoring for entire sequence is

composed of the sum of the scores of each part, and the scoring of each part is composed of two parts. The left part is the feature vector output by the model coding layer, and the right part is the CRF transition matrix.

When only considering the sequence of interactions between two consecutive tags, CRF model decoding usually uses the Viterbi algorithm to find the tag sequence. For NLP tasks, the amount of data in the corpus is huge and the data dimension is high, and the use of Viterbi algorithm will be very complicated. Secondly, CRF is similar to LSTM. It needs to calculate the current time series label based on the decoding result of the previous time series, so it cannot accelerate the operation in parallel. Judging from the fully self-attentive coding model proposed in this paper, it does not use sequence labeling models such as LSTM. Therefore, it is not suitable to directly use the Viterbi algorithm in the field of dynamic programming. At the same time, based on the assumptions put forward in this article, named entity recognition task does not need to understand and model the semantics of the whole sentence. In the same way, for the dependencies between sequences, there is no need to dynamically plan the labels of the entire sentence but only need to perform association modeling for a part of adjacent positions each time. In addition, CRF only performs feature extraction modeling for the front and back dependencies of tags during decoding. It does not perform feature extraction on the information contained in other underlying coding vectors. This article hopes to decode the model in a deeper dimension based on the characteristics of named entity recognition while decoding.

Therefore, this work proposes a decoding method with multivariate convolution, which uses the convolution operation on the adjacent n hidden vectors to replace the CRF to model the dependency of the label before and after it. In the convolution, this paper uses the same convolution kernel with the same number of tags as the named entity recognition task, constructs multiple feature maps, and then uses the multilayer perceptron and softmax function. This enables the decoding process to perform feature extraction in the dimension of the tag type, enlarge the feature of the tag at the current position, and weaken the features of other tag classifications.

3.2.2. Structure. The framework of the multivariate convolutional decoder concatenates each position with its adjacent $k-1$ position vectors and then performs a convolution operation on the resulting matrix. The framework of the MCD is shown in Figure 3.

The input of multivariate convolutional decoding layer is the output from the last neural network. In this article, the word embedding is coded for each word, and the sequence $A = [a_1, a_2, a_3, \ldots, a_n]$ is generated by the self-attentive mechanism.

In the multivariate convolutional decoding, each self-attention vector a_i is concatenated with $k-1$ vectors before and after itself into a matrix with itself as the center:

$$A_i = [a_{1-k+1}, \ldots, a_i, \ldots, a_{i+k-1}]. \tag{6}$$

Each matrix is convolutionally decoded through convolutional layers. Each filter generates a vector of $1 \times k$, and then each filter generates a vector c_i end to end. The formula for generating matrices for all A_i through convolution is

$$C = \mathrm{Concat}(\mathrm{Conv}([A_1, \ldots, A_n])). \tag{7}$$

After each vector c_i is generated by MLP, it is normalized using the softmax function, and finally its corresponding label is output.

3.2.3. Working Mechanism. This work uses multivariate convolution method to decode the output vector of the coding layer. The purpose is to associate and jointly decode the surroundings of the current decoding position during decoding based on the characteristics of named entity recognition of medical text. This solves problem for named entity nesting and label dependency. For the output of the previous layer, each dimension can be individually connected to multiple fully connected layers and finally converted into a vector and then decoded using the softmax function. Using a multilayer perceptron to directly decode a single hidden vector can extract the features of words or characters extracted by itself to the greatest extent. However, it does not combine the vectors of the front and back positions so that it cannot extract the remaining position information related to the named entity at the current position.

Therefore, the model in this article uses a convolution operation to decode the encoding layer. Convolutional neural networks are not like a fully connected layer in a multilayer perceptron, which connects neurons to each other. However, it can make the text sentence problem in natural language processing analogous to the solution of the image problem and perform regionalized decoding to extract the characteristics of a segment of adjacent words in the sentence. Generally, when a convolutional neural network is used in a natural language processing task, it convolves a matrix composed of vectors of the entire sentence, so as to extract the semantics of the entire sentence sequence or the required features in classification tasks such as sentiment. This paper believes that the task of medical text named entity recognition does not need to convolve the entire sequence every time in the decoding stage. First of all, the full self-attentive coding framework used in the previous section has already performed fusion feature extraction for the entire sentence. If feature extraction is performed on the entire sequence in the decoding layer, there will be redundancy. Secondly, for some characteristics of named entity recognition, when decoding, focusing on the adjacent words to determine the type of label will greatly improve the accuracy.

The multivariate convolution decoder designed in this paper takes the current position vector as the center, and the matrix formed by splicing $k-1$ vectors before and after it is the convolution range for two-dimensional convolution. If there are less than $k-1$ vectors before and after the current position vector, padding will be filled. The convolutional neural network used in this article does not use a pooling

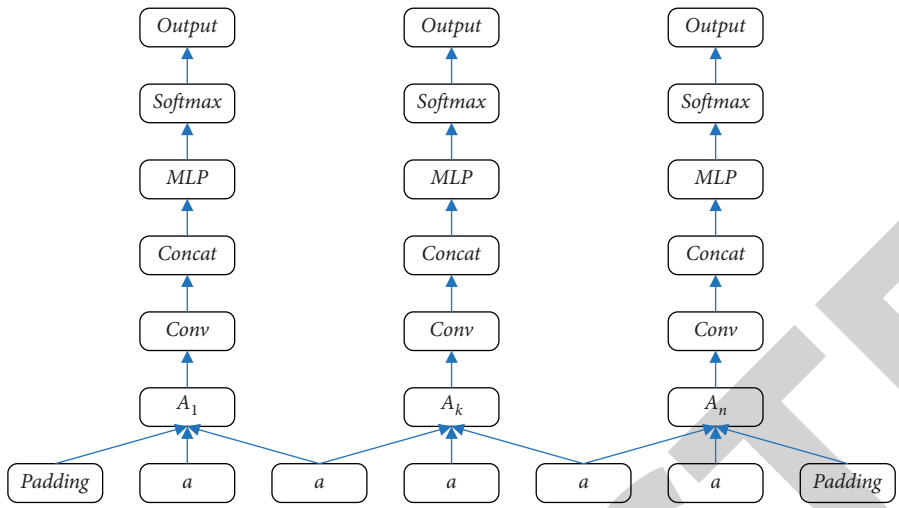

Figure 3: The structure of MCD.

layer after convolution but stitches all the convolution results together as the input of the next layer. Because, as a convolutional neural network for named entity recognition, the result of each convolution reflects the characteristics of the current position and part of the adjacent position, it should be reserved as effective information for the lower layer to extract. In order to reflect the characteristics of the named entity recognition task, for the classification of multiple entity categories, this paper uses multiple filters to convolve the sequence matrix. The number of filters is the number of entity tag categories. The convolution results of each filter are first spliced into a one-dimensional vector. The result of the convolutional layer is the same as that of the multilayer perceptron, and the final output is a $1 \times t$ one-dimensional vector, where t is the number of named entity tag categories. Finally, connect the softmax function for normalization.

3.3. Mixed Loss. The task of medical text named entity recognition needs to distinguish each word (character) in the input sequence as an accurate entity classification or non-entity. Therefore, most of the named entity recognition is a multiclassification task. In view of this feature, the number of filters of the convolutional neural network in the multivariate convolutional decoding layer is set to the number of tag types of the current named entity recognition task. In this way, each coding vector can extract the corresponding characteristics in all the dimensions of the label category. Theoretically, it is hoped that each set filter can correspond to the feature extraction of a tag category, and the features extracted by the filter corresponding to the current word classification should be given a higher weight. Conversely, the features extracted by other filters should be weighted as low as possible.

Therefore, the model needs to be modified during training. The filter of convolutional neural network can extract corresponding label features, and it can make the extracted features distinguish whether the corresponding tag is the tag type of the current location. Therefore, this paper proposes a mixed loss strategy. It uses two classifications and multiple classifications in named entity recognition at the same time, and the multitask loss function is used to train the model to achieve the purpose of improving the model's ability to extract features in the label category dimension. This effectively improves the accuracy of model entity recognition.

The decoding model proposed in this paper is designed to be able to use multiple filters in the feature extraction layer of the convolutional neural network for convolution operations. This allows each filter to extract the features of the encoding vector in a tag category in a targeted manner. In order to achieve this goal, this article is different from the inference model in the training model, which only trains the multiclassification task with the final desired result. However, multiple binary classification tasks are added to the convolutional neural network layer during decoding, allowing it to judge whether the word or character at the current decoding position is in each label category. The specific implementation process is shown in Figure 4.

At the decoder layer, this article sets the number of filters consistent with the number of tag types in the dataset. Each filter will perform a multivariate convolution operation on the current word or character encoding position to obtain a one-dimensional feature vector. For t filters, t feature vectors will be obtained. In order to make the feature vector results obtained by convolution of each filter represent the dimensional features of a specific label type, in the training phase, the model performs a two-classification task training on each feature vector. Each vector in turn corresponds to a label in the set. Each feature vector passes through a multilayer perceptron, and the last output of the perceptron is two nerves, and then the softmax normalization operation is performed on it.

The cross-entropy loss function formula for a filter extraction feature result of a single sample is

$$L_1 = -\sum p(i)\log(q(g(f(i)))), \tag{8}$$

where p is the true label value of the sample and q is the actual output of the model.

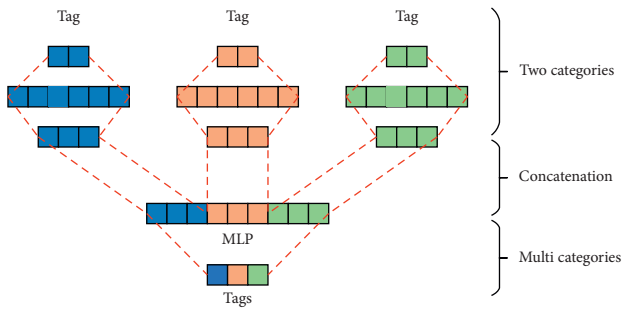

Figure 4: Model multitask training mechanism.

For the coding vector of the word or character at the current position, the training model performs two classifications in addition to each label category. The feature vector generated by each filter must also be spliced to complete the multiclassification task of predicting the type of label. This part is consistent with the principle of the inference model, and its loss function formula is

$$L_2 = -\sum p(C)\log(q(g(C))), \tag{9}$$

where $C = [f_1, f_2, \ldots, f_n]$. The mixed loss function of the multiclassification task and the two-classification task is

$$L = L_1 + L_2. \tag{10}$$

4. Experiment and Discussion

4.1. Dataset and Metric. This article uses a self-made medical text dataset, which is a dataset for named entity recognition and evaluation tasks for electronic medical records. It is mainly composed of hospitalized medical records, including the first page of hospitalized medical records, admission records, course records, and pathological data. The dataset contains five entity types: Anatomy, Symptom, Independent, Drugs, and Operation. The statistical results of the entities are shown in Table 1. Among them, the training set includes 800 current medical history documents, and the test set includes 400 current medical history documents.

Medical text named entity recognition needs to judge the entity boundary and entity type. This paper uses the accurate evaluation method, and only when the boundary and type of the entity are consistent with the true label value is the entity recognition considered correct. At the same time, three evaluation indicators are used to quantitatively analyze the effect of the model, namely, precision, recall, and F1 score.

4.2. Comparison with Other Methods. To verify the effectiveness of our designed model, this section compares our method with other methods including CPM [32], JIC [33], FSCBR [34], and MDD [35]. Experimental result is illustrated in Table 2.

Obviously, compared with the listed methods, our method can obtain the optimal performance. Compared to the best method MDD, our model can obtain 0.9%, 1.4%, and 0.8% gains on precision, recall, and F1 score. This demonstrates the efficiency of our method.

4.3. Evaluation on Network Convergence. In the neural network, the convergence of the model is an important evaluation metric for evaluating network performance. If the network cannot converge, subsequent predictions are meaningless. Therefore, this paper compares the training loss and the testing performance. Experimental result is illustrated in Figure 5.

With the training progresses continuing, the loss of the network gradually decreases, and the test performance of the network gradually increases. When the training epoch is 100, the loss no longer drops, and the test performance no longer rises. The final three performance indicators are 0.924, 0.907, and 0.915. This shows that the network has reached a state of convergence, and the designed network can finally converge and make stable and efficient predictions.

4.4. Evaluation on the Fully Self-Attentive Encoder. In this work, a fully self-attentive encoder is proposed to replace the time series modeling encoder. To verify the effectiveness of this strategy, we compare the encoders using timing model with FSAE. The result is illustrated in Figure 6.

Obviously, when using LSTM or Bi-LSTM to replace the FSAE module proposed in this article, the three performance indicators all have different degrees of decline. This shows that the fully self-attentive mechanism, a nonsequential coding model, can model medical text named entity recognition more effectively.

4.5. Evaluation on the Multivariate Convolutional Decoder. In this work, a multivariate convolutional decoder is proposed to replace the CRF encoder. To verify the effectiveness of this strategy, we compare the model using CRF encoders with FSAE. The result is shown in Figure 7.

Obviously, when using CRF to replace the MCD module proposed in this article, the three performance indicators all have different degrees of decline. This shows that the multivariate convolutional decoder can model medical text named entity recognition more effectively.

4.6. Evaluation on Mixed Loss. In this work, a mixed loss consisting of two-classification loss and multiclassification loss is proposed to optimize the network. The training model is different from the inference model, which only trains the multiclassification task with the final desired result. However, during the decoding process, multiple two-classification tasks are added to the capacity neural network layer, allowing it to decide whether the word or character at the current decoding position is of this class on each label class. To verify the effectiveness, we compare the network only using multiclassification loss with mixed loss. The result is shown in Figure 8.

Obviously, when using the single multiclassification loss to replace the mixed loss proposed in this article, the three performance indicators all have different degrees of decline. This shows that the mixed loss can optimize the network more effectively and guide the network to extract more discriminate features for medical text named entity recognition.

Table 1: Dataset entity statistical result.

Item	Document	Anatomy	Symptom	Independent	Drugs	Operation
Train	800	7534	3019	3407	1658	1427
Test	400	4083	1482	1632	915	748

Table 2: Comparison with other methods.

Method	Precision	Recall	F1
CPM	0.873	0.848	0.861
JIC	0.892	0.871	0.882
FSCBR	0.906	0.885	0.894
MDD	0.915	0.893	0.907
Ours	0.924	0.907	0.915

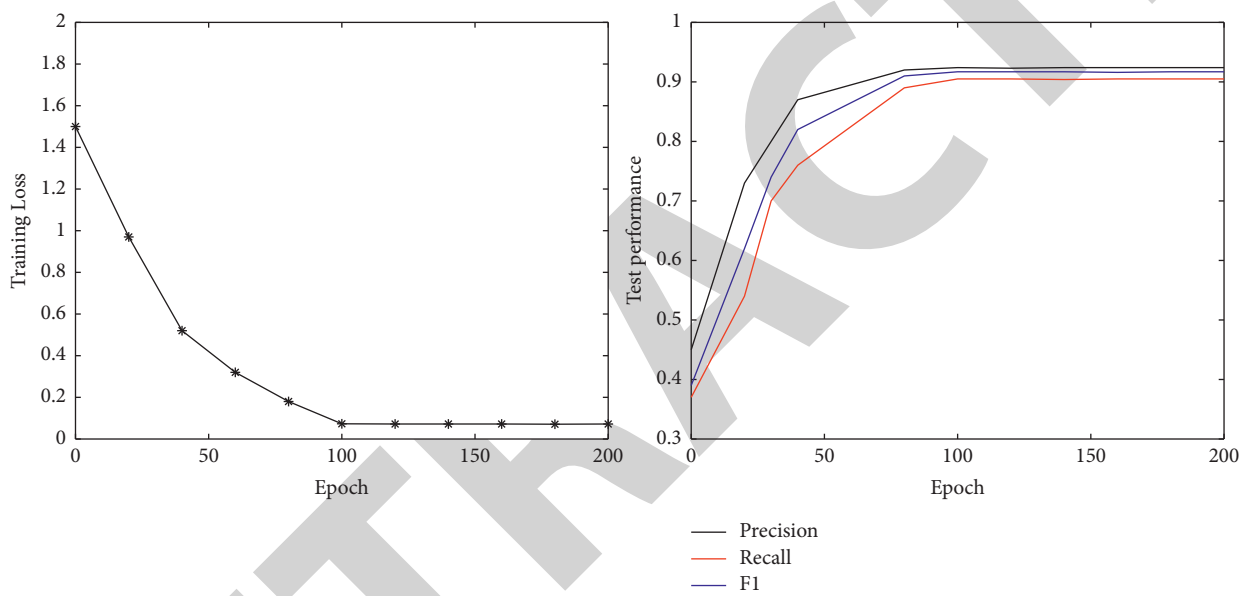

Figure 5: The training loss and test performance.

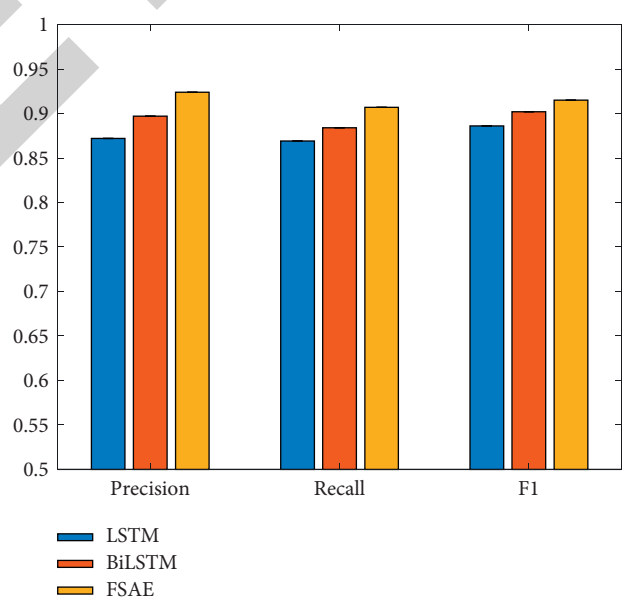

Figure 6: Evaluation on the fully self-attentive encoder.

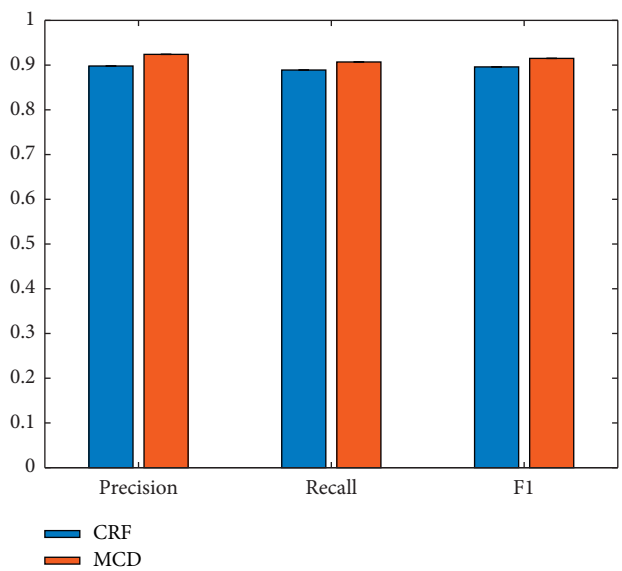

Figure 7: Evaluation on the multivariate convolutional decoder.

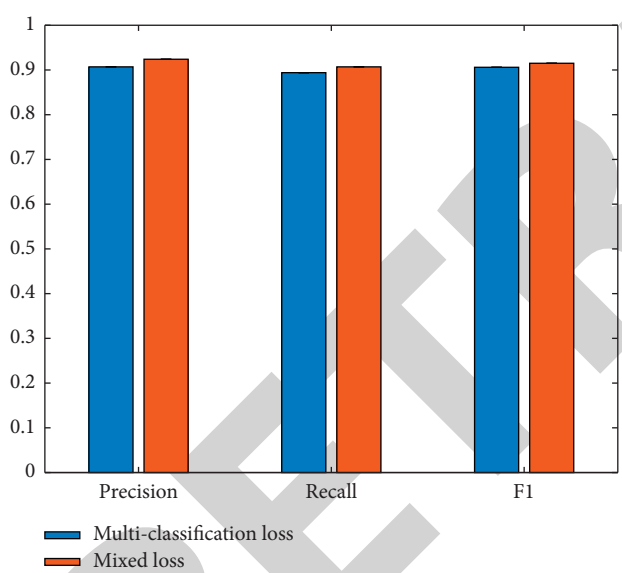

Figure 8: Evaluation on mixed loss.

5. Conclusion

In order to meet the challenge, this paper analyzed some existing medical text named entity recognition models and pointed out their possible shortcomings and proposed a hybrid neural network model. This model improves the performance of medical text named entity recognition. First, this work proposes a coding model based on full self-attention. The words in medical text are more polysemous, and the meanings of some words in the sentence can be clearly judged by reading the whole sentence. Therefore, this paper proposes a fully self-attentive model to replace the temporal model to model the corpus. The fully self-attentive mechanism pays attention to the words in all positions in the sentence when extracting the features of the words in each position. These words are scored according to the degree of influence on the current word. In this way, the feature vector of each word will incorporate contextual information. Second, this paper proposes a decoding method based on multivariate convolution. It uses convolution operation on adjacent hidden vectors instead of CRF to model the dependency relationship between labels. In the convolution, this paper uses the same number of convolution kernels as the number of tags for the named entity recognition task. It constructs multiple feature maps and then uses multilayer perceptron and softmax function. Even the decoding can perform feature extraction in the dimension of the full label, amplify the features of the label at the current position, and weaken the features of other label classifications. Third, multiple binary classification tasks are added to the convolutional neural network layer when the training model is decoded. A large number of experiments verify the effectiveness and reliability of our method.

Data Availability

The datasets used during the current study are available from the corresponding author upon reasonable request.

Conflicts of Interest

The authors declare that there are no conflicts of interest.

References

[1] T. Wolf, J. Chaumond, L. Debut et al., "Transformers: state-of-the-art natural language processing," in *Proceedings of the Conference on Empirical Methods in Natural Language Processing*, pp. 38–45, October 2020.

[2] T. Wolf, L. Debut, V. Sanh et al., "Huggingface's transformers: state-of-the-art natural language processin. Huggingface's transformers: state-of-the-art natural language processing," 2019, https://arxiv.org/abs/1910.03771.

[3] Y. Gu, R. Tinn, H. Cheng et al., "Domain-specific language model pretraining for biomedical natural language processing," *ACM Transactions on Computing for Healthcare*, vol. 3, no. 1, pp. 1–23, 2021.

[4] J. Pei, K. Zhong, J. Li, J. Xu, and X. Wang, "ECNN: evaluating a cluster-neural network model for city innovation capability," *Neural Computing & Applications*, pp. 1–13, 2021.

[5] J. Guo, H. He, and T. He, "GluonCV and GluonNLP: deep learning in computer vision and natural language processing," *Journal of Machine Learning Research*, vol. 21, no. 23, pp. 1–7, 2020.

[6] V. Yadav, S. Bethard, and R. Sharp, "A survey on recent advances in named entity recognition from deep learning models," 2019, https://arxiv.org/abs/1910.11470.

[7] A. Akbik, T. Bergmann, and R. Vollgraf, "Pooled contextualized embeddings for named entity recognition," in *Proceedings of the Conference of the North American Chapter of the Association for Computational Linguistics: Human Language Technologies*, pp. 724–728, Minneapolis, Minnesota, June 2019.

[8] T. Al-Moslmi, G. M. Ocana, and L. A. Opdahl, "Named entity extraction for knowledge graphs: a literature overview," *IEEE Access*, vol. 8, pp. 32862–32881, 2020.

Hindawi
Journal of Healthcare Engineering
Volume 2023, Article ID 9790572, 1 page
https://doi.org/10.1155/2023/9790572

Retraction

Retracted: Biomechanical Analysis of the Human Knee Joint

Journal of Healthcare Engineering

Received 10 October 2023; Accepted 10 October 2023; Published 11 October 2023

This article has been retracted by Hindawi following an investigation undertaken by the publisher [1]. This investigation has uncovered evidence of one or more of the following indicators of systematic manipulation of the publication process:

(1) Discrepancies in scope
(2) Discrepancies in the description of the research reported
(3) Discrepancies between the availability of data and the research described
(4) Inappropriate citations
(5) Incoherent, meaningless and/or irrelevant content included in the article
(6) Peer-review manipulation

The presence of these indicators undermines our confidence in the integrity of the article's content and we cannot, therefore, vouch for its reliability. Please note that this notice is intended solely to alert readers that the content of this article is unreliable. We have not investigated whether authors were aware of or involved in the systematic manipulation of the publication process.

In addition, our investigation has also shown that one or more of the following human-subject reporting requirements has not been met in this article: ethical approval by an Institutional Review Board (IRB) committee or equivalent, patient/participant consent to participate, and/or agreement to publish patient/participant details (where relevant).

Wiley and Hindawi regrets that the usual quality checks did not identify these issues before publication and have since put additional measures in place to safeguard research integrity.

We wish to credit our own Research Integrity and Research Publishing teams and anonymous and named external researchers and research integrity experts for contributing to this investigation.

The corresponding author, as the representative of all authors, has been given the opportunity to register their agreement or disagreement to this retraction. We have kept a record of any response received.

References

[1] S. Wang, "Biomechanical Analysis of the Human Knee Joint," *Journal of Healthcare Engineering*, vol. 2022, Article ID 9365362, 8 pages, 2022.

Hindawi
Journal of Healthcare Engineering
Volume 2022, Article ID 9365362, 8 pages
https://doi.org/10.1155/2022/9365362

Research Article

Biomechanical Analysis of the Human Knee Joint

Sheng Wang

Shanxi University, Taiyuan 030006, China

Correspondence should be addressed to Sheng Wang; adam_sxdx@sxu.edu.cn

Received 17 December 2021; Accepted 31 January 2022; Published 4 March 2022

Academic Editor: Nima Jafari Navimipour

Exercise is an indispensable part of human daily life. The knee joint is inseparable from human movement. The knee is relatively fragile and easy to get injuries. Therefore, the biomechanical properties of knee joints were studied. The VICON T40S 3D motion acquisition and analysis system and the AMTI 3D force measurement platform were used to collect the lower limb kinematics and dynamics data of five male volunteers. Then the knee angle and moment of the human body are analyzed, the foot pressure was obtained by force plate, and the ground reaction force was obtained. The results show that: (1) in terms of knee flexion and extension torques, the peak stretching torques occurred in about 25% and 65% of the gait cycles. At the beginning of the gait, which is the flexion moment, the knee joint produces a moment of −24.65 Nmm, 25% of gait cycles reached the maximum peak value of 896.89 Nmm, 65% of gait cycles reached the second peak value of 315.81 Nmm; (2) The change of reaction force in a gait cycle is: when the ground starts to react, the ground reaction reaches 600 N. At normal times, the ground reaction force rapidly rises to the maximum value of 890 N; when the gait is in the middle of a single support phase, the ground reaction force is 462 N; when the ankle joint moves in plantar flexion, the ground reaction force increases to 830 N again; finally, when the toe is lifted off the ground, the ground reaction force quickly drops to zero; (3) in the course of a gait cycle, the spatial and temporal parameter curve distribution of the subjects was consistent, and the difference was not significant ($P > 0.05$).

1. Introduction

The knee joint is the main joint of the human lower limbs. It has a lot of weight-bearing and a large amount of exercise, and it is the hub of lower limb activities. The structure and function of the knee joint are the most complex joints in the human body. Due to the anatomical complexity of the knee joint (three-component bones: femur, tibia, and patella and their surface cartilage tissue; major ligaments: anterior and posterior cruciate ligaments, medial and lateral collateral ligaments, patellar ligaments, meniscus, attached muscle groups, etc.), kinematic complexity (multiaxis three-dimensional motion) and mechanical complexity (pressure, tensile stress, and shear force are simultaneously applied to the knee during motion and these forces vary dramatically with the gait cycle stage), it is of great theoretical significance to study the mechanical system of knee joint. In the sports population, the improper movement mode often causes knee joint injury, for example, the anterior cruciate ligament, the meniscus, and other related structures are damaged. Among them, anterior cruciate ligament injury is a kind of common potential injury, and it often appears as a kind of noncontact injury in sports, such as landing, changing direction, twisting, and other movements.

Research on knee biomechanics mainly includes the influence of movement, joint contact, and soft tissue deformation and force on joint movement and force. Many scholars have studied this issue. The AMTI 3D three-dimensional force platform is equipped with several piezoresistive sensors to measure the pressure changes in different parts of the entire platform, and the changes in force and torque on the X, Y, and Z axes are calculated. Products are widely used in sports science, clinical medicine, ergonomics, military scientific research, aerospace, and other fields. Therefore, the VICON T40S motion capture system and the AMTI 3D force measurement platform are used to collect the kinematic and dynamic data of the lower limbs. Then, the human knee angle and moment values in the human gait

cycle are analyzed, and the foot pressure is obtained by using the force plate. The ground reaction force was obtained to analyze the biomechanical properties of the knee joint.

Therefore, the development of new therapies is critical to prevent permanent adaptive changes in posture in patients with knee injuries [1]. Biomechanics: knowledge of biomechanics helps predict stresses in different parts of the knee during daily activities. Biomechanical parameters such as contact pressure, contact area, and maximum compressive stress of the fully extended knee during the gait cycle were evaluated [2].

Understanding the complex biomechanical behavior of injured knee joints is critical in a variety of clinical situations [3]. Chen conducted a biomechanical analysis of the knee joint during take-off and landing [4]. Kumbhalkar et al. conducted a biomechanical study on knee replacement [5]. Chang et al. analyzed the biomechanical properties of ankle cartilage and ligament in BKTS, a typical Tai Chi movement [6]. Zhang et al. used finite element analysis to study biomechanical changes in load distribution of longitudinal tear of the knee joint semilunar angle [7]. Tarnita et al. applied finite element analysis (FEA) to a virtual component consisting of an orthotic device and an osteoarthritic knee joint (OAK) using Ansys Workbench 14.5 software, to study the influence of orthopedic devices on the maximum stress value of knee cartilage [8]. Yong-Jun et al. established the finite element model of the discoid meniscus of the knee by fusing CT and MRI data to provide a reliable finite element model for the study of the discoid meniscus [9]. Abidin et al. analyzed the biomechanical effects of different fixators (cross nail technique) on knee stability after ACL-R. Finite element analysis was performed on the knee joint with a DST graft and fixator [10].

The triangular partial grid model and the tetrahedral element solid grid model of the knee joint are established in this paper. The structure of each part of the model is clear and smooth, the grid continuity is good, and the size is right. The mesh is in line with the actual situation. The quality of the mesh is excellent after several times of optimization, and it can be applied to the relevant finite element analysis well.

2. Research Methods

2.1. Experimental Scheme Design. In order to obtain the changes in knee angle, force, and moment during a single gait cycle in healthy subjects, VICON T40S 3D motion acquisition and analysis system was adopted in this experiment. The system has a high sampling rate and good real-time performance, with a maximum of 16 million pixels and the fastest capture speed of 120 fps. The instrument is widely used in VR, biological motion mechanics, human engineering research, physical education, robot design, and other research fields.

The experimental equipment used 10 cameras with a frequency of 100 Hz and sensors with light-emitting spheres, making it easy for the camera to pick it up. In addition, three three-dimensional force measuring plates with an acquisition frequency of 1500 Hz, a T-type calibration frame, and computer and data transmission-related equipment was added. The 3D force plate and the motion capture system are connected with the computer software to collect the gait data needed for the experiment at the same time. Finally, VICON Nexus, a data processing device, corrected the data and calculated the data.

The experiment involved five men, all healthy and able to walk naturally. The lower limbs were normal, and there was no history of knee joint problems. The specific operation is in the shooting area of the laboratory staff around the T-shaped correction frame. The method is to obtain the camera position by collecting the marker movement data. After the calibration begins, the camera continuously collects the data of the marker point, and the marker light on the camera can show the collection situation of the camera. When the blue indicator blinks until the green indicator turns on, the camera has collected enough data. When all 10 cameras complete the collection, the system will automatically stop the collection and start calibration calculation. Successful calibration for each camera is to collect more than 1000 frames of effective data.

In the experiment, each subject was required to add 26 marker points as shown in Figure 1, head (RFHD, LFHD, LBHD, and RBHD), torso (CLAV, C7, RBAK, and T10), points of the pelvis (LASI, LPSI, RASI, and RPSI), lower limbs (RANK, RWRB, RTHI, RKNE, RTIB, LANK, LTIB, LKNE, LTHI, and LWRB), and toes (RTOE, LTOE, LHEE, and RHEE). The points captured by the camera are synthesized by the computer to obtain the kinematic indexes.

2.2. Experimental Data Collection. In order to reduce the influence of various factors on the human body while walking, before the experiment, subjects were asked to do a small amount of walking on their own in the most relaxed state along the route beforehand, familiarize themselves with the route, and experiment when they are not nervous. The experiment process is as follows: first, the basic information of the subject is filled and the measurement data by manual measurement in the computer system; second, the subjects should establish a static model, with their arms spread in a T-shape and their feet spread about 20 cm, in standard standing posture, stand with toes facing forward on the force plate, and hold still. After the markers were identified by VICON, the skeleton model of the subject was established. All subsequent experiments were performed under this model. The line where the flat force plate is located is the route for the subjects to walk. Finally, each participant was asked to walk at a natural walking speed on a set path, ensuring that the force plate had a full gait cycle. There is a five-minute break between each walk so as to not cause fatigue and affect the final results. One subject is required to complete 15 sets of valid data test experiments to ensure that the data has more than 10 sets of optional data. Finally, the data of each cycle of walking in the same direction were extracted from the 15 groups of data.

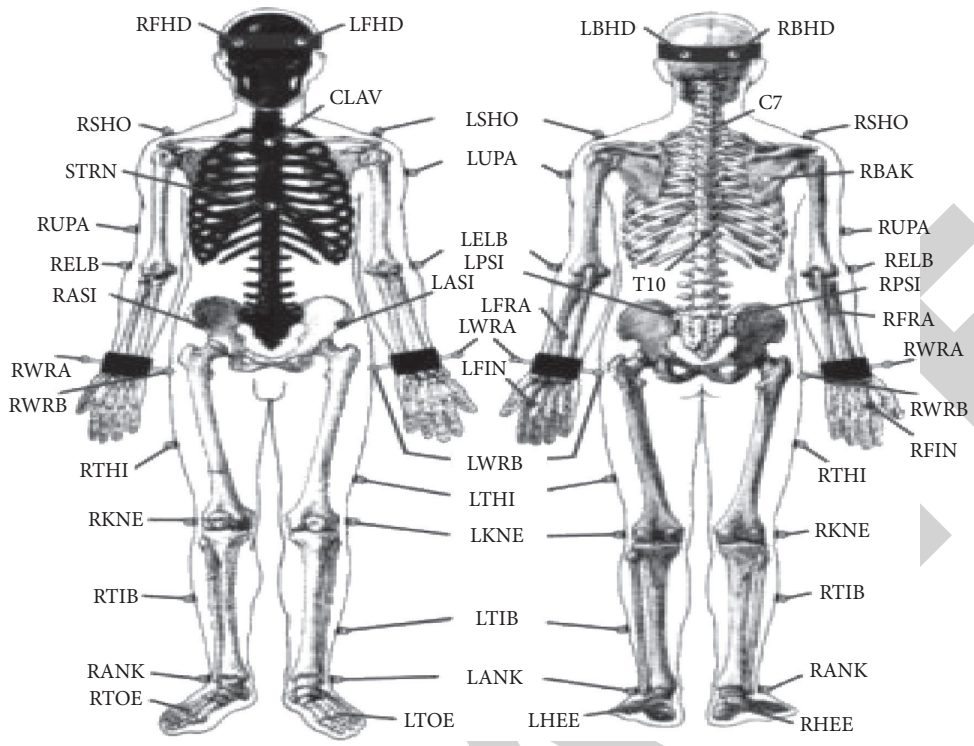

Figure 1: Schematic diagram of human test standard points.

3. Results Analysis and Discussion

The VICON motion capture system defines the angle of the knee joint as follows: the reference line is the extension line of the long axis of the femur, the angle is between the reference line and the long axis of the tibia; knee flexion, adduction, and internal rotation were positive, while the opposite movement was negative; the simulated spatial cartesian coordinate system in the VICON motion capture system defines the X, Y, and Z-axis coordinates of the marked points, where the X-axis coordinates are defined as the left and right directions of the spatial origin, the Y-axis coordinates are defined as the front and back directions of the spatial origin, and the Z-axis coordinates are defined as the upper and lower directions of the spatial origin. Since the knee joint is mainly in the sagittal plane during walking, that is, the Y-axis in the VICON system, the kinematics of this study mainly focus on the movement on the Y-axis.

In order to process the large amount of data obtained in the experiment, the data required in this experiment can be extracted by using Mokka software, Mokka software can directly visualize data information, as shown in Figure 2. The import format is C3d, and the data collected by gait is imported into Mokka, the first and second landing moments of the left and right heels are respectively treated as a gait cycle. Finally, the knee joint angle value, the plantar pressure value on the force plate, the motion trajectory of the marked point on the Y-axis, and the three azimuth torque component values on the knee joint can be extracted and selected during preservation. The observation method of time selection is to intercept a complete gait cycle on the time axis and the data is exported in Excel format.

As shown in Figures 3 and 4, a 27-year-old subject with a weight of 75 kg and a height of 180 cm was taken as an example. The standard deviation of 15 groups of data of knee joint angle and moment was obtained by average processing, and the movement of the knee joint was analyzed accordingly. In the Figures 3(a)–3(d) are the angles and torques of the left and right knee joints, respectively, the solid line of each figure is the average value of the 15 groups of experimental data, and the gray band is the error band.

We select 1, 5, and 10 kinds of materials for the femur model, respectively, and assign values to the femoral materials by the uniform method. That is, we subdivide the gray value of the femoral body mesh into 1, 5, and 10 parts, and each small interval represents an each small area, which is represented by a central gray value, and each material is represented by a different color. Then we determine the expression of the femur, the expression of elastic modulus, and the Poisson's ratio to set the parameters of the material according to the relevant reference books and the referenced literature is

$$\begin{aligned} \text{Density} &= -13.4 + 1017 \times \text{Grayvalue}, \\ E - \text{Modu} \times \text{lus} &= -388.8 + 5925 \times \text{Density}, \\ \text{Poisson Coefficient} &= 0.3. \end{aligned} \tag{1}$$

The time parameters of gait include support time, swing time, and a complete gait cycle time, in which the single support time on one side is consistent with the swing time on the other side. The complete gait cycle time was compared and analyzed. The left leg gait cycle time refers to the time from when the left foot hits the ground until the left foot hits the ground again, and the left foot single support time refers to the time from when the right foot leaves the ground until

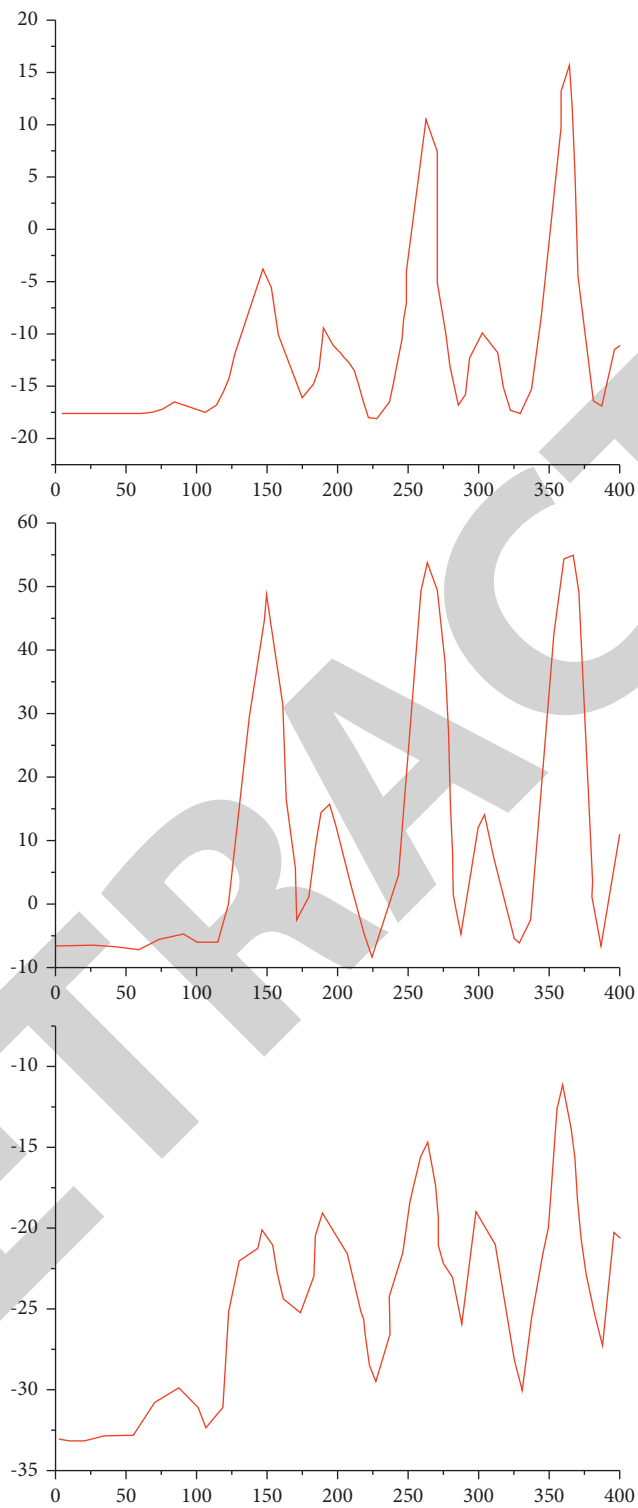

Figure 2: Importing data in Mokka.

the right foot hits the ground again; the same is true for the right side. The range of knee joint changes in adolescent gait is affected by many factors. The magnitude of the change in the knee joint becomes smaller and smaller as the grade increases.

It can be seen that the knee angle changes throughout the gait cycle as follows: the knee angle of the left and right legs is about −5° before bending the knee, and the knee angle reaches about 30° when the heel is off the ground at the beginning. During the first landing in the state of bending the knee, the full extension of the knee joint is close to 0°, during the next swing when the gait cycle is about 78% of the complete gait, the knee flexion angle reaches a peak of about 60°, and the next cycle is the foot

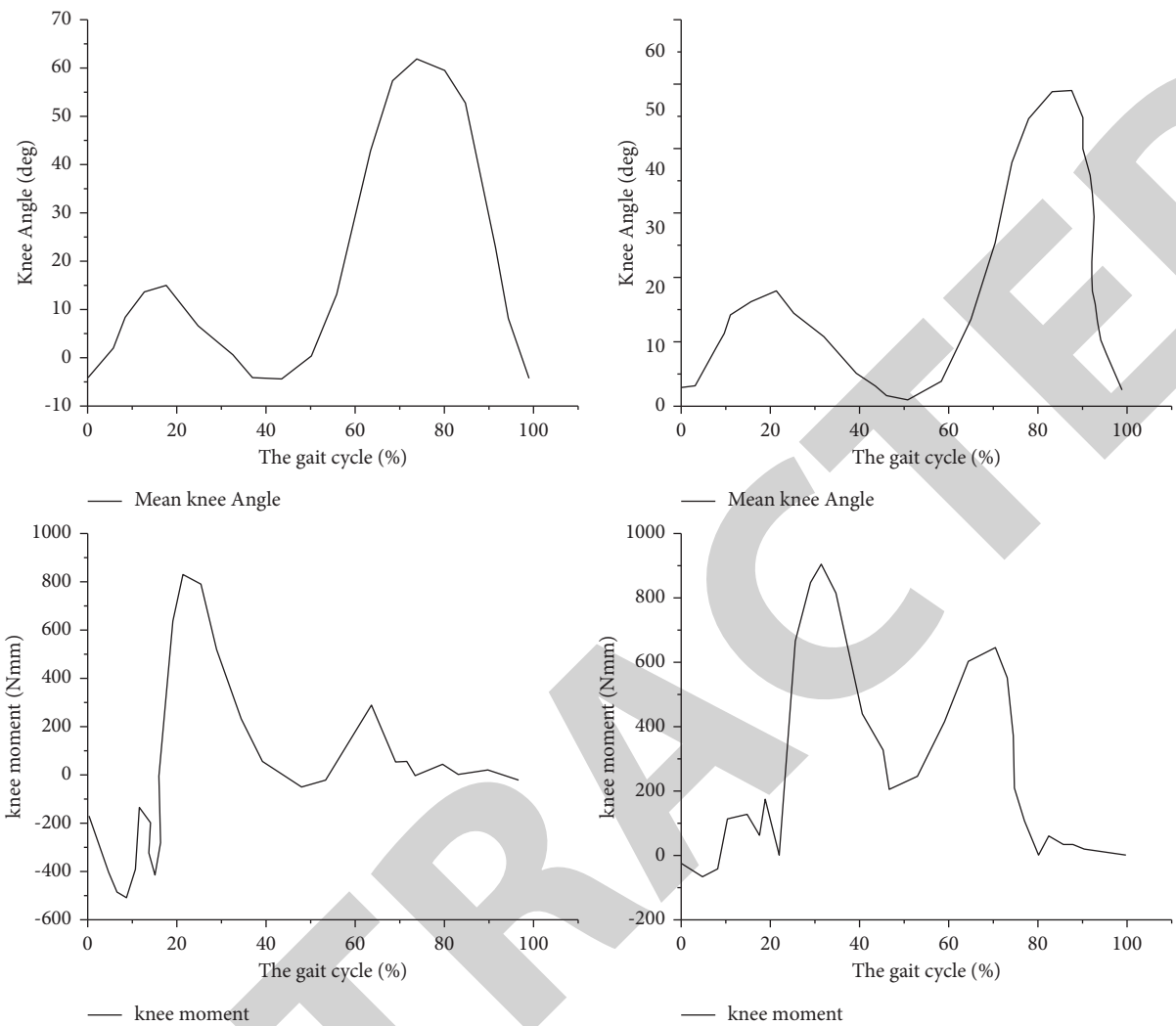

Figure 3: Knee angle and moment.

following the ground. At this point, the knee angle returns to the minimum, as shown in Table 1. However, in the same gait cycle of the left leg and the right leg, the stride length of the left leg is smaller, and the angle difference between the left and right legs is smaller. As can be seen from the figure, the joint angle of the left knee has a slight overextension phenomenon, which is due to the error caused by the inaccuracy between the position of the knee joint sticking point and the standard model.

In terms of knee flexion and extension moments, the peak stretching moments occurred at about 25% and 65% of the gait cycle. At the beginning of the gait, is the flexion moment, the knee produces a moment of −24.65 Nmm 25% of the gait cycle reaches the maximum peak value of 896.89 Nmm, 65% of gait cycles reached the second peak of 315.81 Nmm (see Table 2 for details). The comparison of the initial torque of the gait cycle and the two large peaks of the torque is shown in Figure 5.

In the sagittal plane, the ground reaction curve shows two peaks in a gait cycle. In the early stage of walking, the ground reaction force fluctuates in a small range, and the ground reaction force reaches 600 N after the initial stage of walking. At normal times, the ground reaction force rapidly rises to the maximum value and reaches the maximum value of 890 N. At this time, the ratio of weight to body weight on one limb is 11.8, which is at 20% of the gait cycle. When the gait is in the middle of the single support phase, the value of the force decreases gradually. The curve trough occurs at about 50% of the gait cycle, and the ground reaction force is 462 N. The ratio of this value to the subject's body weight is 6.16. When the ankle is plantar flexion, the ground reaction increases again to a second crest. At this point, it reaches 830 N, which is about 80% of the gait cycle. The ratio of this value to the bodyweight of the walker is 11. Finally, when the toe is off the ground, the ground reaction force quickly drops to zero, as shown in Figure 4. The specific values are shown in Table 3.

In order to verify the validity of the data from this gait experiment, since height also has an impact on the space-time parameters of gait, the left knee joint angles of the subjects aged 22–27 years, average height (175 ± 5) cm, weight (70 ± 5) kg were averaged, and the standard

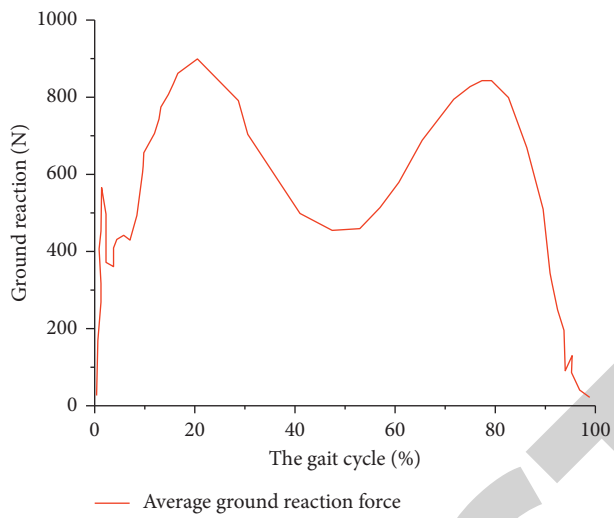

Figure 4: Ground reaction force.

Table 1: Knee angle changes in a gait cycle.

The gait	Bend your knees before	Heel off the ground	First landing	The second time off the ground	Second landing
The angle(°)	−5	30	0	60	−5

Table 2: Peak torque of a gait cycle.

The gait cycle	25%	65%
Peak(Nmm)	896.89	315.81

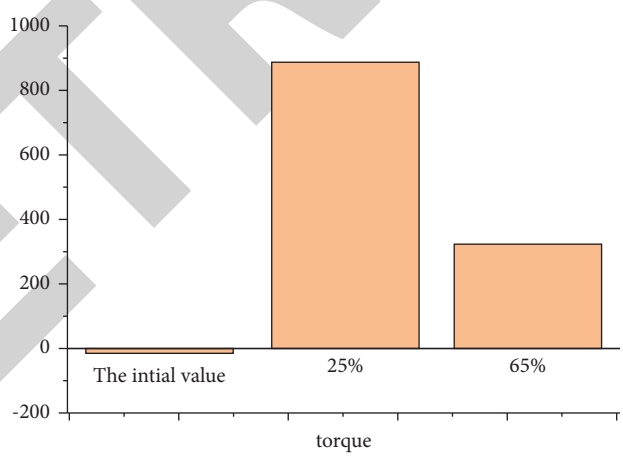

Figure 5: Initial torque and 2 peak torque of a gait cycle.

Table 3: Ground reaction force in a gait cycle.

The gait	Feet on the ground (N)	Foot flat (N)	Single supported phase metaphase (N)	Plantar flexion movement (N)	Toe off the ground (N)
Ground reaction	600	890	462	830	0

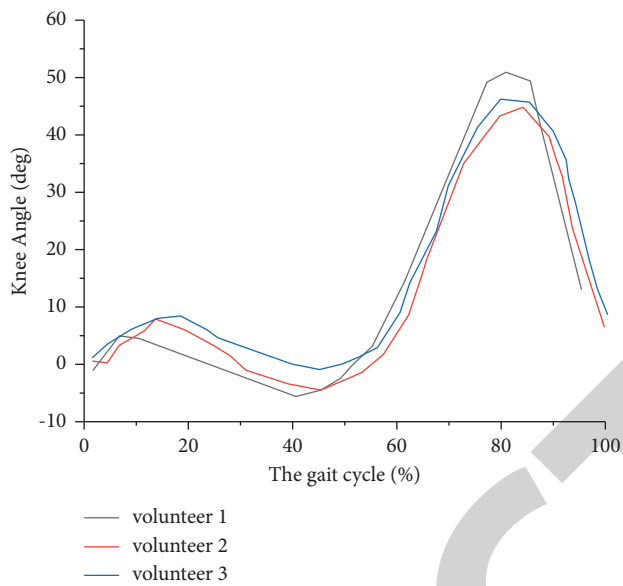

Figure 6: Verification of the validity of gait data.

deviation was obtained, as shown in Figure 6. It can be seen from the results that the spatial and temporal parameter curve distribution of the three subjects in a gait cycle is consistent, and there is no significant difference ($P > 0.05$). Therefore, the results can represent the normal gait pattern.

4. Conclusions

In terms of the present stage, the curative effect of knee joint replacement surgery, may well solve the patients' pain and basic activities in the short term, but after all, the service life of the knee joint prosthesis is limited, postoperative prosthesis and joint wear, the wear and tear of implants and prostheses remains, so the need to do as much as possible to design a perfect prosthesis. The results showed that: (1) at the beginning of the gait, is the flexion moment, and the knee produces a moment of −24.65 Nmm, 25% of the gait cycle reaches the maximum peak value of 896.89 Nmm, and 65% of the gait cycle reaches the second peak value of 315.81 Nmm. (2) When the gait is in the middle of single support phase, the ground reaction force is 462 N; when the ankle joint moves in plantar flexion, the ground reaction force increases to 830 N again. Finally, when the toe is off the ground, the ground reaction force quickly drops to zero. (3) In the course of a gait cycle, the spatial and temporal parameter curve distribution of the subjects was consistent, and the difference was not significant ($P > 0.05$).

Data Availability

The datasets used and/or analyzed during the present study are available from the corresponding author upon reasonable request.

Conflicts of Interest

The authors declare that they have no conflicts of interest.

References

[1] S. Raghav and A. Singh, "Determining the biomechanical changes in lumbar spine among patients with injuries around the knee joint: a systematic review protocol," *International Journal of Community Medicine and Public Health*, vol. 7, no. 8, Article ID 3251, 2020.

[2] A. K. Devaraj, K. K. V. Acharya, R. Adhikari, and R. Adhikari, "Comparison of biomechanical parameters between medial and lateral compartments of human knee joints," *The Open Biomedical Engineering Journal*, vol. 14, no. 1, pp. 74–86, 2020.

[3] A. K. Devaraj, K. K. V. Acharya, and R. Adhikari, "Experimental and finite element investigations on the biomechanical effects of meniscal tears in the knee joint: a review," *Journal of Biomimetics, Biomaterials and Biomedical Engineering*, vol. 50, pp. 1–14, 2021.

[4] Y. D. Cheng, "Biomechanical analysis of knee joint during the process of jumping and landing," *Modeling and Simulation*, vol. 09, no. 1, pp. 77–86, 2020.

[5] M. A. Kumbhalkar, K. S. Rambhad, and N. J. Kanu, "An insight into biomechanical study for replacement of knee joint," *Materials Today: Proceedings*, vol. 47, no. 5, pp. 2957–2965, 2021.

[6] T. Chang, K. Wang, S. Huang, L. Wang, and M. Zhang, "Biomechanical analysis of ankle-foot complex during a typical tai chi movement-brush knee and twist step," *Journal of Biomedical Engineering*, vol. 38, no. 1, pp. 97–104, 2021.

[7] K. Zhang, L. Li, L. Yang et al., "The biomechanical changes of load distribution with longitudinal tears of meniscal horns on knee joint: a finite element analysis," *Journal of Orthopaedic Surgery and Research*, vol. 14, no. 1, p. 237, 2019.

[8] D. Tarnita, D. Pisla, I. Geonea, C. Vaida, M. Catana, and D. N. Tarnita, "Static and dynamic analysis of osteoarthritic

Hindawi
Journal of Healthcare Engineering
Volume 2023, Article ID 9753986, 1 page
https://doi.org/10.1155/2023/9753986

Retraction

Retracted: Study on Correlation between Body Cell Mass Index and Cognitive Impairment in Hemodialysis Maintaining Patients: A Cross-Sectional Study

Journal of Healthcare Engineering

Received 1 August 2023; Accepted 1 August 2023; Published 2 August 2023

This article has been retracted by Hindawi following an investigation undertaken by the publisher [1]. This investigation has uncovered evidence of one or more of the following indicators of systematic manipulation of the publication process:

(1) Discrepancies in scope
(2) Discrepancies in the description of the research reported
(3) Discrepancies between the availability of data and the research described
(4) Inappropriate citations
(5) Incoherent, meaningless and/or irrelevant content included in the article
(6) Peer-review manipulation

The presence of these indicators undermines our confidence in the integrity of the article's content and we cannot, therefore, vouch for its reliability. Please note that this notice is intended solely to alert readers that the content of this article is unreliable. We have not investigated whether authors were aware of or involved in the systematic manipulation of the publication process.

Wiley and Hindawi regrets that the usual quality checks did not identify these issues before publication and have since put additional measures in place to safeguard research integrity.

We wish to credit our own Research Integrity and Research Publishing teams and anonymous and named external researchers and research integrity experts for contributing to this investigation.

The corresponding author, as the representative of all authors, has been given the opportunity to register their agreement or disagreement to this retraction. We have kept a record of any response received.

References

[1] Q. Ou, C. Zhou, M. Tian, X. Yang, and Y. Zha, "Study on Correlation between Body Cell Mass Index and Cognitive Impairment in Hemodialysis Maintaining Patients: A Cross-Sectional Study," *Journal of Healthcare Engineering*, vol. 2022, Article ID 9023562, 9 pages, 2022.

Hindawi
Journal of Healthcare Engineering
Volume 2022, Article ID 9023562, 9 pages
https://doi.org/10.1155/2022/9023562

Research Article

Study on Correlation between Body Cell Mass Index and Cognitive Impairment in Hemodialysis Maintaining Patients: A Cross-Sectional Study

Qinqin Ou,[1] Chaomin Zhou,[2] Maolu Tian,[2] Xiangyan Yang,[1] and Yan Zha[1]

[1]*Zunyi Medical University, Zunyi 563000, China*
[2]*Department of Nephrology, Guizhou Provincial People's Hospital, Guiyang 550002, China*

Correspondence should be addressed to Yan Zha; zhayan72@stu.cpu.edu.cn

Received 25 December 2021; Accepted 1 February 2022; Published 3 March 2022

Academic Editor: Nima Jafari Navimipour

Objective. To investigate the relationship between body cell mass index (BCMI) and cognitive impairment in maintaining hemodialysis (MHD) patients. *Methods*. We collected the general materials, laboratory indexes, and physical measurement indexes of patients undergoing maintenance hemodialysis in hemodialysis centers of 20 tertiary and tertiary general hospitals in Guizhou Province from June to September 2020. The body composition was measured by bioelectrical impedance method, and the BCMI value was calculated. The subjects were divided into normal cognitive function group (score ≥27), mild cognitive impairment group (score 23–26), and severe cognitive impairment group (score <23). Two groups of people with normal cognitive function and cognitive impairment with similar baseline data (gender, age, and education) were obtained by propensity score matching (PSM). *Results*. A total of 2008 subjects were included in this study, including 467 cases (23.3%) in the cognitive impairment group. A total of 814 cases were accurately matched after PSM. Multivariate logistic regression analysis showed that the incidence risk of the BCMI Q1 group was 8.99 times higher than that of the Q4 group (95% CI: 5.74 ~ 14.09, $P < 0.001$). ROC curve analysis showed that the best threshold of BCMI for predicting cognitive impairment in MHD patients was 9.05, the sensitivity and specificity were 71.5% and 62.7%, respectively, and the area under the curve was 0.713 (95% CI: 0.678 ~ 0.748, $P < 0.001$). *Conclusions* BCMI is related to cognitive impairment in MHD patients and has predictive value for the onset of cognitive impairment in MHD patients.

1. Introduction

Cognitive impairment (CI) refers to the defects of one or more key brain functions such as learning, memory, complex attention, executive function, language, perceptual motor function, and its severity can range from mild cognitive impairment (MCI) to severe dementia [1]. Maintenance hemodialysis (MHD) patients often have different degrees of cognitive impairment, and the morbidity rate is as high as 18.8%–60.9% [2–4]. Cognitive impairment can significantly increase the hospitalization rate and mortality of MHD patients and seriously affect the clinical prognosis of patients [5–7]. Therefore, it is particularly important to identify the risk factors of cognitive impairment in MHD patients as soon as possible and carry out early intervention.

Malnutrition is common in patients of maintenance hemodialysis (MHD), featuring decreased protein and energy reserves and decreased muscle mass. Studies have found that malnutrition is an important factor bringing about brain function and neurodegenerative diseases [8–12] and is closely related to the occurrence and development of cognitive dysfunction. It impacts on cognitive function in the following ways: malnutrition leads to the shortage of important micronutrients like vitamins and essential fatty acids, which is likely to stimulate the inflammation to appear in the body, and the increase in inflammatory factors and oxidative stress leads to neuroinflammation and cerebrovascular damage [8, 13]. Second, the β-amyloid 42 (Aβ42) drops and total tau and phosphorylated tau protein levels rise in cerebrospinal fluid (CSF) of malnourished patients,

resulting in the mitochondrial dysfunction and cell death of hippocampal neurons in the brain [14, 15]. Besides energy and hormone metabolism change, and the levels of hormones related to cognitive function, like leptin, are reduced in malnourished patients [15, 16], accompanying with the decreased muscle masses that are related to the reduced volume of prefrontal, cingulate, occipitotemporal, and cerebellar gray matter [15–18].

In the current nutrition guidelines for chronic kidney disease, body mass index (BMI) is chosen as the main nutritional assessment index [19]. However, BMI values cannot differentiate between fluid, fat, and fat-free mass, the decreased muscle mass may be mistaken for increased extracellular water in MHD patients with fluid overload, and it is unable to identify the early malnutrition in MHD patients by monitoring BMI alone [20]. Body cell mass (BCM) is the key to determine the body's energy expenditure, protein requirements, and metabolism; it is a part of lean mass and does not cover extracellular water [21]. Body cell mass index (BCMI) is a BCM normalized by height. Studies have shown that the lower the BCMI, the higher the risk of death in MHD patients, and most patients die of malnutrition [22]. BCMI is linearly correlated with lean mass, positively correlated with serum albumin and blood lipids, serving as a sensitive indicator reflecting muscle wasting [23]. In patients with normal or high BMI, BCMI may be low. In case of malnutrition, especially pathological conditions like dialysis, BCMI is more accurate in assessing changes in muscle mass and protein tissue than BMI [24, 25], and is regarded the best indicator to evaluate the nutritional status in MHD patients [26].

However, whether there is a correlation between BCMI and cognitive impairment in MHD patients has not been reported at home and abroad. This study intends to explore the correlation between BCMI and cognitive impairment in MHD patients through a cross-sectional study of large samples in multiple centers and to evaluate the predictive value of BCMI on cognitive impairment in MHD patients.

2. Methods

2.1. Research Objectives. From June to September 2020, 2008 patients with maintenance hemodialysis in hemodialysis centers of 20 tertiary and tertiary general hospitals in Guizhou Province were selected. Inclusion criteria are (1) dialysis≥6 months, regular dialysis 3 times a week for 12 hours; (2) age ≥18 years; (3) all included patients had been informed to be consent with and sign the informed consent form. Exclusion criteria are (1) patients with severe liver failure, cerebrovascular disease, lung disease, and other related diseases that seriously affect patients' cognitive function; (2) those with mental illness, severe aphasia, and critical illness who cannot cooperate with the questionnaire survey; (3) serious limb defects and deformities or metal stents in the body that cannot be examined by bioelectrical impedance analysis; (4) severe infection in recent one month; (5) patients with definite diagnosis of tumor; and (6) people with alcohol dependence and psychotropic drug dependence.

2.2. Research Methods. General materials: the research group personnel shall issue a unified questionnaire for on-site investigation, including name, gender, age, occupation, education level, dialysis time, and mini mental state examination scale (MMSE), etc.

2.3. Cognitive Function Evaluation. The trained personnel of the research group will issue a unified MMSE questionnaire to all the subjects for on-site investigation. The total score of the evaluation scale is 30 points (including 10 points for orientation force, 3 points for memory, 5 points for attention and calculation, 3 points for memory, and 9 points for language ability). If the score is less than 27 points, it can be considered that there is cognitive impairment [27], of which 23–26 points are mild cognitive impairment, scores <23 were severe cognitive impairment.

2.4. Physical Measurement. All subjects were measured by trained personnel of the research group, including height, weight, etc., and body mass index (BMI) = weight/height^2.

2.5. Measurement on Human Body Composition. Measurement was measured by bioelectrical impedance analyzer (BCM-7BJA4951, Fresenius, Germany), including body cell mass (BCM), lean tissue index (LTI), fat tissue index (FTI), water load (OH), extracellular water (ECW), muscle tissue mass (LTM), etc, and body cell mass index (BCMI) = BCM/height^2.

2.6. Laboratory Indicators. Collect the laboratory indicators of the research subjects in recent 1 ~ 3 months, including blood routine, creatinine, albumin, and other related indicators.

2.7. Statistical Method. SPSS 25.0 software was used for data analysis. The measurement data of normal distribution are expressed in $\bar{x} \pm s$. The independent sample t test is used for the comparison between the two groups, and the one-way ANOVA is used for the comparison between multiple groups, the measurement data of non normal distribution are described by M (P25, p75), and Mann–Whitney U is used for comparison between the two groups, Kruskal–Wallis H test was used for multi group comparison; categorical variables were expressed by the number of cases and percentage (%), and χ^2 inspection was used for inter group comparison; they are all both-side inspection according to the inspection level $\alpha = 0.05$, when $P \leq 0.05$, the difference was statistically significant. The caliper value was taken as 0.001 for propensity score matching (PSM). The matched data were analyzed by logistic regression analysis to analyze the relationship between BCMI and related indicators, and the risk of cognitive impairment in MHD patients and the predictive effect of BCMI on cognitive impairment were analyzed by ROC curve.

3. Results

3.1. Baseline Characteristics of Participants. A total of 2008 MHD patients were included in this study, including 1145 males (57%) and 863 females (43%), aged (53.8 ± 14.7) years, 467 patients with cognitive impairment, with a morbidity rate of 23.3%. The sickness rate of each age segment was 9.9%, 32.8%, 39.6%, and 50.6% respectively. The morbidity rate of cognitive impairment increased with age, and the sickness rate of severe cognitive impairment also increased with age (Figure 1).

3.2. Comparison of Clinical Characteristics between the Normal Pre PSM Cognitive Function Group and the Cognitive Impairment Group. According to the score of cognitive function, the research subjects were divided into the normal cognitive function group and the cognitive impairment group. Compared with the normal cognitive function group, the educational level, dry weight, extracellular water, lean tissue index, muscle mass, body mass index, albumin, and serum creatinine for the cognitive impairment group were lower, and there were fewer male patients for the cognitive impairment group, but age and fat tissue index for the group were higher, and the differences were statistically significant ($P < 0.05$) (Table 1).

3.3. Comparison of Clinical Characteristics of Different BCMI Groups before PSM. According to the three cut-off points of BCMI quartile (7.17, 8.52, 10.08), they are divided into Q1, Q2, Q3, and Q4 groups. Compared with BCMI Q2 ~ Q4 groups, the BCMI Q1 group has fewer male patients, the highest prevalence of cognitive impairment (33.3%), higher age, dialysis age, water load, and fat tissue index, while MMSE score, predialysis BMI, postdialysis BMI, dry weight, extracellular water, lean tissue index, muscle mass, albumin, and serum creatinine were lower, the difference was statistically significant ($P < 0.05$), and there was no significant difference in hemoglobin among different BCMI groups ($P > 0.05$) (Table 2).

3.4. Comparison of Clinical Characteristics after PSM. In order to balance the baseline data of the two groups, taking the cognitive impairment group as the benchmark, 1:1 PSM was matched, and the caliper value was 0.001. A total of 407 pairs were successfully matched, with a total of 814 cases. There was no significant difference in gender, age, and education between the two groups ($P > 0.05$).

Comparison of clinical characteristics between patients with normal cognitive function and patients with cognitive impairment after PSM: compared with the normal cognitive function group, the cognitive impairment group had lower dry weight, extracellular water, lean tissue index, muscle mass, body mass index, albumin, and serum creatinine, but higher dialysis age, water load, and fat tissue index, all differences were statistically significant ($P < 0.05$), there was no significant difference in hemoglobin between the two groups ($P > 0.05$) (Table 3).

3.5. Comparison of Clinical Characteristics of Different BCMI Groups after PSM. They were divided into Q1, Q2, Q3, and Q4 groups according to the three cut-off points of BCMI quartile (7.40, 8.73 and 10.58). Compared with the BCMI Q2 ~ Q4 groups, the BCMI Q1 group had the highest prevalence of cognitive impairment, higher age, dialysis age, water load, fat tissue index, while MMSE score, predialysis BMI, postdialysis BMI, dry weight, extracellular water, lean tissue index, muscle mass, albumin, and serum creatinine were lower, and there were fewer male patients, the difference was statistically significant ($P < 0.05$). There was no significant difference in education and hemoglobin among different BCMI groups ($P > 0.05$) (Table 4).

3.6. Binary Logistic Regression Analysis of the Risk of Cognitive Impairment in Patients with BCMI and MHD after PSM. In 814 patients who were successfully matched with the propensity score matching, binary logistic regression was used so as to analyze the relationship between BCMI and the risk of cognitive impairment in MHD patients. In the uncorrected model, the risk of cognitive impairment in the BCMI Q1 group was 8.992 times higher than that in the Q4 group (95% CI 3.186 ~ 7.530 $P < 0.05$), and the risk of cognitive impairment in the BCMI Q2 and Q3 groups were 4.898 times higher than that in the Q4 group (95% CI 4.462 ~ 13.723 $P < 0.05$), 2.620 times higher than that in the Q4 group (95% CI 1.709 ~ 4.018 $P < 0.05$). After correcting dialysis age, creatinine, albumin, and hemoglobin, the morbidity risk of the BCMI Q1 group was 8.767 times higher than that of the Q4 group (95% CI 5.471 ~ 14.101 $P < 0.05$), the BCMI Q2 group, and the Q3 group were 4.876 times higher than that of the Q4 group (95% CI 3.134 ~ 7.587 $P < 0.05$) and 2.634 times higher (95% CI 1.704 ~ 4.072 $P < 0.05$). After further correction of predialysis BMI, postdialysis BMI, OH, FTI, and ECW, the morbidity risk of the BCMI Q1 group, the Q2 group, and the Q3 group was 7.759 times (95% CI 4.421 ~ 13.620, $P < 0.05$), 4.469 times (95% CI 2.720 ~ 7.341, $P < 0.05$), and 2.435 times (95% CI 1.536 ~ 3.859, $P < 0.05$) than that of the Q4 group (Table 5).

3.7. Binary Logistic Regression Analysis on the Morbidity Risk of Cognitive Impairment in Patients with Predialysis BMI and MHD after PSM. According to the WHO standard of BMI, the research subjects were divided into G1 (BMI < 18.5 kg/m^2), G2 (18.5 kg/m^2 ≤ BMI < 25.0 kg/m^2), G3 (25.0 kg/m^2 ≤ BMI < 30.0 kg/m^2), and G4 (BMI ≥ 30.0 kg/m^2). In 814 patients who were successfully matched with the propensity score matching, binary logistic regression was used so as to analyze the relationship between predialysis BMI and the risk of cognitive impairment in MHD patients. In the uncorrected model, the morbidity risk of the predialysis BMI G1 group was 2.366 times than that of the G4 group (95% CI 1.056 ~ 5.300, $P < 0.05$). After adjusting dialysis age, creatinine, albumin, hemoglobin, and further adjusting dry weight, OH, FTI, and ECW, the correlation between predialysis BMI and the morbidity risk of cognitive impairment in MHD patients was not statistically significant ($P > 0.05$) (Table 6).

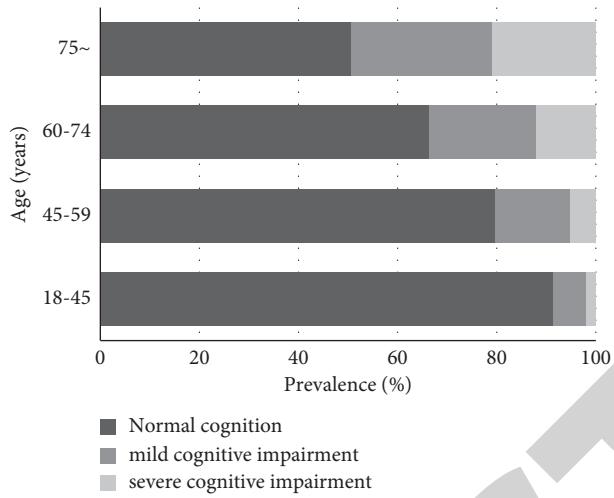

Figure 1: Morbidity rate of cognitive impairment in MHD patients of different age groups.

Table 1: Clinical characteristics of MHD patients with normal cognitive function and cognitive impairment before PSM.

Item	Normal cognition ($n = 1541$)	Cognitive impairment ($n = 467$)	Statistic value	P Value
Male [case(%)]	923(59.9)	222(47.5)	22.336	< 0.001
Age [years old, $\bar{x} \pm s$]	51.44 ± 14.33	61.78 ± 13.23	−14.511	< 0.001
Educational level (below junior high school)	1034(67.1)	398(85.2)	57.557	< 0.001
Dialysis age (months)	42.90(21.00,74.95)	43.80(25.60,74.50)	−0.862	0.389
BMI before dialysis (kg/m^2)	23.29 ± 3.69	23.25 ± 3.75	0.200	0.841
BMI after dialysis(kg/m^2)	22.39 ± 3.63	22.44 ± 3.66	−0.248	0.804
Dry weight(kg)	58.10(51.15,66.40)	57.00(49.90,65.20)	−2.309	0.021
OH(L)	0.50(-0.50,1.60)	0.60(-0.30,1.50)	−1.116	0.264
ECW(L)	14.50(12.60,16.60)	13.90(12.00,16.00)	−3.533	< 0.001
LTI(kg/m^2)	15.20(13.20,17.40)	14.10(12.30,15.90)	−7.26	< 0.001
FTI(kg/m^2)	6.90(4.30,10.07)	8.20(5.45,11.00)	−4.803	< 0.001
LTM(kg)	40.10 ± 9.85	35.89 ± 9.05	8.629	< 0.001
BCMI(kg/m^2)	8.70(7.30,10.30)	7.90(6.60,9.20)	−7.44	< 0.001
Creatinine (μ mol/L)	962.20(772.80,1160.90)	850.20(660.90,1039.90)	−7.229	< 0.001
Hemoglobin (g/L)	109.99 ± 19.98	108.11 ± 20.65	1.761	0.078
Albumin (g/L)	40.50 ± 4.16	39.56 ± 4.60	4.177	< 0.001

Note. MHD is the maintenance hemodialysis; BMI: body mass index; Oh: water load; ECW: extracellular water; FTI: fat tissue index; LTI: lean tissue index; LTM: muscle tissue mass; BCMI: body cell mass index.

3.8. Binary Logistic Regression Analysis on the Morbidity Risk of Cognitive Impairment in Patients with after Dialysis BMI and MHD after PSM. According to the WHO standard of BMI, the research subjects were divided into four groups: D1 (BMI < 18.5 kg/m^2), D2 (18.5 kg/m^2 ≤ BMI < 25.0 kg/m^2), D3 (25.0 kg/m^2 ≤ BMI < 30.0 kg/m^2), and D4 (BMI ≥ 30.0 kg/m^2). In 814 patients who were successfully matched with the propensity score matching, binary logistic regression was used so as to analyze the relationship between after dialysis BMI and the risk of cognitive impairment in MHD patients. In the uncorrected model, the morbidity risk of BMI in the group D1 after dialysis was 3.513 times that in the group D4 (95% CI 1.419 ~ 8.693, $P < 0.05$). After adjusting for dialysis age, creatinine, albumin, and hemoglobin, the morbidity risk of postdialysis BMI D1 group was 3.112 times higher than that of the D4 group (95% CI 1.249 ~ 7.751, $P < 0.05$). After further adjusting for dry weight, OH, FTI, and ECW, there was no significant correlation between postdialysis BMI and the morbidity risk of cognitive dysfunction in MHD patients ($P > 0.05$) (Table 7).

3.9. The ROC Curve after PSM Evaluated the Predictive Value of BCMI, Predialysis BMI and Postdialysis BMI for Cognitive Impairment in MHD Patients. As shown in Figure 2, the sensitivity of BCMI for predicting cognitive impairment in MHD patients was 71.5%, the specificity was 62.7%, the optimal threshold was 9.0, and the area under the curve was 0.713 (95% CI 0.678 ~ 0.748, $P < 0.001$). The area under the curve of BMI before dialysis and BMI after dialysis were 0.571 (95% CI 0.532 ~ 0.610, $P < 0.001$) and 0.570 (95% CI 0.530 ~ 0.609, $P = 0.001$), respectively. The area under the curve of BCMI predicting cognitive impairment in MHD patients was the highest.

Table 2: Comparison of clinical characteristics of MHD patients before PSM grouped by BCMI quartile.

Item	BCMI grouping				Statistic value	P value
	Q1 group ($n = 504$)	Q2 group ($n = 504$)	Q3 group ($n = 504$)	Q4 group ($n = 504$)		
Male [case(%)]	192(38.2)	253(50.4)	306(61.0)	394(78.5)	178.734	< 0.001
Age [years old, $\bar{x} \pm s$]	59.03 ± 14.66	54.44 ± 15.02	51.74 ± 14.42	50.16 ± 13.29	36.717	< 0.001
Educational level (below junior high school)	366(72.9)	343(68.3)	378(75.3)	345(68.7)	8.355	0.039
Dialysis age (months)	50.13(26.55,87.28) (30.80,86.66) (30.80,86.66)	44.13(24.14,75.09)	39.12(19.96,67.92)	37.43(19.13,65.05)	36.359	< 0.001
MMSE score (分)	26.91 ± 4.38	27.79 ± 3.35	28.21 ± 3.04	28.57 ± 2.89	21.234	< 0.001
BMI before dialysis (kg/m^2)	22.40 ± 3.63	22.83 ± 3.43	23.26 ± 3.39	24.63 ± 3.94	35.839	< 0.001
BMI after dialysis (kg/m^2)	21.57 ± 3.56	21.99 ± 3.39	22.34 ± 3.34	23.68 ± 3.87	33.319	< 0.001
Dry weight (kg)	54.50(48.00,62.08)	56.25(49.88,64.78)	58.35(50.80,66.73)	62.60(55.47,69.85)	139.009	< 0.001
OH (L)	0.70(-0.10,1.68)	0.50(-0.50,1.60)	0.40(-0.50,1.63)	0.30(-0.90,1.40)	31.857	< 0.001
EC (L)	12.60(11.13,14.78)	13.80(12.00,15.73)	14.70(13.00,16.43)	16.30(14.60,18.00)	377.157	< 0.001
LTI (kg/m^2)	11.80(11.00,12.40)	14.00(13.50,14.50)	15.90(15.40,16.50)	18.70(17.80,19.80)	1723.404	< 0.001
FTI (kg/m^2)	9.00(6.20,11.40)	7.80(5.10,10.60)	6.65(4.38,9.60)	5.30(3.00,8.50)	162.847	< 0.001
LTM (kg)	29.29 ± 5.33	36.15 ± 4.98	41.29 ± 5.94	49.74 ± 8.65	913.223	< 0.001
Creatinine (μ mol/L)	802.15 (647.38,946.62)	903.97 (738.85,1072.25)	979.85 (777.75,1157.98)	1113.31 (899.73,1290.90)	263.554	< 0.001
Hemoglobin (g/L)	109.05 ± 20.22	110.60 ± 19.73	109.52 ± 19.59	109.03 ± 21.01	0.670	0.571
Albumin (g/L)	39.52 ± 4.45	40.25 ± 4.35	40.54 ± 4.29	40.79 ± 3.94	8.338	< 0.001
Cognitive impairment [case(%)]	167(33.3)	123(24.5)	108(21.5)	69(13.7)	54.921	< 0.001

Note. MHD is the maintenance hemodialysis; BMI: body mass index; Oh: water load; ECW: extracellular water; FTI: fat tissue index; LTI: lean tissue index; LTM: muscle tissue mass; BCMI: body cell mass index.

Table 3: Clinical characteristics of MHD patients with normal cognitive function and cognitive impairment after PSM.

Item	Normal cognition ($n = 407$)	Cognitive impairment ($n = 407$)	Statistic value	P value
Male [case(%)]	206(50.6)	206(50.6)	0	1.000
Age[years old, $\bar{x} \pm s$]	59.85 ± 12.45	59.85 ± 12.45	0	1.000
Educational level(below junior high school)	346(85)	346(85)	0	1.000
Dialysis age (months)	40.23(20.17,68.53)	44.60(26.37,74.73)	−2.581	0.010
BMI before dialysis (kg/m^2)	24.08 ± 3.77	23.17 ± 3.69	3.486	0.001
BMI after dialysis (kg/m^2)	23.22 ± 3.66	22.34 ± 3.60	3.467	0.001
Dry weight (kg)	60.60(52.50,68.70)	57.10(49.90,65.00)	−3.848	< 0.001
OH (L)	0.20(−0.50,1.30)	0.60(-0.30,1.50)	−2.875	0.004
ECW (L)	15.10(13.50,17.30)	14.00(12.10,16.10)	−5.077	< 0.001
LTI (kg/m^2)	16.50(14.50,19.00)	14.30(12.60,16.10)	−9.841	< 0.001
FTI (kg/m^2)	6.00(3.00,9.00)	7.00(5.00,10.00)	−4.745	< 0.001
LTM (kg)	43.29 ± 10.66	36.61 ± 9.90	9.654	< 0.001
BCMI (kg/m^2)	9.65(8.50,11.42)	8.04(6.80,9.29)	−10.53	< 0.001
Creatinine (μ mol/L)	913.60(758.50,1123.30)	874.00(680.00,1059.60)	−2.668	0.008
Hemoglobin (g/L)	106.54 ± 21.07	108.15 ± 20.42	−1.109	0.268
Albumin (g/L)	40.57 ± 5.03	39.67 ± 5.08	2.526	0.012

Note. MHD is the maintenance hemodialysis; BMI: body mass index; Oh: water load; ECW: extracellular water; FTI: fat tissue index; LTI: lean tissue index; LTM: muscle tissue mass; BCMI: body cell mass index.

Table 4: Comparison of clinical characteristics of MHD patients after PSM grouped by BCMI quartile.

Item	BCMI group				Statistic value	P value
	Q1 group ($n = 204$)	Q2 group ($n = 203$)	Q3 group ($n = 204$)	Q4 group ($n = 203$)		
Male[case(%)]	76(37.3)	88(43.3)	104(51)	144(70.9)	52.40	< 0.001
Age[years old, $\bar{x} \pm s$]	64.70 ± 11.48	61.12 ± 12.10	57.84 ± 12.91	55.71 ± 11.38	21.878	< 0.001
Educational level (below junior high school)	178(87.3)	172(84.7)	179(87.7)	163(80.3)	5.56	0.135
Dialysis age (months)	55.16(30.80,86.66)	38.87(25.40,72.63)	42.86(22.33,68.83)	36.17(19.10,66.50)	18.79	< 0.001
MMSE score(分)	24.25 ± 4.81	25.64 ± 4.17	26.73 ± 3.78	27.85 ± 3.32	29.23	< 0.001
BMI before dialysis (kg/m^2)	22.41 ± 3.78	23.36 ± 3.34	23.57 ± 3.65	25.15 ± 3.73	20.05	0.001
BMI after dialysis (kg/m^2)	21.67 ± 3.68	22.57 ± 3.32	22.68 ± 3.56	24.22 ± 3.60	18.16	< 0.001
Dry weight (kg)	54.30(46.80,62.60)	57.30(51.20,64.70)	58.70(50.90,66.80)	63.50(57.10,71.20)	77.22	< 0.001
OH (L)	0.60(-0.10,1.70)	0.60(-0.50,1.50)	0.30(−0.50,1.50)	−0.10(−1.10,1.1)	26.44	< 0.001
ECW (L)	12.9(11.20,14.8)	14.10(12.70,15.90)	14.75(13.00,17.18)	16.60(15.0,18.40)	164.97	< 0.001
LTI (kg/m^2)	12.10(11.00,12.90)	14.30(13.80,14.90)	16.30(15.73,17.0)	19.30(18.50,20.80)	722.77	< 0.001
FTI (kg/m^2)	9.60(7.30,12.1)	7.90(5.80,11.00)	6.05(3.73,8.67)	4.00(2.10,7.20)	167.9	< 0.001
LTM (kg)	29.80 ± 5.15	36.23 ± 4.75	42.20 ± 6.49	51.61 ± 9.21	397.26	< 0.001
Creatinine (μmol/L)	806.90 (630.0,926.00)	837.00 (691.00,1008.00)	930.50 (750.84,1090.67)	1055.0 (853.60,1257.2)	88.68	< 0.001
Hemoglobin (g/L)	107.99 ± 21.17	107.23 ± 20.68	106.93 ± 19.80	107.24 ± 21.46	0.096	0.962
Albumin (g/L)	39.38 ± 4.97	39.51 ± 4.09	41.10 ± 5.55	40.49 ± 5.39	5.39	< 0.001
Cognitive impairment [case(%)]	149(73)	121(59.6)	90(44.1)	47(23.2)	112.16	< 0.001

Note. MHD is the maintenance hemodialysis; BMI: body mass index; Oh: water load; ECW: extracellular water; FTI: fat tissue index; LTI: lean tissue index; LTM: muscle tissue mass; BCMI: body cell mass index.

Table 5: Correlation between BCMI and morbidity risk of cognitive impairment by binary logistic regression analysis.

Grouping	Model 1		Model 2		Model 3	
	OR (95%CI)	P value	OR (95%CI)	P value	OR (95%CI)	P value
BCMI Q1	8.992(5.466~14.064)	< 0.001	8.767(5.471~14.101)	< 0.001	7.759(4.421~13.620)	< 0.001
BCMI Q2	4.874(3.133~ 7.581)	< 0.001	4.876(3.134~7.587)	< 0.001	4.469(2.720~7.341)	< 0.001
BCMI Q3	2.620(1.709~4.018)	< 0.001	2.634(1.704~4.072)	< 0.001	2.435(1.536~3.859)	< 0.001
Reference	Reference	Reference	Reference	Reference	Reference	Reference

Note. (1) Model 1 is an uncorrected model; (2) Model 2 was the model after correcting dialysis age, creatinine, albumin, and hemoglobin; (3) Model 3 is the model after correcting dialysis age, creatinine, albumin, hemoglobin, predialysis BMI, postdialysis BMI, dry weight, OH, FTI, and ECW.

Table 6: Correlation between BMI before dialysis and morbidity risk of cognitive impairment by binary logistic regression analysis.

Grouping	Model 1		Model 2		Model 3	
	OR (95%CI)	P value	OR (95%CI)	P value	OR (95%CI)	P value
BMI G1	2.366(1.056 ~5.300)	0.036	2.027(0.893~4.601)	0.091	1.155(0.434~3.072)	0.773
BMI G2	1.586(0.874~2.877)	0.129	1.558(0.856~2.837)	0.147	1.349(0.669~2.719)	0.403
BMI G3	1.119(0.594~2.110)	0.728	1.103(0.582~2.088)	0.764	1.081(0.539~2.170)	0.826
Reference	Reference	Reference	Reference	Reference	Reference	Reference

Note. (1) Model 1 is an uncorrected model; (2) Model 2 was the model after correcting dialysis age, creatinine, albumin, and hemoglobin; (3) Model 3 was the model after correcting dialysis age, creatinine, albumin, hemoglobin, dry weight, OH, FTI, and ECW.

Table 7: Correlation between BMI after dialysis and the morbidity risk of cognitive impairment by binary logistic regression analysis.

Grouping	Model 1		Model 2		Model 3	
	OR (95%CI)	*P* value	OR (95%CI)	*P* value	OR (95%CI)	*P* value
BMI D1	3.513(1.419~8.693)	0.007	3.112(1.248~7.760)	0.015	1.155(0.434~3.072)	0.773
BMI D2	2.23(0.998~4.984)	0.051	2.172(0.968~4.876)	0.06	1.349(0.669~2.719)	0.403
BMI D3	1.997(0.854~4.670)	0.11	1.946(0.828~4.571)	0.127	1.081(0.539~2.170)	0.826
Reference	Reference	Reference	Reference	Reference	Reference	Reference

Note. (1) Model 1 is an uncorrected model; (2) Model 2 was the model after adjusting dialysis age, creatinine, albumin, and hemoglobin; (3) Model 3 was the model after adjusting dialysis age, creatinine, albumin, dry weight, OH, FTI, and ECW.

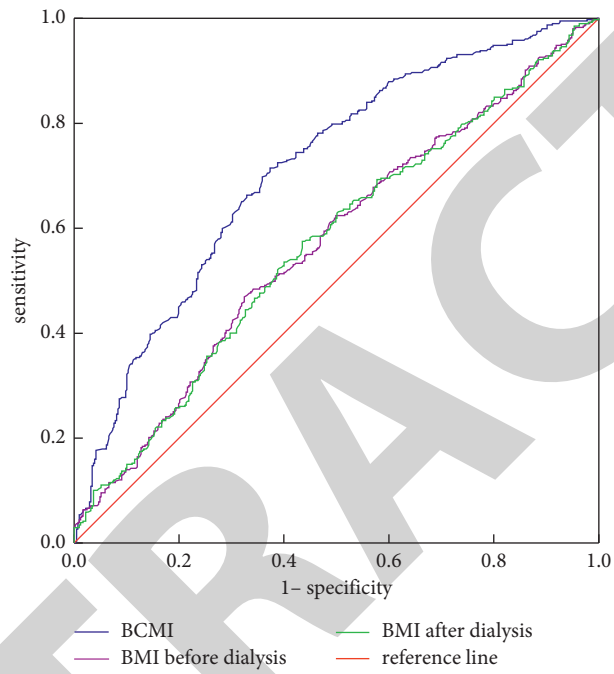

Figure 2: Predictive efficacy of BCMI, predialysis BMI, and postdialysis BMI on cognitive impairment in MHD patients. Note: BCMI is body mass index, BMI is body mass index, and MHD is maintenance hemodialysis.

4. Discussion

Studies have shown that chronic kidney disease (CKD) is an independent risk factor for cognitive dysfunction, and its impact on cognitive impairment has exceeded genetic factors, and morbidity rate is higher in maintenance hemodialysis (MHD) patients [28]. Epidemiological data at home and abroad show that the prevalence of cognitive impairment in MHD patients is as high as 18.8%–60.9% [2–4]. In this study, the prevalence of cognitive impairment in MHD patients was 23.3%, and the prevalence of cognitive impairment was significantly increased in patients aged 45 and over.

MHD patients with cognitive impairment have significantly reduced treatment compliance and quality of life and significantly increased hospitalization rate and mortality, which seriously affects the clinical prognosis of patients [5–7]. Current studies have found that cognitive impairment in MHD patients is related to a variety of factors. Malnutrition can affect energy metabolism, cerebrospinal fluid biochemistry, and brain volume [14, 16–18], which is one of the main risk factors for cognitive impairment in MHD patients. The risk of cognitive impairment in malnourished MHD patients is 20.0% higher than that in well-nourished patients [15]. Body mass index (BMI) is currently recognized as a nutritional evaluation index. However, MHD patients generally have increased water load, BMI cannot distinguish specific human components, and fluid overload in the body will cause false high BMI, thus overestimating the nutritional status of MHD patients [19, 20]. Body cell mass (BCM) is the nonfat content excluding external bone minerals and extracellular water (ECW). Body cell mass index (BCMI) refers to the ratio of BCM to height ^{2}. This index does not include extracellular water (ECW), so it is not affected by body fluid changes. It is more accurate than BMI in assessing the nutritional status of MHD patients [21, 26]. The study of Talluri et al. found that when BCMI is low, it may be accompanied by decreased muscle mass and/or increased fat mass, suggesting poor nutritional status [17]. In this study, compared with the high BCMI (Q4) group, the lean tissue index and muscle mass in the low BCMI (Q1) group were significantly increased, while the fat mass index was significantly reduced, which was consistent with the study results of Talluri et al. This study also suggests that male patients may have higher BCMI values.

This study found that the dry weight, lean8 tissue index, muscle mass, and albumin in the cognitive impairment group were lower than those in the normal cognitive function group, suggesting that malnutrition is related to cognitive impairment in MHD patients. Kim et al. found that the decline of BMI is an independent risk factor for the sharp decline of cognitive function and a predictor of the progress of cognitive impairment [29, 30]. In this study, BMI before and after dialysis is related to the risk of cognitive impairment in MHD patients, but after adjusting for other risk factors, the morbidity risk of cognitive impairment in patients with BMI and MHD before and after dialysis is not statistically significant, which is different from the above research results. It is speculated that it may be related to different research objects and research methods. However, BCMI was independently associated with the morbidity risk of cognitive impairment in patients with MHD. The lower the level of BCMI, the higher the morbidity risk of cognitive impairment, the higher the prevalence. The ROC curve was further used to explore the predictive value of BCMI, predialysis BMI, and postdialysis BMI on cognitive impairment in MHD patients. The results showed that BCMI had the highest AUC for predicting cognitive impairment in MHD patients and had high predictive value for the occurrence of cognitive impairment in MHD patients. The best value for predicting cognitive impairment was 9.0, and cognitive impairment is less likely to occur when it is higher than 9.0.

In conclusion, BCMI is the influencing factor of cognitive impairment in MHD patients and has high predictive value for the occurrence of cognitive impairment. However, this study also has some limitations. First, the research objects of this study are selected from the maintenance hemodialysis center of tertiary hospitals in Guizhou Province in 2020. It is necessary to further study the patients in the dialysis center of secondary and lower hospitals. Second, this study is a cross-sectional study, which cannot reflect the causal relationship between BCMI and cognitive impairment in MHD patients. Therefore, it needs to be further verified by multicenter and large sample cohort study.

Data Availability

The data used to support the findings of this paper are available from the corresponding author upon request.

Ethical Approval

In this paper, all procedures were in line with the international ethical code of ethical conduct for biomedical research involving human subjects (CIOMS) and the declaration of Helsinki. The experimental protocol was approved by the Institutional Review Committee (IRB) of Guizhou Provincial People′s Hospital, and all participants provided written informed consent.

Conflicts of Interest

The authors declare that they have no conflicts of interest.

Acknowledgments

This study was supported by Science and Technology Cooperation Program of Guizhou Province (QKH[2016]7151).

References

[1] D. A. Drew, D. E. Weiner, and M. J. Sarnak, "Cognitive impairment in CKD: pathophysiology, management, and prevention," *American Journal of Kidney Diseases*, vol. 74, no. 6, pp. 782–790, 2019.

[2] X. Pei, S. Lai, X. He et al., "Mild cognitive impairment in maintenance hemodialysis patients: a cross-sectional survey and cohort study," *Clinical Interventions in Aging*, vol. 14, pp. 27–32, 2018.

[3] W. Fadili, A. Al Adlouni, N. Louhab, M. Habib Allah, N. Kissani, and I. Laouad, "Prevalence and risk factors of cognitive dysfunction in chronic hemodialysis patients," *Aging & Mental Health*, vol. 18, no. 2, pp. 207–211, 2014.

[4] S. J. Joseph, S. S. Bhandari, and S. Dutta, "Cognitive impairment and its correlates in chronic kidney disease patients undergoing haemodialysis," *Journal of Evolution of Medical and Dental Sciences*, vol. 8, no. 36, pp. 2818–2822, 2019.

[5] S. Angermann, J. Schier, M. Baumann et al., "Cognitive impairment is associated with mortality in hemodialysis patients," *Journal of Alzheimer's Disease*, vol. 66, no. 4, pp. 1529–1537, 2018.

[6] D. A. Drew, D. E. Weiner, H. Tighiouart et al., "Cognitive function and all-cause mortality in maintenance hemodialysis patients," *American Journal of Kidney Diseases*, vol. 65, no. 2, pp. 303–311, 2015.

[7] M. Di Rosa, S. D'Alia, S. D'Alia et al., "Cognitive impairment, chronic kidney disease, and 1-year mortality in older patients discharged from acute care hospital," *Journal of Clinical Medicine*, vol. 9, no. 7, p. 2202, 2020 Jul 12.

[8] K. Zheng, H. Wang, B. Hou et al., "Malnutrition-inflammation is a risk factor for cerebral small vessel diseases and cognitive decline in peritoneal dialysis patients: a cross-sectional observational study," *BMC Nephrology*, vol. 20, no. 1, p. 366, 2017.

[9] V. E. Bianchi, P. F. Herrera, and R. Laura, "Effect of nutrition on neurodegenerative diseases. A systematic review[J]," *Nutritional Neuroscience*, vol. 4, pp. 1–25, 2019.

[10] E. Tsagalioti, C. Trifonos, A. Morari, K. Vadikolias, and C. Giaginis, "Clinical value of nutritional status in neurodegenerative diseases: what is its impact and how it affects disease progression and management?" *Nutritional Neuroscience*, vol. 21, no. 3, pp. 162–175, 2018.

[11] I. Cova, S. Pomati, L. Maggiore et al., "Nutritional status and body composition by bioelectrical impedance vector analysis: a cross sectional study in mild cognitive impairment and Alzheimer's disease," *PLoS One*, vol. 12, no. 2, Article ID e0171331, 2017.

[12] D. Guenzani, M. Buoli, L. Caldiroli et al., "Malnutrition and inflammation are associated with severity of depressive and cognitive symptoms of old patients affected by chronic kidney disease," *Journal of Psychosomatic Research*, vol. 124, Article ID 109783, 2019.

[13] N. Scarmeas, C. A. Anastasiou, and M. Yannakoulia, "Nutrition and prevention of cognitive impairment," *The Lancet Neurology*, vol. 17, no. 11, pp. 1006–1015, 2018.

[14] A. S. Doorduijn, M. Visser, O. van de Rest et al., "Associations of AD biomarkers and cognitive performance with nutritional

Hindawi
Journal of Healthcare Engineering
Volume 2023, Article ID 9857271, 1 page
https://doi.org/10.1155/2023/9857271

Retraction

Retracted: Data Mining-Based Analysis of Modern Chinese Medicine for the Treatment of Stable Angina Pectoris in Coronary Heart Disease

Journal of Healthcare Engineering

Received 10 October 2023; Accepted 10 October 2023; Published 11 October 2023

This article has been retracted by Hindawi following an investigation undertaken by the publisher [1]. This investigation has uncovered evidence of one or more of the following indicators of systematic manipulation of the publication process:

(1) Discrepancies in scope
(2) Discrepancies in the description of the research reported
(3) Discrepancies between the availability of data and the research described
(4) Inappropriate citations
(5) Incoherent, meaningless and/or irrelevant content included in the article
(6) Peer-review manipulation

The presence of these indicators undermines our confidence in the integrity of the article's content and we cannot, therefore, vouch for its reliability. Please note that this notice is intended solely to alert readers that the content of this article is unreliable. We have not investigated whether authors were aware of or involved in the systematic manipulation of the publication process.

Wiley and Hindawi regrets that the usual quality checks did not identify these issues before publication and have since put additional measures in place to safeguard research integrity.

We wish to credit our own Research Integrity and Research Publishing teams and anonymous and named external researchers and research integrity experts for contributing to this investigation.

The corresponding author, as the representative of all authors, has been given the opportunity to register their agreement or disagreement to this retraction. We have kept a record of any response received.

References

[1] M. Luo, Y. Hu, R. Bai, and Z. Xu, "Data Mining-Based Analysis of Modern Chinese Medicine for the Treatment of Stable Angina Pectoris in Coronary Heart Disease," *Journal of Healthcare Engineering*, vol. 2022, Article ID 3511974, 6 pages, 2022.

Hindawi
Journal of Healthcare Engineering
Volume 2022, Article ID 3511974, 6 pages
https://doi.org/10.1155/2022/3511974

Research Article

Data Mining-Based Analysis of Modern Chinese Medicine for the Treatment of Stable Angina Pectoris in Coronary Heart Disease

Min Luo,[1] Yuying Hu,[2] Rong Bai,[2] and Zongpei Xu[3]

[1]*Graduate School, Tianjin University of Traditional Chinese Medicine, Tianjin 301617, China*
[2]*National Clinical Research Center for Chinese Medicine Acupuncture and Moxibustion, First Teaching Hospital of Tianjin University of Traditional Chinese Medicine, Tianjin 300380, China*
[3]*Library of Tianjin University of Chinese Medicine, Tianjin University of Traditional Chinese Medicine, Tianjin 301617, China*

Correspondence should be addressed to Zongpei Xu; luomin@mail.cu.edu.kg

Received 28 December 2021; Accepted 26 January 2022; Published 28 February 2022

Academic Editor: Alireza Souri

The aim of this study is to explore the clinical effects of Chinese medicine in the treatment of stable angina pectoris in coronary heart disease. Chinese medicine has multitarget, multilevel, and multilink effects in the treatment of coronary angina, which can significantly improve patients' symptoms. Its mechanism of action involves multiple levels such as regulating lipid metabolism, improving platelet function, antioxidant, and protecting endothelial function. The design was based on data mining to analyse the dosing pattern of modern Chinese medicine for the treatment of stable angina pectoris in coronary heart disease. The number of episodes of angina pectoris, the duration of the episodes, and the changes in the electrocardiogram before and after taking the medicine were observed and compared between the two groups. The number and duration of angina attacks ((2.23 ± 0.77) per week and (1.31 ± 0.34) min/time, respectively) in the study group were found to be significantly better than those in the control group ((3.86 ± 1.03) per week and (2.46 ± 1.21) min/time, respectively).

1. Introduction

Coronary atherosclerotic heart disease due to functional changes (stenosis) in the coronary arteries, is collectively known as coronary heart disease [1]. Angina pectoris is a clinical syndrome characterised by chest pain due to temporary myocardial ischaemia and is the most common manifestation of coronary heart disease. The onset of coronary angina is closely related to endothelial dysfunction [2], platelet activation, inflammatory response, plaque rupture, thrombosis, and abnormal serum lipid metabolism. This disease belongs to the category of "chest paralysis and heart pain" in Chinese medicine, and the pathogenesis is "original deficiency and symptomatic deficiency." Chinese medicine treatment of angina pectoris in coronary artery disease follows the principle of evidence-based treatment and adopts treatment methods such as benefiting Qi, nourishing Yin, invigorating Blood, resolving blood stasis, resolving phlegm, and warming Yang, which has shown certain efficacy advantages [3].

The duration of angina pectoris is constantly prolonged. Failure to give effective treatment, therefore, tends to allow unstable angina to progress towards acute myocardial infarction [4]. To this end, 63 patients with unstable angina with coronary artery disease who were admitted and diagnosed in this hospital between January 2017 and May 2018 were used as study subjects to explore the clinical effects of Chinese medicine in the treatment of unstable angina with coronary artery disease, with the aim of providing a more accurate and effective Chinese medicine treatment for unstable angina with coronary artery disease[5].

Unstable angina pectoris is unique in its pathophysiological mechanism and therefore requires a robust and aggressive therapeutic intervention in its prevention and treatment [6]. Modern medicine believes that unstable angina is caused by the rupture of arterial plaque and thrombosis, and treatment is usually with anticoagulant, antiplatelet, calcium antagonist, and other thrombolytic drugs; patients with severe symptoms tend to be treated

surgically, but the medical costs and risks of Western drugs and surgery are relatively high, and Western drugs focus on a single condition and produce more adverse effects [7, 8]. According to the theory of Chinese medicine, the causes of unstable angina pectorals are many and closely related to the patient's body, such as old age and physical decline, disorders of the internal organs, and poor diet, which can lead to Qi stagnation, blood stasis, and internal phlegm, which can block the veins and block the channels, resulting in chest paralysis and damage to the myocardium to form angina pectoris [9]. In the case of unstable angina, Chinese medicine practitioners often identify the evidence according to the patient's condition, and the method is mostly based on medication, supplemented by acupuncture. According to relevant studies [10], the therapeutic effect of combined Chinese and Western medicine is significantly better than that of single Western medicine. Among the many Chinese medicine prescriptions for the treatment of unstable angina pectoris, Radix Codonopsis bilocular, *Panax notoginseng*, and Radix Panax notoginseng are commonly used. For example, *Astragalus membranaceus* is effective in nourishing Qi and fixing the surface of the body, diuretic, and muscle-building and can be used for hypertension, diabetes, and chronic rhinitis; Radix Codonopsis pilosula is effective in nourishing the middle of the body, strengthening the immune system, enhancing the blood-forming function of the organs, and dilating blood vessels and is effective for spleen deficiency and palpitations; *Panax ginseng* is effective in dispersing blood stasis and stopping bleeding and can be used to treat vomiting of blood, blood in the stool, and stabbing pain in the chest and abdomen; *Salvia metrorrhagia* is effective in promoting pain and activating blood circulation to remove blood stasis. It can remove chest paralysis and relieve heat and pain. Compared with Western medicine, Chinese medicine has better therapeutic effects in the clinical practice of treating unstable angina pectoris in coronary artery disease and reducing the number of angina attacks, which are worthy of clinical promotion.

2. Chinese Medicine in the Treatment of Coronary Heart Disease

The action of TCM in treating diseases is achieved through a multisite, multitarget, and multilevel mechanism of holistic regulation, which in turn is achieved through different combinations of TCM.

2.1. Modern Pharmacological Studies on the Active Ingredients of Single-Flavoured Chinese Medicines. Astragalus, commonly used as a treatment for angina pectoris in coronary artery disease [11], improves the environment to which blood vessels are exposed, reduces chronic inflammatory cell infiltration, and causes a significant decrease in serum tumour necrosis factor α, interleukin 1-beta, and interleukin 6 levels. Meanwhile, the main components of *Astragalus*, amino acids, flavonoids, and astragalosides, can dilate coronary arteries, improve cardiac function, increase resistance to hypoxia, prevent lipid peroxidation, increase myocardial contractility, and reduce blood viscosity by acting on Na+-K+-ATPase [12].It also has a strong free radical scavenging effect, limiting the damage to myocardial cells and subcellular structures caused by oxygen-free radicals.

The main treatment for angina pectoris in coronary artery disease is herbal medicine that activates blood circulation and resolves blood stasis. Studies [13] have shown that *Salvia miltiorrhiza* is a good slow calcium channel blocker and can prevent the disruption of membrane structure and function under ischaemic and hypoxic conditions. Johannessen et al. [14] used ginseng injection and danshen powder injection to treat 52 cases of angina pectoris in coronary heart disease. Danshen powder injection has the effect of inhibiting platelet aggregation and increasing coronary blood flow. It [15] was found that *Calendula officinalis* could significantly reduce whole blood viscosity, plasma viscosity, red blood cell pressure volume, and fibrinogen in patients with coronary heart disease ($P < 0.05$), in order to improve myocardial microcirculation obstruction, so that myocardial ischaemia and hypoxia could be improved and the therapeutic effect of coronary heart disease could be enhanced. Palmer et al. [16] found that *Ligusticum chuanxiong* had the effect of protecting myocardial mitochondrial NOS activity and lowering NO content ($P < 0.05$) and suggested that *Ligusticum chuanxiong* had a protective effect on myocardial ischaemic injury in rats, the mechanism of which might be to inhibit mitochondrial calcium overload and reduce mitochondrial NOS activity, thereby reducing NO-induced injury, scavenging free radicals, and reducing lipid peroxide production. Amrutiya et al. [17] concluded that six commonly used blood-activating herbs, namely, Radix Paeoniae, *Salvia miltiorrhiza*, Chuanxiong, *Panax notoginseng*, peach kernel, and wine rhubarb, could interfere with the progression of mature plaques in ApoE gene-deficient mice and have certain plaque stabilizing effects, the mechanism of which may be related to the regulation of lipid metabolism and inhibition of inflammatory response and reduction of low-density lipoprotein (LDL-C) in rats with myocardial ischaemia.

The volatile oil of *Citrus aurantium* has antibacterial effects [18] also indicated that the mechanism of action of *Citrus aurantium* to improve vascular endothelial function, stabilize plaque, and reduce cardiovascular events is unknown and may be related to its hypolipidemic, anti-free radical, and anti-inflammatory effects. The active ingredients of centipede can significantly increase superoxide dismutase (SOD) and nitric oxide (NO) content and significantly reduce malondialdehyde (MDA) in rats with myocardial ischaemia, and the ultrastructure showed a significant reduction in cardiomyocyte damage [19].

2.2. The Pharmacological Effects of Chinese Herbal Formulations. In the literature [20], it has been proved that the representative drug Shengve capsule, which has the effect of benefiting Qi and nourishing Yin, can enhance myocardial contraction, dilate coronary arteries, increase coronary blood flow, achieve the effect of benefiting Qi and

promoting Yang, moving Qi and blood, helping to cure the root cause, thus reducing the attack of angina pectoris.

Heart Ning tablets can increase coronary blood flow, reduce myocardial oxygen consumption, and antiplatelet aggregation, with higher clinical efficacy than compound Dan Shen tablets. The clinical efficacy of Hemifu Bangyu Tang is higher than that of Fuxiang Dan Shen tablets. It can improve the function of the vascular endothelium, thereby improving the efficacy in unstable angina [21].

Lyketos et al. [22] found that heart-supplementing and activating capsules (leech, panel containing, analogue, and astragalus) have definite free radical scavenging ability and antilipid peroxidation effects and have some reversing and protective effects on ischaemic myocardial injury. Yang et al. [21] found that Fuxin Ling granules (Yu Jin, Chuanxiong, Bai Shao, Gan Song, and Ginseng) have improved lipid and blood rheology, regulated endothelin/nitric oxide balance, increased SOD content, and reduced MDA content, thus improving endothelial function and preventing thrombosis and angina attacks. Qishen Yi Qi drops reduces blood lipids and increases ApoA1 levels, which has a beneficial effect in regulating disorders of blood lipid metabolism in patients with coronary heart disease caused by Qi deficiency and blood stasis, thereby alleviating patients' symptoms and reducing the manifestations of TCM symptoms. Banglore et al. [23] found that Fu Zheng and lipid-reducing capsules (*Curcuma longa*, Leech, Da Huang, San Qi, *Astragalus*, etc.) significantly decreased coagulation factor I, D-dimer, and platelet membrane glycoprotein in patients with coronary artery disease ($P < 0.05$), suggesting that the mechanism of action of Fu Zheng and lipid-reducing capsules may be related to improving microcirculation, inhibiting platelet activation and adjusting the coagulation-fibrinolysis balance.

Tongxinluo capsules (ginseng, leech, scorpion, turtle shell, cicada shed, red peony, and ice chips) have the effects of benefiting Qi, activating blood circulation, relieving spasm and pain, significantly inhibiting inflammation and reducing the levels of hs-CRP, tumour necrosis factor-α (TNF-α). It also improves the clinical symptoms and electrocardiogram of patients with intractable angina pectoris who have failed to respond to conventional drug therapy. Musk heart pill (musk, sophora, ice chips, ginseng, toadstool, and nux vomica) has the ability to dilate the coronary arteries, increase coronary flow, increase cardiac output, strengthen the heart, resist myocardial ischaemia, protect the myocardium, and scavenge oxygen radicals and is more effective than nitrates in long-term use.

3. Analysis of Drug Therapy for Coronary Heart Disease

Based on discrete coronary heart disease, a quantitative coronary heart disease development degree is proposed to characterise the relative levels of different coronary heart disease development by constructing central coronary heart disease and hollow coronary heart disease, which represent the two extremes of positive and negative coronary heart disease.

In this paper, the TOPSIS (Technique for Order Preference by Similarity to an Ideal Solution) method is used to evaluate the degree of development of coronary heart disease. Firstly, a standardised evaluation matrix of coronary heart disease development was developed in the form of $\overline{E} = [\overline{e_{ij}}]_{m\times n}$, where i is the number of coronary heart diseases to be evaluated, x_i is the number of coronary heart diseases, and e_{ij} represents the value of the first coronary heart disease for the first developmental characteristic. The standardisation process for cost-based (mobility and energy efficiency) and efficiency-based (size, growth, and balance) characteristics is shown as

$$\overline{e_{ij}} = \frac{\left(\max_i e_{ij} - e_{ij}\right)}{\left(\max_i e_{ij} - \min_i e_{ij}\right)}, \tag{1}$$

$$\overline{e_{ij}} = \frac{\left(e_{ij} - \min_i e_{ij}\right)}{\left(\max_i e_{ij} - \min_i e_{ij}\right)}. \tag{2}$$

Secondly, the standard deviation method was used to calculate the weights of each developmental feature. If the standard deviation of the jth characteristic is σ_j, then, the weight of the nth developmental characteristic is as follows:

$$w_j = \frac{\sigma_j}{\sum_{j=1}^{n} \sigma_j}. \tag{3}$$

Further, the standardised evaluation matrix was weighted to obtain $Z = [z_{ij}]_{m\times n}$, of which $z_{ij} = e_{ij} \times w_j$. The maximum value of each development characteristic was used to construct a positive ideal solution of $Z^+ = [z_1^+, z_2^+, \ldots, z_n^+]$ $(z_j^+ = \max_i z_{ij})$, representing a hollow coronary with the greatest potential for electricity load growth. Similarly, a negative ideal solution of $Z^- = [z_1^-, z_2^-, \ldots, z_n^-]$ $(z_j^- = \max_i z_{ij})$ was constructed to represent a hollow coronary with less potential for electricity consumption.

Finally, the degree of coronary heart disease progression is defined as

$$\begin{cases} D_i = \dfrac{\sqrt{i}^{\,-}}{d_i^+}, \\ d_i^+ = \sqrt{\displaystyle\sum_{j=1}^{n} \left(z_{ij} - z_j^+\right)^2}, \quad i = 1, 2, \ldots, m, \\ d_i^- = \sqrt{\displaystyle\sum_{j=1}^{n} \left(z_{ij} - z_j^-\right)^2}, \end{cases} \tag{4}$$

where d_i^+ and d_i^- are the Euclidean distances of each coronary heart disease from central and hollow coronary heart disease, respectively.

It can be seen that the more developed the coronary heart disease is, the more it tends to be central, and the more likely it is that the implementation of grid construction investment will drive load growth. The less developed coronary heart disease has a significant hollowing out.

Table 1: Number and duration of angina attacks in the study group and control group.

Group	Before treatment		After treatment	
	Number of angina pectoris attacks (times/week)	Attack time of angina pectoris (min/time)	Number of angina pectoris attacks (times/week)	Attack time of angina pectoris (min/time)
Control group ($n = 32$)	8.21 ± 2.67	7.63 ± 2.33	3.83 ± 1.03	2.46 ± 1.21
Study group ($n = 31$)	8.35 ± 2.54	7.42 ± 2.51	2.23 ± 0.77	1.31 ± 0.34
T value	0.682	0.773	3.354	4.645
P value	0.112	0.04	0.001	0.001

Table 2: Comparison of ∑ST and NST values in the study and control group.

Group	∑ST/mm		Number of NST/leads	
	Before treatment	After treatment	Before treatment	After treatment
Control group ($n = 32$)	1.03 ± 0.45	0.71 ± 0.32	3.23 ± 1.11	2.53 ± 0.62
Study group ($n = 31$)	1.01 ± 0.51	0.51 ± 0.29	3.41 ± 1.09	1.79 ± 0.85
T value	0.696	4.561	0.792	4.235
P value	0.078	0.001	0.12	0.002

Coronary heart disease data potential curves and the classification of consumption potential types. First, the data potential ECP can be defined according to a weighted standard evaluation matrix as in equation (5), which quantifies the potential size or level of coronary heart disease data determined by a combination of development characteristics.

$$\mathrm{ECP}_i = \sum_{j=1}^{n} z_{ij}, \quad i = 1, 2, \ldots, m. \tag{5}$$

Further, based on the growth curve function as in (6), the degree of coronary heart disease progression and the corresponding data potential data were fitted to produce a data potential curve.

$$\mathrm{ECP}_i = \frac{1}{\alpha + \beta e^{-\gamma D_i}}. \tag{6}$$

By identifying the inflection points above and below the data potential curve, the different types of coronary data potential can be classified as

$$\begin{cases} \text{Central type}, & D_i \geq D_u, \\ \text{Growth type}, & D_l \leq D_i < D_u, \\ \text{Atlanto subtractive type}, & D_i < D_l. \end{cases} \tag{7}$$

4. Case Studies

Sixty-three patients with unstable angina pectoris of coronary heart disease admitted and diagnosed in the hospital were selected and divided into two groups according to different treatment methods. The ethics committee of the hospital examined the patients, informed their families, communicated and negotiated, and signed a family notification form. In the control group, there were 32 cases; sex: 18 males and 14 females; and age: 40–67 years, average (60.3 ± 12.5) years. In the study group, there were 31 cases; sex: 17 males and 14 females; age: 42–69 years, mean (62.7 ± 10.6) years.

4.1. Results. When comparing the number and duration of angina attacks in the study group with those in the control group, the difference between the study group and the control group before treatment was not statistically significant ($P > 0.05$). After treatment, the number and duration of angina attacks were (2.23 ± 0.77) episodes/week and (1.31 ± 0.34) min/time, respectively, in the study group, which were significantly better than those in the control group ((3.86 ± 1.03) episodes/week and (2.46 ± 1.21) min/time, respectively) ($P < 0.05$). See Table 1.

When comparing the ∑ST and NST values of the two groups after treatment, the ∑ST and NST values of the study group ((0.51 ± 0.29) and (1.79 ± 0.85), respectively) were significantly better than those of the control group ((0.71 ± 0.32) and (2.53 ± 0.62), respectively), with statistically significant differences ($P < 0.05$), as shown in Table 2.

In this paper, the proposed method was validated using the data from our hospital as an example. Factor analysis was performed on the predictor metavariables for the coronary heart disease data, and the main results are shown in Table 3.

The fitted data potential curves are shown in Figure 1. The data potential types for coronary heart disease were classified according to the upper and lower inflection points, with 39%, 55%, and 6% for decaying, growing, and central coronary heart disease, respectively.

As shown in Figure 2, the number of angina episodes (2.23 ± 0.77) and duration (1.31 ± 0.34) min/time in the study group were significantly better than those in the control group ((3.86 ± 1.03) and (2.46 ± 1.21) min/time), with statistically significant differences ($t = 3.354$, $t = 4.645$, $P < 0.05$). The ∑ST and NST values of the study group ((0.51 ± 0.29) and (1.79 ± 0.85), respectively) were significantly better than those of the control group ((0.71 ± 0.32)

Table 3: Ideal solutions for coronary artery disease.

	Positive ideal solution	Negative ideal solution	Weight
Scale	0.78	0.105	0.413
Growth	0.649	0.076	0.034
Mobility	0.478	−0.234	0.184
Balance	0.343	0.05	0.226
Energy saving level	0.774	0.1	0.143

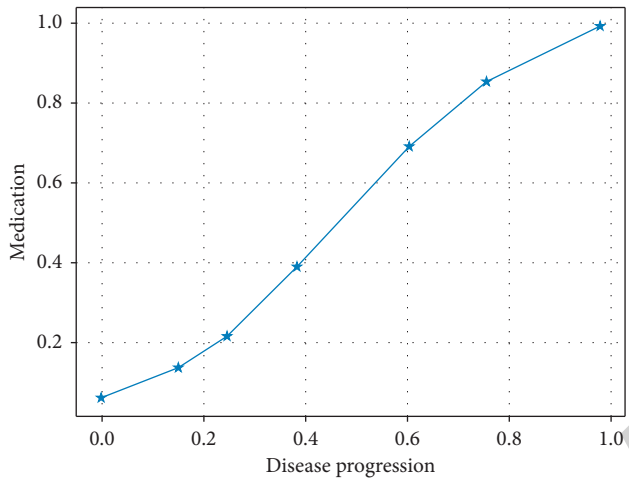

Figure 1: Data potential curve.

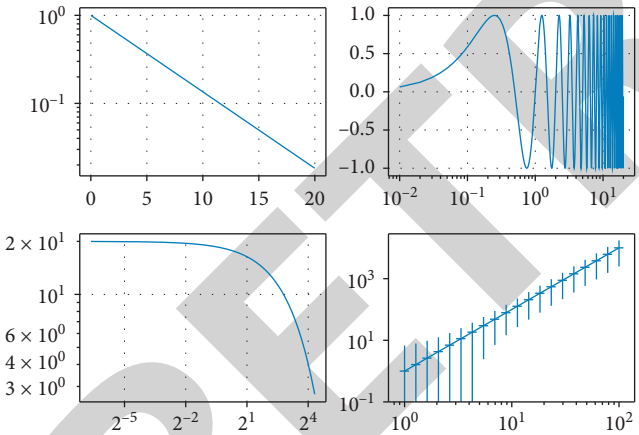

Figure 2: Different dosing patterns.

and (2.53 ± 0.62), respectively), and the differences were statistically significant ($t = 4.561$, $t = 4.235$, $P < 0.05$).

5. Conclusions

Chinese medicine can act on multiple pathological aspects of angina pectoris in coronary heart disease, significantly improving the accompanying symptoms of patients, with relatively few toxic side effects and suitable for long-term application. The mechanisms of action can be summarised as follows: regulation of lipid metabolism and improvement of platelet function and blood rheology. As related clinical and experimental studies continue to be conducted, the mechanism of action of single herbs and compound preparations in the treatment of angina pectoris in coronary artery disease has been further developed, laying the foundation for further elucidation of the mechanism of action of TCM.

Data Availability

The datasets used during the current study are available from the corresponding author on reasonable request.

Conflicts of Interest

The authors declare that they have no conflicts of interest.

References

[1] W.-T. Pang, J.-H. Zhang, J.-B. Zhai et al., "[Tongmai Yangxin Pills in treatment for angina pectoris of coronary heart disease: a systematic review of randomized clinical trails]," *Zhongguo Zhong yao za zhi = Zhongguo zhongyao zazhi = China journal of Chinese materia medica*, vol. 44, no. 11, pp. 2390–2396, 2019.

[2] S. Ramachandran, K. Asokkumar, M. U. Maheswari et al., "Investigation of antidiabetic, antihyperlipidemic, and in vivo antioxidant properties of *Sphaeranthus indicus* linn. In type 1 diabetic rats: an identification of possible biomarkers[J]," *Evidence-Based Complementray and Alternative Medicine*, vol. 2010, pp. 1741–427X, 2011.

[3] M. K. Tamura, V. G. Wadley, B. B. Newsome et al., "Hemoglobin concentration and cognitive impairment in the renal REasons for geographic and racial differences in stroke (REGARDS) study," *Journal of Gerontology*, vol. 65A, no. 12, pp. 1380–1386, 2010.

[4] A. F. Walker, G. Marakis, E. Simpson et al., "Hypotensive effects of hawthorn for patients with diabetes taking prescription drugs: a randomised controlled trial," *British Journal of General Practice the Journal of the Royal College of General Practitioners*, vol. 56, no. 527, pp. 437–443, 2006.

[5] G. Korosoglou, R. G. Weiss, D. A. Kedziorek et al., "Noninvasive detection of macrophage-rich atherosclerotic plaque in hyperlipidemic rabbits using "positive contrast" magnetic resonance imaging," *Journal of the American College of Cardiology*, vol. 52, no. 6, pp. 483–491, 2008.

[6] R. H. Mehta, M. B. Leon, and M. H. Sketch, "The relation between clinical features, angiographic findings, and the target lesion revascularization rate in patients receiving the endeavor zotarolimus-eluting stent for treatment of native coronary artery disease: an analysis of ENDEAVOR I, ENDEAVOR II," *The American Journal of Cardiology*, vol. 100, no. 8, pp. S62–S70, 2007.

[7] M. Geleedst-De Vooght, A.-H. Maitland-van der Zee, T. Schalekamp, A. Mantel-Teeuwisse, and P. Jansen, "Statin prescribing in the elderly in the Netherlands," *Drugs & Aging*, vol. 27, no. 7, pp. 589–596, 2010.

Hindawi
Journal of Healthcare Engineering
Volume 2023, Article ID 9836713, 1 page
https://doi.org/10.1155/2023/9836713

Retraction

Retracted: Finite Element Analysis of Femoral-Acetabular Impingement (FAI) Based on Three-Dimensional Reconstruction

Journal of Healthcare Engineering

Received 10 October 2023; Accepted 10 October 2023; Published 11 October 2023

This article has been retracted by Hindawi following an investigation undertaken by the publisher [1]. This investigation has uncovered evidence of one or more of the following indicators of systematic manipulation of the publication process:

(1) Discrepancies in scope
(2) Discrepancies in the description of the research reported
(3) Discrepancies between the availability of data and the research described
(4) Inappropriate citations
(5) Incoherent, meaningless and/or irrelevant content included in the article
(6) Peer-review manipulation

The presence of these indicators undermines our confidence in the integrity of the article's content and we cannot, therefore, vouch for its reliability. Please note that this notice is intended solely to alert readers that the content of this article is unreliable. We have not investigated whether authors were aware of or involved in the systematic manipulation of the publication process.

In addition, our investigation has also shown that one or more of the following human-subject reporting requirements has not been met in this article: ethical approval by an Institutional Review Board (IRB) committee or equivalent, patient/participant consent to participate, and/or agreement to publish patient/participant details (where relevant).

Wiley and Hindawi regrets that the usual quality checks did not identify these issues before publication and have since put additional measures in place to safeguard research integrity.

We wish to credit our own Research Integrity and Research Publishing teams and anonymous and named external researchers and research integrity experts for contributing to this investigation.

The corresponding author, as the representative of all authors, has been given the opportunity to register their agreement or disagreement to this retraction. We have kept a record of any response received.

References

[1] X. Luo, J. Zhang, G. Cai, Y. Wu, and K. Ma, "Finite Element Analysis of Femoral-Acetabular Impingement (FAI) Based on Three-Dimensional Reconstruction," *Journal of Healthcare Engineering*, vol. 2022, Article ID 2937056, 13 pages, 2022.

Hindawi
Journal of Healthcare Engineering
Volume 2022, Article ID 2937056, 13 pages
https://doi.org/10.1155/2022/2937056

Research Article

Finite Element Analysis of Femoral-Acetabular Impingement (FAI) Based on Three-Dimensional Reconstruction

Xi Luo,[1] Jun Zhang,[2] Guofeng Cai,[3] Yuqiong Wu,[1] and Kun Ma [1]

[1]*College of Architectural Engineering, Kunming University of Science and Technology, Kunming 650500, Yunnan, China*
[2]*Department of Orthopedics, Second Affiliated Hospital of Kunming Medical University, Kunming 651000, Yunnan, China*
[3]*Department of Sports Medicine, First Affiliated Hospital of Kunming Medical University, Kunming 651000, Yunnan, China*

Correspondence should be addressed to Kun Ma; 11305063@kust.edu.cn

Received 26 December 2021; Revised 26 January 2022; Accepted 27 January 2022; Published 27 February 2022

Academic Editor: Nima Jafari Navimipour

In order to solve the problem that people often have pain in the hip joint, it is more meaningful to study femoral-acetabular impingement syndrome in the future. This article aims to study the finite element analysis of femoral-acetabular impingement based on three-dimensional reconstruction. This paper proposes a selective image matching strategy. In the feature matching stage, all images are not matched in pairs, but the corresponding camera distance between the images is calculated initially, which has little effect on the number of features and greatly reduces the time of feature matching, thereby reducing the time cost of 3D reconstruction. In this experiment, a double-blind experiment was used to check the range of motion of all hip joints. Two senior radiologists read the obtained hip joint orthographic films to screen out the hip joint orthographic films that meet the requirements. Experimental data shows that although the initial matching points of the algorithm in this paper are lower than those of the traditional algorithm, the final number of matching points is higher than that of the traditional algorithm. When the final number of patches is fixed to 10000, the initial patch required by the algorithm in this paper is more than that required by the SAD algorithm, nearly 13%, but the total storage requirement is 56.4% of the SAD algorithm, which is a big improvement.

1. Introduction

With the rapid development of computer technology and multimedia technology, signal and image processing technology has received more and more attention. Three-dimensional object and environment reconstruction, as an important branch, has attracted the attention of a large number of scholars at home and abroad and obtained greater progress and a lot of results. Generally speaking, three-dimensional reconstruction is to use existing algorithms or related three-dimensional reconstruction software to model the object or environment, so as to obtain the three-dimensional model that people want.

Among the various ways the human body perceives the external world, vision is the most direct way. In all perceptions of the external world, most of the information comes from vision. Machine vision is based on the perception system that simulates the human eye, so that computers or related machines can obtain and recognize two-dimensional images, so that they have the ability to perform a series of tasks such as three-dimensional positioning, three-dimensional drawing, and three-dimensional reconstruction. On this basis, the extended stereo vision uses images and videos taken by cameras to realize the cognition of the objective world and uses robots to detect areas that cannot be reached by humans or areas that are more dangerous. Shoot to build a three-dimensional model of this type of environment or object. The development of computer vision has promoted human cognition of the unknown world and led to the development of medicine. Because of the abnormal anatomical morphology of the femur and acetabulum, the abnormal collision of the proximal femur and acetabular margin occurs at the end of hip movement. It occurs in young people who exercise a lot and is prone to early hip degeneration.

Parth used two large-capacity hip sparing centers to retrospectively review the hip sparing database of staged bilateral hip arthroscopy from 2008 to 2015 and determine the degree of correlation of imaging measurements, the degree of correlation of intraoperative pathology, and the difference in results on both sides of patients who need to stage bilateral hip arthroscopy [1]. Xie Z believed that femoral-acetabular impingement is a common hip joint disease that may make many patients weak. Hip arthroscopy is used to treat impinging CAM and clamp-shaped acetabular lesions. In view of the low cost of 3D hip printing, no radiation exposure, and tactile multi-angle views, he proposed a safer and more repeatable intraoperative technique than traditional fluoroscopy to achieve better results after femoral-acetabular impact surgery the resection and results [2]. Dutra B believed that in the past ten years arthroscopic treatment of hip joint diseases has been significantly spread and developed, and it currently represents the gold standard for the treatment of athletes' femoral-acetabular impingement. The function of the joint capsule has been better understood, sparking intense debate. He retrospectively included 36 patients (competitive athletes) who underwent hip arthroscopy for femoral-acetabular impingement for two years (2016–2018). It is concluded that the new longitudinal shape of the capsulotomy technique and the unilateral suture of the capsular suture at the end of the athlete's surgery can have a positive effect on the patient's functional outcome [3]. Lutter C analyzed the mechanical environment of the intra-articular structure of femoral-acetabular impingement syndrome, and further understood its pathomechanical characteristics. Based on CT data, a three-dimensional finite element mechanical analysis model of the hip joint including normal articular cartilage and femoral-acetabular impingement syndrome was accurately constructed [4]. Kemp J L reviewed patients who underwent hip arthroscopy at the Children's Hospital for idiopathic femoral-acetabular impingement or acetabular labrum tear and analyzed demographic predictors by using univariate logistic regression with generalized estimating equations. A matched case-control analysis was then performed to determine the radiological predictors of acetabular cartilage lesions by using univariate and multivariate conditional logistic regression. It was found that, in adolescents undergoing hip arthroscopy, older age, men, and higher body mass index were predictors of acetabular cartilage disease. From an imaging point of view, the increased α angle increases the possibility of acetabular cartilage disease, and the presence of the cross sign reduces this possibility. When considering hip arthroscopy to facilitate preoperative planning and more accurately set patient expectations, it is important to predict the presence of acetabular cartilage lesions [5, 6]. Angsutanasombat C believed that a single reconstruction of an object is very important in many applications, where the object is moving, or its shape is non-rigid and changes irregularly. He proposed a single-shot structured light 3D imaging technique, which calculates a phase map based on a distorted line pattern. This technology uses image processing technology to segment and cluster projected structured light patterns from a single captured image. The coordinates of the cluster lines are extracted to form a low-resolution phase matrix and then transformed into a full-resolution phase map by spline interpolation [7]. Vahedi H believed that Morgagni hernia (MH) can be diagnosed by different utilities, but all of these methods are not always 100% accurate. Three-dimensional (3D) reconstruction models help to better understand important anatomical structures. He reported a case of MH that had been misdiagnosed as diaphragmatic valgus in other institutions and provided laparoscopic repair based on the 3D reconstruction model. This case emphasizes that the 3D reconstruction model can be a useful supplementary tool for the diagnosis and preoperative evaluation of MH patients, especially when its diagnosis in clinical practice is confused [8].

The innovations of this article are as follows. (1) Using a double-blind experiment, two senior radiologists read the obtained hip joint orthographic film, and according to the PINCER-type FAI hip joint orthographic film imaging signs inclusion criteria and exclusion criteria, using a double-blind method to check the range of motion of all hip joints. Because machine learning is intelligent and the identified data is more accurate, we used machine learning to evaluate the femoral-acetabular impact finite element analysis. (2) The pathogenesis of FAI is the abnormal anatomical morphology of the hip joint. Three-dimensional reconstruction technology is used to perform imaging signs of the femoral-acetabular impingement. (3) Optimizing the selection of image pairs in the feature matching process, changing from the original full image matching to querying adjacent distance images for matching, which greatly reduces the time complexity and does not affect the quantity and quality of feature point matching. (4) The research on femoral-acetabular impingement is mainly applied to the treatment of femoral-acetabular impingement in the medical field and promotes the development of medicine in this field and makes new breakthroughs in the treatment of femur.

2. Finite Element Analysis Method of Femoral-Acetabular Impingement (FAI) Based on Three-Dimensional Reconstruction

2.1. Femoral-Acetabular Impingement Syndrome

2.1.1. Basic Concepts. The current mainstream view of the disease believes that this so-called "impingement" is a common cause of hip pain in most young patients who have ruled out obvious organic hip disease and classifies it as hip osseous, one of the causes of arthritis [9]. Since the definition was proposed, a large number of scholars have conducted research on it from many directions and have made certain progress and have further in-depth understanding of the disease. According to the different manifestations of imaging, the disease is divided into three types: cam type (CAM-type), clamp type (PINCER-type), and mixed type (MIX type); it is believed that the disease should be diagnosed at an early stage and related treatment [10, 11]. However, with a large number of clinical observations, it has been found that the x-ray signs of the so-called FAI also have a large number of manifestations in people without any hip

symptoms; a study by Laborie et al. found that about half of adults without hip symptoms have at least one or more FAI-related symptoms. X-ray imaging is abnormal. Hartofilakidis et al. conducted a long-term follow-up of 96 patients with FAI-related radiological abnormalities but asymptomatic. Among them, only 17 cases developed osteoarthritis after an average follow-up of 12 years, and the remaining 79 cases were followed up for an average of 18.5 years without bones and joints [12]. In this regard, many scholars have questioned the concept to a certain extent, questioning whether it has over-defined this so-called "impact" [13].

Femoral-acetabular impingement syndrome is a hip joint disease that has been proposed for more than a decade. The current mainstream view is that this so-called "impingement" causes most of the young patients who have ruled out obvious organic hip joint disease, the more common cause of hip pain, and it is listed as one of the causes of hip osteoarthritis [14]. Since this definition was proposed, a large number of scholars believe that the disease should be diagnosed and treated at an early stage. However, with a large number of clinical observations, it has been found that the so-called "impact" signs are also present in a large number of people without any hip symptoms. In this regard, many scholars have questioned the concept to a certain extent, questioning whether it has over-defined this so-called "impact" [15]. Checking the relevant domestic and foreign literature since the concept was put forward, there is no clear diagnosis standard and treatment indication for the disease at present.

2.1.2. Cause. Strictly speaking, the cause of the disease has not yet been fully clarified. According to GANZ, the abnormal anatomy of the proximal femur and acetabulum is the basis of the disease [16]. This so-called abnormal anatomy will reduce the relative movement space of the femur and the acetabulum when the hip joint moves, resulting in abnormal contact. With the in-depth study of the disease, certain acquired factors will cause changes in the anatomical structure of the hip joint, which will also become the cause of FAI [17]. In addition, studies have shown that even if the anatomical structure of the hip joint does not have the above abnormal performance, when its range of motion exceeds the normal range, there will be "impact" between the proximal femur and the acetabular rim, which to some extent also confirms GANZ on the basis of the pathogenesis of the disease, that is, the theoretical view of the abnormal hip joint structure [18].

2.1.3. Imaging Examination. Figure 1, shows an imaging examination of the hip joint. Currently, the most widely used initial diagnosis of FAI is the x-ray examination of the hip joint. The spatial distribution of anatomical structures obtained by plain radiographs is incomparable with CT and MRI, and it plays an irreplaceable role in structural diseases of bones and joints. The imaging diagnosis of FAI mainly relies on the measurement and evaluation of the hip joint anatomy on the plain film of the hip joint. The pelvic orthographic film has incomparable advantages in this respect.

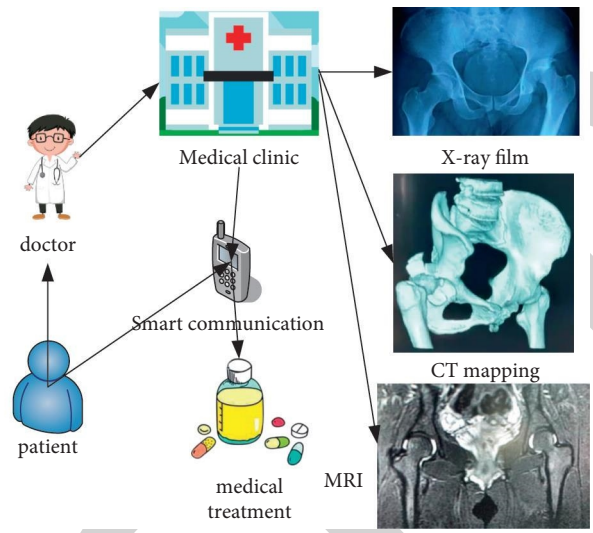

Figure 1: Imaging examination of the hip joint.

The premise is that the obtained hip joint orthographic film is a standard orthographic film. A more satisfactory orthographic film is that the longitudinal distance between the midpoint of the sacrococcygeal joint and the midpoint of the pubic symphysis is less than 3 cm, the lateral distance is less than 1.5 cm, and the pelvis has no obvious tilt. The obtained pelvic radiographs need to be measured for comprehensive evaluation. The most commonly used measurement items are CE angle, eccentricity, cross sign, head socket index, acetabular deep hip index, HTE angle, alpha angle, etc. [19, 20].

Compared with the spatial distribution of plain radiographs, CT scan of bone tissue has a higher spatial resolution, especially the reconstruction of three-dimensional CT, which can more intuitively observe the spatial structure of bones. A CT scan helps to analyze the shape of the acetabulum and femoral head, the eccentricity of the femoral head and neck, etc. On the CT cross section of the acetabulum, it can be observed whether there is excessive coverage of the anterior and posterior walls of the acetabulum. The anatomical morphology of the femoral head-neck junction can be clearly observed in the coronal view, and the presence of retroversion of the acetabulum can be identified in the sagittal view. Some of the main diagnostic indexes of FAI can be determined more accurately, such as femoral head-neck offset, α angle, so as to better assess the FAI classification and the degree of damage [21].

For early FAI pelvic plain film and CT, it is difficult to find bone changes, especially cartilage changes. MRI has obvious advantages [22]. As a non-invasive examination method, MRI can detect abnormal anatomical morphology of the femoral head and neck junction and excessive coverage of the acetabulum. It is currently the only method that can directly show the damage of the labrum and articular cartilage in the early stage of FAI. In addition, there is MRI arthrography. This technology is considered to be the "gold standard" of imaging for the diagnosis of lip and cartilage damage. It has high sensitivity, specificity, and accuracy for lip and cartilage damage.

2.2. Basics of 3D Reconstruction. With the development of high-tech, not only does machine vision continue to gain wider applications in the fields of robot navigation, scene reconstruction, human-computer interaction, etc., people also try to expand its application scope to new fields, such as virtual home, unmanned flying/driving, virtual fitting, 3D printing, etc.

Figure 2, shows the current application of computer vision in daily life.

Three-dimensional reconstruction technology (3D reconstruction) refers to the reconstruction of physical 3D models through relevant knowledge and technology, so as to facilitate the cognition of 3D information. There are two types of three-dimensional structure measurement methods, namely, contact and non-contact. According to the imaging principle, the non-contact method is divided into two types: active and passive. The active method requires laser or infrared and calculates the round-trip flight time or projection of light, or deformation of the pattern to obtain depth, such as laser scanning, structured light, ToF camera, etc. In the passive method, special light sources such as stereo vision technology are not required. Active technology is often limited in viewpoint and has the problem of self-occlusion. Passive technology can only rely on the existing content of the scene. Compared with active technology, its application range is limited [23].

Three-dimensional reconstruction can be divided into position estimation and normal estimation according to the different surface reconstruction methods. The position estimation technology directly estimates the position of the space surface, the technology is robust, and it is very suitable for restoring rough geometry. However, they cannot recover small-scale surface changes. The techniques for directly estimating the 3D position of the surface include not only active technologies such as laser scanning, ToF, and structured light, but also passive technologies such as passive stereo algorithms. The normal estimation technique estimates the direction of the surface given by its normal field, and integrating the normal field can restore the shape of the surface, such as shape restoration from shadows, photometric stereo vision, etc. Since the normal field is very sensitive to small changes on the surface, these techniques perform well in restoring fine structures. However, in practice, integration often introduces low-frequency deviation and noise, making these techniques less suitable for reconstructing rough geometry [24].

Although stereoscopic vision technology is relatively mature, this visual use technology also has its limitations. Its algorithm is very complex, easily interfered by environmental factors, and relies on environmental light sources, and low-light scenes perform poorly. No matter which matching method is still available, it solves the problems of occlusion, lack of texture features, and depth discontinuity [25]. Binocular stereo vision is a classic passive technology and the most commonly used stereo vision technology. Based on the triangulation principle, two images are used to measure the three-dimensional geometric structure, including multiple steps such as camera calibration and stereo matching. Binocular stereo matching can obtain a dense, high-resolution, high-precision disparity map. The structured light system has complex manufacturing process, high cost, short recognition distance, susceptibility to environmental interference, and long response time. The ToF technology can directly obtain depth information, can obtain a denser three-dimensional point cloud than structured light, and has better real-time performance. Its sensor manufacturing process is simple and small in size, has low performance and power consumption requirements, and has no dependence on the surface texture of the object. Its shortcomings are mainly that it will produce unreliable results at the edge of the field of view and the edge of the object, the resolution is relatively low, the measurement depth at short distances is missing, and there is a problem of multipath interference [26]. Therefore, based on the complementary characteristics between ToF depth camera and binocular stereo matching, the combination of ToF depth camera and binocular stereo technology can expand its scope of application and improve performance.

2.3. Camera Model

2.3.1. Camera Model. The camera imaging process can be described by mathematical representations in projective geometry.

$$u' = Ru + t. \tag{1}$$

Assume that the three-dimensional vector u has undergone Euclidean transformation to obtain a new vector u', where R is a $3 * 3$ rotation vector, and t is a $3 * 1$ translation vector.

$$\begin{aligned} u_2 &= R_1 u_1 + t_1, \\ \mathrm{u}_3 &= R_2 u_2 + t_2. \end{aligned} \tag{2}$$

R1, R2 are rotation matrices, and t1, t2 are translation vectors.

It directly means that the transformation from u1 to u3 becomes

$$u_3 = R_2 \left(R_1 u_1 + t_1\right) + t_2. \tag{3}$$

In order to simplify the calculation, the concept of homogeneous coordinates is introduced here. In the three-dimensional projective space, the point Q in homogeneous coordinates is expressed as

$$\begin{aligned} Q &= (X, Y, \mathrm{Z}, W)^T, \\ \mathrm{Q} &\overset{\Delta}{=} \mathrm{k}\,(X, Y, Z, W)^T. \end{aligned} \tag{4}$$

When $W = 0$, Q is the point of infinity. When W is not 0, Q is not a point of infinity.

$$Q' = \left(\frac{X}{W}, \frac{Y}{W}, \frac{Z}{W}\right)^T. \tag{5}$$

That is, the homogeneous coordinates are divided by the last item at the same time. Generally, let $W = 1$.

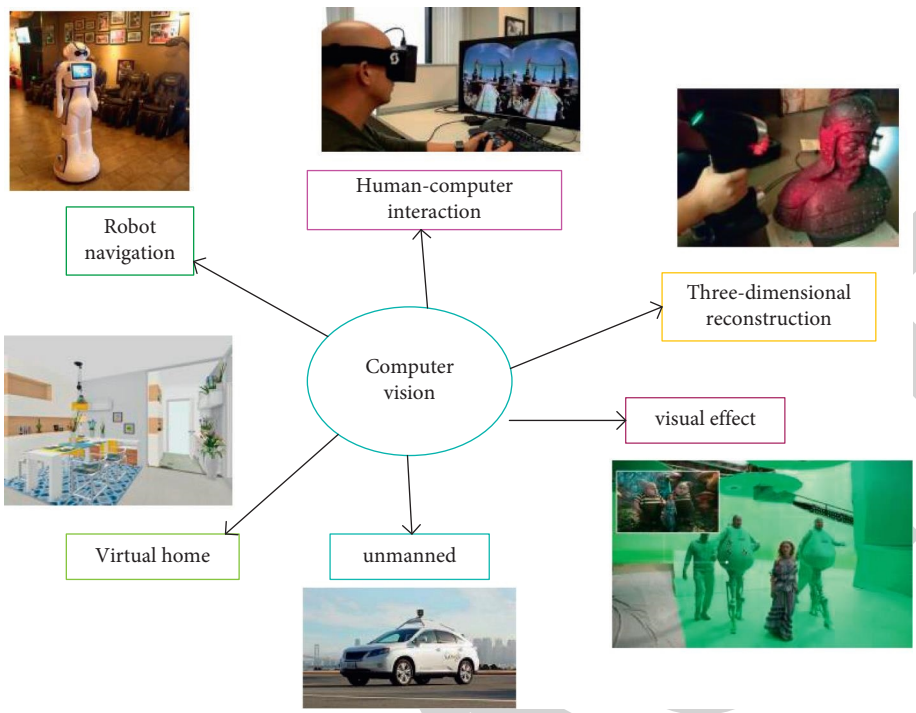

Figure 2: Application of computer vision.

The equation of the plane in the three-dimensional Euclidean space is expressed as

$$AX + BY + CZ + D = 0. \tag{6}$$

The corresponding three-dimensional projective space is expressed as

$$\mathrm{L} = (A, B, C, D)^T. \tag{7}$$

On plane I:

$$Q = (X, Y, Z, W)^T. \tag{8}$$

It satisfies

$$\mathrm{L}^T \cdot Q = 0. \tag{9}$$

Its expression in the two-dimensional projective space is

$$L = (a, b, c)^T. \tag{10}$$

And for any non-zero constant, k represents the same straight line. In the two-dimensional projective space, the necessary and sufficient conditions for the point P to be on the straight line i are

$$Q^T \cdot i = 0. \tag{11}$$

The intersection point of the two straight lines i1 and i2 is the outer product of the two; namely,

$$Q = i1 * i2. \tag{12}$$

The straight line i determined by Q1 and Q2 is expressed as the outer product of the two; namely,

$$i = Q1 * Q2. \tag{13}$$

In homogeneous coordinates, the calculation process of the camera position change becomes linear, and the mathematical expression is

$$\begin{pmatrix} \mathrm{a}' \\ 1 \end{pmatrix} = \begin{pmatrix} R & t \\ 0 & 1 \end{pmatrix} \begin{pmatrix} a \\ 1 \end{pmatrix} = T \begin{pmatrix} a \\ 1 \end{pmatrix}. \tag{14}$$

Among them, the $4 * 4$ matrix T is called the transformation matrix. $\begin{pmatrix} \mathrm{a} \\ 1 \end{pmatrix}$ is the homogeneous coordinate of the camera, and $\begin{pmatrix} \mathrm{a}' \\ 1 \end{pmatrix}$ is the homogeneous coordinate of the camera position after the position change.

2.3.2. Small Hole Camera Model. The camera is a common device to obtain images. Through the camera, a three-dimensional scene can be projected onto a two-dimensional plane. This process can be expressed by a geometric model.

As shown in Figure 3, the small hole camera model can well express most of the existing camera models, and the basic characteristics of its imaging are that the distance is small and the distance is large [27]. The small hole camera imaging process has the following steps.

Q is a three-dimensional point, and Q′ is a point corresponding to Q in the camera coordinate system.

$$\begin{bmatrix} X_c \\ Y_c \\ Z_c \\ 1 \end{bmatrix} = \begin{bmatrix} R & t \\ 0^T & 1 \end{bmatrix} \begin{bmatrix} X_w \\ Y_w \\ Z_w \\ 1 \end{bmatrix}. \tag{15}$$

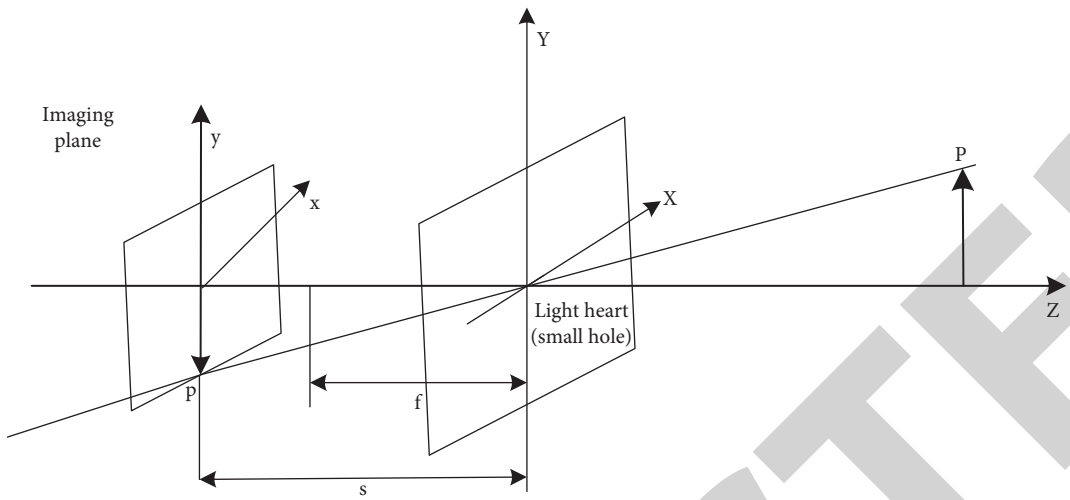

Figure 3: Schematic diagram of the small hole camera model.

Among them, R is the 3 X 3 rotation matrix, and t is the translation coordinate, which is the 3X1 vector. Both can determine the external parameters of the camera.

Then, the imaging process is

$$Z_c \begin{bmatrix} x_u \\ y_u \\ 1 \end{bmatrix} = \begin{bmatrix} f & 0 & 0 & 0 \\ 0 & f & 0 & 0 \\ 0 & 0 & 1 & 0 \end{bmatrix} \begin{bmatrix} X_c \\ Y_c \\ Z_c \\ 1 \end{bmatrix}. \quad (16)$$

Normally, the result of small hole imaging is an upside-down image, which will be automatically turned into an upright image during processing inside the camera. In this process, the corresponding relationship between the various quantities is

$$\begin{cases} x_u = \dfrac{gX_c}{Z_c} \\ y_u = \dfrac{gX_c}{Z_c} \end{cases}. \quad (17)$$

Among them, g is the focal length. The process is

$$\begin{cases} u = \dfrac{x_u}{k} + u_0 \\ v = \dfrac{y_u}{i} + v_0. \end{cases} \quad (18)$$

The focal length and the position of the principal point of the camera are called the internal parameters of the camera.

2.4. Beam Adjustment. When solving the three-dimensional coordinates of the characteristic points, due to factors such as noise points and calculation errors, the obtained camera parameters and three-dimensional coordinates will be deviated. This deviation will have a great impact on the final 3D reconstruction result. In order to improve the accuracy of the results, it is necessary to deal with the errors in the measurement and calculation.

The beam adjustment is the last step of SFM sparse 3D reconstruction, and it is also a very important step. Based on the internal parameters of the camera, it minimizes the reprojection error and, in the sense of nonlinear least squares, performs high-precision reconstruction of the camera parameters and the three-dimensional structure in the image [28].

3. Finite Element Analysis Experiment of Femoral-Acetabular Impingement (FAI) Based on Three-Dimensional Reconstruction

3.1. Subjects. All the hip joint anterior radiographs in the hospital were screened out, regardless of gender, aged 14–50 years old, and BMI below 28 kg/m2. According to the proposed inclusion criteria and exclusion criteria, a total of 265 patients (530 hips) were included as the research subjects.

As shown in Table 1, for the proposed inclusion and exclusion criteria, all patients in this experiment have the right to know. Without forcing the patients to conduct the experiment, the patients agreed to cooperate in the study and signed the relevant informed consent.

As shown in Table 2, for the demographic data of the study subjects, a total of 265 patients (530 hips) were included as the study subjects. In addition, 50 patients without any FAI imaging signs were selected according to the above inclusion and exclusion criteria (100 hips) as the normal group (control group).

3.2. Experimental Process. Figure 4 shows the research flow chart of the whole experiment. After obtaining a standard hip joint anterior view, and then selecting 100 normal hip joints without any abnormal signs, and using the range of motion of all hip joints, it was examined by double-blind method and six matching points were taken for comparison. The hip joints with PINCER-type FAI imaging signs were

Table 1: Inclusion criteria and exclusion criteria.

Inclusion criteria	Exclusion criteria
Age 14-50 years old	Femoral head necrosis
No gender limit	Various types of hip arthritis
Body mass index (BMI) 19–28 Kg/m2	Lumbar disc herniation
	History of hip injury and surgery
	Inguinal hernia
There are imaging signs of PINCER-type FAI	Special occupations (martial arts, dance, etc.)
	There are CAM-type FAI imaging signs

Table 2: Demographic data of the research subjects.

	PINCER-type sign group	Normal group
Age	32 ± 11	34 ± 9
Gender (male/female)	104/161	27/23
Body mass index (BMI)	24.1 ± 2.5	23.6 ± 1.2

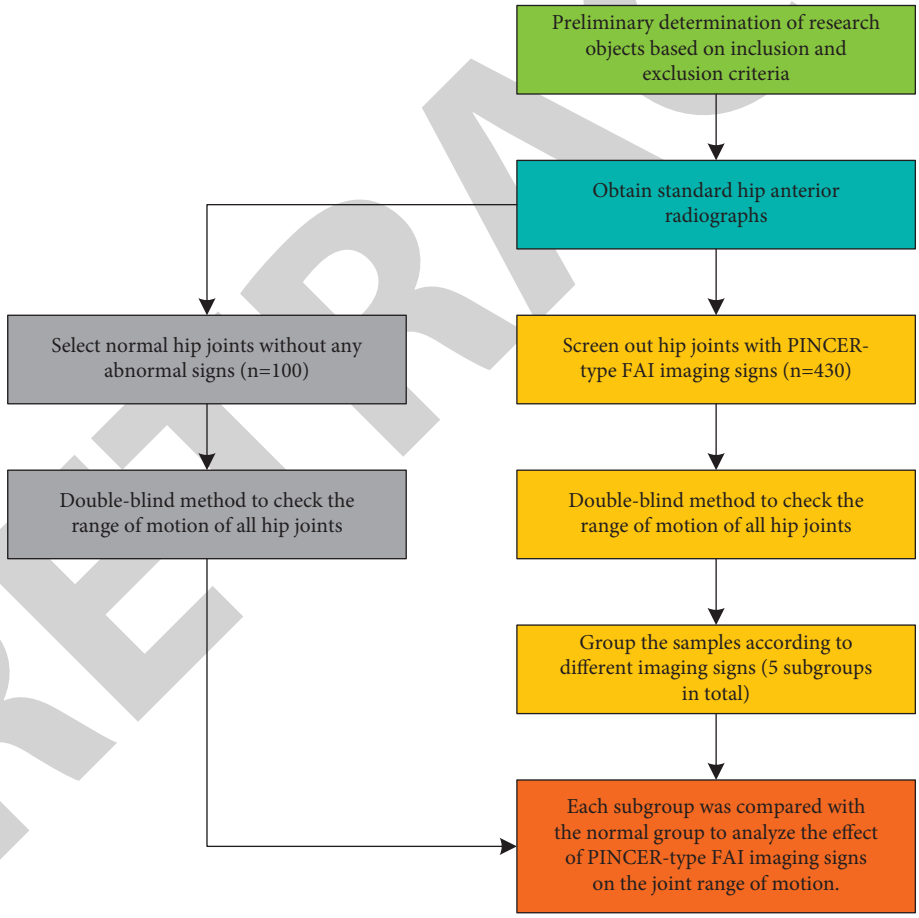

Figure 4: Experimental flowchart.

selected from the experimental subjects, and the range of motion of all hip joints was checked using a double-blind method. The samples were divided into five subgroups according to different imaging signs. Finally, each subgroup was analyzed. The activities of the groups were compared with those of the normal group, and the finite element analysis was carried out using three-dimensional reconstruction technology.

3.3. Experimental Method

3.3.1. Obtaining Method of Hip Joint Orthographic Film. The three-dimensional reconstruction system was used to complete, and all the anatomical structures of the hip joint were clear; the longitudinal distance between the midpoint of the sacrococcygeal joint and the midpoint of the pubic symphysis was less than 3 cm, the lateral distance was less than 1.5 cm, and the pelvis had no obvious tilt.

3.3.2. Under the Principle of Random Double-Blind. Two senior radiologists read the obtained hip joint anterior radiographs, according to the inclusion and exclusion criteria of the PINCER FAI hip joint orthographic radiographs.

As shown in Table 3, it is based on the inclusion and exclusion criteria of the PINCER-type FAI hip joint orthographic imaging signs. The four signs are associated with corresponding symptoms.

As shown in Table 4, it is based on the inclusion and exclusion criteria of the CAM-type FAI hip joint orthographic imaging signs. Among them, it was found that femoral hip impingement occurred at the early stage of hip flexion (α angle >40), which was more serious (α angle >78) and the anterior CAM deformity may cause earlier femoral hip impaction.

3.3.3. Checking the Passive Range of Motion of the Hip Joint. At the same time, under the principle of random double-blind, two senior joint surgeons used the same method to check all the above-mentioned hip joint motions, measured and recorded the results with a protractor, and took two physicians to measure the motion of each hip joint.

4. Finite Element Analysis of Femoral-Acetabular Impingement (FAI) Based on Three-Dimensional Reconstruction

4.1. 3D Reconstruction System. As shown in Figure 5, the left side of the picture is the original 3D reconstruction image, and the right side is the rotated sideways image, in order to verify the effect of the proposed improved algorithm under different influencing factors, including image rotation, noise interference, and illumination changes and other influencing factors.

Figure 6 shows a traditional stereo matching SAD algorithm. This traditional algorithm is often used for image block matching. The absolute value of the difference between the corresponding values of each pixel is summed to evaluate the similarity of two image blocks.

Figure 7 shows the algorithm matching graph optimized in this paper. It can be clearly seen that the final matching points obtained by the optimized algorithm are far more than that of the traditional SAD algorithm, which shows that the matching accuracy of this algorithm is much higher than that of the traditional algorithm.

4.2. Algorithm Performance Analysis. As shown in Figure 8, the traditional SAD algorithm is compared with the optimized algorithm in this paper. First, three algorithms are used to detect the feature points of the image to obtain the initial matching points. Since there are a large number of mismatches in the initial matching points, it is necessary to remove the mismatched points in the initial matching points to obtain higher accuracy. It can be found from the figure that, in the first set of data, the matching accuracy of the algorithm in this paper is 59.71%, the matching accuracy of the traditional algorithm is 33.93%, the first group is 25.78% higher, the second group is 10.68% higher, and the third group is 29.98% higher. It can be seen that as the number of initial matching points is higher, the matching accuracy will be greater.

The experiment first uses the algorithm to generate sparse matching points and uses the generated matching points as the input of the PMVS algorithm to generate a denser spatial point cloud, so as to realize the three-dimensional reconstruction of the object or the environment.

As shown in Figure 9, the left side is the initial number of faces, and the right side is the final number of faces. It can be seen that when the fixed initial number of patches is the same, the final number of patches obtained by the algorithm in this chapter is 1390 less than that of the traditional SAD algorithm, but the dimension of the feature point vector proposed by the algorithm in this paper is only half of the dimension of the feature point vector of the SAD algorithm. That is, the storage requirement is reduced by 50% compared with the SAD algorithm. Although the final number of patches is reduced by nearly 13%, the result is acceptable. When the final number of patches is fixed to 10,000, the initial patch required by the algorithm in this paper is nearly 13% more than that required by the SAD algorithm, but the total storage requirement is 56.4% of the SAD algorithm.

4.3. Analysis of Femoral-Acetabular Impingement Sign. As shown in Figure 10, the image on the left is the comparison of the mobility of the simple cross sign and the normal group, and the image on the right is the comparison of the mobility of the simple acetabulum and the normal group. Compared with the normal group, the range of motion of the hip joints with "cross sign" on the anterior and posterior radiographs of the hip was mainly in forward flexion, internal rotation, and adduction. The results of the two groups were statistically different ($P < 0.05$). There was no significant difference in the range of motion of the hip joint in the anteroposterior view of the hip as "too deep acetabulum" compared with the normal group ($P > 0.05$).

Table 3: Signs and signs of PINCER femoral-acetabular impingement.

Cross sign	The anterior wall of the acetabulum is on the outside of the posterior wall
Deep acetabulum	The inner wall of the acetabulum overlaps with the iliac sitting line or is on its inner side
Acetabular protrusion	The inner edge of the femoral head overlaps the iliac seat line or is inside
Posterior sign	The center of the femoral head is inside the projection of the posterior wall of the acetabulum

Table 4: Signs and signs of CAM femoral-acetabular impingement.

Pistol-like deformity	The depression at the junction of the femoral head and neck disappears or even bulges
Femoral neck α angle	>40°
Femoral head and neck eccentricity	<10 mm

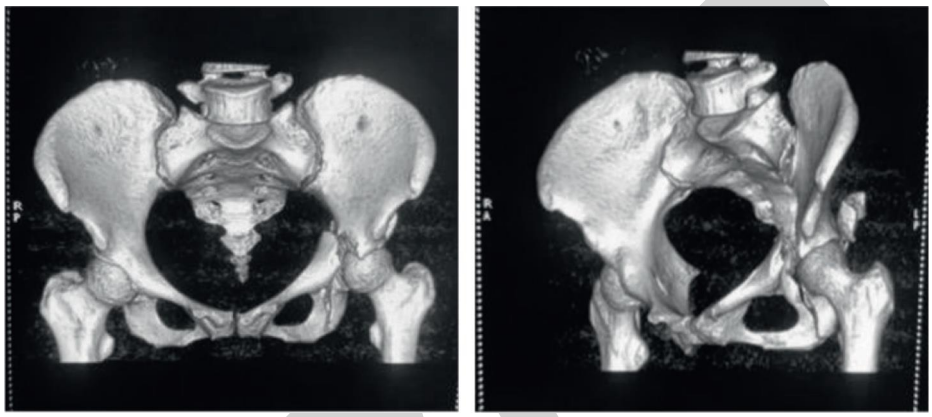

Figure 5: Original image (a), rotated sideways image (b).

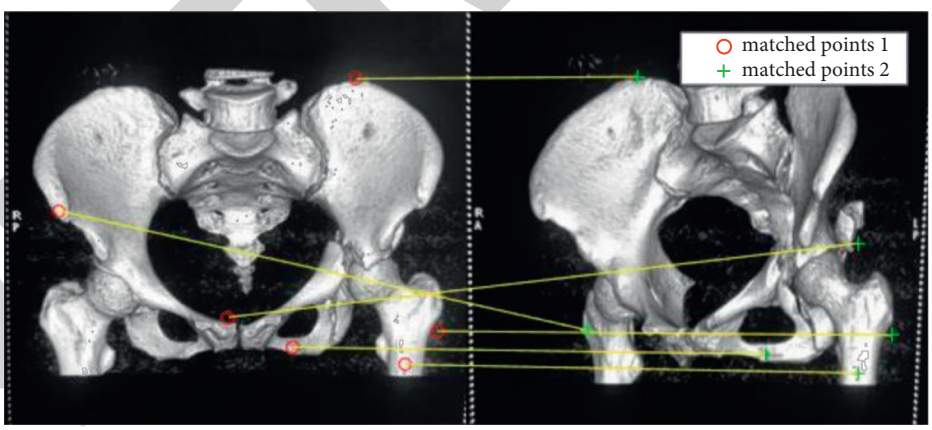

Figure 6: Traditional SAD algorithm.

As shown in Figure 11, the left image is a comparison of mobility between the "cross sign + deep acetabulum" group and the normal group, and the right image is a comparison of mobility between the "cross sign + deep acetabulum" group and the normal group. The main differences in the former were flexion, internal rotation, and adduction. The results of the two groups were statistically different ($P < 0.05$). The main differences in the latter are extension, internal rotation, and external rotation. The results of the two groups were statistically different ($P < 0.05$).

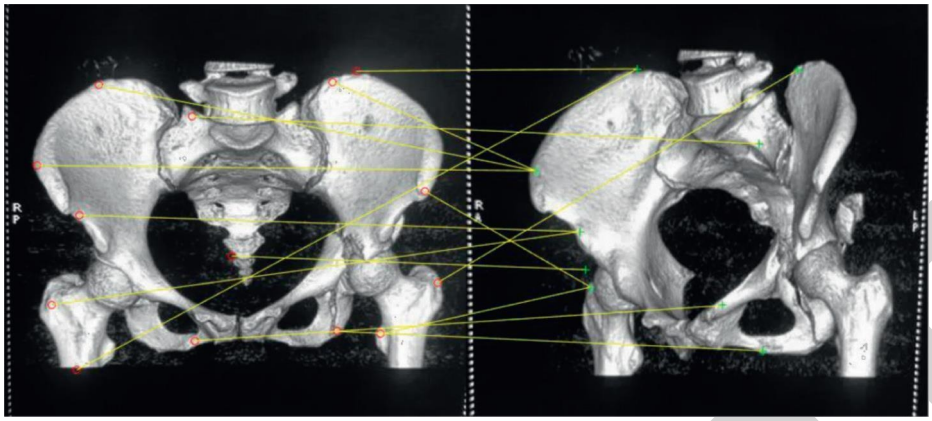

Figure 7: The optimized algorithm.

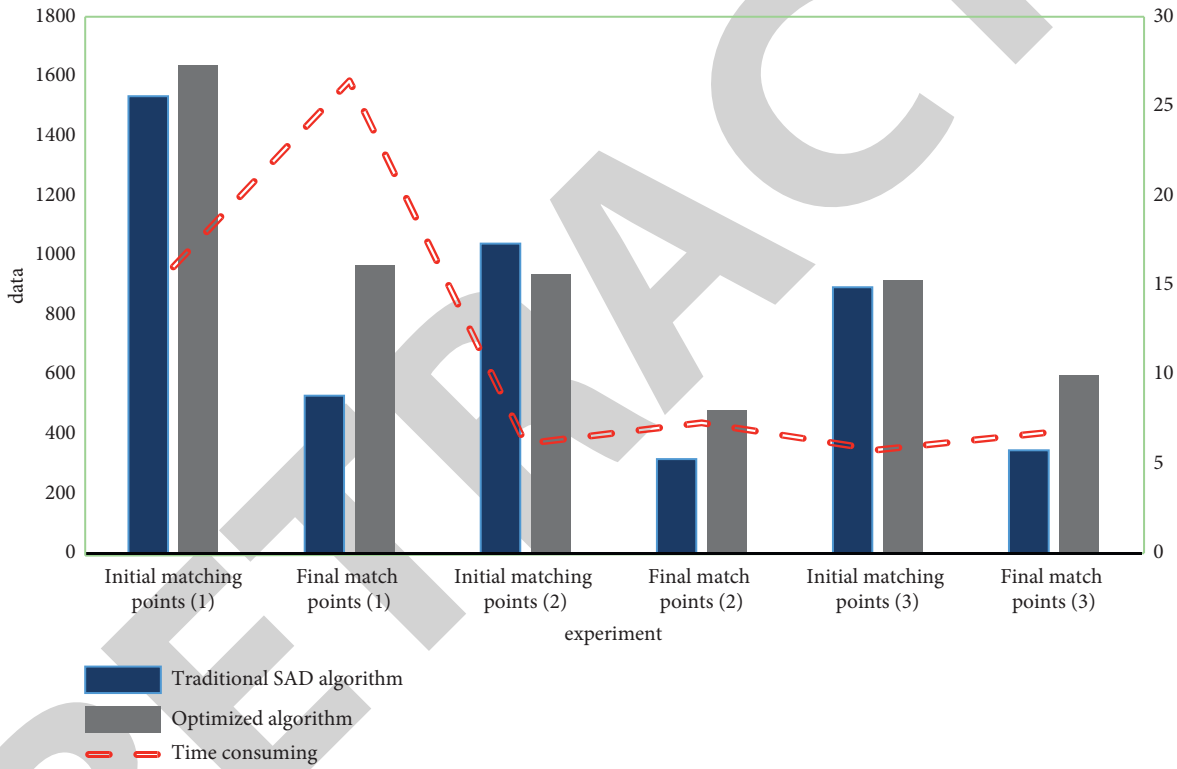

Figure 8: Algorithm performance comparison.

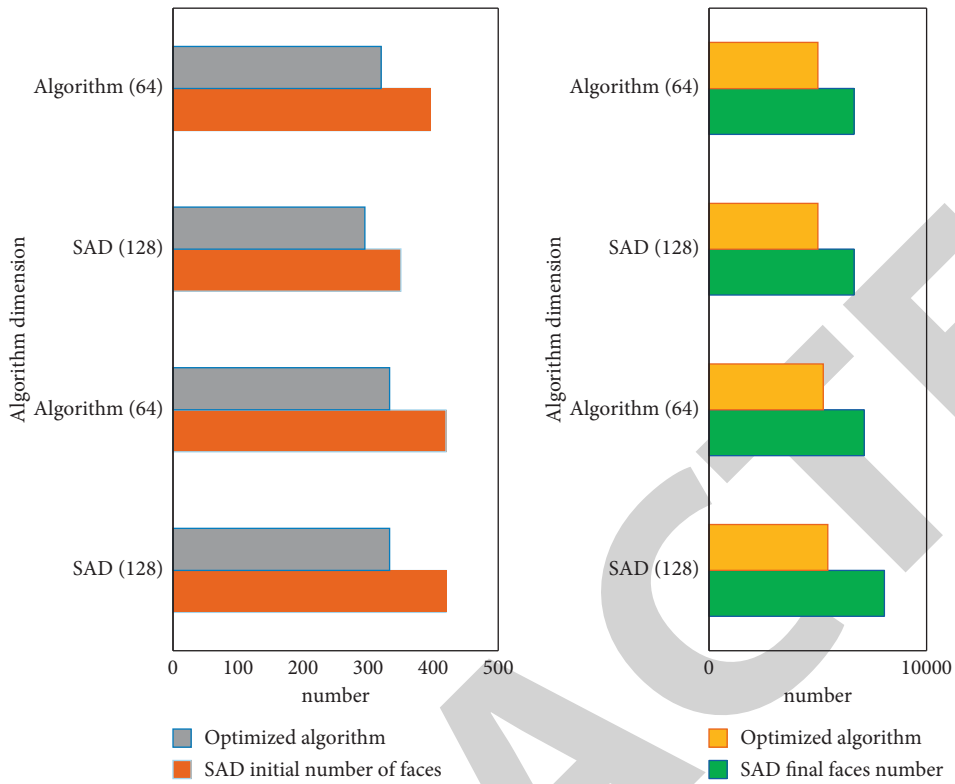

Figure 9: 3D reconstruction initial number of faces (a), 3D reconstruction final number of faces (b).

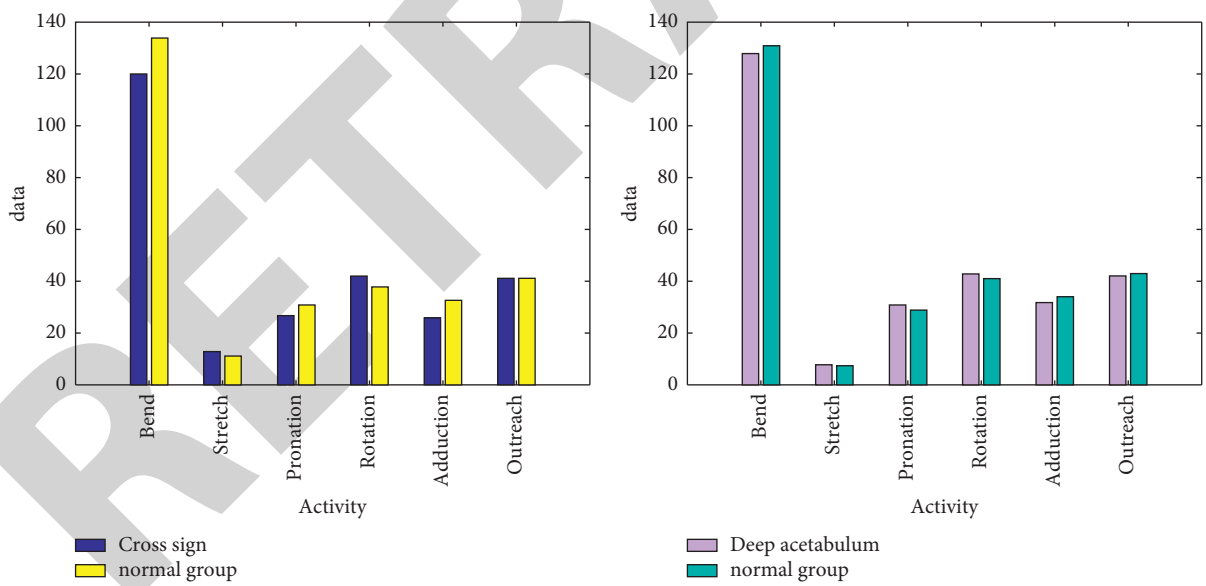

Figure 10: Comparison of mobility between simple cross sign and normal group (a), comparison of mobility between simple acetabular deep and normal group (b).

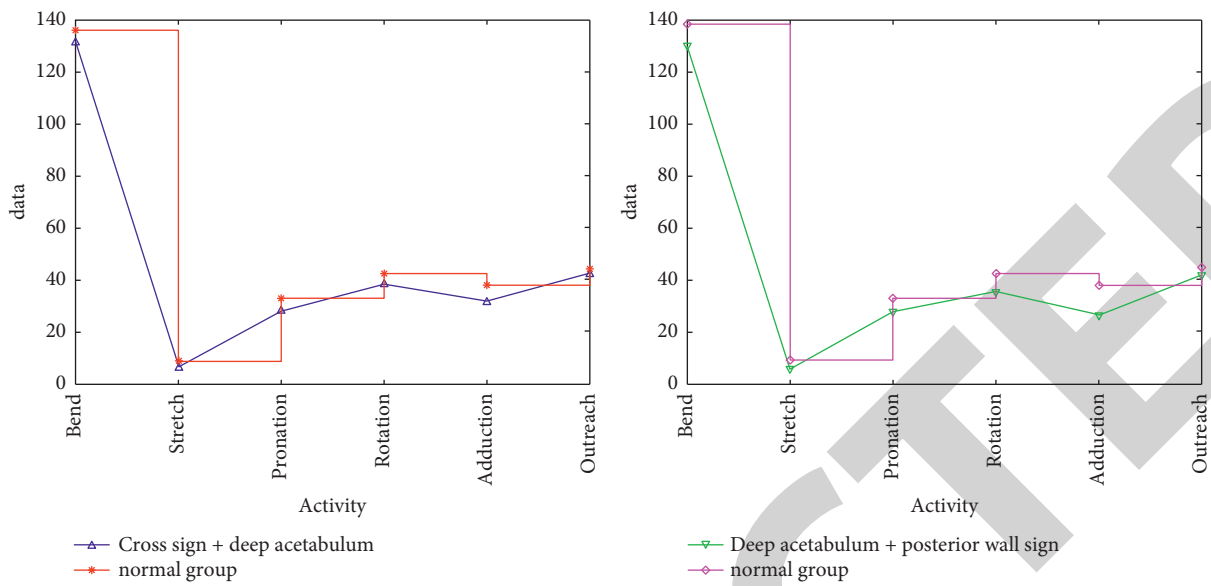

Figure 11: Comparison of mobility between the "cross sign + deep acetabulum" group and the normal group (a), comparison of mobility between the "cross sign + deep acetabulum" group and the normal group (b).

5. Conclusion

The FAI concept has been formally put forward for more than 10 years, but there are still many disputes about it. The previous research literature on FAI has many imaging indicators for its diagnosis, and it is also mentioned that the clinical symptoms of the disease are mostly pain in the groin area during flexion, adduction, and internal rotation. However, there is no clear research on the relationship between the so-called imaging signs and joint range of motion. This study focused on the influence of related imaging signs of PINCER FAI on the range of motion of the hip joint. The results proved that when there is only one FAI imaging sign, it will also affect the range of motion of the hip joint, such as the "cross sign." In addition, the results of this study indicate that the "excessive acetabulum," an imaging sign used to evaluate PINCER-type FAI, may not have clinical significance when it exists alone. When "posterior wall sign" exists, in addition to extension and external rotation being affected, internal rotation will also be affected; when "posterior wall sign" combined with "acetabular protrusion," in addition to extension, internal rotation, and external rotation, internal revenue will also be affected. The disadvantage of this article is that all samples included in this study have no hip pain in daily life. Whether the hip joint with FAI imaging signs will develop osteoarthritis requires long-term follow-up. Although the 3D reconstruction process is suitable for images collected in various ways, including images obtained by image acquisition devices such as drones and consumer cameras, the requirements for image quality are still very high. In the case of poor lighting conditions, the reconstruction effect of the image is still poor. In addition, the image collected by the mobile phone is often because the image at the focal length is clear, and the other positions are very blurred, which greatly affects the solution of the parameters. For these situations, in order to get a good modeling effect, the algorithm needs to be more robust.

Data Availability

The data that support the findings of this study are available from the corresponding author upon reasonable request.

Disclosure

Xi Luo and Jun Zhang are co-first authors.

Conflicts of Interest

The authors declare that they have no conflicts of interest.

Authors' Contributions

Xi Luo and Jun Zhang contributed equally to this work as co-first authors.

References

[1] P. Lodhia, C. Gui, TJ. Martin, S. Chandrasekaran, C. Suarez-Ahedo, and BG. Domb, "Central acetabular impingement is associated with femoral head and ligamentum teres damage: a cross-sectional matched-pair analysis of patients undergoing hip arthroscopy for acetabular labral tears," *Arthroscopy: The Journal of Arthroscopic & Related Surgery*, official publication of the Arthroscopy Association of North America and the International Arthroscopy Association, vol. 34, no. 1, pp. 135–143, 2018.

[2] Z. Xie, D. Jin, and J. Shen, C. Zhang, Mid-term effectiveness of arthroscopic surgery for femoroacetabular impingement," *Chinese Journal of Reparative and Reconstructive Surgery*, vol. 32, no. 2, pp. 129–133, 2018.

[3] B. Dutra, M. V. Roos, and A. C. Júnior, EMU. Lima, MF. Fontana, and RP. Okamoto, Subspine hip impingement:

Hindawi
Journal of Healthcare Engineering
Volume 2023, Article ID 9790589, 1 page
https://doi.org/10.1155/2023/9790589

Retraction

Retracted: Recognition of Volleyball Player's Arm Motion Trajectory and Muscle Injury Mechanism Analysis Based upon Neural Network Model

Journal of Healthcare Engineering

Received 10 October 2023; Accepted 10 October 2023; Published 11 October 2023

This article has been retracted by Hindawi following an investigation undertaken by the publisher [1]. This investigation has uncovered evidence of one or more of the following indicators of systematic manipulation of the publication process:

(1) Discrepancies in scope
(2) Discrepancies in the description of the research reported
(3) Discrepancies between the availability of data and the research described
(4) Inappropriate citations
(5) Incoherent, meaningless and/or irrelevant content included in the article
(6) Peer-review manipulation

The presence of these indicators undermines our confidence in the integrity of the article's content and we cannot, therefore, vouch for its reliability. Please note that this notice is intended solely to alert readers that the content of this article is unreliable. We have not investigated whether authors were aware of or involved in the systematic manipulation of the publication process.

Wiley and Hindawi regrets that the usual quality checks did not identify these issues before publication and have since put additional measures in place to safeguard research integrity.

We wish to credit our own Research Integrity and Research Publishing teams and anonymous and named external researchers and research integrity experts for contributing to this investigation.

The corresponding author, as the representative of all authors, has been given the opportunity to register their agreement or disagreement to this retraction. We have kept a record of any response received.

References

[1] J. Zhao and Z. Li, "Recognition of Volleyball Player's Arm Motion Trajectory and Muscle Injury Mechanism Analysis Based upon Neural Network Model," *Journal of Healthcare Engineering*, vol. 2022, Article ID 8114740, 15 pages, 2022.

Hindawi
Journal of Healthcare Engineering
Volume 2022, Article ID 8114740, 15 pages
https://doi.org/10.1155/2022/8114740

Research Article

Recognition of Volleyball Player's Arm Motion Trajectory and Muscle Injury Mechanism Analysis Based upon Neural Network Model

Jinxiang Zhao and Zengli Li

Physical Education Department, Hebei Academy of Fine Arts, Shijiazhuang 050700, Hebei, China

Correspondence should be addressed to Zengli Li; lzl@hbafa.edu.cn

Received 17 December 2021; Revised 20 January 2022; Accepted 21 January 2022; Published 17 February 2022

Academic Editor: Nima Jafari Navimipour

At present, in sports training for volleyball, it still mainly depends on the personal experience of the coach. Training costs are high, and the quality is difficult to maintain stable. Even with the introduction of training assistance software, it is often necessary to manually enter complex data, and the research samples are mostly single individuals. Serving is one of the basic and important technical movements of volleyball, and its standardization is of great significance to the stable performance of the scene. This article proposes an analysis of the volleyball player's arm trajectory based on the background of human posture recognition and analysis, based on the neural network model. The changes in the angles of the shoulders, elbows, and wrist when serving the ball reflect the different trajectories of the arm. Experiments show that the height of the throwing arm from the ground accounts for 98% of the height. The horizontal angle of the throwing arm at the moment the ball leaves the hand is positively correlated with the throwing time and height, and the reasonable trajectory has an impact on the stability of the throwing ball. The closer the trajectory of the tossing arm is to the vertical, the more stable the tossing is.

1. Introduction

The article takes serving training in volleyball training as an application scenario. Based on the monocular video research method to obtain the athlete's body posture evaluation index, the volleyball player's arm trajectory is recognized. And through the comparison of shoulder and elbow angle changes, this article explores the difference of serve movement and forms the evaluation result of the training quality of serve movement. It provides a reference basis for coaches to find problems in a targeted manner. The change of the arm's trajectory during the serve has an important role in accumulating force for the next stage of explosion. Therefore, we study the running trajectory of the throwing arm to provide information for training and teaching and improve the quality of serve.

Nowadays, people's attention to sports competition, based on the in-depth analysis of big data technology, has made many scholars' more in-depth research on the recognition and analysis of sports gestures. With the support of neural networks, the recognition and analysis of motion trajectories have new endpoints. Shu W uses an improved neural network to extract the trajectory features of the athletes in the football game video and trains the network on a large number of data objects containing similar objects, which improves the algorithm's ability of distinguishing the trajectories of the athletes. Experimental results show that the algorithm has a good effect in the field of football, with an accuracy rate of over 90% [1]. Rock climbing trajectory is the basic data for coaches to select athletes and formulate follow-up training plans. Zhang J proposed a bolt-shaped friction nanogenerator (BS-TENG), which can be used for trajectory detection during rock climbing training. The peak value of the output voltage pulse is between 4 and 7 V, which has a strong signal-to-noise ratio and anti-interference ability [2]. Based on the internal model assumptions, during the planning and execution of voluntary tracking exercises, Shevtsova et al. numerically model the motion control

process of the higher regions of the human brain. They used measures such as Kalman filter, linear quadratic estimator, and linear quadratic regulator. Based on the analysis of the tracking motion trajectory, they proposed a method to determine the activation time of the control [3]. Melo et al. accurately detect the line and ball position by applying color filters and transformations in combination with a support vector machine. They use different pictures to track the ball's position and use mathematical models to estimate the ball's trajectory and help predict the moment of contact. In this work, they applied the extended Kalman filter to reduce the measurement error and improve the detection performance by predicting the future position of the ball. The results show that this method has excellent performance and technical feasibility for deployment in low-cost embedded computers [4]. Liu et al. proposed a nonbackstepping predictive controller based on a dynamic linearized multilayer feedforward neural network (MFNN) model. This method does not require an inverse model of inherent hysteresis, and the control law can be obtained explicitly. Experimental results show that the method proposed has satisfactory tracking performance even under high-frequency reference [5]. Nikitin et al. solve the video-based face recognition problem. They proposed a new neural network model that uses a person's facial image input set to generate a compact, fixed-dimensional descriptor. These feature vectors are weighted according to their utility estimates to produce a feature representation of the image set. Experiments show that the feature aggregation method based on face quality evaluation proposed is always better than the traditional aggregation method [6]. The proposals of these theories have a more in-depth effect on the application of neural networks to a certain extent. Although it has a wider application range, they all have certain defects more or less and cannot be considered comprehensively. Moreover, the experimental process is relatively complicated, there are many calculation places, and problems such as calculation errors are prone to occur.

The innovation of this article is the gesture recognition of today's sports athletes, which is mostly group or single individual gesture recognition. This article is based on the background of deep neural network to recognize the volleyball player's arm trajectory. Through the analysis of the trajectory of the throwing arm and the angles of the shoulder and elbow joints, it draws the attention points that are more conducive to the training of volleyball players for better training [7].

2. Neural Network Model Based on Volleyball Arm Recognition

2.1. Neural Network Based on Volleyball Arm Trajectory Recognition

2.1.1. Fully Convolutional Network. Fully Convolutional Networks (FCN) can classify images at the pixel level, and the network structure is shown in Figure 1. Compared with the traditional convolutional neural network CNN, there is a slight difference [8]. There are two key technologies in FCN.

2.1.2. Convolution. The schematic diagram of the convolution is shown in Figure 2. The classic convolutional neural network CNN classification network is usually the fully connected layer at the end [9]. However, this will lose the spatial information of the feature [10, 11]. The output of the two-dimensional segmentation map required for image semantic segmentation is Mask. To obtain a two-dimensional matrix, a convolutional layer is used to replace the fully connected layer in the last layer. That is the meaning of convolution [12].

2.1.3. Upsampling. Upsampling is the process of generating a heat map. The specific performance is that after the network performs convolutional pooling for 5 times, the image will be reduced by a square number, such as 2, 4, and 8 times. Until the last layer is upsampled by 32 times, it is possible to obtain a picture with the same size as the original picture. Now, we need to restore the image size of the convolutional layer to the original image size. The upsampling method is used in FCN, and the specific implementation is deconvolution [13]. The extraction diagram is shown in Figure 3.

2.2. Recurrent Neural Network.

Recurrent Neural Network (RNN for short) is a view based on the following: "human cognition is the past experience and memory." Different from general neural networks, RNN is a special neural network structure [14]. The problem with RNN and CNN is that it not only considers the input at the previous moment, but also provides the network with the "storage" function of the previous content [15]. The reason RNN is called a Recurrent Neural Network is that, in the hidden layer within the neural network of the network, no connections between neuron nodes will be replaced by links and the outputs of the previous hidden layer and the input layer together form inputs to the hidden layer.

2.2.1. RNN Model Structure. As shown in Figure 4, it can be seen that the RNN hierarchical structure ratio is mainly composed of the input layer, the hidden layer, and the output layer. The arrow in the "hidden layer" indicates that the data is being updated regularly [16].

This section expands the hidden layer structure diagram of the RNN as shown in Figure 4, using q as the sample input. At this time, the memory of the sample at time s is represented by T_s, so $T_s = f(M \cdot T_{s-1} + N \cdot q_s)$. The M table starts with the weight of the input, and N is the weight of the input during the process, and the weight of the output of the R table is used.

When $s = 1$, initialize $T_0 = 0$ as the input value and M, N, and R randomly, and calculate the following equation:

$$\begin{aligned} e_1 &= Nq_1 + MT_0 \\ T_1 &= f(e_1) \\ c_1 &= y(NT_1) \end{aligned} \tag{1}$$

In the equation, f can represent multiple activation functions, such as tanh, Relu, and Sigmoid. And y, which

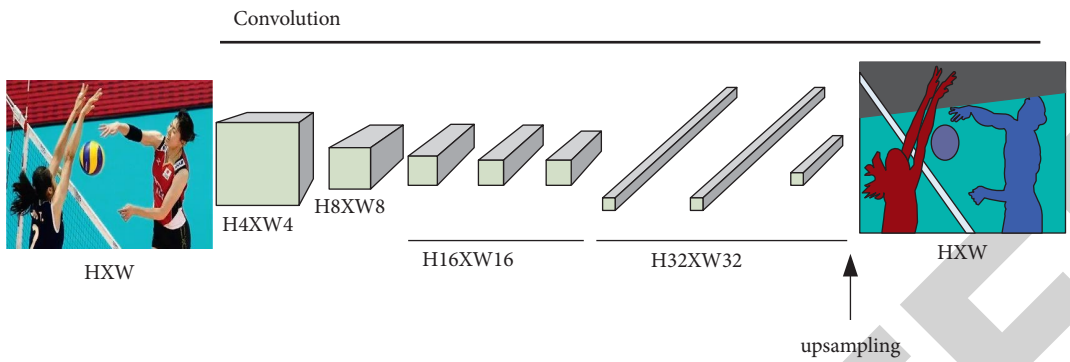

Figure 1: FCN network structure diagram.

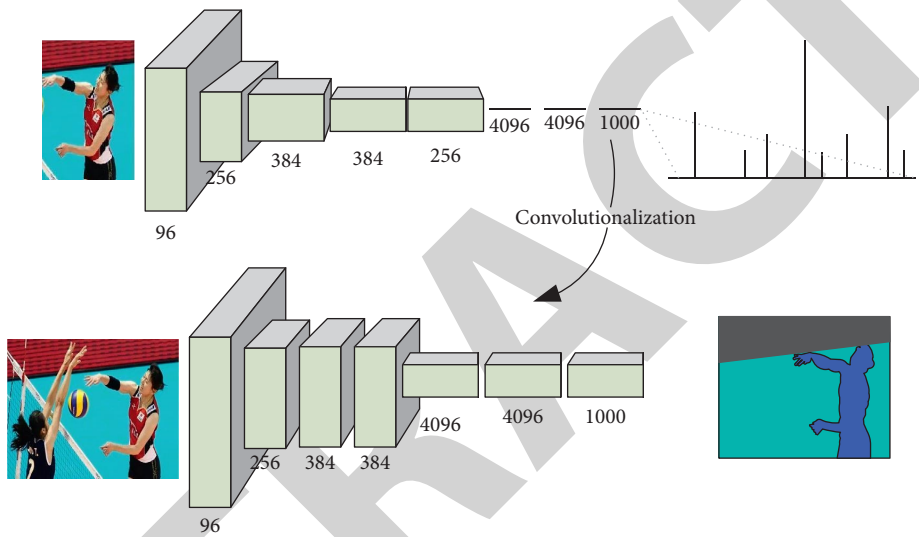

Figure 2: Schematic diagram of convolution.

also represents the activation function, usually only represents Softmax. As time grows, the prediction equation of the storage state of the T1 table at time 1 is as follows:

$$\begin{aligned} e_2 &= Nq_2 + MT_1, \\ T_2 &= f(e_2), \\ c_2 &= y(NT_2). \end{aligned} \tag{2}$$

As shown in Figure 5, the derivation is based on this

$$\begin{aligned} e_t &= Nq_2 + MT_{s-1}, \\ T_s &= f(e_s), \\ c_s &= y(NT_s). \end{aligned} \tag{3}$$

2.2.2. Backpropagation of RNN. The previous section introduced the basic method of forward propagation. This section updates the M, N, and R weight parameters of the neural network's reverse transmission. That is, in the representation method $H = \sum hs$ of the output value cs and the error value to the total error hs, when the square loss or cross entropy is used as the loss function, the output of each step is not only affected by the current network, but also by the influence of the network status of the upper layer, so it is also called the backpropagation of time. The error value of this transmission method is mainly updated by the gradient descent method; namely,

$$\begin{aligned} H &= \sum_s hs, \\ \Delta N &= \frac{\alpha H}{\alpha N} = \sum_s \frac{\alpha h_s}{\alpha N}, \\ \Delta R &= \frac{\alpha H}{\alpha R} = \sum_s \frac{\alpha h_s}{\alpha R}, \\ \Delta M &= \frac{\alpha H}{\alpha M} = \sum_s \frac{\alpha h_s}{\alpha M}. \end{aligned} \tag{4}$$

Based on the parameter update method, M is updated as the sum of each bit deviation. Here, the update method of M needs to be solved first. Assuming $s = 5$, according to the chain derivation, it can be expressed as

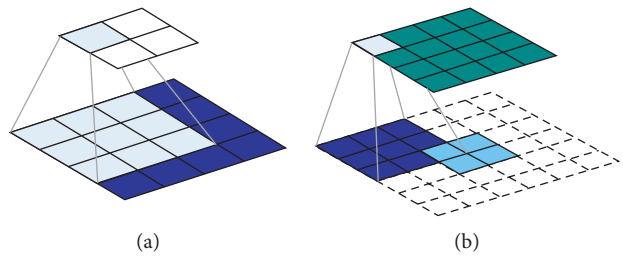

Figure 3: Schematic diagram of (a) convolution and (b) deconvolution in upsampling.

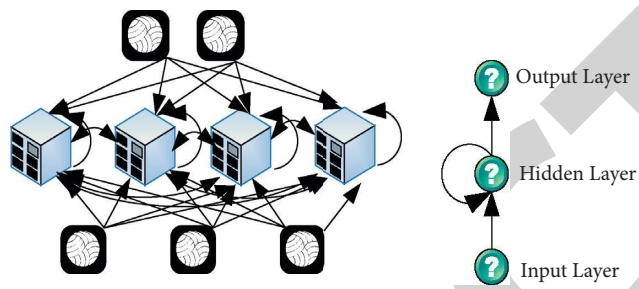

Figure 4: Schematic diagram of the middle-level structure of the RNN model.

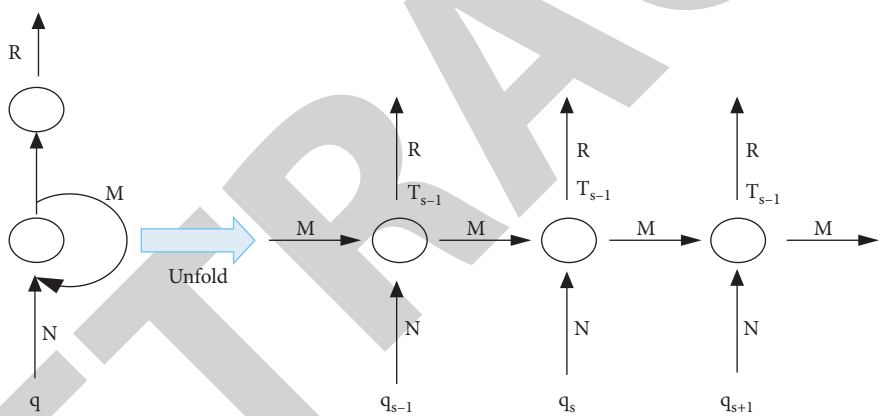

Figure 5: Schematic diagram of hidden layer expansion.

$$\frac{\alpha H_5}{\alpha M} = \frac{\alpha H_5}{\alpha c_5}\frac{\alpha c_5}{\alpha t_5}\frac{\alpha t_5}{\alpha M}. \tag{5}$$

At this time, it can be found that, in addition to M, t_5 and t_4 at the previous moment are also related. According to the equation $T_s = f(M \cdot T_{s-1} + N \cdot q_s)$, t_5 can be extended; namely,

$$\frac{\alpha H_5}{\alpha R} = \frac{\alpha H_5}{\alpha c_5}\frac{\alpha c_5}{\alpha R}. \tag{6}$$

The expansion of t_4 can be expressed as

$$\frac{\alpha t_4}{\alpha M} = \frac{\alpha t_4}{\alpha t_4}\cdot\frac{\alpha t_4^+}{\alpha M} + \frac{\alpha t_4}{\alpha t_3}\cdot\frac{\alpha t_3}{\alpha M}. \tag{7}$$

At this time, t_1 can be extended; namely,

$$\frac{\alpha t_1}{\alpha M} = \frac{\alpha t_1}{\alpha t_1}\cdot\frac{\alpha t_1^+}{\alpha M} + \frac{\alpha t_1}{\alpha t_0}\cdot\frac{\alpha t_0}{\alpha M}. \tag{8}$$

Integrate the three equations:

$$\frac{\alpha t_5}{\alpha M} = \sum_{r=1}^{5}\frac{\alpha t_5}{\alpha t_r}\cdot\frac{\alpha t_r^+}{\alpha M}. \tag{9}$$

We can get

$$\frac{\alpha h_5}{\alpha M} = \sum_{r=0}^{5}\frac{\alpha h_5}{\alpha c_5}\frac{\alpha c_5}{\alpha t_5}\frac{\alpha t_5}{\alpha t_r}\frac{\alpha^+ t_r}{\alpha M}. \tag{10}$$

Equation (9) can show that t_5's derivative M is not affected by t_4 and the update of N is similar to M. The expression equation is

$$\frac{\alpha H_5}{\alpha M} = \sum_{r=0}^{5}\frac{\alpha H_5}{\alpha c_5}\frac{\alpha c_5}{\alpha t_5}\frac{\alpha\left(M^{5-r}a_r\right)}{\alpha N}. \tag{11}$$

Finally, the update method of R is only related to the output 0, and the update equation expression of R is

$$\frac{\alpha H_5}{\alpha R} = \frac{\alpha H_5}{\alpha c_5} \cdot \frac{\alpha c_5}{\alpha R}. \tag{12}$$

2.3. Pooling Method of Convolutional Neural Network. In convolutional neural networks, pooling operations are usually used after convolution [17]. Through pooling, the feature vector output by the convolutional layer can be reduced, making it less prone to overfitting. As we all know, "static" is the biggest attribute of an image. In an image, the discriminative features of one area point are very likely to be applicable to other areas [18, 19]. Therefore, it appears to calculate the mean or maximum value of the features in a certain area of the image and use it to represent the features of the area. The following will introduce 4 common pooling methods.

(1) General pooling: it is mostly used where there is no overlap in a certain image, which is also different from the convolutional layer. In general, pooling each window is unique, and it can also be understood that the window size is the same as the step size [20].

(2) Average pooling: on the basis of general pooling, the average value of the area corresponding to the window needs to be calculated as the pooled value of the area [21].

(3) Max pooling: on the basis of general pooling, it is necessary to calculate the maximum value of the area corresponding to the window and use it to represent the pooling value of this area [22].

(4) Stochastic pooling: it is a simple and effective way to standardize CNN. It can reduce the overfitting of max pooling and improve the generalization ability. For the input of the pooling layer, based on the polynomial distribution of the input, a value is randomly selected as the output [23].

3. Volleyball Serve Experiment Based on Multilayer Features of Neural Network

Based on the improved human pose estimation technology, this chapter constructs a pose-based action evaluation index. And, based on this, a comparative analysis of volleyball serve moves, forming an automated method to compare and assess the quality of volleyball serve. It can provide valuable information for volleyball training [24]. This article selects 6 volleyball players as sample data. Under the mechanism of attention, attention in computer vision is to make the system learn to focus on the area of interest. On the one hand, neural networks with attention mechanisms can learn attention autonomously. On the other hand, the attention mechanism can help us understand the world that the neural network sees.

During data collection, the hardware part and the software part are required to cooperate to complete. The design of the hardware part is mainly the placement angle of the camera and the parameters of the camera body, and the software part defines the data collection interface. The base class camera of the data acquisition software interface provides five functions, which are used to detect the camera, set the camera ID, parameter setting, and display, and obtain continuous image output through the function outputtIng. The standard volleyball court is rectangular, with a length of 18 meters, a width of 9 meters, and a barrier-free area of at least 3 meters. The center line divides the field into two areas, each with an offensive line 3 meters from the center line. Suppose here that the volleyball player is doing serve training at the bottom line of the left area in the figure.

On the other hand, the attention mechanism can help us understand the world that the neural network sees [25, 26]. The design of the hardware part is mainly the placement angle of the camera and the parameters of the camera body, and the software part defines the data collection interface [27]. The base class camera of the data acquisition software interface provides five functions, which are used to detect the camera, set the camera ID, parameter setting, and display, and obtain continuous image output through the function outputting [28, 29]. In the process of video-based action alignment, it is not accurate to directly calculate the Euclidean distance between the joint points of the two poses. Here, we will extract the key features for the alignment of the pose sequence and then normalize the pose features [30].

3.1. Attitude Preprocessing

3.1.1. Joint Coordinate Processing. As shown in Figure 6, the joint points of the human skeleton posture, each node has its coordinates, temporarily represented by (A, B). Considering the characteristics of the body, the neck is the most stable part. We use the neck as the origin to recalculate the joint coordinates to solve the problem of inconsistent coordinates. The translation equation of the coordinate system is

$$\begin{aligned} A' &= A - bA, bA = A_0, \\ B' &= B - bB, = bB = B_0. \end{aligned} \tag{13}$$

In the equation, bA, bB represents the position offset of the origin of the coordinates in the directions of the A-axis and the B-axis. The offsets are equal to the A and B coordinates of the neck on Ao, Bo, respectively.

Depending on the resolution of the image, the length and body shape of each person's limbs will be different, and the style will be scaled in equal proportions, as shown in Figure 7.

3.2. Attitude Distance Calculation. In the process of video-based action alignment, it is not accurate to directly calculate the Euclidean distance between the joint points of the two poses. Here, we will extract the key features for the alignment of the pose sequence and then normalize the pose features. The smaller the characteristic distance between the two postures, the more similar the postures. Conversely, the larger the characteristic distance between the postures, the greater the posture difference. First, we convert each group of 17 key points into vectors and draw them all in a high-dimensional space:

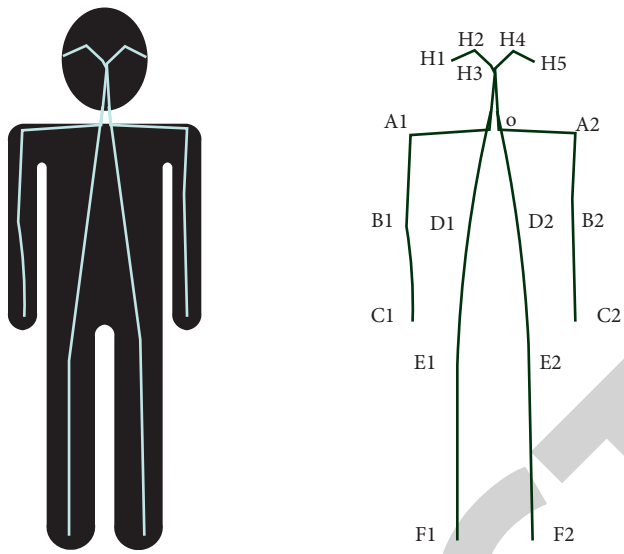

Figure 6: Schematic diagram of human posture skeleton.

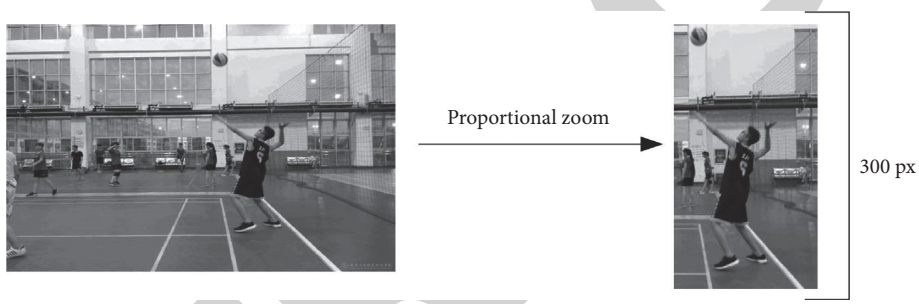

Figure 7: Pose proportional zoom.

$$Q = (A_1, A_2, \ldots, A_{17}, B_1, B_2, \ldots, B_{17})M = (m_1, m_2, \ldots .m_{34}), \tag{14}$$

Then, the similar measurement task of the two poses will be transformed into calculating the angle between the two vectors, and we use the cosine similarity to calculate the angle. However, based on the coordinate system centered on the neck, the direct cosine similarity calculation will encounter some problems. The main action is that when the athlete jumps to serve, there will be two steps before the jump, so the distance between the feet will be a good description of the athlete's moment. After the athlete jumps off the ground, the right arm will rotate vigorously before hitting the ball. The angle of the right arm is also an ideal feature.

Normalize the posture information:

$$\begin{aligned} norm(q)' &= \sqrt{A_1^2 + A_2^2 + \cdots + A_{17}^2 + B_1^2 + B_2^2 + \cdots B_{17}^2}, \\ A'' &= \frac{A'}{norm(q)'}, \\ B'' &= \frac{B'}{norm(q)'}. \end{aligned} \tag{15}$$

After recalculating the coordinates and normalizing the two skeleton vectors q_1 and q_2, using cosine to express the distance between the twois

$$Di(q1'', q2'') = \sqrt{2 \cdot (1 - conSim(q1'', q2''),} \tag{16}$$

Based on the problem of different confidence levels, the skeleton distance equation can be expressed as

$$Di(q1'', q2'') = \frac{1}{\sum_{r=1}^{34} Tr} \times \sum_{r=1}^{34} (q_{1r}'' - q_{2r}''), \tag{17}$$

3.3. The Trajectory and Function of the Throwing Arm. (1) Tossing time: the time it takes for the throwing arm to throw the ball up is the time to throw the ball. The longer the tossing time is, the longer the athlete can hit the ball, and it can give enough time for the body to push upwards.

(2) The height of the throwing arm from the ground: whether the throwing height is reasonable is a key link in the throwing technique. The height of the tossing arm plays a decisive role in the height of the tossing. Whether the height of the tossing is appropriate is the most important factor in whether the

Table 1: The height of the throwing arm from the ground and the height of the throwing ball after the ball leaves the hand.

Serial number	Height	Throwing arm high above the ground	Account for height (%)	Toss height
A	1.85	1.8	97.3	3.3
B	1.82	1.8	99.5	3.27
C	1.8	1.8	99.4	3.3
D	1.8	1.78	98.4	3.28
E	1.85	1.8	95.3	3.27
F	1.84	1.83	99.5	3.5
Average value	1.83	1.8	98.2	3.3

whole serving rhythm is reasonable. Therefore, it is also one of the key factors affecting the quality of serving.

For the convenience of registration, the professional athletes who collected the samples were drawn and sorted by letters from *A* to *F*, and then the height, throwing height, and arm height of the six athletes were detected, and the height and throwing height were calculated. The basic information of the detection is as follows:

The height of the throwing arm from the ground corresponds to the height of the throwing ball and the time of throwing the ball. The moment the ball is thrown away from the hand and the arm of the throwing ball is higher than the ground, the height of the throwing ball will be higher, and the throwing time will be longer. Since the height of the toss reflects the strength of the lower limbs and the rebound amplitude of the trunk back, it is a condition for striving for the height of the hitting point. Therefore, ensuring the height of the throwing arm from the ground is the basis for ensuring the throwing height and success rate, to ensure the space and time of the athlete's lower limbs. It can be seen from Table 1 that the height of the throwing arm from the ground accounts for 98% of the height on average. From an individual point of view, *F* athlete's throwing arm is the highest from the ground, accounting for 99.52% of the height, and the throwing height is also the highest. Although the height of *E* athlete's throwing arm from the ground is not the lowest, it accounts for the lowest percentage of height, accounting for 95.26% of the height. In Table 1, the throwing time used by *E* is the shortest.

(3) Analysis of the vertical movement trajectory of the throwing arm:

Figure 8 uses the vertical line as the standard to see if the athlete's throw is close to vertical. The vertical angles of *A*, *B*, and *C* of the experimental objects are small, less than 9° close to the vertical line, the thrown ball is vertical, and the throwing ball has high stability. The ball is close to vertical, which is helpful for the athlete to better judge the position of the ball and can ensure the stability of the athlete's next swing.

(4) The angles of the shoulder, elbow, and wrist joints of the throwing arm from the moment the ball leaves the hand to the highest point of the throwing ball are as follows.

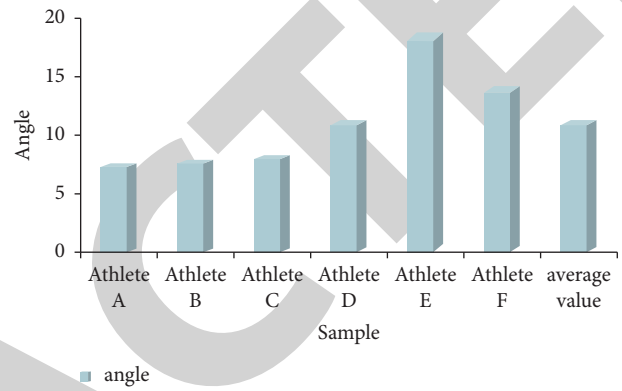

Figure 8: The angle of the perpendicular to the highest point of the toss.

Table 2: Changes in the angles of the shoulder, elbow, and wrist joints of the throwing arm from the ball to the highest point.

Serial number	Throw the ball away			Toss the ball to the highest point		
	Shoulder	Elbow	Wrist	Shoulder	Elbow	Wrist
A	108.9	163.4	171.1	156.5	169.5	212.7
B	113	162.1	171.4	158.6	170.7	219.1
C	110.9	159.4	171	151.7	167.6	214.7
D	96.7	158.1	169.3	149.1	169.3	189.5
E	96.7	154.1	167.3	141.3	158.7	187.3
F	100.3	153.6	170.3	150.2	155.4	188.6
Average value	104.4	158.4	170.1	151.2	165.2	202

For the athletes from *A* to *F*, the angles of the shoulder joint, elbow joint, and wrist joint are detected at the moment of throwing the ball and when the ball reaches the highest point. The results are as follows:

The throwing arm should be fully extended during the upward throwing process, and there should be no elbow flexion, throwing, or forceful throwing action with the fingers backwards. Toss the ball according to the reasonable trajectory of the throwing arm and the correct angles of the shoulder, elbow, and wrist joints to ensure that the trajectory of the throwing ball is relatively stable. Keeping the throwing arm extending upward and forward is helpful to judge the position of the hitting point, and it is easy to achieve the purpose of precise control of the throwing ball. Table 2 and Figure 8 show that the elbow joints of the

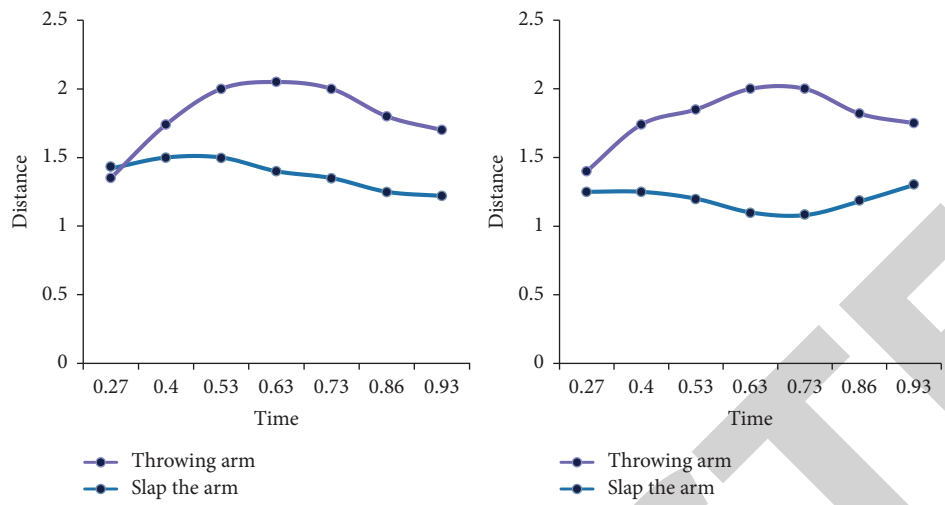

Figure 9: The trajectory of the two arms in the process of throwing the ball.

experimental subjects' shoulder joints, elbow joints, and wrist joints are relatively stable during the ball throwing process. The angle of the wrist joint increased from close to 180 degrees to more than 180 degrees, and the shoulder joint increased from 100.3 to 150.2 degrees at the moment of leaving the hand. In the process of throwing the ball, the main movement of the throwing arm is an upward movement driven by the shoulder joint. From the analytical data, it can be seen that the shoulder and elbow joints of the throwing arm of the athlete are not straight when throwing the ball away from the hand and the average is about 150.2° and 155.4°. The closer the shoulder and elbow joints are to 180°, the more stable the ball will be. Failure to meet the standard will result in low ball stability. The elbow joint of the experimental subject has a small change of 6.8°, and the wrist joint has a larger change, with a change of 32°. This shows that the subject's elbow joint is relatively stable and the wrist joint movement is large, which will affect the stability of the throwing ball.

(5) Tossing rhythm during the tossing stage: because the individual differences of athletes, the height, height of the tossing, and personal habits are not used, there is a slight difference in the rhythm of the tossing of the athletes. However, generally speaking, the tossing rhythm in the serve action is composed of slow to fast and balanced force.

It can be seen from Figure 9 that the data of both arms have a downward trend. As the tossing arm lifts the ball, the batting arm directly charges backwards to do elbow bend and shoulder-sinking movements, and the body's center of gravity also shifts forward and downwards as the tossing arm lifts. Therefore, the height of the arms has also decreased. The throwing arm first starts to throw the ball upwards and then holds the racket arm directly back to accumulate energy, forming a posture of accumulating energy. The throwing arm increased from 1.4 meters to 1.75 meters, showing a downward trend from 0.73 to 0.93 seconds, while the batting arm did not change significantly. It grew from 1.25 meters to 1.3 meters and began to show a downward trend at 0.64 seconds. 0.53 seconds is the moment the ball leaves the hand. At this stage, the racket arm starts to draw the racket, and the data shows a downward trend.

4. Volleyball Arm Trajectory Based on Neural Network

4.1. The Arm Trajectory during the Hitting Stage. The swinging and hitting stage is the main stage of force in the serve. All techniques in the throwing stage are to be able to hit the ball better during the swinging and hitting stage and deliver a high-quality ball.

The functions of the nonhitting arm are as follows: to ensure the stability of the toss during the serve, to assist the force when jumping the serve and spiking; to increase the means of attack, to maintain the balance and support of the body, and so on. Through the comparison of the pictures, it can be seen that the input action is consistent with the body curve baseline of the standard action, but the waist and legs do not exert backward force, and the waist strength is insufficient, which affects the hitting force.

As shown in Figures 10 and 11, when the ball rises to the highest point, the angle of the arm and shoulder joint of the throwing ball is about 148 degrees, and the body presents the state of top hip. The joint angle of the throwing arm is 148, and the joint angle of the slap arm is 79. The transition from the action to the next action is that the articulation of the throwing arm shows a downward trend, while the batting arm shows an upward trend, forming a kind of angular balance between the two arms. On the whole, the balance formed by the two can keep the volleyball player's body in balance. The throwing arm assists the batting arm in the process of hitting the ball upwards.

Combining Table 3 and Figure 12, when the ball is removed from the hand, the shoulder joint of the throwing arm is higher than the shoulder joint of the slap arm, the shoulder joint of the throwing arm is 0.34

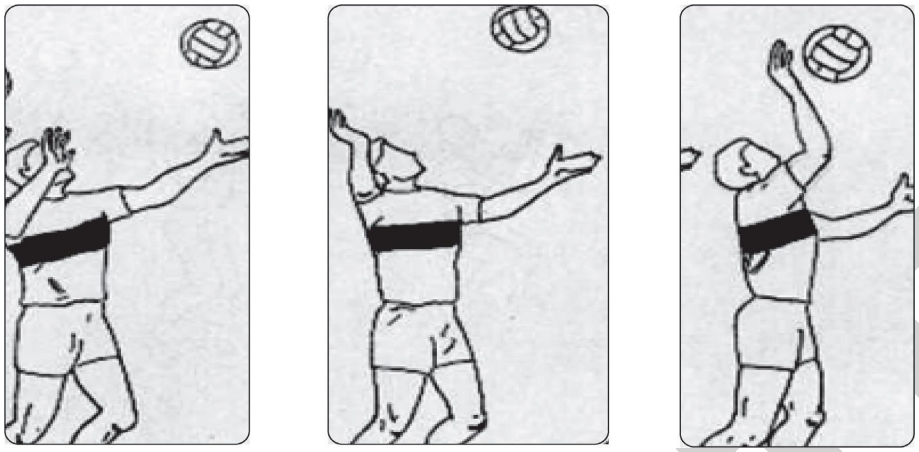

Figure 10: Schematic diagram of serving action.

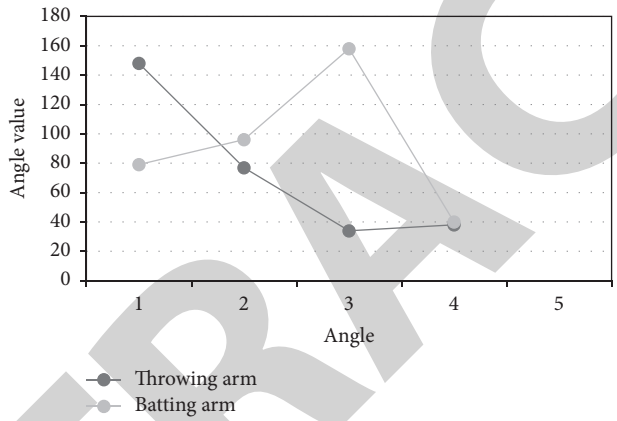

Figure 11: The relationship between the angle changes of the shoulders.

Table 3: The distance between the shoulder joint of the slap arm and the horizontal line.

Serial number	Ball off hand	The highest point of the toss	Back scratching	Hitting moment	End of action
A	0.42	0.69	0.35	0.19	0.5
B	0.4	0.75	0.25	0.1	0.57
C	0.44	0.8	0.29	0.21	0.46
D	0.46	0.85	0.26	0.23	0.46
E	0.36	0.66	0.26	0.1	0.38
F	0.34	0.91	0.27	0.1	0.48
Average value	0.4	0.77	0.28	0.14	0.48

meters, and the shoulder joint of the slap arm is 0.40 meters; the difference is not big. On the same level, the shoulder joint of the throwing arm is closer to the horizontal line. At this time, the function of the throwing arm is mainly to throw the ball upwards. When the ball is tossed to the highest point, the shoulder joint of the throwing arm is still higher than the shoulder joint of the slap arm, the shoulder joint of the throwing arm is 0.5 meters, and the shoulder joint of the batting arm is 0.8 meters; the difference is large. It forms a posture where the tossing arm shoulder joint is holding the racquet arm shoulder joint, the tossing arm shoulder joint is closer to the horizontal line, and the slap arm shoulder joint is minimized. At this time, the function of the throwing arm is to fully extend backwards, creating conditions for the top hip movement, and to make the slap arm the lowest point of the power reserve before hitting the ball. At the end of the final action, the shoulder joint of the throwing arm and the shoulder joint of the slap arm are almost back to the same level. The shoulder joint of the throwing arm is 0.4 meters, and the shoulder joint of the hitting arm is 0.5 meters. In the whole serving action, the tossing arm shoulder joint and the slap arm shoulder joints complete each stage of the action in this one-up and one-down sequence. The shoulder joints of both arms are balanced and hard, and the throwing arm plays a role in balancing the body, driving the rhythm, and assisting the force at all stages.

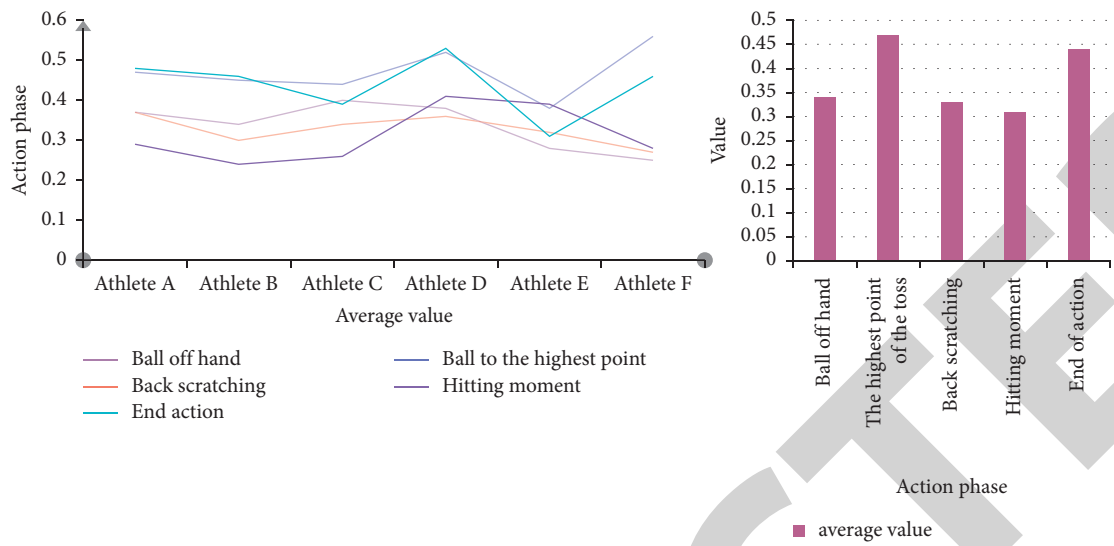

Figure 12: The distance between the shoulder joint of the throwing arm and the horizontal line.

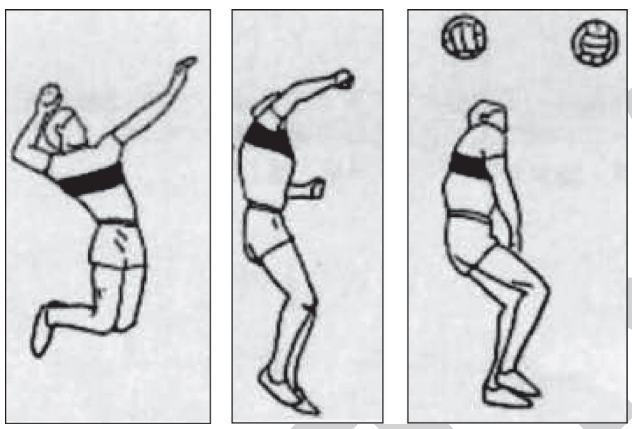

Figure 13: The trajectory diagram of the arm of the crank arm type ending action.

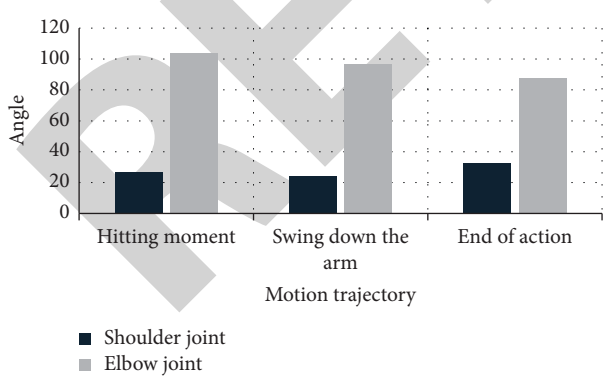

Figure 14: The angle of the lower shoulder and elbow changes at the end of the crank arm.

4.2. The Arm Trajectory of the Crank Arm End Action

4.2.1. Trajectory of the Throwing Arm at the End of the Crank Arm. For example, Figure 13 is a diagram of the arm's trajectory and action at the end of the crank arm, and Figure 14 is a diagram of the angle changes of the shoulder and elbow joints of the throwing arm. It can be seen from Figure 14 that, at the end of the action, the two trajectory lines overlap at the end of the trajectory. Because it is a curved arm ending action, the throwing arm remains at the abdomen position after the hit. From the action diagram in Figure 13, the tossing arm of the curved arm ending action is retracted to the abdomen position after the ball is hit, mainly to assist the torso in the abdomen movement. From Figure 14, there is a slight downward trend in the elbow joint, from 104 at the moment of hitting to 97° at the end of the action, and the change is not obvious. There is no obvious change in the shoulder joint from the moment of hitting the ball to the lowering of the ball. There is a slight upward trend in the process from the hand down to the end of the action, from the downward swing of 24° to 33° at the end of the action. The data shows that, from the time the ball is shot to the end of the action, there is no obvious change in the shoulder and elbow joints, the angle remains stable, and the trajectory of the movement is also stable. It is good for keeping the balance of the body after the abdomen is closed and the action is over.

4.2.2. The Function of the Throwing Arm of the Crank Arm Type Ending Action

(1) Auxiliary Force. As shown in Figure 15, from the angle changes of the shoulder and elbow joints of the throwing arm, after the moment of hitting the ball, it is the process of the ball flying forward and the shooting arm moving forward and downward. At this time, the torso is continuing to rotate and move the upper body forward and downward, and the angular velocity of the shoulder and elbow joints has increased significantly. It shows that the shoulder and elbow joints of the tossing arm can play the role of assisting force in the process of pressing the arm downwards after hitting the ball, mainly assisting the forward and downward force of the slap arm.

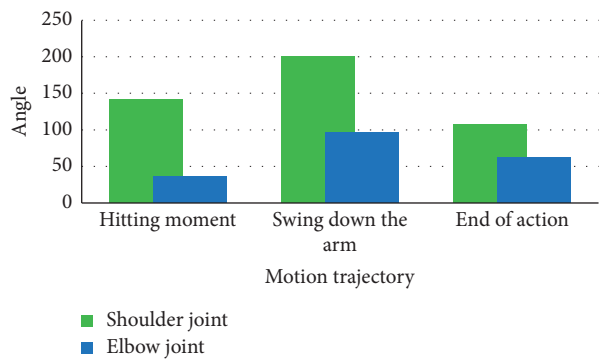

Figure 15: Angle changes of the shoulder and elbow joints at the end of the crank arm.

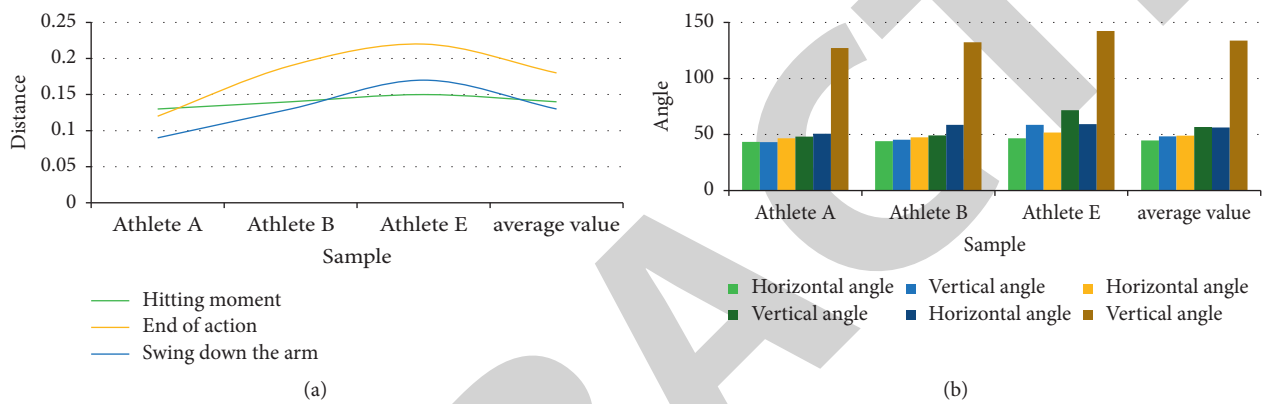

Figure 16: The distance between the forearm and the body and the angle of the horizontal vertical line at the end of the bent arm.

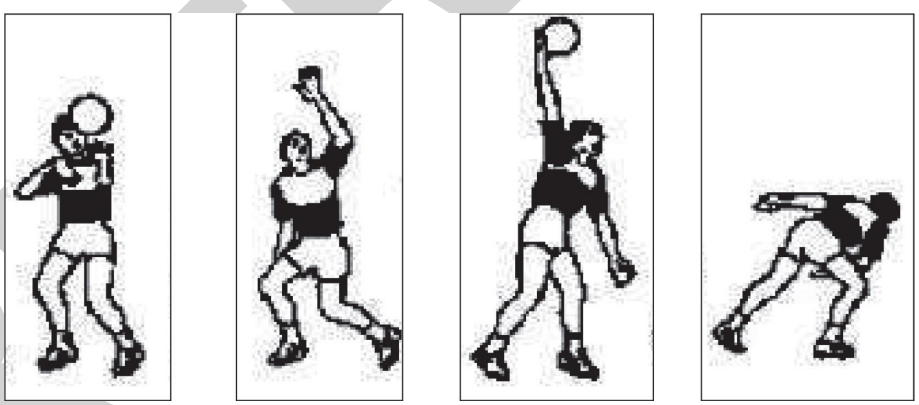

Figure 17: The arm movement trajectory of the back swing and action hitting the ball.

(2) Auxiliary Torso Rotation and Abdomen Function. Figure 16(a) shows the schematic diagram of the distance from the forearm to the body. From the perspective of the overall direction, the forearm is closer to the body at the end of the curved arm action, and the distance between the forearm and the body at the moment of hitting and the end of the action is 0.14 m and 0.18 m. It shows that, from the moment of hitting the ball to the end of the action, the distance from the forearm to the body does not change much and it is closer to the body. As shown in Figure 16(b), the horizontal angle of the forearm does not change much at the end of the crank arm, but the vertical angle is gradually increasing. Combining with the trajectory of the arm when throwing the ball, the angle of the forearm close to the abdomen, shoulder, and elbow joints and the increase in speed in the curved arm ending action are all conducive to the downward pressure of the trunk and the racket arm after the ball is hit. The closer the forearm is to the body, the more it can bend the arm, speeding up the torso and reducing the abdomen. Generally speaking, when the arm of the throwing ball is closer to the abdomen, the horizontal angle is stable, and the vertical angle increases. The increase in angular velocity is conducive to the abdomen movement of the trunk and assists the turning and pressing of the body's center of gravity to complete the final ending movement.

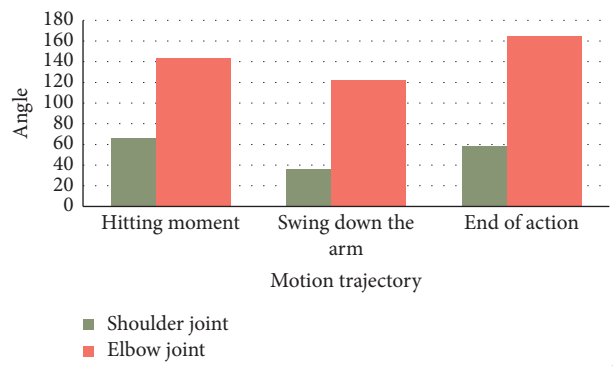

Figure 18: The angle changes of the shoulder and elbow joints at the end of the back swing.

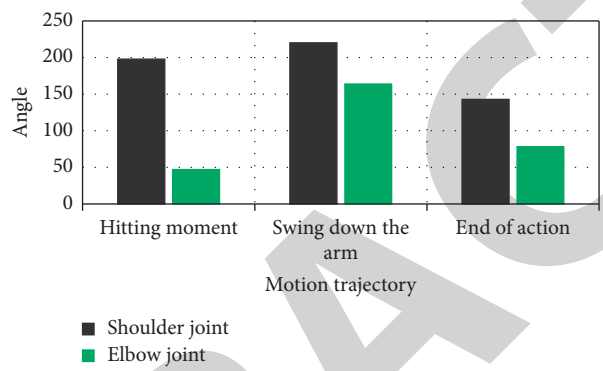

Figure 19: Angle changes of the shoulder and elbow joints of the throwing arm.

4.3. The Running Trajectory of the End Action Arm

4.3.1. Trajectory of the Throwing Arm at the End of the Backward Swing. Figure 17 shows the trajectory of the arm movement at the end of the back swing, from the moment of hitting the ball to the end of the movement, and the gap between the two increases in segments. The data shows that when the arm is pressed down after the ball is hit, the shoulder and elbow joints of the throwing arm that end the swing in the back swing can also play an auxiliary force role. It can be seen from Figure 18 that the angles of the shoulder and elbow joints of the back swing type are greater than the angles of the shoulder and elbow joints at the end of the curved arm type. The data shows that the angle of the elbow joint has a downward trend from the moment of hitting the ball to the downward swing, from 144° to 122°. And when the batting arm swings forward and down at the end of the action, there is a significant upward trend, from the 122° downward rise of the batting arm to 165° at the end of the action; the change is more obvious.

4.3.2. The Function of the Throwing Arm of the Back Swing End Action

(1) The Role of Auxiliary Forces. Figure 19 shows the angle change diagram of the shoulder joint and elbow joint of the throwing arm. The change values of the shoulder and elbow joints of the back swing type ending movement are greater than the change values of the crank arm type ending movement. The data shows that when the arm is pressed down after the shot, the shoulder and elbow joints of the throwing arm that end the swing back swing can also play an auxiliary force.

(2) The Role of Auxiliary Rotation. As shown in Figure 20(a), as a whole, the forearm is far away from the body, and the distance at the moment of hitting the ball and the distance at the end of the action are 0.34 m and 0.45 m, respectively. As shown in Figure 20(b), in the finishing action of the back swing, the forearm of the throwing arm has a relatively high degree of change in the horizontal and vertical angles, showing a more obvious undulating state. During the time the ball is flying away from the hand, the arm gradually moves backward, and the vertical angle between the forearm and the body is close to 180 degrees.

Through the data statistics of the appeal, the two ending actions are compared. Comparing these two ending actions, the throwing arm in the first type of curved arm ending action can play a more important role in assisting the force. The main reason is that the throwing arm of the curved arm ending action is closer to the abdomen of the body, the angle of the shoulder and elbow joints of the throwing arm is smaller, and the angle change with the horizontal and vertical lines is small. These are conducive to the depression of the torso and can assist the force and complete the serve action. Although the ending action of the second back swing has the effect of assisting the body to press down, because the throwing arm is far from the body, the angle of the shoulder

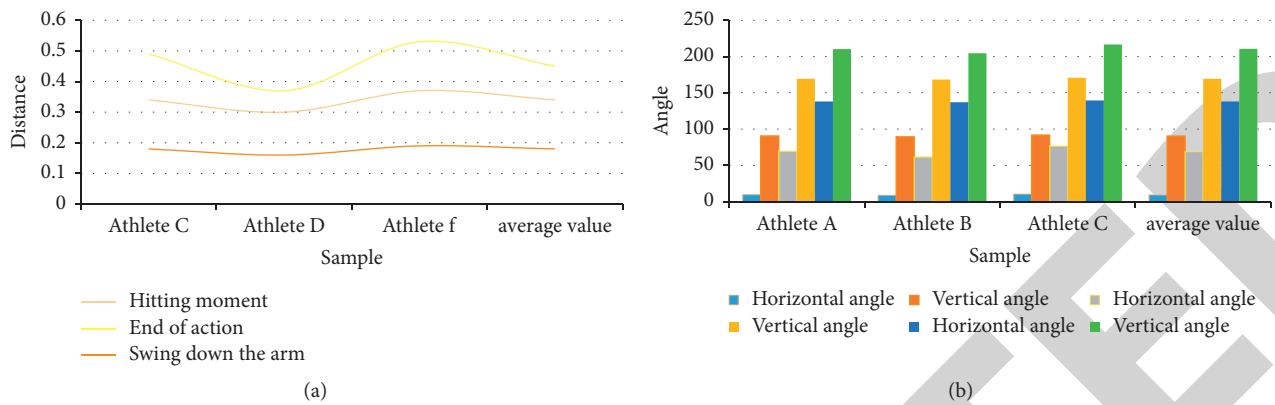

(a) (b)

Figure 20: The distance between the forearm and the body and the angle of the horizontal and vertical lines at the end of the back swing.

Table 4: Comparison of recognition degrees of different algorithms.

Method	Single person behavior recognition (%)	Group behavior recognition (%)
Algorithm	85.8	83.8
Two-stage Hierarchical Model	81.9	—
CERN	83.3	69
Social Scene	83.8	81
Hierarchical LSTM	70.3	—

joint and the elbow joint of the throwing arm is larger. The angle changes of the horizontal and vertical lines are also large, and the effect is not as good as the crank arm type. In addition, the trajectory of the throwing arm of the swing back ending action tends to swing backwards by a large margin when the action is about to end. Although it is conducive to body rotation, it is not conducive to maintaining balance and will cause excessive rotation. The trajectory of the throwing arm of the crank arm ending action swings back slightly. That is to say, it can assist in turning and pressing down, and it can also maintain the balance of the body in the process of turning and prevent excessive turning.

As shown in Table 4, under the condition of the same dataset and two tasks being evaluated at the same time, the accuracy rate of the algorithm in this paper reaches 85.8% in group recognition and 83.8% in single person recognition. All are significantly higher than Two-stage Hierarchical Model, CERN, Social Scene, Hierarchical LSTM, and other algorithms. The experimental results show that the use of attention mechanism helps to better enhance the feature representation and greatly improves the recognition accuracy and its effectiveness is verified.

5. Conclusion

The running trajectory of the throwing arm is divided into two different running trajectories: the crank arm type and the back swing type. Comparing the two running trajectories, the curved arm running trajectory has a small radian and is close to vertical, and the throwing of the ball is relatively stable, which is conducive to the movement of the trunk and abdomen. The back swing type has a large arc; during the flight of the ball, the forearm of the throwing arm begins to swing to the left and rear of the body. The angle between the forearm and the vertical was almost 180°, and the angle between the forearm and the vertical line increased from 90° to more than 180°. At the end of the action, the throwing arm is straight behind the left side of the body and the throw is unstable, which will cause excessive rotation. The throwing arm is 98% of the height above the ground. The horizontal angle of the throwing arm at the moment the ball leaves the hand is positively correlated with the throwing time and height. The reasonable running trajectory has an impact on the stability of the throwing ball. The closer the trajectory of the tossing arm is to the vertical, the more stable the tossing is. Crank arm ending action has a more positive effect on serve than the back swing ending action. The distance between the forearm and the body at the end of the movement is 0.18 meters, with a minimum of 0.12 meters and a maximum of 0.22 meters. The overall look is very close to the body, close to the abdomen. The bent arm style is closer to the abdomen, which is good for the torso to press down and play a role in assisting the force. The back swing is far from the abdomen, which is conducive to torso rotation, but too much swing back will cause excessive rotation. It is necessary to pay attention to the importance of the throwing arm trajectory, and practice according to the reasonable trajectory of the throwing arm. In this way, the stability of the throwing ball is strengthened, the drop of the throwing ball is reduced, and the time of scratching the ball is shortened. By strengthening the stability of the upward throwing trajectory of the throwing arm, the arc is reduced, the ball is closer to the vertical, and the stability of the throwing ball is increased. When throwing the ball, pay

attention to the angle of the throwing arm to be close to 45 degrees. Increasing the angle of the joints of the throwing arm when throwing the ball upwards, the angle between the high point and the vertical line of the ball is close to perpendicular. In the future, tossing the ball, the elbow joints, wrist joints of the tossing arm, and the movement trajectory of the tossing arm should be kept fixed. And it ensures that the height of the arm of the throwing ball is the same as the height at the moment the ball is thrown away from the hand, which increases the control distance of the ball [25–30].

Data Availability

All the data used are included within the article.

Conflicts of Interest

The authors declare that they have no conflicts of interest.

References

[1] X. Dai and S. Li, "Volleyball data analysis system and method based on machine learning," *Wireless Communications and Mobile Computing*, vol. 2021, pp. 1–11, 2021.

[2] J. Zhang, C. Wu, and Q. Zhou, "Bolt-shaped triboelectric nanogenerator for rock-climbing training trajectory detection," *IEEE Sensors Journal*, vol. 21, no. 3, pp. 2693–2701, 2021.

[3] I. G. Shevtsova, A. A. Navolotskii, N. A. Eremich, and M. P. Shestakov, "Way of assessing an athlete's upright posture control while performing tracking movements," *Moscow University Computational Mathematics and Cybernetics*, vol. 44, no. 4, pp. 203–217, 2020.

[4] A. G. Melo, M. F. Pinto, A. L. M. Marcato, I. Z. Biundini, and N. M. S. Rocha, "Low-cost trajectory-based ball detection for impact indication and recording," *Journal of Control, Automation and Electrical Systems*, vol. 32, no. 2, pp. 367–377, 2021.

[5] W. Liu, L. Cheng, Z. G. Hou, J. Yu, and M. Tan, "An inversion-free predictive controller for piezoelectric actuators based on a dynamic linearized neural network model," *IEEE-ASME TRANSACTIONS ON MECHATRONICS*, vol. 21, no. 1, pp. 214–226, 2016.

[6] M. Y. Nikitin, V. S. Konushin, and A. S. Konushin, "Neural network model for video-based face recognition with frame quality assessment," *National Research University, Higher School of Economics*, vol. 41, no. 5, pp. 732–742, 2017.

[7] B. Kasap and A. V. Opstal, "A spiking neural network model of the midbrain superior colliculus that generates saccadic motor commands," *Biological Cybernetics*, vol. 111, no. 3-4, pp. 249–268, 2017.

[8] K. B. Yong, Y. Yoon, and W. M. Jin, "Development of artificial neural network model for predicting the optimal setback application of the heating systems," *Kieae Journal*, vol. 16, no. 3, pp. 89–94, 2016.

[9] M. G. Kim, H. Ko, and S. B. Pan, "A study on user recognition using 2d ecg based on an ensemble of deep convolutional neural networks," *Journal of Ambient Intelligence and Humanized Computing*, vol. 11, no. 2, pp. 1859–1867, 2020.

[10] N. M. Ramli, M. A. Hussain, and B. M. Jan, "Multivariable control of a debutanizer column using equation-based artificial neural network model inverse control strategy," *Neurocomputing*, vol. 194, no. jun.19, pp. 135–150, 2016.

[11] Y. Li, "Research on sports video image analysis based on the fuzzy clustering algorithm," *Wireless Communications and Mobile Computing*, vol. 2021, pp. 1–8, 2021.

[12] C.-H. Chen, F. Song, F.-J. Hwang, and L. Wu, "A probability density function generator based on neural networks," *Physica A: Statistical Mechanics and Its Applications*, vol. 541, Article ID 123344, 2020.

[13] B. Grandjean and M. A. Maier, "Emergence of gamma motor activity in an artificial neural network model of the corticospinal system," *Journal of Computational Neuroscience*, vol. 42, no. 1, pp. 53–70, 2017.

[14] T. S. Pedersen, K. M. Nielsen, J. Hindsborg, P. Reichwald, K. Vinther, and R. Izadi-Zamanabadi, "Predictive functional control of superheat in a refrigeration system using a neural network model," *IFAC-PapersOnLine*, vol. 50, no. 1, pp. 43–48, 2017.

[15] J. S. Rath, P. H. Hutton, L. Chen, and S. B. Roy, "A hybrid empirical Bayesian artificial neural network model of salinity in the San Francisco Bay-Delta estuary," *Environmental Modelling & Software*, vol. 93, no. Jul, pp. 193–208, 2017.

[16] S. K. Park, H. J. Moon, K. C. Min, C. Hwang, and S. Kim, "Application of a multiple linear regression and an artificial neural network model for the heating performance analysis and hourly prediction of a large-scale ground source heat pump system," *Energy and Buildings*, vol. 165, no. apr, pp. 206–215, 2018.

[17] M. Adil, M. K. Khan, M. Jamjoom, and A. Farouk, "MHADBOR: AI-enabled administrative distance based opportunistic load balancing scheme for an agriculture internet of things network," *IEEE Micro*, vol. 2021, p. 1, 2021.

[18] A. Parziale, R. Senatore, and A. Marcelli, "Exploring speed–accuracy tradeoff in reaching movements: a neuro-computational model," *Neural Computing & Applications*, vol. 32, pp. 13377–13403, 2020.

[19] F. Zhu, C. Zhang, Z. Zheng, and A. Farouk, "Practical network coding technologies and softwarization in wireless networks," *IEEE Internet of Things Journal*, vol. 8, no. 7, pp. 5211–5218, 2021.

[20] M. Elhoseny, G. Ramírez-González, O. M. Abu-Elnasr, S. A. Shawkat, N. Arunkumar, and A. Farouk, "Secure medical data transmission model for IoT-based healthcare systems," *Ieee Access*, vol. 6, pp. 20596–20608, 2018.

[21] B. Shin, C. Kim, J. Kim, S. Lee, C. Kee, and T. Lee, "Motion recognition-based 3D pedestrian navigation system using smartphone," *IEEE Sensors Journal*, vol. 16, no. 18, pp. 6977–6989, 2016.

[22] A. E. F. Da Gama, T. M. de Chaves, P. Fallavollita, L. S. Figueiredo, and V. Teichrieb, "Rehabilitation motion recognition based on the international biomechanical standards," *Expert Systems with Applications*, vol. 116, no. FEB, pp. 396–409, 2019.

[23] M. Balazia and K. N. Plataniotis, "Human gait recognition from motion capture data in signature poses," *ACM Transactions on Multimedia Computing, Communications, and Applications*, vol. 14, no. 2, pp. 129–137, 2016.

[24] T. Hachaj, M. R. Ogiela, and K. Koptyra, "Human actions recognition from motion capture recordings using signal resampling and pattern recognition methods," *Annals of Operations Research*, vol. 265, no. 2, pp. 1–17, 2016.

[25] F. Hammo, "A comparative study of some (kinematics) variables between the loope drive of top spin style by forehand and backhand of the racket in the table tennis," *Al-Rafidain Journal For Sport Sciences*, vol. 21, no. 67, pp. 293–310, 2019.

[26] P. Fassina, G. Q. Nunes, F. S. Adami, M. I. Goettert, and C. F. V. de Souza, "Importance of cheese whey processing:

Hindawi
Journal of Healthcare Engineering
Volume 2023, Article ID 9807545, 1 page
https://doi.org/10.1155/2023/9807545

Retraction

Retracted: Analysis of the Model for Sports Enhancing Human Health Using Data Mining

Journal of Healthcare Engineering

Received 10 October 2023; Accepted 10 October 2023; Published 11 October 2023

This article has been retracted by Hindawi following an investigation undertaken by the publisher [1]. This investigation has uncovered evidence of one or more of the following indicators of systematic manipulation of the publication process:

(1) Discrepancies in scope
(2) Discrepancies in the description of the research reported
(3) Discrepancies between the availability of data and the research described
(4) Inappropriate citations
(5) Incoherent, meaningless and/or irrelevant content included in the article
(6) Peer-review manipulation

The presence of these indicators undermines our confidence in the integrity of the article's content and we cannot, therefore, vouch for its reliability. Please note that this notice is intended solely to alert readers that the content of this article is unreliable. We have not investigated whether authors were aware of or involved in the systematic manipulation of the publication process.

In addition, our investigation has also shown that one or more of the following human-subject reporting requirements has not been met in this article: ethical approval by an Institutional Review Board (IRB) committee or equivalent, patient/participant consent to participate, and/or agreement to publish patient/participant details (where relevant).

Wiley and Hindawi regrets that the usual quality checks did not identify these issues before publication and have since put additional measures in place to safeguard research integrity.

We wish to credit our own Research Integrity and Research Publishing teams and anonymous and named external researchers and research integrity experts for contributing to this investigation.

The corresponding author, as the representative of all authors, has been given the opportunity to register their agreement or disagreement to this retraction. We have kept a record of any response received.

References

[1] R. Wang and L. Han, "Analysis of the Model for Sports Enhancing Human Health Using Data Mining," *Journal of Healthcare Engineering*, vol. 2022, Article ID 3416255, 9 pages, 2022.

Hindawi
Journal of Healthcare Engineering
Volume 2022, Article ID 3416255, 9 pages
https://doi.org/10.1155/2022/3416255

Research Article

Analysis of the Model for Sports Enhancing Human Health Using Data Mining

Ruiqing Wang[1] and Lei Han[2]

[1]*School of Physical Education, Harbin University, Harbin 150086, China*
[2]*School of Environmental and Chemical Engineering, Dalian Jiaotong University, Dalian 116028, China*

Correspondence should be addressed to Lei Han; hl@djtu.edu.cn

Received 3 January 2022; Accepted 26 January 2022; Published 11 February 2022

Academic Editor: Alireza Souri

The problems of low reliability and the high fitting degree of mutual information feature extraction of traditional sports to human health enhancement model are analyzed. We analyze and study the sports to human health enhancement model using data mining. The model consists of a data layer, a logic layer, and a presentation layer. Sports project data, real-time sports data, and health monitoring data are collected in the data layer, and the collected data are transmitted to the logic layer. The logical layer uses the dynamic difference feature classification algorithm of data mining to fuse human health data, extract the mutual information features of human health, and input the features into the long short-term memory (LSTM) neural network, which outputs the pattern recognition results of sports health after forward and reverse operations. The results of sports health pattern recognition are input into the display layer, and the enhancing effect of sports on human health is presented for users by constructing a model of sports on human health. The results show that the effect of sports on human health enhancement analyzed by the model in this paper is extremely accurate, which can significantly improve the health level of community residents and college students. When the number of data is about 600, it remains at about 0.05, indicating that this model has high reliability, and the fitting degree of mutual information feature extraction is up to 99.82%. It has certain practical application value.

1. Introduction

Obese people have a higher incidence of hypertension, arteriosclerosis, and osteoporosis. Therefore, more and more people pay attention to their health. Kenneth Cooper, an American expert, put forward that as long as you participate in sports, you will benefit, and sports are additives to human health. As early as in the BC period, Aristotle also proposed the idea of "life lies in movements." Many sports health concepts and living habits promote people to exercise more and more. However, different exercise intensities and exercise modes can enhance human health at varying degrees. At present, there is no reasonable evaluation system or model to evaluate such problems, so that people do not fully understand the relationship between exercise and health, and it is a long-term and continuous process for exercise to enhance human health, during which people cannot grasp the health enhancement effect of current kinds of exercise in time, which is easy to make the sports population lose their self-restraint on exercise. In the face of the above situation, Islam and Alajlan [1] designed a human health recognition model, analyzed the impact of sports on human health enhancement by analyzing the distance of aligning heartbeat within individuals and measuring the recognition ability of human health with different alignment methods, and obtained relevant analysis results. Baqueri et al. [2] established the exercise schedule of relevant research objects by simulating residents' travel and activities outside the study area, preprocessed all data with fees, and analyzed high-intensity tourism activities with relevant data to achieve the effect of human health enhancement. Parmezan Bonidia et al. [3] tested whether there were differences in exercise variability and complexity only above exercise intensity during running and whether exercise would increase running speed and neuromuscular fatigue. Combined with the analysis results and human physiological parameters, they constructed a

model of sports enhancing human health and obtained relevant analysis results. Chen [4] studied the impact model of physical training on physical health. The model integrates sports training and diet management. Using the model, we can obtain such information as to whether people's current diet is reasonable and the impact of sports training intensity on their health. Zheng and Haifeng [5] studied the model of the effect of exercise with the same intensity on the amount of abdominal visceral fat, which can be used to obtain the changes of human visceral fat at different exercise intensities.

In the process of sports, the human body can produce a large amount of various data [6, 7], which makes the subsequent data analysis more difficult. Therefore, a model and analysis method of sports on human health enhancement is designed in this paper based on data mining. The main contributions of this paper are as follows: (1) Data mining is an algorithm that mines available information from a large amount of data. It is the most commonly used algorithm in machine learning algorithms. Using this algorithm can improve mining efficiency and accuracy. (2) The dynamic difference feature classification algorithm in data mining is used to fuse human health data, extract human health mutual information features, and input the feature into the LSTM neural network. The neural network outputs the results of motion health pattern recognition after forward and reverse operations, so as to improve the recognition accuracy. (3) The results of sports health pattern recognition are input into the display layer. Through constructing the model of sports on human health enhancement, the effect of sports on human health enhancement is presented to users, the visualization of relevant information is realized, and the impact results of their current sports behavior on their health enhancement are provided.

2. Methodology

2.1. Structure of Sports on Human Health Enhancement Model. According to the hierarchical concept, a model of sports on human health enhancement based on data mining is designed, as shown in Figure 1.

According to Figure 1, the human health enhancement model of sports based on data mining is composed of a data layer, a logic layer, and a display layer. The data layer is used to obtain the human body's sports project data, sports real-time data, and health monitoring data, and the above data are transmitted to the logic layer [8, 9]. The logic layer is used to extract the mutual information features of the human body's exercise data and health data. After sports health pattern recognition and logical calculation of sports intensity, the relevant calculation results are input into the display layer to provide users with sports project management, sports intensity viewing, sports health mode, and other information, so that users can fully understand the health enhancement effect of current sports.

2.2. Extraction of Features of Human Health Mutual Information. During exercise, the human body will produce a large number of health data, such as current pulse beat, blood circulation times, changes in body water, and fat

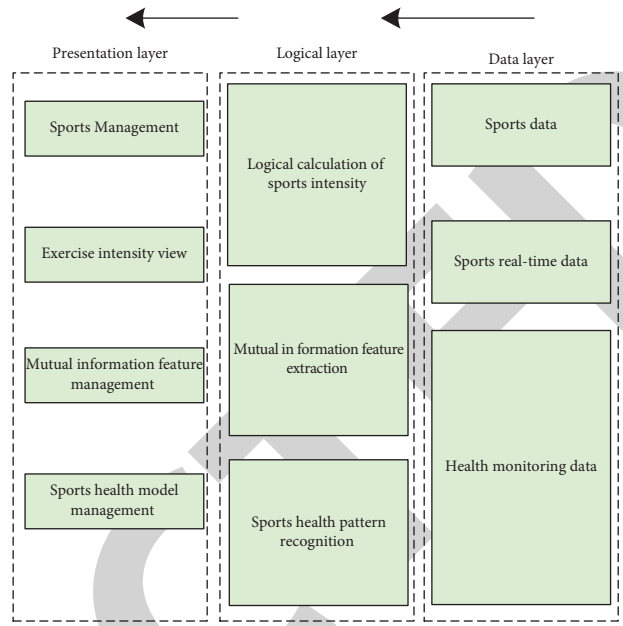

Figure 1: Structure of sports on the human health enhancement model.

[10, 11]. Their data sources are different, and their preservation formats are also different, forming a multisource heterogeneous complex data source. In order to extract useful health data from complex data sources, the dynamic difference feature classification method in data mining is used to fuse multisource heterogeneous human health data and extract human health mutual information features. The detailed process is as follows.

Let the scalar time series of human health data be $o = [\cdots, o_i, \cdots, o_j^i, \cdots]^T \in R^{nN}$, and the dynamic difference feature classification method is used to decompose the scalar time series in the windowed time domain. The expression equation is as follows:

$$o(t) = \iint_{a,b} \rho(a,b) \frac{da\ db}{\sqrt{|a|} * a^2} \frac{f(t-b)}{f(t)}, \tag{1}$$

where $f(\bullet)$ refers to transient sampling value at sampling time; $\rho(a,b)$ refers to the joint distribution state of mutual information of human health data; a and b refer to matching parameters and frequency-domain decomposition spectrum; and t refers to the time.

Fuzzy control is applied to the time-domain sequence in the windowed area of equation (1) to mine the feature vector of human health data, and the state function expression equation of the feature vector is as follows:

$$o_i' = \min\{f_i(o_i, u_i) D(o_i)\}, \tag{2}$$

where o_i refers to the vector of human health data distribution state, u_i refers to weight input vector, and $D(o_i)$ refers to eigenvector distribution distance.

The fuzzy clustering algorithm is used to cluster the time series mean of the results of equation (2) to obtain the linear average time series of human health data. The expression equation is as follows:

$$\langle o(n)\rangle = \frac{\sum_{n=1}^{N} x(o)}{N}, \tag{3}$$

where N refers to the amount of human health data, and $n \in N$. The frequency response of the time series of linear average human health data is configured to obtain the autocorrelation feature state of human health data. The expression equation is as follows:

$$o_n = ot_0 + no\Delta t = h(t_0 + n\Delta t) + \omega_n, \tag{4}$$

where n refers to the data dimension; ω_n refers to the phase space distribution interval when the dimension is n; $n\Delta t$ refers to the time interval; t_0 refers to the initial time; and h refers to the rounding operation function.

The geometric invariants of human health data in phase space are calculated, and redundant interference data are removed [12]. The expression equation is as follows:

$$z(t) = s(t) + js(t) \otimes h(t), \tag{5}$$

where j refers to adjustable parameters; j refers to eigenvector amplitude; and $h(t)$ refers to corrected periodic function.

After the redundant interference data of human health data are removed, the limited dataset of human health data is obtained by clustering algorithm [13]. The expression equation is as follows:

$$O = \{o_1, o_2, \cdots o_n\} \in R^n. \tag{6}$$

Recursively process equation (6), perform differential evolution calculation on each data sample in the human health dataset, and obtain the output scalar timing of the human health dataset. The expression equation is as follows:

$$o = (o_{i1}, o_{i2}, \cdots, o_{in})^T. \tag{7}$$

Let the clustering category threshold be ζ. According to the threshold, the number of feature data clusters in the limited human health dataset is calculated. The expression equation is as follows:

$$V = \{v_{ij}\}, \tag{8}$$

where V_i refers to the finite dataset clustering center of the i time-domain distribution feature point. The output component of data mining is calculated according to the clustering center. The expression equation is as follows:

$$\Delta o_i = a + bo_n - ao_n. \tag{9}$$

The clustering center partition matrix of the data mining output component in equation (9) is calculated by using the perturbation variable difference algorithm. The expression equation is as follows:

$$U = \{\mu_{ik}\}. \tag{10}$$

Equation (10) is normalized to obtain the mutual information features of human health data. The expression equation is as follows:

$$o_i' = o_i / \|o_i\|. \tag{11}$$

After the mutual information features of human health data are obtained according to the above equation, the LSTM neural network is used to identify the mutual information feature to obtain human sports health [14].

2.3. Human Sports Health Pattern Recognition. As we all know, human health models are divided into three models: healthy, subhealth, and unhealthy [15, 16]. In order to clearly show the effect of sports on enhancing human health after exercise, the three human health models are divided into three levels: I, II, and III. The smaller the level, the worse the health status in the health model. The mutual information features of human health data obtained in the previous section are input into the long-term and short-term memory neural network to identify human health patterns. The essence of human health pattern recognition is the classification and processing of signal sequences. Because human motion is a continuous process, the motions of the human body can be divided into several cycles [17, 18], and the human health pattern can be identified according to the time relationship of mutual information features of human health data. The process is as follows.

The internal state c_t is set in the LSTM neural network layer. Then, it is used to record the historical information before the deadline of a certain time, and the values of input gate, forgetting gate, and output gate of the LSTM neural network are calculated [19]. The expression equation is as follows:

$$\begin{cases} i_t = \sigma U_i h_{t-1} + \sigma \psi_i x_t + \sigma b_i, \\ f_t = \sigma U_f h_{t-1} + \sigma \psi_f x_t + \sigma b_f, \\ p_t = \sigma U_0 h_{t-1} + \sigma \psi_0 x_t + \sigma b_0, \end{cases} \tag{12}$$

where i_t, f_t and p_t are human health feature values output by input gate, forgetting gate, and output gate; σ refers to the activated function; h_t refers to the output value of the hidden layer of the neural network; f, U, and ψ refer to the nonlinear activation function, state weight matrix, and input weight matrix; and b refers to the offset value.

The numerical value of the internal state c_t of the LSTM neural network layer is calculated. The expression equation is as follows:

$$c_t = f_t * c_{t-1} + i_t * \tanh U_c h_{t-1} + i_t * \tanh \sigma_c x_t + i_t * \tanh b_c. \tag{13}$$

The value h_t of the hidden layer output of neural network is calculated [20]. The expression equation is as follows:

$$h_t = p_t * \tanh(c_t). \tag{14}$$

Equations (12) and (14) are the forward calculation of the LSTM neural network, but there are two hidden layers in the LSTM neural network [21]. In order to make the output human health model results more authoritative, the mutual information features of human health data are calculated again according to the forward calculation results [22].

Let ϑ be the forward calculation results of the LSTM neural network. The reverse calculation expression equation is as follows:

$$\begin{cases} \left[h_t^{f\_1}, c_t^{f\_1}\right] = \vartheta\left(h_{t-1}^{f\_1}, c_{t-1}^{f\_1}, p_t; \theta^{f\_1}\right), \\ \left[h_t^{f\_2}, c_t^{f\_2}\right] = \vartheta\left(h_{t-1}^{f\_2}, c_{t-1}^{f\_2}, h_t^{f\_1}; \theta^{f\_2}\right), \\ \left[h_t^{b\_1}, c_t^{f\_2}\right] = \vartheta\left(h_{t-1}^{b\_1}, c_{t-1}^{b\_1}, p_{W+1-t}; \theta^{b\_1}\right), \\ \left[h_t^{b\_2}, c_t^{b\_2}\right] = \vartheta\left(h_{t-1}^{b\_2}, c_{t-1}^{b\_2}, h_t^{b\_1}; \theta^{b\_2}\right), \end{cases} \tag{15}$$

where f_1, b_1, f_2, and b_2 are the forward and reverse outputs of the first and second hidden layers of the LSTM neural network, respectively; θ refers to the weight parameters of hidden layer; and o refers to the output vector.

According to the above calculation method, the gradient Adam optimization algorithm is used to train the LSTM neural network model. The steps are as follows:

Step 1: use equations (12) to (14) to calculate the cell output value of the LSTM neural network.

Step 2: after inverse calculation with equation (15), the cross-entropy error term of the LSTM neural network is obtained. The expression equation is as follows:

$$Loss_i = -\log\left(\left(e^{H*\psi_{0,i}} + b_{o,i}\right) / \sum_{j=1}^{N} e^{H*\psi_{o,j}} + b_{o,j}\right), \tag{16}$$

where H refers to the output value of the hidden layer, N refers to the total number of human health mutual information features, and $Loss_i$ refers to the classification loss of the LSTM neural network in recognizing human health patterns.

Step 3: according to the result of equation (16), the weight gradient of the human health mutual information feature is calculated.

Step 4: use the gradient Adam optimization algorithm to gradient the weight of human health mutual information features, and reinput the optimization results into the hidden layer of the LSTM neural network. After reverse calculation, the human health pattern recognition results are output, and the sports health pattern recognition results are input into the display layer. By constructing the model of sports on human health enhancement, the effect of sports on human health enhancement is presented to users.

The process of sports on the human health enhancement model is shown in Figure 2.

The data layer is used to collect sports data, real-time sports data, and health monitoring data, and the collected data is transmitted to the logic layer. The logic layer uses the dynamic difference feature classification algorithm in the data mining to fuse the human health data, extract the human health mutual information feature, and input the feature into LSTM neural network. The neural network outputs the results of sports health pattern recognition after forward and reverse operations. The results of sports health pattern recognition are input into the display layer, and the enhancement effect of sports on human health is presented to users by constructing the enhancement model of sports on human health.

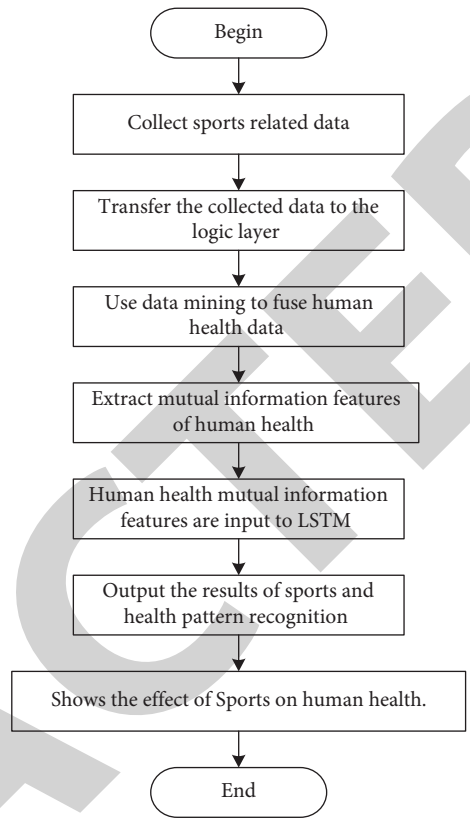

Figure 2: The process of sports on the human health enhancement model.

3. Experimental Design and Result Analysis

3.1. Datasets and Experimental Indexes. The CPU of this experiment is Intel (R) Core (TM) i5-9400 and the operating system is Windows 10. The deep learning framework is the PyTorch deep learning framework. The development language is Python.

The 2019 sports health data of residents aged 30 to 40 years in a community and the sports health of college students in a university are taken as the experimental objects and labeled as dataset as A and dataset B, respectively. This model is used to recognize the physical health patterns of community residents and college students after exercise and analyze the effect of sports on human health. Dataset A: community residents use spacewalker, ladder, waist back massager, pedal, rib frame, Tai Chi massage device, leg pressing trainer, horse riding machine, and vertical waist twisting device for training and test the physiological parameters of residents every month. Dataset B: a university student participates in sports associations, such as basketball, badminton, volleyball, and other track and field sports, and tests the physiological parameters of residents every month. Dataset A and Dataset B are divided in such a way that 80% of the data are used for training and 20% of the data are used for testing.

In order to highlight the reliability of the model in this paper, experiments are carried out using the model in literature [1], literature [2], literature [3], literature [4], and literature [5]. The model in literature [1] to the model in literature [5] represent the heartbeat of the sport recognition model, outdoor sports model, high-intensity running linear analysis model, sports impact analysis model, and different intensity sports impact recognition model, respectively.

(1) Health enhancement effect of community residents and college students after sports: after the model in this paper is applied, the more the number of community residents and college students in a healthy state, the better the enhancement effect.

(2) Human health index of community residents and college students: the body mass index (BMI) is about 18, indicating that the healthier the community residents and college students are, the better the practical application effect of the model is.

(3) Human health pattern recognition accuracy: the model recognition results in this paper are compared with the actual health level. The closer the two values are, the higher the human health pattern recognition accuracy is. The calculation equation of this index is as follows:

$$r = \frac{z}{x} \times 100\%, \tag{17}$$

where z represents the amount of correctly identified human health model data and x represents the total amount of human health model data.

(4) Reliability test results: taking the classification loss value when identifying human health mode as the measurement index and dataset A as the experimental object, test the change of classification loss value during identification under different human health data samples. The loss value is calculated as follows:

$$A = \frac{S}{K}, \tag{18}$$

where S represents the amount of data lost in the classification process and K represents the total amount of data.

(5) Mutual information feature extraction fit: it refers to the similarity between feature extraction results and actual mutual information features.

$$r = \frac{z}{d} \times 100\%, \tag{19}$$

where z represents the number of mutual information features actually extracted and d represents the total amount of mutual information features.

3.2. Results and Discussion

3.2.1. Comparison of Physical Health Enhancement Effect. In order to more clearly describe the practical application effect of this model, taking the proportion of different health models as the measurement index, this paper analyzes the health enhancement effect of community residents and college students after sports in 2019 as shown in Figure 3.

According to Figure 3, after using this model to output the human health enhancement data of community residents and college students after sports, it can be seen that the overall physical quality of community residents and college students has been enhanced. At the two time nodes at the beginning and end of 2019, the proportion of health in the health model of college students and community residents increased greatly, while the proportion of subhealth and unhealthy decreased. On the whole, the physical quality of college students is higher than that of community residents. The reason is that college students have regular work and rest time, diet, relatively young age, and rapid metabolism. On the contrary, the work and life pressure of community residents are relatively large, and different working hours or single dietary structure has a great impact on their health. In conclusion, this model can effectively identify human health patterns and has good applicability.

3.2.2. Comparison of Changes in Human Health Index. Taking human health index BMI as the index and dataset A and dataset B as the experimental objects, this model is used to output the changes of BMI values of community residents and college students when they exercise for one year, as shown in Figure 4.

We observe from Figure 4 that the human health indexes of community residents and college students decrease with the increase of exercise months, and the human health index of college students is lower than that of community residents. The initial BMI of college students and community residents exceeded 20, but after continuous sports, their BMI decreased to about 18, which is the normal standard of the human body. The above results show that continuous sports can effectively improve the BMI of the human body and enhance physical quality.

3.2.3. Comparison of Human Health Pattern Recognition Accuracy. Taking a resident in data set A as the experimental terrain and the recognition accuracy as the measurement index, this model is used to recognize the changes of the health model in 2019, compare it with the actual health model, and analyze the impact of sports on human health enhancement as shown in Figure 5.

It is seen from Figure 5 that the health grade output of the model in this paper is exactly the same as the actual health grade of the residents, and its output accuracy is as high as 100%. The resident kept doing sports in 2019, during

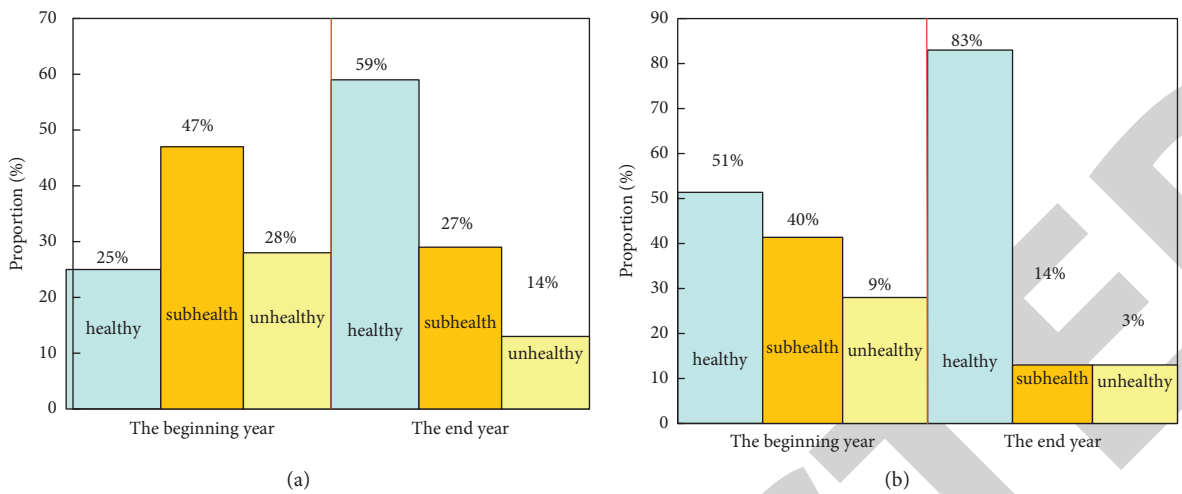

Figure 3: Community residents and college students' physical health enhancement effect after sports. (a) Dataset A. (b) Dataset B.

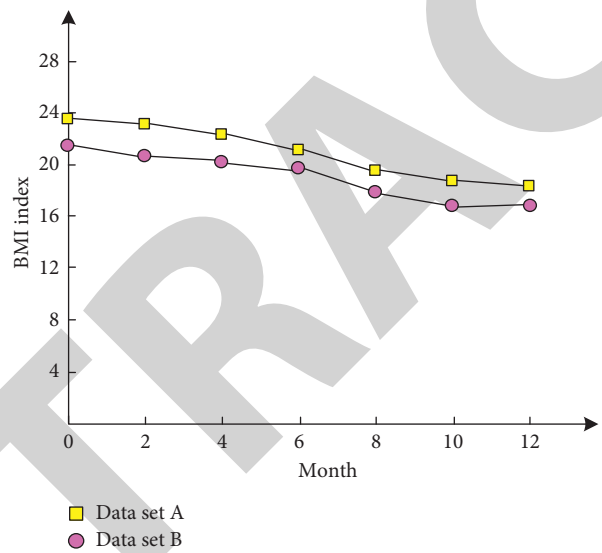

Figure 4: Changes in the human health index of community residents and college students.

which his health level gradually rose from the initial unhealthy level II to healthy level II. The above results show that the output results of this model are very accurate, and the output results can fully describe the enhancement effect of sports on human health and explain the change of residents' health level.

The accuracy of human health pattern recognition by different methods is detected, and the results are shown in Figure 6.

By analyzing the data in Figure 6, it can be seen that the accuracy of human health pattern recognition of the model in literature [1] varies from 79% to 88%, and the accuracy of human health pattern recognition of the model in literature [2] varies from 63% to 69%. The accuracy of human health pattern recognition of the model in literature [3] varies from 59% to 78%, and the accuracy of human health pattern recognition of the model in literature [4] varies from 63% to 76%. The accuracy of human health pattern recognition of the model in literature [5] varies from 52% to 58%. Compared with these methods, the accuracy of human health pattern recognition of this model is always more than 95%, which can realize the accurate recognition of human health patterns.

3.2.4. Comparison of Reliability Test Results. The reliability test result is shown in Figure 7.

According to Figure 7, when analyzing the effect of sports on health enhancement, the loss value curves of the six models decrease rapidly with the increase of the amount of data before the amount of human health data is 1000, but when the amount of human health data exceeds 1000, the loss value curves of the six models are not affected by the amount of human health data, showing a gentle trend. The maximum loss value of this model is lower than that of the other five models, and it begins to show a stable trend when the amount of data is about 600, and the loss value is 0.05. The above results show that the

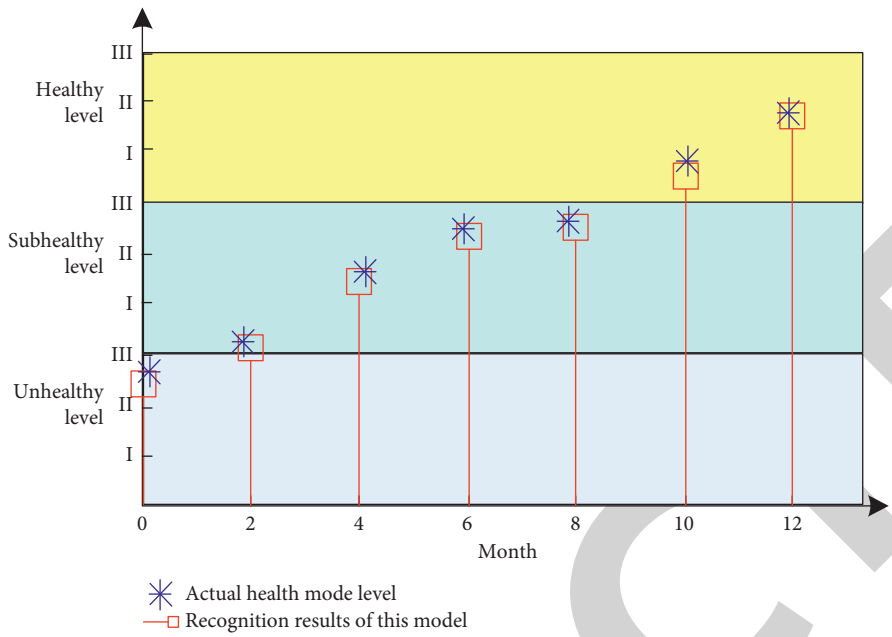

Figure 5: Comparison of human health pattern recognition results.

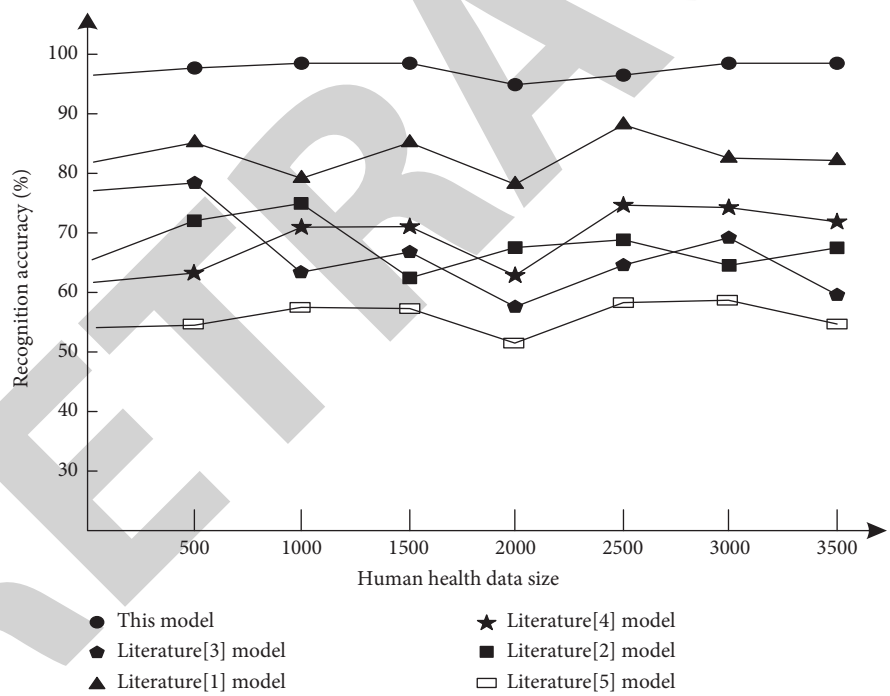

Figure 6: Comparison of human health pattern recognition accuracy.

loss value of this model in analyzing the effect of sports on human health enhancement is the smallest, and its output result is reliable.

3.2.5. Comparison of Mutual Information Feature Extraction Fit. Taking 5000 groups of community residents' human health data in data set A as the experimental object, the fitness of mutual information features extracted by this model is tested, as shown in Table 1.

According to Table 1, the fit degree of the output results of the six models decreased with the increase of the health array. Before the health data group was 3000, the decrease of the fit of the output results of the six models was low. When the lecture data group continued to increase, the decrease of the fit of all model output results gradually increased. When the data group of the model in this paper is 5000 groups, the consistency of the output results is 98.01%, which is 3.91%, 8.09%, 7.94%, 7.9%, and 9.87% higher than the model in literature [1] and the model in literature [5]. From the above

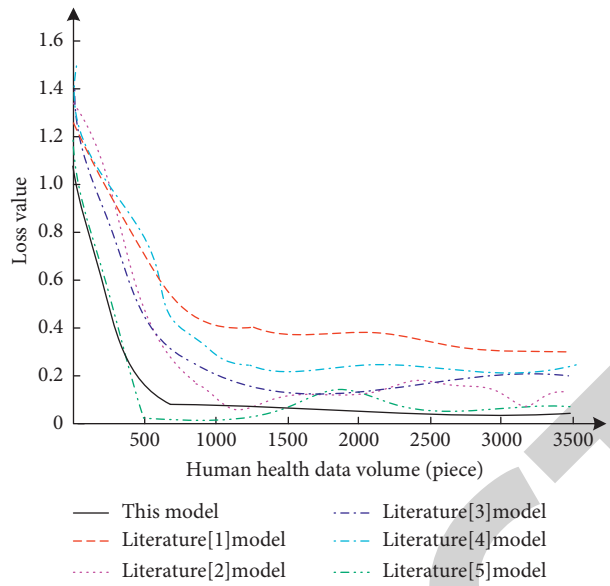

Figure 7: Comparison of reliability test results.

Table 1: Comparison of mutual information feature extraction fit degree (%).

Human health data group	This model	Literature [1] model	Literature [2] model	Literature [3] model	Literature [4] model	Literature [5] model
500	99.82	99.81	97.64	99.24	98.57	95.46
1000	99.79	99.72	97.09	98.97	98.41	94.82
1500	99.75	99.70	96.88	98.54	98.24	93.55
2000	99.73	99.54	95.41	98.02	97.33	92.89
2500	99.68	99.46	95.03	97.55	96.06	91.77
3000	99.54	99.31	94.25	97.31	95.89	91.54
3500	99.33	98.09	94.06	95.88	95.13	90.49
4000	99.01	97.22	93.39	94.27	94.22	89.22
4500	98.86	96.55	92.17	93.05	93.09	89.03
5000	98.01	94.10	89.92	90.07	90.11	88.14

results, it can be concluded that the output results of the model in this paper have the highest fit, which shows that it has good applicability.

4. Conclusions and Future Works

This paper designs a model of sports to human health enhancement based on data mining and uses the model to analyze the sports health data of residents and college students in a community in 2019. The analysis results show that the physical quality of college students is slightly higher than that of community residents, but after continuous sports, their physical health BMI decreases to the standard value, indicating that continuous sports can effectively enhance human health. However, this study also has some shortcomings, that is, it does not use more data for experimental testing to verify the applicability of this model. Therefore, future work is to use more data to test the model based on this study to further verify the reliability of the experimental results.

Data Availability

The data used to support the findings of this study are available from the corresponding author upon request.

Conflicts of Interest

The authors declare that there are no conflicts of interest with any financial organizations regarding the material reported in this manuscript.

Acknowledgments

This work was supported by the Key Project of Heilongjiang Province's "13th Five-Year Plan" for Education Science in 2019: "Research on the Application of Micro-course-MooC-Flipped Classroom Three-dimensional Teaching Model in Theoretical Teaching of Physical Education Major in Colleges and Universities" (no. GJB1319076).

References

[1] M. S. Islam and N. Alajlan, "Model-based alignment of heartbeat morphology for enhancing human recognition capability," *Computer Journal*, vol. 58, no. 10, pp. 2622–2635, 2018.

[2] S. F. A. Baqueri, M. Adnan, B. Kochan, and T. Bellemans, "Activity-based model for medium-sized cities considering external activity-travel: enhancing feathers framework,"

Hindawi
Journal of Healthcare Engineering
Volume 2023, Article ID 9894289, 1 page
https://doi.org/10.1155/2023/9894289

Retraction

Retracted: Evaluation of Cardiac Space-Occupying Lesions by Myocardial Contrast Echocardiography and Transesophageal Echocardiography

Journal of Healthcare Engineering

Received 1 August 2023; Accepted 1 August 2023; Published 2 August 2023

This article has been retracted by Hindawi following an investigation undertaken by the publisher [1]. This investigation has uncovered evidence of one or more of the following indicators of systematic manipulation of the publication process:

(1) Discrepancies in scope
(2) Discrepancies in the description of the research reported
(3) Discrepancies between the availability of data and the research described
(4) Inappropriate citations
(5) Incoherent, meaningless and/or irrelevant content included in the article
(6) Peer-review manipulation

The presence of these indicators undermines our confidence in the integrity of the article's content and we cannot, therefore, vouch for its reliability. Please note that this notice is intended solely to alert readers that the content of this article is unreliable. We have not investigated whether authors were aware of or involved in the systematic manipulation of the publication process.

In addition, our investigation has also shown that one or more of the following human-subject reporting requirements has not been met in this article: ethical approval by an Institutional Review Board (IRB) committee or equivalent, patient/participant consent to participate, and/or agreement to publish patient/participant details (where relevant).

Wiley and Hindawi regrets that the usual quality checks did not identify these issues before publication and have since put additional measures in place to safeguard research integrity.

We wish to credit our own Research Integrity and Research Publishing teams and anonymous and named external researchers and research integrity experts for contributing to this investigation.

The corresponding author, as the representative of all authors, has been given the opportunity to register their agreement or disagreement to this retraction. We have kept a record of any response received.

References

[1] M. Ren, L. Huang, X. Ye, Z. Xv, C. Ouyang, and Z. Han, "Evaluation of Cardiac Space-Occupying Lesions by Myocardial Contrast Echocardiography and Transesophageal Echocardiography," *Journal of Healthcare Engineering*, vol. 2022, Article ID 2066033, 10 pages, 2022.

Hindawi
Journal of Healthcare Engineering
Volume 2022, Article ID 2066033, 10 pages
https://doi.org/10.1155/2022/2066033

Research Article

Evaluation of Cardiac Space-Occupying Lesions by Myocardial Contrast Echocardiography and Transesophageal Echocardiography

Mingming Ren, Lei Huang, Xiaoqiang Ye, Zhifeng Xv, Chun Ouyang, and Zhen Han

Department of Cardiovascular Surgery, Peking University Shenzhen Hospital, Shenzhen 518036, Guangdong, China

Correspondence should be addressed to Zhen Han; hanzhen0431@sohu.com

Received 14 December 2021; Revised 5 January 2022; Accepted 6 January 2022; Published 25 January 2022

Academic Editor: Nima Jafari Navimipour

Heart space-occupying lesions are a disease that occurs frequently in clinical setting, and therefore, it is important to diagnose and treat this type of pathologies properly. Angiographic echocardiography and transesophageal sonogram are widely used for clinical diagnosis. Their application provides a guarantee for the diagnosis of cardiac space-occupying lesions. In this paper, the application of cardiac contrast echocardiography and transesophageal echocardiography in cardiac space-occupying lesions was studied. Prediction of cardiac lesions can accurately determine the nature of cardiac occupancies and provide a basis for clinical diagnosis and management judgments. The results of pathological analysis and experimental comparison showed that myocardial contrast echocardiography can accurately distinguish tumor and thrombus and make contribution to patients taking appropriate medical measures. At the same time, it can compare conventional transthoracic echocardiography and transesophageal echocardiography. The results showed that TEE could clearly show the cardiac lesions. The experimental data of 76.9% confirmed cases showed that the diagnostic accuracy is greatly improved. TEE can also clearly show small thrombus that TTE cannot, in which 2DTEE can clearly show the boundary between the space-occupying and surrounding tissues, and whether there is a clear boundary between the space-occupying and surrounding tissues is an important distinguishing point of benign and malignant tumors. In addition, the TEE probe can also be used for large angle imaging and multiangle rotation, so as to determine the tumor boundary and the spatial position relationship between the tumor and the surrounding tissue. All in all, myocardial contrast echocardiography and transesophageal echocardiography have better clinical application effect on cardiac space-occupying lesions.

1. Introduction

Space-occupying lesions are a special term in medical imaging diagnosis. The results appear in X-ray, B-ultrasound, CT, and other examinations. It points to something that is not grown out of the original part of an organ [1]. This kind of extra growth can press on the previous organ and cause a movement of the original apparatus. Space-occupying lesions usually include malignant or benign tumors, parasites, stones, and hematoma but are not caused by their own disease. Space-occupying lesions are different from cancers. In clinical examinations, experienced doctors can analyze the patient's condition through symptoms.

Heart-occupying lesions (that is, the growth of excess in the heart area will compress the heart) are one of the heart diseases that seriously threatens the life of patients [2]. The reason for space occupancy will differ depending on its size, the position, and whether it causes the symptoms and signs of blood fluids. Clinically, primary heart tumors, metastases, cancer thrombi, tumors, thrombi, etc. are common pre-occupational lesions, the most common of which are tumors, thrombi, and primary heart tumors. Examination is particularly important when determining the disease, so an accurate examination should be performed.

In the study of heart-occupying lesions, many experts and scholars have conducted intensive research. Dong et al.

studied four patients with space-occupying cardiomyopathy using electronic focusing high-resolution two-dimensional echocardiography [3]. In two patients with high-intensity echo clusters at different depths on the epicardial surface, histology confirmed the diagnosis of lymphosarcoma, showing patchy, malignant infiltration of varying thickness. The remaining two patients have very different characteristics: the lesion appears to be inherent to the left posterior wall. A patient with arrhythmia and a small package of noncontractive masses was histologically confirmed as rhabdomyosarcoma. In the second patient, histology confirmed fibroids. In these two patients, the location of the lesion has been determined by angiography [4]. Alexandra used transesophageal echocardiography (TEE) to detect the left atrium, revealing the potential source of cardiac embolism in 12 patients (26%). All patients had clinical evidence of heart disease. TEE detected 32 patients (69%) with potential source of cardiac embolism; 7 (21%) of them had no clinical evidence of heart disease. It was concluded that TEE is a technology superior to TTE, which can be used to identify potential sources of embolized heart and should be recommended for early treatment and prevention of further stroke in patients with potential heart disease or unexplained cerebrovascular accidents [5]. Italy's Ren and other agents have demonstrated improved image quality and diagnostic confidence, and its practicality is now widely accepted [6]. One of the advantages of contrast echocardiography is that it can integrate the best imaging of LV function (by analyzing wall motion) and myocardial perfusion imaging. In clinical trials, using various contrast agent-specific methods, several contrast agents have been shown to provide excellent myocardial contrast effects. In two recent studies evaluating stress ischemia, perfusion imaging by contrast echocardiography can provide more information than conventional wall motion analysis. The technique of deriving quantitative information from contrast echocardiographic images is still mainly used in research, not in clinical settings. Conclusion. Contrast echocardiography can comprehensively assess left ventricular function and myocardial perfusion, has a high spatial and temporal resolution, and has the potential for quantification [7, 8]. Machine learning is the study of how computers can simulate or implement human learning behavior in order to acquire new knowledge or skills and reorganize existing knowledge structures to continuously improve their performance; joint learning is a method in which two events are repeated in close proximity to each other in time, eventually forming connections in the brain over time.

This article briefly introduces the damage of heart-occupying lesions to patients and the application of new medical technology, introduces the application of ultrasound technology in the medical field, and further introduces myocardial ultrasound contrast and transesophageal echocardiography technology, using practical research methods. The application of myocardial contrast echocardiography and transesophageal echocardiography in heart-occupying lesions is analyzed. The incomparable results indicated that the use of cardiomyogram echocardiography and transesophageal sonography can effectively improve the diagnosis of an occupied cardiac lesion in patients. The next surgical steps for patients had contributed a lot.

2. Proposed Method

2.1. Heart Occupying Lesions and the Application of Ultrasound Technology. Space-occupying lesions are one of the more common clinical diseases. With the population aging in China, the growing incidence of cardiovascular and the rising incidence of cardiac preoccupying lesions has caused significant concern among a number of physicians and scholars. Space-occupying lesions include benign, malignant tumors, thrombosis, hematoma, and abscesses [9, 10]. The pathological classification of tumors is diverse, and common benign tumors include myxoma, lipoma, hemangioma, and rhabdomyosarcoma [11]. Malignant tumors include primary and secondary malignant tumors; the former is the most common sarcoma, and the latter is secondary to other organ tumors; the most common primary lesions are lung cancer, breast cancer, lymphoma, and liver cancer. Nonneoplastic lesions are often accompanied by a history of basic heart disease or cardiac surgery. Patients with thrombosis usually suffer from valve disease, dilated cardiomyopathy, or coronary heart disease. Patients with cardiac hematoma usually have a recent history of interventional therapy. Benign tumors can usually be cured by surgical removal. Based on the pathological and disease characteristics, we use chemotherapy, radiotherapy, and photoresection to be able to treat malignant tumors. Depending on the extent of the disease and the length of the medical history, nonneoplastic lesions are treated with drugs or surgery. It can be seen that the treatment methods for different types of space-occupying lesions are different [12, 13]. Therefore, it is particularly important to clarify the nature of space-occupying lesions before treatment.

With the advancement of technology, ultrasound technology has been applied in the medical field [14]. Compared with other medical shaping methods, ultrasound medical imaging technology has many advantages. It has no radiation, and in most cases, ultrasound diagnosis is noninvasive and will not cause harm to patients or doctors [15]. Therefore, ultrasonic medical imaging is considered a safe imaging method and has become a routine inspection method. In addition, ultrasound imaging equipment is relatively cheap, and the cost of diagnosis is relatively low. In addition, ultrasound can also image soft tissues, displaying the visceral anatomy and actual activity in real time. Therefore, at present, echocardiography has been widely used in the diagnosis of cardiovascular diseases. The heart is an organ with very complicated structure and movement. It is difficult to describe it accurately with traditional two-dimensional ultrasound, so in recent years, a three-dimensional reconstruction system of ultrasound medical images has emerged, using a series of two-dimensional ultrasound images in three-dimensional space. The three-dimensional shape of the heart is reconstructed, so that the heart can be observed from any angle, and some post-processing methods are used to achieve accurate

measurement of the heart cavity volume and free heart wall to achieve the purpose of accurate diagnosis [16, 17]. Ultrasound imaging is a new type of noninvasive diagnostic clinical medicine developed in the late 1950s. By studying the application of the physical properties and imaging rationale of ultrasound, as well as the knowledge of the anatomical, physiological, and pathological properties of human tissues and anatomies of organs and the basic knowledge of clinical physics, we observed the sound and image performance of human tissues, organ morphology, and function changes and then analyzed and discussed the occurrence and development of diseases, so as to achieve the purpose of disease diagnosis and treatment [18]. Transthoracic echocardiography (thoracic echocardiography, TTE) is one of the main methods for diagnosing heart-occupying lesions. It can observe the hemodynamic changes caused by the size, shape, location, and occupation of the space-occupying space in real time, but regarding this technique, due to its limitations, its results are susceptible to interference from many factors, such as the patient's body type. Such images are of poor quality and are not clear enough to define the specific spatial location of the lesion. It is easy to cause missed diagnosis and misdiagnosis, taking huge risks. Because of this, more precise methods and instruments are needed to accurately determine the type of lesion [19, 20]. In this form, ultrasound contrast and transesophageal echocardiography came into being [21, 22]. As early as the late 1980s, transesophageal echocardiography (TEE) was clinically applied, but the technology at that time was immature and, at the same time, affected by other factors such as cost; this technology has not been widely applied. Compared with transthoracic echocardiography, the transesophageal method can obtain a better acoustic window, thereby obtaining a better quality image of the heart [23, 24]. In particular, the development of real-time transesophageal three-dimensional echocardiography (RT3D-TEE) can display the heart in real time and three-dimensionally, providing clinicians with richer and more accurate information. In recent years, ultrasound contrast technology has been maturely used in the diagnosis of liver, thyroid, breast, and other organ occupying lesions. It can display the tiny blood vessels and low-speed blood flow of the occupying lesions, which helps evaluate its properties; there are also research applications. Myocardial contrast-enhanced ultrasound (MCE) determines the nature of cardiac tumors and believes that the degree of MCE enhancement can help distinguish between benign and malignant tumors [25, 26]. Computers can find patterns of heart disease onset and predict and evaluate heart disease with the help of different machine learning methods.

2.2. Myocardial Contrast Echocardiography and Transesophageal Echocardiography. Myocardial echocardiography (MCE) is currently a commonly used method for detecting cardiac function. In recent years, with the use of acoustic contrast agents, to observe myocardial perfusion by performing an echocardiogram has been made possible. This is known as myocardial echocardiography. It is also known as echocardiography of the corpus cavernosa. During the MCE examination, a specific microbubble contrast agent needs to be injected into the blood vessel. The microbubbles in the contrast agent are encapsulated by a high molecular weight gas (nitrogen or fluorocarbon gas) in a phospholipid or albumin shell. They cannot penetrate the endothelial cell layer and have similar dynamics to human red blood cells in blood vessels. They can be ruptured under the action of ultrasound and observed and recorded by relevant ultrasound equipment. The operation of heart echocardiography is simple, the cost is low, and there is no radiation. It is easier to be accepted by the majority of patients, and it has been gradually applied in clinical practice. In fact, the development of ultrasound contrast agents has also experienced three stages of leaping development; so far, the third generation of contrast agents has appeared [27, 28]. The first generation of contrast agents was produced in the 1980s. Its predecessor was a saccharide microbubble contrast agent. This discovery can be said to be a milestone in contrast agents. Since then, the development of ultrasonic microbubble contrast agents has entered an era of rapid development. Subsequently, some researchers obtained the transpulmonary circulation contrast agent with a diameter smaller than erythrocytes by acoustic vibration, which was the first generation of ultrasonic microbubble contrast agent. It was the first left heart acoustic contrast agent approved by the US FDA. The first generation of ultrasound microbubble contrast agent is also the first pulmonary transcontrast agent approved by the Ministry of Health of China. The second generation ultrasound microbubble contrast agent is mainly encapsulated with fluorocarbon gas or other inert gas, and its physical stability is improved compared with the first generation contrast agent. In addition, there are two kinds of contrast agent shells that are polymer composites, containing nitrogen or perfluorobutane, which can be used for cardiac cavity or myocardial imaging, have completed three key clinical trials, and have not yet officially put on the market. The third-generation targeted ultrasound microbubble contrast agent is still in the experimental stage. Generally speaking, the third-generation contrast agent is an improved version of the second-generation ultrasound microbubble contrast agent [29]. At present, myocardial ultrasound contrast is mainly used in the following aspects: application one to better identify the endocardial boundary: myocardial ultrasound contrast can better identify the endocardial boundary through enhanced cardiac cavity visualization, assess the wall thickness, and provide more accurate assessment. The left ventricular ejection fraction is also more accurate in evaluating the motor function of the wall segment. Diagnosis of two coronary heart diseases and evaluation of its therapeutic effect and prognosis is applied. Diagnosis of triple myocardial infarction and its complications is applied. We applied the diagnosis and characteristics of occupying lesions of the four cavities. MCE can detect the density of blood vessels in the space-occupying lesions in the heart, so as to roughly assess its properties. Intracardiac thrombus is generally free of blood vessels. MCE shows no obvious contrast agent filling; benign tumors in the heart generally have fewer blood vessels. MCE shows

less contrast agent filling; and there are more blood vessels in cardiac malignant tumors, and MCE shows more abundant contrast agents. Filling: application of five cardiomyopathy diagnoses. Regarding hypertrophic cardiomyopathy, especially apical hypertrophy, MCE is a very good noninvasive diagnosis. Diagnosis of six myocardial insufficiency is applied. MCE can clearly show the boundary of the endocardium, can better find and diagnose the left ventricular nondensified myocardial segment, and can also identify asymptomatic myocardial densification patients early.

While the conventional transthoracic echo cardiogram can determine most of the oncotic lesions and is by far the most widely used means of visualization of oncotic lesions, its restrictions are also very well established. In order to be able to accurately determine the heart occupying, the nature of the lesions has been gradually applied and popularized by transesophageal echocardiography. In principle, transesophageal echocardiography (TEE) refers to an ultrasound imaging method, in which an ultrasound probe is placed in the esophagus to detect changes in the morphological structure and function of the heart and blood vessels from the back of the heart and blood vessels [30]. Its scanning method has undergone changes in single plane, double plane, and multiplane scanning and can be displayed more clearly. At present, multiplanar TEE has been widely used in the diagnosis of various heart diseases and the monitoring of thoracotomy and interventional surgery. Transesophageal echocardiography (TEE) was first used in the clinical field in the 1980s. Compared with transthoracic echocardiography, the transesophageal method can obtain a better acoustic window and thus a better quality of the heart. Image. Using the method of rotating transesophageal ultrasound probe to obtain two-dimensional sequence images of the heart and reconstruct the left ventricle to evaluate its morphology and volume, a microcontroller similar to an endoscope was designed to obtain multiplanar transesophageal echocardiography. With a modification of the esophageal ultrasound probe to control its rotation through a process to obtain pyramidal ultrasound montanic volume data, this method is utilized to the advantage of TEE to have a high quality reconstruction being achieved. In this paper, we have evaluated the diagnostic aspects of the prediction method and found that MCE is effective in differentiating between tumors and thrombi and improves the accuracy of the diagnosis of occupying lesions.

3. Experiments

3.1. Study of Myocardial Contrast-Enhanced Ultrasound on Heart Occupying Lesions

3.1.1. Research Object. At a hospital, a total of 50 patients, 28 being men and 22 being women, aged 25–85 years, diagnosed with preoccupation of the heart by transthoracic radiology, were selected for the study. Patients diagnosed with the presence of cardiac thrombus based on clinical data, etiology, and TTE presentation were excluded. Of the 50 patients, 10 had previous history of malignant tumors of other organs; 45 tumors were confirmed by pathology, 5 tumors had reduced volume after chemotherapy, and 4 had reduced volume after thrombolytic therapy. Fifty patients were divided into benign tumor group (25 cases), malignant tumor group (20 cases), and thrombosis group (5 cases) according to clinicopathology and clinical diagnosis. This experiment is based on two latitudes of tumor detection time and size to determine tumor category. In general, tumors that do not change significantly in size over time are classified as benign. This example uses the most simplified two-dimensional model to visualize the sample data and produce the following graph, where the horizontal axis is the mass size, and the vertical axis is the time of detection. Each point represents the size of the tumor and the time of onset for a different patient, and the tumor is judged to be benign or malignant based on its color.

3.1.2. Research Instruments. Using the PhilipsiE33 ultrasound system, the patient was lying on the left side, connected to an electrocardiogram, and conventional ultrasound was used to observe the size, shape, position, internal echo, and adjacent conditions of the tumor, and to store the image. Sign the informed consent for ultrasound imaging. Select an appropriate section, so that the tumor is displayed on the same section as the ventricular septum or the left ventricular posterior wall, enable the MCE mode, the mechanical index is 0.10, the frequency is 2.5~3.5 MHz, and slowly push the Novi contrast agent 2.5 through the left median elbow vein ml, speed 1.25 mL/min, postinjection of normal saline 5 mL to flush the injection channel, observe the tumor and normal myocardial enhancement, and store dynamic images. Instruct the patient to keep quiet and not move during the entire imaging process.

3.1.3. Research Methods. MCE semiquantitative analysis: visual observation: the degree of contrast enhancement of space-occupying lesions is divided into (1) high enhancement: the enhancement intensity inside the space-occupying lesion is higher than the adjacent myocardial tissue; (2) enhancement: enhancement intensity of the space-occupying lesion is equal to that of the adjacent myocardial tissue; (3) low enhancement: the enhancement intensity of the occupying lesion is lower than that of the adjacent myocardial tissue; (4) no enhancement: no enhancement agent is filled inside the occupying lesion. Diagnose malignant tumors with high-enhanced space-occupying lesions, whole-area-enhanced space-occupying lesions as normal myocardial tissue, and overall low-enhanced space-occupying lesions with benign tumors, and the morphological rules remain unchanged. The positional lesions were diagnosed as dense thrombi, and the space-occupying lesions that were significantly lobed after the angiography and had no internal enhancement were diagnosed as fresh thrombus with loose texture. The quantitative index of MCE uses the QLAB10.8 software computer region of interest ROI technology to select the region of interest and dynamically track it to obtain the contrast intensity-time curve of the heart-occupying lesion and the adjacent normal myocardium, and according to the formula $y\ (t) = A\ \ (1 - e - Bt) + \mathrm{C}$ line

perfusion curve fitting, record the peak intensity A value of the space-occupying lesion and the adjacent myocardium (reflecting the blood volume of the area of interest), and record it as $A1$ and $A2$, respectively, and calculate $A1/A2$ ratio; the ratio is greater than 1 diagnosed as malignant tumor, the ratio is diagnosed as benign tumor or thrombosis in the range of (0,1), and the ratio is equal to 0 diagnosed as thrombosis. Use SPSS18.0 professional statistical software analysis. MCE semiquantitative index results are adopted. The absolute value indicates that the chi-square test is used to compare the semiquantitative indexes of MCE between benign and malignant heart tumor groups; the results of the quantitative indexes of MCE are described by $x \pm s$, and the independent sample t-test is used to compare the quantitative indexes of MCE between benign and malignant heart tumor groups; $P < 0.05$ means that the difference was statistically significant.

3.2. Transesophageal Echocardiography Study of Heart Occupying Lesions

3.2.1. Research Object. 52 patients were selected for TEE examination in a hospital, 22 males and 30 females, aged 20–60 years. Of the 52 cases, 8 had no obvious symptoms, and the physical examination found that the heart occupied, and the remaining 44 had obvious symptoms and signs (including varying degrees of palpitations, shortness of breath, chest tightness, heart murmur, and 10 of them with brain Infarction). Examination found that the heart occupied space. Ten of 52 patients occupy a history of malignant tumor. An occupying lesion is a general term for a group of conditions, in which the body's tissues occupy a certain spatial position. The majority of occupying heart lesions are caused by heart disease, but some are also caused by bruising inside the heart or by cysts.

3.2.2. Research Instruments. Ultrasonic examination uses Philips iE33 colour ultra-Doppler ultrasound diagnostic instrument, equipped with C5-1 transthoracic probe and X7-2t three-dimensional transesophageal real-time probe. Transesophageal real-time 3D has a real-time three-dimensional display mode (Live-3D) and ECG-gated three-dimensional full-volume display mode (3DFullVolume).

3.2.3. Research Method-Comparative Analysis of Conventional Transthoracic Echocardiography and Transesophageal Echocardiography. TTE examination method: first, let the patient take the supine position, with the left ventricular long-axis view, left ventricular short-axis view, left ventricular apex four-chamber view, etc. as the standard part of cardiac ultrasound scanning. To measure the size of each cardiac chamber regularly and to attentiveness to the specific characteristics of the defect and its association with the surviving tissues. TEE examination method: before the examination, it is necessary to make sure that the patient has no contraindications, the consent form has been signed, and the examination room is equipped with the necessary first aid equipment. Instruct patients to fast for more than 16 hours, take the left position, connect the ECG; use X7-2t probe, 2DTEE multi-angle scanning observation, measure relevant indicators and store images and data; then, use RT3DTEE imaging; first use real-time 3D mode display, observe the position, shape, and size of the cardiac cycle, and then switch to 3DFullVolume (maximum fan angle width 104., thickness 101.) mode, adjust the fan angle and thickness, wide-angle display space, and surrounding structure, and continuously store 4~7. During the cardiac cycle, rotate and cut the stored 3DFullVolume image, observe carefully, clearly show the lesion, and measure its maximum footprint. Using SPSS18.0 software analysis, the maximum meridian of the space-occupying lesion is represented by $z \pm s$. Use the £ test to compare the size of the heart-occupying lesions measured by various methods with the size of pathological specimens, and the size of the heart-occupying lesions measured by various methods, and compare the size correlation using the pathological specimens Pearson method. $P < 0.05$ indicates that the difference is statistically significant.

4. Discussion

4.1. Analysis of Myocardial Ultrasound Contrast Results

4.1.1. Pathological Results. Of the 50 heart-occupying cases, 25 cases were (25/50, 50%) in the benign tumor group, including 15 cases of myxoma, 3 cases of lipoma and hemangioma, 2 cases of fibroids, and 2 cases of intracardiac leiomyoma, and 25 benign tumors were confirmed by surgery: 20 cases of malignant tumors (20/50, 40%), including 8 cases of lung cancer heart metastasis, 3 cases of malignant thymoma heart metastasis, and 3 cases of liver cancer heart metastasis and lymphoma and pericardial osteosarcoma. Pericardial angiosarcoma and neuroectodermal malignant tumors each had a heart metastasis; 20 cases of malignant tumors were confirmed by surgery in 10 cases (3 cases of malignant thymoma, liver cancer heart metastasis, lung cancer heart metastasis 2 cases, pericardial osteosarcoma, pericardial angiosarcoma 1 in each case of lymphoma), 7 of the remaining 10 unoperated patients had shrinkage after chemotherapy (all lung cancer metastases), and 3 were confirmed by biopsy under CT biopsy (2 cases were neuroectodermal malignant tumors with heart metastasis, 1 (Case of lymphoma); 5 cases (5/50, 10%) in the thrombus group, based on medical history (respectively, chronic renal failure with central venous catheterization, 1 year after pulmonary valve stenosis, right atrial tumor (1 year after surgery and 5 years of palpitations) and TTE could not confirm the diagnosis of thrombosis, and they were included in this study, the volume after thrombolytic therapy is small, and final clinical diagnosis of cardiac thrombosis is applied.

4.1.2. Analysis of Semiquantitative Indicators of Cardiac Space-Occupying MCE. See Table 1 for semiquantitative indicators of cardiac space-occupying MCE.

According to Table 1, in 25 cases of benign tumor group, 18 cases of tumor edge smoothing (18/25, 72%), 7 cases of

Table 1: Comparison of semiquantitative indexes in benign and malignant tumor group of heart.

Pathological diagnosis	Quantity	Is the far edge smooth after angiography		Whether the enhancement is even		Strengthen	
		Yes	No	Yes	No	Low	High
Malignant	20	0	20	0	20	6	14
Benign	25	18	7	17	8	20	5
X^2		19.2		19.2		11.8	
P		0		0		0	

tumor edge smoothing (7/25, 28%), of which 6 cases were myxoma intracardiac leiomyomatosis; 20 of 25 benign tumors showed low enhancement (20/25, 80%), 5 tumors showed high enhancement (5/25, 20%), and 3 were hemangiomas and 2 cases of lipoma; 17 of 25 cases of benign tumors showed uniform enhancement (17/25, 68%), 8 cases of tumors showed uneven enhancement (8/25, 32%), of which 3 cases were myxoma. There were 1 case of lipoma, 2 cases of hemangioma, and 1 case of intracardiac leiomyomatosis. In the 20 cases of malignant tumor group, 20 cases had uneven tumor edges (20/20, 100%); 20 cases had uneven enhancement (20/20, 100%); 14 of 20 malignant tumors showed high enhancement (14/20,70%), and 6 cases showed low enhancement, including 2 cases of lung cancer heart metastases, 2 cases of liver cancer heart metastases, and 2 cases of heart lymphoma. Of the thrombotic group, MCE displayed no enhancement in 5 cases. The semiquantitative results of MCE in the benign and malignant tumor groups were of statistical significance ($P < 0.05$). The results of MCE semiquantitative indicators of various tumors are shown in Table 2.

According to Table 2, 18 cases of myxoma in the benign tumor group showed low enhancement (18/18, 100%) after imaging, 6 cases showed uneven enhancement (6/18, 33.3%), and 8 cases had uneven edges. (8/18, 44.4%), and these 18 cases of myxoma showed typical changes; that is, they were all located in the atrium, the tumor pedicle was located in the oval fossa or the free wall of the atrium and lobulated, and the degree of activity was greater (14 can travel between the atrioventricular, 4 cases fluttered in the atrium with the cardiac cycle), combined with its MCE enhancement degree was diagnosed as a benign tumor with low blood supply; intraoperative and pathological findings showed 8 cases of myxoma tumors with uneven edges after angiography. It is lobulated, and thrombosis can be seen on the surface. Six cases showed unevenly enhanced tumor volume after angiography (4.3 mm × 4.9 mm~4.2 mm × 6.9 mm), with brown or brown-red areas of visible calcification, fibrosis, and cystic changes. The posterior edges of 3 cases of lipoma MCE were smooth, but the degree of enhancement and the uniformity of the enhancement were different. During the operation, the tumor with uneven enhancement was larger in volume (5.2 cm × 5.6 cm), and old bleeding was seen inside.

4.1.3. Analysis of Quantitative Indexes of Cardiac Tumor MCE. The quantitative index of cardiac tumor MCE is shown in Figure 1.

As can be seen from Figure 1, the curve obtained by the MCE quantitative analysis software shows that, in the malignant tumor group, 15 tumors in 20 cases had higher TIC than the surrounding myocardium, 5 tumors had lower TIC than the surrounding myocardium (2 cases of lung cancer metastasis, 2 cases of liver cancer heart metastasis Lymphoma), in 20 cases of benign tumor group, and 20 tumors had lower TIC than peripheral myocardium, 5 tumors had higher TIC than peripheral myocardium (3 hemangiomas, 2 lipomas), which was consistent with the semi-quantitative MCE enhancement index. Compared with tumor A/myocardial A and curve slope, the malignant tumor group was higher than the benign tumor group, and the differences were statistically significant; compared with the peak time (TTP), the malignant tumor group was lower than the benign tumor group, but the difference was not statistically significant.

Through the above analysis, the tumor and thrombus can be identified by MCE, and the thrombus MCE shows no enhancement; semiquantitative and quantitative indicators help judge the blood supply status of cardiac tumors: most benign tumors are of low enhancement, and there are also small ones in malignant tumors. Some have low enhancement; unevenly enhanced MCE and uneven edges have high diagnostic value for the diagnosis of malignant tumors; but for typical myxoma, the diagnostic value of conventional echocardiography is higher than MCE; for some tumors (this Lipoma, heart metastases of lung cancer, and lymphoma in the study), the same pathological type shows different degrees of enhancement, so more cases need to be collected for discussion. Secondly, MCE is different from the ultrasound contrast of liver, breast, thyroid, and other organs. First, MCE takes intravenous drip, which is different from intravenous bolus injection, so the heart develops longer, and the quantitative index results are different from other organs; second, the heart is a pulsating organ, which brings difficulties to MCE quantitative analysis. Software analysis will be affected by heart beats, especially tumors with long tumor pedicles. The operation of software analysis is more complicated; third, the requirements for the cut surface are more than others. Visceral ultrasonography is

Table 2: MCE semiquantitative indexes of different pathological types of cardiac tumors.

Pathological type	Quantity	Is the far edge smooth after angiography		Whether the enhancement is even		Strengthen	
		Yes	No	Yes	No	Low	High
Myxoma	18	10	8	12	6	18	0
Lipoma	3	3	0	2	1	2	1

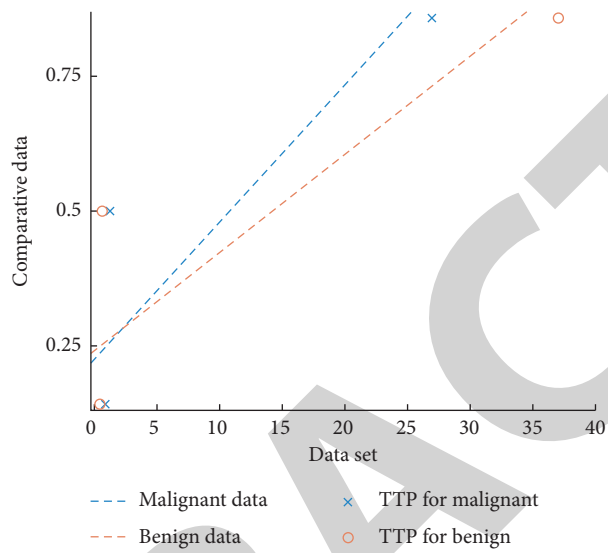

Figure 1: Comparison of quantitative indexes of benign and malignant tumor group.

high, and MCE requires that the lesion is located at the same depth as normal tissue, so the operator is required to be proficient in each section of TTE, both to select a section to display the lesion and normal tissue at the same depth, but the depth cannot be too large; otherwise, the contrast of the effect is not good, and at the same time, it is necessary to avoid adverse factors such as rib sound windows.

4.2. Transesophageal Echocardiography Results Analysis

4.2.1. Pathological Results. Pathological analysis is shown in Figure 2.

According to Figure 2, 30 of 52 cases of benign tumors (8 cases of hemangioma, 18 cases of myxoma, 2 cases of lipoma and 2 cases of fibroma) accounted for 57.7%, and all 30 cases were confirmed by surgery; cases accounting for 19.3%, of which 8 cases were confirmed by surgery, 6 cases of thrombosis accounting for 11.5%, significantly reduced after diagnosis by TEE and anticoagulation; 4 cases of thickened boundary ridge, accounting for 7.7%, diagnosed by TEE; two cases of hematoma, accounting for 3.8%, were confirmed by surgery. It is clear from this data that a large proportion of tumour cases are benign and can be diagnosed and treated with the aid of modern medical procedures.

4.2.2. Results of Conventional Transthoracic Echocardiography and Transesophageal Echocardiography. An example of transesophageal echocardiography is shown in Figure 3.

The results of conventional transthoracic echocardiography and transesophageal echocardiography are shown in Figure 4.

It can be seen that Figure 4 compares the three sets of data in total, which are confirmed cases of 52 patients under the analysis of 2DTTE and TEE technology and cases of benign tumors and misdiagnosis. From the data comparison, we can see that the type of heart-occupying lesions in the 52 patients participating in the study was 20 cases diagnosed by 2DTTE, and the diagnosis rate was 38.5%. 40 cases were diagnosed by TEE, and the diagnosis rate was up to 76.9%. Under 2DTTE imaging, there were 30 cases of benign tumors, 12 cases were definitely diagnosed by 2DTTE, and 2 cases were misdiagnosed, while, under TEE imaging, 30 cases of benign tumors were diagnosed without misdiagnosis. It can be seen from the above that 2DTTE is subject to many restrictions in actual use, and it is easy to be interfered by internal and external factors to cause error in results, which may cause misdiagnosis and missed diagnosis. The diagnosis rate of TEE technology is much higher than 2DTTE.

Figure 5 is a comparison of three kinds of 2DTTE, 2DTEE, and RT3DTEE ultrasound methods to estimate the heart size and surgical specimens.

According to Figure 5, with the comparison of the size of the heart occupied by 2DTTE, 2DTEE, and RT3DTEE and the size of the surgical specimen, the difference is greater than the statistical value of 0.05, so there is no statistical significance. Based on the above research, we can

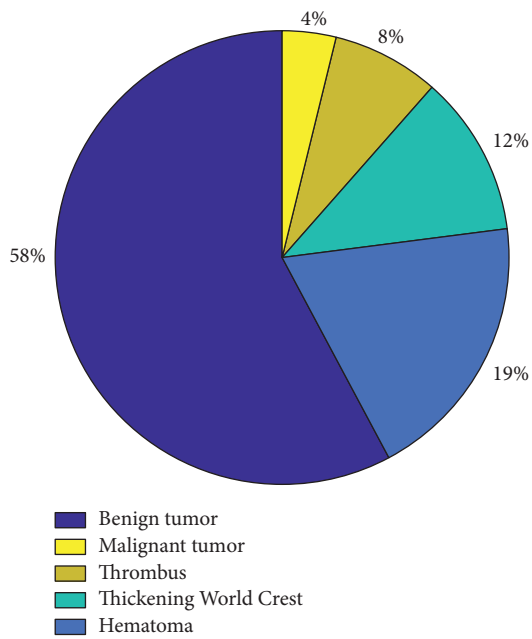

Figure 2: Transesophageal echocardiography results.

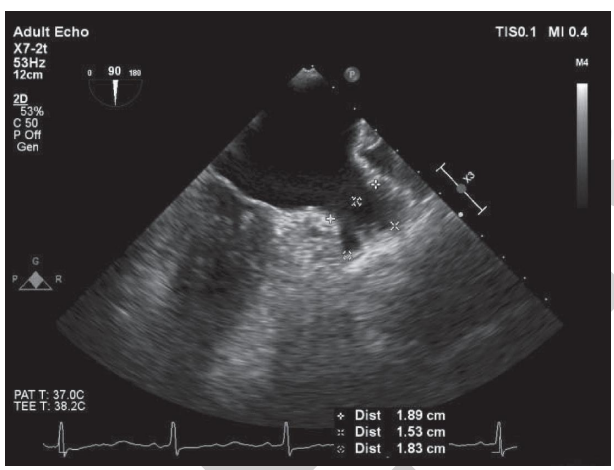

Figure 3: Example of transesophageal echocardiography.

draw the following conclusions: first, TEE technology can clearly show heart disease changes, greatly improving the accuracy of diagnosis, which is undoubtedly a huge boon for patients, greatly reducing the risk of misdiagnosis and missed diagnosis. As far as the research in this article is concerned, in 52 cases of experimental data, the diagnosis rate under 2DTTE imaging reached only 38.5%, less than half, while, under TEE technology, 40 cases were diagnosed, and the diagnosis rate was 76.9%, an increase of 100% compared with 2DTTE. The second is that the TEE technology can display the fine structure of the lesion more clearly, helping the surgeon make a more accurate diagnosis. For the present case, TEE may reveal tumor peduncles in 20 fibroid and 2 papillary elastic cases in this subset of vasculature. The third TEE imaging can clearly show the boundary between the occupying lesion and the surrounding tissue. In summary, TEE can not only

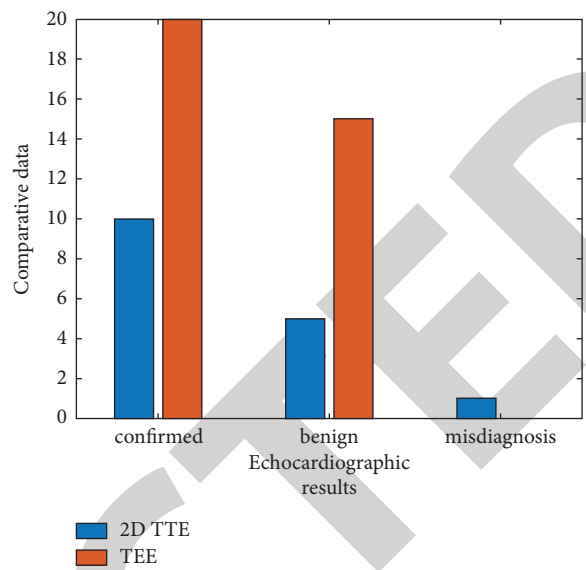

Figure 4: Comparison of conventional transthoracic echocardiography and transesophageal echocardiography.

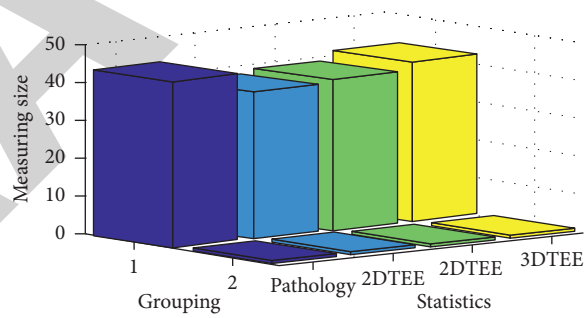

Figure 5: Comparison of the measured heart footprint with the size of the surgical specimen.

improve the diagnosis rate, because of its clear image, but also help surgeons obtain more preoperative information, which helps make surgical plans.

5. Conclusions

It has to be said that heart occupation is one of the heart diseases that seriously threatens the lives of patients, and it will cause huge interference to patients and their families. The placeholder will show different symptoms and signs due to its own characteristics. Clinically, primary heart tumors, metastases, cancer thrombi, neoplasms, thrombi, etc. are all common heart-occupying lesions.

An investigation based on thermography echocardiography and transesophageal echocardiography in the clinical of occupant cardiac lesions is presented in this article. Cardiac echocardiography is simple to perform, is of low cost, and is radiation free. It is more acceptable to most patients and is gradually being used in clinical practice, but it is not possible to accurately determine the nature of the occupying cardiac lesion and to make the most accurate

diagnostic modality. Using it, myocardial echocardiography and transesophageal echocardiography were in fact found to make an outstanding contribution to the diagnosis of occupying cardiac lesions.

Through the application study of myocardial contrast echocardiography and transesophageal echocardiography in the clinical practice of cardiac space-occupying lesions, the following conclusions are drawn: (1) MCE can effectively distinguish tumors from thrombus and thrombus and improve the accuracy of diagnosis of space-occupying lesions. (2) TEE can clearly show the change of heart disease. The experimental data confirmed 76.9% of the cases, and the diagnosis accuracy rate is greatly improved compared with 2D TTE (the diagnosis rate is only 38.5%). (3) TEE can also clearly display small blood clots, tumor pedicles, and other details and the boundary with the surrounding tissue, which is helpful to form a more accurate judgment. In summary, the application of myocardial contrast echocardiography and transesophageal echocardiography in the clinical practice of heart-occupying lesions is conducive to more comprehensive observation and evaluation of the diagnostic accuracy of heart-occupying lesions.

Data Availability

This article does not cover data research. No data were used to support this study.

Conflicts of Interest

The authors declare that they have no conflicts of interest.

Acknowledgments

This work was supported by the Guangdong Province Medical Technology Research fund, A2016145, and Shenzhen City Health Bureau, 201501023.

References

[1] Y. Zhao, H. Li, S. Wan et al., "Knowledge-aided convolutional neural network for small organ segmentation," *IEEE journal of biomedical and health informatics*, vol. 23, no. 4, pp. 1363–1373, 2019.

[2] T. Araki, N. Ikeda, F. Molinari et al., "Effect of geometric-based coronary calcium volume as a feature along with its shape-based attributes for cardiological risk prediction from low contrast intravascular ultrasound," *Journal of Medical Imaging And Health Informatics*, vol. 4, no. 2, pp. 255–261, 2014.

[3] Y. Dong, X. L. Zhang, and F. Mao, "Contrast-enhanced ultrasound features of histologically proven small (≤20 mm) liver metastases," *Scandinavian Journal of Gastroenterology*, vol. 52, no. 1, pp. 1–6, 2016.

[4] A. Dogra, B. Goyal, S. Agrawal, U. J. Tanik, S. Kumar, and R. S. Nayak, "Enhanced vascular and osseous information fusion: disagreement of quantitative and qualitative analysis," *Neural Computing & Applications*, vol. 32, no. 20, Article ID 15885, 2020.

[5] A. M. Kowalewski, R. Wilkens, A. Wilson, J. Ruan, and S. R. Wilson, "Quantitative contrast-enhanced ultrasound parameters in crohn disease: their role in disease activity determination with ultrasound," *American Journal of Roentgenology*, vol. 206, no. 1, pp. 64–73, 2016.

[6] J. Ren, "Application of contrast-enhanced ultrasound after liver transplantation: current status and perspectives," *World Journal of Gastroenterology*, vol. 22, no. 4, 2016.

[7] X. Diao, J. Zhan, L. Chen, Y. Chen, and Y. Liu, "Quantification of solid hypo-echoic thyroid nodule enhancement with contrast-enhanced ultrasound," *Translational Cancer Research*, vol. 6, no. 6, pp. 1078–1087, 2017.

[8] T. K. Kim, S. Y. Noh, S. R. Wilson et al., "Contrast-enhanced ultrasound (CEUS) liver imaging reporting and data system (LI-RADS) 2017-a review of important differences compared to the CT/MRI system," *Clinical and Molecular Hepatology*, vol. 23, no. 4, pp. 280–289, 2017.

[9] J. Luo, J. D. Chen, Q. Chen et al., "Contrast-enhanced ultrasound improved performance of breast imaging reporting and data system evaluation of critical breast lesions," *World Journal of Radiology*, vol. 8, no. 6, pp. 610–617, 2016.

[10] A. Giorgio, L. Montesarchio, P. Gatti et al., "Contrast-enhanced ultrasound: a simple and effective tool in defining a rapid diagnostic work-up for small nodules detected in cirrhotic patients during surveillance," *Journal of Gastrointestinal and Liver Diseases*, vol. 25, no. 2, pp. 205–211, 2016.

[11] S. C. Tenant and C. M. Gutteridge, "The clinical use of contrast-enhanced ultrasound in the kidney," *Ultrasound*, vol. 24, no. 2, pp. 94–103, 2016.

[12] L. L. Zhou, L. Fan, and Y. Liu, "Contrast-Enhanced Ultrasound for differential diagnosis of pancreatic mass lesions: a meta-analysis," *Medical Ultrasonography*, vol. 18, no. 2, pp. 163–169, 2016.

[13] C. Lowe, A. Abbas, and S. Rogers, "Three-dimensional contrast-enhanced ultrasound improves endoleak detection and classification after endovascular aneurysm repair," *Journal of Vascular Surgery*, vol. 65, no. 5, pp. 1453–1459, 2016.

[14] Y. Zhang, L. Sun, H. Song, and X. Cao, "Ubiquitous WSN for healthcare: recent advances and future prospects," *IEEE Internet of Things Journal*, vol. 1, no. 4, pp. 311–318, 2014.

[15] Y. Wang, F. Yang, J. Zhang, H. Wang, X. Yue, and S. Liu, "Application of artificial intelligence based on deep learning in breast cancer screening and imaging diagnosis," *Neural Computing & Applications*, vol. 33, no. 15, pp. 9637–9647, 2021.

[16] V. Kumar, "Evaluation of computationally intelligent techniques for breast cancer diagnosis," *Neural Computing & Applications*, vol. 33, no. 8, pp. 3195–3208, 2021.

[17] D. Hunt and J. Romero, "Contrast-enhanced ultrasound," *Magnetic Resonance Imaging Clinics of North America*, vol. 25, no. 4, pp. 725–736, 2017.

[18] M. R. Kramer, N. Bhagat, and J. B. Susan, "Influence of contrast-enhanced ultrasound administration setups on microbubble enhancement: a focus on pediatric applications," *Pediatric Radiology*, vol. 48, no. 1, pp. 1–8, 2017.

[19] S. L. W. Denham, L. F. Alexander, and M. L. Robbin, "Contrast-enhanced ultrasound: practical review for the assessment of hepatic and renal lesions," *Ultrasound Quarterly*, vol. 32, no. 2, pp. 116–125, 2016.

[20] M. Garbajs and P. Popovic, "Contrast-enhanced ultrasound for assessment of therapeutic response after percutaneous radiofrequency ablation of small renal tumors," *Journal of B.u.on. Official Journal of the Balkan Union of Oncology*, vol. 21, no. 3, pp. 685–690, 2016.

[21] J. Ye, X. Xie, Y. Lin et al., "Imaging features of combined hepatocellular-cholangiocarcinoma on contrast-enhanced

Hindawi
Journal of Healthcare Engineering
Volume 2023, Article ID 9809423, 1 page
https://doi.org/10.1155/2023/9809423

Retraction

Retracted: Exercise Rehabilitation Improves Heart Function and Quality of Life in Elderly Patients with Chronic Heart Failure

Journal of Healthcare Engineering

Received 10 October 2023; Accepted 10 October 2023; Published 11 October 2023

This article has been retracted by Hindawi following an investigation undertaken by the publisher [1]. This investigation has uncovered evidence of one or more of the following indicators of systematic manipulation of the publication process:

(1) Discrepancies in scope
(2) Discrepancies in the description of the research reported
(3) Discrepancies between the availability of data and the research described
(4) Inappropriate citations
(5) Incoherent, meaningless and/or irrelevant content included in the article
(6) Peer-review manipulation

The presence of these indicators undermines our confidence in the integrity of the article's content and we cannot, therefore, vouch for its reliability. Please note that this notice is intended solely to alert readers that the content of this article is unreliable. We have not investigated whether authors were aware of or involved in the systematic manipulation of the publication process.

In addition, our investigation has also shown that one or more of the following human-subject reporting requirements has not been met in this article: ethical approval by an Institutional Review Board (IRB) committee or equivalent, patient/participant consent to participate, and/or agreement to publish patient/participant details (where relevant).

Wiley and Hindawi regrets that the usual quality checks did not identify these issues before publication and have since put additional measures in place to safeguard research integrity.

We wish to credit our own Research Integrity and Research Publishing teams and anonymous and named external researchers and research integrity experts for contributing to this investigation.

The corresponding author, as the representative of all authors, has been given the opportunity to register their agreement or disagreement to this retraction. We have kept a record of any response received.

References

[1] X. Peng and L. Tang, "Exercise Rehabilitation Improves Heart Function and Quality of Life in Elderly Patients with Chronic Heart Failure," *Journal of Healthcare Engineering*, vol. 2022, Article ID 8547906, 12 pages, 2022.

Hindawi
Journal of Healthcare Engineering
Volume 2022, Article ID 8547906, 12 pages
https://doi.org/10.1155/2022/8547906

Research Article

Exercise Rehabilitation Improves Heart Function and Quality of Life in Elderly Patients with Chronic Heart Failure

Xingyun Peng[1] and Liuquan Tang[2]

[1]*School of Smart Healthcare Industry, Chongqing City Management College, Shapingba 401331, Chongqing, China*
[2]*The Department of Basic Education, Chongqing City Vocational College, Yongchuan 402160, Chongqing, China*

Correspondence should be addressed to Liuquan Tang; tangliuquan123@163.com

Received 7 October 2021; Accepted 22 November 2021; Published 12 January 2022

Academic Editor: Alireza Souri

With the acceleration of the aging process, there are more and more elderly patients with chronic heart failure. Chronic heart failure has severely affected the heart function and quality of life of the elderly. This article aims to study the further improvement of the heart function and the quality of life of elderly patients with chronic heart failure through exercise rehabilitation. In this paper, experimental analysis and comparative analysis are adopted, the experimental group and the control group are designed, the adaptive heart rate and breathing rate algorithm is adopted, the heart failure symptom assessment scale and the quality of life assessment tool are selected, and the two groups of different rehabilitation forms are compared. Data collection, sorting, and analysis of the patient's conditions are utilized. Through the use of exercise rehabilitation, the heart failure process will be slower and the recovery of heart strength will be faster than the control group. Before the experiment, the probability of shortness of breath in the two groups of patients with chronic heart failure symptoms was as high as 84.08%, and the symptom clusters were more serious; after the experiment, the SV and EF values after exercise rehabilitation were higher than those of the control group ($p < 0.05$). The quality of life in the realm, emotional realm, and other realms has been significantly improved. For elderly patients with chronic heart failure, reasonable exercise rehabilitation training can provide them with effective preventive measures and protective measures, improve the patients' heart function and quality of life, and play an important and key role.

1. Introduction

Chronic heart failure (CHF) is the initial myocardial infarction caused by some myocardial damage and other reasons, which leads to complex clinical symptoms. Myocardial infarction, myocardial disease, and overload of blood circulation mechanics (severe, myocarditis, etc.) can cause changes in myocardial structure and function and ultimately lead to a decrease in ventricular pump or filling function. Chronic heart failure is a disease with high morbidity and mortality. It is also the advanced stage of various cardiovascular diseases, which greatly reduces the quality of life and well-being of patients. The mortality of chronic heart failure is positively correlated with the age of the patients. In our country, as the aging of the population accelerates the process, the prevention and treatment of heart failure is an important public health issue.

Exercise rehabilitation is an effective secondary prevention measure for CHF patients. In 2013, according to the guidelines of the American College of Cardiology Foundation, rehabilitation training was recorded as an important recommendation for HR patients. Many foreign studies have shown that while reducing treatment costs, restarting exercise can effectively reduce the prevalence and mortality of heart failure, thereby improving the exercise resistance and quality of life of HR patients. In recent years, HR sports rehabilitation has developed in our country, but many medical staff still lack understanding of it. HR patients and their families cannot effectively use sports training for self-management and support. This article will observe the sports

rehabilitation of HR patients, provide a basis for the sports rehabilitation of HR patients, and promote the development of cardiac rehabilitation training in China.

Ba proposed a deep learning system for sports injury medical rehabilitation based on MRI image analysis. Warm-up activities refer to a variety of physical exercises purposefully carried out before sports, training, and competitions in order to maximize physical activity and prevent injury preparations. Therefore, how to use MRI images for numerical analysis of the above tasks is very necessary. Combined with the deep learning model, a new image enhancement recognition model is proposed to undertake medical tasks. However, the medical rehabilitation cycle for sports injuries is long, and there are too many uncontrollable factors, which cannot guarantee the medical rehabilitation effect [1]. Mao et al. stated that chronic heart failure (CHF) is a clinical syndrome caused by a variety of cardiovascular diseases (CVDs), which is increasingly becoming the main cause of global morbidity and mortality. They have previously proved that a 4-day forest bathing trip can provide adjuvant treatment effects for CHF patients. In order to further study the duration of the effects of CHF patients and the optimal frequency of forest bathing, we recruited subjects who experienced forest bathing again after 4 weeks and randomly divided them into two groups, namely, the urban control group (city) and the forest bathing group (forest). After the second 4-day forest bathing trip, they observed that the levels of brain natriuretic peptide, a biomarker of heart failure, continued to decrease, and the inflammation and oxidative stress were weakened. Therefore, this exploratory study proves the additional benefits of two forest baths for elderly CHF patients, which will further pave the way for the analysis of the impact of such interventions on cardiovascular disease. However, their experimental subjects are relatively narrow, and the experimental results are not very representative [2]. Yu et al. investigated the characteristics of clinical treatment drugs for elderly chronic heart failure (CHF) with various degrees of renal failure. Elderly CHF patients who received treatment from October (2010) to October (2015) were selected, and retrospective case collection was used. The revised equation of diet therapy for kidney disease (MDRD) was used to study the spiral filtration rate. Patients were divided into normal renal function group, mild renal function group, and moderate to severe renal function group. The statistical analysis of the three groups of characteristic drugs was compared. Compared with the results of the normal renal function group and the mildly decreased group, the difference between the normal renal function group and the mildly decreased group was significant ($p < 0.05$). The use of ACEI and beta blockers from moderate to severely reduced groups is very small. Diuretics and spironolactone were used ($p < 0.05$). Compared with the normal renal function group, the use rate of ACEIs is low, and the use rate of diuretics is low. However, their experimental method has limitations and there are many restrictive factors [3].

The innovations of this article are as follows: (1) the adaptive heart rate and respiration rate algorithm is used to observe the patient's heart function data at any time during the exercise rehabilitation process to strengthen the monitoring of the patient's health; (2) theoretical analysis and empirical analysis are comparable. Theoretically combine the advantages of sports rehabilitation with the data of the research experiments in this article, and demonstrate the effects of sports rehabilitation.

2. Research Methods for Exercise Rehabilitation to Improve Heart Function and Quality of Life in Elderly Patients with Chronic Heart Failure

2.1. Chronic Heart Failure in the Elderly. Chronic heart failure (CHF) is a clinical syndrome caused by various heart abnormalities and dysfunctions caused by abdominal filling. This is the final stage formed by various heart diseases such as hypertension, valvular heart disease, and pulmonary heart disease [4]. According to the latest data, the incidence of heart failure in developed countries is 1.5%~2.0%, and the incidence of people over 70 years old is 10%. A random sampling of urban and rural residents aged 35–74 in my country shows that the morbidity rate of heart failure is 0.9%, and the older the age, the higher the prevalence rate [5, 6]. The 3-year survival rate is only 44%, and the 5-year survival rate is equivalent to malignant tumors. At present, there are about 4 to 5 million patients with heart failure in our country, which has brought a huge economic burden to the society [7, 8]. Therefore, the symptom management of elderly patients with chronic heart failure has attracted the attention of medical staff.

Almost all CHF patients exhibit 2–9 symptoms at the same time during their illness, such as dyspnea, fatigue, edema, and other characteristic symptoms of heart failure [9, 10]. Pain, drowsiness, sadness and tension, loss of appetite, and other symptoms are related to underlying diseases, and psychological related symptoms such as restlessness and depression. These symptoms do not appear alone in the onset of the disease, but a variety of symptoms will appear at the same time, indicating the "symptoms" of the "complex" phenomenon of interaction [11, 12].

Regarding the treatment of the symptoms of heart failure patients, before the 1970s, CHF patients were considered necessary to restrict physical activity accompanied by exercise recovery and pain. However, prolonged rest may cause skeletal muscle atrophy, venous thrombosis, pulmonary embolism, pressure ulcers, reduced exercise tolerance, worsening symptoms, etc. [13, 14]. By 1979, studies pointed out that exercise rehabilitation was safe for CHF patients, and it was possible to improve the exercise resistance of CHF patients. In order to restore the motor function of CHF patients, many studies have been conducted overseas, and its effectiveness and safety have been confirmed to various degrees in China [15, 16]. In 2005, the European Society of Cardiology recommended exercise as an important part of cardiac rehabilitation training to stabilize patients with heart failure, as an effective secondary preventive measure. In the American College of Cardiology 2013 (ACCF)/AHA Heart

Failure Management Guidelines, IA lists exercise rehabilitation training for heart failure recommended by patients with chronic heart failure [17, 18].

2.2. Sports Rehabilitation. Cardiac rehabilitation exercise refers to the use of various forms of exercise to improve cardiovascular and physiological functions, prevent or delay the onset of diseases, achieve the purpose of rehabilitation, reduce the risk of vascular events, and enable patients to obtain better functional status [19, 20]. Research and analysis believe that exercise recovery can improve vascular endothelial function, increase the strength of skeletal muscles, lower blood pressure, strengthen sympathetic nerves, improve exercise resistance, and increase skeletal creatinase activity [21, 22]. Possible effects include improvement in left ventricular excitation rate (LVEF) and final volume of left ventricular dilation, increase in heart rate, decrease in plasma neurohormonal levels, and changes in histological characteristics of skeletal muscle.

At present, there is insufficient demand for clinical rehabilitation training in sports activities in my country. Sports rehabilitation training is not recognized and evaluated by almost all hospitals and medical staff. Only a few hospitals and regions have developed sports rehabilitation [23, 24]. CHF patients have not yet received standard sports rehabilitation training instructions. The continuity and coordination of sports rehabilitation are is not strong, and many hospitals have increased the burden on patients, medical care, and social economy [25]. This article aims to provide beneficial clinical rehabilitation exercises for more heart failure patients with complex causes, multiple diseases, and low exercise capacity for elderly CHF patients and to explore effective forms of CHF exercise recovery to improve physical health. Provide theoretical support for the training effect of sports rehabilitation.

2.3. Quality of Life. Quality of life (QOL) is also called living conditions, including economic conditions, religious beliefs, emotions, physiology, psychology and society. Quality of life is a complex and multidimensional concept. There is no unified definition at present. It is divided into two research fields: health and nonhealth. Generally, it includes three aspects: happiness, subjective health, and the meaning of life.

Health-Related Quality of Life (HRQOL) is a subjective feeling. Compared with quality of life, the scope only relates to the health field, which specifically reflects the difference between the patient's actual functional status of the body and its expected functional status perception. Wenger believes that HRQOL has a multidimensional structure, which refers to the patient's subjective perception of the impact of physiological symptoms, health perception, and functional status on daily life. Physiological symptoms refer to disease-related symptoms and their effects on functional status and health perception; health perception is closely related to mortality and is similar to life satisfaction and happiness; functional status integrates self-care activities, interpersonal fields, social support, sleep, mental function, coping, and emotions.

The factors affecting the quality of life of patients with chronic heart failure are divided into four aspects: demographic sociological factors, disease-related factors, psychosocial factors, and other factors. (1) Demographic sociological factors research shows that the demographic sociological characteristics of patients with chronic heart failure, such as age, gender, personality traits, and marital status, are important factors affecting the quality of life. (2) Research on disease-related factors shows that the disease-related characteristics of patients with chronic heart failure, such as heart rate, heart failure type, cardiac function classification, ejection fraction, blood B-type Brain Natriuretic Peptide (BNP), symptoms, and comorbidities are important factors affecting the quality of life. The independent predictors of quality of life are gender, age, body mass index, systolic blood pressure, cardiac function classification, symptom burden, functional status, and use of Angiotensin-Converting Enzyme Inhibitors (ACEI) drugs. The functional status of elderly patients with chronic heart failure is poor, but their quality of life is better than that of young patients with low ejection fraction. The degree of damage to the quality of life is not related to ejection fraction. The relationship between quality of life and ejection fraction reflects the complexity of the development of symptoms in the process of chronic heart failure, suggesting that the understanding of symptoms needs to go beyond traditional pathophysiological models. (3) Psychosocial factors research shows that the psychosocial factors of patients with chronic heart failure, such as psychological distress, mental status, self-efficacy, social support, coping style, are closely related to the quality of life. (4) Other factors: studies have found that the self-management, disease knowledge, functional status, rehabilitation exercise, and other conditions of patients with chronic heart failure are related to the patient's quality of life.

2.4. Adaptive Heart Rate and Breathing Rate Algorithm

2.4.1. Bayesian Principle. Bayes' theorem refers to the theorem of conditional or critical probability of random events A and B. Its conditional probability is expressed by

$$P(AB) = P(A)P(B \mid A) = P(B)P(A \mid B). \tag{1}$$

In the formula, $P(A \mid B)$ refers to the probability of occurrence of A under the condition that B occurs, and $P(B \mid A)$ is the probability of occurrence of B under the condition of occurrence of A. We can use the formula of conditional probability to derive the Bayesian formula as

$$P(B \mid A) = P(A \mid B) \cdot \frac{P(B)}{P(A)}. \tag{2}$$

In other words, $P(B \mid A)$ can be calculated by $P(A \mid B)$, $P(A)$, and $P(B)$. Suppose B is a probability space $\{B1, B2, \ldots Bn\}$ composed of mutually independent events. Then, it can be expanded in the form of full probability:

$$P(A) = P(A \mid B_1)P(B_1) + P(A \mid B_2)P(B_2) + \cdots + P(A \mid B_n)P(B_n). \tag{3}$$

Bayesian formula is represented as formula:

$$P(B_i \mid A) = \frac{P(A \mid B_i)P(B_i)}{P(A \mid B_1)P(B_1) + \cdots + P(A \mid B_n)P(B_n)}. \quad (4)$$

$P(Bi \mid A)$ is often called the posterior probability, and $P(A \mid Bn)P(Bn)$ is the prior probability. $P(Bi)$ is called the basic probability. In this algorithm, the three important estimators in the Bayesian probability fusion algorithm are adopted.

2.4.2. Adaptive Heart Rate and Breathing Rate. The adaptive process is a process of continuously approaching the target. The path it follows is represented by a mathematical model, which constructs a mathematical model of the patient's heart rate and combines the physiological characteristics of heart rate and breathing to form a signal monitoring process for analysis. In this algorithm, we will use a short window to continuously slide on the signal for iterative calculations. During each sliding process, the length of the heartbeat and breathing interval in the sliding window will be estimated, so we need to set the heartbeat and breathing separately. The expected heart rate range in this algorithm is 40–160 beats/minute; that is, the expected heartbeat interval min = 60/160 s, max = 60/40 s; the expected range of breathing is 6–40 beats/minute, which is expected. The respiratory interval min = 60/40 s, max = 60/6 s. In order to accurately detect the heartbeat and respiration, ensure that the sliding window contains at least two complete heartbeats or respirations, and the length of the sliding judgment window is at least two maximum intervals. Use j to represent the j-th sliding window, mj to represent the center of the j-th sliding window, gs to represent the sampling rate, and $x\ (m)$ to represent the signal after signal preprocessing and filtering without body movement; then, the j-th window is expressed as

$$Q_j[b] = x\left[m_j + b\right], b \in \{-\max, g_s, \cdots, \max \cdot g_s\}. \quad (5)$$

In this algorithm, we will evaluate each possible interval length of each analysis window $Qj[b]$ of the heartbeat signal and breathing signal through three estimators ($M \in \{M_{\min}, \cdots, M_{\max}\}, M_{\min} = Y_{\min} \cdot g_s, M_{\max} = Y_{\max} \cdot g_s$), and calculate the most likely Yj.

(1) Three Estimators Improve Autocorrelation. Autocorrelation is widely used in signal processing, and the similarity of signals can be detected through autocorrelation. In this algorithm, we use a mature and improved autocorrelation function to estimate the length of each possible interval of each analysis window $Qj[b]$ of the heartbeat signal and breathing signal. The autocorrelation function formula is shown in

$$T[M] = \frac{1}{M}\sum_{b=0}^{M} Q[b]Q[b-M]. \quad (6)$$

(2) Improve the Average Amplitude Difference. The traditional average amplitude difference takes the minimum value of $Q[b] - Q[b-M]$ when the signals are similar. This parameter can be used to infer the similarity of the signal. In this algorithm, we unify the value of the estimator and obtain the maximum value when the signal has high similarity, so the traditional average amplitude difference is reversed, so that it is unified with the values of other estimators and is convenient for analysis. The specific improved average amplitude difference formula is shown in

$$T_{\mathrm{MDF}}[M] = \left(\frac{1}{M}\sum_{b=0}^{M} |Q[b] - Q[b-M]|\right)^{-1}. \quad (7)$$

(3) Maximum Amplitude Pair. The maximum amplitude pair is the best representation of the amplitude information of the signal. In the successive periods before and after the signal, the amplitude sum of N corresponding to the peak of the signal and the peak is the largest, which is beneficial to the direct detection of the signal peak. Because this estimator relies on the peak amplitude information of the signal, it is susceptible to the influence of signal quality, but it can greatly improve the accuracy of signal estimation while combining the first two estimates. The calculation formula of the specific maximum amplitude pair is shown in the following formula:

$$T_{\mathrm{MAP}}[M] = \max_{b\in\{0,\cdots,M\}} (Q[b] + Q[b-M]). \quad (8)$$

In this algorithm, we will calculate three estimator values $b \in \{-Y_{\max} \cdot g_s, \cdots, Y_{\max} \cdot g_s\}$ in different interval threshold ranges $M \in \{M_{\min}, \cdots, M_{\max}\}$ for each sliding window $Qj[b]$. Calculate the most likely local signal interval length by combining the values of three different estimators at different points.

2.4.3. Estimator Fusion. The estimator through the above calculation method provides a possible value of the interval at which each M is correct. In this algorithm, we look at the output of the above three estimators (autocorrelation, average amplitude difference, and maximum amplitude pair) separately. It is formed into three Bayesian posterior probability density functions. These three probability density functions describe the probability of each estimator so that its output N is the true signal interval length. The N with the highest probability is the most common interval length:

$$M = \max_{M} p(M \mid T, T_{\mathrm{MDF}}, T_{\mathrm{MAP}}). \quad (9)$$

According to the Bayesian principle, the probability density function can be described as

$$P(M \mid T, T_{\mathrm{MDF}}, T_{\mathrm{MAP}}) = \frac{p(T, T_{\mathrm{MDF}}, T_{\mathrm{MAP}} \mid M)p(M)}{p(T, T_{\mathrm{MDF}}, T_{\mathrm{MAP}})}. \quad (10)$$

Assuming that the similarity between estimators is only related to the true interval length of the signal and not related to the output of other estimators, formula (10) can be simplified according to the Bayes principle as

$$P(M \mid T, T_{\mathrm{MDF}}, T_{\mathrm{MAP}}) \infty p(T, T_{\mathrm{MDF}}, T_{\mathrm{MAP}} \mid M)p(M). \quad (11)$$

Using Bayesian principle again, we can get

$$p(M \mid T, T_{\mathrm{MDF}}, T_{\mathrm{MAP}}) \infty p(T \mid M) p(T_{\mathrm{MDF}} \mid M) p(T_{\mathrm{MAP}} \mid M) p(M). \tag{12}$$

Ignore the fixed factors that have nothing to do with M and use Bayesian formula to get

$$p(M \mid T, T_{\mathrm{MDF}}, T_{\mathrm{MAP}}) \infty p(M \mid T) p(M \mid T_{\mathrm{MDF}}) p(M \mid T_{\mathrm{MAP}}) p(M)^{-2}. \tag{13}$$

We regard P (M) as a prior probability with uniform distribution; then, formula (13) is simplified to obtain

$$p(M \mid T, T_{\mathrm{MDF}}, T_{\mathrm{MAP}}) \infty p(M \mid T) p(M \mid T_{\mathrm{MDF}}) p(M \mid T_{\mathrm{MAP}}). \tag{14}$$

The three posterior probability density functions can be calculated by the following formula:

$$p(M \mid T) = \sum_{n=0}^{K} [T(m) - \min(T)]^{T(M) - \min(T)}. \tag{15}$$

By fusing the three estimators, the maximum probability N obtained is the maximum data length of the most likely local interval, and then it can be converted to the signal local interval time length by the following formula (13)

$$Y = \frac{M}{g_d}. \tag{16}$$

3. Exercise Rehabilitation to Improve the Heart Function and Quality of Life of Elderly Patients with Chronic Heart Failure

This article conducted a research experiment to improve the heart function and quality of life in elderly patients with chronic heart failure. The experimental group and the control group were selected for comparative experiments. The experimental group adopted exercise rehabilitation and the control group adopted traditional rehabilitation methods to compare the performance between the two groups. Changes in heart function and improvement in quality of life were noticed. This article selects heart failure symptom assessment scale and quality of life assessment tools to investigate from physical, emotional, and other fields. The experimental results show that exercise rehabilitation is beneficial to the recovery of heart function in elderly patients with chronic heart failure, and it can also improve the quality of life of patients and life happiness.

3.1. Experimental Research Objects. In this experiment, a total of 163 patients who were diagnosed and hospitalized in the Department of Cardiology, Geriatrics, and Cardiology Rehabilitation Department of Y Hospital from March (2019) to July (2019) were selected. It is divided into experimental group and control group. The experimental group takes the form of exercise rehabilitation, and the control group takes traditional rehabilitation. Through comparative experiments, the cardiac function and quality of life of the two groups of patients are studied. Table 1 shows the inclusion and exclusion criteria of experimental research objects.

The included experimental subjects of heart failure patients must be unconscious and have basic communication skills. In addition, their participation in this trial has been approved by their family members. Those with liver and kidney failure, advanced malignant tumors, and other serious diseases should be excluded. It is mainly aimed at the physiological and psychological states of these patients under different intervention periods.

3.2. Research Methods

(1) Patient general information questionnaire: This questionnaire is designed by the author to understand basic information such as age, course of disease, prevalence, gender, education level, and other basic information of patients. Among them, the symptoms of elderly patients were collected specifically during the data collection process.

(2) Heart failure symptom assessment scale: This scale selects MSAS-HF, which includes the patient's physical, psychological, and heart failure symptoms, and has more than 30 subitems for testing to understand whether the patient has heart failure, degree of heart failure, frequency of occurrence, distress, etc.

(3) Quality of life evaluation tools: The quality of life evaluation tools for patients with chronic heart failure are divided into nonspecific quality of life evaluation tools and specific quality of life evaluation tools.

3.3. Experimental Process. Both groups of patients received physical rehabilitation training on the basis of conventional drug treatment. The experimental group received sports rehabilitation, and the control group took traditional rehabilitation methods. The specific process is as follows:

Experimental group: According to the different degrees of heart failure of patients, exercise training with different intensities is designed. The training mainly includes aerobic exercise; muscle strength training; flexibility training, including walking, jogging, Tai Chi, aerobic gymnastics; and reasonable control of exercise duration; all exercises are carried out under no physical load, and exercise frequency is average exercise every other day making appropriate adjustments based on your physical condition.

Control group: Traditional rehabilitation training adopts conservative treatment methods. Exercise is not suitable, and it is best to maintain a happy mood.

The whole process of exercise is monitored by adaptive heart rate and breathing rate algorithm, and the stroke volume (SV) and left ventricular ejection fraction (EF) of all patients before and after exercise are measured. And the

Table 1: Inclusion and exclusion criteria of experimental research objects.

Standard	Detailed items
Inclusion criteria	According to the Chinese Guidelines for the Diagnosis and Treatment of Heart Failure (2014), CHF was diagnosed as CHF by a physician at or above the level of attending a cardiovascular specialist hospital, and it is in the I–IV grade according to the New York Heart Association (NYHA) heart function classification Age ≥60 years old Unconscious obstacles, with basic communication skills
Exclusion criteria	Patients after surgery such as heart transplantation or heart valve replacement People with mental illness People with cognitive impairment Accompanied by severe diseases such as liver and kidney failure, advanced malignant tumors, etc. Those who cannot understand or accurately provide relevant information

patient wear a monitoring bracelet to keep abreast of their cardiac function status and record the mood status, changes in the situation, appetite, and other related indicators every day.

3.4. Investigation Method. This experiment explained the situation of all patients, signed an informed consent form, and completed the questionnaire independently. Researchers completed and sorted out the questionnaire on the spot to ensure the validity and completeness of the questionnaire.

3.5. Statistical Analysis. The experimental data in this article are all used SPSS17.0 for data sorting and analysis. The measurement data are expressed in $x \pm s$, and some are expressed in medians. All data are valid; this article also uses multifactor analysis to analyze the impact on the quality of life of patients and heart function research.

4. Exercise Rehabilitation Improves Heart Function and Quality of Life in Elderly Patients with Chronic Heart Failure

4.1. Comparison of General Data of the Two Groups of Patients. General data and clinical data surveys were conducted on the 163 study subjects that were finally included. The results of the survey are shown in Table 2. Among them, males accounted for 53.37% and females accounted for 46.63%; the average age was (68.78 ± 8.65) years; the vast majority of the subjects had a high school or technical secondary school degree or above (61.96%); 93.25% of the subjects had a spouse; family monthly income was 98.16% of the subjects with more than 1,000 yuan; about two-thirds of the subjects with NYHA classification are at level II (66.87%); the medical payment method for the vast majority of subjects is medical insurance (98.69%). The number of study subjects over 5 years accounted for 76.06%; 89.57% of the study subjects had more than 1 comorbidity; nearly half of the study subjects were equipped with stents (47.24%); and the difference in baseline data between the two groups was not statistically significant, indicating that the two groups of studies had comparable objects.

Figure 1 shows the change process of a patient's heart failure. The leftmost is the initial symptom. With a partial infarction, after a few hours to a few days, the infarct area becomes larger, and then after a long time without treatment, the heart undergoes a global renewal (plastic). The whole process demonstrates the deepening of the disease of patients with chronic heart failure, which seriously affects the health of patients.

4.2. Symptoms of Elderly Patients with Chronic Heart Failure. It can be seen from Table 3 that the top 10 symptoms in elderly patients with chronic heart failure in descending order are shortness of breath (84.08%), leg and arm edema (75.13%), dizziness (62.18%), cough (50.74) %), palpitations (50.35%), lack of energy (44.78%), sleep awake at night (41.73%), difficulty breathing when lying down (40.34%), dry mouth (37.82%), and lack of appetite (35.83%). The median score for the severity and distress of the above symptoms is 2 to 3 points.

It can be seen from Figure 2 that the symptom group of the experimental group after exercise rehabilitation has been significantly improved. Not only the mental state has improved, but the mood is also relaxed, and it will not be so easy to feel sleepy, nervous, and sad. Compared with the control, the effect of the group after ordinary rehabilitation is much better, and the severity of the overall symptom group has been reduced. Therefore, the form of rehabilitation through exercise is conducive to the patient's mental, psychological, and physical recovery and brings the patient a good exercise, to improve the patient's quality of life.

4.3. Exercise Rehabilitation Improves Heart Function Changes in Elderly Patients with Chronic Heart Failure. We measured the ventricular systolic function of patients, and the test results are shown in Table 4. It can be seen from the table that the SV and EF values of the two groups of patients before and after rehabilitation are statistically different, and the SV and EF values of the experimental group after exercise rehabilitation are higher than those of the control group ($p < 0.05$). The difference in the original data between the two groups was not large. After the intervention of the test group, the maximum value of SV increased from 39.3 to 45.41; the maximum value of EF increased from 44.26 to 51.01. Regardless of SV or EF, the data of the control group and the experimental group have increased to a certain extent before the intervention, but it is obvious that the data

Table 2: Comparison of general data and clinical data of the experimental group and the control group.

Project	Category	Test group	Control group	t	p
Gender	Male	43	44	0.005	0.942
	Female	39	38		
Age	—	68.29	70.12	−1.638	0.064
Education level	Junior high school and below	31	32	1.403	0.496
	High school or technical secondary school	29	34		
	College degree and above	23	15		
Marital status	Married	77	74	0.085	0.772
	No spouse	5	6		
Family monthly income	< 1000	2	2	2.771	0.251
	1000–4000	68	63		
	> 4000	12	19		
Classification	II level	56	54	0.374	0.543
	III level	25	28		
Medical payment method	Public medical	18	16	0.454	0.797
	Medical insurance	59	59		
	Other	5	7		
Course of disease	1–3 year	19	22	0.256	0.613
	3–5 year	64	61		
Number of comorbidities	0	9	8	0.744	0.689
	1–3	46	52		
	3–5	27	23		
Whether it is equipped with bracket	Yes	41	36	0.717	0.392
	No	40	46		

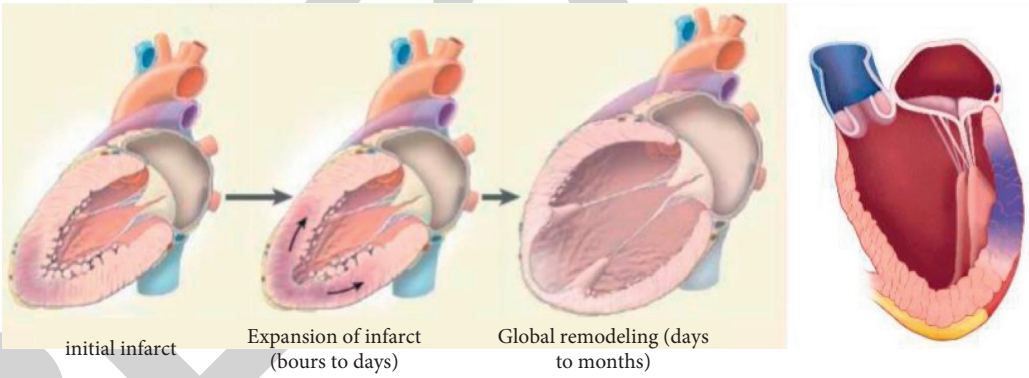

Figure 1: Heart changes in patients with chronic heart failure.

presented by the test group have greater fluctuations, indicating that the left ventricular systolic function is more. With coordination, the patient's heart rate tends to move more toward the normal range, indicating that the intervention has a significant therapeutic effect on heart rate failure.

The results of disease characteristics classification variables are shown in Figure 3. Among all chronic heart failure patients, 47.1% of patients have normal BMI, and 39.4% of patients with chronic heart failure are diagnosed for the first time. (54.0%) The heart function is the most in grade III, accounting for 57.7%, the patients with two causes are the most, accounting for 54.7%, the patients with one disease account for 40.5%, and the patients using 5-6 drugs account for 66.4%. The continuous variable data of disease characteristics showed that the average systolic blood pressure of the patients was (133.82 ± 21.42), the average diastolic blood pressure was (80.81 ± 13.68), and the average ejection fraction was (43.42 ± 9.07).

Factors affecting their quality of life mainly include changes in their physiological functions, decreased exercise endurance (due to insufficient cardiac output and insufficient oxygen), high psychological stress (anxiety, depression), cognitive impairment, individual psychological characteristics (cardiovascular patients are affected by functional recovery impact), and lack of social support (burden and pressure on family members). According to the Pearson correlation analysis between the heart function indexes (6MWT distance, LVEF, NT-proBNP) of patients with chronic heart failure and the Minnesota heart failure

Table 3: Symptoms in elderly patients with heart failure.

Sort	Symptoms	The occurrence of symptoms		Severity of symptoms	Level of distress
		n	Incidence	Median	Median
1	Shortness of breath	168	84.08	3	3
2	Edema of legs or arms	152	75.13	2	2
3	Dizziness	125	62.18	2	2
4	Cough	103	50.74	2	2
5	Palpitations	101	50.35	2	3
6	Exhausted	91	44.78	3	3
7	Sleep and wake up at night	85	41.73	3	3
8	Difficulty breathing when lying down	82	40.34	2	3
9	Dry mouth	77	37.82	2	2
10	Lack of appetite	72	35.83	2	2
11	Sweating	61	29.86	2	2
12	Chest pain	49	23.88	3	3
13	Trouble sleeping	46	23.36	3	3
14	Bloating	46	23.35	2	2
15	Nausea	28	13.42	2	0
16	Numbness in hands and feet	23	10.95	2	1.5
17	Decline in physical fitness	22	10.44	2	1
18	Hard to concentrate	18	8.45	2	2
19	Vomiting	15	6.96	2	2
20	Anxiety	15	6.96	2	2
21	Itchy skin	14	6.45	2	2

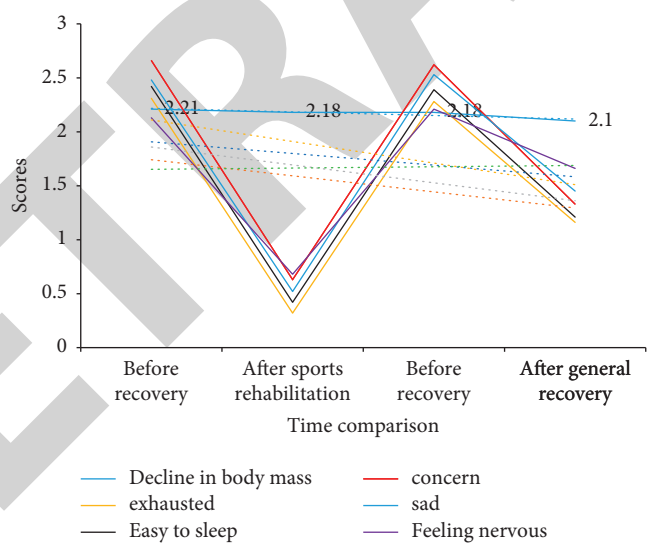

Figure 2: Comparative analysis of the symptom cluster severity scores of the experimental group and the control group.

Table 4: Comparison of changes in left ventricular systolic function before and after rehabilitation between the two groups.

Group	Number of cases	SV (ml)		EF (%)	
		Before intervention	After the intervention	Before intervention	After the intervention
Control group	58	37.25 ± 3.32	41.38 ± 1.54	40.15 ± 5.56	45.12 ± 3.58
Test group	65	37.15 ± 2.15	43.2 ± 2.21	39.78 ± 4.48	46.82 ± 4.19

quality of life scores, the results in Figure 4 show that the 6MWT distance and LVEF of elderly patients with chronic heart failure are related to the quality of life. Obviously it has negative correlation ($r = -0.494/-0.385$, $p < 0.01$); NT-proBNP is significantly positively correlated with quality of life ($r = 0.331$, $p < 0.01$).

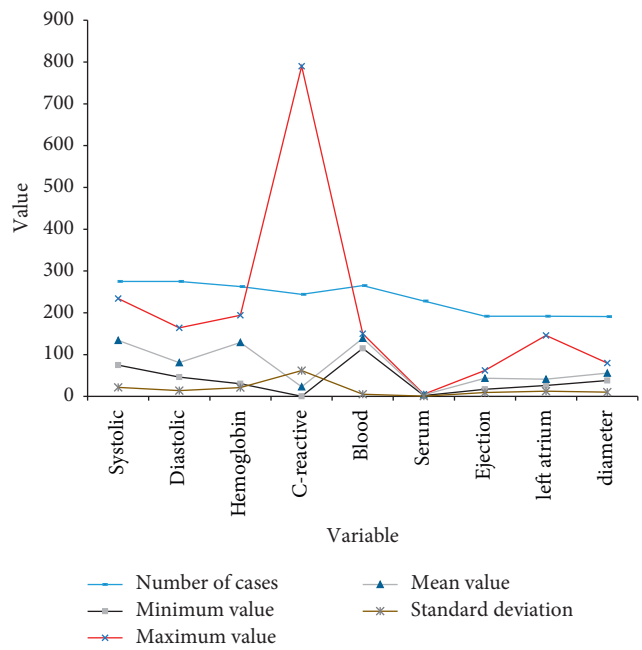

Figure 3: Results of continuous variables in the disease-related data of the research subjects.

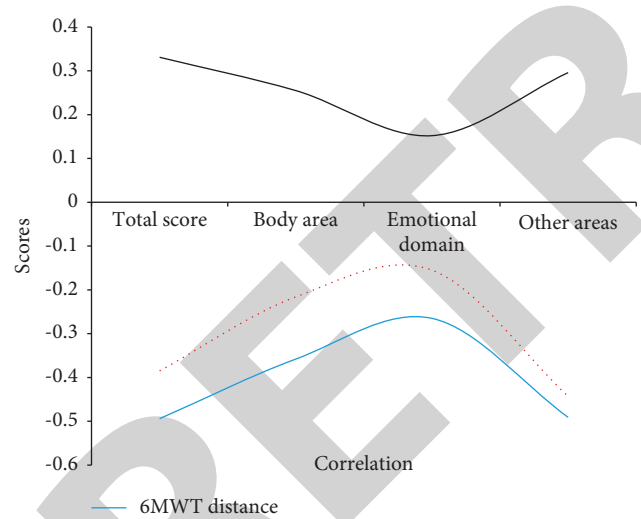

Figure 4: Correlation analysis of heart function and quality of life in elderly patients with chronic heart failure.

4.4. Exercise Rehabilitation Improves the Quality of Life of Elderly Patients with Chronic Heart Failure. In order to verify the influence of other factors on the survey results, this paper assigns a single factor and introduces a multifactor logistic regression model for analysis. The assignment results are shown in Table 5.

The step-by-step method is adopted, with 0.05 as the significance level of the introduced variable and 0.10 as the significance level of the excluded variable. This is based on the algorithm of the expected range of heartbeat and respiration. In the previous article, the multifactor analysis method was used to estimate and predict the amplitude of

Table 5: Variable setting and assignment.

Variable name	Assignment
Number of hospitalizations due to heart failure in the past year	0 = 0; 1~3 = 1; 3~5 = 2
Heart function classification	II = 0; III = 1; IV = 2
Medical payment method	Medical insurance = 0; self-pay = 1
Whether it is equipped with bracket	No = 0; Yes = 1
Anxiety/depression	0~7 = 1; 8~10 = 2; 11~21 = 3
Difficulty breathing	Yes = 1; No = 0
Edema	Yes = 1; No = 0
Complications	0 = 0; 1~3 = 1; 3~5 = 2
Heart failure quality of life score	≤30 = 0; >30 = 1

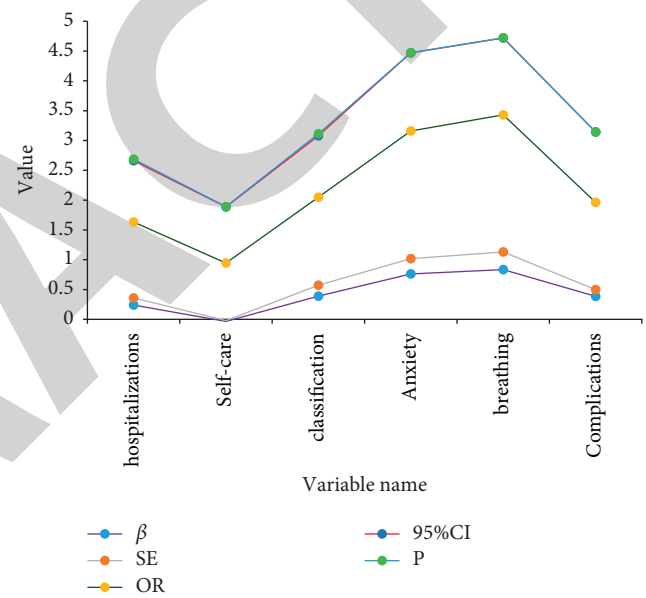

Figure 5: Logistic analysis of factors affecting the quality of life in elderly patients with chronic heart failure.

this fluctuation. Pearson correlation analysis can provide sufficient basis for it. The results in Figure 5 show that the number of hospitalizations due to heart failure, self-care ability, cardiac function classification, anxiety, dyspnea, and comorbidities in the past year are independent factors affecting the quality of life of patients with chronic heart failure. The quality of life has a greater impact.

Two-factor (group factor and time factor) repeated measures analysis of variance was used to compare the differences in the total quality of life scores between the two groups of patients. The experimental results are shown in Figure 6. Group factors include test group and control group, and time factors include 5 levels (baseline, 1 month of recovery, 3 months of recovery, 6 months of recovery, and 12 months of recovery). The results of repeated measures analysis of variance showed that there were differences in the total quality of life scores between different groups ($F = 11.48$, $p = 0.001$); there were differences in the total quality of life scores between different time points

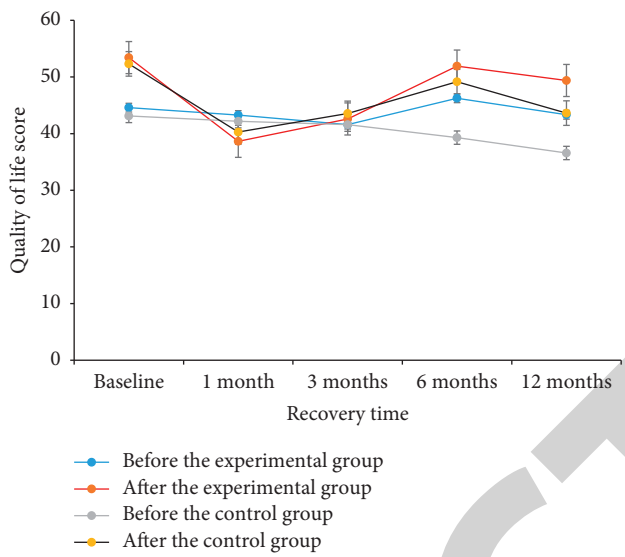

Figure 6: Comparison of the quality of life scores of the two groups of patients after different recovery time.

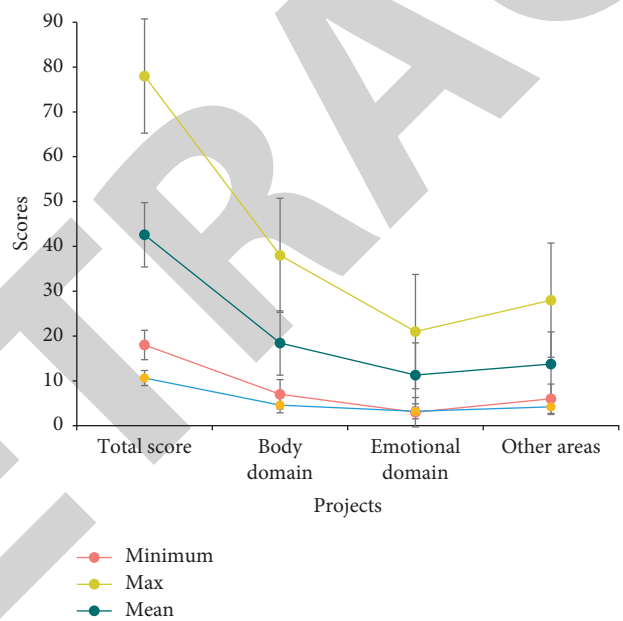

Figure 7: The quality of life scores of elderly patients with chronic heart failure in different fields.

($F = 117.78$, $p < 0.001$) and rehabilitation There is an interaction between method and time ($F = 34.68$, $p < 0.001$).

It can be seen from Figure 7 that the total quality of life of patients with chronic heart failure is (42.59 ± 10.62), the score in the physical domain is (18.45 ± 4.59), the score in the emotional domain is (10.39 ± 3.20), and the score in other domains is (13.74 ± 4.08). According to the quality of life, each dimension is equally divided; from high to low, they are the physical domain, other domains, and the emotional domain.

It can be seen from Figure 8 that according to the results of a single factor analysis of the quality of life of patients with chronic heart failure, the differences in the quality of life of patients with chronic heart failure in groups of different per capita income, first-visit heart failure, heart failure type, heart function classification, and combined different diseases are statistically significant ($p < 0.05$). The results show that different per capita income, heart failure at first diagnosis, and the number of combined diseases enter the regression equation, which can explain 14.8% of the variation in quality of life.

In order to further reveal the relationship between symptom burden, self-efficacy, social support, and quality of life, the quality of life is used as a dependent variable, with different per capita income, heart failure at first diagnosis, number of combined diseases and symptom burden, self-

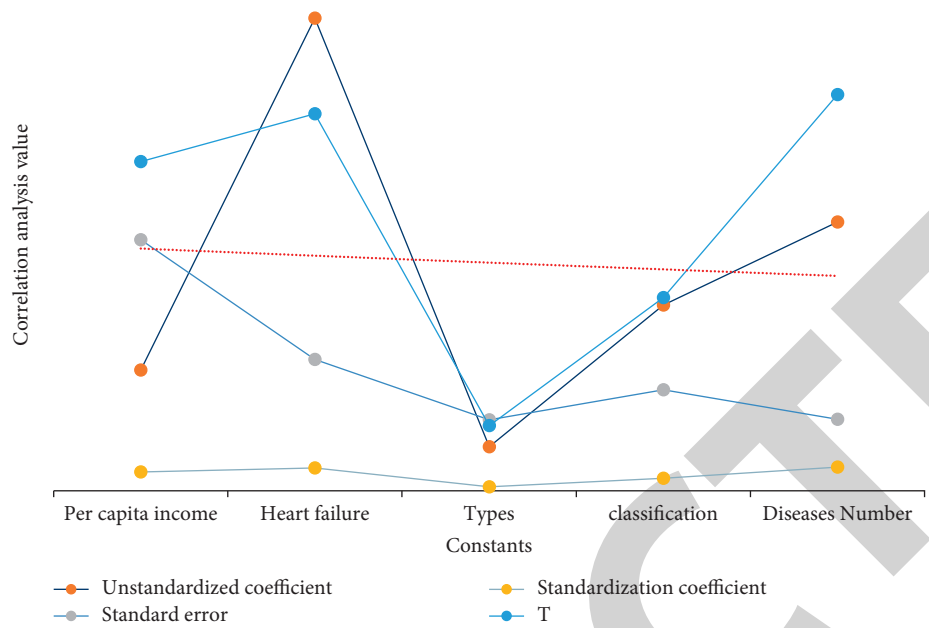

Figure 8: Multifactor analysis of quality of life in elderly patients with chronic heart failure.

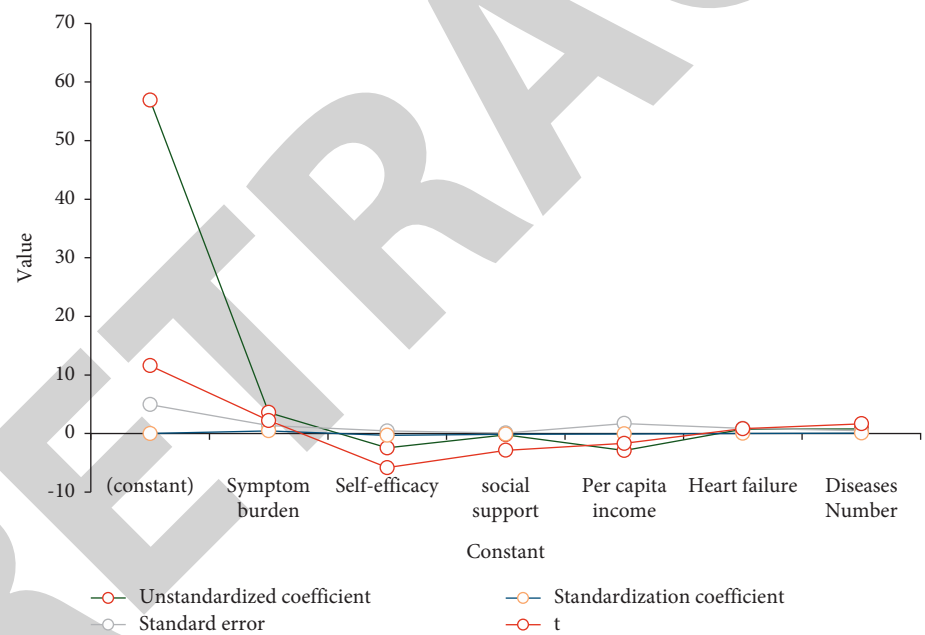

Figure 9: Regression analysis of symptom burden, self-efficacy, social support, and quality of life.

efficacy, and social support. Carry out regression analysis for the independent variables and incorporate all the independent variables into the regression equation. The results are shown in Figure 9. It can be seen from the results that symptom burden, self-efficacy, and social support can explain 59.8% of the variation in quality of life.

5. Conclusion

This article mainly focuses on the research of exercise rehabilitation to improve the heart function and quality of life of elderly patients with chronic heart failure. Through literature data method, experimental analysis method, and comparative analysis method, it shows that exercise rehabilitation can effectively improve the elderly patients with chronic heart failure. Cardiac function, self-efficacy, social support, and other aspects have been very effective, which can effectively improve the quality of life of patients. The innovation of this paper is to use adaptive heart rate and respiration rate algorithm to detect the heart function of the patient. While protecting the health of the patient, observe the changes of the patient's heart rate and other indicators to keep abreast of the patient's heart function. And this article has strong pertinence in topic selection and design, and it is